frontiers | Research Topics

Bridging gaps in neuroimaging: enhancing diagnostic precision in cerebrovascular disease

Edited by
Liang Jiang, Shuai Ren, Xindao Yin and Sonu Bhaskar

Published in
Frontiers in Neurology

ISSN 1664-8714
ISBN 978-2-8325-6824-8
DOI 10.3389/978-2-8325-6824-8

Generative AI statement
Any alternative text (Alt text) provided alongside figures in the articles in this ebook has been generated by Frontiers with the support of artificial intelligence and reasonable efforts have been made to ensure accuracy, including review by the authors wherever possible. If you identify any issues, please contact us.

About Frontiers

Frontiers is more than just an open access publisher of scholarly articles: it is a pioneering approach to the world of academia, radically improving the way scholarly research is managed. The grand vision of Frontiers is a world where all people have an equal opportunity to seek, share and generate knowledge. Frontiers provides immediate and permanent online open access to all its publications, but this alone is not enough to realize our grand goals.

Frontiers journal series

The Frontiers journal series is a multi-tier and interdisciplinary set of open-access, online journals, promising a paradigm shift from the current review, selection and dissemination processes in academic publishing. All Frontiers journals are driven by researchers for researchers; therefore, they constitute a service to the scholarly community. At the same time, the *Frontiers journal series* operates on a revolutionary invention, the tiered publishing system, initially addressing specific communities of scholars, and gradually climbing up to broader public understanding, thus serving the interests of the lay society, too.

Dedication to quality

Each Frontiers article is a landmark of the highest quality, thanks to genuinely collaborative interactions between authors and review editors, who include some of the world's best academicians. Research must be certified by peers before entering a stream of knowledge that may eventually reach the public - and shape society; therefore, Frontiers only applies the most rigorous and unbiased reviews. Frontiers revolutionizes research publishing by freely delivering the most outstanding research, evaluated with no bias from both the academic and social point of view. By applying the most advanced information technologies, Frontiers is catapulting scholarly publishing into a new generation.

What are Frontiers Research Topics?

Frontiers Research Topics are very popular trademarks of the *Frontiers journals series*: they are collections of at least ten articles, all centered on a particular subject. With their unique mix of varied contributions from Original Research to Review Articles, Frontiers Research Topics unify the most influential researchers, the latest key findings and historical advances in a hot research area.

Find out more on how to host your own Frontiers Research Topic or contribute to one as an author by contacting the Frontiers editorial office: frontiersin.org/about/contact

Bridging gaps in neuroimaging: enhancing diagnostic precision in cerebrovascular disease

Topic editors

Liang Jiang — Nanjing Medical University, China

Shuai Ren — Affiliated Hospital of Nanjing University of Chinese Medicine, China

Xindao Yin — Nanjing Medical University, China

Sonu Bhaskar — Department of Cerebrovascular Medicine and Neurology, National Cerebral and Cardiovascular Center, Japan

Citation

Jiang, L., Ren, S., Yin, X., Bhaskar, S., eds. (2025). *Bridging gaps in neuroimaging: enhancing diagnostic precision in cerebrovascular disease*.

Lausanne: Frontiers Media SA. doi: 10.3389/978-2-8325-6824-8

Table of contents

frontiers | Frontiers in Neurology

TYPE Systematic Review
PUBLISHED 02 August 2024
DOI 10.3389/fneur.2024.1447964

OPEN ACCESS

EDITED BY
Sonu M. M. Bhaskar,
National Cerebral and Cardiovascular Center, Japan

REVIEWED BY
Minho Han,
Yonsei University, Republic of Korea
Vincenzo Inchingolo,
Home for Relief of Suffering (IRCCS), Italy

*CORRESPONDENCE
Mei-Fang Pan
csyx_panmf@163.com

RECEIVED 12 June 2024
ACCEPTED 25 July 2024
PUBLISHED 02 August 2024

CITATION
Zhang D, Jiang L, Chen Y-N and Pan M-F (2024) The diagnostic value of contrast-enhanced transcranial Doppler and contrast-enhanced transthoracic echocardiography for right to left shunt in patent foramen ovale: a systematic review and meta-analysis.
Front. Neurol. 15:1447964.
doi: 10.3389/fneur.2024.1447964

The diagnostic value of contrast-enhanced transcranial Doppler and contrast-enhanced transthoracic echocardiography for right to left shunt in patent foramen ovale: a systematic review and meta-analysis

Dian Zhang, Li Jiang, Yue-Nan Chen and Mei-Fang Pan*

Department of Ultrasound, Xiangcheng People's Hospital, Suzhou, China

Purpose: To evaluate and compare the diagnostic value of contrast-enhanced transcranial Doppler (c-TCD) and contrast-enhanced transthoracic echocardiography (c-TTE) for right to left shunt (RLS) in patent foramen ovale (PFO) by meta-analysis.

Methods: The literature included in the Cochrane Library, PubMed, and Embase were searched by using "contrast-enhanced transcranial Doppler (c-TCD), contrast-enhanced transthoracic echocardiography (c-TTE), patent foramen ovale (PFO), and right to left shunt (RLS)" as the keywords from inception through April 30, 2024. The diagnostic accuracy research quality assessment tool (QUADAS-2) was used to evaluate the quality of the included literature. The combined sensitivity, specificity, positive likelihood ratio (PLR), negative likelihood ratio (NLR), and Diagnostic odds ratio (DOR) were pooled, and a comprehensive ROC curve analysis was performed. Statistical software StataSE 12.0 and Meta-Disc 1.4 were used for data analysis.

Results: A total of 8,536 articles were retrieved, and 9 articles that met all inclusion criteria were included in this meta-analysis. The meta-analysis results show that the combined sensitivity, specificity, PLR, NLR, DOR, and area under the SROC curve of c-TCD for the diagnose of PFO-RLS were 0.91 (95% CI, 0.88–0.93), 0.87 (95% CI: 0.84–0.91), 6.0 (95% CI, 2.78–12.96), 0.10 (95% CI, 0.06–0.18), 91.61 (95% CI, 26.55–316.10), and 0.9681, respectively; the corresponding values of c-TTE were 0.86 (95% CI, 0.84–0.89), 0.88 (95% CI, 0.84–0.91), 5.21 (95% CI, 2.55–10.63), 0.16 (95% CI, 0.09–0.31), 71.43 (95% CI, 22.85–223.23), and 0.9532. The ROC curve shows that c-TCD has slightly higher diagnostic value for PFO than c-TTE, but there is no significant statistical difference ($Z = 0.622$, $p > 0.05$). Deek funnel pattern showed no significant publication bias.

Conclusion: Both c-TCD and c-TTE have high diagnostic values for PFO-RLS. However, c-TCD has slightly higher sensitivity and lower specificity in diagnosing PFO-RLS compared to c-TTE.

Systematic review registration: identifier [CRD42024544169].

KEYWORDS

contrast transcranial Doppler, contrast transthoracic echocardiography, patent foramen ovale, right to left shunt, meta-analysis

1 Introduction

Patent foramen ovale (PFO) is a passage left in the atrial septum of the heart during embryonic development, with a detection rate of approximately 25–30% in adults (1). Especially in young patients with cryptogenic stroke, the incidence rate is higher. Right to left shunt (RLS) refers to the direct blood flow from the venous circulation system to the arterial circulation system through abnormal channels, without filtration through the lungs (2). PFO is currently the most common cause among RLS types, reaching 95% (3). Multiple diseases such as occult stroke, transient ischemic attack, unexplained syncope, and migraine have been confirmed to be associated with PFO-RLS (3–6). At present, the main diagnostic methods for PFO-RLS ultrasound examination were transesophageal echocardiography (TEE), contrast-enhanced transthoracic echocardiography (c-TTE), and contrast-enhanced transcranial Doppler ultrasound (c-TCD) (7). There are differences in the detection of PFO-RLS among these three examination methods. TEE with right heart contrast echocardiography can display the characteristics of the atrial septal structure, size, and shape of the foramen ovale, and is currently the gold standard for diagnosing patent foramen ovale (8). However, due to its time-consuming and invasive nature, this test is unsuitable for screening PFO. The advantages of non-invasive, easy-to-operate, and high reproducibility of c-TCD and c-TTE during use have gradually made them important methods for screening PFO-RLS (9, 10). However, there are significant differences in opinions on which of the two detection methods had a greater advantage in detecting PFO-RLS (11, 12). Therefore, this study conducted a comprehensive systematic review and meta-analysis to compare the diagnostic value of c-TCD and c-TTE for PFO-RLS, to improve the understanding of the clinical application of the two methods and provide a decision-making basis for clinical doctors.

2 Materials and methods

2.1 Search strategy

We searched PubMed, Embase, and Cochrane Library from inception through April 30, 2024. The following keywords and MeSH terms were used: ["contrast transcranial Doppler" or "c-TCD"] and ["contrast transthoracic echocardiography" or "c-TTE"] and ["patent foramen ovale" or "PFO"] and ["right to left shunt" or "RLS"]. We also performed a manual search to find other potential articles. Two investigators (DZ and LJ) searched online to obtain the original data, and the reference lists of all relevant articles were also scanned. All retrieved citations were exported to Zotero and checked for duplicates.

2.2 Inclusion and exclusion criteria

The inclusion criteria of this study were as follows:(1) Clinical cohort study or diagnostic test; (2) English research; (3) All patients were examined by c-TCD and c-TTE; (4) TEE was used as reference standards. If TEE was not the gold standard, then use TEE as a reference to calculate the appropriate parameters (5) All studies can directly or indirectly obtain original data such as true positive (TP), false positive (FP), false negative (FN), true negative values (TN). Exclusion criteria: (1) Abstracts, reviews, or case reports; (2) Repeated publication of data; (3) Incomplete original data.

2.3 Data extraction

Two evaluators (LJ and DZ) independently screened the literature according to the inclusion and exclusion criteria of the literature, and finally obtained two copies of data, and then cross-checked the data. If there were different opinions, discuss and negotiate together or ask a third party to help decide. Extract literature data from the data, including the first author, publication year, country, research type, number of cases, average age of patients, ultrasound system parameters, and echo-contrast medium. This study was conducted by the Preferred Reporting Items for Systematic Reviews and Meta-Analyses (PRISMA) guidelines (13), the protocol was registered in the PROSPERO:(CRD42024544169).

2.4 Evaluation of research quality

Use the QUADAS-2 scale in Review Manager software (RevMan, version 5.4, Cochrane IMS) to evaluate bias risk and applicability and create a bias risk and applicability assessment diagram. Risk assessment of bias comprises four areas: patient selection, index test, reference standards, and flow and timing; Applicability assessment covers three areas: patient selection, index test, and reference standards. The evaluation results for each field are evenly divided into high-risk, low-risk, and unclear.

2.5 Statistical analysis

Meta-DiSc version 1.4 (Universidad Complutense, Madrid, Spain) software was used for meta-analysis. The sensitivity (Sen), specificity (Spe), positive likelihood ratio (LR+), and negative likelihood ratio (LR-) are calculated, and the threshold effect is evaluated using the 95% confidence interval (CI). The summary receiver operating characteristic (SROC) curve and the corresponding area under the curve were determined. Quality evaluation chart and ROC curve were created using Review Manager (RevMan, version 5.4, Cochrane IMS). The heterogeneity of the diagnostic odds ratio (DOR) of each study was analyzed by Meta-Disc 1.4 software. If $I2 > 50\%$ or $p < 0.05$ among the included literature, there is a high heterogeneity between the results; $I2 < 25\%$ indicates that the heterogeneity between results is small, and $25\% \leq I2 \leq 50\%$ indicates that the heterogeneity of results is medium; $p \geq 0.05$ indicates that there is no heterogeneity in the results. If there is heterogeneity, try to explore the source of heterogeneity by using Meta-regression. The sensitivity analysis was carried out by StataSE 12 (Stata Corporation, College Station, TX). Z-test was used to compare the diagnostic value of c-TCD and c-TTE. $p < 0.05$ indicated a statistically significant difference.

3 Results

3.1 Literature research and screening results

Figure 1 shows the PRISMA flowchart we studied. After reading the title, the abstract, the full text, and the duplicate articles, 155

articles were selected. After eliminating duplicate results and abstract screening, the number of complete publications that may meet the criteria was reviewed, and finally, 9 articles were included (14–22). Other 146 articles were excluded because of non-c-TCD and c-TTE results, duplication, unrelated research, inappropriate data, review, case, conference, and non-English research.

3.2 Basic characteristics and quality assessment of the included literature

The detailed characteristics of the included study are shown in Table 1, including the name of the first author, year of publication, the age range of patients, gender distribution (male/female), design,

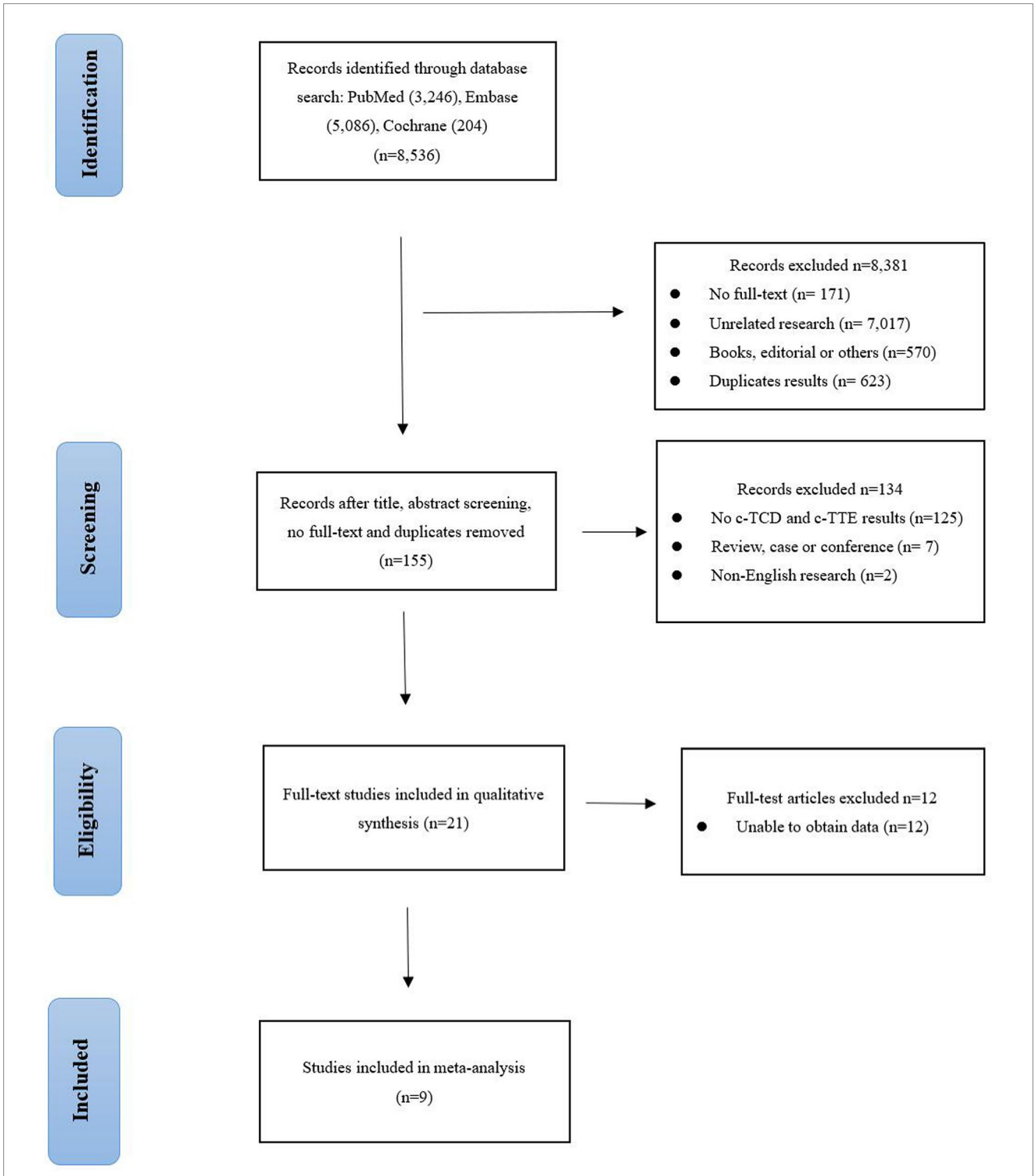

FIGURE 1
Flowchart of the study selection process.

TABLE 1 Included studies and the basic characteristics.

Author (Year)	Country	Design	Sex (M/F)	Age (mean ± SD)	PFO/ total cases (*n*)	VM position	TCD system	TTE system	Echo-contrast medium
González-Alujas T (2011) (14)	Spain	Prospective	75/59	46.4 ± 14.2	93/134	Left lateral	100 ML system and MultiDop X4	Vivid 7	saline solution and air
Maffè S (2010) (15)	United States	NA	28/47	49 ± 13	62/75	Left lateral	Philips iE33 platform	Philips iE33	saline solution and air
Souteyrand G (2005) (16)	France	NA	67/40	56	42/107	supine	SONOS 5500	SONOS 5500	saline solution and air
Zito C (2009) (17)	Italy	Prospective	33/39	49 ± 13	46/72	Supine	Prosound α-10, ALOKA echo-machine	ALOKA echo-machine	agitated saline solution mixed with urea-linked gelatine
Stendel R (2000) (18)	Germany	Prospective	47/45	51	24/92	Supine	Medasonics CDS	Ultramark 9	D-galactose microspheres and generates air-filled microbubbles
Liu *F* (2020) (19)	China	NA	86/75	42.0 ± 15.6	141/161	Left lateral	Multi-DopX4 Transcranial Doppler	GE Vivid E9 or E95 Philips EPIQ7	saline solution and air
Yang J (2020) (20)	China	NA	68/145	41 ± 12	161/213	–	–	GE or Siemens	saline solution and air
Yang X (2020) (21)	China	Prospective	40/62	41.9 ± 13	98/102	Supine	Vivid 7	Philips Epiq7c	saline, patient's blood, and room air
Lu J (2022) (22)	China	Retrospective	51/79	c-TCD group:66.32 ± 15.34 c-TTE group:68.80 ± 16.10	64/130	Supine	–	Philips iE	saline, patient's blood, and room air

VM, valsalva maneuver; PFO, patent foramen ovale; c-TCD, contrast-enhanced transcranial Doppler; c-TTE, contrast-enhanced transthoracic echocardiography; NA, Not Applicable.

sample size, echo-contrast medium, and equipment. All these articles were published from 2000 to 2022. The study was conducted in European countries ($n = 4$), China ($n = 4$), and United States ($n = 1$). The sample size is between 72 and 213. A total of 1,086 cases were included in these studies. After excluding invalid nodules, there were 355 non-PFO and 731 PFO cases, respectively. The methodological quality of the included studies based on QUADAS-2. The risk of bias and adherence of individual studies to these items. All included studies had a low risk of bias and were of high quality (Supplementary Figures S1, S2).

3.3 Threshold effects and heterogeneity

The Spearman correlation coefficients were 0.433 and 0.733 by heterogeneity analysis ($p > 0.05$), indicating that there was no threshold effect. At the same time, the results showed that heterogeneity for sensitivity (I2 = 78.6%), specificity (I2 = 90%) in the c-TCD group, and sensitivity (I2 = 93.8%), specificity (I2 = 89.1%) in the c-TTE group. The included literature has high heterogeneity, so it is necessary to use a random effect model to summarize and evaluate, and draw SROC curve.

3.4 Sensitivity analysis

To observe the stability of the synthetic results, the data included in the literature were excluded one by one and the sensitivity and specificity were summarized again. It showed that the combined effect of various indicators changed little, indicating that the stability of the included literature was good and the reliability of the results was high (Supplementary Figure S3).

3.5 Meta-regression analysis

As a result of the significant heterogeneity, meta-regression analysis was used to explore the source of heterogeneity. The covariates of the regression model are set as follows: (1) The sample size ≥100 is set as 1, and the sample size<100 is set as 0; (2) The age ≥ 50 years old is set as 0, and the age < 50 years old is set as 1; (3) The prospective study was set as 0, others study was set at 1; (4) The research object from China is set as 0, and that from other countries is set as 1. Meta-regression analysis of the c-TCD group showed that there was a significant difference between the sources of heterogeneity and age

($p = 0.03$). There was no significant difference between the sources of heterogeneity and the covariates in the c-TTE group ($p > 0.05$).

3.6 Diagnostic accuracy

A random effect model was used to analyze the combined effect quantity of the diagnostic four-grid data of c-TCD and c-TTE included in the literature. The combined sensitivity of c-TCD and c-TTE in the diagnosis of PFO-RLS was 0.91 (95% CI: 0.88–0.93) and 0.86 (95% CI: 0.84–0.89), respectively; The combined specificity was 0.87 (95% CI: 0.84–0.91) and 0.88 (95% CI: 0.84–0.91) respectively; The positive likelihood ratios were 6.0 (95% CI: 2.78 ~ 12.96) and 5.21 (95% CI: 2.55 ~ 10.63) respectively; The negative likelihood ratios were 0.10 (95% CI, 0.06 ~ 0.18) and 0.16 (95% CI, 0.09 ~ 0.31) respectively; The DOR were 91.61 (95% CI, 26.55 ~ 316.10) and 71.43 (95% CI, 22.85 ~ 223.23) respectively. The ROC curve shows that c-TCD has slightly higher diagnostic value for PFO than c-TTE. The area under the SROC curve is 0.9681 and 0.9532, respectively. However, there is no significant statistical difference ($Z = 0.622$, $p > 0.05$) (Figures 2–4).

3.7 Evaluation of publication bias and clinical applicability

The meta-analysis of the value of c-TCD and c-TTE showed no significant asymmetry ($p > 0.05$), that is, there was no significant publication bias (Supplementary Figure S4). At the same time, it can be seen from the Fagan diagram that the post-test probability of c-TCD and c-TTE is 91% respectively, which is 50% higher than the pre-test probability. The combined negative likelihood ratio of c-TCD and c-TTE in the diagnosis of PFO-RLS is more than 0.1, and the combined positive likelihood ratio is less than 10, indicating that both methods are effective in the diagnosis of PFO-RLS (Supplementary Figure S5).

4 Discussion

The foramen ovale is an important physiological channel in the embryonic atrial septum. PFO is a dynamic and open channel structure, the pressure in the right atrium is lower than that in the left atrium, and the foramen ovale valve is well-fitted to prevent shunting

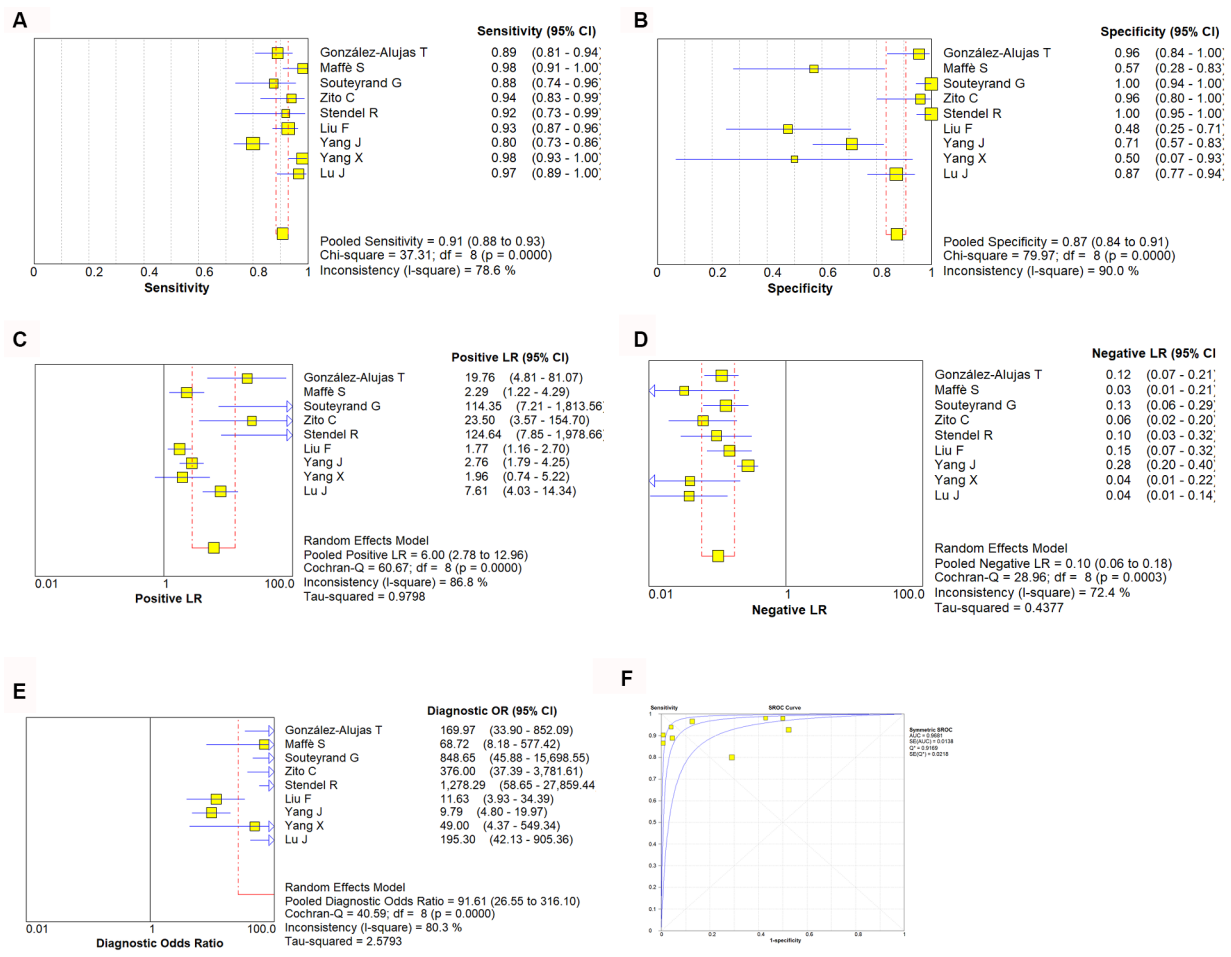

FIGURE 2
Estimates of c-TCD assessment for the diagnosis of PFO-RLS. **(A–E)** Forest plots illustrate pooled estimates (diamonds) for sensitivity **(A)**, specificity **(B)**, positive likelihood ratio (LR) **(C)**, negative LR **(D)**, and diagnostic odds ratio **(E)** and corresponding 95% CIs for pooled estimates. **(F)** Summary receiver operating characteristic (SROC) plot for assessing accuracy with corresponding curves indicative of upper and lower bounds of 95% CI. AUC, area under curve; SE, standard error; Q*, summary measure of accuracy derived from the SROC curve.

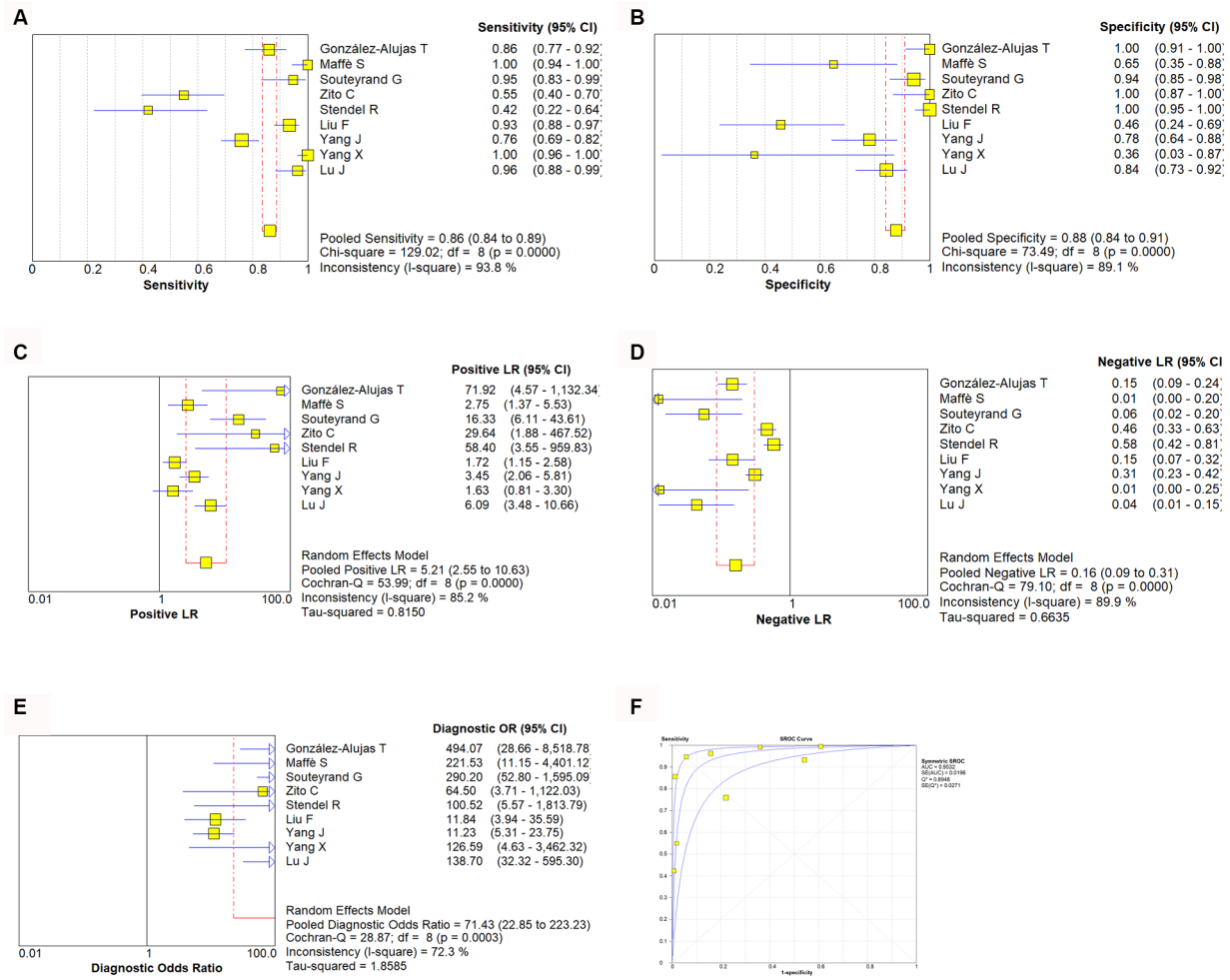

FIGURE 3
Estimates of c-TTE assessment for the diagnosis of PFO-RLS. **(A–E)** Forest plots illustrate pooled estimates (diamonds) for sensitivity **(A)**, specificity **(B)**, positive likelihood ratio (LR) **(C)**, negative LR **(D)**, and diagnostic odds ratio **(E)** and corresponding 95% CIs for pooled estimates. **(F)** Summary receiver operating characteristic (SROC) plot for assessing accuracy with corresponding curves indicative of upper and lower bounds of 95% CI. AUC, area under curve; SE, standard error; Q*, summary measure of accuracy derived from the SROC curve.

(23). When the pressure in the left and right atria changes, the foramen ovale valve cannot tightly fit, causing blood to flow between the atria. The direction of shunting depends on the pressure difference between the left and right atria. When the left atrial pressure is lower than the right atrial pressure, the PFO channel opens, and the emboli in the right heart and venous system enter the left heart and arterial system in the opposite direction (23). Research has shown that PFO is closely related to the occurrence of most cerebrovascular diseases (24–26). The reason may be that during deep breathing, severe coughing, or performing the Valsalva maneuver, the right atrial end-diastolic pressure temporarily increases, causing blood clots, air, fat, and vasoactive substances to enter the arterial circulation through the PFO-RLS from the venous circulation. According to statistics, the incidence of PFO in patients with unexplained stroke is much higher than that in the normal healthy population (27). Palazzo found that the prevalence of PFO in patients with cryptogenic stroke ranged from 44 to 66%, while the prevalence of PFO in stroke patients with common causes was only 10 to 27% (28). The detection of PFO has increasingly become a hot topic in clinical research. c-TEE, as the gold standard for diagnosing PFO and RLS, can provide anatomical support for transcatheter PFO occlusion (29, 30). However, during the examination process, patients generally feel uncomfortable and may even cause serious complications such as esophageal perforation and vocal paralysis. In addition, these discomforts can lead to poor coordination of Valsalva movements, resulting in false negatives (8). The principle of c-TCD exploration of PFO-RLS is mainly to inject a microbubble contrast agent into the elbow vein mass and detect at least one side of the middle cerebral artery through TCD to determine whether there is a microembolic signal entering the middle cerebral artery. The principle of c-TTE is to first perform transthoracic echocardiography detection, select the four-chamber view below the xiphoid process, inject microbubble contrast agent through the elbow vein mass, and observe whether microbubbles enter the left atrium. In addition, c-TTE combined with RoPE score can effectively identify high-risk PFO and the probability of related stroke (31). Due to the advantages of simplicity, non-invasive, and low cost, c-TTE and c-TCD are currently routinely performed in most hospitals, but the reliability of these tests is still controversial. Previous research showed

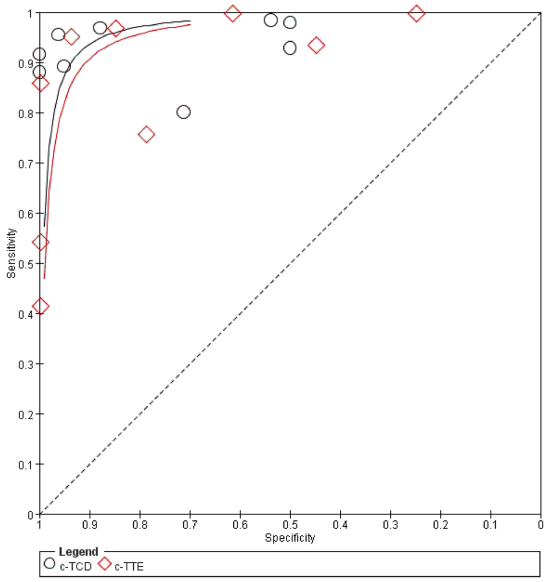

FIGURE 4
Comparison of ROC curves for the diagnostic value of c-TCD and c-TTE in PFO.

that the negative predictive value of c-TCD is greater than that of c-TTE, indicating that c-TCD excludes PFO-RLS better than c-TTE (16). However other research showed that the sensitivity of c-TCD in diagnosing PFO-RLS is lower than that of c-TTE, and the specificity is higher than that of c-TTE (14). Therefore, this study conducted a comprehensive systematic review and meta-analysis to compare the diagnostic value of c-TCD and c-TTE for PFO-RLS, to improve the understanding of the clinical application of the two methods and provide a decision-making basis for clinical doctors.

This study used the diagnostic experimental evaluation tool QUADAS-2 to evaluate the quality of the included literature. The results indicate that the overall quality of the included studies is high and the risk of bias is low. However, the heterogeneity included in the study is significant, but heterogeneity testing indicates the absence of threshold effects, and heterogeneity may be mainly caused by non-threshold effects. This may be due to the characteristics of the patients included in each study, the technical level of the operators, the type of study design, different diagnostic criteria, and different contrast agents. Meta-regression analysis shows that there is a certain relationship between the heterogeneity of c-TCD and age, and the relationship between c-TTE and covariates is not statistically significant. It is speculated that the operator's dependence on related measurements may also bring some bias. The heterogeneity of this study was not caused by threshold effects; therefore, a random model was used for summary analysis. In addition, this study is a diagnostic meta-analysis, so there is inevitably clinical heterogeneity.

This study found that the combined sensitivity of c-TCD in the diagnosis of PFO-RLS was 91%, specificity was 87%, PLR was 6.0, NLR was 0.10, DOR was 91.61, and the area under the SROC curve (AUC) was 0.9681. The sensitivity and specificity of c-TTE in diagnosing PFO-RLS were 86 and 88%, respectively. The PLR was 5.21, the NLR was 0.16, the DOR was 71.43, and the area under the SROC curve (AUC) was 0.9532. The sensitivity of c-TCD to PFO-RLS detection is higher than that of c-TTE, and the specificity is lower than that of c-TTE. The possible reasons for the analysis may be: The price of c-TCD is cheaper than that of c-TTE, which allows for examination of disabled patients at the bedside, repeated experiments in different positions, and patients are more likely to perform standard Valsalva movements to improve detection sensitivity (32, 33); c-TCD is used to detect both intracardiac and extracardiac RLS, while PFO belong to intracardiac RLS, so specificity is low; The low sensitivity of c-TTE may be due to poor detection image quality, and during Valsalva maneuver, the patient's chest wall activity is too large, which affects image acquisition and result judgment (34, 35); c-TTE can visually detect the specific conditions of the cardiac structure and surrounding tissues such as the atrial septum, identify the source of RLS, and improve specificity (17). The different techniques used by doctors during operation, the patient's physical conditions, and the characteristics of testing instruments can all affect the results. For patients with high suspicion of PFO, such as unexplained stroke, migraine, dizziness, and transient ischemic attacks, it is more necessary to consider specificity, while if only clinical screening is used, sensitivity is preferred. In practical clinical work, it is necessary to comprehensively consider the above methods to enable patients to receive more personalized diagnoses and treatment.

The SROC curve is a comprehensive indicator that directly observes the accuracy of diagnostic tests, reflecting the sensitivity and specificity of diagnostic tests and targeted diseases. The AUC value is an important indicator of testing accuracy. The closer to 1, the better the diagnostic efficiency of this diagnostic method. The meta-analysis results showed that c-TCD has slightly higher sensitivity and lower specificity in diagnosing PFO-RLS compared to c-TTE. The AUC values are both greater than 0.9, indicating that both c-TCD and c-TTE have high diagnostic values for PFO-RLS.

This study has the following limitations: (1) In order to determine which detection method is more accurate, we strictly followed the procedure of reviewing the article and selected case studies that use both detection techniques simultaneously, resulting in a relatively small number of included studies and patient cases; (2) Although continuous patient enrollment has been reported in most studies, selection bias cannot be completely ruled out when c-TCD is used as a trial to be evaluated, as there may be some patients with poor temporal window detection. The biggest limitation of c-TCD is poor temporal window detection, which makes it impossible for 10 to 15% of patients over 60 years old to undergo examination (36); (3) After undergoing Valsalva maneuver, the positive detection rate of PFO-RLS in patients increases. Therefore, the standardization of Valsalva maneuver has a significant impact on the detection results. The accuracy of the experiment is also indirectly affected by the standardization of the Valsalva test. Non-standardization of the Valsalva test will increase the false negative rate of the experiment results. The degree to which Valsalva maneuver increases right atrial end-diastolic pressure in various examinations may not be completely consistent, which may cause bias in the results (37). (4) The research language is limited to English and case–control studies, and there may be publication bias, selection bias, and language bias. (5) The heterogeneity of this study is high, therefore, subgroup analysis and sensitivity analysis were used. Although there is a certain relationship between c-TCD heterogeneity and age, more research is still needed,

with more subgroups to confirm the reasons for heterogeneity between studies. (6) The variability of different machines and differences in contrast agents may affect the presented results. Therefore, more rigorous research is needed in the future to address the methodological limitations of these issues.

In summary, c-TCD has slightly higher sensitivity and lower specificity in diagnosing PFO-RLS compared to c-TTE. Therefore, the diagnosis of PFO requires a multidisciplinary and multi-instrument approach. The high sensitivity of c-TCD in detecting RLS should be utilized, and in positive cases, c-TTE should be used to confirm whether shunting is actually due to PFO or other anatomical conditions, such as atrial defects or pulmonary arteriovenous fistulas. Both c-TCD and c-TTE have high diagnostic value for PFO-RLS and can be used as screening methods for PFO-RLS.

Data availability statement

The original contributions presented in the study are included in the article/Supplementary material, further inquiries can be directed to the corresponding author.

Author contributions

DZ: Writing – original draft, Writing – review & editing. LJ: Writing – review & editing. Y-NC: Writing – review & editing. M-FP: Writing – review & editing.

Funding

The author(s) declare that no financial support was received for the research, authorship, and/or publication of this article.

Conflict of interest

The authors declare that the research was conducted in the absence of any commercial or financial relationships that could be construed as a potential conflict of interest.

Publisher's note

Supplementary material

The Supplementary material for this article can be found online at: https://www.frontiersin.org/articles/10.3389/fneur.2024.1447964/full#supplementary-material

SUPPLEMENTARY FIGURE S1
Percentage of included studies with the risk of bias and suitability evaluation results by QUADAS-2 tool. Green bar = "low" risk, yellow bar = "unclear" risk, and red bar = "high" risk.

SUPPLEMENTARY FIGURE S2
The assessment of risk of bias for included study. Quality is represented by colors using green (+) as yes (high quality), yellow (?) as unclear, and red (−) as no (low quality).

SUPPLEMENTARY FIGURE S3
Sensitivity analysis of studies.

SUPPLEMENTARY FIGURE S4
Funnel diagram of c-TCD and c-TTE. Panel A is the funnel diagram of c-TCD; panel B is the funnel diagram of c-TTE.

SUPPLEMENTARY FIGURE S5
Fagan diagram of c-TCD and c-TTE. Panel A is Fagan diagram of c-TCD; panel B is the Fagan diagram of c-TTE.

References

1. Alakbarzade V, Keteepe-Arachi T, Karsan N, Ray R, Pereira AC. Patent foramen ovale. *Pract Neurol*. (2020) 20:225–33. doi: 10.1136/practneurol-2019-002450

2. Burkett DA. Common left-to-right shunts. *Pediatr Clin N Am*. (2020) 67:821–42. doi: 10.1016/j.pcl.2020.06.007

3. Ailani J. Migraine and patent foramen ovale. *Curr Neurol Neurosci Rep*. (2014) 14:426. doi: 10.1007/s11910-013-0426-4

4. Kanemaru K, Ueno Y, Kikuno M, Tateishi Y, Shimizu T, Kuriki A, et al. High-risk patent foramen ovale and elderly in cryptogenic stroke. *J Stroke Cerebrovasc Dis*. (2023) 32:107344. doi: 10.1016/j.jstrokecerebrovasdis.2023.107344

5. Mazzucco S, Li L, Binney L, Rothwell PMOxford Vascular Study Phenotyped Cohort. Prevalence of patent foramen ovale in cryptogenic transient ischaemic attack and non-disabling stroke at older ages: a population-based study, systematic review, and meta-analysis. *Lancet Neurol*. (2018) 17:609–17. doi: 10.1016/S1474-4422(18)30167-4

6. Zhang B, Li D, Song A, Ren Q, Cai S, Wang P, et al. Characteristics of patent foramen Ovale: analysis from a single center. *Cardiol Res Pract*. (2022) 2022:5430598–6. doi: 10.1155/2022/5430598

7. Mac Grory B, Ohman EM, Feng W, Xian Y, Yaghi S, Kamel H, et al. Advances in the management of cardioembolic stroke associated with patent foramen ovale. *BMJ*. (2022) 376:e063161. doi: 10.1136/bmj-2020-063161

8. Song JK. Pearls and pitfalls in the transesophageal echocardiographic diagnosis of patent foramen Ovale. *J Am Soc Echocardiogr*. (2023) 36:895–905.e3. doi: 10.1016/j.echo.2023.05.004

9. Filomena D, Cimino S, Maestrini V, Monosilio S, Birtolo LI, Vicenzini E, et al. The evolving role of echocardiography in the assessment of patent foramen ovale in patients with left-side thromboembolism. *Echocardiography*. (2021) 38:657–75. doi: 10.1111/echo.15018

10. Floria M, Năfureanu ED, Iov DE, Dranga M, Popa RF, Baroi LG, et al. Multimodality imaging approach of patent foramen ovale: practical considerations for transient ischemic attack/stroke. *J Clin Ultrasound*. (2022) 50:1166–76. doi: 10.1002/jcu.23325

11. Kumar P, Rusheen J, Tobis JM. A comparison of methods to determine patent foramen ovale size. *Catheter Cardiovasc Interv*. (2020) 96:E621–9. doi: 10.1002/ccd.28665

12. Chen J, Chen L, Hu W, Ni X, Zhang Z, Feng X, et al. A comparison of contrast transthoracic echocardiography and contrast transcranial Doppler in cryptogenic stroke patients with patent foramen ovale. *Brain Behav*. (2019) 9:e01283. doi: 10.1002/brb3.1283

13. Knobloch K, Yoon U, Vogt PM. Preferred reporting items for systematic reviews and meta-analyses (PRISMA) statement and publication bias. *J Craniomaxillofac Surg*. (2011) 39:91–2. doi: 10.1016/j.jcms.2010.11.001

14. González-Alujas T, Evangelista A, Santamarina E, Rubiera M, Gómez-Bosch Z, Rodríguez-Palomares JF, et al. Diagnosis and quantification of patent foramen ovale. Which is the reference technique? Simultaneous study with transcranial Doppler, transthoracic and transesophageal echocardiography. *Rev Esp Cardiol*. (2011) 64:133. doi: 10.1016/j.recesp.2010.10.009

15. Maffè S, Dellavesa P, Zenone F, Paino AM, Paffoni P, Perucca A, et al. Transthoracic second harmonic two- and three-dimensional echocardiography for detection of patent foramen ovale. *Eur J Echocardiogr*. (2010) 11:57–63. doi: 10.1093/ejechocard/jep165

16. Souteyrand G, Motreff P, Lusson JR, Rodriguez R, Geoffroy E, Dauphin C, et al. Comparison of transthoracic echocardiography using second harmonic imaging, transcranial Doppler and transesophageal echocardiography for the detection of patent foramen ovale in stroke patients. *Eur J Echocardiogr*. (2006) 7:147–54. doi: 10.1016/j.euje.2005.04.007

17. Zito C, Dattilo G, Oreto G, Di Bella G, Lamari A, Iudicello R, et al. Patent foramen ovale: comparison among diagnostic strategies in cryptogenic stroke and migraine. *Echocardiography*. (2009) 26:495–503. doi: 10.1111/j.1540-8175.2008.00852.x

18. Stendel R, Gramm HJ, Schröder K, Lober C, Brock M. Transcranial Doppler ultrasonography as a screening technique for detection of a patent foramen ovale before surgery in the sitting position. *Anesthesiology*. (2000) 93:971–5. doi: 10.1097/00000542-200010000-00016

19. Liu F, Kong Q, Zhang X, Li Y, Liang S, Han S, et al. Comparative analysis of the diagnostic value of several methods for the diagnosis of patent foramen ovale. *Echocardiography*. (2021) 38:790–7. doi: 10.1111/echo.15058

20. Yang J, Zhang H, Wang Y, Zhang S, Lan T, Zhang M, et al. The efficacy of contrast transthoracic echocardiography and contrast transcranial Doppler for the detection of patent foramen Ovale related to cryptogenic stroke. *Biomed Res Int*. (2020) 2020:1513409–6. doi: 10.1155/2020/1513409

21. Yang X, Wang H, Wei Y, Zhai N, Liu B, Li X. Diagnosis of patent foramen Ovale: the combination of contrast transcranial Doppler, contrast transthoracic echocardiography, and contrast transesophageal echocardiography. *Biomed Res Int*. (2020) 2020:8701759–7. doi: 10.1155/2020/8701759

22. Lu J, Li J, Huang H, Ye Q. Diagnostic value of Micro-bubble transcranial Doppler combined with contrast transthoracic echocardiography in cryptogenic stroke patients with patent foramen Ovale. *Neurol India*. (2022) 70:1403–6. doi: 10.4103/0028-3886.355122

23. Teshome MK, Najib K, Nwagbara CC, Akinseye OA, Ibebuogu UN. Patent foramen Ovale: a comprehensive review. *Curr Probl Cardiol*. (2020) 45:100392. doi: 10.1016/j.cpcardiol.2018.08.004

24. Desai AJ, Fuller CJ, Jesurum JT, Reisman M. Patent foramen ovale and cerebrovascular diseases. *Nat Clin Pract Cardiovasc Med*. (2006) 3:446–55. doi: 10.1038/ncpcardio0597

25. Meier B. Permeables foramen ovale (PFO) als Todesursache [patent foramen ovale with a license to kill]. *Med Klin Intensivmed Notfmed*. (2020) 115:94–100. German. doi: 10.1007/s00063-019-0561-z

26. Cho KK, Khanna S, Lo P, Cheng D, Roy D. Persistent pathology of the patent foramen ovale: a review of the literature. *Med J Aust*. (2021) 215:89–93. doi: 10.5694/mja2.51141

27. He D, Shi Q, Xu G, Hu Z, Li X, Li Q, et al. Clinical and infarction patterns of PFO-related cryptogenic strokes and a prediction model. *Ann Clin Transl Neurol*. (2018) 5:1323–37. doi: 10.1002/acn3.647

28. Palazzo P, Ingrand P, Agius P, Belhadj Chaidi R, Neau JP. Transcranial Doppler to detect right-to-left shunt in cryptogenic acute ischemic stroke. *Brain Behav*. (2019) 9:e01091. doi: 10.1002/brb3.1091

29. Hahn RT, Abraham T, Adams MS, Bruce CJ, Glas KE, Lang RM, et al. Guidelines for performing a comprehensive transesophageal echocardiographic examination: recommendations from the American Society of Echocardiography and the Society of Cardiovascular Anesthesiologists. *J Am Soc Echocardiogr*. (2013) 26:921–64. doi: 10.1016/j.echo.2013.07.009

30. Vitarelli A. Patent foramen Ovale: pivotal role of transesophageal echocardiography in the indications for closure, assessment of varying anatomies and post-procedure follow-up. *Ultrasound Med Biol*. (2019) 45:1882–95. doi: 10.1016/j.ultrasmedbio.2019.04.015

31. Arslan A, Yılmaz DÇ, Adıyaman M, Kara C, Örsçelik Ö, Yılmaz IA. Study of transesophageal echocardiography in young patients with cryptogenic stroke: prevalence of patent foramen Ovale and interpretation of the RoPE score. *Turk Kardiyol Dern Ars*. (2022) 50:314–9. doi: 10.5543/tkda.2022.21306

32. Sharma VK, Tsivgoulis G, Lao AY, Alexandrov AV. Role of transcranial Doppler ultrasonography in evaluation of patients with cerebrovascular disease. *Curr Neurol Neurosci Rep*. (2007) 7:8–20. doi: 10.1007/s11910-007-0016-4

33. Tsivgoulis G, Alexandrov AV, Sloan MA. Advances in transcranial Doppler ultrasonography. *Curr Neurol Neurosci Rep*. (2009) 9:46–54. doi: 10.1007/s11910-009-0008-7

34. Clarke NR, Timperley J, Kelion AD, Banning AP. Transthoracic echocardiography using second harmonic imaging with Valsalva manoeuvre for the detection of right to left shunts. *Eur J Echocardiogr*. (2004) 5:176–81. doi: 10.1016/S1525-2167(03)00076-3

35. Daniëls C, Weytjens C, Cosyns B, Schoors D, De Sutter J, Paelinck B, et al. Second harmonic transthoracic echocardiography: the new reference screening method for the detection of patent foramen ovale. *Eur J Echocardiogr*. (2004) 5:449–52. doi: 10.1016/j.euje.2004.04.004

36. Alexandrov AV, Babikian VL, Adams RJ, Tegeler CH, Caplan LR, Spencer MP, et al. The evolving role of transcranial doppler in stroke prevention and treatment. *J Stroke Cerebrovasc Dis*. (1998) 7:101–4. doi: 10.1016/s1052-3057(98)80135-3

37. Jauss M, Zanette E. Detection of right-to-left shunt with ultrasound contrast agent and transcranial Doppler sonography. *Cerebrovasc Dis*. (2000) 10:490–6. doi: 10.1159/000016119

frontiers | Frontiers in Neurology

TYPE Original Research
PUBLISHED 06 September 2024
DOI 10.3389/fneur.2024.1461258

OPEN ACCESS

EDITED BY
Liang Jiang,
Nanjing Medical University, China

REVIEWED BY
Xiaoquan Xu,
Nanjing Medical University, China
Ying Wang,
Second Hospital of Hebei Medical University, China

*CORRESPONDENCE
Yuehua Li
liyuehua77@sjtu.edu.cn

RECEIVED 08 July 2024
ACCEPTED 27 August 2024
PUBLISHED 06 September 2024

CITATION
Wang D, Sun Z and Li Y (2024) Horizontal analysis and longitudinal cohort study of chronic renal failure correlates and cerebral small vessel disease relationship using peak width of skeletonized mean diffusivity. *Front. Neurol.* 15:1461258. doi: 10.3389/fneur.2024.1461258

Horizontal analysis and longitudinal cohort study of chronic renal failure correlates and cerebral small vessel disease relationship using peak width of skeletonized mean diffusivity

Dan Wang, Zheng Sun and Yuehua Li*

Institute of Diagnostic and Interventional Radiology, Shanghai Sixth People's Hospital Affiliated to Shanghai Jiao Tong University School of Medicine, Shanghai, China

Background and purpose: Peak width of skeletonized mean diffusivity (PSMD) is an MRI-based biomarker that may reflect white matter lesions (WML). PSMD is based on skeletonization of MR DTI data and histogram analysis. Both chronic renal failure (CRF) and WML may be affected by multisystemic small-vessel disorder. We aimed to explore the relationship between PSMD and estimated glomerular filtration rate (eGFR).

Methods: Fifty followed-up CRF patients matched for age, sex, hypertension and smoking status were enrolled and classified into a progressive group ($n = 16$) and stable group ($n = 34$) based on eGFR levels. Longitudinal and horizontal differences of PSMD were compared between the progressive and stable groups at the initial and follow-up time points. Pearson's correlation was used for correlation of eGFR with PSMD and WML (per Fazekas scale score). ROC was used to measure the sensitivity of PSMD and WML score to changes of eGFR.

Results: At the follow-up time point, PSMD of the progressive group was significantly higher than at the initial time point ($p < 0.001$), and PSMD of the progressive group was significantly higher than stable group ($p < 0.001$). PSMD and eGFR were significantly correlated. AUC curves explored that ΔPSMD (PSMD changes at the follow-up and initial time points) and follow-up PSMD was better for the classification of progressive and stable groups.

Conclusion: PSMD has significant correlation with eGFR, PSMD can reveal a close relationship between WML and CRF.

KEYWORDS

MRI, PSMD, chronic renal failure, white matter lesion, cerebrovascular

Highlights

- PSMD is based on skeletonization of MR DTI data and histogram analysis.
- CRF and WML may be affected by multisystemic small-vessel disorder.
- To explore the relationship between PSMD and eGFR.

Introduction

Chronic renal failure is often accompanied by nervous system pathology. The earliest chronic renal failure (CRF)-associated lesion occurring in the nervous system is damage to small blood vessels including small arteries, arterioles, capillaries, and small veins (1). These vessels have poor collateral anastomoses, causing increased ischemic susceptibility to the deep white matter of the central nervous system. White matter lesion (WML) is a part of cerebral small vessel disease (CSVD) (2–5).

The correlation between CRF and WML is mainly because of similar hemodynamics, and anatomical and functional features of the kidney and brain (4). Therefore, CRF-associated pathological changes in small vessels of the kidneys may also exist in the small arteries of the brain (6).

Recently, Baykara et al. (7–9) used a new imaging marker called the peak width of skeletonized mean diffusivity (PSMD) in the brain to assess CSVD. PSMD is based on DTI, white matter tract skeletonization, and histogram analysis (7). Skeletonization focuses the analysis of mean diffusivity (MD) on the main fiber tracts, thereby largely eliminating CSF contamination (7). Whole-brain histogram analysis is particularly appropriate when dealing with diffuse diseases and when quantifying total disease burden. In some studies, PSMD appears to be robust and promising for studies on WML in large populations (8, 10, 11).

PSMD has been provided to be related to cerebral small vessel diseases, especially sensitive to small vessel-related white matter abnormalities. However, despite the common nature and high prevalence of cerebrovascular disease in patients with renal failure, the potential application of PSMD in renal failure has scarcely been investigated.

In this study, we used PSMD to explore the progression of WML in CRF based on MR diffusion images, and the relationship of cerebral WML and CRF.

Materials and methods

Participants

This retrospective analysis, conducted between December 2015 and December 2019, involved a cohort of 50 patients diagnosed with chronic renal failure (CRF) primarily caused by glomerulonephritis, hypertension, and diabetes et al., leading to chronic kidney dysfunction. The inclusion criteria were based on the clinical diagnostic guidelines outlined by the Kidney Disease Outcomes Quality Initiative (KDOQI), requiring patients to meet the criteria for stage III or IV CRF. CRF is characterized by prolonged renal damage lasting for more than 3 months, along with various causes of chronic kidney dysfunction. These causes may manifest as abnormal blood or urine components, abnormal imaging results, or a persistent decrease in estimated glomerular filtration rate (eGFR) below 60 mL/min/1.73 m^2 for more than 3 months.

The patients were followed up for a duration of 10 to 20 months. Those who exhibited a decline in eGFR greater than 10 mL/min/year or showed progression in CRF severity were classified into the progressive group (12). Conversely, patients with a decline in eGFR less than 10 mL/min were categorized into the stable group (Flow chart and data is showed in Figure 1 and Table 1).

MR examination

All participants underwent MR examinations from December 2015 to December 2019. A 3 T MR scanner (MAGNETOM Verio, Siemens Healthcare, Erlangen, Germany) with a 32-channel head coil was used. The imaging sequences included conventional MR sequences (T1- and T2-weighted image) and diffusion tensor images (DTI). Protocols were as follows: DTI was performed for six *b*-values (0, 50, 500, 1,000, 1,500, 2,000, and 2,500 s/mm^2) and 30 directions: FOV, 230 mm; TR/TE, 5100/109 ms; voxel size, $1.8 \times 1.8 \times 3\,mm^3$; slice thickness, 3 mm; and number of slices: 32, DTI sequence takes 10 min 38 s.

Processing of PSMD

PSMD calculations include skeletonization of MR DTI data and histogram analysis Baykara et al. (7–9). (1) Preprocessing algorithms: include removing non-brain tissue and eddy current correction. (2) Skeletonization of MR DTI data: FA images of participants were registered to the FMRIB 1-mm standard space. Then, the FA data of each subject was projected onto the skeleton. According to the generated mapping matrix, the MD is projected onto the skeleton. Finally, the threshold was further set to reduce the influence of CSF on the MD skeleton. (3) Histogram analysis: PSMD is calculated as the difference between the 95th and 5th percentiles of the MD skeleton histogram analysis. All steps from (1) to (3) automatic calculation processes of PSMD follows the program described by Baykara et al. (7–9)[1] (Data is showed in Figures 2–4).

Image analysis: WML Fazekas scale evaluation

One neuroradiologist with 9 years of experience was highly trained before reviewing images and recording WML locations and ratings.

A WML was defined as a signal abnormality of variable size in the white matter consisting of hyperintensity on FLAIR without cavitation and decreased signal on T1-weighted images, according to previous studies (2). Fazekas scale (0–3 points) was used as follows: grade 0 (normal), grade 1 (spot lesion), grade 2 (fusion lesion), and grade 3 (large fusion lesion) (13).

Statistics

After passing the variance equality test, paired sample *t*-tests were used to compare the longitudinal differences in WML score and PSMD within the two groups (the comparison is the difference between initial and follow-up time for the progressive group and stable group). $p < 0.05$ was statistically significant. Two-sample *t*-test of WML and PSMD was used to compare the horizontal difference between the two groups at two time points (initial and follow-up). Covariance analysis was used to remove the influence of different

Abbreviations: PSMD, Peak width of skeletonized mean diffusivity; WML, White matter lesions; CRF, Chronic renal failure; eGFR, Estimated glomerular filtration rate; CRF, Chronic renal failure.

1 http://www.psmd-marker.com

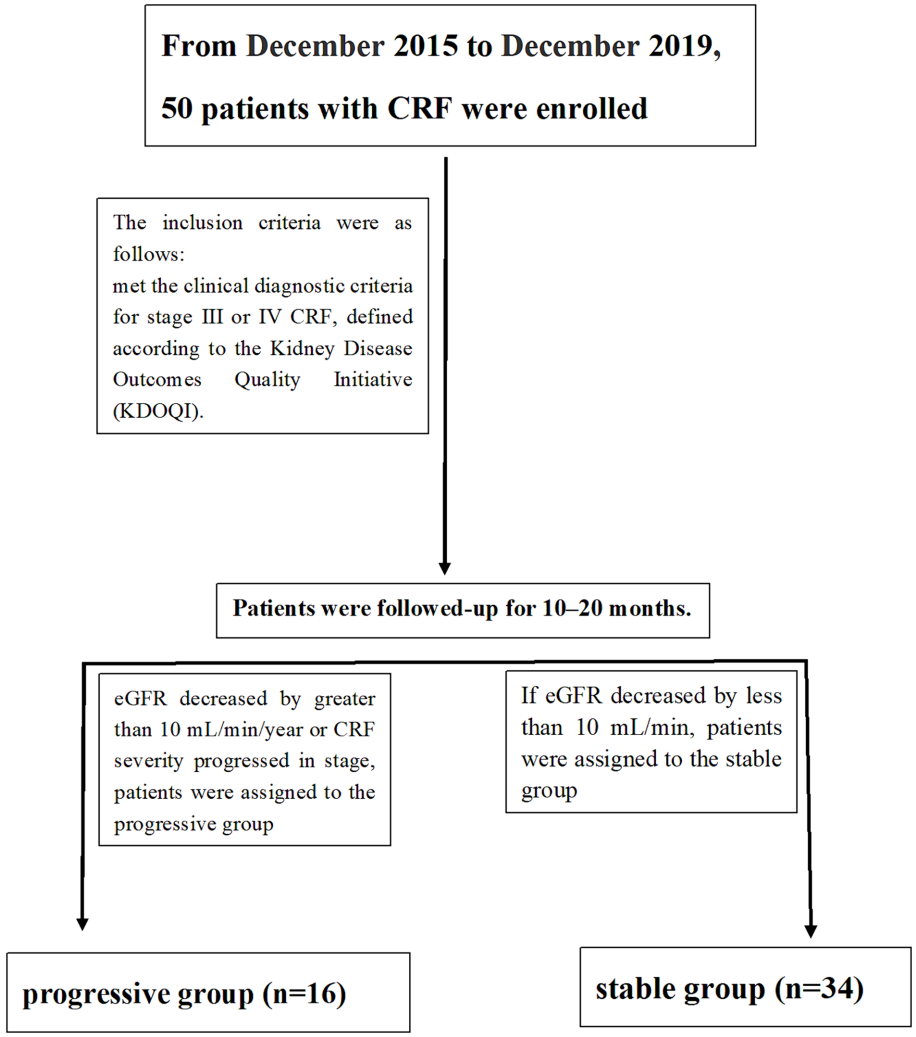

FIGURE 1
Flow chart.

follow-up time. Further, the ΔPSMD difference was also compared by covariance analysis, as was ΔWML (WML changes of follow-up and initial time point).

Pearson's correlation was used for correlation of eGFR with PSMD and WML, and Pearson's correlation was also used for correlation of ΔGFR with ΔPSMD and ΔWML.

AUC curves were plotted to explore which parameter is better for the classification of progressive group and stable group.

We conducted the statistical analysis using SPSS VERSION 27 software.

Results

Participants

In all, 50 patients with CRF were enrolled and classified into a progressive group ($n = 16$) and stable group ($n = 34$). There was no significant difference between the two groups with respect to age, sex, hypertension, diabetes, and smoking status. Covariance analysis was used to compare data between groups without the influence of follow-up time.

PSMD

Longitudinal comparison at different time points in the same group

In the progressive group, PSMD at the follow-up time point was significantly higher than PSMD at the initial time point ($p < 0.001$). There is no significant difference between two time points of the stable group ($p = 0.130$) (Data is showed in Figure 5).

Horizontal comparison between the two groups at same time points

At the follow-up time point, the PSMD of progressive group was significantly higher than the PSMD of stable group ($p < 0.001$).

TABLE 1 Clinical data for participants (progressive group and stable group).

	Progressive group	Stable group	Comparisons between two groups (*p*-value)
Number (*N*)	16	34	
Age (years)	52.35 ± 6.99	54.46 ± 8.73	
Sex (male/female)	11/5	19/15	0.39
Proportion who are smokers (y/n)	7/9	12/22	0.57
Hypertension (%)	4 (25%)	8 (23.53%)	0.91
Diabetes (type 2)	4 (25%)	9 (26.47%)	0.91
Total cholesterol (TC) (mmol/L)	4.87 + 0.93	5.29 + 0.97	0.15
Triglycerides (TG)	1.43 + 0.45	1.51 + 0.47	0.56
Fasting blood glucose (FBG)	5.41 + 0.48	5.63 + 0.45	0.13
Urine erythrocytes	2.44 + 1.46	1.65 + 1.5	0.09
Urine protein			
<0.2 g/L	$n = 0$	$n = 2$	
0.2 g to 1.0 g/L	$n = 3$	$n = 7$	
1.0 to 2.0 g/L	$n = 4$	$n = 8$	
2.0 to 4.0 g/L	$n = 3$	$n = 12$	
>4.0 g/L	$n = 6$	$n = 5$	
eGFR			
Initial eGFR	35.868 + 10.086	37.253 + 11.865	
Follow-up eGFR	23.28 + 8.10	36.95 + 11.05	
Horizontal comparisons between initial and follow up groups	*$p < 0.001$	$p = 0.807$	
Initial CKF stage			
Stage III	11	21	
Stage IV	5	13	
CKF stage at follow-up			
Stage III	3	21	
Stage IV	13	13	

*$p < 0.05$ indicated statistical significance. eGFR, estimated glomerular filtration rate; CRF, chronic renal failure.

At the initial time point, there was no significant difference between the two groups ($p = 0.629$) (Data is showed in Figure 5).

ΔPSMD (PSMD changes of follow-up time point and the initial time point)

The PSMD of the progressive group showed significantly higher increase than the stable group ($p < 0.001$).

WML

Only WMLs in the progressive group were exacerbated, there was no significant difference between the two groups at the same time point.

Longitudinal comparison at different time points in the same group

WMLs in the progressive group were exacerbated at follow-up compared to the initial exam ($p = 0.029$).

There was no significant difference between the initial time point and follow-up time point of the stable group ($p = 0.083$) (Data is showed in Figure 5 and Table 2).

Horizontal comparison between the two groups at the same time points

At two time points, there was no significant difference between the two groups either at the initial time point ($p = 0.544$) or at the follow-up time point ($p = 0.127$) (Data is showed in Figure 5 and Table 3).

ΔWML (WML changes to follow-up time point and initial time point)

ΔWML of progressive group significantly higher than stable group ($p = 0.032$).

Pearson's correlation for eGFR with PSMD and WML

Initial PSMD with initial eGFR, follow-up PSMD with follow-up eGFR, PSMD with ÄGFR all significantly correlated respectively (Pearson correlation coefficients were −0.405, −0.445, and −0.438, respectively). Follow-up WML was significantly correlated to follow-up eGFR (Pearson correlation coefficient was 0.352) (Data is showed in Table 4).

AUC curve results

The highest AUC is ΔPSMD (0.912), the second-highest AUC is follow-up PSMD (0.829) (Data is showed in Figure 6).

Discussion

This is a study about using PSMD to study the relationship between renal failure and cerebral small vessel disease. Results of this study supported the stability of PSMD as an MR biomarker for cerebrovascular disease, especially sensitive to small vessel-related white matter abnormalities. This study found out that with deterioration of renal function, as reflected by decreased eGFR, the PSMD increases more in the progressive group than the stable group. PSMD is a more sensitive biomarker than WML score. These observations suggest that PSMD increased with CRF progressed.

PSMD has been proved to be a sensitive biomarker for small vessel disease (14–19). DTI images are more sensitive than conventional MRI T1W, T2W, and FLAIR images in detecting white matter changes. Histograms of MR parameter values measured in the whole brain are increasingly being used to characterize subtle disease that affects large parts of the brain. Based of DTI, PSMD uses MD skeletonization and histogram analysis, so it is advantageous in assessing the effect of CRF of cerebral small vessel white matter lesions (1). Studies have shown that histogram peak height measures were associated with cognitive function and CSVD (20).

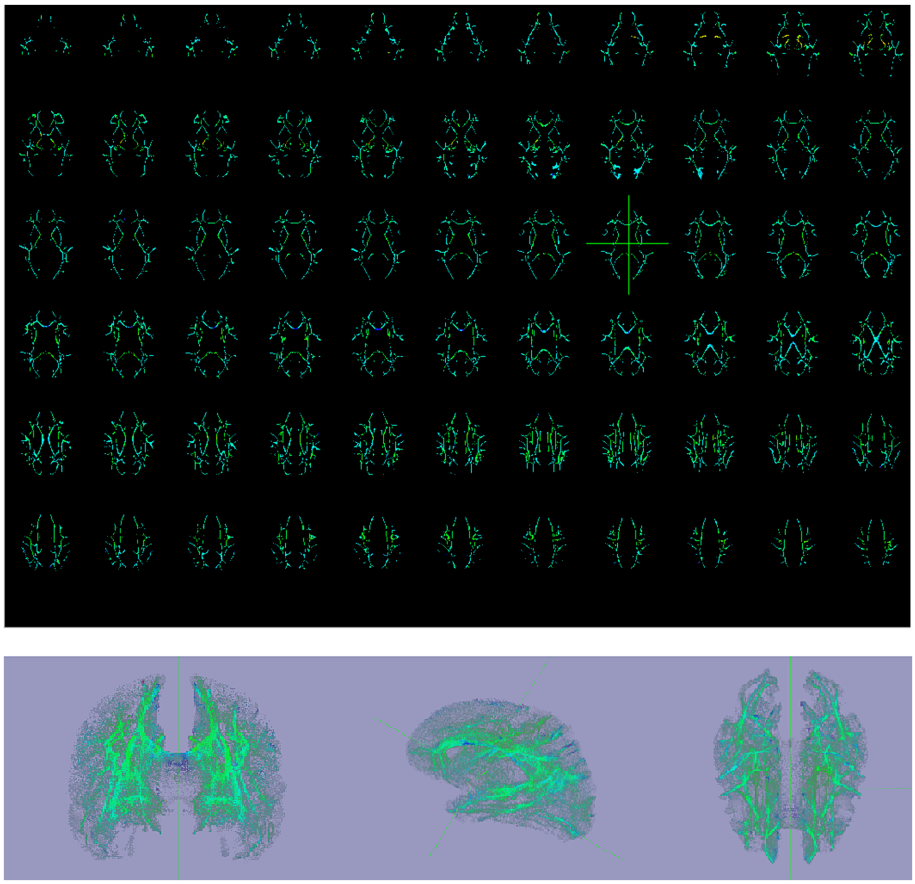

FIGURE 2
Initial MR examination, PSMD skeletonization images, and 3D PSMD skeletonization images of a 59-year-old patient in the progressive group. (1) PSMD skeletonization images were calculated, axial skeleton images of MD from top to base of the skull and 3D PSMD skeleton image. (2) 3D PSMD skeletonization images in axial, sagittal, and coronal orientations.

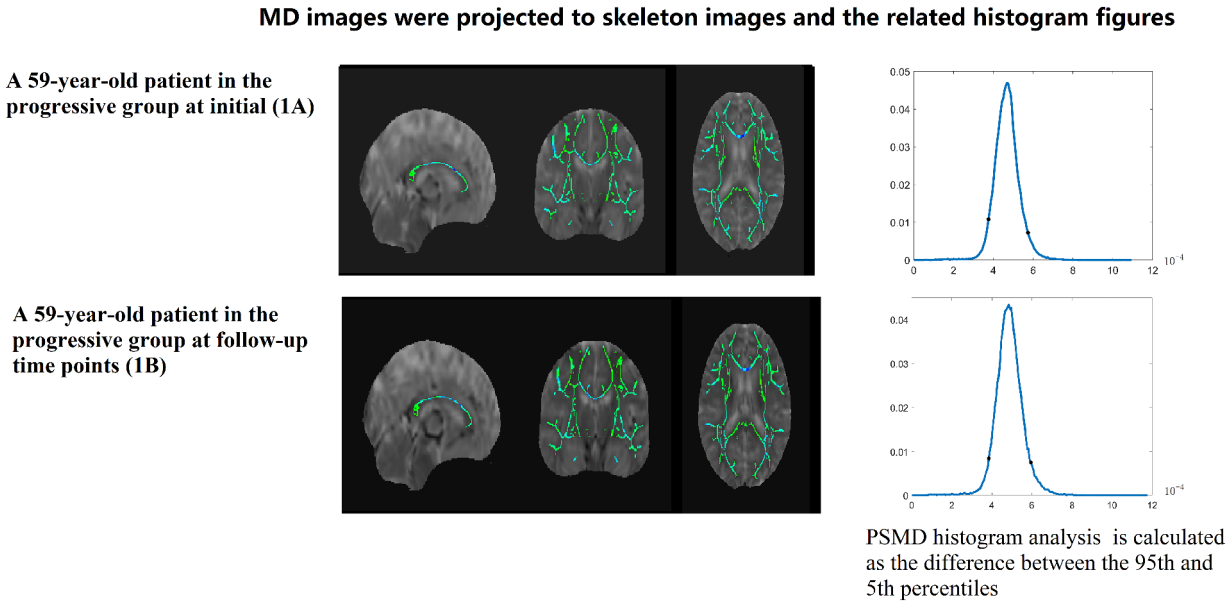

FIGURE 3
A 59-year-old patient in the progressive group at initial (1A) and follow-up time points (1B). MD images were projected to skeleton images and the related histogram figures. PSMD histogram analysis of the MD data is calculated as the difference between the 95th and 5th percentiles.

FIGURE 4
A 56-year-old patient in the stable group at initial (2A) and follow-up (2B) time points. MD images were projected to skeleton images and the related histogram figures. PSMD histogram analysis of the MD data is calculated as the difference between the 95th and 5th percentiles.

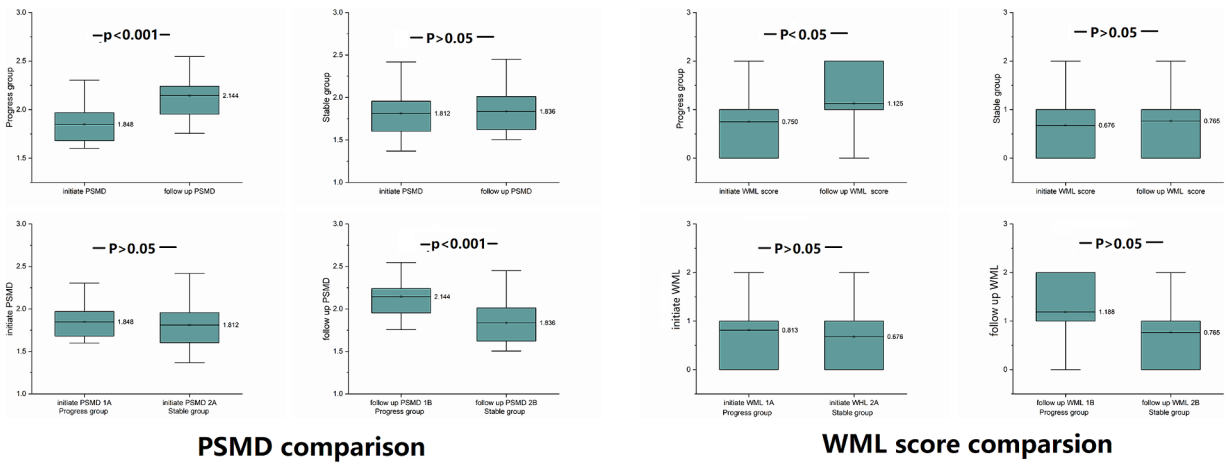

FIGURE 5
PSMD and WML differences were compared between the progressive and stable groups at the same time point, and comparison within groups at the initial and follow-up time points: at the follow-up time point, PSMD of the progressive group was significantly higher than at the initial time point ($p < 0.001$), and PSMD of the progressive group was significantly higher than that of the stable group ($p < 0.001$).

Chronic renal failure and PSMD and white matter lesions

Kidney hemodynamics are similar to that of brain, as both of their vascular beds have very low resistance and are sensitive to fluctuations in blood pressure. Moreover, it is widely accepted that chronic renal insufficiency is an independent risk factor for cerebrovascular disease (4, 21).

In this study, PSMD results support previous studies that PSMD is sensitive to small vessel-related white matter abnormalities (9). PSMD showed higher AUC than WML Fazekas scale scores, indicating that PSMD is a more sensitive MR biomarker to detect white matter lesion. Additionally, at the follow-up time point, PSMD detected worse white matter lesion in the progressive than stable group. eGFR is a reliable indicator of renal function, and is commonly used clinically to assess and monitor kidney function.

Relationship of PSMD and renal function

The results of the this study are consistent with these conclusions, specifically that declining renal function, the greater the degree of white matter degeneration, the higher the PSMD value (4, 20, 21).

TABLE 2 Intra-group longitudinal comparison of PSMD, WML Fazekas scores and eGFR and at initial and after follow-up time points: [progressive group at initial exam (group 1A), progressive group at follow-up (group 1B), stable group at initial exam (group 2A), stable group at follow-up (group 2B)].

	Number	eGFR		ΔeGFR		PSMD		ΔPSMD		WML Fazekas scores		ΔWML Fazekas scores	
		Mean	SD	Mean	SD	Mean	SD	Mean	SD	Mean	SD	Mean	SD
Group 1A	16	35.868	10.086			1.848	0.208			0.75	0.683		
Group 1B	16	23.28	8.10	−10.092	8.948	2.144	0.223	0.296	0.22	1.125	0.719	0.25	0.577
Comparison 1A vs. 1B *p*-value		<0.001*				<0.001*				0.029			
Group 2A	34	37.253	11.865			1.812	0.259			0.676	0.768		
Group 2B	34	36.95	11.05	−0.302	7.132	1.836	0.255	0.024	0.091	0.765	0.781	0.088	0.288
Comparison 2A vs. 2B *p*-value		0.807				0.13				0.083			
Comparison group1 vs. group 2 *p*-value				<0.001*				<0.001*				0.032	

ΔPSMD (PSMD changes of follow-up time point and initial time point). *$p < 0.05$ indicated statistical significance.

TABLE 3 Horizontal comparison of PSMD, WML Fazekas scores and eGFR between the progressive group and stable groups at the same time point [progressive group at initial exam (group 1A), progressive group at follow-up (group 1B), stable group at initial exam (group 2A), stable group at follow-up (group 2B)].

	Number	eGFR		PSMD		WML Fazekas scores	
		Mean	SD	Mean	SD	Mean	SD
Group 1A	16	35.868	10.086	1.848	0.208	0.813	0.655
Group 2A	34	37.253	11.865	1.812	0.259	0.676	0.768
Comparison between group 1A vs. 2A	*t* value	0.403		0.487		0.611	
	p-value	0.689		0.629		0.544	
Group 1B	16	23.28	8.10	2.144	0.223	1.188	0.655
Group 2B	34	36.95	11.05	1.836	0.255	0.765	0.781
Comparison between group 1B vs. 2B	*F* value	19.492		16.749		2.408	
	p-value	<0.001*		<0.001*		0.127	

*$p < 0.05$ indicated statistical significance.

TABLE 4 Pearson's correlation for eGFR with PSMD and WML Fazekas scores, and Pearson's correlation for ΔeGFR with ΔPSMD and ΔWML Fazekas scores.

Correlation coefficients	Initial GFR	Initial PSMD	Initial WML Fazekas scores	Follow-up PSMD	Follow-up WML Fazekas scores	ΔWML Fazekas scores score	ΔPSMD
Initial eGFR	Pearson corr.	−0.405	−0.223				
	p-value	0.004*	0.119				
Follow-up eGFR	Pearson corr.			−0.445	−0.352		
	p-value			0.001*	0.012*		
ΔeGFR	Pearson corr.					−0.225	−0.438
	p-value					0.117	0.001*

Two-tailed test of significance was used. *Correlation is significant at the 0.05 level.

The clinical application of PSMD

CSVD is increasingly recognized as a significant contributor to vascular cognitive disorders, including mild cognitive impairment and vascular dementia. The early detection of CSVD is pivotal for initiating targeted interventions that may include pharmacological treatments, lifestyle modifications, and cognitive training. These interventions are essential for mitigating the progression of cognitive impairment.

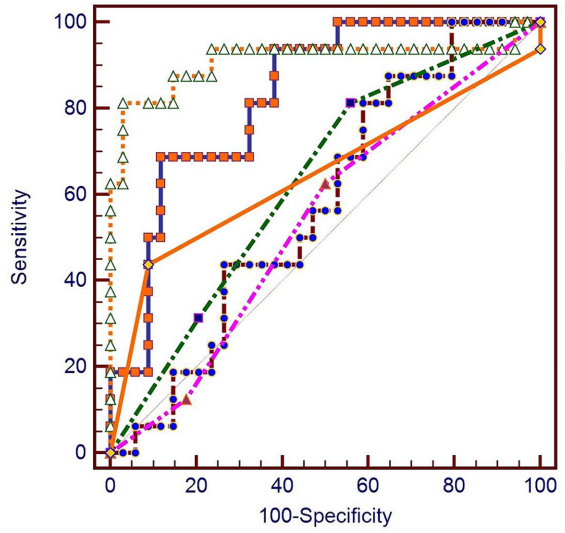

Variable	AUC	SE [a]	95% CI [b]
follow_up_PSMD	0.829	0.0586	0.696 to 0.921
initiate_PSMD	0.577	0.083	0.429 to 0.716
ΔPSMD	0.912	0.0604	0.797 to 0.973
follow_up_WML__score	0.631	0.0778	0.482 to 0.763
initiate_WML_score	0.539	0.0797	0.392 to 0.681
ΔWML__score	0.646	0.0792	0.498 to 0.776

FIGURE 6
AUC was used to measure the sensitivity of PSMD and WML score to changes in eGFR. The highest AUC was of ΔPSMD (0.912), and the second-highest AUC was of the follow-up PSMD (0.829). AUC curve showed that ΔPSMD (PSMD changes of follow-up time point and the initial time point) and follow-up PSMD were better for the classification of progressive group and stable group.

Moreover, to deepen the understanding of the linkages between CSVD and CKD and explore novel diagnostic and therapeutic modalities. Collectively, these efforts contribute to the advancement of patient care and the overall improvement of clinical outcomes in the management of CKD and CSVD.

Conclusion

This study is a first attempt to try to explore the progression of WML in CRF with PSMD. Previously, PSMD technology was rarely used to study the situation of cerebral small vessel disease in renal failure patients. This study revealed two important findings. Firstly, this study certificated that PSMD is closely related to eGFR and CRF. This study expands the understanding of the link between cerebral small vessel disease and renal failure. Secondly, there is bold speculation that when white matter lesions progress, renal function in patients with CRF may correspondingly decline. Conversely, when CRF declines, CSVD may also progress and is require more careful attention of physicians and patients. But imitated to the numbers of participants and follow-up time, these speculations require further validation in future large-sampled studies.

Data availability statement

The original contributions presented in the study are included in the article/supplementary material, further inquiries can be directed to the corresponding author.

Ethics statement

The studies involving humans were reviewed and approved by the Ethics Review Board of the Shanghai Sixth People's Hospital, affiliated with the Shanghai Jiao Tong University. The studies were conducted in accordance with the local legislation and institutional requirements. The participants provided their written informed consent to participate in this study.

Author contributions

DW: Writing – original draft, Writing – review & editing. ZS: Data curation, Writing – original draft. YL: Conceptualization, Funding acquisition, Methodology, Writing – review & editing.

Funding

The author(s) declare that financial support was received for the research, authorship, and/or publication of this article. This study was supported by the following grants: National Key R&D Program NO. 2023YFF1204800 and 2023YFF1204804; The National Natural Science Foundation of China Grant Nos. 8225024 and 1871329; the Shanghai Medical Rising Star Talent Fund; Shanghai Science and Technology Innovation Action Plan (20S31907300).

Conflict of interest

The authors declare that the research was conducted in the absence of any commercial or financial relationships that could be construed as a potential conflict of interest.

Publisher's note

References

1. Arba F, Quinn T, Hankey GJ, Ali M, Lees KR, Inzitari D, et al. Cerebral small vessel disease, medial temporal lobe atrophy and cognitive status in patients with ischaemic stroke and transient ischaemic attack. *Eur J Neurol*. (2017) 24:276–82. doi: 10.1111/ene.13191

2. Doubal FN, MacLullich AM, Ferguson KJ, Dennis MS, Wardlaw JM. Enlarged perivascular spaces on MRI are a feature of cerebral small vessel disease. *Stroke*. (2010) 41:450–4. doi: 10.1161/STROKEAHA.109.564914

3. Wardlaw JM, Smith C, Dichgans M. Small vessel disease: mechanisms and clinical implications. *Lancet Neurol*. (2019) 18:684–96. doi: 10.1016/S1474-4422(19)30079-1

4. Wardlaw JM, Smith EE, Biessels GJ, Cordonnier C, Fazekas F, Frayne R, et al. Neuroimaging standards for research into small vessel disease and its contribution to ageing and neurodegeneration. *Lancet Neurol*. (2013) 12:822–38. doi: 10.1016/S1474-4422(13)70124-8

5. Vogels SC, Emmelot-Vonk MH, Verhaar HJ, Koek HL. The association of chronic kidney disease with brain lesions on MRI or CT: a systematic review. *Maturitas*. (2012) 71:331–6. doi: 10.1016/j.maturitas.2012.01.008

6. Mogi M, Horiuchi M. Clinical interaction between brain and kidney in small vessel disease. *Cardiol Res Pract*. (2011) 2011:306189. doi: 10.4061/2011/306189

7. Baykara E, Gesierich B, Adam R, Tuladhar AM, Biesbroek JM, Koek HL, et al. A novel imaging marker for small vessel disease based on skeletonization of white matter tracts and diffusion histograms. *Ann Neurol*. (2016) 80:581–92. doi: 10.1002/ana.24758

8. Beaudet G, Tsuchida A, Petit L, Tzourio C, Caspers S, Schreiber J, et al. Age-related changes of peak width skeletonized mean diffusivity (PSMD) across the adult lifespan: a multi-cohort study. *Front Psychiatry*. (2020) 11:342. doi: 10.3389/fpsyt.2020.00342

9. Raposo N, Zanon Zotin MC, Schoemaker D, Xiong L, Fotiadis P, Charidimou A, et al. Peak width of skeletonized mean diffusivity as neuroimaging biomarker in cerebral amyloid angiopathy. *AJNR Am J Neuroradiol*. (2021) 42:875–81. doi: 10.3174/ajnr.A7042

10. Deary IJ, Ritchie SJ, Munoz Maniega S, Cox SR, Valdes Hernandez MC, Luciano M, et al. Brain peak width of skeletonized mean diffusivity (PSMD) and cognitive function in later life. *Front Psychiatry*. (2019) 10:524. doi: 10.3389/fpsyt.2019.00524

11. Lam BYK, Leung KT, Yiu B, Zhao L, Biesbroek JM, Au L, et al. Peak width of skeletonized mean diffusivity and its association with age-related cognitive alterations and vascular risk factors. *Alzheimers Dement*. (2019) 11:721–9. doi: 10.1016/j.dadm.2019.09.003

12. Engelbertz C, Reinecke H, Breithardt G, Schmieder RE, Fobker M, Fischer D, et al. Two-year outcome and risk factors for mortality in patients with coronary artery disease and renal failure: the prospective, observational CAD-REF registry. *Int J Cardiol*. (2017) 243:65–72. doi: 10.1016/j.ijcard.2017.05.022

13. Fazekas F, Chawluk JB, Alavi A, Hurtig HI, Zimmerman RA. MR signal abnormalities at 1.5 T in Alzheimer's dementia and normal aging. AJR. *Am J Roentgenol*. (1987) 149:351–6. doi: 10.2214/ajr.149.2.351

14. Low A, Mak E, Stefaniak JD, Malpetti M, Nicastro N, Savulich G, et al. Peak width of skeletonized mean diffusivity as a marker of diffuse cerebrovascular damage. *Front Neurosci*. (2020) 14:238. doi: 10.3389/fnins.2020.00238

15. Vinciguerra C, Giorgio A, Zhang J, Nardone V, Brocci RT, Pasto L, et al. Peak width of skeletonized mean diffusivity (PSMD) and cognitive functions in relapsing-remitting multiple sclerosis. *Brain Imaging Behav*. (2020) 15:2228–33. doi: 10.1007/s11682-020-00394-4

16. Wei N, Deng Y, Yao L, Jia W, Wang J, Shi Q, et al. A neuroimaging marker based on diffusion tensor imaging and cognitive impairment due to cerebral white matter lesions. *Front Neurol*. (2019) 10:81. doi: 10.3389/fneur.2019.00081

17. Zanon Zotin MC, Yilmaz P, Sveikata L, Schoemaker D, van Veluw SJ, Etherton MR, et al. Peak width of skeletonized mean diffusivity: a neuroimaging marker for white matter injury. *Radiology*. (2023) 306:e212780. doi: 10.1148/radiol.212780

18. Horn MJ, Gokcal E, Becker JA, Das AS, Schwab K, Zanon Zotin MC, et al. Peak width of skeletonized mean diffusivity and cognitive performance in cerebral amyloid angiopathy. *Front Neurosci*. (2023) 17:1141007. doi: 10.3389/fnins.2023.1141007

19. Jochems ACC, Munoz Maniega S, Clancy U, Jaime Garcia D, Arteaga C, Hewins W, et al. Associations of peak-width skeletonized mean diffusivity and post-stroke cognition. *Life*. (2022) 12:–1362. doi: 10.3390/life12091362

20. Miwa K, Tanaka M, Okazaki S, Furukado S, Yagita Y, Sakaguchi M, et al. Chronic kidney disease is associated with dementia independent of cerebral small-vessel disease. *Neurology*. (2014) 82:1051–7. doi: 10.1212/WNL.0000000000000251

21. Hainsworth AH, Fisher MJ. A dysfunctional blood-brain barrier and cerebral small vessel disease. *Neurology*. (2017) 88:420–1. doi: 10.1212/WNL.0000000000003561

frontiers | Frontiers in Neurology

TYPE Original Research
PUBLISHED 19 September 2024
DOI 10.3389/fneur.2024.1477811

OPEN ACCESS

EDITED BY
Shuai Ren,
Affiliated Hospital of Nanjing University of Chinese Medicine, China

REVIEWED BY
Lei Gao,
Wuhan University, China
Long Teng,
Hong Kong Polytechnic University, Hong Kong SAR, China

*CORRESPONDENCE
Wei Wang
✉ waywang@126.com

†These authors have contributed equally to this work and share first authorship

‡PRESENT ADDRESS
Yong-xin Li,
School of Automation and Intelligence, Beijing Jiaotong University, Beijing, China

RECEIVED 08 August 2024
ACCEPTED 09 September 2024
PUBLISHED 19 September 2024

CITATION
Qu H, Tang H, Gao D-y, Li Y-x, Zhao Y, Ban Q-q, Chen Y-C, Lu L and Wang W (2024) Target-based deep learning network surveillance of non-contrast computed tomography for small infarct core of acute ischemic stroke.
Front. Neurol. 15:1477811.
doi: 10.3389/fneur.2024.1477811

Target-based deep learning network surveillance of non-contrast computed tomography for small infarct core of acute ischemic stroke

Hang Qu[1†], Hui Tang[2†], Dong-yang Gao[3†], Yong-xin Li[4‡], Yi Zhao[1], Qi-qi Ban[1], Yu-Chen Chen[5], Lu Lu[1] and Wei Wang[1*]

[1]Department of Radiology, Affiliated Hospital of Yangzhou University, Yangzhou, Jiangsu Province, China, [2]Department of Health Science and Kinesiology, Georgia Southern University, Statesboro, GA, United States, [3]School of Computer Science and Engineering, Nanjing University of Science and Technology, Nanjing, Jiangsu Province, China, [4]Chinese Institute of Brain Research, Beijing, China, [5]Department of Radiology, Nanjing Medical University Affiliated First Hospital, Nanjing, China

Purpose: Rapid diagnosis of acute ischemic stroke (AIS) is critical to achieve positive outcomes and prognosis. This study aimed to construct a model to automatically identify the infarct core based on non-contrast-enhanced CT images, especially for small infarcts.

Methods: The baseline CT scans of AIS patients, who had DWI scans obtained within less than 2 h apart, were included in this retrospective study. A modified Target-based deep learning model of YOLOv5 was developed to detect infarctions on CT. Randomly selected CT images were used for testing and evaluated by neuroradiologists and the model, using the DWI as a reference standard. Intraclass correlation coefficient (ICC) and weighted kappa were calculated to assess the agreement. The paired chi-square test was used to compare the diagnostic efficacy of physician groups and automated models in subregions. $p < 0.05$ was considered statistically significant.

Results: Five hundred and eighty four AIS patients were enrolled in total, finally 275 cases were eligible. Modified YOLOv5 perform better with increased precision (0.82), recall (0.81) and mean average precision (0.79) than original YOLOv5. Model showed higher consistency to the DWI-ASPECTS scores (ICC = 0.669, $\kappa = 0.447$) than neuroradiologists (ICC = 0.452, $\kappa = 0.247$). The sensitivity (75.86% vs. 63.79%), specificity (98.87% vs. 95.02%), and accuracy (96.20% vs. 91.40%) were better than neuroradiologists. Automatic model had better diagnostic efficacy than physician diagnosis in the M6 region ($p = 0.039$).

Conclusion: The deep learning model was able to detect small infarct core on CT images more accurately. It provided the infarct portion and extent, which is valuable in assessing the severity of disease and guiding treatment procedures.

KEYWORDS

target-based deep learning network, small infarct core, acute ischemic stroke, you only look once (YOLO), non-contrast CT

1 Introduction

Acute ischemic stroke (AIS) is a clinical syndrome of rapid onset of focal cerebral deficit (1), which represents a major public health problem worldwide (2). Since its high mortality, disability and morbidity, emergent diagnosis and treatment is critical for patient prognosis. The current first-choice examination method is non-contrast computed tomography (NCCT) of the head, valued for its speed of acquisition and wide availability (3). However, early AIS does not change significantly on CT, resulting in the previous interpretation of CT signs achieved low sensitivity (40–60%) within the first 3 h after symptom onset (4).

To better assess tissue damage and guide AIS treatments, Alberta Stroke Program Early CT score (ASPECTS) was designed to summarize early signs of ischemia in AIS patients. ASPECTS is a standardized semi-quantitative CT grading system used to quantify early ischemic changes in patients with ischemic changes within 10 regions of the cerebral hemisphere supplied by the middle cerebral artery (5). It is more systematic than the one-third middle cerebral artery territory rule and has been reported highly correlated to clinical outcomes. Therefore, many guidelines for early AIS management use an ASPECTS evaluation of ≥6 as an inclusion criterion for intravascular thrombectomy treatment (6, 7). Recent study also suggested patients with lower APECTS scores May still benefit from thrombectomy (8).

Noticeably, even with the convenience of NCCT, the interpretation of core infarct areas can be subjective and highly dependent on the radiologists' experience (9). A systematic review found that, given the various levels of agreement among clinicians assessing ASPECTS in thrombectomy candidates (ICC 0.672–0.811, kappa 0.042–0.469), the inconsistency is significant enough to question its reliability for treatment decisions (10). The sensitivity of stroke diagnosis by physicians based on NCCT within 24 h is 57–71%, with only 12% in the early 3 h (11). Accurately identifying small infarct foci on NCCT is more challenging in patients with ASPECTS scores ≥6 compared to those with large infarcts (10).

However, the development of artificial intelligence (AI) technology has helped address this issue. Automated software based on machine learning (ML) has been widely used in the differential diagnosis and prognosis prediction of cerebrovascular diseases (12–14). Studies have shown that automatic ASPECTS evaluation programs, such as the e-ASPECTS, RAPID, and Frontier programs, can perform statistically non-inferior, or even equivalent, to experienced neuroradiologists (6, 15, 16). However, these existing automated ASPECTS scoring software employ homogeneous principles in ML methods and rely heavily on comparisons of Hounsfield units (HU) between ipsilateral and contralateral brain regions. This approach has limitations in patients with subtle ischemic changes, as well as when images have low signal-to-noise ratios and motion artifacts (17). Further, some automated ASPECTS models use CT perfusion imaging (CTP) as reference gold standard of infarct core (18, 19), which is controversial due to its low resolution and unreliable precise core infarct foci information (20, 21).

Diffusion MRI, recognized as the gold standard for determining the core of acute ischemic infarction (22), provides the most accurate assessment but is limited by scanning preparation time and MR-related contraindications, restricting its wide application in immediate AIS diagnosis. Therefore, accurate diagnosis of AIS by NCCT and rapid identification of small infarct foci within the effective time window are important for clinicians to select surgical options and predict patient prognosis (23).

In this study, we proposed using YOLOv5 as the basic target detection model to automatically identify the core area of AIS infarcts (especially for small infarcts, i.e., ASPECTS score ≥ 6) on NCCT. By comparing and optimizing the loss function as well as using DWI infarcts (within 2 h after NCCT) as a reference, our network trained the model to achieve higher diagnostic performance. In addition, we compared the diagnostic efficacy of this model to manual assessments using the DWI-ASPECTS scoring system as the standard.

2 Methods

2.1 Study cohort

In the current study, we retrospectively collected AIS patients who underwent examinations in the radiology department of our hospital from January 2018–2022. Our hospital has established a "green channel" for emergency stroke care, also referred to as a priority pathway, ensuring that patients with acute stroke receive prompt diagnostic and treatment services.

Inclusion criteria: (1) clinical symptoms, signs, and imaging manifestations were consistent with the diagnosis of ischemic stroke (24); (2) completion of NCCT examination with images available for assessment (no obvious motion artifacts, etc.); (3) completion of MRI examination (including DWI, ADC, T2-Flair and 3D-TOF images) with images available for assessment; (4) patients underwent NCCT examinations within 6 h of symptom onset and did not receive any recanalizing/reperfusion treatments, as confirmed by interviews and the attending emergency physician; (5) NCCT and MRI examination interval < 2 h; (6) ASPECTS score ≥ 6.

Exclusion criteria: presence of infarct foci in the posterior circulation blood supply area, incomplete clinical data, patients with intracranial hemorrhage, cranial tumor, post-cranial surgery, and wake-up stroke patients (25).

2.2 Image acquisition

2.2.1 Unenhanced CT acquisition

Unenhanced brain CT images were acquired using a Somatom Definition Flash or a Somatom Force CT machine (Siemens Healthcare, Forchheim, Germany). For all examinations, automated tube voltage selection (Care kV, Siemens Healthcare) was used with a quality reference tube voltage of 120 kVp. Automatic tube current modulation (CARE Dose 4D; Siemens Healthcare) was applied with a quality reference tube current time product of 330 mAs (Flash) and 273 mAs (Force).

2.2.2 MRI acquisition

MRI images were scanned on Discovery MR750W 3.0-T MRI scanner (GE Healthcare, Waukesha, WI, United States) with a 16-channel head/neck combined coils. DWI images were obtained with the following parameters: TR = 4,300 ms, TE = 109 ms, averages = 2; acquisition matrix = 192 × 192, slice thickness = 6 mm, and slice =16. 3D TOF-MRA images were obtained with parameters of TR = 19 ms,

TE = 3.6 ms, averages = 1, FOV = 220 mm × 80.5 mm, acquisition matrix = 512 × 512; slice thickness = 0.7 mm. The T2-weighted FLAIR sequences were: TR = 7,000 ms, TE = 94 ms; averages = 1; FOV = 220 mm × 100 mm; acquisition matrix = 256 × 256; slice thickness = 6 mm, slice =6.

2.3 Image analysis

2.3.1 Image analysis by neuroradiologists

According to the ASPECTS criteria, all unenhanced brain CT images within 6 h of symptom onset were reviewed retrospectively and independently by two board-certified neuroradiology physicians (with 25 and 26 years of experience, respectively). Basic clinical information or lateralization of symptoms/stroke were disclosed to neuroradiologists. Final consensus of the AIS infarct core diagnosis would be achieved after discussion of two physicians. The manual diagnosis of CT-ASPECTS would be compared to the reference standard scores that based on the ASPECTS scores summarized from DWI images observed by two radiologists (31 and 32 years of experience, respectively).

2.3.2 Image preprocessing

All CT images displaying AIS core infarcts were manually labeled by radiologists using Labelme software. All CT images were assigned to two board-certified radiologists to delineate ground truth via consensus. A third board-certified radiologist was consulted in cases of disagreement.

Initially, the DWI images were registered to the corresponding CT images using the Dual Attention VoxelMorph Network (26), which offers enhanced registration accuracy and model sensitivity with minimal computational overhead. After registration, radiologists labeled the core infarcts on the annotated CT images while referring to the registered CT-DWI images.

We applied a series of preprocessing steps to the NCCT images. These steps included standardizing the resolution of all images to 640 × 640 pixels, normalizing the image contrast using brain window settings (window level: 30 HU, window width: 60 HU) for all head NCCT images, applying z-score normalization, and augmenting the data through random horizontal flipping and cropping.

The 10 paired ASPECTS regions from the preprocessed CT images were segmented using the widely employed V-net architecture (27). V-net has been extensively utilized for medical image segmentation, particularly in brain tissue segmentation (28, 29).

2.3.3 Image analysis by proposed model

Our proposed model adopted a single-stage detection method from YOLOv5 (30). Shown as Figure 1, the structure of YOLOv5 model consists of backbone, neck and head. Cross Stage Partial Networks (CSPNet) based on DenseNet architecture were used as the backbone to extract rich and useful features from an input image. The neck included PANet and SPP, where SPP (spatial pyramid pooling) enhances the model's detection of objects with different scales and PANet (Path aggregation network) is the neck for feature aggregation (30) and to generate feature pyramids. The head model is used for final inspection, where anchor boxes are used to feature the map and generate the final output vector with class probabilities, object scores, and bound boxes.

Although the YOLOv5 reports high inference speed and small model sizes to allow a convenient translation to mobile use cases via model export (31), the imbalance of positive and negative samples in this study restricts the application of basic YOLOv5 model. We modified the R-Mish activation function and intersection over union (IoU) loss function (32, 33) of YOLOv5 to detect infarct cores correctly even on the complex surfaces. Specific details will be disclosed in the Supplementary materials.

For constructing baseline models, we employed a workstation with 11400F CPU, 32GB system memory and NVIDIA RTX3070GPU with 8GB memory. Both stages used the default set of hyper parameters (including parameters related to the data augmentation procedures) offered by the YOLO framework, which was based on Pytorch framework. We used different bounding box loss functions for testing. The parameters were modified based on the current data. The main parameter in this paper were: the number of image categories, the number of training times is based on 100, appropriately increased to 300, and the size of the training image: 512*512. Before training we set the threshold value to 0.5, that is, the result predicted by the neural network model in the training process is greater than this value can be regarded as a positive sample, and vice versa as a negative sample. After a certain number of training sessions, the model with the best training result will be obtained, which will be used to assist in finding the lesion area in CT images. The mean Average Precision (mAP%) is used as a reference indicator for good model training results.

2.4 Statistical analysis

Normality distribution data was assessed by Kolmogorove-Smirnov test ($\alpha = 0.05$). Otherwise, medians, interquartile ranges, and ranges are given. The agreement among neuroradiologists, model and reference standard of DWI on the ASPECTS evaluation was calculated by means of the intraclass correlation coefficient (ICC) and weighted kappa. The sensitivity, specificity and accuracy of each subregion (M1-M6, insula, lenticular nucleus, caudate nucleus, and internal capsule) in the ASPECTS scoring system was calculated by confusion matrix. To assess the models' performance, we used the IoU metric to measure overlap between predicted and ground truth boxes. A detection was considered correct (True Positive, TP) if the IoU exceeded 0.5; otherwise, it was classified as a False Negative (FN). The IoU threshold was set at 0.5. In the ASPECTS scoring system, if the model detected a lesion with a probability greater than 0.5, one point was subtracted from the maximum score of 10 for that region. The paired chi square test was used to compare the diagnostic efficacy of physician groups and automated models in subregions. $p < 0.05$ was considered statistically significant.

3 Results

3.1 Demographics of the study cohort

Between 2018 and 2022, in a total of 584 AIS patients underwent examinations in the radiology department. However, only 275 cases were eligible for the current study, the exclusion cases were: 25 cases of motion artifacts, 78 cases that core infarct area accumulated in the

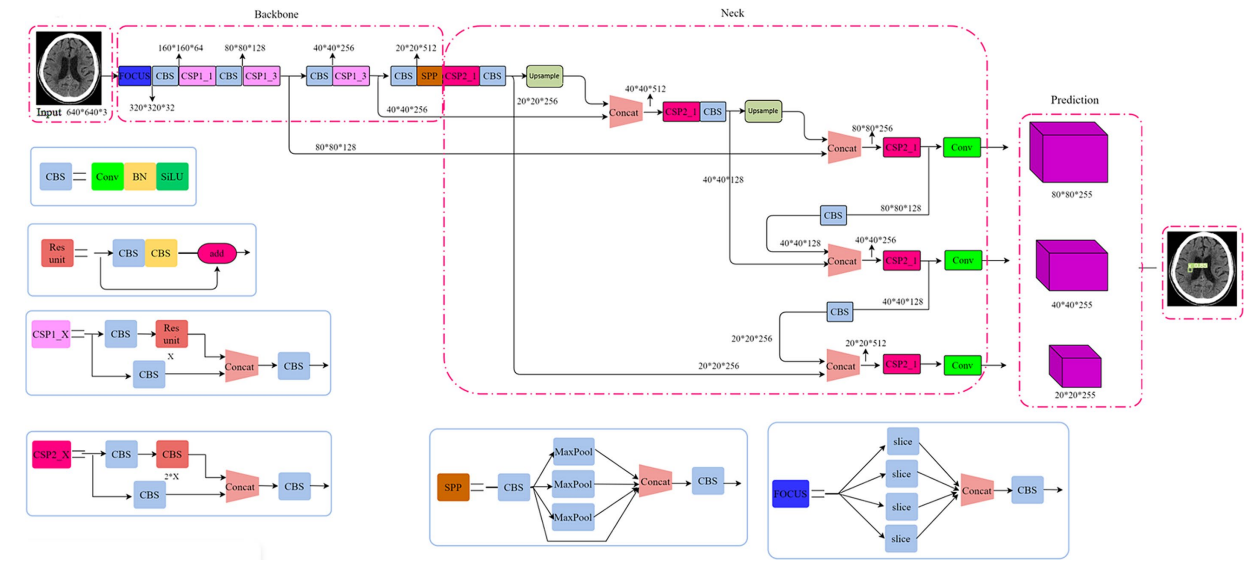

FIGURE 1
The structure of the YOLOv5 model.

posterior circulation area, 71 cases that stroke symptoms occurred more than 6 h before coming to the hospital for NCCT, 43 cases that the interval between NCCT and MRI examination was more than 2 h, 55 cases with large infarcts due to postoperative or incomplete medical records, and 37 cases with ASPECTS score < 6.

The 275 cases were completely randomly divided into a training set and an independent testing set at a 10:1 ratio. Clinical and imaging indices were shown in the Table 1.

3.2 Outcomes of the deep learning recognition of core infarct area

After experimental testing, our modified complete IoU (M-CIoU) module had the best training outcomes than the CIoU and DIoU (Distance IoU) loss function. Detailed results were shown in the Figure 2 and Table 2.

3.3 Results of consistency analysis

The ICC between our model diagnosed ASPECTS scores and DWI ASPECTS scores was 0.669 (95% interval [CI] 0.380–0.839, $p < 0.001$). The ICC between physician scored ASPECTS and DWI ASPECTS was 0.452 (95% interval [CI] 0.077–0.715, $p = 0.010$).

The consistency testing between our model scored ASPECTS and the DWI ASPECTS achieved kappa of 0.477 (95% interval [CI] 0.255–0.699, $p < 0.001$). The consistency between physician scores and the DWI ASPECTS achieved the kappa of 0.247 (95% interval [CI] −0.017–0.510, $p = 0.054$).

In addition, the sensitivity, specificity, and accuracy results of three different diagnoses of AIS were shown in the Table 3. The paired Chi-square test showed that the automatic model had better diagnostic efficacy than the physician diagnosis in the M6 region ($p = 0.039$).

TABLE 1 Patient's clinical record in the training and testing tests.

Category	Training set(250 cases)	Testing set(25 cases)
Average age (years)	68.08 ± 11.70	67.16 ± 9.38
Male [n (%)]	172(68.8)	19(76.00)
History of ischemic stroke [cases (%)]	139(55.6)	15(60.00)
Hypertension [cases (%)]	120(48.0)	19(76.00)
Diabetes [cases (%)]	157(62.8)	15(60.00)
Smoking history [n (%)]	147(58.8)	18(72.00)
Mean time to onset of stroke from NCCT examination (h)	3.85 ± 1.82	3.68 ± 1.15
NCCT interval from MRI examination<1 h [n (%)]	131(52.4)	9(36.00)
NCCT interval from MRI examination1^2h [n (%)]	119(47.6)	16(64.00)
DWI-ASPECTS [M (P25, P75), scores]	8(7, 8)	8(7, 9)

3.4 Case demonstration

Case 1, 2 were typical cases in the missed cases during physicians' diagnoses, indicating the difficulty of recognition of small core infarct area (Figure 3).

In case 1, the ASPECTS score was 9, the lesion was located on the hind limb of the left internal capsule. Figures 3-1A was the NCCT. Figures 3-1B was the automatic diagnosed figure, where the green box indicated the core infarct area, with a 73% probability of the area being an acute infarct. Figures 3-1C was the DWI image, and the Figures 3-1D was the ADC image.

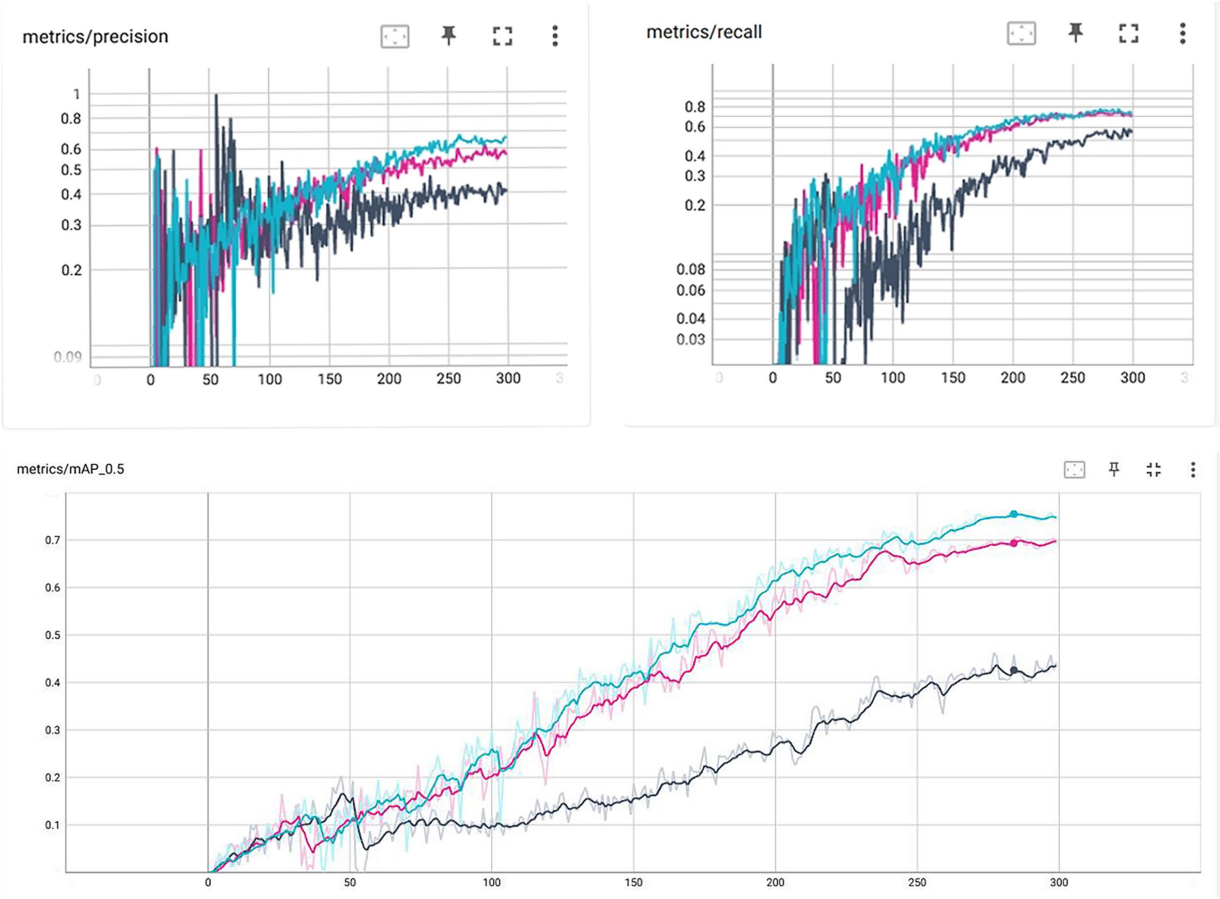

FIGURE 2
Parameter change curves for different loss functions during the training process. M-CIoU is in color blue, CIoU is in color pink and the DIoU is in gray.

TABLE 2 Testing results of three different loss function.

	CIoU (pink)	DIou (gray)	M-CIoU (blue)
Precision	0.616	0.8014	0.8237
Recall	0.7377	0.5942	0.8101
IoU (map@0.5)	0.706	0.4629	0.7851

In case 2, the ASPECTS score was 9, and the lesion location was M5. Figures 3-2A was the NCCT, Figures 3-2B showed the automatic diagnosed image, where the green box indicted the identified core infarct area with an 85% of probability of the area being an acute infarct. Figures 3-2C and Figures 3-2D showed the DWI image and ADC image, respectively.

Figure 4 illustrates Case 3, which showed mixed foci with the infarct extent spanning two brain regions simultaneously, and an ASPECTS score of 6 with lesion locations in M2, M3,M5, and M6. The Figure 4A showed the NCCT image. Figure 4B showed the automatic diagnosed images, where the purple boxes demonstrated the core infarcts areas, with the 92, 74, 94, 95, and 83% of probabilities of being acute infarcts areas indicated the acute infarcts probabilities, respectively. Figure 4C was DWI image and Figure 4D as ADC image.

4 Discussion

This study aimed to employ a target-based deep learning network to improve the accuracy of NCCT based AIS diagnosis so to identify small infarct foci within the effective time window. The results showed our proposed modified YOLOv5 model is a fast and compact object detection model for automated identification of AIS infarct core area on NCCT images. Compared to the traditional physician interpretation, which takes a few minutes, the proposed automated model reads AIS in only 10 s (23). In addition, the ASPECTS scores of the automated recognition model showed higher consistency to the DWI-ASPECTS scores than the ASPECTS scores graded by the physician group. The diagnostic efficacy of multiple regions was higher than that of the physician group, especially for small areas of acute cerebral infarction (Figure 5).

Our proposed model showed a superior consistency with the reference standard score (ICC = 0.669, $\kappa = 0.447$) than neuroradiologists (ICC = 0.452, $\kappa = 0.247$) who had particular expertise in evaluating diagnostic studies in acute stroke patients, also the mean sensitivity, specificity, and accuracy of nearly every subregion were better than neuroradiologists. Previous studies have confirmed the challenge of detection of subtle signs of early ischemia for even experienced physicians (34). Prior analytic results showed that ASPECTS achieved

TABLE 3 Sensitivity, specificity and accuracy of the CT manual ASPECTS scoring system.

	Sensitivity (%)		Specificity (%)		Accuracy (%)	
	Model	Physician	Model	Physician	Model	Physician
M1	33.30	66.67	100.00	93.62	96.00	92.00
M2	80.00	40.00	100.00	97.78	98.00	92.00
M3	100.00	75.00	97.83	97.83	98.00	96.00
M4	50.00	83.33	100.00	90.91	94.00	90.00
M5	90.00	75.00	96.67	93.33	94.00	86.00
M6	85.71	28.57	100.00	93.02	98.00	84.00
Insula	33.33	33.33	97.87	93.62	94.00	90.00
Lenticular nucleus	100.00	100.00	100.00	100.00	100.00	100.00
Caudate	50.00	100.00	100.00	100.00	98.00	100.00
Internal capsule	66.67	50.00	95.45	88.64	92.00	84.00
Total	75.86	63.79	98.87	95.02	96.20	91.40

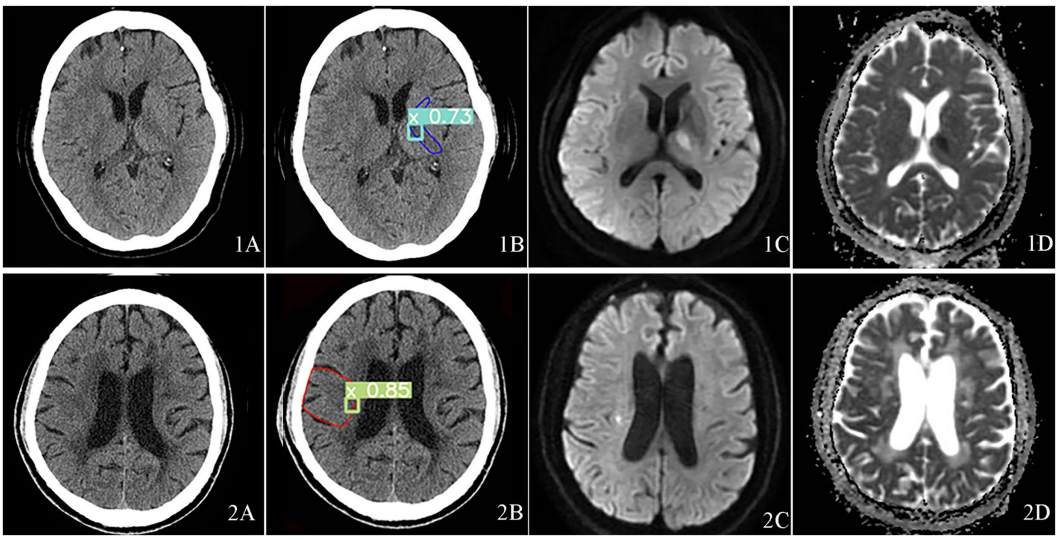

FIGURE 3
Visualization of acute core infarct recognition on NCCT images using the deep learning model for case 1 and case 2. Case 1 was shown at the top and Case 2 at the bottom. Case 1 and 2 images were shown as NCCT (labeled as **1A** and **2A**), automatic model diagnosed images (labeled as **1B** and **2B**), DWI images (labeled as **1C** and **2C**) and ADC images(labeled as **1D** and **2D**).

insufficient agreement between clinicians for ASPECTS to be reliably used as a criterion for treatment decisions, inter-rater agreement was slight to moderate (κ = 0.129–0.315). Even in the best of cases, when ASPECTS was dichotomized as 0–5 vs. 6–10, interrater agreement did not reach a substantial level (κ = 0.561) (10). Wilson AT et al. point out that as the development of automated computational tools to assess ASPECTS on NCCT, the inter-rater reliability issue May become less pertinent than the issue of human versus computer performance (35). The detection rate of AIS lesions within 3 Hours of onset was low by neurologists and CT-ASPECTS scores could not predict the favorable and non-favorable outcome groups (36).

The present study chose DL algorithms for a reason. The drawbacks of ML based software cannot be neglected. For example, there are several popular commercial software in the clinical settings. Studies have shown software programs such as e-ASPECTS, RAPID and syngo.via Frontier ASPECTS prototype can be statistically non-inferior or equivalent to three independent neuroradiologists (NRADs) when diagnosing early ischemic damage (15, 16). These programs used ML highly depend on first-order image features to discover the presence of infarct foci in certain regions, such as Hounsfield unit (HU) or density (6). These first-order image features have limitations in patients with subtle ischemic changes and when images have low signal-to-noise ratios and motion artifacts (17). Additionally, ML-based approaches greatly rely on comparisons of the ipsilateral and contralateral brain regions, as this is how humans interpret images (17). This would result in low sensitivity. The e-ASPECTS software revealed such low sensitivity in both two studies, 44 and 46.46%, respectively (15, 37). Although the RAPID showed the best agreement to the consensus score (k = 0.9), its restricted application cannot be ignored. When patients with ASPECTS

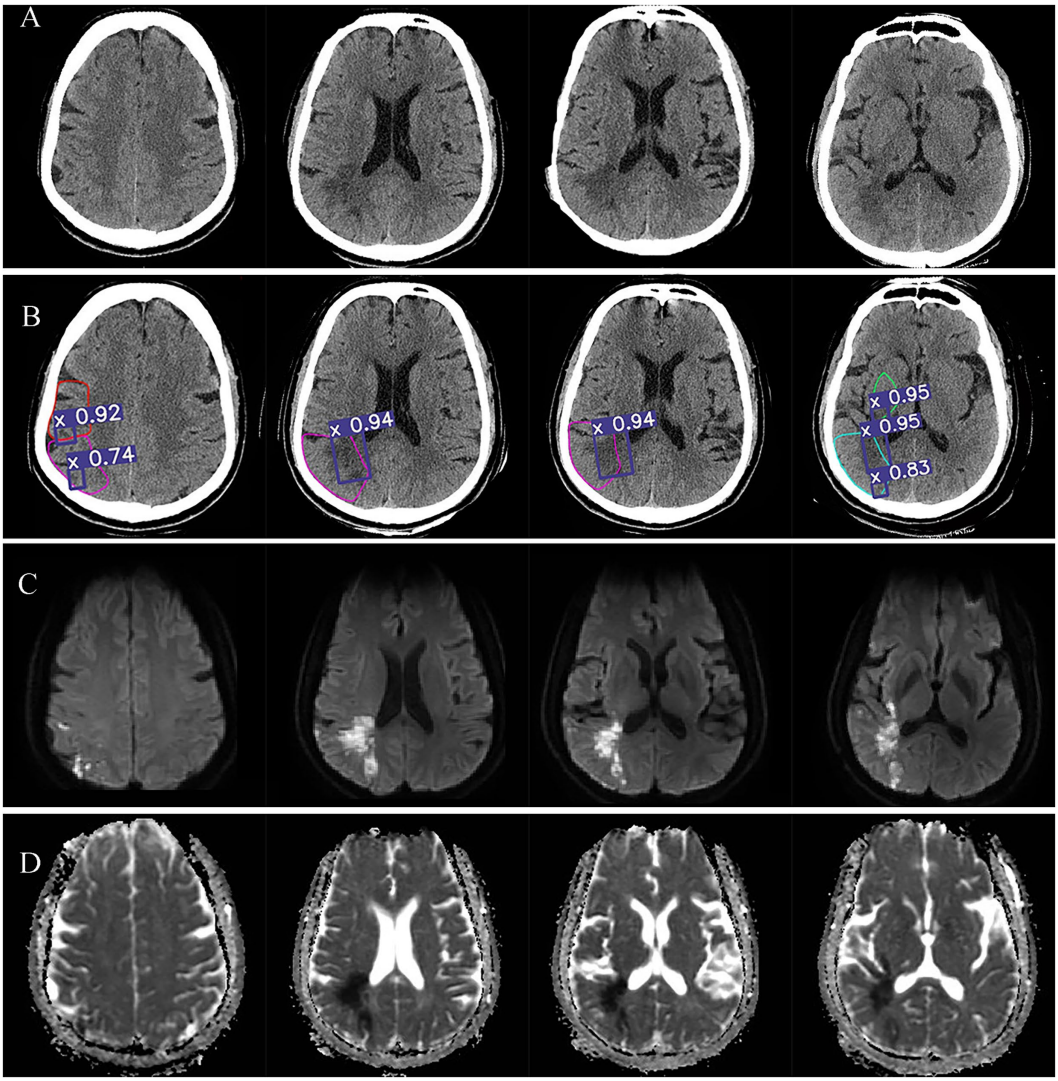

FIGURE 4
Visualization of acute core infarct recognition on NCCT images using the deep learning model for case 3. Case 3 images were shown as NCCT (labeled as **A**), automatic model diagnosed images (labeled as **B**), DWI images (labeled as **C**) and ADC images (labeled as **D**).

score ≥ 7, the probability of detecting infarction by RAPID decreased substantially. Only about 20% (22 of 100 in cohort 1, 10 of 52 in cohort 2) of the CT data sets could not be analyzed by using RAPID (6).

Given the aforementioned limitations of ML models, more recent studies have optimized the extraction of features in the ML models. For example, Kuang et al. introduced multiple high order computational textural features into the ML model and showed a more accurate and reliable ASPECTS reading compared to that on acute DWI (17). This method used nonlinear self-registration to correct brain asymmetry and calculated bilateral differences at different scales to tolerate suboptimal symmetry. However, it would result in the increasing variability and complexity of ML model and May introduce unpredictability into their model. Therefore, the current models based on ML algorithms cannot overcome the defects, such as poor generalization ability. So that the diagnosis is more unreliable when the case is an acute ischemic stroke in bilateral brain regions.

Notably, the major strengths of convolutional neural network (CNN) from DL can overcome the weak contrast of the infarct tissue in the early stage and naked eye's low ability in detecting subtle differences. The modified target detection method proposed in the current study can acquire and learn high-dimensional information of images directly from the data. The algorithm not only gives the detected target class, but the location and range of lesion. Among object detection models such as faster R-CNN and YOLO, we chose to use YOLO for the following reasons. Firstly, it is well recognized that realizing CNN feature extraction on each candidate frame and calculations would take up a large amount of memory space and overlaps. YOLO model can be superior in the detection speed. It uses the entire image as the input to the network to convert detection problem into a single regression problem and directly return the target frame of its position in multiple positions of the image and the category to which the target belongs (38). Secondly, YOLOv5 has demonstrated reliable detection performance with an overall high precision over different model configurations (31). The present study proposed a lightweight detection and classification method based on modified YOLOv5 to detect infarct core of AIS. Improvements of activation function R-Mish and CIoU loss have

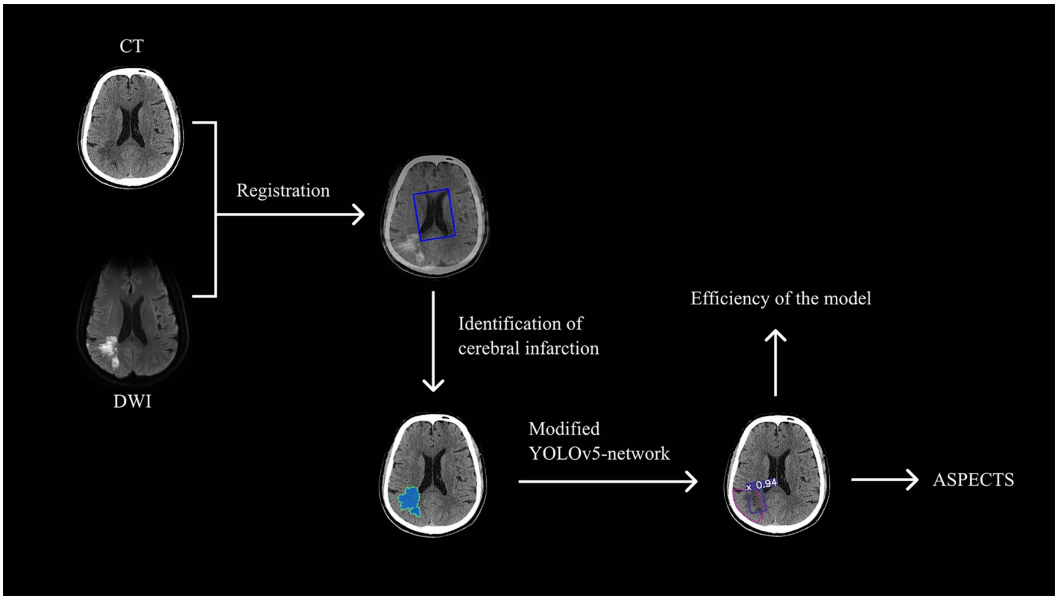

FIGURE 5
The technical pipeline of the study.The study begins with the registration of CT and DWI images using the Dual Attention VoxelMorph Network. Radiologists then labeled the core infarcts on the CT images, which were subsequently used to train the Modified YOLOv5-based model. Finally, the trained model efficiently recognizes acute infarct cores and calculates the ASPECTS score.

showed superiority in the detection of lesions, especially in our dataset that had fewer positive samples. The results showed that modified versions of YOLOv5 perform better with incensed precision (0.82), recall (0.81) and mAP (0.79) than original YOLOv5. Due to its reasonable performance and rapid end-to-end technique for detecting objects, our model only takes a few seconds to detect a single case, which is much faster than the 5-min reported previously (12). Moreover, our model is small and can be easily transplanted on mobile devices, making it applicable in other fields.

Our results reported that our proposed model can quickly identify small cerebral infarcts that could not be quickly detected by some physicians at NCCT (shown as Figures 3, 4). The better performance of this model can be explained by the subtle changes corresponding to DWI image. Our model favorably detected subtle changes without follow-up imaging procedures. Our observations can be surpassing many previous studies. For example, Pan et al. used a DL residual network (ResNet) to detect the infarct core on NCCT images based on DWI to improve the accuracy of acute ischemic stroke diagnosis (39). However, the insufficient number of cases and absence of ASPECTS areas segmentation making it difficult to evaluate its clinical applicability. Barros et al. used separate three CNNs for the segmentation of the final infarct on follow-up NCCT scans and reported an excellent agreement with the manually reference with an ICC of 0.88 (40). However, the absence of gold-standard makes it impossible to identify the early ischemic injury. Same problem also existed in some other studies (41), where using experts' manual contouring as the reference standard can cause considerable observer variability. For data-driven approach, the uncertainty and variability of reference standard May introduce unpredictability into the DL model, thereby increasing the complexity of the problem. Although some DL models tried to construct the gold standard for CTP, it remains controversial to use CTP to determine the infarct core due to is low resolution and debatable cutoff value, and lacking of reliable information about the precise core infarct foci (20, 21). A recent study used CTP to detect ischemic regions for ASPECTS scoring. It designed a depth-asymmetric network (DA-Net) on an asymmetric structure to detect differences between the left and right hemispheres in order to estimate their ischemic status (18). Accordingly, it can automatically calculate the ASPECTS score. Due to the lack of DWI reference for the core infarct region, they mainly evaluate the performance of estimating whether the ASPECTS score is higher than 6. In addition, this asymmetric network model for determining ischemic brain regions does not visualize the core infarct foci, which provides limited assistance to the imaging physician when performing image analysis.

Therefore, our proposed model included spatial information to improve the performance in detecting small focal lesions. The gold standard is built based on the MR (DWI, T2-FLAIR, 3D-TOF, ADC) within 2 h after NCCT. DWI is a highly sensitive MRI technique that can provide more reliable information for AIS such as core infarct area and infarct extent, and is relatively better able to distinguish the infarct core from the old lesions (42).

The present study used AIS patients for retrospective analysis, from which the patient acute state is defined as patients within 6 h after onset of stroke symptoms. This period is important since assessing the extent of infarction within 6 h is critical for determining the most appropriate treatment strategies moving forward (7). Images included in the dataset of this study were heterogeneous, including images of different manufacturers, parameters, and layer thicknesses. It is noticeable that we obtained higher accuracy but lower average sensitivity in the detection and analysis of sub-regions. The sensitivity of M1, M4 and insula was lower than 50%. This was mainly caused by the small number of positive samples are in these subregions. Since we adopted the subregion-based detection model, number of

positive samples in these areas in the test set is small and some misjudged samples will appear. False negative identification results would appear due to some reasons such as insufficient data set of the model. The model in the present study could still provide more reference information to the imaging physicians and save the diagnosis time. The rate of missed diagnosis can be significantly reduced.

In addition, this study screened the dataset was targeted to include only small infarcts with ASPECTS scores ≥6 to test the model, so it was more challenging in terms of diagnostic difficulty, but the diagnostic efficacy of the automated model in this study in terms of consistency (ICC = 0.669), total sensitivity (75.86%), total specificity (98.87%) and total accuracy (96.20%) has been comparable to current models that do not target small cerebral infarction. We selected patients with ASPECTS scores ≥6 to align with current clinical guidelines for interventions like mechanical thrombectomy (7). This focus ensures clinical relevance but May limit applicability to patients with lower scores. Future studies should include a wider range of ASPECTS scores to assess the model's performance across different patient populations.

There are several limits in the present study. First, the proposed model is only trained to test the MCA blood supply area, and acute ischemic stroke in the posterior circulation is more difficult to detect these lesions than by anterior circulation stroke due to ray-hardening artifacts, so further research is needed. Secondly, the number of cases is relatively small. To improve the robustness and generalization ability of the algorithm, we also need to further build a feedback mode for clinical practice. A feedback mode could realize the software data polycentric so that to improve the software accuracy. Last but not the least, NCCT images can be used for rapid identification of a variety of diseases, including ischemic, hemorrhagic cerebrovascular disease, large vessel occlusion, and can rapidly assess the ischemic semi dark zones by CT. If the future model can recognize stroke types, it would be more beneficial.

5 Conclusion

In this paper, we construct a deep learning target detection network-based model for automated identification of infarct cores in acute ischemic stroke in NCCT by optimizing the loss function of target detection model using the gold standard of DWI. The results showed that the model was more effective than the physician group in identifying the infarct core in the acute phase of AIS patients, especially for small areas of acute cerebral infarction (ASPECTS score ≥ 6). The modified YOLOv5 achieved better diagnostic performance and accuracy than original version. The deep learning network based on target detection not only gives more accurate ASPECTS scores, but also provides a simple and intuitive understanding of the infarct portion and extent, which is valuable in assessing the severity of disease and selecting treatment procedures. Due to its reasonable performance and rapid end-to-end technique for detecting, this model only takes a few seconds to detect a single case which should help clinicians optimize the process of cerebrovascular disease and reduce the rate of missed diagnoses more effectively.

Data availability statement

The raw data supporting the conclusions of this article will be made available by the authors, without undue reservation.

Ethics statement

The studies involving humans were approved by the Affiliated Hospital of Yangzhou University. The studies were conducted in accordance with the local legislation and institutional requirements. The participants provided their written informed consent to participate in this study.

Author contributions

HQ: Conceptualization, Supervision, Writing – original draft. HT: Methodology, Writing – review & editing. D-yG: Conceptualization, Writing – review & editing. Y-xL: Methodology, Writing – review & editing. YZ: Writing – review & editing. Q-qB: Formal analysis, Writing – original draft. Y-CC: Writing – review & editing. LL: Formal analysis, Writing – original draft. WW: Resources, Writing – review & editing.

Funding

The author(s) declare that financial support was received for the research, authorship, and/or publication of this article. This program was funded by Jiangsu Provincial Special Program of Medical Science (No. BE2021604).

Conflict of interest

The authors declare that the research was conducted in the absence of any commercial or financial relationships that could be construed as a potential conflict of interest.

Publisher's note

Supplementary material

The Supplementary material for this article can be found online at: https://www.frontiersin.org/articles/10.3389/fneur.2024.1477811/full#supplementary-material

References

1. Lee TY, Murphy BD, Aviv RI, Fox AJ, Black SE, Sahlas DJ, et al. Cerebral blood flow threshold of ischemic penumbra and infarct core in acute ischemic stroke: a systematic review. *Stroke*. (2006) 37:2201–3. doi: 10.1161/01.STR.0000237068.25105.aa

2. Chemerinski E, Robinson RG. The neuropsychiatry of stroke. *Psychosomatics*. (2000) 41:5–14. doi: 10.1016/S0033-3182(00)71168-6

3. Musuka TD, Wilton SB, Traboulsi M, Hill MD. Diagnosis and management of acute ischemic stroke: speed is critical. *CMAJ: Canadian Med Assoc J = journal de l'Association medicale canadienne*. (2015) 187:887–93. doi: 10.1503/cmaj.140355

4. El-Koussy M, Schroth G, Brekenfeld C, Arnold M. Imaging of acute ischemic stroke. *Eur Neurol*. (2014) 72:309–16. doi: 10.1159/000362719

5. Barber PA, Demchuk AM, Zhang J, Buchan AM. Validity and reliability of a quantitative computed tomography score in predicting outcome of hyperacute stroke before thrombolytic therapy. ASPECTS study group. Alberta stroke Programme early CT score. *Lancet (London, England)*. (2000) 355:1670–4. doi: 10.1016/s0140-6736(00)02237-6

6. Maegerlein C, Fischer J, Mönch S, Berndt M, Wunderlich S, Seifert CL, et al. Automated calculation of the Alberta stroke program early CT score: feasibility and reliability. *Radiology*. (2019) 291:141–8. doi: 10.1148/radiol.2019181228

7. Powers WJ, Rabinstein AA, Ackerson T, Adeoye OM, Bambakidis NC, Becker K, et al. Guidelines for the early Management of Patients with Acute Ischemic Stroke: 2019 update to the 2018 guidelines for the early Management of Acute Ischemic Stroke: a guideline for healthcare professionals from the American Heart Association/American Stroke Association. *Stroke*. (2019) 50:e344–418. doi: 10.1161/STR.0000000000000211

8. Yoo AJ, Berkhemer OA, Fransen PSS, van den Berg LA, Beumer D, Lingsma HF, et al. Effect of baseline Alberta stroke program early CT score on safety and efficacy of intra-arterial treatment: a subgroup analysis of a randomised phase 3 trial (MR CLEAN). *Lancet Neurol*. (2016) 15:685–94. doi: 10.1016/S1474-4422(16)00124-1

9. von Kummer R, Nolte PN, Schnittger H, Thron A, Ringelstein EB. Detectability of cerebral hemisphere ischaemic infarcts by CT within 6 h of stroke. *Neuroradiology*. (1996) 38:31–3. doi: 10.1007/BF00593212

10. Farzin B, Fahed R, Guilbert F, Poppe AY, Daneault N, Durocher AP, et al. Early CT changes in patients admitted for thrombectomy: Intrarater and interrater agreement. *Neurology*. (2016) 87:249–56. doi: 10.1212/WNL.0000000000002860

11. Köhrmann M, Schellinger PD. Acute stroke triage to intravenous thrombolysis and other therapies with advanced CT or MR imaging: pro MR imaging. *Radiology*. (2009) 251:627–33. doi: 10.1148/radiol.2513081074

12. Qiu W, Kuang H, Teleg E, Ospel JM, Sohn SI, Almekhlafi M, et al. Machine learning for detecting early infarction in acute stroke with non-contrast-enhanced CT. *Radiology*. (2020) 294:638–44. doi: 10.1148/radiol.2020191193

13. Bentley P, Ganesalingam J, Carlton Jones AL, Mahady K, Epton S, Rinne P, et al. Prediction of stroke thrombolysis outcome using CT brain machine learning. *NeuroImage Clin*. (2014) 4:635–40. doi: 10.1016/j.nicl.2014.02.003

14. Gomolka RS, Chrzan RM, Urbanik A, Nowinski WL. A quantitative method using head noncontrast CT scans to detect Hyperacute nonvisible ischemic changes in patients with stroke. *J Neuroimag: official J American Society of Neuroimag*. (2016) 26:581–7. doi: 10.1111/jon.12363

15. Nagel S, Sinha D, Day D, Reith W, Chapot R, Papanagiotou P, et al. E-ASPECTS software is non-inferior to neuroradiologists in applying the ASPECT score to computed tomography scans of acute ischemic stroke patients. *Int J Stroke: Official J Int Stroke Society*. (2017) 12:615–22. doi: 10.1177/1747493016681020

16. Wolff L, Berkhemer OA, van Es ACGM, van Zwam WH, Dippel DWJ, Majoie CBLM, et al. Validation of automated Alberta stroke program early CT score (ASPECTS) software for detection of early ischemic changes on non-contrast brain CT scans. *Neuroradiology*. (2021) 63:491–8. doi: 10.1007/s00234-020-02533-6

17. Kuang H, Najm M, Chakraborty D, Maraj N, Sohn SI, Goyal M, et al. Automated ASPECTS on noncontrast CT scans in patients with acute ischemic stroke using machine learning. *AJNR Am J Neuroradiol*. (2019) 40:33–8. doi: 10.3174/ajnr.A5889

18. Cao Z, Xu J, Song B, Chen L, Sun T, He Y, et al. Deep learning derived automated ASPECTS on non-contrast CT scans of acute ischemic stroke patients. *Hum Brain Mapp*. (2022) 43:3023–36. doi: 10.1002/hbm.25845

19. Wei J, Shang K, Wei X, Zhu Y, Yuan Y, Wang M, et al. Deep learning-based automatic ASPECTS calculation can improve diagnosis efficiency in patients with acute ischemic stroke: a multicenter study. *Eur Radiol*. (2024). doi: 10.1007/s00330-024-10960-9

20. Wintermark M, Reichhart M, Thiran JP, Maeder P, Chalaron M, Schnyder P, et al. Prognostic accuracy of cerebral blood flow measurement by perfusion computed tomography, at the time of emergency room admission, in acute stroke patients. *Ann Neurol*. (2002) 51:417–32. doi: 10.1002/ana.10136

21. Wintermark M, Fischbein NJ, Smith WS, Ko NU, Quist M, Dillon WP. Accuracy of dynamic perfusion CT with deconvolution in detecting acute hemispheric stroke. *AJNR Am J Neuroradiol*. (2005) 26:104–12.

22. Nael K, Khan R, Choudhary G, Meshksar A, Villablanca P, Tay J, et al. Six-minute magnetic resonance imaging protocol for evaluation of acute ischemic stroke: pushing the boundaries. *Stroke*. (2014) 45:1985–91. doi: 10.1161/STROKEAHA.114.005305

23. von Kummer R, Dzialowski I. Imaging of cerebral ischemic edema and neuronal death. *Neuroradiology*. (2017) 59:545–53. doi: 10.1007/s00234-017-1847-6

24. Yew KS, Cheng EM. Diagnosis of acute stroke. *Am Fam Physician*. (2015) 91:528–36.

25. Huisa BN, Raman R, Ernstrom K, Tafreshi G, Stemer A, Meyer BC, et al. Alberta stroke program early CT score (ASPECTS) in patients with wake-up stroke. *J Stroke Cerebrovasc Dis*. (2010) 19:475–9. doi: 10.1016/j.jstrokecerebrovasdis.2010.03.003

26. Li YX, Tang H, Wang W, Zhang XF, Qu H. Dual attention network for unsupervised medical image registration based on VoxelMorph. *Sci Rep*. (2022) 12:16250. doi: 10.1038/s41598-022-20589-7

27. Milletari F, Navab N, Ahmadi SA. V-net: fully convolutional neural networks for volumetric medical image segmentation. In: *2016 Fourth International Conference on 3D Vision (3DV)*. IEEE, 565–71. (2016). doi: 10.1109/3DV.2016.79

28. Park JS, Fadnavis S, Garyfallidis E. Multi-scale V-net architecture with deep feature CRF layers for brain extraction. *Commun Med*. (2024) 4:29. doi: 10.1038/s43856-024-00452-8

29. Huang F, Xia P, Vardhanabhuti V, Hui SK, Lau KK, Ka-Fung Mak H, et al. Semisupervised white matter hyperintensities segmentation on MRI. *Hum Brain Mapp*. (2023) 44:1344–58. doi: 10.1002/hbm.26109

30. Liu S., Qi L., Qin H., Shi J., Jia J. (2018). "Path aggregation network for instance segmentation." In *2018 IEEE/CVF conference on computer vision and pattern recognition (CVPR)* (pp. 8759–8768). IEEE.

31. Yap MH, Hachiuma R, Alavi A, Brüngel R, Cassidy B, Goyal M, et al. Deep learning in diabetic foot ulcers detection: a comprehensive evaluation. *Comput Biol Med*. (2021) 135:104596. doi: 10.1016/j.compbiomed.2021.104596

32. Zheng Z, Wang P, Liu W, Li J, Ye R, Ren D. Distance-IoU loss: faster and better learning for bounding box regression. *Proceed AAAI Conference on Artificial Intel*. (2020) 34:12993–3000. doi: 10.1609/aaai.v34i07.6999

33. He K, Zhang X, Ren S, Sun J. Spatial pyramid pooling in deep convolutional networks for visual recognition. *IEEE Trans Pattern Anal Mach Intell*. (2015) 37:1904–16. doi: 10.1109/TPAMI.2015.2389824

34. Dippel DW, Ry D, van Beest Holle M, van Kooten F, Koudstaal PJ. The validity and reliability of signs of early infarction on CT in acute ischaemic stroke. *Neuroradiology*. (2000) 42:629–33. doi: 10.1007/s002340000369

35. Wilson AT, Dey S, Evans JW, Najm M, Qiu W, Menon BK. Minds treating brains: understanding the interpretation of non-contrast CT ASPECTS in acute ischemic stroke. *Expert Rev Cardiovasc Ther*. (2018) 16:143–53. doi: 10.1080/14779072.2018.1421069

36. Mitomi M, Kimura K, Aoki J, Iguchi Y. Comparison of CT and DWI findings in ischemic stroke patients within 3 hours of onset. *J Stroke Cerebrovasc Dis*. (2014) 23:37–42. doi: 10.1016/j.jstrokecerebrovasdis.2012.08.014

37. Herweh C, Ringleb PA, Rauch G, Gerry S, Behrens L, Möhlenbruch M, et al. Performance of e-ASPECTS software in comparison to that of stroke physicians on assessing CT scans of acute ischemic stroke patients. *Int J Stroke: Official J Int Stroke Society*. (2016) 11:438–45. doi: 10.1177/1747493016632244

38. Wan J, Chen B, Yu Y. Polyp detection from Colorectum images by using attentive YOLOv5. *Diagnostics (Basel, Switzerland)*. (2021) 11:2264. doi: 10.3390/diagnostics11122264

39. Pan J, Wu G, Yu J, Geng D, Zhang J, Wang Y. Detecting the early infarct Core on non-contrast CT images with a deep learning residual network. *J Stroke Cerebrovasc Dis*. (2021) 30:105752. doi: 10.1016/j.jstrokecerebrovasdis.2021.105752

40. Sales Barros R, Tolhuisen ML, Boers AM, Jansen I, Ponomareva E, Dippel DWJ, et al. Automatic segmentation of cerebral infarcts in follow-up computed tomography images with convolutional neural networks. *J Neurointerventional Surg*. (2020) 12:848–52. doi: 10.1136/neurintsurg-2019-015471

41. Stoel BC, Marquering HA, Staring M, Beenen LF, Slump CH, Roos YB, et al. Automated brain computed tomographic densitometry of early ischemic changes in acute stroke. *J Medical Imag (Bellingham)*. (2015) 2:014004. doi: 10.1117/1.JMI.2.1.014004

42. Kranz PG, Eastwood JD. Does diffusion-weighted imaging represent the ischemic core? An evidence-based systematic review. *AJNR Am J Neuroradiol*. (2009) 30:1206–12. doi: 10.3174/ajnr.A1547

frontiers | Frontiers in Neurology

TYPE Original Research
PUBLISHED 09 October 2024
DOI 10.3389/fneur.2024.1476937

OPEN ACCESS

EDITED BY
Sonu Bhaskar,
National Cerebral and Cardiovascular Center, Japan

REVIEWED BY
Yuto Uchida,
Johns Hopkins Medicine, United States
Zhengge Wang,
Nanjing Drum Tower Hospital, China
Guofeng Zhou,
Fudan University, China

*CORRESPONDENCE
Fei Chen
✉ shuibin1988@163.com
Zhenyu Dai
✉ ycsydzy@163.com
Yijun Dong
✉ 295243804@qq.com

†These authors have contributed equally to this work and share first authorship

RECEIVED 06 August 2024
ACCEPTED 27 September 2024
PUBLISHED 09 October 2024

CITATION
Li Q, Jiang C, Qian L, Yang J, Mu T, Dong C, Wang S, Wang Z, Liu H, Dong Y, Dai Z and Chen F (2024) Prognostic value of multi-PLD ASL-based cerebral perfusion ASPECTS in acute ischemic stroke.
Front. Neurol. 15:1476937.
doi: 10.3389/fneur.2024.1476937

Prognostic value of multi-PLD ASL-based cerebral perfusion ASPECTS in acute ischemic stroke

Qingqing Li[1,2†], Chaojun Jiang[3†], Linqing Qian[1], Jing Yang[1], Tianchi Mu[2], Congsong Dong[2], Shu Wang[2], Zhenyu Wang[2], Hengheng Liu[2], Yijun Dong[4*], Zhenyu Dai[2*] and Fei Chen[2,5*]

[1]Department of Radiology, Suzhou Wuzhong People's Hospital, Suzhou, Jiangsu, China, [2]Department of Radiology, Affiliated Hospital 6 of Nantong University, Yancheng, Jiangsu, China, [3]Department of Radiology, The People's Hospital of Danyang, Affiliated Danyang Hospital of Nantong University, Danyang, Jiangsu, China, [4]Department of Ultrasound, Affiliated Hospital 6 of Nantong University, Yancheng, Jiangsu, China, [5]Department of Radiology, Affiliated Yancheng Third People's Hospital of Jiangsu Vocational College of Medicine, Yancheng, Jiangsu, China

Introduction: We aimed to verify the application value of the Alberta Stroke Program Early CT Score (ASPECTS) based on multiple post-labeling delay (multi-PLD) arterial spin labeling (ASL) for outcome assessment in acute ischemic stroke (AIS) patients.

Method: The endpoint was modified Rankin scale score at 90 days (90-day mRS). Patients were divided into the good outcome (0–2) and poor outcome (3–6) groups. The independent samples *t*-test, Mann-Whitney *U*-test, and χ^2-test were used to compare clinical and imaging parameters between groups. We used partial correlation analysis to evaluate the relationships between ASPECTS and outcomes. Multivariate logistic regression analysis was used to examine potential independent prognostic indicators. The receiver operating characteristic (ROC) curve analysis was used to evaluate the performance of the independent prognostic indicators in predicting outcomes.

Results: Fifty-five AIS patients were included. The good outcome group had a lower baseline National Institutes of Health Stroke Scale (NIHSS; $Z = -3.413$, $P < 0.001$) and infarct core volume (ICV; $Z = -3.114$, $P = 0.002$) as well as higher cerebral blood flow (CBF)-ASPECTS ($Z = -3.835$, $P < 0.001$) and cerebral blood volume (CBV)-ASPECTS ($Z = -4.099$, $P < 0.001$). Higher CBF-ASPECTS ($r = -0.459$, $P = 0.001$), and CBV-ASPECTS ($r = -0.502$, $P < 0.001$) were associated with a lower 90-day mRS. The baseline NIHSS, CBF-ASPECTS, and CBV-ASPECTS were identified as independent prognostic indicators. The AUCs of the baseline NIHSS, CBF-ASPECTS, and CBV-ASPECTS were 83.3, 87.4, and 89.9%, respectively. Combining NIHSS with CBF-ASPECTS and CBV-ASPECTS, the AUC significantly improved to 96.3%. The combined three factors showed a significant difference compared to the baseline NIHSS ($Z = 2.039$, $P = 0.041$) and CBF-ASPECTS ($Z = 2.099$, $P = 0.036$), but no difference with CBV-ASPECTS ($Z = 1.176$, $P = 0.239$).

Conclusions: The ASPECTS based on multi-PLD ASL is a valuable tool for identifying independent prognostic indicators and assessing clinical outcomes in AIS patients. The baseline NIHSS, combined with CBF-ASPECTS and CBV-ASPECTS, enhances the predictive efficacy of clinical outcomes in AIS

patients. The CBV-ASPECTS alone can offer comparable predictive efficacy to the combination.

KEYWORDS

acute ischemic stroke, Alberta Stroke Program Early CT Score, arterial spin labeling, cerebral blood flow, cerebral blood volume

1 Introduction

Acute ischemic stroke (AIS) is now the most fatal condition in China, and its global impact is on the rise (1, 2). Permanent damage to brain cells can occur within minutes of losing blood supply. The most successful way to rescue patients and reduce their disabilities is to rapidly restore the flow of blood to the brain (3, 4). A growing attention has been paid to cerebral perfusion, particularly represented in quantitative parameters, as a strong association has been found between the presence of good brain perfusion and favorable radiological and clinical outcomes in patients with AIS (5).

Arterial spin labeling (ASL) is a non-invasive imaging approach that enables quantitative measurements of cerebral perfusion in AIS patients (6). However, the accuracy can be affected by several factors, the most significant being the applied post-labeling delay (PLD) (7). For different populations, the duration for hydrogen protons in the blood to progress from the initiation of the labeling procedure to the location of collection, i.e., the arterial transit time (ATT) may be dissimilar. Earlier studies utilizing single-PLD ASL have been observed to either overestimate or underestimate cerebral blood flow (CBF) (8, 9). Multiple acquisitions can reduce bias, and obtain additional information, such as cerebral blood volume (CBV) and ATT (10). However, it also increases time costs. Recently, multiple post-labeling delay (multi-PLD) ASL has been shown to improve signal-to-noise ratio (SNR) and temporal efficiency as a single-acquisition, time-coded quantitative technology (11–14). In several trials, multi-PLD ASL has been proven to be accurate and consistent in measuring cerebral perfusion in healthy adults and children (15–17). To summarize, this imaging method requires a shorter scanning duration but improves the accuracy, sensitivity, and reliability of cerebral perfusion (18–21).

The Alberta Stroke Program Early CT Score (ASPECTS) provides a simple means of evaluating early ischemic changes in the middle cerebral artery (MCA) blood supply area of individuals with AIS (22). ASPECTS was originally designed for unenhanced CT images. However, the ideal ASPECTS would be to assess the area of early ischemic changes on a perfusion map to identify the core of the infarct (23). Computed tomography perfusion and magnetic resonance perfusion imaging are considered the benchmark for assessing cerebral perfusion. However, their applications were restricted due to its invasive nature and the potential risk of allergic reactions to contrast agents. Thus, examining the ASPECTS based on ASL is highly significant. Nevertheless, there is a scarcity of research on the correlation between ASPECTS determined by ASL and the prognosis of ischemic stroke. Currently, there are only two studies that rely on single-PLD ASL and solely employ visual artificial analysis on the CBF parameter map (24, 25). However, both the assessment of CBF by single-PLD ASL and the CBF-ASPECTS based on visual were lacking in accuracy. Therefore, we hypothesized that the ASPECTS based on multi-PLD ASL could detect imaging independent prognostic indicators of AIS patients, and was an effective tool for prognostic assessment.

In this study, we used multi-PLD ASL to quantitatively assess CBF, ATT, and CBV in the brain tissue of AIS patients with non-major vessel occlusion. The ASPECTS of CBF, ATT, and CBV were calculated. Combined with clinical data, we analyzed whether perfusion ASPECTS were correlated with the clinical outcome of AIS patients, whether they were independent prognostic indicators, and their efficacy in predicting the clinical outcome.

2 Materials and methods

2.1 Patients

A total of 55 AIS patients (36 men [65.45%]; mean [SD] age, 66.61 [11.56] years) were enrolled between December 2020 and March 2022 (Figure 1). All patients underwent MRI examinations within 24–48 h after symptom onset. The trial was approved by the ethics committee of Yancheng Third People's Hospital (Ethics No. 2020-77). All participants in this trial provided informed consent.

The inclusion criteria were as follows: (1) a confirmed diagnosis of AIS according to the guidelines (26); (2) patients who have exceeded the time window and cannot be treated with thrombolysis or embolization; (3) adults aged 18 or older.

The exclusion criteria were as follows: (1) images with artifacts; (2) AIS in the posterior or bilateral anterior circulation; (3) hemorrhagic transformation; (4) lesions with a minimum diameter of $\leq$0.5 cm; (5) a history of previous stroke; (6) diffusion or cerebral perfusion abnormalities due to non-acute ischemic stroke; (7) patients with serious diseases of other systems.

2.2 Clinical assessment

All participants received standard medical therapy, including antiplatelet aggregation, anticoagulation and lipid lowering. Every patient received a neurological score based on the National Institutes of Health Stroke Scale (NIHSS; range, 0–42, with higher scores indicating greater deficit) on admission. The clinical and demographic parameters of the patient were noted from the electronic medical record (Table 1), including age, sex, history of atrial fibrillation, hyperlipidemia, diabetes mellitus, hypertension, alcohol abuse, and smoking. According to the modified Rankin Scale score at 90 days (90-day mRS), scores range from 0 to 6, with scores higher than 2 indicating a poor outcome. Therefore,

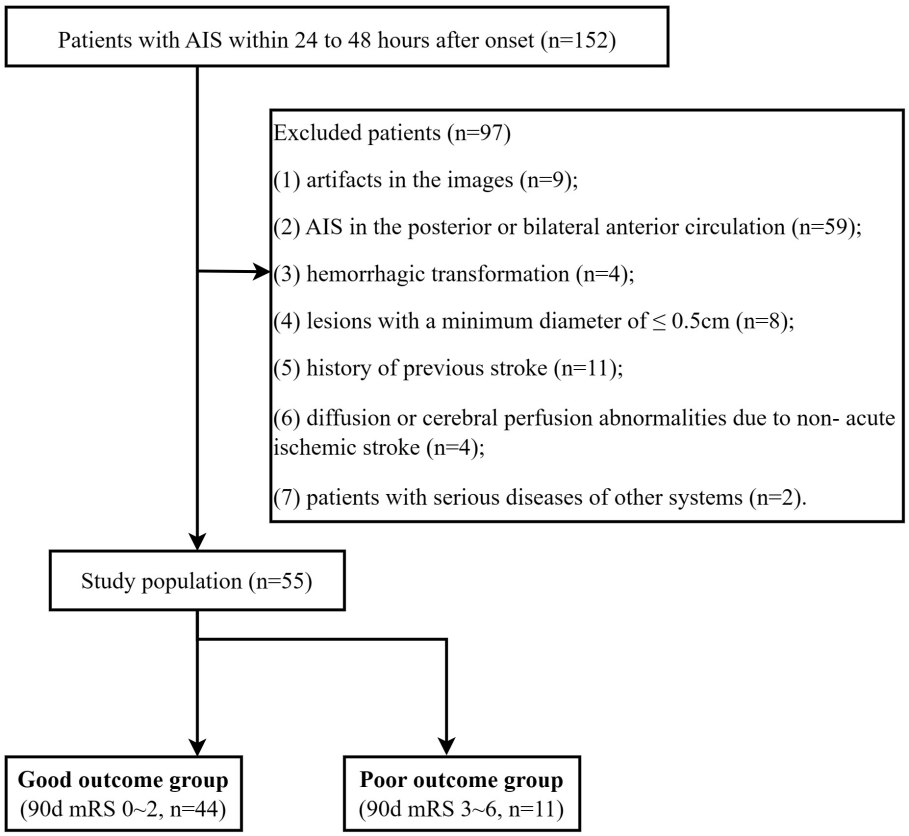

FIGURE 1
Study flow diagram.

patients were divided into the good outcome group (0–2) and the poor outcome group (3–6).

2.3 MR imaging protocol

In this trial, MRI examination was conducted using a 3 T unit (Discovery 750, GE Healthcare, Waukesha, WI, USA) with a 24-channel head and neck coil. The routine MRI protocol included T_2-weighted imaging (T_2WI; TR: 4,357 ms, TE: 1,000 ms), T_2-based fluid attenuation inversion recovery (T_2WI-FLAIR; TR: 9,000 ms, TE: 140 ms), T_1-weighted imaging (T_1WI; TR: 2,213.1 ms, TE: 77.2 ms), diffusion weighted imaging (DWI; TR: 3,586 ms, TE: 77.2 ms, b: 1,000 s/mm^2), 3D time-of-flight (TOF) MRA (TR: 20 ms; TE: 3.4–5 ms). Multi-PLD ASL was simulated with the following parameters: PLD_{1-7} = 1.0, 1.22, 1.48, 1.78, 2.1, 2.63, 3.32 s; TR: 5,978 ms, TE: 11.5 ms, FOV: 22 cm × 22 cm, thickness: 4.5 mm, number of layers: 106, resolution: 4.67 mm × 4.67 mm, NEX: 1, scan duration: 4 min 2 s.

2.4 Imaging assessment

The infarct core was defined as the area with ADC <620 ($\times 10^{-6}$ mm^2/s), and the infarct core volume (ICV) was automatically obtained by Astroke software (version 1.0, Animage Beijing Technology Co, Ltd) based on the ADC map (27, 28).

Multi-PLD ASL data were quantitatively analyzed through an automatic software CereFlow (http://www.cereflow.cn; Animage Beijing Technology Co, Ltd; Figures 2, 3). The processing steps were as follows: Firstly, physiological noise and motion correction were performed between the marker and control pictures, followed by pairwise subtraction (29). Using a conventional non-linear iterative curve fitting method based on the traditional single-chamber perfusion model, mean perfusion maps of multi-PLD ASL were generated. These maps were based on quantitative values of CBF and CBV, which were corrected for ATT. The SimpleITK (http://www.simpleitk.org) normalization tool was applied to the estimated perfusion images to generate the ATT, CBF, and CBV values for ASPECTS. The difference index of perfusion between the left and right brain regions was calculated, using the quantification algorithm given as follows:

$$\frac{(L-R)}{(L+R)}2. \quad (1)$$

The regions where the difference index ≥0.2 were considered to be regions with ischemic changes (24). Based on the above formula and thresholds, we recorded the number of regions with cerebral ischemic changes in the ASPECTS brain regions and

TABLE 1 Demographic, clinical characteristics, and ASL parameters of the good and poor outcome groups.

Characteristic	Good ($n = 44$)	Poor ($n = 11$)	$t/Z/\chi^2$	P-value
Age, year[a]	68 ± 11	75 ± 11	−1.986	0.052
Male sex, *n* (%)	28 (63.64)	8 (72.73)	0.322	0.571
ICV, ml[b]	6.71 (2.09, 19.89)	11.67 (6.96, 31.76)	−3.114	0.002*
Risk factors, *n* (%)				
Atrial fibrillation	6 (13.64)	2 (18.18)	0.146	0.702
Hypertension	36 (81.82)	11 (100)	2.340	0.126
Diabetes mellitus	15 (34.09)	1 (9.09)	2.666	0.102
Hyperlipidemia	20 (45.45)	6 (54.55)	0.292	0.589
Smoking history	12 (27.27)	4 (36.36)	0.353	0.553
Alcohol abuse	11 (25)	2 (18.18)	0.227	0.634
NIHSS[b]	3 (1, 6)	8 (4, 13)	−3.413	<0.001*
ASL parameters				
CBF-ASPECTS[b]	7 (5, 9)	3 (2, 4)	−3.835	<0.001*
CBV-ASPECTS[b]	7 (6, 9)	4 (2, 4)	−4.099	<0.001*
ATT-ASPECTS[b]	10 (10, 10)	10 (9, 10)	−1.772	0.181

n, number of cases.
[a]($\overline{\chi}$±s).
[b][M (Q1, Q3)].
NIHSS, baseline National Institutes of Health Stroke Scale; ASPECTS, Alberta Stroke Program Early CT Score; ICV, infarct volume; CBF-ASPECTS, CBF-based ASPECTS; CBV-ASPECTS, CBV-based ASPECTS; ATT-ASPECTS, ATT-based ASPECTS.
The marked with "*" is statistically significant ($P < 0.05$).

calculated ASPECTS based on CBF, CBV, and ATT, respectively, by subtracting the number of regions from 10.

All participants in this study underwent imaging evaluations by two neuroradiologists (F.C. and C.J.J.), each with at least 10 years of experience in MR imaging. Conflicts were resolved through consensus, and the mean level was measured for statistical analysis.

2.5 Statistical methods

Analyses were performed using SPSS software (Version 26, IBM, Armonk, NY, USA) and MedCalc software (Version 20, Belgium, GER). To compare the variables of the good outcomes group and the poor outcomes group, we employed independent samples *t*-test or Mann-Whitney *U*-test (non-normal distribution) for continuous variables and χ^2-test for categorical variables. The relationship between ASPECTS and clinical outcomes (90-day mRS) was analyzed using partial correlation analysis. Based on the between-group comparison results, binary logistic regression was utilized to investigate potential independent prognostic indicators, with a *p*-value selected at $P < 0.1$. Due to the collinearity among the ASPECTS of perfusion parameters, it is necessary to develop logistic regression models separately with clinical data for conducting multi-factor analysis. The receiver operating characteristic (ROC) curve was used to evaluate the effectiveness of individual prognostic indicators or their combination in differentiating AIS patients with different clinical outcomes. The DeLong test was used to statistically compare the areas under the curves (AUC). Statistical significance was defined as $P < 0.05$.

3 Results

3.1 Clinical and imaging comparison between the good outcome group and the poor outcome group

The images of AIS with different outcome were shown in Figures 2, 3. Compared to the poor outcome group, the good outcome group had a lower baseline NIHSS ($Z = -3.413$, $P < 0.001$), ICV ($Z = -3.114$, $P = 0.002$), and higher CBF-ASPECTS ($Z = -3.835$, $P < 0.001$), and CBV-ASPECTS ($Z = -4.099$, $P < 0.001$; Table 1). There were no significant differences in age, sex, atrial fibrillation, hypertension, diabetes, hyperlipidemia, smoking, alcohol abuse, or ATT-ASPECTS between the two groups (all $P > 0.05$).

3.2 Correlation between ASPECTS of perfusion parameters and clinical outcome

With the partial correlation analysis, the clinical outcome (90-day mRS) showed separate negative correlations with CBF-ASPECTS ($r = -0.459$, $P = 0.001$), and CBV-ASPECTS ($r = -0.502$, $P < 0.001$), correcting for baseline NIHSS and ICV as covariates (Figure 4). Nevertheless, there was no correlation found between ATT-ASPECTS and clinical outcomes ($r = -0.099$, $P = 0.482$).

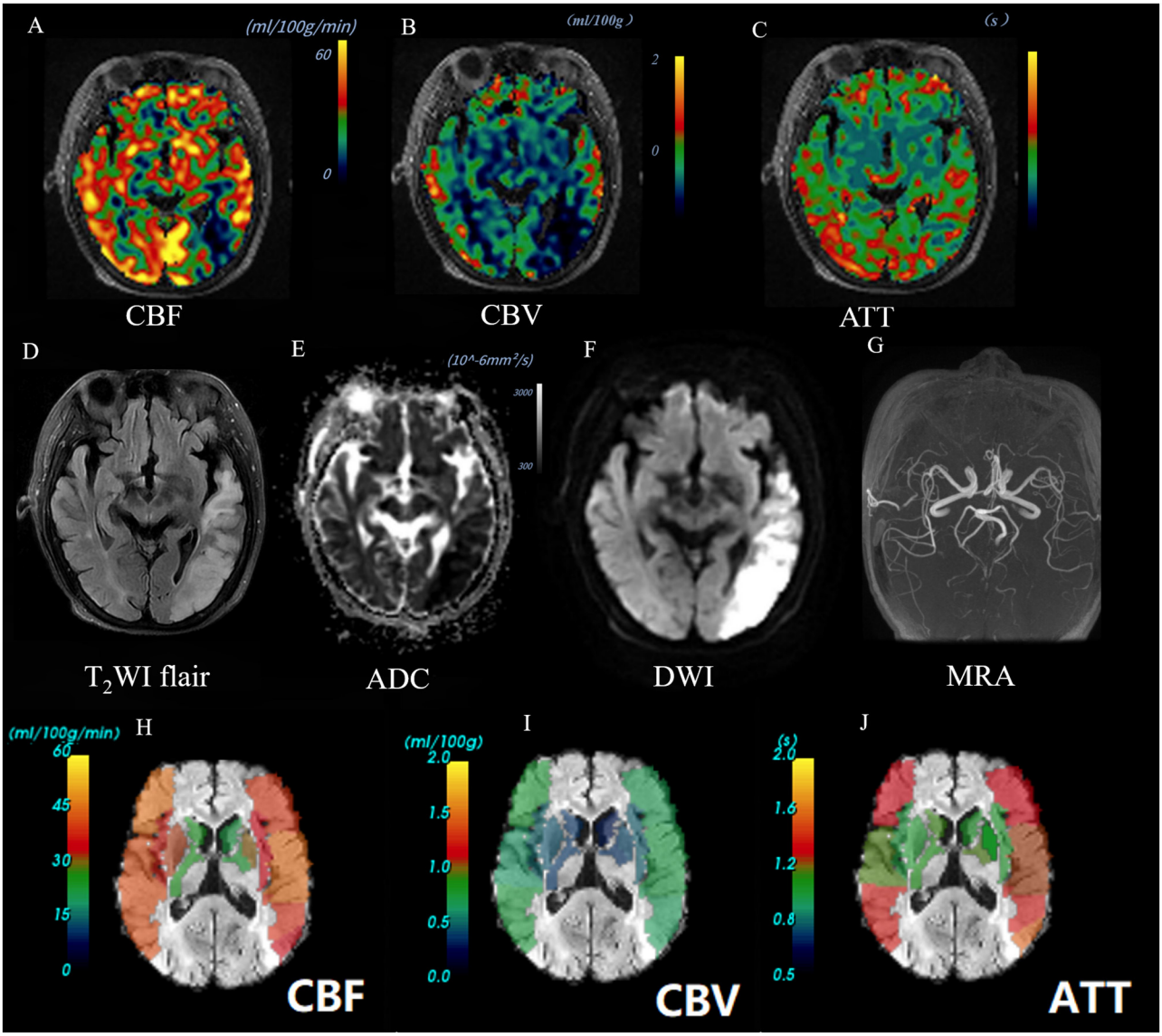

FIGURE 2
Images of an AIS patient with a good outcome (90-day mRS = 0). A 66-year-old female patient was diagnosed with AIS in the left temporal lobe. Baseline NIHSS score of 1 point, 90-day mRS score of 0 point. The CBF perfusion map **(A)** and CBV perfusion map **(B)** showed low perfusion of the lesion. The ATT perfusion map **(C)** revealed an insignificant change. The lesion showed high signal on T_2Flair **(D)** and DWI map (b = 1,000) **(F)**, and the ADC value decreased **(E)**. The 3D-TOF-MRA map showed no obvious stenosis or occlusion **(G)**. The ASPECTS template was used to standardize the perfusion parameters across 10 different zones. **(H–J)** The scores obtained were as follows: CBF-ASPECTS: 8 points, CBV ASPECTS: 9 points, ATT-ASPECTS: 10 points. Warm-to-cold color bars represent values from high to low.

3.3 Multivariate logistic regression analysis of prognostic indicators

Potential prognostic indicators including age, ICV, baseline NIHSS, CBF-ASPECTS, and CBV-ASPECTS were identified based on the comparison between groups with different clinical outcomes. Due to the collinear relationship between CBF-ASPECTS and CBV-ASPECTS, two logistic regression models were constructed separately. Model 1 (Table 2) showed that the baseline NIHSS (OR = 1.67, $P = 0.023$) and CBF-ASPECTS (OR = 0.32, $P = 0.016$) were independent prognostic indicators. Model 2 (Table 3) showed that the baseline NIHSS (OR = 1.55, $P = 0.030$) and CBV-ASPECTS (OR = 0.41, $P = 0.016$) were independent prognostic indicators.

3.4 The predictive efficacy analysis of independent prognostic indicators

The Receiver Operating Characteristic (ROC) analysis was employed to evaluate the potential of independent prognostic indicators and their combination in accurately distinguishing the different clinical outcomes of AIS patients (Figure 5). Table 4 showed that the baseline NIHSS had an AUC of 83.3% [$P < 0.001$,

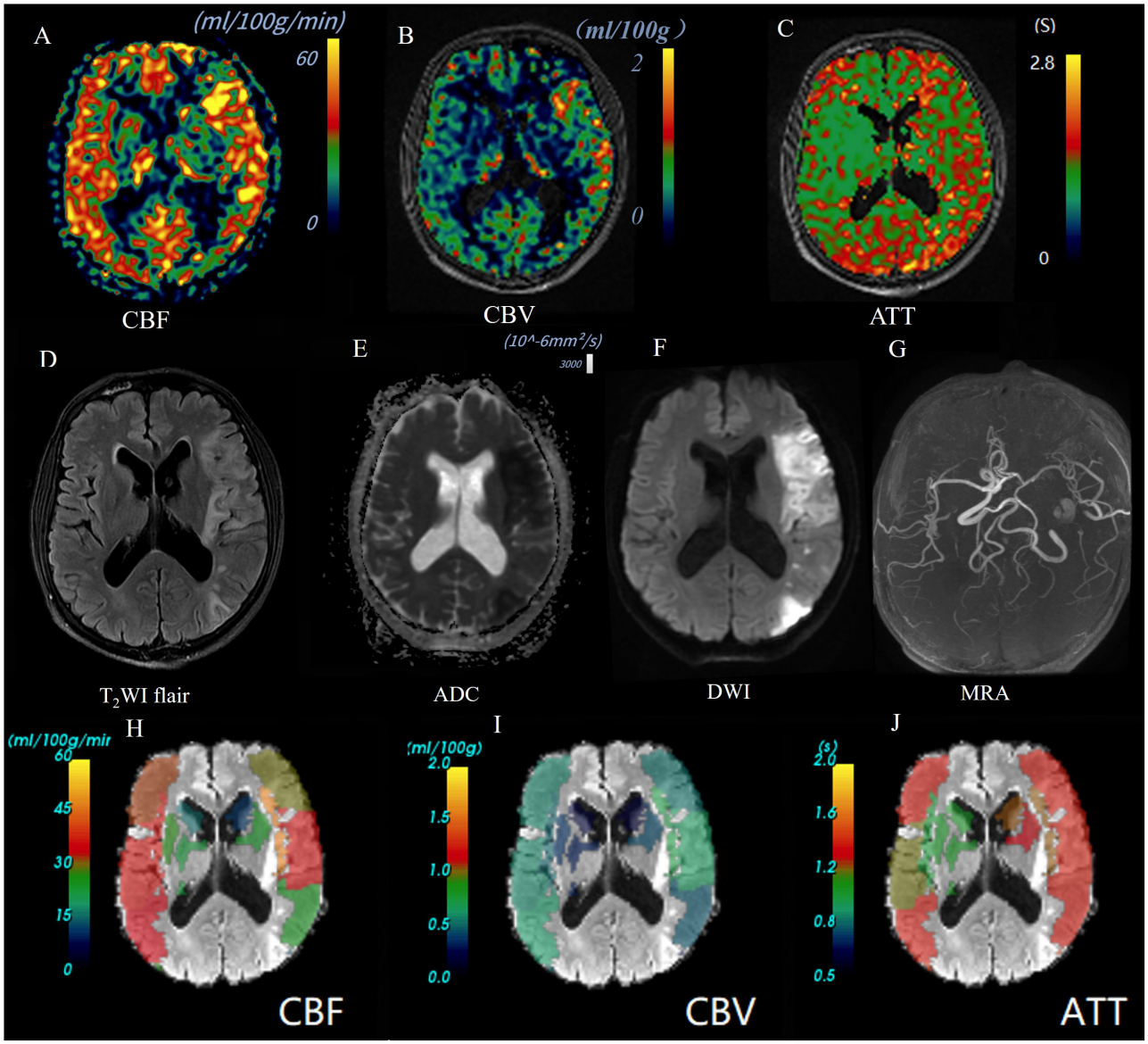

FIGURE 3
Images of an AIS patient with a poor outcome (90-day mRS = 4). A 55-year-old male patient was diagnosed as AIS in left temporal parietal occipital lobe. Baseline NIHSS score 10 points, 90 d mRS score 4 points. CBF perfusion map **(A)** and CBV perfusion map **(B)** showed high perfusion of the lesion; ATT perfusion map revealed extended arrival time **(C)**. The lesion showed high signal on T2Flair **(D)** and DWI map (b = 1,000) **(F)**, and the ADC value decreased **(E)**. 3D-TOF-MRA map showed the left middle cerebral artery is narrow but not occluded **(G)**. Warm-to-cold color bars represent values from high to low. The ASPECTS template was used to standardize the perfusion parameters across 10 different zones. **(H–J)** The scores obtained were as follows: CBF-ASPECTS: 6 points, CBV ASPECTS: 9 point, ATT-ASPECTS: 8 points.

95% confidence interval [CI] = 0.698–0.968, with a cut-off value of 3]; the CBF-ASPECTS had an AUC of 87.4% ($P < 0.001$, 95% CI = 0.777–0.971, with a cut-off value of 8); and the CBV-ASPECTS had an AUC of 89.9% ($P < 0.001$, 95% CI = 0.793–1.000, with a cut-off value of 6). The sensitivity of the baseline NIHSS, CBF-ASPECTS, and CBV-ASPECTS were 0.727, 0.818, and 0.818, and the specificity were 0.864, 0.795, and 0.886, respectively. When adding CBF-ASPECTS and CBV-ASPECTS to the baseline NIHSS, the AUC significantly improved to 96.3% ($P < 0.001$, 95% CI = 0.916–1.000). Both sensitivity and specificity were increased to 0.909. The combination of the three indicators was found to have a significant difference compared to the baseline NIHSS ($Z = 2.039$, $P = 0.041$), CBF-ASPECTS ($Z = 2.099$, $P = 0.036$), but no difference with CBV-ASPECTS ($Z = 1.176$, $P = 0.239$).

4 Discussion

This study showed that the baseline NIHSS, ICV, CBF-ASPECTS, and CBV-ASPECTS significantly differed between AIS patients with good or poor outcomes. A higher CBF-ASPECTS or CBV-ASPECTS was associated with a good outcome.

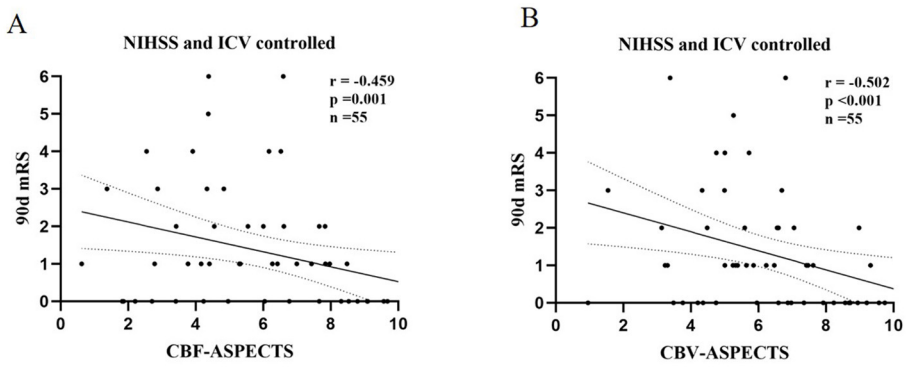

FIGURE 4
The partial correlation analysis of CBF-ASPECTS **(A)** / CBV-ASPECTS **(B)** and clinical outcome (90-day mRS) with baseline NIHSS and ICV controlled.

TABLE 2 Multivariate logistic regression analysis of independent prognostic indicators (model 1).

Prognostic indicators	B	S.E.	Wald χ^2	Exp (B)	95% CI	*P*-value
Age	0.048	0.058	0.697	1.05	0.94–1.18	0.404
NIHSS	0.511	0.226	5.136	1.67	1.07–2.60	0.023*
ICV (ml)	0.047	0.036	1.720	1.05	0.98–1.13	0.190
CBF-ASPECTS	−1.131	0.469	5.812	0.32	0.13–0.81	0.016*

NIHSS, baseline National Institutes of Health Stroke Scale; ASPECTS, Alberta Stroke Program Early CT Score; ICV, infarct core volume; CBF-ASPECTS, CBF-based ASPECTS.
The marked with "*" is statistically significant ($P < 0.05$).

TABLE 3 Multivariate logistic regression analysis of independent prognostic indicators (model 2).

Prognostic indicators	B	S.E.	Wald χ^2	Exp(B)	95% CI	*P*-value
Age	0.056	0.064	0.761	1.06	0.93–1.20	0.383
NIHSS	0.436	0.202	4.653	1.55	1.04–2.30	0.030*
ICV (ml)	0.028	0.029	0.922	1.03	0.97–1.10	0.337
CBV-ASPECTS	−0.895	0.372	5.780	0.41	0.20–0.85	0.016*

NIHSS, baseline National Institutes of Health Stroke Scale; ASPECTS, Alberta Stroke Program Early CT Score; ICV, infarct core volume; CBV-ASPECTS, CBV-based ASPECTS.
The marked with "*" is statistically significant ($P < 0.05$).

Furthermore, baseline NIHSS, CBF-ASPECTS and CBV-ASPECTS were independent prognostic indicators. When adding CBF-ASPECTS and CBV-ASPECTS to the baseline NIHSS, the predictive efficacy of clinical outcome significantly improved. Moreover, the CBV-ASPECTS by itself could offer comparable predictive accuracy to the combination.

The multi-PLD ASL technique is currently one of the most advanced non-invasive imaging methods for detecting brain perfusion (7). By setting multiple PLDs, it avoids the influence of blood flow velocity differences on brain perfusion measurement (13). Multi-PLD ASL has been used in the evaluation of various neurological disorders such as stroke, epilepsy, cognitive impairment, and more. Specifically, diffusion-prepared multi-PLD ASL can be utilized for assessing neurological disorders by detecting the blood-brain barrier function (30, 31). This study leveraged the accurate measurement characteristics of multi-PLD ASL to analyze perfusion changes at the voxel level in patients with AIS. Subsequently, the ASPECTS template was used for localization to analyze the perfusion ASPECTS of these AIS patients.

Consistent with previous trials (32, 33), we found that the good outcome group had a lower baseline NIHSS, ICV. This implies that a smaller baseline injury leads to a better prognosis, which is a logical outcome. A recent study employing multi-PLD ASL found that a higher rCBF, as indicated by ROI analysis, was associated with better early neurological outcomes in AIS patients (6). Manual tracking of ROIs, despite being the most popular method, has many shortcomings. Firstly, ROI-based values are inaccurate, especially when the ROIs contain partial volume effects. Secondly, the infarct areas of stroke patients often contain cortical and gray matter, making it difficult to accurately measure. Thirdly, in longitudinal studies, it is challenging to precisely replicate the same ROI manually, which can also cause bias in the results. In our investigation, we refrained from using the commonly utilized ROI-based analysis method. Instead of that, we employed an analysis method that combines voxel analysis with the ASPECTS template.

In this study, we found that the poor outcome group had lower CBF-ASPECTS and CBV-ASPECTS, and that both CBF-ASPECTS and CBV-ASPECTS were negatively correlated with clinical outcomes (90-day mRS). Lower CBF-ASPECTS based on pseudo-continuous ASL (single-PLD = 2,000 ms) was associated with a poor prognosis for AIS patients, which has been verified in a previous study (24). Moreover, there was a collinear relationship between CBF and CBV, so it is reasonable that there was a consistent rule between CBV-ASPECTS and the prognosis of AIS. To date, there is a lack of studies on the relationship between CBF-ASPECTS and CBV-ASPECTS based on multi-PLD ASL as a more accurate non-invasive perfusion detection method, and the clinical outcome of AIS. In our study, we also found conclusions that are consistent with the study of single PLD ASL. The association between CBF-ASPECTS and CBV-ASPECTS and clinical outcome was observed, with baseline NIHSS and ICV serving as control variables. Our results indicate that there was no statistical difference in ATT-ASPECTS between two groups of AIS patients with different outcomes, and it was not correlated with the clinical outcome. However, ATT has a significant impact on perfusion measurements (12). Additionally, in this study, CBF and CBV measured by multi-PLD ASL were also corrected based on ATT. One possible reason could be that all cases in this group were AIS patients without large vessel occlusion, resulting in no significant changes in ATT and thus no statistical difference between the two prognosis groups. Further investigation is needed to determine the value of ATT-ASPECTS in clinical prognosis assessment of AIS patients with large vessel occlusion. Given the significant correlation between CBF-ASPECTS/CBV-ASPECTS and patient outcomes, multi-PLD ASL could be considered as a non-invasive alternative to CT perfusion for prognostic evaluation, especially in AIS patients with non-major vessel occlusion.

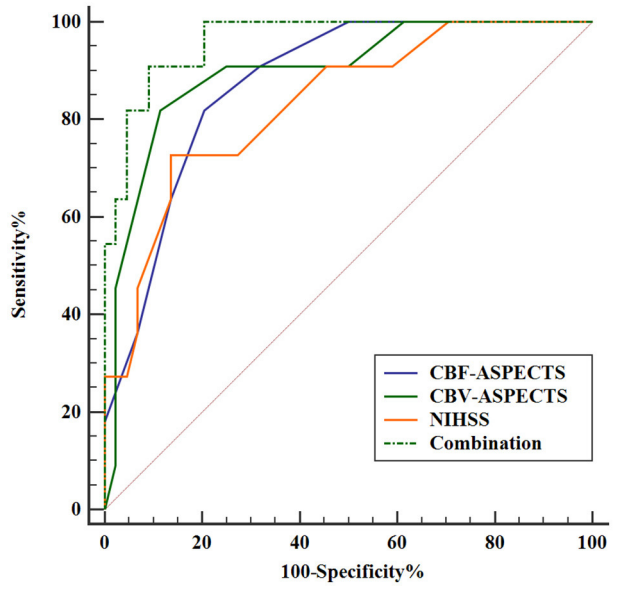

FIGURE 5
ROC curves analysis of independent prognostic indicators and their combination for predicting clinical outcomes.

Additionally, the ischemic penumbra is also an important factor influencing the clinical prognosis of AIS patients. Studies have reported that the oxygen extraction fraction map, based on quantitative susceptibility mapping (QSM), holds significant value in detecting the ischemic penumbra in AIS patients (34). Future research can incorporate it into multi-factor prognostic models as a prognostic indicator for analysis. Moreover, studies have shown that the longitudinal changes in magnetic susceptibility values within ischemic lesions based on QSM are significantly related to neurological functional prognosis (35). This provides new insights into exploring non-invasive methods for prognosis assessment in AIS patients.

In our study, independent prognostic indicators were screened from potential prognostic indicators by constructing binary logistic regression models. Given the collinearity between CBF-ASPECTS and CBV-ASPECTS, we constructed two logistic regression models, results shown that CBF-ASPECTS, CBV-ASPECTS, and baseline NIHSS were independent prognostic indicators. The baseline NIHSS serves as an independent prognostic indicator in AIS patients, as evidenced by previous studies (24, 30). Our study was the first to find that CBF-ASPECTS and CBV-ASPECTS based on multi-PLD ASL were independent prognostic indicators in AIS patients. The OR values for CBF-ASPECTS and CBV-ASPECTS were 0.32 and 0.41, respectively, suggesting that the increase in CBF-ASPECTS and CBV-ASPECTS was an inhibiting factor for poor prognosis. It provides a basis for clinical identification of AIS patients with poor prognosis and timely targeted treatment to improve prognosis.

Further analysis of independent prognostic indicators revealed strong predictive efficacy. Baseline NIHSS, CBF-ASPECTS, and CBV-ASPECTS demonstrated good areas under the curve for predicting various outcomes in AIS patients: 0.833, 0.874, and 0.899, respectively. The optimal thresholds for CBF-ASPECTS and CBV-ASPECTS are 8 and 6, respectively, both exhibiting a sensitivity of 0.818. In contrast, the optimal threshold for

TABLE 4 ROC curves analysis of independent prognostic indicators and their combination for predicting clinical outcomes.

Variables	AUC	SE	*P*-value	95%CI	Sensitivity	Specificity	Youden J
NIHSS	0.833	0.0493	<0.001	0.698–0.968	0.727	0.864	0.591
CBF-ASPECTS	0.874	0.0540	<0.001	0.777–0.971	0.818	0.795	0.613
CBV-ASPECTS	0.899	0.068	<0.001	0.793–1.000	0.818	0.886	0.704
Combination	0.963	0.023	<0.001	0.916–1.000	0.909	0.909	0.818

NIHSS, baseline National Institutes of Health Stroke Scale; ASPECTS, Alberta Stroke Program Early CT Score; CBF-ASPECTS, CBF-based ASPECTS; CBV-ASPECTS, CBV-based ASPECTS; Combination, combination of NIHSS, CBF-ASPECTS, and CBV-ASPECTS.

baseline NIHSS is 3, demonstrating a relatively low sensitivity of 0.727. The specificity values ranged from 0.795 for CBF-ASPECTS to 0.886 for CBV-ASPECTS, with the baseline NIHSS falling in between at 0.864. The results presented above demonstrate that both the baseline NIHSS and CBF-ASPECTS or CBV-ASPECTS were effective in identifying potential poor outcomes in AIS patients, with CBV-ASPECTS displaying relatively better predictive capability.

By integrating baseline NIHSS with perfusion indicators CBF-ASPECTS and CBV-ASPECTS, the combined area under the curve improved to 0.963, enhancing both sensitivity and specificity to 0.909. The AUC of this combined indicator demonstrates a statistically significant improvement over the baseline NIHSS. It is evident that enhancing the perfusion ASPECTS information from multi-PLD ASL improves the predictive accuracy for patient prognosis in clinical practice. Simultaneously, we observed no statistical variance between the AUC of the combined indicator and the AUC of CBV-ASPECTS. The results suggested that CBV-ASPECTS can provide a similar predictive efficacy as the baseline NIHSS combined with CBF/CBV-ASPECTS. In essence, this suggested that in scenarios with insufficient clinical data, evaluating ASPECTS based on multi-PLD ASL could still provide valuable insights into the prognosis of stroke patients. The discovery is of great significance. As it is common in clinical practice to not acquire accurate baseline clinical neurological function assessment data for patients.

There are several shortcomings in this study. Firstly, the sample size of the trial was relatively small. Secondly, this study only included AIS patients with non-major vessel embolization who were treated with conservative medical therapy. Future studies should include larger cohorts and patients treated with thrombolysis or thrombectomy to better generalize the findings. Thirdly, the factors affecting the long-term prognosis of stroke are complex and diverse, and this study standardized the baseline clinical characteristics as much as possible by including only AIS patients with first-ever unilateral anterior circulation infarction and standard medical clinical treatment. Fourthly, the clinical prognostic value of multi-PLD ASL has not been directly compared with other advanced imaging techniques. In future research, we will conduct a direct comparison of the prognostic value of multi-PLD ASL with dynamic susceptibility contrast MRI, QSM or positron emission tomography imaging in AIS patients to further establish the utility of multi-PLD ASL.

5 Conclusion

In conclusion, the ASPECTS based on multi-PLD ASL is a valuable tool for identifying independent prognostic indicators and assessing clinical outcomes in AIS patients. CBF-ASPECTS and CBV-ASPECTS, as independent prognostic indicators, are significantly associated with clinical outcomes. Furthermore, the baseline NIHSS combined with CBF-ASPECTS and CBV-ASPECTS enhances the predictive efficacy of clinical outcomes in AIS patients. CBV-ASPECTS alone can offer a comparable predictive efficacy to the combination. Thus, the incorporation of multi-PLD ASL into routine clinical evaluation may significantly enhance the precision of prognosis, thereby allowing for more tailored interventions in AIS patients.

Data availability statement

The datasets presented in this article are not readily available because, the raw data supporting the conclusions of this article will be made available by the authors, without undue reservation. Requests to access the datasets should be directed to Qingqing Li, lsh946901143@163.com.

Ethics statement

The studies involving humans were approved by Ethics Committee of the Yancheng Third People's Hospital. The studies were conducted in accordance with the local legislation and institutional requirements. The participants provided their written informed consent to participate in this study.

Author contributions

QL: Methodology, Writing – original draft. CJ: Supervision, Writing – review & editing. LQ: Formal analysis, Methodology, Writing – review & editing. JY: Data curation, Formal analysis, Methodology, Writing – review & editing. TM: Conceptualization, Data curation, Writing – review & editing. CD: Conceptualization, Methodology, Supervision, Writing – review & editing. SW: Methodology, Supervision, Writing – review & editing. ZW: Data curation, Methodology, Writing – review & editing. HL: Data curation, Methodology, Writing – review & editing. YD: Conceptualization, Methodology, Writing – review & editing. ZD: Project administration, Supervision, Writing – review & editing. FC: Data curation, Supervision, Writing – review & editing.

Funding

The author(s) declare financial support was received for the research, authorship, and/or publication of this article. This work was supported by the Foundation Plan for Outstanding People of The Sixth Peak of Jiangsu Province of China (No. 2019-WSN-313), the Foundation Plan for The Fifth Scientific Research Project of "333 Project" of Jiangsu Province of China (No. BRA2019031), the Research Foundation of Science and Technology Bureau of Yancheng (No. YCBK2023041), the Foundation Plan for Suzhou "Science, Education and Health" Youth Science and Technology Program (No. KJXW2023084), the Special Project of Clinical Medicine of Nantong University (No. YXY-Z2023003), and the School-Local Collaborative Innovation Research Project of Jiangsu Vocational College of Medicine (No. 20239102). The funders had no role in study design, data collection and analysis, decision to publish, or preparation of the manuscript.

Conflict of interest

The authors declare that the research was conducted in the absence of any commercial or financial relationships that could be construed as a potential conflict of interest.

Publisher's note

References

1. The Lancet Neurology. The fight against stroke must go on. *Lancet Neurol.* (2020) 19:369. doi: 10.1016/S1474-4422(20)30107-1

2. Yi X, Luo H, Zhou J, Yu M, Chen X, Tan L, et al. Prevalence of stroke and stroke related risk factors: a population based cross sectional survey in southwestern China. *BMC Neurol.* (2020) 20:5. doi: 10.1186/s12883-019-1592-z

3. Chen H, Khunte M, Colasurdo M, Malhotra A, Gandhi D. Thrombectomy vs. medical management for posterior cerebral artery stroke: systematic review, meta-analysis, and real-world data. *Neurology.* (2024) 102:e209315. doi: 10.1212/WNL.0000000000209315

4. Wei B, Wang Z, Wu S, Orgah J, Zhu J, Song W. Improving collateral circulation: a potential adjunctive strategy to prevent or slow the progression of vascular dementia. *Neuropsychiatr Dis Treat.* (2021) 17:3061–7. doi: 10.2147/NDT.S328446

5. Brugnara G, Herweh C, Neuberger U, Bo Hansen M, Ulfert C, Mahmutoglu MA, et al. Dynamics of cerebral perfusion and oxygenation parameters following endovascular treatment of acute ischemic stroke. *J Neurointerv Surg.* (2022) 14:17163. doi: 10.1136/neurintsurg-2020-017163

6. Luijten SPR, Bos D, van Doormaal P-J, Goyal M, Dijkhuizen RM, Dippel DWJ, et al. Cerebral blood flow quantification with multi-delay arterial spin labeling in ischemic stroke and the association with early neurological outcome. *Neuroimage Clin.* (2023) 37:103340. doi: 10.1016/j.nicl.2023.103340

7. Hernandez-Garcia L, Lahiri A, Schollenberger J. Recent progress in ASL. *Neuroimage.* (2019) 187:3–16. doi: 10.1016/j.neuroimage.2017.12.095

8. Hara S, Tanaka Y, Ueda Y, Hayashi S, Inaji M, Ishiwata K, et al. Noninvasive evaluation of CBF and perfusion delay of Moyamoya disease using arterial spin-labeling MRI with multiple postlabeling delays: comparison with 15O-Gas PET and DSC-MRI. *Am J Neuroradiol.* (2017) 38:696–702. doi: 10.3174/ajnr.A5068

9. Golay X, Ho ML. Multidelay ASL of the pediatric brain. *Br J Radiol.* (2022) 95:20220034. doi: 10.1259/bjr.20220034

10. Wang DJ, Alger JR, Qiao JX, Gunther M, Pope WB, Saver JL, et al. Multi-delay multi-parametric arterial spin-labeled perfusion MRI in acute ischemic stroke—comparison with dynamic susceptibility contrast enhanced perfusion imaging. *Neuroimage Clin.* (2013) 3:1–7. doi: 10.1016/j.nicl.2013.06.017

11. von Samson-Himmelstjerna F, Madai VI, Sobesky J, Guenther M. Walsh-ordered hadamard time-encoded pseudocontinuous ASL (WH pCASL). *Magn Reson Med.* (2016) 76:1814–24. doi: 10.1002/mrm.26078

12. Ishida S, Kimura H, Isozaki M, Takei N, Fujiwara Y, Kanamoto M, et al. Robust arterial transit time and cerebral blood flow estimation using combined acquisition of Hadamard-encoded multi-delay and long-labeled long-delay pseudo-continuous arterial spin labeling: a simulation and *in vivo* study. *NMR Biomed.* (2020) 33:e4319. doi: 10.1002/nbm.4319

13. Cohen AD, Agarwal M, Jagra AS, Nencka AS, Meier TB, Lebel RM, et al. Longitudinal reproducibility of MR perfusion using 3D pseudocontinuous arterial spin labeling with hadamard-encoded multiple postlabeling delays. *J Magn Reson Imaging.* (2020) 51:1846–53. doi: 10.1002/jmri.27007

14. Ya J, Zhou D, Ding J, Rajah GB, Wu Y, Yang X, et al. Arterial spin labeling-MR may be an alternative to SPECT for evaluating cerebral perfusion in patients with unilateral middle cerebral artery stenosis. *Neurol Res.* (2020) 42:621–9. doi: 10.1080/01616412.2020.1782080

15. Guo J, Holdsworth SJ, Fan AP, Lebel MR, Zun Z, Shankaranarayanan A, et al. Comparing accuracy and reproducibility of sequential and Hadamard-encoded multidelay pseudocontinuous arterial spin labeling for measuring cerebral blood flow and arterial transit time in healthy subjects: a simulation and *in vivo* study. *J Magn Reson Imaging.* (2018) 47:1119–32. doi: 10.1002/jmri.25834

16. Xu X, Tan Z, Fan M, Ma M, Fang W, Liang J, et al. Comparative study of multi-delay pseudo-continuous arterial spin labeling perfusion MRI and CT perfusion in ischemic stroke disease. *Front Neuroinform.* (2021) 15:719719. doi: 10.3389/fninf.2021.719719

17. Lou X, Yu S, Scalzo F, Starkman S, Ali LK, Kim D, et al. Multi-delay ASL can identify leptomeningeal collateral perfusion in endovascular therapy of ischemic stroke. *Oncotarget.* (2017) 8:2437–43. doi: 10.18632/oncotarget.13898

18. Pellerin A, Khalifé M, Sanson M, Rozenblum-Beddok L, Bertaux M, Soret M, et al. Simultaneously acquired PET and ASL imaging biomarkers may be helpful in differentiating progression from pseudo-progression in treated gliomas. *Eur Radiol.* (2021) 31:7395–405. doi: 10.1007/s00330-021-07732-0

19. Puig O, Henriksen OM, Vestergaard MB, Hansen AE, Andersen FL, Ladefoged CN, et al. Comparison of simultaneous arterial spin labeling MRI and (15)O-H(2)O PET measurements of regional cerebral blood flow in rest and altered perfusion states. *J Cereb Blood Flow Metab.* (2020) 40:1621–33. doi: 10.1177/0271678X19874643

20. Dolui S, Li Z, Nasrallah IM, Detre JA, Wolk DA. Arterial spin labeling versus (18)F-FDG-PET to identify mild cognitive impairment. *Neuroimage Clin.* (2020) 25:102146. doi: 10.1016/j.nicl.2019.102146

21. Schertz M, Benzakoun J, Pyatigorskaya N, Belkacem S, Sahli-Amor M, Navarro V, et al. Specificities of arterial spin labeling (ASL) abnormalities in acute seizure. *J Neuroradiol.* (2020) 47:20–6. doi: 10.1016/j.neurad.2018.11.003

22. Prakkamakul S, Yoo AJ. ASPECTS CT in acute ischemia: review of current data. *Top Magn Reson Imaging.* (2017) 26:103–12. doi: 10.1097/RMR.0000000000000122

23. Chu Y, Shen G-C, Ma G, Xu X-Q, Lu S-S, Jiang L, et al. Diagnostic accuracy of using Alberta Stroke Program Early Computed Tomography Score on CT perfusion map to predict a target mismatch in patients with acute ischemic stroke. *Neuroradiology.* (2022) 64:1321–30. doi: 10.1007/s00234-021-02892-8

24. Yu S, Ma SJ, Liebeskind DS, Yu D, Li N, Qiao XJ, et al. ASPECTS-based reperfusion status on arterial spin labeling is associated with clinical outcome in acute ischemic stroke patients. *J Cereb Blood Flow Metab.* (2018) 38:382–92. doi: 10.1177/0271678X17697339

25. Kidoguchi M, Akazawa A, Komori O, Isozaki M, Higashino Y, Kawajiri S, et al. Prediction of occurrence of cerebral infarction after successful mechanical thrombectomy for ischemic stroke in the anterior circulation by arterial spin labeling. *Clin Neuroradiol.* (2023) 33:965–71. doi: 10.1007/s00062-023-01295-x

26. Lou M, Ding J, Hu B, Bai Y, Wang B, Qu Y, et al. Chinese Stroke Association guidelines for clinical management of cerebrovascular disorders: executive summary and 2019 update on organizational stroke management. *Stroke Vasc Neurol.* (2020) 5:250–9. doi: 10.1136/svn-2019-000321

27. Liu H, Li T, Ding Y, Zhu L, Hui FK, Zhou T, et al. Predictive accuracy of an ADC map for hemorrhagic transformation in acute ischemic stroke patients after successful recanalization with endovascular therapy. *Ann Transl Med.* (2022) 10:591. doi: 10.21037/atm-22-2255

28. Juan C-J, Lin S-C, Li Y-H, Chang C-C, Jeng Y-H, Peng H-H, et al. Improving interobserver agreement and performance of deep learning models for segmenting acute ischemic stroke by combining DWI with optimized ADC thresholds. *Eur Radiol.* (2022) 32:5371–81. doi: 10.1007/s00330-022-08633-6

29. Shao X, Wang Y, Moeller S, Wang DJJ. A constrained slice-dependent background suppression scheme for simultaneous multislice pseudo-continuous arterial spin labeling. *Magn Reson Med.* (2018) 79:394–400. doi: 10.1002/mrm.26643

30. Uchida Y, Kan H, Sakurai K, Horimoto Y, Hayashi E, Iida A, et al. APOE ε4 dose associates with increased brain iron and β-amyloid via blood-brain barrier dysfunction. *J Neurol Neurosurg Psychiat.* (2022) 2022:93. doi: 10.1136/jnnp-2021-328519

31. Uchida Y, Kan H, Sakurai K, Oishi K, Matsukawa N. Contributions of blood-brain barrier imaging to neurovascular unit pathophysiology of Alzheimer's disease and related dementias. *Front Aging Neurosci.* (2023) 15:1111448. doi: 10.3389/fnagi.2023.1111448

32. Yoshimura S, Sakai N, Yamagami H, Uchida K, Beppu M, Toyoda K, et al. Endovascular therapy for acute stroke with a large ischemic region. *N Engl J Med.* (2022) 386:1303–13. doi: 10.1056/NEJMoa2118191

33. Suomalainen OP, Elseoud AA, Martinez-Majander N, Tiainen M, Forss N, Curtze S. Comparison of automated infarct core volume measures between non-contrast computed tomography and perfusion imaging in acute stroke code patients evaluated for potential endovascular treatment. *J Neurol Sci.* (2021) 426:117483. doi: 10.1016/j.jns.2021.117483

34. Uchida Y, Kan H, Inoue H, Oomura M, Shibata H, Kano Y, et al. Penumbra detection with oxygen extraction fraction using magnetic susceptibility in patients with acute ischemic stroke. *Front Neurol.* (2022) 13:752450. doi: 10.3389/fneur.2022.752450

35. Uchida Y, Kan H, Kano Y, Onda K, Sakurai K, Takada K, et al. Longitudinal changes in iron and myelination within ischemic lesions associate with neurological outcomes: a pilot study. *Stroke.* (2024) 55:1041–50. doi: 10.1161/STROKEAHA.123.044606

frontiers | Frontiers in Neurology

TYPE Original Research
PUBLISHED 19 November 2024
DOI 10.3389/fneur.2024.1478583

OPEN ACCESS

EDITED BY
Shuai Ren,
Affiliated Hospital of Nanjing University of Chinese Medicine, China

REVIEWED BY
Leonard Yeo,
National University Health System, Singapore
Fei Chen,
Yancheng Third People's Hospital, China

*CORRESPONDENCE
Li Zhu
9363923@qq.com
Wei Wang
waywang@126.com

†These authors have contributed equally to this work and share first authorship

RECEIVED 10 August 2024
ACCEPTED 04 November 2024
PUBLISHED 19 November 2024

CITATION
Ren K, He J, Zhu L, Gu Y, Qu H, Zhao Y and Wang W (2024) Assessing stroke recurrence in sICAS: a study on mCSVD score and culprit plaque magnetic resonance characteristics. *Front. Neurol.* 15:1478583.
doi: 10.3389/fneur.2024.1478583

Assessing stroke recurrence in sICAS: a study on mCSVD score and culprit plaque magnetic resonance characteristics

Kaixuan Ren[1†], Juan He[2†], Li Zhu[3*], Yue Gu[1], Hang Qu[1], Yi Zhao[1] and Wei Wang[1*]

[1]Department of Medical Imaging, The Affiliated Hospital of Yangzhou University, Yangzhou University, Yangzhou, China, [2]Department of Neurology, The Affiliated Hospital of Yangzhou University, Yangzhou University, Yangzhou, China, [3]Department of Medical Imaging, The Second Affiliated Hospital of Nantong University, Nantong, China

Background: Recurrent ischemic stroke in patients with symptomatic intracranial atherosclerotic stenosis (sICAS) can be attributed to two main causes: intracranial atherosclerotic stenosis (ICAS) and cerebral small vessel disease (CSVD). This study investigates the potential associations between stroke recurrence and the modified cerebral small vessel disease (mCSVD) burden score, as well as the characteristics of culprit plaques related to intracranial artery high-resolution vessel wall imaging (HR-VWI).

Methods: A total of 145 patients presenting sICAS underwent intracranial artery HR-VWI and routine cranial MRI at two large Chinese hospitals from December 2019–2022 were participants of this retrospective analysis. Standard MRI scans were used to calculate the mCSVD score. Following a 12-month observation period, the patients were categorized into two distinct groups depending on whether or not they experienced a subsequent stroke.

Results: Within 12 months, 32 patients experienced stroke recurrence. The recurrence group's mCSVD score was higher compared to the non-recurrence group ($p < 0.001$). Their luminal stenosis and culprit plaque thickness and burden were also higher ($p < 0.05$). Additionally, higher rates of diabetes, T1WI hyperintensity of culprit plaques, and significant plaque enhancement were observed in the recurrence group ($p < 0.05$). The adjusted Cox regression model indicated that the mCSVD score (HR = 1.730, 95% CI 1.021–2.933, $p = 0.042$) and T1WI hyperintensity of the culprit plaque (HR = 6.568, 95% CI 1.104–39.059, $p = 0.039$) remained significantly independent risk variables. The combination of the mCSVD score and T1WI hyperintensity of the culprit plaque demonstrated the highest efficacy in predicting stroke recurrence ($z = 2.678$, $p < 0.05$).

Conclusion: The mCSVD score, associated with T1WI hyperintensity of culprit plaque, effectively predicts stroke recurrence and can be easily obtained, offering high clinical value.

KEYWORDS

small vessel disease burden, stroke recurrence, vessel wall imaging MRI, acute ischemic stroke, intracranial atherosclerotic stenosis

Introduction

Intracranial atherosclerotic stenosis (ICAS) is a major causative factor for ischemic stroke worldwide. Patients with symptomatic ICAS experience stroke recurrence risk between 20 and 30%. The rates of morbidity and mortality associated with recurrent strokes are significantly higher than those observed after the initial onset (1, 2). Research has shown a strong association between the features of intracranial arterial culprit plaques, as detected by high-resolution vessel wall imaging (HR-VWI), and the recurrence of stroke (3–5). Many studies have primarily examined the characteristics of intracranial large arteries, overlooking the effect of cerebral small vessel disease (CSVD) burden on stroke recurrence.

CSVD involves brain damage from cerebral arterioles, veins, and capillaries, leading to clinical, imaging, and pathological changes (6, 7). Multiple CSVD imaging biomarkers are frequently detected in individuals with stroke, and CSVD heightens the possibility of stroke occurrence and recurrence (8). Currently, the presence of lacunes, cerebral microbleeds (CMBs), enlarged perivascular spaces (EPVS), and white matter hyperintensity (WMH) was used to compute the total CSVD burden score (tCSVD score; 0–4 points) (9). It has been demonstrated that the tCSVD score is a predictive measure of cognitive impairment and stroke recurrence (10, 11). Nevertheless, this scoring method is relatively simple and does not adequately capture the severity of each imaging biomarker. Amin et al. developed a modified CSVD burden score (mCSVD score) with a maximum of 7 points, incorporating both the overall burden of CSVD and the severity of individual imaging biomarkers. Their research, which was confirmed by three cohort studies, showed that the modified cerebral small vessel disease (mCSVD) score improved the ability to predict dementia and cognitive decline compared to the traditional CSVD (tCSVD) score (12). However, to evaluate the predictive value of this score for stroke recurrence, more research is necessary.

This study hypothesizes that integrating intracranial arterial plaque characteristics with the mCSVD score may improve the prediction of stroke recurrence in patients. This research uses HR-VWI to evaluate plaque characteristics and the mCSVD score to assess the overall burden of CSVD in the brain. The study aims to develop a predictive model and evaluate its efficacy in predicting stroke recurrence in ischemic stroke patients, thereby equipping clinicians with a tool for early assessment of recurrence risk.

Methods

Patient data, inclusion, and exclusion criteria

The ischemic stroke patients ($n = 199$) were admitted to our hospital's Department of Neurology between December 2019 and December 2022 and were the participants of a retrospective analysis. Magnetic resonance angiography (MRA), electrocardiogram (ECG), carotid ultrasound, and magnetic resonance imaging (MRI) were among the diagnostic assessments that each patient received. Within 1 week, an HR-VWI examination was conducted in cases where these diagnostic techniques identified the stroke under the TOAST criteria as large artery atherosclerosis or suggested that intracranial atherosclerosis was the cause of the ischemic event. The availability of all baseline data and the finding of the HR-VWI assessment indicating plaque development in all culprit's vessels were the inclusion criteria for this investigation. All patients received conservative therapy with basic pharmacological interventions during hospitalization. The following were the exclusion criteria: (1) non-atherosclerotic vascular conditions, such as vasculitis of the primary nervous system (5 cases) or vascular malformation (2 cases); (2) cases of the culprit vessels where stenosis was absent (11 cases); (3) 50% or more of the ipsilateral extracranial carotid artery stenosis (8 cases); (4) possibility of cardiogenic embolism risk factors, including atrial fibrillation (13 cases); and (5) low image quality (15 cases). The unit's ethical committee authorized the trial, which involved 145 patients after the consent of the participants or their legal guardians was obtained (Figure 1).

Data collection

Gender, age, smoking, diabetes, hypertension, and coronary heart disorder were among the baseline data that were collected. Moreover, a venous blood sample (5 mL) of individuals who had fasted was acquired on the second day of post-hospitalization to evaluate blood lipids, high-sensitivity C-reactive protein, lipoprotein-associated phospholipase A2, fasting blood glucose, homocysteine, and cystatin C.

mCSVD score assessment

Following the international imaging standard for cerebral small vessel disease 2 (STRIVE-2) (6) and the results of MRI examinations conducted during hospitalization, the mCSVD score was assessed. According to the number of lacunes, they were given a score between 0 and 3 (0 = none, 1 = 1–2, 2 = 3–5, and 3 = more than 5). White matter hyperintensities (WMH) were scored from 0 to 3 according to the Fazekas scale. If cerebral microbleeds (CMBs) were found, they received a score of 1. The cumulative mCSVD burden score totaled 7 points.

HR-VWI protocol

The Siemens Verio 3.0T MR imaging equipment (Siemens, Erlangen, Germany) was utilized in this work. The scanning protocol included magnetic resonance time-of-flight angiography (TOF-MRA), diffusion-weighted imaging (DWI), T2 fluid-attenuated inversion recovery (T2-FLAIR), susceptibility-weighted imaging (SWI), and three-dimensional T1 variable flip angle fast spin echo (3D-T1-SPACE). 3D-T1-SPACE sequence performed both pre-and post-injection of the gadoxetic acid (contrast agent). The scan lasted for 7 min and 16 s. The contrast agent was administered with 0.1 mmol/kg. The whole presentation of the bilateral internal carotid artery, the anterior cerebral artery, the middle cerebral artery, the posterior cerebral artery, the basilar artery, the intracranial segment of the vertebral artery, and the P1–P2 segment of the posterior cerebral artery were all included in the scanning range.

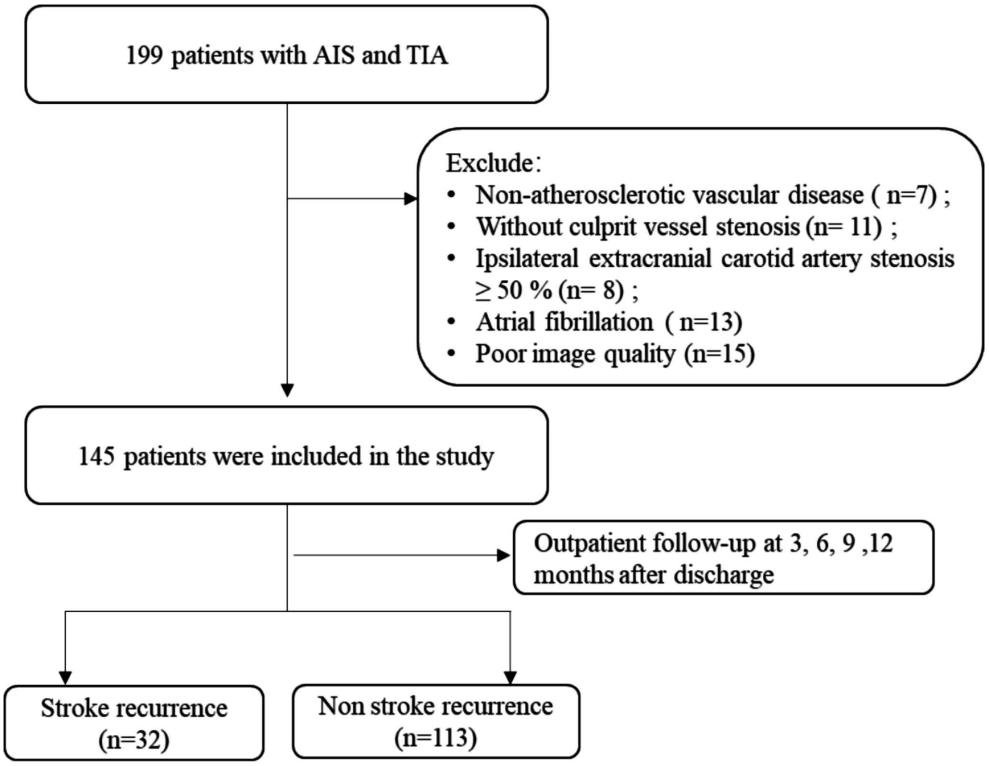

FIGURE 1
Schematic representation of the process for enrolling patients. AIS, acute ischemic stroke; TIA, transient ischemic attack.

Culprit plaque characteristics assessment

Based on DWI symptoms and signs of acute infarction or clinical neurological impairments that were reported, the culprit vessels were identified. The culprit plaque was determined to produce the largest stenosis of the culprit vessel on HR-VWI. Culprit plaque analysis involved measuring plaque thickness, residual lumen area, plaque burden, and lumen stenosis, evaluating the T1WI hyperintensity, positive remodeling, and significant plaque enhancement (13). A five-year-experienced neuroradiologist and a second-year graduate student in neuroimaging evaluated all images. By consulting with a third neuroradiologist with 10 years of expertise, disagreements were settled (Figure 2).

Stroke recurrence assessment

Upon discharge, all patients were prescribed antiplatelet and lipid-lowering drugs for an average duration of 25 days or more each month. Outpatient follow-up assessments were carried out three, six, nine, and twelve months after discharge. DWI showed the existence of additional acute infarcts in the same vascular area, which was used to diagnose stroke recurrence. In the absence of imaging data for suspected stroke recurrence, follow-up clinicians determined the occurrence of outcome events depending on the presence of new neurological impairment symptoms characterized by sudden neurological deterioration. It was considered neurological deterioration when new neurological problems continued for more than 24 h or when the National Institutes of Health Stroke Scale (NIHSS) rose by more than 4 points. The time interval between discharge and the endpoint event's occurrence was designated as the recurrence time. In cases where no endpoint event occurred, it was defined as the duration from discharge to the last outpatient follow-up (14).

Statistical analysis

The SPSS software (version 21.0; IBM Corp., Armonk, NY, USA) was used in the present study for all statistical analysis. With the Kolmogorov–Smirnov test, the distribution of the data was assessed for normality. Variables were analyzed and compared using the *t*-test, with a normal distribution, and indicated as mean ± standard deviation (SD). When a variable did not have a normal distribution, it was presented as the median (interquartile range), and the Mann–Whitney U test was used for comparison. The data of the counts were analyzed via chi-square analysis and displayed as frequency (percentage). The mCSVD burden score was compared between the groups with and without recurrence using the rank sum test. The variables with a *p*-value less than 0.05 were incorporated from the univariate analysis into the multivariate Cox regression model, using the backward stepwise approach to ascertain independent variables. Variables including age, gender, hypertension history, smoking history, and those found in the univariate analysis with a *p*-value less than 0.05 were included in the binary logistic regression analysis to calculate propensity scores. The propensity score covariate adjustment approach was used to mitigate confounding variables in the prediction model. The model's performance was evaluated via the Receiver

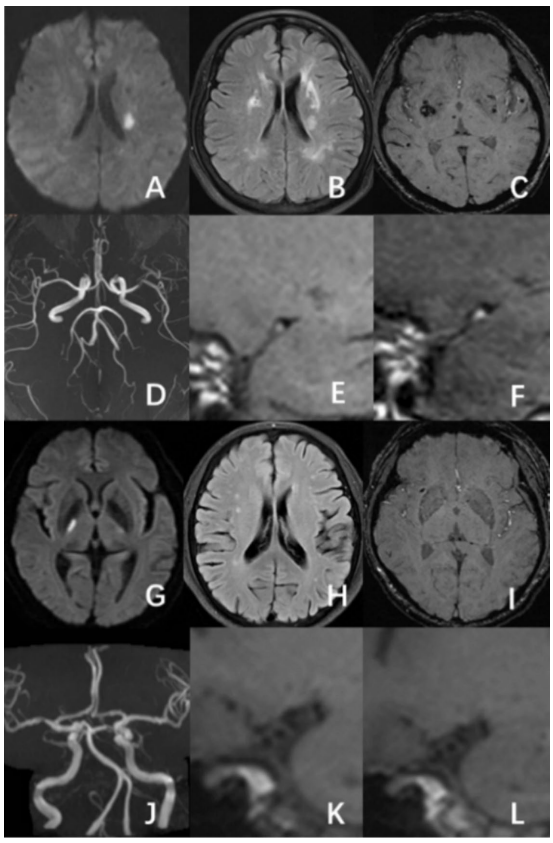

FIGURE 2
A male patient, aged 58, had an acute ischemic stroke in the left basal ganglia area, with a mCSVD score of 5 points. HR-VWI demonstrated hyperintensity on T1WI and significant enhancement on the culprit plaque present at the left middle cerebral artery **(A–F)**. A 65-year-old male patient was experiencing an acute ischemic stroke in the right thalamus. The patient has a mCSVD score of 2 points. HR-VWI revealed T1WI iso-intensity and mild enhancement in the right middle cerebral artery culprit plaque **(G–L)**.

Operating Characteristic (ROC) curve and the area under the curve (AUC). A p-value of less than 0.05 was considered statistically significant.

Results

A total of 145 patients (96 = males; 49 = females) with symptomatic intracranial atherosclerotic stenosis were included in this study. The mean age of the participants was 63 ± 12 years. Notably, 22.1% (32 out of 145) of the patients experienced stroke recurrence within 12 months. Diabetes was much more common in the recurrent group in relation to the group without recurrence (53.1% vs. 27.1%, $p = 0.010$). Additionally, the levels of fasting blood glucose and glycosylated hemoglobin comparing the two groups differed significantly ($p < 0.05$). As shown in Table 1, the recurrence group's serum HDL levels were significantly ($p < 0.05$) lower in relation to the group without recurrence.

The recurrence group exhibited a higher number of lacunes, a greater WMH Fazekas grade, and an increased count of CMBs than the non-recurrence group, showing significant outcomes (all $p < 0.05$). As shown in Table 2, a significant difference in the median mCSVD load score was present between both groups, with the recurrence group scoring 4 points and the non-recurrence scoring 2 ($p < 0.001$).

No significant disparity was observed in the proportion of anterior circulation between the two groups (50.0% vs. 57.5%, $p = 0.546$), nor did the proportion of AIS patients (81.3% vs. 67.3%, $p = 0.187$). The plaque thickness (1.75 ± 0.53 vs. 1.50 ± 0.36), plaque burden (77.53 ± 10.26 vs. 70.81 ± 10.12), and lumen stenosis degree (51.81 ± 21.29 vs. 39.62 ± 17.21) of the recurrence group were reported to be significantly greater in relation to the group without recurrence (all $p < 0.05$). In comparison to the non-recurrence group, the recurrence group had a higher incidence of T1WI hyperintensity (53.1% vs. 21.2%, $p = 0.001$). Table 3 shows that the recurrent group had a higher incidence of significant plaque enhancement (53.1% vs. 25.7%, $p = 0.010$) than the non-recurrent group.

After stepwise backward selection, three variables were eventually retained in the Cox regression model: HDL, mCSVD score, and T1WI hyperintensity of the culprit plaque. The mCSVD score (HR = 1.730, 95% CI 1.021 ~ 2.933, $p = 0.042$) and T1WI hyperintensity of the culprit plaque (HR = 6.568, 95% CI 1.104 ~ 39.059, $p = 0.039$) were significant independent risk factors after adjusting the Cox regression model for covariate propensity score (Table 4).

The cutoff value for the mCSVD score in predicting stroke recurrence was determined to be 4 points, according to ROC curve analysis, which also revealed the AUC value to be 0.775, the sensitivity was equal to 62.50%, and the specificity was 87.51%. The AUC of T1WI hyperintensity was 0.659 for the prediction of stroke recurrence, with a sensitivity and a specificity of 53.13 and 76.76%, respectively. In predicting stroke recurrence, the AUC for the mCSVD score, combined with the T1WI hyperintensity of the culprit plaque, was 0.819. Moreover, the specificity and the sensitivity were 80.53 and 71.87%, respectively, showing the results of the Delong test analysis, revealing the culprit plaque's T1WI hyperintensity, in conjunction with the mCSVD score, that had the strongest predictive power for stroke recurrence ($z = 2.678$, $p < 0.05$) (Figure 3). The Kaplan–Meier survival curve indicated that individuals with a mCSVD score exceeding 4 points ($p < 0.001$) and T1WI hyperintensity of the culprit plaque ($p < 0.001$) exhibited an elevated risk of stroke recurrence during follow-up (Figure 4).

Discussion

Intracranial atherosclerotic stenosis and cerebral small vessel disease are essential causes of recurrent stroke patients. However, both follow different pathophysiological mechanisms, but intracerebral atherosclerosis and CSVD typically coexist and share vascular risk factors. Both have a common effect on the occurrence of stroke (15, 16). This study aims to examine the combined effect of two risk variables on stroke recurrence in patients. The study used HR-VWI to determine the type of the culprit plaques in stroke patients. Moreover, the mCSVD score was used to assess the whole brain CSVD disease burden in stroke patients.

Research indicates that individuals with a mCSVD score > 4 points had a 1.730-fold greater chance of experiencing recurrent stroke. The mCSVD score, together with the total CSVD burden score and the severity of prevalent imaging biomarkers of CSVD, offers a reliable

TABLE 1 The baseline clinical data of the non-recurrence and recurrence groups of the study participants.

Characteristic	Non-recurrence group (n = 113)	Recurrence group (n = 32)	$t/z/\chi^2$	p-value
Age [y]	62.82 ± 12.93	65.58 ± 9.84	−1.102	0.272
Male [n (%)]	71 (62.8)	25 (78.1)	−2.607	0.139
Smoking history [n (%)]	25 (22.1)	12 (37.5)	−3.102	0.107
History of hypertension [n (%)]	84 (74.3)	19 (51.4)	−2.713	0.123
History of diabetes [n (%)]	31 (27.4)	17 (53.1)	−7.433	0.010
Admission NIHSS score	2.86 ± 3.77	3.12 ± 3.49	−0.315	0.753
FBG (mmol/L)	6.08 ± 2.55	7.26 ± 2.50	−2.269	0.025
HbA1c (mmol/L)	6.73 ± 1.33	7.32 ± 1.67	−2.012	0.046
TG (mmol/L)	1.68 ± 1.11	1.75 ± 1.00	−0.282	0.778
TC (mmol/L)	4.14 ± 1.05	3.98 ± 1.37	0.681	0.562
HDL (mmol/L)	1.21 ± 0.34	1.07 ± 0.26	2.112	0.037
LDL (mmol/L)	3.33 ± 7.46	2.51 ± 1.26	0.595	0.553
Apolipoprotein A/B	1.33 ± 0.46	1.38 ± 0.59	−0.443	0.658
Lp-PLa2 (ng/ml)	353.86 ± 217.37	327.89 ± 175.31	0.572	0.568
hs-CRP (mg/L)	3.26 ± 10.10	4.51 ± 14.91	−0.734	0.464
Hcy (μmol/L)	14.00 ± 8.08	12.32 ± 4.02	1.397	0.163
Cystatin-C (pg/mL)	21.01 ± 111.61	29.03 ± 139.02	−0.312	0.756

*$p < 0.05$ = statistically significant result.
FBG, fasting blood glucose; NIHSS, national institutes of health stroke scale; Lp-PLa2, lipoprotein-associated phospholipase a2; HbA1c, glycosylated hemoglobin; TC, total cholesterol; TG, triglyceride; LDL, low-density lipoprotein; HDL, high-density lipoprotein; Hcy, homocysteine; hs-CRP, high-sensitivity C-reactive protein.

TABLE 2 Comparison of the CSVD imaging biomarkers and mCSVD score between the recurrence and non-recurrence groups of patients.

Characteristic score	Non-recurrence group (n = 113)	Recurrence group (n = 32)	χ''	p-value
Lacune [n (%)]			17.121	0.001
0	67 (59.3)	8 (25.0)		
1	26 (23.0)	9 (28.1)		
2	18 (15.9)	11 (34.4)		
3	2 (1.8)	4 (12.5)		
WMH [n (%)]			11.05	0.011
0	19 (16.8)	1 (3.1)		
1	54 (47.8)	10 (31.3)		
2	39 (34.5)	21 (65.6)		
3	1 (0.9)	0 (0)		
CMBs [n (%)]			10.884	0.001
0	69 (61.1)	44 (38.9)		
1	9 (28.1)	23 (71.9)		
mCSVD score	2 (1, 3)	4 (3, 5)	−4.843	< 0.001

*$p < 0.05$ = statistically significant result.
WMH, white matter hyperintensity; CMBs, cerebral microbleeds.

assessment of small vessel disease severity across the brain. Initial data from this study indicate the potential effectiveness in predicting stroke recurrence. However, more prospective clinical investigations are necessary to validate these findings. Moreover, stroke patients exhibiting T1WI hyperintensity of the culprit plaque had a 6.568-fold increased risk of recurrence compared to those lacking T1WI hyperintensity. Previous studies on carotid plaques (17, 18) have shown that T1WI hyperintensity of the culprit plaque often signifies the presence of a lipid-rich necrotic core (LRNC) and intraplaque hemorrhage (IPH), with IPH regarded as a component of LRNC. Organizational research studies have demonstrated that plaque fragility is affected by its internal constituents, with LRNCs and IPH

TABLE 3 Comparison of the culprit plaques in the recurrence and non-recurrence groups.

Characteristic	Non-recurrence group ($n = 113$)	Recurrence group ($n = 32$)	$t/z/\chi^2$	p-value
AIS [n (%)]	76 (67.3)	26 (81.3)	2.341	0.187
Plaque thickness (mm)	1.50 ± 0.36	1.75 ± 0.53	−2.467	0.018
Remaining lumen area (mm^2)	4.47 ± 2.58	4.43 ± 3.89	0.188	0.852
Degree of stenosis (%)	39.62 ± 17.21	51.81 ± 21.29	−3.350	0.001
Plaque burden (%)	70.81 ± 10.12	77.53 ± 10.26	−3.309	0.001
Significant enhancement [n (%)]	29 (25.7)	17 (53.1)	6.861	0.010
T1WI hyperintensity [n (%)]	24 (21.2)	17 (53.1)	12.502	0.001

*$p < 0.05$ = statistically significant result.
AIS, acute ischemic stroke; T1WI, T1 weight imaging.

TABLE 4 Cox regression analysis of stroke recurrence risk variables.

Characteristic	Unadjusted		Adjusted	
	HR (95% CI)	p value	HR (95% CI)	p value
HDL	0.377 (0.105 ~ 1.356)	0.135	0.349 (0.065 ~ 1.884)	0.221
mCSVD score	1.675 (1.288 ~ 2.179)	<0.001	1.730 (1.021 ~ 2.933)	0.042
T1WI hyperintensity	5.868 (2,565 ~ 13.427)	<0.001	6.568 (1.104 ~ 39.059)	0.039

*$p < 0.05$ = statistically significant result.
HDL, high-density lipoprotein; T1WI, T1 weight imaging; HR, hazard ratio; CI, confidence interval.

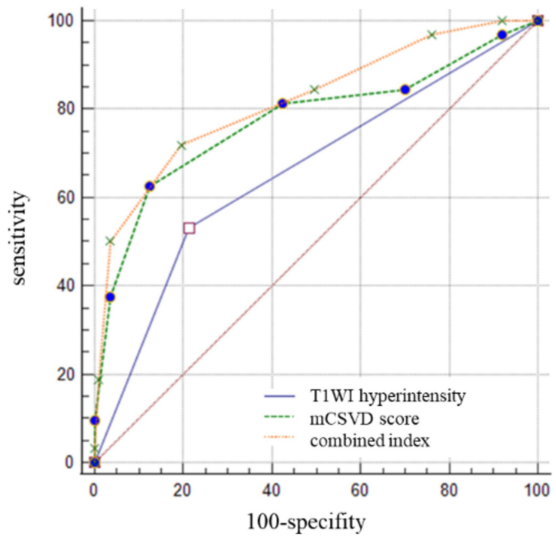

FIGURE 3
The ROC curve analysis of mCSVD, T1WI hyperintensity, and the combined index in predicting stroke recurrence.

potentially increasing the likelihood of plaque rupture and arterial embolism, thereby leading to stroke recurrence (19, 20).

This work has established an integrated prediction model defined by the mCSVD score and T1WI hyperintensity of the culprit plaque. The results reveal that the integrated predictive model has significant effectiveness in predicting stroke recurrence within 1 year among stroke patients. With a specificity of 80.53% and a sensitivity of 71.87%, the combined AUC value of the mCSVD score and the T1WI hyperintensity of culprit plaque was 0.819, greater than any single risk factor, according to the data. Thus demonstrating a robust predictive value. The combined index not only integrated the severity of common imaging subtypes of CSVD but also included the nature of intracranial arterial culprit plaque, which was an important factor influencing the recurrence of stroke. It has a strong clinical and practical value and is simple to promote in clinical environments. This tool can assist clinicians in the preliminary evaluation of recurrence risk in ischemic stroke patients and improve strategies for secondary stroke prevention.

The recurrence group in this study had a higher median mCSVD score, WMH Fazekas grade, CMB number, and number of lacune than the non-recurrence group. According to earlier research, the percentage of WMH detected on MRI in stroke patients might range from 67 to 98% (21). After following up on 7,101 ischemic stroke patients for a year, Ryu et al. verified the correlation between WMH load and hemorrhagic transformation, stroke recurrence, and all-cause mortality. Moreover, the prevalence of WMH in all patients was reported to be 86 and 97% in the group of patients who experienced recurrences (22). However, previous studies have found that the number of cerebral microbleeds is related to cognitive impairment and cerebral hemorrhage after intravenous thrombolysis (23, 24). Large cohort studies are required to investigate the association between CMBs and stroke recurrence in depth. Plaque enhancement, characteristic of susceptible plaques, is associated with capillary growth, inflammation-induced vascular wall stimulation, and endothelial injury (25). Research by Song et al. (4) demonstrates that plaque enhancement independently corresponds with the recurrence of ischemic stroke, with higher enhancement levels increasing the probability of recurrence. In this study, univariate analysis revealed that the proportion of significantly larger plaques in the recurrent group was significantly greater than in the non-recurrent group. In multivariate analysis, the association between stroke recurrence and plaque enhancement was observed to diminish. It was speculated that the differences might be due to Song

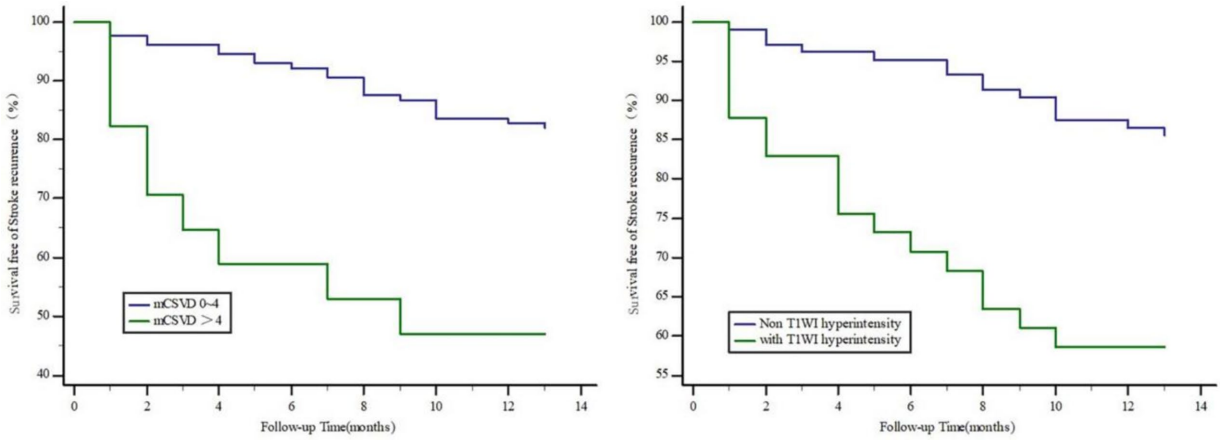

FIGURE 4
Kaplan–Meier survival curve in patients with stroke recurrence. Patients with mCSVD score > 4 points ($p < 0.001$) and T1WI hyperintensity of the culprit plaque ($p < 0.001$) had a higher risk of stroke recurrence at follow-up.

et al. (4) grading the degree of plaque enhancement. In contrast, plaque enhancement was only a categorical variable in the present study. Therefore, more research is necessary to establish the relationship between plaque enhancement and recurrence.

The study found that the occurrence of diabetes was more common in the recurrence group in comparison to the group without recurrence. Additionally, the recurrence group showed elevated fasting blood glucose levels and glycosylated hemoglobin relative to the group without recurrence. Jiao et al. (26) observed a definitive correlation between blood glucose management and the attributes of cerebral atherosclerotic plaques in individuals diagnosed with type 2 diabetes. Inadequate regulation of blood glucose levels will impact the severity and susceptibility of intracranial atherosclerotic plaques, thereby contributing to the higher risk of stroke recurrence. Further investigation is required to understand the precise mechanism by which controlling blood glucose levels affects the likelihood of stroke recurrence in individuals with type 2 diabetes. It was also observed that, in the recurrent group, the blood HDL level was lowered ($p < 0.05$) in contrast to the non-recurrent group. This difference may be attributed to the anti-atherosclerosis impact of HDL (27).

This study has several limitations. Firstly, regarding the selection of research participants and sample size, patients with severe stroke symptoms were often omitted owing to inadequate image quality, possibly leading to a bias toward patients with less severe stroke presentations. Moreover, the sample size and the follow-up period were limited. Further research will mitigate these limitations by augmenting the sample size and prolonging the follow-up duration to enable a more thorough investigation of stroke recurrence. Secondly, regarding imaging data collection, the 3 T MRI demonstrates limited resolution relative to the 5 T and 7 T MRI systems, making it less effective at illustrating intricate characteristics of plaque components, including plaque surface ulcers and fibrous caps. This study obtained data on plaque thickness, stenosis degree, and burden by manual delineation and semi-automated measuring methods. Despite the execution of repeatability examinations, the possibility of error in the results persists. Future initiatives will focus on augmenting image resolution and reducing measurement errors through integrating higher field strength magnetic resonance machines and deploying artificial intelligence software for the automated segmentation and quantification of diverse plaque components. Thirdly, the efficacy of the prediction model has yet to be confirmed. Future initiatives will entail executing multicenter studies to externally evaluate the study results, aiming to improve clinical practitioners' ability to detect patients at elevated risk for stroke recurrence in their standard practice.

Conclusion

Both the mCSVD score and the T1WI hyperintensity of the culprit plaque associated with intracranial arterial were the independent factors related to the risk for stroke recurrence. In conjunction with the T1WI hyperintensity of the culprit plaque, the mCSVD score provides a strong predictive potential for stroke recurrence, allowing for the establishment of a tailored treatment plan and the hierarchical management of sICAS patients.

Data availability statement

The raw data supporting the conclusions of this article will be made available by the authors, without undue reservation.

Ethics statement

The studies involving humans were approved by the Ethics Committee of Yangzhou University Affiliated Hospital (2022-YKL8-(K03)). The studies were conducted in accordance with the local legislation and institutional requirements. The participants provided their written informed consent to participate in this study.

Author contributions

KR: Data curation, Formal analysis, Writing – original draft. JH: Conceptualization, Data curation, Investigation, Methodology,

Writing – original draft. LZ: Data curation, Writing – review & editing. YG: Investigation, Methodology, Writing – original draft. HQ: Conceptualization, Software, Writing – review & editing. YZ: Formal analysis, Resources, Writing – review & editing. WW: Funding acquisition, Writing – review & editing.

Funding

The author(s) declare financial support was received for the research, authorship, and/or publication of this article. This work was supported by the 333 Project of Jiangsu Province (BRA2018196), Yangzhou Municipal Science and Technology Bureau (YZ2019062).

Conflict of interest

The authors declare that the research was conducted in the absence of any commercial or financial relationships that could be construed as a potential conflict of interest.

Publisher's note

References

1. Kleindorfer DO, Towfighi A, Chaturvedi S, Cockroft KM, Gutierrez J, Lombardi-Hill D, et al. 2021 guideline for the prevention of stroke in patients with stroke and transient ischemic attack: a guideline from the American Heart Association/American Stroke Association. *Stroke*. (2021) 52:e364–364e467. doi: 10.1161/STR.0000000000000375

2. de Havenon A, Turan TN. Past, present, and future of intracranial atherosclerosis treatment. *Stroke*. (2024) 55:471–3. doi: 10.1161/STROKEAHA.123.044270

3. Kim JM, Jung KH, Sohn CH, Moon J, Shin JH, Park J, et al. Intracranial plaque enhancement from high resolution vessel wall magnetic resonance imaging predicts stroke recurrence. *Int J Stroke*. (2016) 11:171–9. doi: 10.1177/1747493015609775

4. Song X, Zhao X, Liebeskind DS, Wang L, Xu W, Xu Y, et al. Incremental value of plaque enhancement in predicting stroke recurrence in symptomatic intracranial atherosclerosis. *Neuroradiology*. (2020) 62:1123–31. doi: 10.1007/s00234-020-02418-8

5. Ran Y, Wang Y, Zhu M, Wu X, Malhotra A, Lei X, et al. Higher plaque burden of middle cerebral artery is associated with recurrent ischemic stroke: a quantitative magnetic resonance imaging study. *Stroke*. (2020) 51:659–62. doi: 10.1161/STROKEAHA.119.028405

6. Duering M, Biessels GJ, Brodtmann A, Chen C, Cordonnier C, de Leeuw FE, et al. Neuroimaging standards for research into small vessel disease-advances since 2013. *Lancet Neurol*. (2023) 22:602–18. doi: 10.1016/S1474-4422(23)00131-X

7. Mahammedi A, Wang LL, Williamson BJ, Khatri P, Kissela B, Sawyer RP, et al. Small vessel disease, a marker of brain health: what the radiologist needs to know. *AJNR Am J Neuroradiol*. (2022) 43:650–60. doi: 10.3174/ajnr.A7302

8. Nam KW, Kwon HM, Lim JS, Han MK, Nam H, Lee YS. The presence and severity of cerebral small vessel disease increases the frequency of stroke in a cohort of patients with large artery occlusive disease. *PLoS One*. (2017) 12:e0184944. doi: 10.1371/journal.pone.0184944

9. Staals J, Makin SD, Doubal FN, Dennis MS, Wardlaw JM. Stroke subtype, vascular risk factors, and total MRI brain small-vessel disease burden. *Neurology*. (2014) 83:1228–34. doi: 10.1212/WNL.0000000000000837

10. Ölmez B, Togay Işikay C, Peker E, Sorgun MH. The relationship between renal function and imaging markers and Total burden of cerebral small vessel disease. *Neurologist*. (2022) 27:157–63. doi: 10.1097/NRL.0000000000000388

11. Wardlaw JM, Smith C, Dichgans M. Small vessel disease: mechanisms and clinical implications. *Lancet Neurol*. (2019) 18:684–96. doi: 10.1016/S1474-4422(19)30079-1

12. Amin Al Olama A, Wason J, Tuladhar AM, van Leijsen E, Koini M, Hofer E, et al. Simple MRI score aids prediction of dementia in cerebral small vessel disease. *Neurology*. (2020) 94:e1294–302. doi: 10.1212/WNL.0000000000009141

13. Lindenholz A, van der Kolk AG, Zwanenburg J, Hendrikse J. The use and pitfalls of intracranial Vessel Wall imaging: how we do it. *Radiology*. (2018) 286:12–28. doi: 10.1148/radiol.2017162096

14. Feng X, Chan KL, Lan L, Abrigo J, Liu J, Fang H, et al. Stroke mechanisms in symptomatic intracranial atherosclerotic disease: classification and clinical implications. *Stroke*. (2019) 50:2692–9. doi: 10.1161/STROKEAHA.119.025732

15. Li Q, Yu M, Yang D, Han Y, Liu G, Zhou D, et al. Association of the coexistence of intracranial atherosclerotic disease and cerebral small vessel disease with acute ischemic stroke. *Eur J Radiol*. (2023) 165:110915. doi: 10.1016/j.ejrad.2023.110915

16. Hainsworth AH, Markus HS, Schneider JA. Cerebral small vessel disease, hypertension, and vascular contributions to cognitive impairment and dementia. *Hypertension*. (2024) 81:75–86. doi: 10.1161/HYPERTENSIONAHA.123.19943

17. Brinjikji W, Huston J 3rd, Rabinstein AA, Kim GM, Lerman A, Lanzino G. Contemporary carotid imaging: from degree of stenosis to plaque vulnerability. *J Neurosurg*. (2016) 124:27–42. doi: 10.3171/2015.1.JNS142452

18. van Dam-Nolen D, Truijman M, van der Kolk AG, Liem MI, Schreuder F, Boersma E, et al. Carotid plaque characteristics predict recurrent ischemic stroke and TIA: the PARISK (plaque at RISK) study. *JACC Cardiovasc Imaging*. (2022) 15:1715–26. doi: 10.1016/j.jcmg.2022.04.003

19. Turan TN, Bonilha L, Morgan PS, Adams RJ, Chimowitz MI. Intraplaque hemorrhage in symptomatic intracranial atherosclerotic disease. *J Neuroimaging*. (2011) 21:e159–61. doi: 10.1111/j.1552-6569.2009.00442.x

20. Ren K, Jiang H, Li T, Qian C, Gong S, Wang T, et al. Predictive value of the combination between the intracranial arterial culprit plaque characteristics and the Essen stroke risk score for short-term stroke recurrence. *J Stroke Cerebrovasc Dis*. (2022) 31:106624. doi: 10.1016/j.jstrokecerebrovasdis.2022.106624

21. Moran C, Phan TG, Srikanth VK. Cerebral small vessel disease: a review of clinical, radiological, and histopathological phenotypes. *Int J Stroke*. (2012) 7:36–46. doi: 10.1111/j.1747-4949.2011.00725.x

22. Ryu WS, Schellingerhout D, Hong KS, Jeong SW, Jang MU, Park MS, et al. White matter hyperintensity load on stroke recurrence and mortality at 1 year after ischemic stroke. *Neurology*. (2019) 93:e578–89. doi: 10.1212/WNL.0000000000007896

23. Tsivgoulis G, Zand R, Katsanos AH, Turc G, Nolte CH, Jung S, et al. Risk of symptomatic intracerebral hemorrhage after intravenous thrombolysis in patients with acute ischemic stroke and high cerebral microbleed burden: a meta-analysis. *JAMA Neurol*. (2016) 73:675–83. doi: 10.1001/jamaneurol.2016.0292

24. Wilson D, Ambler G, Lee KJ, Lim JS, Shiozawa M, Koga M, et al. Cerebral microbleeds and stroke risk after ischaemic stroke or transient ischaemic attack: a pooled analysis of individual patient data from cohort studies. *Lancet Neurol*. (2019) 18:653–65. doi: 10.1016/S1474-4422(19)30197-8

25. Huang LX, Wu XB, Liu YA, Guo X, Ye JS, Cai WQ, et al. Qualitative and quantitative plaque enhancement on high-resolution vessel wall imaging predicts symptomatic intracranial atherosclerotic stenosis. *Brain Behav*. (2023) 13:e3032. doi: 10.1002/brb3.3032

26. Jiao S, Huang J, Chen Y, Song Y, Gong T, Lu J, et al. Impacts of glycemic control on intracranial plaque in patients with type 2 diabetes mellitus: a vessel wall MRI study. *AJNR Am J Neuroradiol*. (2021) 42:75–81. doi: 10.3174/ajnr.A6878

27. Toh R. Assessment of HDL cholesterol removal capacity: toward clinical application. *J Atheroscler Thromb*. (2019) 26:111–20. doi: 10.5551/jat.RV17028

frontiers | Frontiers in Neurology

TYPE Original Research
PUBLISHED 16 December 2024
DOI 10.3389/fneur.2024.1518911

OPEN ACCESS

EDITED BY
Shuai Ren,
Affiliated Hospital of Nanjing University of Chinese Medicine, China

REVIEWED BY
Warda Syeda,
University of Melbourne, Australia
Yuto Uchida,
Johns Hopkins Medicine, United States

*CORRESPONDENCE
Jianquan Zhong
✉ zhongjianquan.2010@qq.com

†These authors have contributed equally to this work

RECEIVED 29 October 2024
ACCEPTED 04 December 2024
PUBLISHED 16 December 2024

CITATION
Zhou L, Yang J, Zhang W, Han L, Zhou S, Zheng C, Feng H and Zhong J (2024) Evaluating iron deposition in gray matter nuclei of patients with acute ischemic stroke using quantitative susceptibility mapping. *Front. Neurol.* 15:1518911. doi: 10.3389/fneur.2024.1518911

Evaluating iron deposition in gray matter nuclei of patients with acute ischemic stroke using quantitative susceptibility mapping

Li Zhou†, Jie Yang†, Wei Zhang, Limei Han, Shenghai Zhou, Chunyan Zheng, Hao Feng and Jianquan Zhong*

Department of Radiology, Zigong First People's Hospital, Zigong, Sichuan, China

Objectives: Understanding the microscopic pathophysiological mechanisms underlying acute ischemic stroke (AIS) is vital for facilitating early clinical diagnosis and intervention. In this study, we aimed to quantitatively assess brain iron changes in gray matter (GM) nuclei in patients with AIS via quantitative susceptibility mapping (QSM).

Methods: Thirty-four patients with AIS and thirty age-and sex-matched healthy controls (HCs) were included. QSM and conventional magnetic resonance imaging were performed. Intergroup differences in regional susceptibility values were calculated for the bilateral caudate nucleus (CN), globus pallidus (GP), putamen (PUT), red nucleus (RN), substantia nigra (SN), thalamus (THA), and dentate nucleus (DN). A receiver operating characteristic curve was plotted to evaluate the classification and diagnostic performance of susceptibility values in distinguishing patients with AIS from HCs. Multiple linear regression analysis was used to investigate the impact of clinical variables on susceptibility values. Correlation analysis was used to assess the correlation between regional iron variations and clinical scores. A paired t test was used to calculate the differences in susceptibility values between the bilateral hemispheres in the participants.

Results: Compared with the HCs, the patients with AIS had significantly increased susceptibility values in the bilateral CN and PUT ($p < 0.05$, FDR correction). The highest diagnostic performance was observed in the combination of susceptibility values with differences between groups (AUC = 0.722). Multiple linear regression analysis revealed that increased susceptibility in the right CN was significantly associated with smoking ($p < 0.05$). The susceptibility values were not significantly correlated with the clinical scores ($p > 0.05$), but age was positively correlated with the modified Rankin Scale scores at admission ($p < 0.05$). The susceptibility values of the SN exhibited lateral asymmetry in patients with AIS.

Conclusion: This study revealed increased iron concentrations in the GM nuclei of patients with AIS. Iron deposition in GM nuclei may be a potential biomarker for further understanding the pathophysiological mechanism underlying AIS.

KEYWORDS

acute ischemic stroke, brain iron, quantitative susceptibility mapping, gray matter nuclei, caudate nucleus, putamen

1 Introduction

Stroke is one of the leading causes of death and disability worldwide, imposing significant social and financial burdens (1). The stroke encompasses both ischemic and hemorrhagic stroke, with ischemic stroke accounting for approximately 85% of all cases (2). In the United States alone, nearly 800,000 people suffer a stroke annually, out of which around 700,000 are acute ischemic stroke (AIS) (3). AIS is characterized by high incidence rate, mortality rate, disability rate, and recurrence rate (5), necessitating advanced non-invasive magnetic resonance imaging (MRI) for further comprehension of its pathophysiological characteristics. When the ischemic stroke progresses to subacute stage, most ischemic lesions tend to evolve into a complete infarction and the fate of the ischemic lesion is basically determined (4).

The gray matter (GM) nuclei play an important role in motor control and cognitive function, and the normal metabolism of iron in the GM nuclei is essential for maintaining these functions. And then, the GM nuclei produce high levels of neurotransmitters involved in the information processing and present a progressive iron accumulation with age, so high levels of iron are exhibited in the GM nuclei (5, 6). Brain iron is a double-edged sword: on the one hand, it is crucial for various neurophysiological functions, such as oxygen binding and transportation, synthesis of neurotransmitter and protein, myelin production, and ATP production; on the other hand, it can also contribute to the development of diseases by causing reactive oxygen species production and oxidative stress (5, 7, 8). Quantitative susceptibility mapping (QSM) is one of the sophisticated processing methods for gradient-echo MRI, extensively employed for the quantification of the spatial distribution of magnetic susceptibility in biological tissues (9–11). Magnetic susceptibility refers to the response of magnetic materials in human tissue to an applied external magnetic field and different tissues show different susceptibilities (12, 13). It is currently believed that the susceptibility of GM is dominated by tissue iron, which is mainly stored in ferritin macromolecules (9). Ferritin complex is a kind of paramagnetic substance, indicating that iron increases the overall magnetic susceptibility of the tissue. Tissue susceptibility has been shown to have a positive linear relationship with iron concentration in deep GM nuclei (9, 14). The main source of magnetic susceptibility in GM nuclei has been reported to be iron, and quantitative evaluation of iron in these regions using QSM has emerged as a reliable non-invasive method (6, 9). Studies on QSM have reported excessive iron deposition in GM nuclei in various neurodegenerative diseases, such as Alzheimer's disease, schizophrenia, Parkinson's disease, and multiple sclerosis (15–21). Visualization and quantitative evaluation of changes in brain iron concentration could contribute to understand the underlying pathophysiological mechanisms of these diseases.

Ischemic stroke leads to hypoxic–ischemic of brain tissue, disrupting iron homeostasis and resulting in a surge of iron deposition in local brain tissue (22, 23). Ferroptosis is an iron-dependent and reactive oxygen species reliant cell death, which caused by massive lipid peroxidation mediated membrane damage (24). A study examined the model of unilateral, transient middle cerebral artery occlusion in rats and revealed an elevation of iron level within the lesioned hemisphere (25). Xia et al. reported the susceptibility value of the asymmetrically prominent cortical veins in the stroke hemisphere was significantly higher compared to that in the contralateral hemisphere and HCs (26). Hypertension is a prominent risk factor among stroke survivors, and the susceptibility value of subcortical structures in patients with hypertension was found to be significantly increased compared to that of healthy controls (HCs) (27, 28). Studies have found that patients with cerebral artery stenosis/occlusion showed significantly elevated susceptibility values in GM nuclei, which were found to be associated with several risk factors of cerebrovascular disease (23, 29). Previous studies have demonstrated that cerebral ischemia induces alterations of iron deposition in GM nuclei, which holds significant implications for comprehending pathological mechanism of cerebral ischemia; however, there remains a dearth of research on iron deposition resulting from AIS.

The aim of this study was to utilize QSM technology to identify alterations of iron accumulation in the GM nuclei among patients with AIS, and subsequently investigate its association with clinical scales. The identification of iron level abnormalities associated with early stage of ischemic stroke holds promise for informing clinical interventions and development of therapeutic drugs to enhance the neurological prognosis of patients.

2 Materials and methods

2.1 Participants

A total of thirty-four patients diagnosed with AIS and thirty HCs were recruited from Zigong First People Hospital. The following demographic and clinical information were collected: name, gender, age, race, risk factors of cerebrovascular disease (hypertension, hyperlipidemia, and diabetes), and time of onset, etc. In addition, the extent of neural function deficiency and prognosis of patients with AIS was assessed upon admission and discharge using the National Institutes of Health Stroke Scale (NIHSS) and modified Rankin Scale (mRS). This study was approved by the Ethics Committee and obtained informed consent from all participants.

The inclusion criteria of patients with AIS were as follows: (1) a diagnosis of AIS was established by at least two clinician and two radiologists based on comprehensive physical examination, neurological assessment, and MRI image; (2) the clinical diagnosis of AIS was based on the "Chinese Guidelines for the Diagnosis and Treatment of Acute Ischemic Stroke 2018"; (3) there were complete clinical data and good MRI image quality.

The exclusion criteria of patients with AIS were as follows: (1) history of severe neurological disorders, such as intracranial hemorrhage, brain tumor and brain surgery; (2) the brain infarction lesions affected region of interest (ROI) (bilateral caudate nucleus (CN), globus pallidus (GP), putamen (PUT), red nucleus (RN), substantia nigra (SN), thalamus (THA) and dentate nucleus (DN)); (3) unsuccessful MRI scans, due to factors such as the metallic implants or claustrophobia; (4) history of organic lesions in important organs.

The inclusion criteria for HCs were as follows: (1) no history of neuropsychiatric disorders; (2) no contraindications for MRI; (3) no history of severe organic lesions, such as cerebrovascular disease, brain injury, neurological disorders; (4) no history of alcohol and drug abuse.

10.3389/fneur.2024.1518911

2.2 Image acquisition

The complete image data, including QSM, T1-weighted imaging (T1WI), T2-weighted imaging (T2WI), and T2 fluid-attenuated inversion recovery (T2-FLAIR), diffusion weighted imaging (DWI) was collected on a 3.0 T MRI scan (MAGNETOM Vida; Siemens Healthineers, Erlangen, Germany), and the 64-channel head coil was selected for scanning.

QSM was conducted using an eight echo gradient-echo (GRE) sequence: repetition time (TR) = 55 ms, echo time (TE) = 6.15 ms, flip angle = 15°, field of view (FOV) = 220 × 220 mm^2, thickness = 2 mm, number of slices = 72, voxel size = 0.9 × 0.9 × 2 mm^3, acceleration mode: GRAPPA with 2X acceleration factor, and total scan time was 8 min 7 s.

2.3 Data analysis

2.3.1 Data analysis of QSM

The QSM data were analyzed using the MEDI toolbox (Morphology Enabled Dipole Inversion) based on the Matlab 2018a software platform (Mathworks, Natick, MA, USA), following a structured workflow to ensure accurate and reliable results: (1) The image was unwrapped with Laplacian algorithm. (2) The FSL BET algorithm in MEDI toolbox was used to extract the brain mask. (3) The projection onto dipole fields (PDF) algorithm was used to remove the background field. (4) The susceptibility map was generated by MEDI local field inversion algorithm.

2.3.2 Extracting the ROI

The susceptibility value of each ROI was quantified using ITK-SNAP by two radiologists who were blinded to the neurologic and clinical diagnosis. The ROIs included the bilateral CN, GP, PUT, RN, SN, THA, and DN. To enhance accuracy, the susceptibility value of each ROI was evaluated in three consecutive slices, and the average susceptibility value and standard deviation (SD) for each region were obtained.

2.4 Statistical analysis

SPSS 27.0 was used for statistical analysis. Independent t-test were used to compare the ages between patients with AIS and HCs. The $\chi 2$ test was used to compare gender data between the two groups.

The interclass correlation coefficient (ICC) was utilized to evaluate the interrater reliability of manual segmentation and the ICC $\geq$ 0.75 was considered excellent. The differences in corresponding ROI susceptibilities between patients with AIS and HCs were compared using either independent t-test or Mann–Whitney U tests, depending on the normal distribution of the data. The receiver operating characteristic (ROC) curve was plotted to evaluate the classification and diagnostic performance of the susceptibility values with significant differences between groups. Additionally, multiple linear regression analysis was used to investigate the impact of independent variables (demographic and clinical data) on the susceptibility values in GM nuclei. The correlation between regional iron variations and clinical scores were explored using either Pearson correlation or Spearman correlation test, depending on the normal distribution of the data. The paired t test was employed to calculate the differences of susceptibility values between the bilateral hemispheres in both patients with AIS and HCs. A value of $p < 0.05$ was considered to indicate statistical significance.

3 Results

3.1 Study population

A total of thirty-four patients with AIS (mean age: 71.32 years) and thirty HCs (mean age: 66.90 years) were included in this study. The demographics and clinical characteristics of patients with AIS and HCs are shown in Table 1. There were significant differences in the smoking history and hypertension history between the two groups ($p < 0.001$). There was no significant difference in other demographics or clinical characteristics between the two groups ($p > 0.05$).

3.2 Comparisons of susceptibility values between groups

The representative axial QSM sections are shown in Figure 1. The boundary of GM nuclei can be clearly seen on the QSM images, thereby demonstrating the feasibility of direct manual segmentation. The results of ICC analysis revealed excellent absolute agreement between raters in all segmented GM nuclei (0.823 ≤ ICCs ≤0.981, Table 2).

The susceptibility values in bilateral CN and PUT were significantly increased in patients with AIS compared to HCs (susceptibility values in left CN: 0.07300 ± 0.02882 vs. 0.05570 ± 0.02277; susceptibility values in right CN: 0.07076 ± 0.02737 vs. 0.05405 ± 0.02256; susceptibility values in left PUT:

TABLE 1 The demographic and clinical data of participants.

	Patients with AIS	Healthy controls	*p* value
	n = 34	*n* = 30	
Age (years)	71.32 ± 10.10	66.90 ± 7.81	0.057
Gender (male/female)	19/15	11/19	0.124
Smoking history (yes/no)	18/16	3/27	<0.001*
Alcohol history (yes/no)	10/24	3/27	0.054
Hypertension (yes/no)	24/10	0/30	<0.001*
Hyperlipidemia (yes/no)	5/29	3/27	0.570
Diabetes (yes/no)	7/27	2/28	0.110
NIHSS score at admission	2.0 (4.25)	-	-
NIHSS score at discharge	1.0 (2.25)	-	-
mRS score at admission	2.0 (2.0)	-	-
mRS score at discharge	1.0 (1.25)	-	-

*$p < 0.05$; –, not applicable; values are given in means ± standard deviations or median (interquartile range). AIS, acute ischemic strokes; mRS, modified Rankin Scale; NIHSS, National Institutes of Health Stroke Scale.

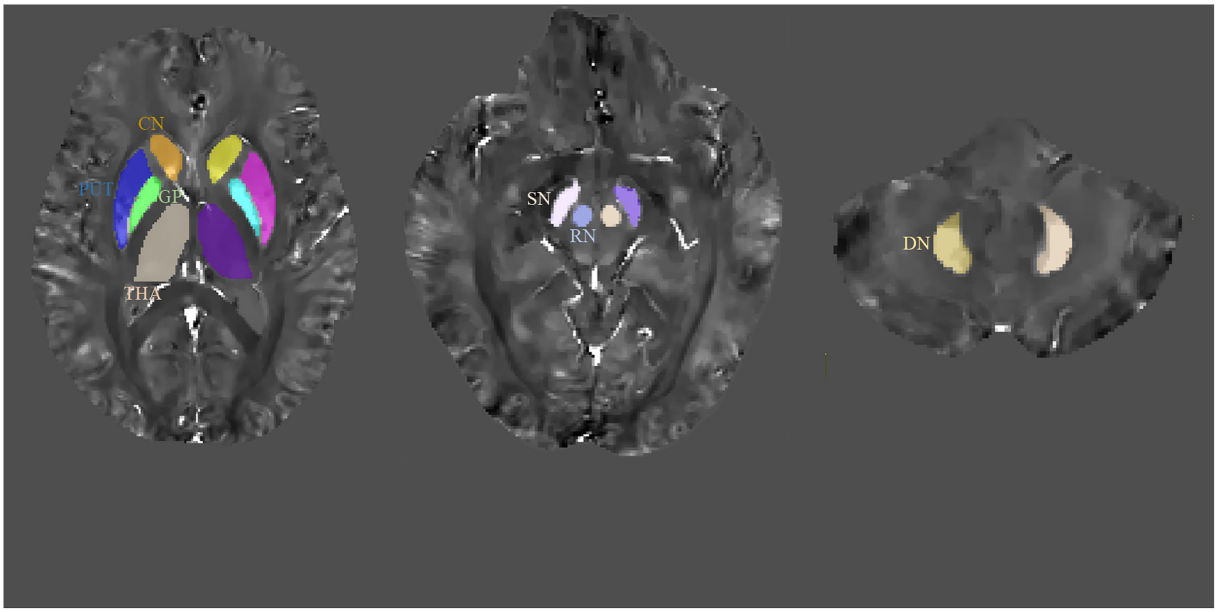

FIGURE 1
Regions-of-interest (ROIs) depicted on quantitative susceptibility mapping (QSM) images. CN, caudate nucleus; GP, globus pallidus; PUT, putamen; RN, red nucleus; SN, substantia nigra; THA, thalamus; DN, dentate nucleus.

0.08580 ± 0.03239 vs. 0.06429 ± 0.02839; susceptibility values in right PUT: 0.08828 ± 0.03053 vs. 0.06531 ± 0.02670; $p < 0.05$, FDR corrected). The susceptibility values of other GM nuclei (bilateral GP, RN, SN, THA and DN) did not exhibit significantly different between the two groups (Table 3; Figure 2).

3.3 ROC curve analysis

The results of the ROC curve analysis revealed that susceptibility values in the bilateral CN and PUT had some effect in distinguishing patients with AIS from HCs. The combination of susceptibility values in the bilateral CN and PUT showed better classification and diagnostic performance (AUC = 0.722) (Table 4; Figure 3).

3.4 Multivariable linear regression analysis

Due to the relatively small sample size, variables with p values <0.1 in the univariate analysis were selected as independent variables for subsequent multiple linear regression analysis (Table 5). The results of multiple linear regression analysis showed that patients with smoking exhibited higher susceptibility values in the right CN ($p = 0.012$) (Table 6).

3.5 Correlation analysis

There was no statistically significant correlation between susceptibility values and clinical scores ($p > 0.05$), but the age of patients with AIS was positively correlated with the modified Rankin Scale scores at admission ($p = 0.006$, $r = 0.501$) (Figure 4).

3.6 The asymmetry of susceptibility values

The left–right asymmetry in the susceptibility values of SN was observed in patients with AIS by the paired t-test (the right side higher than left, susceptibility values in right SN = 0.149768 ± 0.059665, susceptibility values in left SN = 0.135634 ± 0.067580, $p = 0.0083$) (Figure 5). Comparable levels of susceptibility values were observed in other GM nuclei across bilateral hemispheres in patients with AIS. Susceptibility values of all ROIs in HCs did not exhibit left–right asymmetry.

4 Discussion

In the study, we utilized the QSM method to quantitatively compare iron concentrations in GM nuclei between patients with AIS and HCs. The results showed a significant increase in susceptibility values in bilateral CN and PUT in patients with AIS. Susceptibility values in bilateral CN and PUT had some effect in distinguishing patients with AIS from HCs. The result of multiple linear regression analysis indicate that smoking may have an impact on susceptibility values in CN in patients with AIS. The results of correlation analysis suggest that older patients with AIS may have worse neurological recovery outcomes. The susceptibility values of SN exhibited lateral asymmetry in patients with AIS, suggesting that alterations of iron level may not necessarily be paralleled between bilateral cerebral hemispheres.

The blood–brain barrier (BBB) plays a crucial role in regulating the physiological transport and metabolism of brain iron. The impairment of BBB endothelial cells can severely affect the normal iron absorption in hypoxic conditions that accompany AIS, leading to the release of excessive iron into brain tissue (22, 23). Iron overload can enhance Fenton reactions known as Haber-Weiss reaction ($Fe^{++} + H_2O_2 \rightarrow Fe^{+++} + OH^{\bullet} + OH^{-}$), leading to an excessive production of

10.3389/fneur.2024.1518911

TABLE 2 Absolute ICCs for agreement between the raters for segmentation of the gray matter nuclei in patients with AIS and healthy controls.

		CN		GP		PUT		RN		SN		THA		DN	
		Left	Right	Left	Right	Left	Right	Left	Right	Left	Right	Left	Right	Left	Right
ICC	Patients with AIS	0.939	0.953	0.978	0.961	0.86	0.905	0.923	0.922	0.945	0.89	0.959	0.955	0.944	0.956
	Healthy controls	0.823	0.905	0.907	0.981	0.958	0.902	0.895	0.882	0.917	0.917	0.946	0.932	0.962	0.959

AIS, acute ischemic strokes; CN, caudate nucleus; DN, dentate nucleus; GP, globus pallidus; ICC, intraclass correlation coefficient; PUT, putamen; RN, red nucleus; ROI, region of interest; SN, substantia nigra; THA, thalamus.

TABLE 3 ROI susceptibilities of the patients with AIS and healthy controls.

		Patients with AIS	Healthy controls	*P-FDR* value
CN	Left	0.07300 ± 0.02882	0.05570 ± 0.02277	0.042*
	Right	0.07076 ± 0.02737	0.05405 ± 0.02256	0.047*
GP	Left	0.17203 ± 0.05722	0.14285 (0.08172)	0.729
	Right	0.17960 ± 0.06094	0.15132 (0.06268)	0.564
PUT	Left	0.08580 ± 0.03239	0.06429 ± 0.02839	0.049*
	Right	0.08828 ± 0.03053	0.06531 ± 0.02670	0.028*
RN	Left	0.13421 ± 0.04802	0.12057 ± 0.03732	0.375
	Right	0.13429 ± 0.04533	0.12074 ± 0.03871	0.412
SN	Left	0.13194 (0.08458)	0.11392 (0.05587)	0.438
	Right	0.14977 ± 0.05966	0.13040 ± 0.04453	0.423
THA	Left	−0.00198 ± 0.01035	−0.00350 ± 0.00724	0.586
	Right	−0.00274 ± 0.00959	−0.00207 ± 0.00774	0.760
DN	Left	0.09596 (0.04371)	0.08232 (0.04186)	0.448
	Right	0.09071 (0.04433)	0.08779 ± 0.04074	0.467

*$p < 0.05$, FDR corrected; values are given in means ± standard deviations or median (interquartile range). AIS, acute ischemic strokes; CN, caudate nucleus; DN, dentate nucleus; GP, globus pallidus; PUT, putamen; RN, red nucleus; ROI, region of interest; SN, substantia nigra; THA, thalamus.

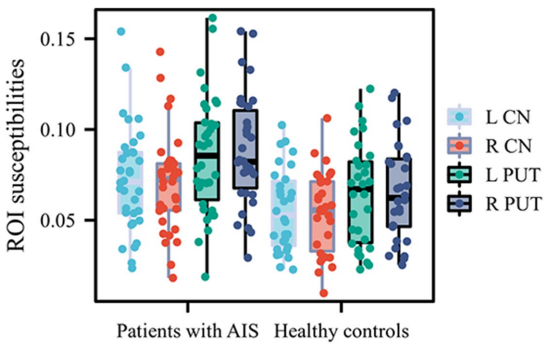

FIGURE 2
Quantitative comparison of susceptibility values in bilateral CN and PUT between patients with AIS with and healthy controls. CN, caudate nucleus; PUT, putamen; AIS, acute ischemic stroke.

hydroxyl (OH), and the highly reactive free radicals have the potential to cause damage to DNA, proteins, and lipids (30–32). Lipids play a crucial role in the cellular structure and function (such as cell membranes), and oxidative destruction of the lipids can ultimately lead to cytotoxic edema and subsequent cellular demise (29, 33). And then, aberrations in iron homeostasis *in vivo* are also associated with predisposing factors for ischemic stroke, such as cardiovascular disease, diabetes mellitus, hyperlipidemia, and hypertension (34–37). Disturbances of brain iron homeostasis may be involved in pathogenesis and progression of cerebral ischemia and stroke.

The findings of the study indicate that iron content in bilateral CN and PUT increases in patients with AIS, indicating alterations of microscopic and molecular properties in GM nuclei. Result of the ROC analysis showed that susceptibility values in bilateral CN and PUT could help us to distinguish patients with AIS from HCs. Similar to our finding, Mao et al. found that patients with middle cerebral artery stenosis/occlusion showed increased iron deposition in the PUT, GP, and SN, and the susceptibility values of GM nuclei exhibited correlations with risk factor variables for cerebrovascular disease (29). Du et al. revealed significant alterations in the susceptibility levels of GM nuclei in patients with middle cerebral artery occlusion, suggesting a potential involvement of iron metabolism disorder in the pathophysiological mechanisms underlying cerebrovascular disease (23). A study found that iron content in PUT and GP in patients with long-term cerebral ischemia significantly increased compared to HCs, which is consistent with our findings (38). The susceptibility values of infarct regions in patients with AIS were found to exhibit a significant increase compared to both HCs and the non-infarct region of the responsible artery (14). Patients with cerebral ischemia and stroke show abnormal iron accumulation in the brain, which may provide a novel perspective for comprehending the pathophysiological alterations of ischemic stroke.

The results of a study about computed tomographic perfusion and computed tomographic angiography suggest that advanced imaging variables (such as acute ischemic core volume, acute penumbra volume and collateral circulation grade) are strong predictors of prognosis in patients with AIS (39). Another study suggests collateral circulation grade is a prognostic indicator for patients who achieve recanalization, but not for patients who do not achieve recanalization (40). However, a review suggests that the low consistency of stroke trials with different imaging modalities may affect the development of new treatment strategies for AIS (41). A study found that oxygen extraction fraction map generated based on QSM can help identify the ischemic penumbra in patients with AIS, suggesting that advanced MRI has the potential to guide treatment choices for patients with AIS (42). A QSM-based study found that longitudinal changes in iron and myelination within ischemic lesions were associated with neurologic prognosis, and that increased iron concentrations within ischemic lesions were associated with less improvement in neurologic prognosis (43). Although the diagnostic accuracy of susceptibility values in CN

10.3389/fneur.2024.1518911

TABLE 4 Diagnostic performance of ROI susceptibilities in patients with AIS and healthy controls.

Indicators		AUC	95%CI	Sensitivity	Specificity	Accuracy
CN	Left	0.672	0.538–0.805	0.433	0.853	0.656
	Right	0.684	0.552–0.815	0.900	0.412	0.641
PUT	Left	0.683	0.552–0.814	0.833	0.471	0.641
	Right	0.699	0.569–0.829	0.633	0.735	0.688
Combination of above indicators		0.722	0.569–0.847	0.633	0.794	0.719

AIS, acute ischemic strokes; AUC, area under the curve; CI, confidence interval; CN, caudate nucleus; PUT, putamen.

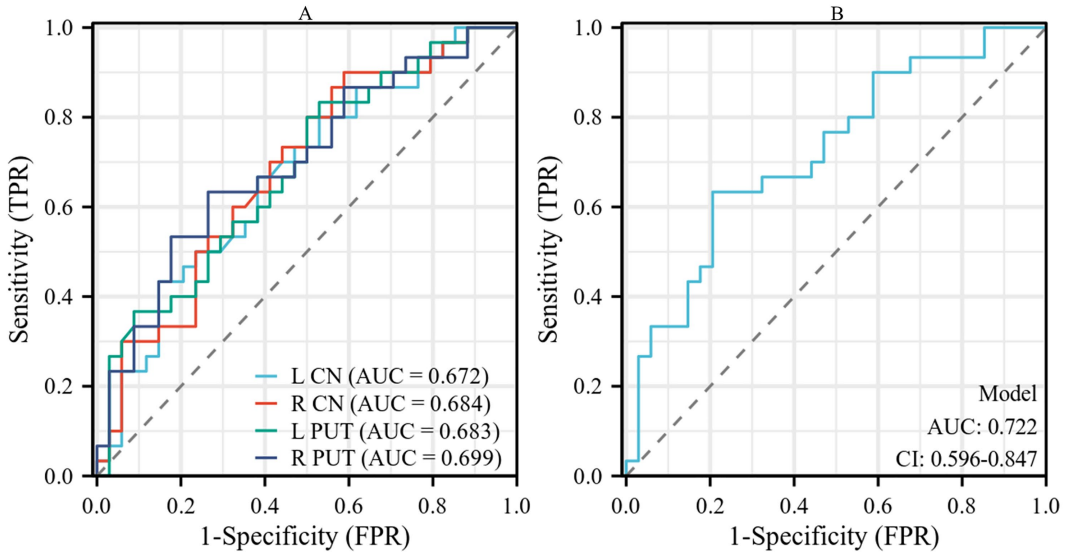

FIGURE 3
(A) Performance of susceptibility values of the bilateral CN and PUT in the diagnosis of patients with AIS. **(B)** The combined analysis of susceptibility values of bilateral CN and PUT showed a certain improvement in diagnostic performance. CN, caudate nucleus; PUT, putamen; AIS, acute ischemic stroke.

TABLE 5 Summary of univariate analysis linking demographic and clinical data with susceptibility values in the bilateral CN and PUT.

	L CN		R CN		L PUT		R PUT	
	β	*P*	*β*	*P*	*β*	*P*	*β*	*P*
Age	−0.043	0.809	−0.055	0.791	−0.029	0.869	−0.043	0.809
Smoking	−0.329	0.057*	−0.425	0.012*	−0.405	0.017*	−0.323	0.062*
Drinking	−0.131	0.460	−0.200	0.257	−0.402	0.018*	−0.272	0.120
Hypertension	−0.137	0.440	−0.196	0.267	−0.156	0.379	−0.138	0.437
Hyperlipidemia	−0.112	0.528	−0.146	0.409	−0.215	0.222	−0.136	0.441
Diabetes	−0.210	0.234	−0.221	0.210	−0.21	0.233	−0.278	0.111
NIHSS score at admission	0.194	0.314	0.165	0.394	0.364	0.052*	0.355	0.058*
NIHSS score at discharge	−0.090	0.662	−0.094	0.648	0.160	0.435	0.07	0.734
mRS score at admission	0.065	0.738	0.040	0.836	0.217	0.259	0.152	0.432
mRS score at discharge	−0.055	0.791	−0.094	0.646	0.074	0.719	0.095	0.645

*$p < 0.1$. CN, caudate nucleus; L, left; PUT, putamen; R, right.

and PUT has moderate predictive value in this study, enhanced use of advanced imaging biomarkers may help us find the underlying molecular-level pathophysiologic basis of AIS. Study of iron deposition in GM nuclei of patients with AIS may provide new ideas for prevention and therapeutic drug development of stroke. We will deeply explore the relationship between susceptibility values of deep GM nuclei and other imaging biomarkers about AIS as well as the prognosis of AIS in the future.

The CN and PUT form the dorsal striatum, which coordinates various functions including motor activity, motivation and learning

TABLE 6 Summary of multivariable linear regression models linking demographic and clinical data with susceptibility values in the bilateral CN and PUT.

	Univariate analysis	*β*	*t*	*P*	Adjusted R^2 of model	*F of model*	*P* of model
L CN	Smoking	−0.329	−1.973	0.057	0.081	3.895	0.057
R CN	Smoking	−0.425	−2.658	0.012	0.155	7.064	0.012*
L PUT	Smoking	−0.303	−1.44	0.162	0.168	2.887	0.056
	Drinking	−0.087	−0.377	0.709			
	NIHSS score at admission	0.299	1.557	0.132			
R PUT	Smoking	−0.106	−0.529	0.601	0.069	2.040	0.150
	NIHSS score at admission	0.312	1.558	0.131			

*$p < 0.05$. CN, caudate nucleus; L, left; PUT, putamen; R, right.

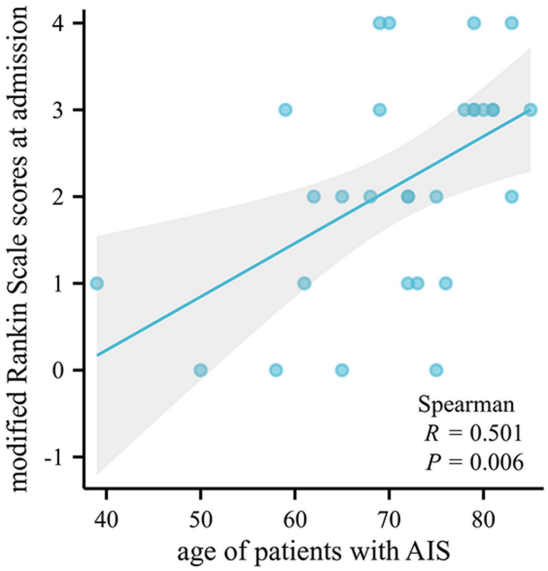

FIGURE 4
Bivariate scatter plots showing a positive correlation between the age of patients with AIS and the modified Rankin Scale scores at admission. AIS, acute ischemic stroke.

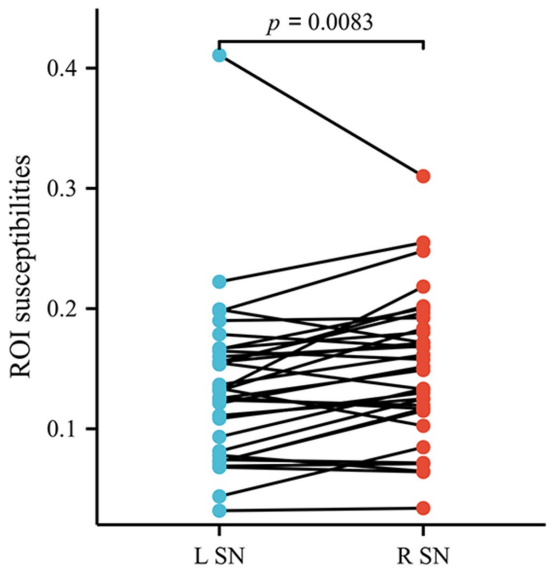

FIGURE 5
The susceptibility values of SN exhibited lateral asymmetry in patients with AIS. SN, substantia nigra; AIS, acute ischemic stroke.

(44). When focusing on functional connections, the PUT showed a high degree of co-activation with the primary motor cortex, whereas the CN showed a high degree of co-activation with the area of high-level cognitive functions (45). Previous studies have demonstrated a significant accumulation of iron in CN and PUT in patients with neurodegenerative diseases, such as Alzheimer's disease, Parkinson's disease and Wilson's disease (46–49). Iron overload within the CN and PUT may contributes to iron-dependent cell death, and the neuronal death of the CN and PUT could result in neurological impairment and cognition deficit (23, 50). The result in the present study may provide a plausible explanation for motor and cognition deficit in patients with AIS. As a final note, our study has specifically focused on the susceptibility values of the head region of the CN, and do not focus on the body or tail.

AIS causes rapid neuronal damage and death in the central area of the infarction and in the surrounding hypoperfused region. In addition to this, cerebral ischemia also induces neuronal degeneration in distal regions which are connected to the area of ischemic core (51). For example, after cerebral infarction in the middle cerebral artery region, neuronal death, gliosis, and axonal degeneration were also found in the ipsilateral THA, SN, and distal pyramidal tract that outside the middle cerebral artery region (52). An animal study from rat models demonstrated significant atrophy and neurodegeneration in the ipsilateral SN after middle cerebral artery occlusion (53). Several days after the basal ganglia infarction, DWI showed degeneration in the ipsilateral SN of the patient (52). The SN plays an important role in motor control along with the basal ganglia, so degeneration of SN may be associated with poor functional or motor outcomes of the patient with AIS (54). Degeneration of SN cells and decreased dopamine synthesis are the main causes of Parkinson's disease. A large population-based analysis found that cerebrovascular risk factors such as a history of stroke were strongly associated with a subsequent diagnosis of Parkinson's disease (55). We hypothesized that stroke may cause degeneration of SN cells leading to Parkinson's disease. Our findings revealed that the susceptibility values of SN showed lateral asymmetry in patients with AIS but not in HCs, suggesting that alterations of iron

level may not necessarily be paralleled between left and right after the onset of stroke. Notably, conventional MRI including T1WI, T2WI, T2-FLAIR, and DWI in our experiments did not reveal any abnormalities in SN signals in patients with AIS. Therefore, we hypothesized that the change in iron content in SN may have occurred prior to neuronal degeneration and cytotoxic edema. It should be noted that whether lateral asymmetry of the SN is related to the site of cerebral infarction require further examination in the future.

This study had several limitations. First, the number of participants was relatively small. A larger sample size, especially patients with AIS, is required to validate the finding of the current study. Second, the current study focused on the brain iron changes in the GM nuclei, while the study of susceptibility values in white matter and cerebral cortex may also contribute to the understanding of AIS. Third, as a cross-sectional study, this research still cannot be used to accurately speculate on the cause-and-effect relationship between abnormal iron accumulation and AIS. Fourth, the lack of measurements of ROI volume is a limitation, as it may affect the evaluation of susceptibility value and the experimental results. Nevertheless, we ensured that ROI was evaluated in similar slices of different participant as much as possible to reduce the impact on the experimental results. And then, the average susceptibility value and standard deviation of each ROI was evaluated on three consecutive slices to improve the accuracy of the experiment. In future studies, we will include ROI volume as a covariate in statistical models to improve the reliability and validity of the study.

5 Conclusion

As measured by QSM, iron levels in the bilateral CN and PUT were significantly increased in patients with AIS. Abnormal iron accumulation in the basal ganglia region might be related to the pathophysiological changes of AIS. These findings may open the door to in-depth study of the pathophysiological mechanisms of AIS.

Data availability statement

The raw data supporting the conclusions of this article will be made available by the authors, without undue reservation.

Ethics statement

The studies involving human participants were reviewed and approved by the Ethics Committee of Zigong First People's Hospital. The studies were conducted in accordance with the local legislation and institutional requirements. The participants provided their written informed consent to participate in this study.

Author contributions

LZ: Data curation, Writing – original draft, Writing – review & editing. JY: Data curation, Methodology, Software, Writing – original draft, Writing – review & editing. WZ: Data curation, Writing – original draft. LH: Data curation, Writing – original draft. SZ: Data curation, Writing – original draft. CZ: Data curation, Writing – original draft. HF: Data curation, Writing – original draft. JZ: Conceptualization, Project administration, Supervision, Writing – original draft, Writing – review & editing.

Funding

The author(s) declare that financial support was received for the research, authorship, and/or publication of this article. This study was supported by the Zigong Public Hospital Reform and High-Quality Development Demonstration Project in 2023 (No. ZG-KY-2023-008) and Zigong Key Science and Technology Plan (Collaborative Innovation Project of Zigong Academy of Medical Sciences) in 2023 (No. 2023YKYXT08).

Conflict of interest

The authors declare that the research was conducted in the absence of any commercial or financial relationships that could be construed as a potential conflict of interest.

Generative AI statement

The author(s) declare that no Gen AI was used in the creation of this manuscript.

Publisher's note

References

1. Schadlich IS, Winzer R, Stabernack J, Tolosa E, Magnus T, Rissiek B. The role of the ATP-adenosine axis in ischemic stroke. *Semin Immunopathol*. (2023) 45:347–65. doi: 10.1007/s00281-023-00987-3

2. Donnan GA, Fisher M, Macleod M, Davis SM. Stroke. *Lancet*. (2008) 371:1612–23. doi: 10.1016/S0140-6736(08)60694-7

3. Mendelson SJ, Prabhakaran S. Diagnosis and Management of Transient Ischemic Attack and Acute Ischemic Stroke. *JAMA*. (2021) 325:1088. doi: 10.1001/jama.2020.26867

4. Oku N, Kashiwagi T, Hatazawa J. Nuclear neuroimaging in acute and subacute ischemic stroke. *Ann Nucl Med*. (2010) 24:629–38. doi: 10.1007/s12149-010-0421-7

5. Eskreis-Winkler S, Zhang Y, Zhang J, Liu Z, Dimov A, Gupta A, et al. The clinical utility of QSM: disease diagnosis, medical management, and surgical planning. *NMR Biomed*. (2017) 30:3668. doi: 10.1002/nbm.3668

6. Otani S, Fushimi Y, Iwanaga K, Tomotaki S, Shimotsuma T, Nakajima S, et al. Evaluation of deep gray matter for early brain development using quantitative susceptibility mapping. *Eur Radiol*. (2023) 33:4488–99. doi: 10.1007/s00330-022-09267-4

7. Crichton RR, Dexter DT, Ward RJ. Brain iron metabolism and its perturbation in neurological diseases. *J Neural Transm (Vienna)*. (2011) 118:301–14. doi: 10.1007/s00702-010-0470-z

8. Lotharius J, Brundin P. Pathogenesis of Parkinson's disease: dopamine, vesicles and alpha-synuclein. *Nat Rev Neurosci*. (2002) 3:932–42. doi: 10.1038/nrn983

9. Langkammer C, Schweser F, Krebs N, Deistung A, Goessler W, Scheurer E, et al. Quantitative susceptibility mapping (QSM) as a means to measure brain iron? A post mortem validation study. *Neuroimage*. (2012) 62:1593–9. doi: 10.1016/j.neuroimage.2012.05.049

10. Probst J, Rohner M, Zahn M, Piccirelli M, Pangalu A, Luft A, et al. Quantitative susceptibility mapping in ischemic stroke patients after successful recanalization. *Sci Rep*. (2021) 11:16038. doi: 10.1038/s41598-021-95265-3

11. Vinayagamani S, Sheelakumari R, Sabarish S, Senthilvelan S, Ros R, Thomas B, et al. Quantitative susceptibility mapping: technical considerations and clinical applications in neuroimaging. *J Magn Reson Imaging*. (2021) 53:23–37. doi: 10.1002/jmri.27058

12. Du L, Zhao Z, Cui A, Zhu Y, Zhang L, Liu J, et al. Increased Iron deposition on brain quantitative susceptibility mapping correlates with decreased cognitive function in Alzheimer's disease. *ACS Chem Neurosci*. (2018) 9:1849–57. doi: 10.1021/acschemneuro.8b00194

13. Reichenbach JR. The future of susceptibility contrast for assessment of anatomy and function. *NeuroImage*. (2012) 62:1311–5. doi: 10.1016/j.neuroimage.2012.01.004

14. Yang J, Lv M, Han L, Li Y, Liu Y, Guo H, et al. Evaluation of brain iron deposition in different cerebral arteries of acute ischaemic stroke patients using quantitative susceptibility mapping. *Clin Radiol*. (2024) 79:e592–8. doi: 10.1016/j.crad.2024.01.007

15. Kim HG, Park S, Rhee HY, Lee KM, Ryu CW, Rhee SJ, et al. Quantitative susceptibility mapping to evaluate the early stage of Alzheimer's disease. *Neuroimage Clin*. (2017) 16:429–38. doi: 10.1016/j.nicl.2017.08.019

16. Uchida Y, Kan H, Sakurai K, Arai N, Kato D, Kawashima S, et al. Voxel-based quantitative susceptibility mapping in Parkinson's disease with mild cognitive impairment. *Mov Disord*. (2019) 34:1164–73. doi: 10.1002/mds.27717

17. Uchida Y, Kan H, Sakurai K, Horimoto Y, Hayashi E, Iida A, et al. APOE varepsilon 4 dose associates with increased brain iron and beta-amyloid via blood-brain barrier dysfunction. *J Neurol Neurosurg Psychiatry*. (2022) 93:772–8. doi: 10.1136/jnnp-2021-328519

18. Uchida Y, Kan H, Sakurai K, Inui S, Kobayashi S, Akagawa Y, et al. Magnetic susceptibility associates with dopaminergic deficits and cognition in Parkinson's disease. *Mov Disord*. (2020) 35:1396–405. doi: 10.1002/mds.28077

19. Uchida Y, Kan H, Sakurai K, Oishi K, Matsukawa N. Quantitative susceptibility mapping as an imaging biomarker for Alzheimer's disease: the expectations and limitations. *Front Neurosci*. (2022) 16:938092. doi: 10.3389/fnins.2022.938092

20. Xu M, Guo Y, Cheng J, Xue K, Yang M, Song X, et al. Brain iron assessment in patients with first-episode schizophrenia using quantitative susceptibility mapping. *Neuroimage Clin*. (2021) 31:102736. doi: 10.1016/j.nicl.2021.102736

21. Yan Z, Liu H, Chen X, Zheng Q, Zeng C, Zheng Y, et al. Quantitative susceptibility mapping-derived Radiomic features in discriminating multiple sclerosis from Neuromyelitis Optica Spectrum disorder. *Front Neurosci*. (2021) 15:765634. doi: 10.3389/fnins.2021.765634

22. Campos-Escamilla C. The role of transferrins and iron-related proteins in brain iron transport: applications to neurological diseases. *Adv Protein Chem Struct Biol*. (2021) 123:133–62. doi: 10.1016/bs.apcsb.2020.09.002

23. Du L, Zhao Z, Liu X, Chen Y, Gao W, Wang Y, et al. Alterations of Iron level in the bilateral basal ganglia region in patients with middle cerebral artery occlusion. *Front Neurosci*. (2020) 14:608058. doi: 10.3389/fnins.2020.608058

24. Dusek P, Hofer T, Alexander J, Roos PM, Aaseth JO. Cerebral Iron deposition in neurodegeneration. *Biomol Ther*. (2022) 12:714. doi: 10.3390/biom12050714

25. Tuo QZ, Lei P, Jackman KA, Li XL, Xiong H, Li XL, et al. Tau-mediated iron export prevents ferroptotic damage after ischemic stroke. *Mol Psychiatry*. (2017) 22:1520–30. doi: 10.1038/mp.2017.171

26. Xia S, Utriainen D, Tang J, Kou Z, Zheng G, Wang X, et al. Decreased oxygen saturation in asymmetrically prominent cortical veins in patients with cerebral ischemic stroke. *Magn Reson Imaging*. (2014) 32:1272–6. doi: 10.1016/j.mri.2014.08.012

27. Li X, Jin D, Zhu Y, Liu L, Qiao Y, Qian Y, et al. Quantitative susceptibility mapping to evaluate brain iron deposition and its correlation with physiological parameters in hypertensive patients. *Ann Transl Med*. (2021) 9:1582. doi: 10.21037/atm-21-5170

28. Wang W, Jiang B, Sun H, Ru X, Sun D, Wang L, et al. Prevalence, incidence, and mortality of stroke in China: results from a Nationwide population-based survey of 480 687 adults. *Circulation*. (2017) 135:759–71. doi: 10.1161/CIRCULATIONAHA.116.025250

29. Mao H, Dou W, Chen K, Wang X, Wang X, Guo Y, et al. Evaluating iron deposition in gray matter nuclei of patients with unilateral middle cerebral artery stenosis using quantitative susceptibility mapping. *Neuroimage Clin*. (2022) 34:103021. doi: 10.1016/j.nicl.2022.103021

30. Salvador GA. Iron in neuronal function and dysfunction. *Biofactors*. (2010) 36:103–10. doi: 10.1002/biof.80

31. Selim MH, Ratan RR. The role of iron neurotoxicity in ischemic stroke. *Ageing Res Rev*. (2004) 3:345–53. doi: 10.1016/j.arr.2004.04.001

32. Stankiewicz J, Panter SS, Neema M, Arora A, Batt CE, Bakshi R. Iron in chronic brain disorders: imaging and neurotherapeutic implications. *Neurotherapeutics*. (2007) 4:371–86. doi: 10.1016/j.nurt.2007.05.006

33. Hirschhorn T, Stockwell BR. The development of the concept of ferroptosis. *Free Radic Biol Med*. (2019) 133:130–43. doi: 10.1016/j.freeradbiomed.2018.09.043

34. Harrison AV, Lorenzo FR, McClain DA. Iron and the pathophysiology of diabetes. *Annu Rev Physiol*. (2023) 85:339–62. doi: 10.1146/annurev-physiol-022522-102832

35. Hilton C, Sabaratnam R, Drakesmith H, Karpe F. Iron, glucose and fat metabolism and obesity: an intertwined relationship. *Int J Obes*. (2023) 47:554–63. doi: 10.1038/s41366-023-01299-0

36. Savarese G, von Haehling S, Butler J, Cleland JGF, Ponikowski P, Anker SD. Iron deficiency and cardiovascular disease. *Eur Heart J*. (2023) 44:14–27. doi: 10.1093/eurheartj/ehac569

37. Xi X, Wu Q, Wang X, Sun X, Yu G, Jiang L, et al. The association between iron metabolism with the change of blood pressure and risk of hypertension: a large cross-sectional study. *J Trace Elem Med Biol*. (2023) 79:127193. doi: 10.1016/j.jtemb.2023.127193

38. Mao H, Dou W, Wang X, Chen K, Wang X, Guo Y, et al. Iron deposition in gray matter nuclei of patients with intracranial artery stenosis: a quantitative susceptibility mapping study. *Front Neurol*. (2021) 12:785822. doi: 10.3389/fneur.2021.785822

39. Bivard A, Levi C, Lin L, Cheng X, Aviv R, Spratt NJ, et al. Validating a predictive model of acute advanced imaging biomarkers in ischemic stroke. *Stroke*. (2017) 48:645–50. doi: 10.1161/STROKEAHA.116.015143

40. Tong E, Patrie J, Tong S, Evans A, Michel P, Eskandari A, et al. Time-resolved CT assessment of collaterals as imaging biomarkers to predict clinical outcomes in acute ischemic stroke. *Neuroradiology*. (2017) 59:1101–9. doi: 10.1007/s00234-017-1914-z

41. Harston GW, Rane N, Shaya G, Thandeswaran S, Cellerini M, Sheerin F, et al. Imaging biomarkers in acute ischemic stroke trials: a systematic review. *AJNR Am J Neuroradiol*. (2015) 36:839–43. doi: 10.3174/ajnr.A4208

42. Uchida Y, Kan H, Inoue H, Oomura M, Shibata H, Kano Y, et al. Penumbra detection with oxygen extraction fraction using magnetic susceptibility in patients with acute ischemic stroke. *Front Neurol*. (2022) 13:752450. doi: 10.3389/fneur.2022.752450

43. Uchida Y, Kan H, Kano Y, Onda K, Sakurai K, Takada K, et al. Longitudinal changes in Iron and myelination within ischemic lesions associate with neurological outcomes: a pilot study. *Stroke*. (2024) 55:1041–50. doi: 10.1161/STROKEAHA.123.044606

44. De Deurwaerdere P, Gaetani S, Vaughan RA. Old neurochemical markers, new functional directions?: an editorial for 'Distinct gradients of various neurotransmitter markers in caudate nucleus and putamen of the human brain' on page 650. *J Neurochem*. (2020) 152:623–6. doi: 10.1111/jnc.14929

45. Grahn JA, Parkinson JA, Owen AM. The cognitive functions of the caudate nucleus. *Prog Neurobiol*. (2008) 86:141–55. doi: 10.1016/j.pneurobio.2008.09.004

46. Nathoo N, Gee M, Nelles K, Burt J, Sun H, Seres P, et al. Quantitative susceptibility mapping changes relate to gait issues in Parkinson's disease. *Can J Neurol Sci*. (2023) 50:853–60. doi: 10.1017/cjn.2022.316

47. Rao IY, Hanson LR, Johnson JC, Rosenbloom MH, Frey WH 2nd. Brain glucose Hypometabolism and Iron accumulation in different brain regions in Alzheimer's and Parkinson's diseases. *Pharmaceuticals*. (2022) 15:551. doi: 10.3390/ph15050551

48. Yang A, Du L, Gao W, Liu B, Chen Y, Wang Y, et al. Associations of cortical iron accumulation with cognition and cerebral atrophy in Alzheimer's disease. *Quant Imaging Med Surg*. (2022) 12:4570–86. doi: 10.21037/qims-22-7

49. Yuan XZ, Li GY, Chen JL, Li JQ, Wang XP. Paramagnetic metal accumulation in the deep gray matter nuclei is associated with neurodegeneration in Wilson's disease. *Front Neurosci*. (2020) 14:573633. doi: 10.3389/fnins.2020.573633

50. Wan J, Ren H, Wang J. Iron toxicity, lipid peroxidation and ferroptosis after intracerebral haemorrhage. *Stroke Vasc Neurol*. (2019) 4:93–5. doi: 10.1136/svn-2018-000205

51. Rodriguez-Grande B, Blackabey V, Gittens B, Pinteaux E, Denes A. Loss of substance P and inflammation precede delayed neurodegeneration in the substantia nigra after cerebral ischemia. *Brain Behav Immun*. (2013) 29:51–61. doi: 10.1016/j.bbi.2012.11.017

52. Zhang J, Zhang Y, Xing S, Liang Z, Zeng J. Secondary neurodegeneration in remote regions after focal cerebral infarction: a new target for stroke management? *Stroke*. (2012) 43:1700–5. doi: 10.1161/STROKEAHA.111.632448

53. Nakanishi H, Tamura A, Kawai K, Kawai K, Yamamoto K, Yamamoto K. Electrophysiological studies of rat substantia nigra neurons in an in vitro slice preparation after middle cerebral artery occlusion. *Neuroscience*. (1997) 77:1021–8. doi: 10.1016/s0306-4522(96)00555-6

54. Lee H, Lee K, Kim YD, Nam HS, Lee HS, Cho S, et al. Association between substantia nigra degeneration and functional outcome in patients with basal ganglia infarction. *Eur J Neurol*. (2024) 31:e16111. doi: 10.1111/ene.16111

55. Kummer BR, Diaz I, Wu X, Aaroe AE, Chen ML, Iadecola C, et al. Associations between cerebrovascular risk factors and parkinson disease. *Ann Neurol*. (2019) 86:572–81. doi: 10.1002/ana.25564

frontiers | Frontiers in Neurology

TYPE Original Research
PUBLISHED 10 January 2025
DOI 10.3389/fneur.2024.1485921

OPEN ACCESS

EDITED BY
Shuai Ren,
Affiliated Hospital of Nanjing University of Chinese Medicine, China

REVIEWED BY
Huilin Zhao,
Shanghai Jiao Tong University, China
Li'an Huang,
First Affiliated Hospital of Jinan University, China

*CORRESPONDENCE
Hui-Ling Ren
✉ renhuiling2010@163.com

†These authors have contributed equally to this work

RECEIVED 25 August 2024
ACCEPTED 27 December 2024
PUBLISHED 10 January 2025

CITATION
Zhang G-S, Bu W, Meng L-H, Li W-J, Dong Y-J, Cao X-Y, Gao Q, Zhang X-Y and Ren H-L (2025) The correlation between intracranial atherosclerosis and white matter hyperintensities in cerebral small vessel disease: a high-resolution magnetic resonance imaging study.
Front. Neurol. 15:1485921.
doi: 10.3389/fneur.2024.1485921

The correlation between intracranial atherosclerosis and white matter hyperintensities in cerebral small vessel disease: a high-resolution magnetic resonance imaging study

Gui-Song Zhang[1†], Wei Bu[2†], Ling-Hui Meng[3], Wen-Jun Li[1], Yu-Juan Dong[1], Xiao-Yun Cao[1], Qi Gao[4], Xuan-Ye Zhang[4] and Hui-Ling Ren[1*]

[1]Department of Neurology, The Third Hospital of Hebei Medical University, Shijiazhuang, China, [2]Department of Neurosurgery, The Third Hospital of Hebei Medical University, Shijiazhuang, China, [3]Department of Radiology, The Third Hospital of Hebei Medical University, Shijiazhuang, China, [4]School of Basic Medicine, Hebei Medical University, Shijiazhuang, China

Objective: Recent studies have indicated a close relationship between intracranial arterial stenosis and white matter hyperintensities (WMHs), but few have reported on the correlation between the characteristics of intracranial arterial wall plaques and WMHs. The aim of this study was to comprehensively assess the correlation between intracranial atherosclerosis plaques and WMHs using 3.0T high-resolution magnetic resonance imaging (HR-MRI).

Patients and methods: Ninety-two ischemic stroke patients with middle cerebral artery (MCA) stenosis <50% on cranial magnetic resonance angiography (MRA) underwent conventional MRI and HR-MRI examinations. T2-weighted fluid-attenuated inversion recovery (T2-FLAIR) images were processed using 2D VBNeT automatic segmentation technology to segment WMH volume. HR-MRI images were analyzed using ImageJ software to evaluate the luminal area, outer wall area, plaque distribution, luminal stenosis rate, remodeling patterns, and other plaque parameters at the stenosis site and reference points of the MCA M1 segment. The correlation between the presence of plaques, plaque distribution, luminal stenosis rate, T1 hyperintensity, remodeling patterns, remodeling ratio (RR), eccentric plaques, and plaque burden with the volume of cerebral WMHs was analyzed.

Results: Compared with the no-plaque group, the plaque group had significantly higher age, male ratio, total WMH volume, periventricular WMH (PVWMH) volume, deep WMH (DWMH) volume, and juxtacortical WMH (JCWMH) volume (all $p < 0.05$). The Kruskal-Wallis H test showed that patients with plaques on the superior and dorsal sides of the MCA M1 segment had higher levels of total WMH volume, PVWMH volume, DWMH volume, and JCWMH volume than patients with plaques on the inferior and ventral sides (all $p < 0.05$). Age, diabetes, previous stroke events, plaque distribution, positive remodeling, eccentric plaques, and RR were positively correlated with total WMH volume, PVWMH volume, and JCWMH volume (all $p < 0.05$). The presence of plaques, plaque distribution, and positive remodeling were independent risk factors for total WMH volume (all $p < 0.05$).

Conclusion: The presence of intracranial atherosclerotic plaques, plaque distribution, and positive remodeling are closely associated with increased cerebral WMHs burden in patients with ischemic stroke, which further supports the relationship between large artery atherosclerosis and CSVD.

KEYWORDS

white matter hyperintensities, middle cerebral artery, atherosclerosis, high-resolution magnetic resonance imaging, volume, ischemic stroke, positive remodeling

Highlights

- Question: Intracranial atherosclerosis and white matter hyperintensities (WMHs) are commonly found in patients with ischemic stroke. However, the relationship between the characteristics of intracranial arterial wall plaques and WMHs remains unclear.
- Findings: In patients with ischemic stroke, the characteristics of intracranial arterial wall plaques, such as plaque distribution and positive remodeling, are closely associated with the development of WMHs.
- Meaning: Research based on HR-MRI indicates that the characteristics of intracranial atherosclerotic plaques in patients with ischemic stroke can exacerbate the white matter burden, providing a theoretical foundation for the effective prevention and treatment of WMHs.

1 Introduction

Cerebral small vessel disease (CSVD) is characterized by affecting the perforating cerebral arterioles, capillaries, and venules, which can lead to a variety of clinical manifestations and imaging features. White matter hyperintensities (WMHs) serve as a critical imaging biomarker that reflects the underlying vascular pathology of CSVD, while the etiology and mechanisms of WMHs are multifactorial. In the context of CSVD, ischemia triggers a series of pathophysiological alterations, the breakdown of the blood–brain barrier, facilitating the infiltration of inflammatory mediators and exacerbating the tissue damage (1), thereby impairing the normal functioning of the brain's white matter tracts.

Numerous studies have confirmed the coexistence of atherosclerotic stenosis with cerebral WMHs (2). A large artery and small vessel disease may share common vascular risk factors, such as advanced age, hypertension, and diabetes, that could play a mediating role. A meta-analysis showed that the presence of ≥50% atherosclerotic stenosis in both intracranial and extracranial arteries was associated with an increased risk of WMHs and increased volume of WMHs, even after accounting for the effects of vascular risk factors (3). Another CT-based brain perfusion study found WMHs attributable to cerebral hypoperfusion secondary to cranial vascular stenosis (4). Thus, the pathophysiological link between the two is thought to be a reduction in cerebral blood flow, leading to chronic ischemia in the white matter.

In addition to atherosclerotic stenosis of the large cerebral arteries, plaque composition characteristics have been reported to be strongly associated with the severity of WMHs (5). A CARE-II study (6) showed that carotid atherosclerotic plaque characteristics were more useful in assessing the severity of WMHs than the degree of stenosis within intracranial arteries. In recent years, the presence of atherosclerotic plaques (especially complex plaques) has also been shown to be strongly associated with imaging markers of CSVD (7). High-resolution magnetic resonance imaging (HR-MRI) allows non-invasive visualization of intracranial vessel walls, making it possible to comprehensively explore the structure and composition of unstable plaques. An HR-MRI study discussed the significant role of intracranial arterial vulnerable plaque characteristics, particularly intraplaque hemorrhage, and plaque enhancement in the severity of WMHs (8). Therefore, the study provides us with a new perspective to explore the pathophysiological mechanisms of CSVD. In addition to alterations in cerebral hemodynamics, mechanisms such as inflammatory responses, microembolism, and vascular dysfunction are likely to contribute to disease progression.

Therefore, based on the HR-MRI study, we deeply assess the presence and characteristics of atherosclerotic plaques in the middle cerebral artery (MCA) and their association with WMHs. The aim was to identify potential independent risk factors for the volume of WMHs, and further explore the underlying vascular pathology of CSVD.

2 Methods

2.1 Patients

Patients were selected from the Third Hospital of Hebei Medical University. A retrospective study of consecutive patients with cerebral ischemic stroke who underwent HR-MRI was performed between January 2021 and April 2024. Inclusion criteria were: (1) age ≥ 18; (2) diffusion-weighted imaging (DWI) showed evidence of acute infarct foci in the blood-supplying region of the MCA; (3) MRI was performed within 2 weeks of symptoms onset; (4) presence of at least one atherosclerosis risk factor; (5) all the enrolled patients underwent HR-MRI, T2-weighted fluid-attenuated inversion recovery (T2-FLAIR) and magnetic resonance angiography (MRA). Exclusion criteria were: (1) ≥ 50% stenosis of one carotid artery or MCA on brain MRA; (2) presence of nonatherosclerotic vascular diseases, such as vasculitis, moyamoya, dissection, arterial sequestration, etc.; (3) presence of massive cerebral infarction, intracerebral hemorrhage, intracranial infections, intracranial tumor, multiple sclerosis, cerebral white matter dystrophy, other CNS demyelinating diseases and degenerative diseases, etc.; (4) presence of contraindications to MRI; (5) poor image quality of HR-MRI or conventional MRI for accurate quantitative analysis of dilated arterial borders.

The basic clinical information was collected, including age, sex, hypertension, diabetes, coronary artery disease, hyperlipidemia,

previous stroke events, smoking, drinking, and systolic and diastolic blood pressure on admission. The next morning after admission, fasting venous blood was collected from all the enrolled patients and then sent to the clinical laboratory, the levels for fasting plasma total cholesterol (TC), triglyceride (TG), high-density lipoprotein (HDL), low-density lipoprotein (LDL), very low-density lipoprotein (VLDL), homocysteine (HCY) and uric acid (UA) were recorded.

2.2 MR imaging protocol

All participants underwent magnetic resonance imaging at the Third Hospital of Hebei Medical University with a 3.0 T MRI scanner (Signal Architect, GE Medical Systems, America) with a 19-channel head–neck coil. Conventional MRI and HR-MRI scanning protocols are included: T2-FLAIR, DWI, three-dimensional time-of-flight MRA (3D-TOF MRA), 3D CUBE T1-weighted imaging (3D CUBE T1WI), and 3D proton density-weighted imaging CUBE (3D PDWI CUBE). Sequence parameters for T2-FLAIR imaging were as follows: Repetition time (TR) = 9,000 ms; echo time (TE) = 100 ms; slice thickness = 5 mm; slices = 23; field of view (FOV) = 240 × 240 mm2; matrix = 288 × 200; pixel = 0.8 × 1.2. Sequence parameters for DWI imaging were as follows: TR = 4,351 ms; TE = 76 ms; slice thickness = 5 mm; slices = 23; FOV = 240 × 240 mm2; matrix = 128 × 160; pixel = 1.9 × 1.5. Sequence parameters for 3D-TOF MRA imaging were as follows: TR = 19 ms; TE = 3.4 ms; slice thickness = 0.7 mm; slices = 168; FOV = 220 × 220 mm2; matrix = 384× 160; pixel = 0.6 × 1.4; voxel size = 0.6 × 1.4 × 1.4. Sequence parameters for 3D CUBE T1WI imaging were as follows: TR = 702 ms, TE = 13.27 ms, slice thickness = 0.4 mm; slices = 272; FOV = 200 × 200 mm2; matrix = 280 × 280; pixel = 0.7 × 0.7; voxel size = 0.7 × 0.7 × 0.8. Sequence parameters for 3D PDWI CUBE imaging were as follows: TR = 1,500 ms, TE = 40 ms, slice thickness = 0.4 mm; slices = 272; FOV = 200 × 200 mm2; matrix = 260 × 260; pixel = 0.8 × 0.8; voxel size = 0.8 × 0.8 × 0.8. The use of a 3D-TOF MRA localizer ensured that HR-MRI cross-sectional images were perpendicular to the M1 segment of the middle cerebral artery.

2.3 MR image analysis

All patient MRI images were reviewed by two experienced neuroradiologists (M.LH and R.BB, each with 5 years of experience in neuroimaging), both of them were unaware of demographic and clinical information, and peer-reviewed by another senior neuroradiologist (P.ZG, 10 years of experience in neuroimaging) in cases of disagreement in the image analysis results. Evaluators used ImageJ software designed by the National Institutes of Health for post-processing.

2.4 Assessment of plaque characteristics

The image quality of the intracranial arterial vessel wall images was assessed and the image quality was categorized into four classes (9): Grade 1, the borders of the vessel lumen and outer wall were poorly displayed, severe artifacts were present, and the signal characteristics of the wall could not be analyzed; Grade 2, some of the borders of the vessel lumen and outer wall were displayed, a few artifacts were present, and the signal characteristics of the wall still could not be analyzed; Grade 3, the borders of the vessel lumen and outer wall were displayed, a few artifacts were present, and the signal characteristics of the wall could be analyzed; Grade 4, the borders of the vessel lumen and outer wall were displayed, no artifacts were present, and the signal characteristics of the vessel wall could be analyzed. MRI images with a grade of ≥2 were included.

Plaque assessment of MCA was performed using 3D CUBE T1WI and 3D PDWI CUBE sequences. Using multiplanar reconstruction (MPR), the three-dimensional localization points were adjusted to be located in the center of the lumen in sagittal, coronal, and axial positions. And at the same time, the cross-sections were adjusted to be perpendicular to the long axis of the vessel, to obtain a cross-sectional image of the stenosis at the narrowest point of the M1 segment of MCA. Plaque characteristics were analyzed based on cross-sectional images: (1) To determine the presence or absence of plaque in the MCA M1 segment of the subjects; (2) To assess the distribution of plaque in the narrowest part of the MCA M1 segment: on the cross-sectional images, centered on the lumen, it was divided into 4 quadrants equally: including the superior wall, the inferior wall, the ventral wall, and the dorsal wall. Quadrants accrued by plaques were recorded, and when 2 or more quadrants were accrued, the quadrant with the greatest plaque thickness was selected (10); (3) Determination of the presence of intraplaque hemorrhage in MCA M1 segment plaques: intraplaque hemorrhage was considered to be present when there was a high-signal area within the plaque at the narrowest point of the MCA M1 segment on the 3D CUBE T1WI image (with a signal intensity of >150% of 150% of the area of the adjacent vessel wall of the reference wall) (11); (4) Analysis of quantitative plaque characteristics: the vessel with the largest stenosis in the MCA M1 segment was selected, the reference vessel was preferred to be a no-plaque normal vessel proximal to the level of the largest stenosis, and if the proximal reference vessel was unavailable, an adjacent distal no-plaque normal vessel was used. Cross-sectional images of the lumen were magnified by 300% by two neuroradiologists. The lumen and wall borders were manually outlined on ImageJ software according to the region of interest (ROI), the outer wall area (OWA), the lumen area (LA), the maximum wall thickness, and the minimum wall thickness of the largest stenosis in the MCA M1 segment and the reference vessel were measured and recorded semi-automatically, respectively. The degree of lumen stenosis, remodeling ratio, eccentricity, and plaque burden were calculated based on the measurement results. The formulas for the relevant parameters were as follows: degree of luminal stenosis = (1 - LA stenosis / LA reference) × 100% (MCA stenosis was classified as mild stenosis 0–49%, moderate stenosis 50–69%, and severe stenosis 70–99%) (12); remodeling ratio (RR) = OWA stenosis / OWA reference (RR > 1.05 indicates positive remodeling; $0.95 \leq RR \leq 1.05$ indicates no remodeling; RR < 0.95 indicates negative remodeling) (13); eccentric plaques (eccentricity ≥0.5) (eccentricity = (maximum wall thickness - minimum wall thickness) / maximum wall thickness (14)); plaque burden was quantified using the normal wall index (NWI), plaque burden = (OWA stenosis - LA stenosis) / OWA stenosis (15) (Figure 1).

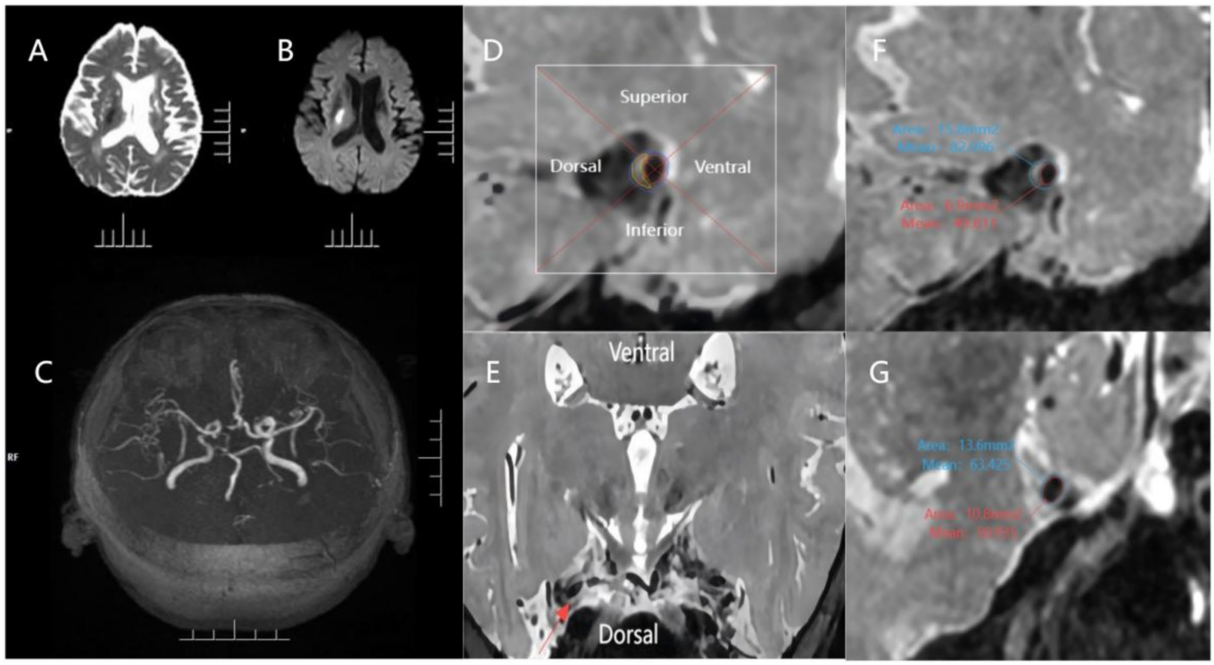

FIGURE 1
An example of evaluating plaque characteristics. The patient is a 70-year-old male who has experienced an acute ischemic stroke. **(A,B)** Diffuse right basal ganglia area is confined, with the hypointense signal on the ADC map and confined hyperintense signal on the b = 1,000 map; **(C)** 3D-TOF-MRA image showing mild stenosis of the M1 segment of middle cerebral artery bilaterally; **(D,E)** The cross-section of the plaque was divided into 4 quadrants (superior, inferior, ventral, and dorsal) using 2 perpendiculars dashed lines intersecting at the center of the lumen, as shown in the magnified image of the plaque. The red line indicates the lumen area, the blue line indicates the outer wall area and the yellow line indicates the estimated plaque. The relevant quadrant of the plaque was further verified using the reconstructed axial view of the MCA wall; **(F)** 3D PDWI CUBE measurements of the narrowest portion of the MCA M1 segment plaque: OWA 15.80 mm 2, LA 6.90 mm 2; **(G)** 3D PDWI CUBE measurement of the reference site: OWA 13.60 mm 2, LA 10.80. Remodeling ratio = 15.80 mm 2 / 13.60 mm 2 = 1.16 (positive remodeling); degree of stenosis = (1−6.90 mm 2 / 10.80 mm 2) = 36.11%.

2.5 WMH volume measurements

The T2-FLAIR images were collected and downloaded in Dic.com format before uploading them to the United Imaging Intelligence MR CSVD Intelligent Analysis System for post-processing (16) which uses a convolutional neural network algorithm with a 2D VB-Net to segment the WMHs, and which outperforms the other state-of-the-art methods in segmenting the WMHs (such as HughesNet, 3D V-Net, and VisualGeometryGroup Network). The total WMH volume (total WMH volume = periventricular WMH volume + deep WMH volume + juxtacortical WMH volume), periventricular WMH volume (PVWMH, PVWMH = lateral ventricular rim WMH volume + lateral paraventricular WMH volume), deep WMH volume (DWMH), and juxtacortical WMH volume (JCWMH) were calculated (Figure 2).

2.6 Statistical analysis

We used a statistical package for the social sciences (SPSS 26) to conduct statistical analysis and used GraphPad Prism 9 to plot. When comparing the baseline characteristics and imaging characteristics of the plaque group and the no-plaque group. Continuous variables that conformed to normal distribution were expressed as mean ± standard deviation. Continuous variables that were not normally distributed were expressed as median and interquartile spacing, and categorical variables were expressed as frequency and percentage. Continuous variables were tested using the student-*t* test or the Mann–Whitney *U* test, and categorical variables were tested using the $\chi 2$ test or the Fisher exact test. For the plaque group, the Kruskal-Wallis H test was used to compare the relationship between the quadrant in which the different plaques were located and the WMH volume. Spearman correlation analysis was used to determine the relationship of clinical characteristics and plaque characteristics with total WMH volume, PVWMH volume, DWMH volume, and JCWMH volume. Independent variables controlling for $p < 0.1$ in Spearman's correlation analysis were included in a multifactorial generalized linear model to analyze the relationship between different plaque parameters and WMH volume. The variance inflation factors (VIFs) among variables were checked to avoid multicollinearity among independent variables. Two-tailed *p*-values less than 0.05 were considered statistically significant.

3 Results

3.1 Clinical characteristics

A total of 136 patients with acute ischemic stroke who visited our hospital from January 2021 to May 2024 were included. Among them, 92 patients met the inclusion and exclusion criteria for enrollment. The flow chart of subject enrolment is shown (Figure 3). The 92 patients

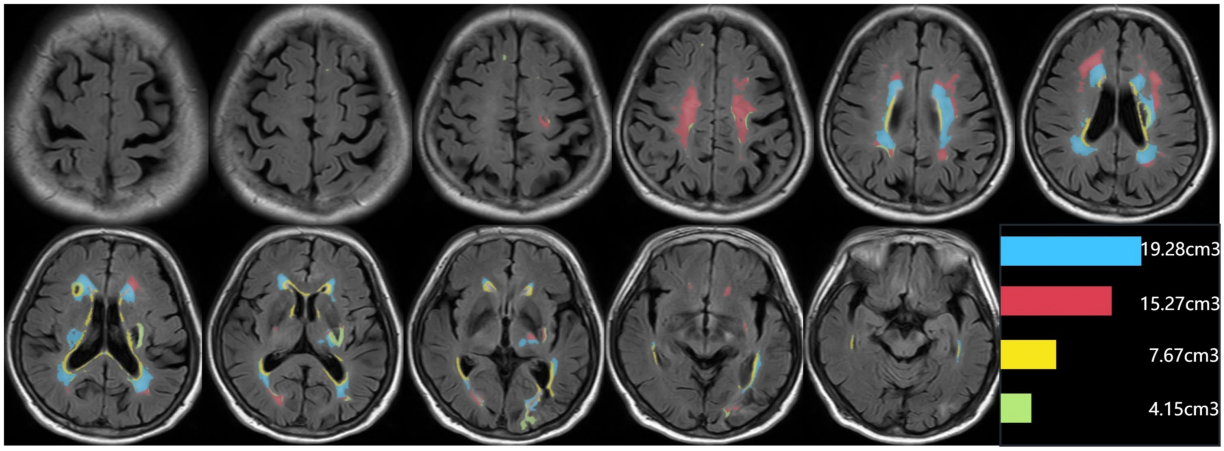

FIGURE 2
An example of segmentation results for subclassified WMHs. Display the segmentation map and the volumes of each subclassified WMH area. The regions of each subclassified WMH are represented by different colors (blue zone = lateral paraventricular WMH volume; red zone = deep WMH volume; yellow zone = lateral ventricular rim WMH volume; green = juxtacortical WMH volume).

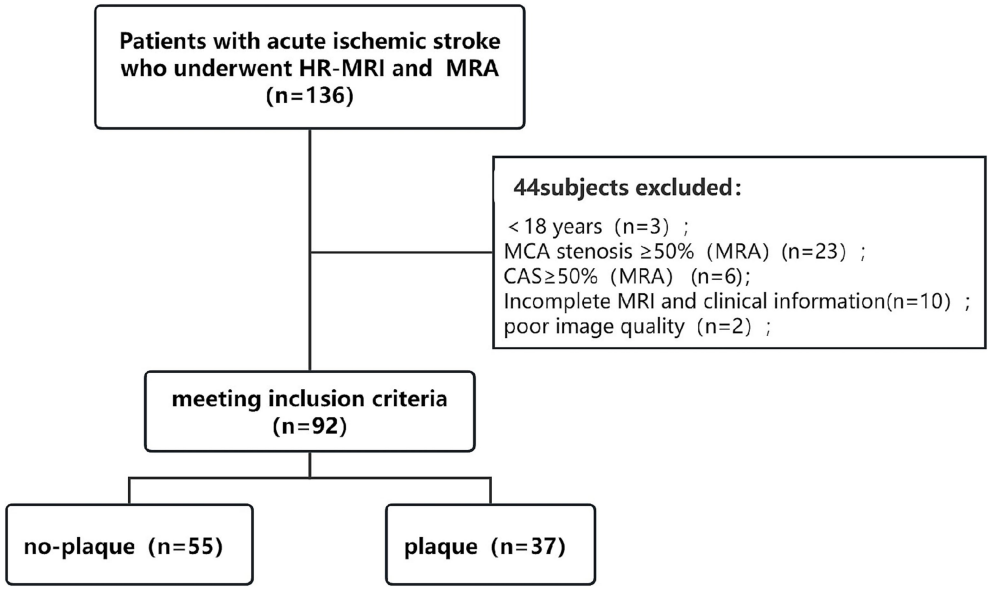

FIGURE 3
Flow chart. HR-MRI, high-resolution magnetic resonance imaging; MRA, magnetic resonance angiography; MCA, middle cerebral artery; CAS, carotid artery stenosis.

finally included in the statistical analysis had a mean age of 55.50 ± 12.87 years, 64 males, 65 with hypertension, 29 with diabetes, 12 with coronary artery disease, 21 with hyperlipidemia, 19 smokers, 21 drinkers, and 32 previous strokes. Among the subjects of this study, no-plaque was seen in the MCA M1 segment in 55 patients (59.78%) and the plaque was present in the MCA M1 segment in 37 patients (40.22%).

3.2 Comparison of clinical and imaging characteristics between plaque group and no-plaque group

Compared to the no-plaque group (n = 55), the plaque group (n = 37) had higher levels of age, percentage of males, total WMH volume, PVWMH volume, DWMH volume, and JCWMH volume (Table 1 and Figure 4) (all $p < 0.05$).

3.3 Comparison of WMH volume for different plaque distributions

For patients with plaques, the difference between the four groups of total WMH volume, PVWMH volume, DWMH volume, and JCWMH volume was statistically significant. The total WMH volume, PVWMH volume, DWMH, and JCWMH volume were higher in patients with plaques on the superior and dorsal sides of the MCA M1 segment than in those with plaques on the inferior and ventral sides (Figure 5) (all $p < 0.05$).

TABLE 1 Comparison of clinical and imaging characteristics between the plaque group and the no-plaque group.

Characteristic	No-plaque group (n = 55)	Plaque group (n = 37)	p-value
Age (years), mean [SD]	53.33 ± 13.09	58.73 ± 12.00	0.048
Sex male, n (%)	34 (61.8%)	30 (81.1%)	0.049
Vascular risk factor			
Hypertension, n (%)	37 (67.3%)	28 (75.7%)	0.385
Diabetes, n (%)	14 (25.5%)	15 (40.5%)	0.127
Coronary artery disease, n (%)	5 (9.1%)	7 (18.9%)	0.170
Hyperlipidemia, n (%)	11 (20.0%)	10 (27.0%)	0.431
Smoking, n (%)	8 (14.6%)	11 (29.7%)	0.078
Drinking, n (%)	9 (16.4%)	12 (32.4%)	0.072
Previous stroke events, n (%)	18 (32.7%)	14 (37.8%)	0.614
Laboratory parameters			
Systolic blood pressure, mean [SD], mmHg	138.49 ± 20.41	144.92 ± 21.15	0.148
Diastolic blood pressure, mean [SD], mmHg	87.35 ± 18.03	88.68 ± 12.81	0.700
HCRP, median [IQR], mmol/L	2.49 (1.11, 8.24)	2.07 (1.11, 6.13)	0.516
Hcy, median [IQR], mmol/L	12.30 (10.50, 17.19)	13.20 (10.79, 16.55)	0.946
TC, median [IQR], mmol/L	4.56 (3.66, 5.32)	4.56 (3.96, 5.22)	0.933
TG, median [IQR], mmol/L	1.35 (1.04, 1.84)	1.33 (0.98, 2.29)	0.729
HDL, median [IQR], mmol/L	1.07 (0.90, 1.28)	1.00 (0.89, 1.18)	0.534
LDL, mean [SD], mmol/L	2.66 ± 0.81	2.58 ± 0.72	0.602
VLDL, median [IQR], mmol/L	0.61 (0.47, 0.84)	0.60 (0.45, 1.04)	0.723
UA, median [IQR], mmol/L	328.00 (276.00, 397.00)	337.00 (261.50, 414.50)	0.927

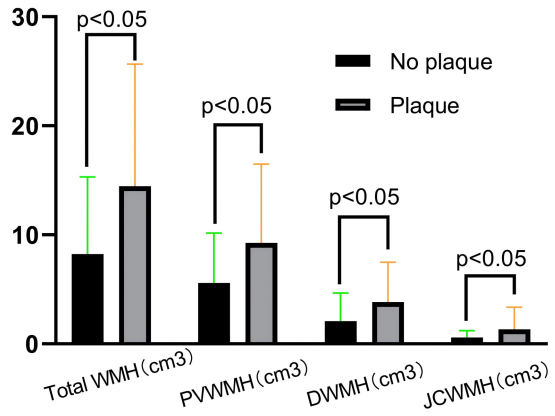

FIGURE 4
Imaging characteristics of patients between the plaque group and the no-plaque group.

3.4 Correlation of clinical and plaque characteristics with WMH volume

For all patients, age, diabetes, and previous stroke events were positively correlated with total WMH volume, PVWMH volume, and JCWMH volume; for patients with plaques, plaque distribution, positive remodeling, eccentric plaques, and RR were positively correlated with total WMH volume, PVWMH volume, DWMH volume, and JCWMH volume (Table 2 and Figure 6) (all $p > 0.05$).

3.5 Multifactor generalized linear model for WMH volume

Independent variables with $p < 0.1$ in Spearman's correlation analysis were selected as control variables and included in the multifactor generalized linear model shown: the presence of plaques, plaque distribution, and positive remodeling were independent risk factors for the total volume of WMH (Table 3) (all $p > 0.05$).

4 Discussion

4.1 Findings of our study

Our study focused on specific characteristics of atherosclerotic plaques with less than 50% MCA stenosis, including plaque distribution, plaque burden, and remodeling patterns. Our findings confirm that, after adjusting for significant risk factors such as age and previous stroke events, the presence of plaques at the orifice of the perforating arteries of the MCA is significantly positively correlated with WMH volume. Additionally, among the 37 patients with arterial plaque formation, plaque distribution and positive remodeling are independent risk factors for the total volume of WMHs. Furthermore, patients with a higher vascular remodeling ratio tend to have a larger volume of WMHs.

10.3389/fneur.2024.1485921

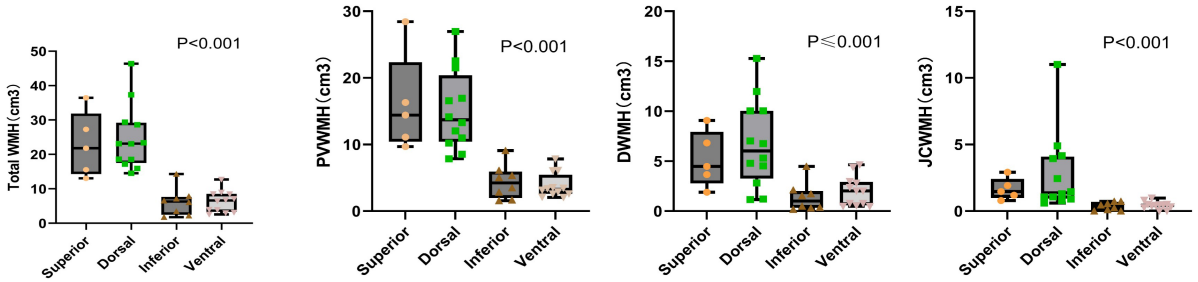

FIGURE 5
Comparison of WMH volume for different plaque distributions.

TABLE 2 Correlation of clinical and plaque characteristics with WMH volume.

Characteristic	Total WMH (cm^3)		PVWMH (cm^3)		DWMH (cm^3)		JCWMH (cm^3)	
	r	*p*-value	*r*	*p*-value	*r*	*p*-value	*r*	*p*-value
Clinical characteristics								
Age	0.388	<0.001	0.435	<0.001	0.204	0.051	0.353	0.001
Diabetes	0.274	0.008	0.277	0.008	0.162	0.123	0.263	0.011
Previous stroke events	0.344	0.001	0.322	0.002	0.284	0.006	0.432	<0.001
Diastolic blood pressure	−0.095	0.370	−0.104	0.322	−0.074	0.486	−0.218	0.037
Plaque characteristics								
Plaque	0.293	0.005	0.270	0.009	0.298	0.004	0.271	0.009
Plaque distribution	0.858	<0.001	0.853	<0.001	0.655	<0.001	0.818	<0.001
Moderate or severe stenosis	0.000	1.000	0.018	0.917	−0.150	0.374	0.115	0.498
T1 hyperintensity	−0.246	0.142	−0.201	0.232	−0.218	0.194	−0.112	0.509
Positive remodeling	0.710	<0.001	0.684	<0.001	0.642	<0.001	0.676	<0.001
Eccentric plaques	0.726	<0.001	0.705	<0.001	0.647	<0.001	0.676	<0.001
Plaque burden	0.197	0.242	0.199	0.238	0.108	0.524	0.335	0.042

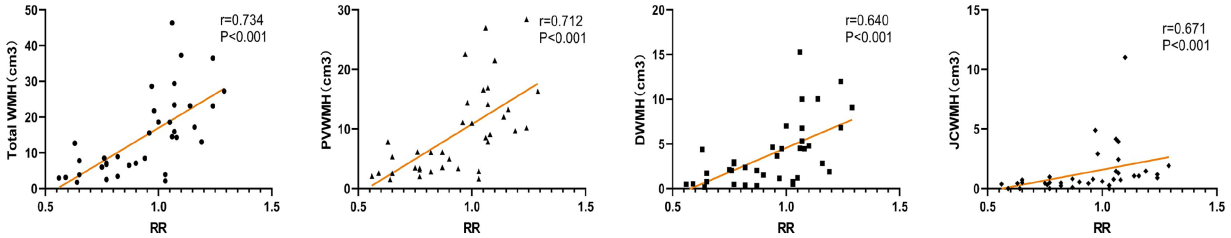

FIGURE 6
Correlation between RR and WMH volume.

4.2 Comparison with previous studies

The large artery is a new perspective to explore CSVD. A meta-analysis (3) involving 10,841 participants, which searched 21 eligible cross-sectional studies, found that the presence of both intracranial and extracranial atherosclerotic stenosis was associated with an increased risk of WMHs, but that this association was significant in the extracranial atherosclerotic stenosis (ECAS) but less so in the intracranial atherosclerotic stenosis (ICAS). Ni et al. (17), when assessing the relationship between WMHs burden and unilateral ICAS by examining luminal stenosis, plaque enhancement, and cerebral perfusion, concluded that the volume of DWMH ipsilateral to the site of ICAS was significantly greater than that of the contralateral site, which all suggests that ICAS contributes to the formation of WMHs. Another 3-year retrospective longitudinal study (18) yielded that patients with more severe ICAS were more likely to have progression of WMHs and had a significant correlation. Whereas the present study did not find an association between the degree of stenosis of the intracranial arteries and WMHs, probably because the MCA stenosis of our included subjects was <50% on MRA, which was not sufficient

TABLE 3 Multifactor generalized linear model for WMH volume.

Characteristic	Total WMH (cm^3)		PVWMH (cm^3)		DWMH (cm^3)		JCWMH (cm^3)	
	B	*p*-value	*B*	*p*-value	*B*	*p*-value	*B*	*p*-value
Plaque	4.614	0.008	2.415	0.026	1.634	0.011	0.632	0.019
Plaque distribution								
Superior or dorsal	9.446	0.004	6.683	0.002	1.751	0.253	0.995	0.284
Degree of stenosis								
Moderate or severe stenosis	1.631	0.482	0.972	0.518	0.259	0.812	0.383	0.558
Plaque vulnerability								
T1 hyperintensity	−5.219	0.220	−4.186	0.125	−0.738	0.709	−0.495	0.685
Positive remodeling	5.960	0.037	2.826	0.128	2.679	0.044	0.525	0.514
Eccentric plaques	2.785	0.301	1.189	0.496	1.274	0.302	0.203	0.789
Plaque burden	2.152	0.767	1.618	0.731	−0.564	0.865	1.507	0.459

to cause a significant hypoperfusion of the cerebral blood flow, we did find that some of the plaque features were correlated with WMHs. Therefore, we speculate that plaque features are more valuable in assessing the progression of WMHs when intracranial arterial MRA shows stenosis <50%. These may provide clues to understand the mechanism of WMHs progression.

4.3 The presence of intracranial atherosclerotic plaques contributes to the progression of WMHs

The presence of intracranial atherosclerotic plaques in large arteries aggravated WMHs in our study. This finding is consistent with the results of Zhu and colleagues, who studied patients diagnosed with CSVD or embolic stroke of undetermined source (ESUS) (7) that intracranial non-stenotic atherosclerotic plaques, especially complex plaques, were strongly associated with CSVD imaging markers, while this study also found a significant association between intracranial atherosclerotic plaques (IAPs) and the presence of WMHs, which further suggests that non-stenotic plaques may contribute to white matter changes. The observed correlation could be due to the intracranial large arteries due to the lack of external elasticity plates, exhibit a markedly slower metabolism compared with the extracranial arteries, and a relatively slower autoregulatory function. As a result, the formation of cerebral aortic plaques often signals that a certain degree of injury already exists in small vessels throughout the body.

4.4 Plaques located superiorly or dorsally to the MCA M1 segment exhibit a greater burden of WMHs

Our study enrolled patients with less than 50% stenosis of the MCA, who are traditionally classified as having small vessel occlusions. These penetrating arteries, which include the lenticulostriate arteries (LSA), usually originate at acute angles from the parent artery. This anatomical feature predisposes to the formation of atheromatous plaque. This region is also one of the common sites for leukoaraiosis (LA) lesions, considered one of the manifestations of CSVD. A previous study focusing on basilar artery branching atherosclerotic disease (BABAD) found (19) that patients with BABAD had a higher severity of WMHs in the periventricular region of the brain, and also demonstrated a significant association between WMHs and BABAD, and this association was independent of vascular risk factors. Our study reached similar conclusions, showing that atherosclerosis in penetrating arteries is significantly correlated with WMH volume. The recent ZOOM@SVDs study utilized the advantage of 7T MRI to show the fine structural function of small perforating vessels and found that perforating arteries were strongly associated with CSVD (20). Another cohort study demonstrated that ischemic stroke patients with BAD are often accompanied by a high prevalence of cerebral white matter lesions (21).

Our results showed that total WMH volume and PVWMH volume were greater in patients with plaques located on the superior or dorsal side of the MCA. After also controlling for the plaque intrinsic characteristics variable, plaques located on the superior or dorsal side remained an independent risk factor for total WMH volume, suggesting that it is plaque distribution rather than plaque intrinsic characteristics that determine the progression of WMHs. Our study contributes to further understanding of the pathophysiology of WMHs and thus monitors the relationship between cerebral atherosclerosis and WMHs. However, the relatively small sample size of this study may have led to insufficient statistical power and an increased risk of Type II errors, so caution is needed in interpreting these results. Therefore, we used HR-MRI to detect atherosclerotic plaques in patients' MCA branch arteries and concluded that patients with plaques located superiorly or dorsally to the MCA M1 segment had a greater WMHs burden, and the correlation may be because the perforating arteries often open superiorly or dorsally to the MCA (22), and plaque located at the orifice of a perforating artery often leads to altered hemodynamics (23) in the downstream region, which in turn causes ischemic damage to white matter. Not only can this ischemia lead to oligodendrocyte death and axonal degeneration, causing an increase in white matter volume, but reduced cerebral perfusion can lead to impaired cerebrovascular reactivity (24), which is the ability of the cerebral vessels to dilate in response to changes in metabolic demand, can lead to inefficient cerebral blood flow regulation. This impairment can contribute to white matter ischemia and atrophy. This

is not a simple CSVD, but a result of atherosclerosis of the large arteries.

4.5 Positive remodeling increases the WMHs burden

Previous studies have found that structural cranial arterial remodeling may be important in the pathophysiology of WMHs (25). Chen et al. concluded that cerebral arterial remodeling scores are positively associated with severe WMHs and that patients with large cranial arterial diameters may have a heavier CSVD burden (26). It has also been suggested that cerebral arterial outward remodeling may be a biomarker of systemic arterial stiffness (27). A large number of recent research has established a close association between cerebral arterial stiffness and the development of CSVD (28), which indirectly suggests that cerebral arterial remodeling about WMHs. Meanwhile, a recent systematic evaluation and meta-analysis showed that intracranial arterial dilatation was associated with a high prevalence of CSVD imaging markers in patients with ischemic stroke (29). Our study further established a close correlation between plaque vulnerability parameters (i.e., positive remodeling) and WMHs. The correlation may be because intracranial large arteries, as a bridge between extracranial large arteries and small cerebral vessels, function to reduce systemic pressure and pulsatility of blood delivery to cerebral capillaries, and cerebral arteriolar ectopic remodeling may reduce physiological cerebral self-regulation, leading to the transmission of hemodynamic loads to the downstream small blood vessels, thus causing CSVD (30). Thus, our findings suggest that remodeling of cranial arteries may play an important role in the development of large artery disease and small vessel disease.

Outward remodeling of intracranial arteries, as an early response to atherosclerotic plaque formation, has the potential to delay luminal stenosis but also increases the risk of plaque rupture and has unknown effects on the brain. Previously Zhang et al. (31) in their study of the relationship between remodeling patterns and ischemic stroke in patients with atherosclerotic MCA stenosis, found that positive remodeling was associated with an increase in plaque area, whereas this suggests that the atherosclerotic disease burden of the MCA is increasing, and that an increase in the plaque burden further increases the overall cerebrovascular event risk. Whereas the correlation between atherosclerotic changes in intracranial arteries without significant stenosis on MRA and small vessel disease has rarely been explored, our study focused on examining the remodeling of intracranial arterial walls, looking in particular for evidence of positive remodeling (i.e., outward expansion of the arterial wall) and discussing in-depth the impact of the pattern of remodeling on the progression of white matter, and the results of the present study suggest that positive remodeling may be associated with more severe WMHs.

4.6 Potential limitations

The present study has some limitations: (1) the sample size of this study was limited, and although multifactor analysis revealed a close association between plaque characteristics and WMHs, a small number of data points are more susceptible to random fluctuations. This affects the robustness of the statistical analysis and restricts the generalizability of the findings. Future studies should aim to expand the sample size to better assess the true relationship between atherosclerotic plaques and WMHs; (2) the retrospective design of the present study does not allow for the assessment of the causal relationship between intracranial atherosclerosis and WMHs, whereas prospective and longitudinal follow-up studies help to observe the dynamic course of the relationship between plaque characteristics and WMHs; (3) the present study lacks hemodynamic indices, and future studies may investigate whether plaque distribution, positive remodeling, and other plaque characteristics affecting white matter lesions are mediated by hemodynamic factors; (4) the present study did not explore CSVD imaging markers other than WMHs, limiting the comprehensive assessment of cranial atherosclerosis's impact on brain injury.

5 Conclusion

In conclusion, our study found that the presence of atheromatous plaques, their geometric distribution, and positive remodeling were closely associated with the volume of WMHs, contributing to the progression of white matter lesions. HR-MRI provided *in vivo* evidence that intracranial atherosclerosis, particularly plaque characteristics, can lead to white matter lesions, which further demonstrated that atherosclerotic alterations in the brain may contribute to the development of WMHs. Therefore, more attention should be paid to the interconnectedness of cerebral large-vessel and CSVD. HR-MRI can also serve as a valuable tool for assessing plaque characteristics, aiding in the stratification of future clinical risk and supporting the development of individualized treatment strategies.

Data availability statement

The raw data supporting the conclusions of this article will be made available by the authors, without undue reservation.

Ethics statement

The studies involving humans were approved by the ethics committee of the Third Hospital of Hebei Medical University (approval code: 2023-016-1). The studies were conducted in accordance with the local legislation and institutional requirements. The participants provided their written informed consent to participate in this study.

Author contributions

G-SZ: Conceptualization, Data curation, Methodology, Writing – original draft, Writing – review & editing. WB: Conceptualization, Formal analysis, Investigation, Writing – original draft, Writing – review & editing. L-HM: Software, Writing – review & editing. W-JL: Software, Writing – review & editing. Y-JD: Data curation, Writing – review & editing. X-YC: Data curation, Writing – review & editing. QG: Investigation,

Writing – review & editing. X-YZ: Investigation, Writing – review & editing. H-LR: Funding acquisition, Methodology, Project administration, Writing – review & editing.

Funding

The author(s) declare financial support was received for the research, authorship, and/or publication of this article. This study was supported by the Key Science and Technology Research Programme of Hebei Province, China (grant number: 20240760) and 2024 Government-funded Clinical Medicine Talent Training Project (grant number: ZF2024090).

Conflict of interest

The authors declare that the research was conducted in the absence of any commercial or financial relationships that could be construed as a potential conflict of interest.

Publisher's note

References

1. Litak J, Mazurek M, Kulesza B, Szmygin P, Litak J, Kamieniak P, et al. Cerebral small vessel disease. *Int J Mol Sci*. (2020) 21:9729. doi: 10.3390/ijms21249729

2. Li Q, Yu M, Yang D, Han Y, Liu G, Zhou D, et al. Association of the coexistence of intracranial atherosclerotic disease and cerebral small vessel disease with acute ischemic stroke. *Eur J Radiol*. (2023) 165:110915. doi: 10.1016/j.ejrad.2023.110915

3. Zhang W, Fu F, Zhan Z. Association between intracranial and extracranial atherosclerosis and white matter hyperintensities: a systematic review and meta-analysis. *Front Aging Neurosci*. (2024) 15:1240509. doi: 10.3389/fnagi.2023.1240509

4. Feng F, Kan W, Yang H, Ding H, Wang X, Dong R. White matter hyperintensities had a correlation with the cerebral perfusion level, but no correlation with the severity of large vessel stenosis in the anterior circulation. *Brain Behav*. (2023) 13:e2932. doi: 10.1002/brb3.2932

5. Zhang X, Li J, Zeng JJ. The association between white matter lesions and carotid plaque score: a retrospective study based on real-world populations. *Eur Rev Med Pharmacol Sci*. (2022) 26:9365–71. doi: 10.26355/eurrev_202212_30687

6. Shen R, Tong X, Zhao C, Qiao H, Ning Z, Li J, et al. Atherosclerotic plaque characteristics in extracranial carotid artery may indicate closer association with white matter hyperintensities than intracranial arteries: a CARE-II study. *Eur J Radiol*. (2024) 170:111208. doi: 10.1016/j.ejrad.2023.111208

7. Zhu KL, Shang ZY, Liu BJ, Wang Y, Li J, Yang BQ, et al. The association of intracranial atherosclerosis with cerebral small vessel disease imaging markers: a high-resolution magnetic resonance imaging study. *Sci Rep*. (2023) 13:17017. doi: 10.1038/s41598-023-44240-1

8. Li J, Tian Y, Shi Y, Cui Y, Lian J, Liu P. Association of vulnerable plaques with white matter hyperintensities on high-resolution magnetic resonance imaging. *Quant Imaging Med Surg*. (2024) 14:3606–18. doi: 10.21037/qims-23-1856

9. Zhou Z, Li R, Zhao X, He L, Wang X, Wang J, et al. Evaluation of 3D multi-contrast joint intra- and extracranial vessel wall cardiovascular magnetic resonance. *J Cardiovasc Magn Reson*. (2015) 17:41. doi: 10.1186/s12968-015-0143-z

10. Xu WH, Li ML, Niu JW, Feng F, Jin ZY, Gao S. Intracranial artery atherosclerosis and lumen dilation in cerebral small-vessel diseases: a high-resolution MRI study. *CNS Neurosci Ther*. (2014) 20:364–7. doi: 10.1111/cns.12224

11. Ran Y, Wang Y, Zhu M, Wu X, Malhotra A, Lei X, et al. Higher plaque burden of middle cerebral artery is associated with recurrent ischemic stroke: a quantitative magnetic resonance imaging study. *Stroke*. (2020) 51:659–62. doi: 10.1161/STROKEAHA.119.028405

12. Kasner SE, Lynn MJ, Chimowitz MI, Frankel MR, Howlett-Smith H, Hertzberg VS, et al. Warfarin aspirin symptomatic intracranial disease (WASID) trial investigators. Warfarin vs aspirin for symptomatic intracranial stenosis: subgroup analyses from WASID. *Neurology*. (2006) 67:1275–8. doi: 10.1212/01.wnl.0000238506.76873.2f

13. Qiao Y, Anwar Z, Intrapiromkul J, Liu L, Zeiler SR, Leigh R, et al. Patterns and implications of intracranial arterial remodeling in stroke patients. *Stroke*. (2016) 47:434–40. doi: 10.1161/STROKEAHA.115.009955

14. Yamagishi M, Terashima M, Awano K, Kijima M, Nakatani S, Daikoku S, et al. Morphology of vulnerable coronary plaque: insights from follow-up of patients examined by intravascular ultrasound before an acute coronary syndrome. *J Am Coll Cardiol*. (2000) 35:106–11. doi: 10.1016/s0735-1097(99)00533-1

15. Yuan W, Liu X, Yan Z, Wu B, Lu B, Chen B, et al. Association between high-resolution magnetic resonance vessel wall imaging characteristics and recurrent stroke in patients with intracranial atherosclerotic steno-occlusive disease: a prospective multicenter study. *Int J Stroke*. (2024) 19:569–76. doi: 10.1177/17474930241228203

16. Zhu W, Huang H, Zhou Y, Shi F, Shen H, Chen R, et al. Automatic segmentation of white matter hyperintensities in routine clinical brain MRI by 2D VB-net: a large-scale study. *Front Aging Neurosci*. (2022) 14:915009. doi: 10.3389/fnagi.2022.915009

17. Ni L, Zhou F, Qing Z, Zhang X, Li M, Zhu B, et al. The asymmetry of white matter Hyperintensity burden between hemispheres is associated with intracranial atherosclerotic plaque enhancement grade. *Front Aging Neurosci*. (2020) 12:163. doi: 10.3389/fnagi.2020.00163

18. Zhong T, Qi Y, Li R, Zhou H, Ran B, Wang J, et al. Contribution of intracranial artery stenosis to white matter hyperintensities progression in elderly Chinese patients: a 3-year retrospective longitudinal study. *Front Neurol*. (2022) 13:922320. doi: 10.3389/fneur.2022.922320

19. Lin PC, Chang FC, Huang HC, Tsai JY, Lin YY, Chung CP. Greater periventricular white matter hyperintensity severity in basilar artery branch atheromatous disease. *BMC Neurol*. (2017) 17:135. doi: 10.1186/s12883-017-0918-y

20. Van Den Brink H, Pham S, Siero JC, Arts T, Onkenhout L, Kuijf H, et al. Assessment of small vessel function using 7T MRI in patients with sporadic cerebral small vessel disease: the ZOOM@SVDs study. *Neurology*. (2024) 102:e209136. doi: 10.1212/WNL.0000000000209136

21. Men X, Wu A, Zhang B, Li H, Zhang L, Chen S, et al. Leukoaraiosis and NIHSS score help to differentiate subtypes of intracranial branch atheromatous disease in southern Han Chinese patients with stroke. *Neurol Sci*. (2013) 34:1727–33. doi: 10.1007/s10072-013-1322-z

22. Won SY, Cha J, Choi HS, Kim YD, Nam HS, Heo JH, et al. High-resolution intracranial Vessel Wall MRI findings among different middle cerebral artery territory infarction types. *Korean J Radiol*. (2022) 23:333–42. doi: 10.3348/kjr.2021.0615

23. Huang YC, Tsai YH, Lee JD, Weng HH, Lin LC, Lin YH, et al. Hemodynamic factors may play a critical role in neurological deterioration occurring within 72 hrs after lacunar stroke. *PLoS One*. (2014) 9:e108395. doi: 10.1371/journal.pone.0108395

24. Ashimatey BS, D'Orazio LM, Ma SJ, Jann K, Jiang X, Lu H, et al. Lower retinal capillary density in minimal cognitive impairment among older Latinx adults. *Alzheimers Dement*. (2020) 12:e12071. doi: 10.1002/dad2.12071

25. Rundek T, Della-Morte D, Gardener H, Dong C, Markert MS, Gutierrez J, et al. Relationship between carotid arterial properties and cerebral white matter hyperintensities. *Neurology*. (2017) 88:2036–42. doi: 10.1212/WNL.0000000000003951

26. Chen Z, Li H, Wu M, Chang C, Fan X, Liu X, et al. Caliber of intracranial arteries as a marker for cerebral small vessel disease. *Front Neurol*. (2020) 11:558858. doi: 10.3389/fneur.2020.558858

27. Pico F, Labreuche J, Amarenco P. Pathophysiology, presentation, prognosis, and management of intracranial arterial dolichoectasia. *Lancet Neurol*. (2015) 14:833–45. doi: 10.1016/S1474-4422(15)00089-7

28. Zhong W, Xia Y, Ying Y, Wang Y, Yang L, Liang X, et al. Cerebral pulsatility in relation with various imaging markers of cerebral small vessel disease: a longitudinal community-based study. *Ther Adv Neurol Disord*. (2024) 17:17562864241227304. doi: 10.1177/17562864241227304

29. Thiankhaw K, Ozkan H, Ambler G, Werring DJ. Relationships between intracranial arterial dolichoectasia and small vessel disease in patients with ischaemic stroke: a systematic review and meta-analysis. *J Neurol*. (2024) 271:772–81. doi: 10.1007/s00415-023-12094-2

30. Shi Y, Thrippleton MJ, Blair GW, Dickie DA, Marshall I, Hamilton I, et al. Small vessel disease is associated with altered cerebrovascular pulsatility but not resting cerebral blood flow. *J Cereb Blood Flow Metab*. (2020) 40:85–99. doi: 10.1177/0271678X18803956

31. Zhang DF, Chen YC, Chen H, Zhang WD, Sun J, Mao CN, et al. A high-resolution MRI study of relationship between remodeling patterns and ischemic stroke in patients with atherosclerotic middle cerebral artery stenosis. *Front Aging Neurosci*. (2017) 9:140. doi: 10.3389/fnagi.2017.00140

frontiers | Frontiers in Neurology

TYPE Original Research
PUBLISHED 13 January 2025
DOI 10.3389/fneur.2024.1544578

OPEN ACCESS

EDITED BY
Shuai Ren,
Affiliated Hospital of Nanjing University of Chinese Medicine, China

REVIEWED BY
Xiaowei Han,
Quzhou City People's Hospital, China
Jiajia Zhu,
First Affiliated Hospital of Anhui Medical University, China
Yuto Uchida,
Johns Hopkins Medicine, United States

*CORRESPONDENCE
Fei Chen
✉ shuibin1988@163.com
Zhenyu Dai
✉ ycsydzy@163.com
Pinglei Pan
✉ panpinglei@163.com

†These authors have contributed equally to this work and share first authorship

RECEIVED 13 December 2024
ACCEPTED 30 December 2024
PUBLISHED 13 January 2025

CITATION
Wang Z, Shen Y, Zhang X, Li Q, Dong C, Wang S, Sun H, Chen M, Xu X, Pan P, Dai Z and Chen F (2025) Prognostic value of multi-PLD ASL radiomics in acute ischemic stroke.
Front. Neurol. 15:1544578.
doi: 10.3389/fneur.2024.1544578

Prognostic value of multi-PLD ASL radiomics in acute ischemic stroke

Zhenyu Wang[1†], Yuan Shen[2†], Xianxian Zhang[2†], Qingqing Li[3], Congsong Dong[4], Shu Wang[4], Haihua Sun[2], Mingzhu Chen[2], Xiaolu Xu[2], Pinglei Pan[2,5*], Zhenyu Dai[1*] and Fei Chen[4,6*]

[1]Department of Radiology, Affiliated Hospital 6 of Nantong University, Medical School of Nantong University, Nantong, Jiangsu, China, [2]Department of Neurology, Affiliated Hospital 6 of Nantong University, Yancheng Third People's Hospital, Yancheng, Jiangsu, China, [3]Department of Radiology, Suzhou Wuzhong People's Hospital, Suzhou, Jiangsu, China, [4]Department of Radiology, Affiliated Hospital 6 of Nantong University, Yancheng Third People's Hospital, Yancheng, Jiangsu, China, [5]Department of Central Laboratory, Affiliated Hospital 6 of Nantong University, Yancheng Third People's Hospital, Yancheng, Jiangsu, China, [6]Medical Imaging Institute of Jiangsu Medical College, Yancheng, Jiangsu, China

Introduction: Early prognosis prediction of acute ischemic stroke (AIS) can support clinicians in choosing personalized treatment plans. The aim of this study is to develop a machine learning (ML) model that uses multiple post-labeling delay times (multi-PLD) arterial spin labeling (ASL) radiomics features to achieve early and precise prediction of AIS prognosis.

Methods: This study enrolled 102 AIS patients admitted between December 2020 and September 2024. Clinical data, such as age and baseline National Institutes of Health Stroke Scale (NIHSS) score, were collected. Radiomics features were extracted from cerebral blood flow (CBF) images acquired through multi-PLD ASL. Features were selected using least absolute shrinkage and selection operator regression, and three models were developed: a clinical model, a CBF radiomics model, and a combined model, employing eight ML algorithms. Model performance was assessed using receiver operating characteristic curves and decision curve analysis (DCA). Shapley Additive exPlanations was applied to interpret feature contributions.

Results: The combined model of extreme gradient boosting demonstrated superior predictive performance, achieving an area under the curve (AUC) of 0.876. Statistical analysis using the DeLong test revealed its significant outperformance compared to both the clinical model (AUC = 0.658, $p < 0.001$) and the CBF radiomics model (AUC = 0.755, $p = 0.002$). The robustness of all models was confirmed through permutation testing. Furthermore, DCA underscored the clinical utility of the combined model. The prognostic prediction of AIS was notably influenced by the baseline NIHSS score, age, as well as texture and shape features of CBF.

Conclusion: The integration of clinical data and multi-PLD ASL radiomics features in a model offers a secure and dependable approach for predicting the prognosis of AIS, particularly beneficial for patients with contraindications to contrast agents. This model aids clinicians in devising individualized treatment plans, ultimately enhancing patient prognosis.

KEYWORDS

acute ischemic stroke, radiomics, arterial spin labeling, cerebral blood flow, machine learning

1 Introduction

Stroke is defined by a range of clinical syndromes featuring focal neurological impairments triggered by cerebrovascular occurrences, standing as the third leading contributor to mortality and disability worldwide (1, 2). Acute ischemic stroke (AIS) is the predominant type of stroke, accounting for approximately 87% of all cases (3). A negative prognosis confronts approximately one-third of patients with AIS, causing a marked deterioration in their quality of life and imposing a significant financial burden on society (4). The mortality and incidence rates of AIS have decreased in recent years due to advancements in medical technology. Nevertheless, the increasing global aging population could compound the existing burden (5). Therefore, it is crucial for clinicians to promptly and precisely evaluate the prognosis of AIS to tailor individualized treatment approaches.

AIS occurs when arteries become obstructed in certain regions, causing brain tissue to death due to inadequate oxygen and glucose delivery (6). The survival of brain tissue and functional recovery, as well as the prognosis of AIS, are directly influenced by cerebral blood flow (CBF) in the infarcted area (7). The evaluation of CBF is predominantly conducted through imaging modalities, such as dynamic susceptibility contrast perfusion-weighted imaging (DSC-PWI) and computed tomography perfusion (CTP) (8). However, the use of gadolinium or iodine contrast agents is limited by allergic reactions and potential renal function impairment, which restricts their widespread clinical application (9). Arterial spin labeling (ASL) is a magnetic resonance imaging (MRI) technique that quantifies CBF by applying a pulse signal to water molecules in arterial blood, serving as an endogenous contrast agent (10). Compared to traditional imaging techniques, ASL eliminates the need for exogenous contrast agents and provides several notable advantages, such as repeated usability within a short timeframe, non-radiative properties, and reduced examination costs (11). In recent years, there has been a growing utilization of ASL imaging for evaluating blood perfusion in AIS (12, 13).

Post-labeling delay (PLD) is a critical parameter in ASL technology, representing the time between the application of the labeling pulse and the acquisition of the signal (14). However, variations in arterial transit time (ATT) across brain tissues lead to a certain degree of underestimation of CBF in single-PLD ASL technology (15). To address this limitation, multi-PLD ASL technology encodes multiple PLDs within a single scan, allowing for the measurement of ATT in brain tissue and the correction of CBF for ATT (12). This effectively addresses the problem of underestimating CBF due to single-PLD scanning (16). In areas of infarction characterized by reduced blood flow, it is essential to make this correction to prevent underestimation of perfusion (17). Multi-PLD ASL has shown robust agreement with CBF measurements acquired through DSC-PWI or CTP (18–20).

Mihoko et al. employed multi-PLD ASL technology to determine the correlation between CBF and the initial severity of AIS (21). Furthermore, Li et al. discovered that the Alberta Stroke Program Early CT Score, determined through multi-PLD ASL, serves as a standalone prognostic indicator in AIS (22). Consequently, multi-PLD ASL shows promise as an alternative method for assessing the severity and prognosis of AIS. However, the quantification of CBF in the aforementioned studies offers a restricted evaluation of perfusion status and overlooks the heterogeneity present within the lesion.

Radiomics enables the rapid, objective, and high-throughput extraction of numerous features from biomedical images (23). This process reflects subtle changes that are challenging to detect visually, thereby offering a more comprehensive array of biological information (24). Guo et al. uncovered a significant correlation between the dynamic radiomics features of DSC-PWI in the infarcted region and the clinical prognosis of AIS patients at 90 days (25). However, research focusing on the ASL radiomics features of AIS patients remains limited. Therefore, we hypothesize that CBF radiomics features based on multi-PLD-ASL have significant value in the prognostic assessment of AIS patients.

In this study, our aim is to utilize machine learning (ML) techniques to construct multi-PLD ASL radiomics models for predicting the prognosis of AIS. Moreover, relevant clinical risk factors will be incorporated to improve predictive precision and determine the optimal prognostic model.

2 Materials and methods

2.1 Patients

A cohort of 102 patients with AIS (45.10% female; mean [SD] age, 67.98 [12.49] years) was recruited at the Third People's Hospital of Yancheng between December 2020 and September 2024. The screening procedures and research analysis are depicted in Figure 1.

The inclusion criteria were: (1) a confirmed diagnosis of AIS according to the guidelines (26); (2) the ability to cooperate with brain MRI scans within 24–72 h after symptom onset; (3) a modified Rankin Scale (mRS) score of 0 before symptom onset; and (4) individuals aged 18 or older.

The exclusion criteria were: (1) posterior circulation infarction; (2) intracranial occupying lesions such as tumors or arachnoid cysts; (3) significant MRI artifacts; (4) evidence of hemorrhagic transformation; and (5) patients with severe diseases in other systems.

2.2 Clinical assessment

Demographic and clinical data were gathered for all participants, including age, gender, onset to therapy time, baseline National Institutes of Health Stroke Scale (NIHSS) score, treatment strategies, atrial fibrillation, hypertension, diabetes mellitus, hyperlipidemia, coronary heart disease, smoking history, alcohol abuse and history of stroke. To aid in the modeling process, the continuous variables in the dataset were standardized to mitigate disparities in data distribution. The mRS score was assessed through a telephone follow-up at 90 days

Abbreviations: AIS, acute ischemic stroke; CBF, cerebral blood flow; DSC-PWI, dynamic sensitivity contrast perfusion weighted imaging; CTP, computed tomography perfusion; ASL, arterial spin labeling; MRI, magnetic resonance imaging; PLD, post-labeling delay; ATT, arterial transit time; ML, machine learning; mRS, modified Rankin Scale; NIHSS, National Institutes of Health Stroke Scale; DWI, diffusion weighted imaging; ROI, region of interest; ICC, interclass correlation coefficient; XGBoost, extreme gradient boosting; LOOCV, leave-one-out cross-validation; LASSO, least absolute shrinkage and selection operator; ROC, receiver operating characteristic; AUC, area under the curve; PR-AUC, precision-recall AUC; DCA, decision curve analysis; SHAP, Shapley Additive exPlanations; CI, confidence interval.

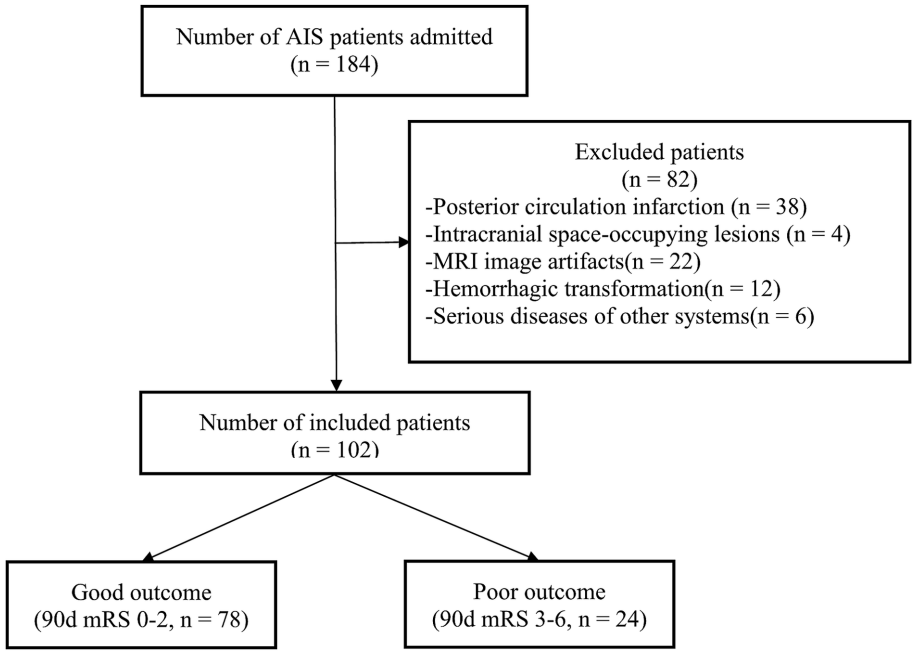

FIGURE 1
Study enrollment process. AIS, acute ischemic stroke; MRI, magnetic resonance imaging; mRS, modified Rankin Scale.

post-onset, classifying prognosis as either good (mRS score ≤ 2) or poor (mRS score > 2).

2.3 MRI acquisition

All participants underwent head MRI scans (3.0T, GE Discovery 750 W, USA), including diffusion weighted imaging (DWI) and multi-PLD ASL sequences within 24–72 h after symptom onset. Multi-PLD ASL employs a three-dimensional pseudo-continuous scanning method, with the following specific parameters: echo time: 5978 ms; repetition time: 11.5 ms; field of view: 22 × 22 cm; slice thickness: 4.5 mm; slice number: 106; resolution: 4.67 mm * 4.67 mm; NEX: 1; PLDs: 1.0 s, 1.22 s, 1.48 s, 1.78 s, 2.1 s, 2.63 s, 3.32 s; scan duration: 6 min 2 s. The ATT-corrected CBF image is obtained by averaging the individual CBF images calculated for each PLD directly on the MRI scanner.

2.4 Lesion segmentation and radiomics feature extraction

To improve the image quality, N4 bias field correction was applied to the obtained CBF images to minimize the impact of magnetic field inhomogeneity. Subsequently, the DWI images were used as a template to conduct image registration with the CBF images. Two radiologists independently delineated the infarct area slice-by-slice on DWI images using ITK-SNAP[1] to define the region of interest (ROI). The ROI was then transferred to the corresponding registered CBF images. PyRadiomics software (version: 3.1.0) was utilized to extract 1,032 features from the CBF image ROI. The intraclass correlation coefficient (ICC) was computed to evaluate the consistency of the extracted features. Features with an ICC exceeding 0.75 were deemed highly consistent, standardized, and incorporated into the model development process.

2.5 Model building and evaluation

Eight different ML methods were employed to build models, including logistic regression, support vector machine, random forest, k-nearest neighbors, naive Bayes, extreme gradient boosting (XGBoost), light gradient boosting machine and deep neural networks. Given the limited sample size included in this study, leave-one-out cross-validation (LOOCV) was employed instead of partitioning the subjects into training and testing sets. This method involves utilizing (N-1) samples for training across N iterations, while reserving one sample as the test set in each iteration. This strategy aims to enhance data utilization and increase accuracy levels (27). In each training cycle, the least absolute shrinkage and selection operator (LASSO) regression was used to select features with non-zero coefficients through 10-fold cross-validation.

Class-weighted loss functions were utilized in model training to address the effects of class imbalance. In order to reduce bias toward the majority class (good prognosis), the minority class (poor prognosis) was assigned higher weights to amplify its influence on the loss function. Grid search was utilized for hyperparameter tuning across all models. This approach systematically investigated various combinations of model-specific hyperparameters (e.g., the penalty parameter C for logistic regression, the kernel type and gamma for

1 http://www.itk-snap.org, version 4.0.

TABLE 1 Demographic and clinical characteristics of the good and poor prognosis groups.

Characteristics	Good (n = 78)	Poor (n = 24)	$t/Z/\chi^2$	p value
Age, year[a]	66 ± 12	73 ± 13	−2.283	0.025*
Female, n (%)	33 (42.31)	13 (54.17)	1.042	0.307
Onset to therapy time, hour[a]	13.42 ± 14.90	13.23 ± 13.89	0.055	0.956
Baseline NIHSS score[b]	3 (1, 6)	8 (4, 12)	4.505	<0.001*
Reperfusion therapy, n (%)	18 (23.08)	6 (25.00)	0.038	0.846
Atrial fibrillation, n (%)	12 (15.38)	5 (20.83)	0.392	0.531
Hypertension, n (%)	58 (74.36)	18 (75.00)	0.004	0.950
Diabetes mellitus, n (%)	22 (28.21)	6 (25.00)	0.095	0.758
Hyperlipidemia, n (%)	16 (20.51)	5 (20.83)	0.001	0.973
Coronary heart disease, n (%)	3 (3.85)	2 (8.33)	0.793	0.373
Smoking history, n (%)	19 (24.36)	4 (16.67)	0.622	0.430
Alcohol abuse, n (%)	13 (16.67)	3 (12.50)	0.241	0.624
History of stroke, n (%)	10 (12.82)	7 (29.17)	3.531	0.060

n, number of cases.
[a]($\bar{x} \pm s$).
[b][M (Q1, Q3)].
NIHSS, National Institutes of Health Stroke Scale. The marked with "*" is statistically significant ($p < 0.05$).

support vector machine, the number of estimators and maximum depth for random forest, XGBoost, and light gradient boosting machine) to determine the optimal configuration for each method. The optimal hyperparameters were chosen according to performance metrics obtained from cross-validation.

We constructed CBF radiomics models using radiomics features and clinical models using clinical data. Furthermore, combined models were established by integrating radiomics features and clinical data. Receiver operating characteristic (ROC) curves were generated for all models to evaluate performance based on the area under the curve (AUC), sensitivity, specificity, accuracy, and F1 score. The model's performance on the minority class (poor prognosis) was also examined through the evaluation of precision, recall, F1-score, and the area under the precision-recall AUC (PR-AUC). Additionally, the robustness of the models was validated through 5,000 permutation tests. The DeLong test was utilized to statistically compare the predictive performance of the models. Decision curve analysis (DCA) was performed to assess the potential clinical net benefits of the models. Finally, feature importance was determined within the models using SHapley Additive exPlanations (SHAP).

2.6 Statistical analysis

Statistical analysis was conducted using SPSS software (Version 26.0, IBM, Armonk, NY, USA). Clinical data were evaluated for normality and homogeneity of variance. Data following a normal distribution were expressed as mean ± standard deviation. In cases where the data showed a non-normal distribution, the descriptive measure employed was the median (first quartile, third quartile). Continuous variables were analyzed using the independent samples t-test or the Mann–Whitney U test, whereas categorical variables were analyzed with the chi-square test. Statistical significance was defined as $p < 0.05$.

A statistical power analysis was conducted to assess the adequacy of the sample size in supporting the study's conclusions. The analysis was based on the observed AUC values and a null hypothesis AUC of 0.5 (random classification).

Python (version 3.11)[2] was used for image processing and model construction. The 'sklearn' package was used to perform LASSO regression analysis for feature selection. The 'matplotlib' package was used to generate ROC and DCA curves. The 'SHAP' package was implemented to calculate SHAP values for the features.

3 Results

3.1 Demographic characteristics of patients

The demographic and clinical data of the included AIS patients are detailed in Table 1. Among all patients, 78 exhibited a good prognosis, while 24 had a poor prognosis. In comparison to patients with a good prognosis, those with a poor prognosis were older ($p = 0.025$) and displayed a higher baseline NIHSS score ($p < 0.001$). No significant differences were observed between the two groups in terms of gender, onset to therapy time, treatment strategies, atrial fibrillation, hypertension, diabetes mellitus, hyperlipidemia, coronary heart disease, smoking history, alcohol abuse, or history of stroke.

3.2 Model building and performance

Out of the eight ML methods, the model constructed with the XGBoost algorithm exhibited superior performance. The

2 https://www.python.org

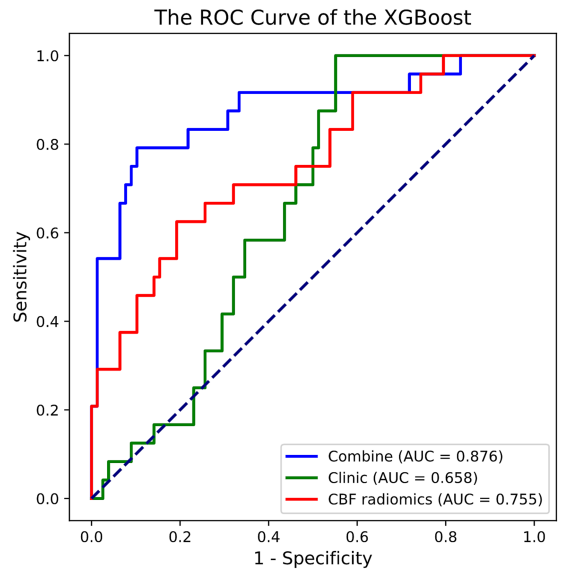

FIGURE 2
ROC curve of the XGBoost models in predicting prognosis of acute ischemic stroke. ROC, receiver operating characteristic; XGBoost, extreme gradient boosting; AUC, area under the curve; CBF, cerebral blood flow.

hyperparameters for XGBoost were configured with a maximum depth of 6, a learning rate of 0.3, 100 estimators, a subsample of 1, and column sampling by tree set to 1. Figure 2 and Table 2 display the ROC curves and key diagnostic performance metrics for each XGBoost models. The results of the models created using the remaining seven ML algorithms are elucidated in the Supplementary material.

Among the XGBoost models, the combined model demonstrated superior performance, attaining an AUC of 0.876 (95% CI, 0.768–0.960), indicating its significant capability in discriminating between good and poor prognoses. In comparison, the AUC for the clinical model was 0.658 (95% CI, 0.547–0.755), while the AUC of the CBF radiomics model was 0.755 (95% CI, 0.635–0.869). The DeLong test demonstrated that the combined model exhibited markedly better predictive performance compared to both the clinical model ($p < 0.001$) and the CBF radiomics model ($p = 0.002$). Furthermore, there was no statistically significant difference between the clinical model and the CBF radiomics model ($p = 0.222$). During the 5,000 permutation tests, it is noteworthy that all models exhibited a relatively high level of robustness. In Figure 3, the DCA for all models reveals that the combined model exhibits superior net benefit compared to both the clinical model and the CBF radiomics model across a broad spectrum of threshold probabilities, ranging from 0.1 to 0.9.

Based on the observed AUC of the combined model (AUC = 0.876) and a null hypothesis AUC of 0.5, a statistical power analysis resulted in a standard error of 0.034 and a Z-value of 10.970 ($p < 0.05$), demonstrating that the current dataset possesses adequate power (>80%) to validate the observed AUC. Furthermore, the combined model achieved a precision of 0.79, recall of 0.83, PR-AUC of 0.85, and F1-score of 0.81 for the minority group, indicating its ability to accurately identify cases with poor prognosis.

3.3 Model interpretability

As illustrated in Figure 4, we used the SHAP values from the best-performing XGBoost combined model to identify the important variables for predicting AIS prognosis. Positive SHAP values were linked to an elevated risk of poor prognosis, while negative SHAP values were indicative of a greater chance of poor prognosis. Notably, the baseline NIHSS score and age played significant roles in predicting the prognosis of AIS. Additionally, several texture and shape features derived from the CBF images also contributed significantly to the predictive performance of the model.

4 Discussion

This study proposes a novel approach that integrates multi-PLD ASL radiomics features with clinical variables for predicting AIS prognosis. Among the models developed, the XGBoost algorithm exhibited the highest AUC value of 0.876, underscoring its predictive accuracy for AIS prognosis. It can assist clinicians in early prognostic assessment and the implementation of personalized treatment plans, ultimately aiming to reduce the incidence of poor prognosis.

The fundamental aspect of AIS involves tissue necrosis caused by embolism in the supplying artery. CBF serves as a direct reflection of the hemodynamic condition within the infarcted region, making it a pivotal indicator of brain tissue injury and a key role in evaluating neurological rehabilitation (28). In contrast to conventional DSC-PWI, multi-PLD ASL technology produces CBF images without the need for contrast agents (29). Moreover, radiomics techniques enable the extraction of multidimensional features from medical images, providing a more thorough assessment of the heterogeneity of blood perfusion within lesions in comparison to visual evaluation or basic CBF quantification (30). Guo et al. developed ten ML models based on the dynamic radiomics features of DSC-PWI in the infarcted area to predict the prognosis of AIS, achieving a maximum AUC of 0.882 (25). However, there is a scarcity of studies investigating the correlation between the radiomics features of CBF in the infarcted region and the prognosis of AIS. Therefore, we aimed to develop a CBF radiomics model for AIS prognosis prediction based on multi-PLD ASL imaging. Our model attained a maximum AUC of 0.755 in the results, indicating the viability of utilizing multi-PLD ASL technology for predicting neurological recovery in AIS patients. After including age and baseline NIHSS score, the model achieves an AUC of 0.876, which aligns closely with the findings of Guo et al.'s model (25). Therefore, this method presents a safer and more reproducible avenue for prognostic prediction in AIS patients, particularly for those with contraindications to contrast agents. Moreover, the absence of contrast agents renders ASL a more economical method.

When examining the demographic and clinical profiles of AIS patients, it was observed that those with poorer prognoses were characterized by advanced age and a higher baseline NIHSS score. The development of a predictive model utilizing demographic and clinical factors yielded limited performance, as indicated by an AUC of 0.658, which falls below that of the CBF radiomics model. While the DeLong test did not indicate a statistically significant distinction between the two models, the test's power may have been constrained by the small sample size (31). Consequently, there is justification to argue for the

TABLE 2 The performance of XGBoost models in predicting prognosis of AIS patients.

Models	AUC (95% CI)	Sensitivity	Specificity	Accuracy	F1 score	Permutation test
Clinic	0.658 (0.547–0.755)	1	0.449	0.578	0.527	0.012*
CBF radiomics	0.755 (0.635–0.869)	0.625	0.808	0.765	0.556	0.002*
Combined	0.876 (0.768–0.960)	0.792	0.897	0.873	0.745	<0.001*

XGBoost, extreme gradient boosting; AIS, acute ischemic stroke; CBF, cerebral blood flow; AUC, area under the curve; CI, confidence interval. The marked with "*" is statistically significant ($p < 0.05$).

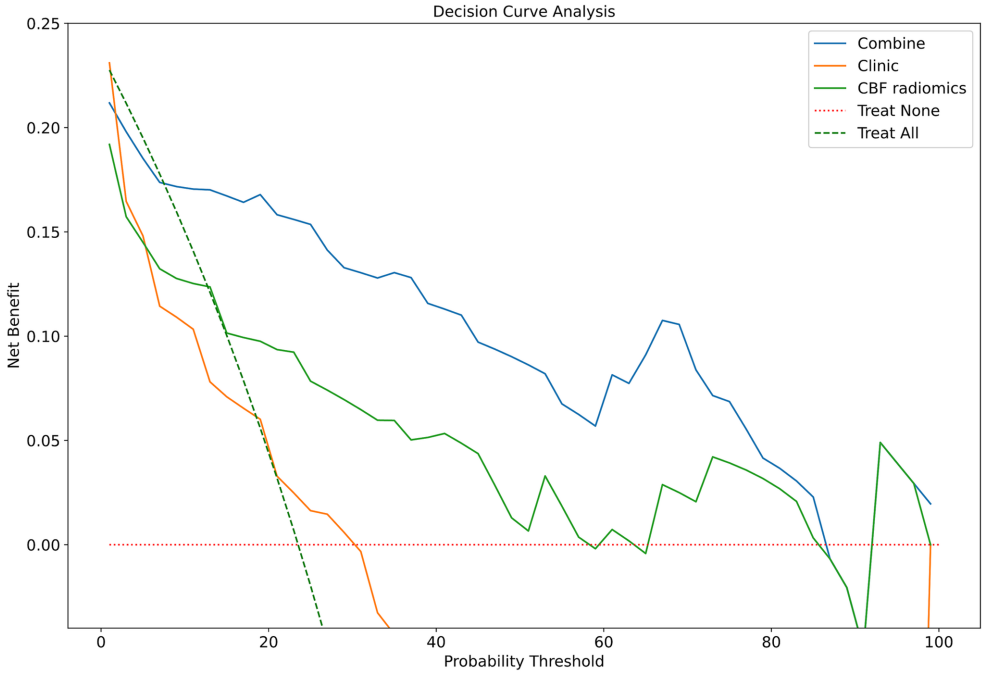

FIGURE 3
Clinical decision curve analysis of the XGBoost models. XGBoost, extreme gradient boosting; CBF, cerebral blood flow.

superiority of the CBF radiomics model compared to the clinical model. During the acute phase of AIS, the CBF radiomics model may function as an alternative to the clinical model for prognostic prediction, especially beneficial for patients with insufficient clinical data.

The combined model, which integrates clinical data with CBF radiomics features, achieved an AUC of 0.876. The DeLong test demonstrated that the combined model significantly outperformed both the clinical model and the CBF radiomics model. This finding implies that clinical data provide only partial insight into prognosis. In contrast, CBF radiomics features provide distinct information on alterations in cerebral blood perfusion status that clinical data alone cannot encompass. This discovery is in line with results from various studies, underscoring the essential role of the complementarity of multimodal information in radiomics research (32). Additionally, the DCA demonstrated that the combined model yielded a higher net benefit across a wide range of threshold probabilities. This suggests that the model has the potential for application in clinical practice, with the only requirement being the extraction of relevant clinical and imaging data from electronic medical records and imaging systems. It can assist clinicians in delivering consistent prognostic evaluations in diverse clinical scenarios, enhancing the management of AIS by facilitating prompt interventions and optimizing resource distribution.

In order to determine the factors influencing the prognosis of AIS, we conducted SHAP analysis to assess the individual contribution of each feature to the predictive accuracy of the combined model. The baseline NIHSS score and age emerged as the most significant predictors among the clinical variables, aligning with prior studies (33–35). The baseline NIHSS score reflects stroke severity, correlating strongly with infarct size and functional outcomes in AIS patients (36). Advanced age, characterized by diminished neural plasticity and a higher prevalence of comorbidities, is a firmly established risk factor for poor outcomes in AIS (37, 38). Texture features and shape features derived from multi-PLD ASL CBF were identified as important contributors to the model. Among the texture features, the gray level run length matrix made the greatest contribution, quantifying gray intensity patterns and their spatial relationships within the ischemic area (39). Ischemic regions often exhibit varying degrees of blood flow reduction and tissue damage, and texture features can capture these variations, distinguishing areas of hypoperfusion, penumbra, and infarct core. Moreover, alterations in tissue density induced by cytotoxic and vasogenic edema may manifest in texture

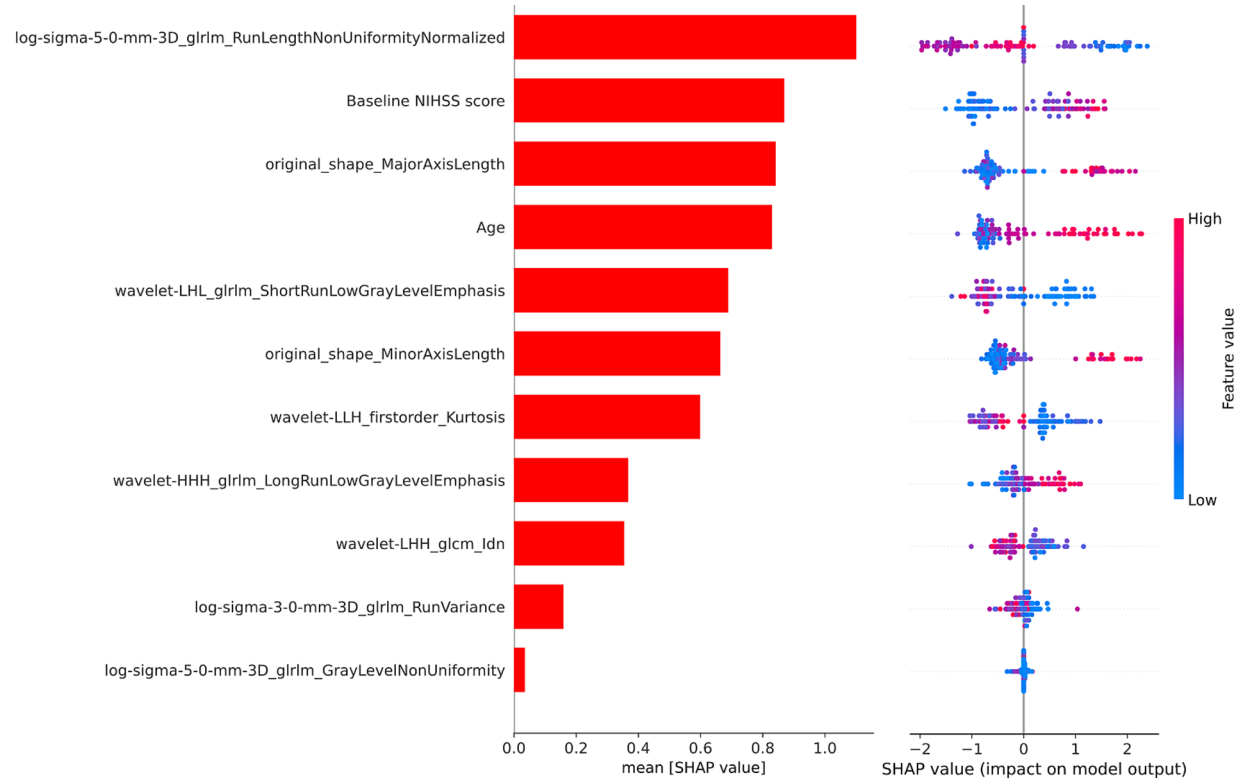

FIGURE 4
The SHAP values of the XGBoost combined model. SHAP, SHapley Additive Explanations; XGBoost, extreme gradient boosting; NIHSS, National Institutes of Health Stroke Scale.

characteristics, elucidating the advancement of secondary damage (40). Additionally, microstructural disruptions, such as the loss of neural integrity or capillary breakdown, may manifest as increased texture irregularities in radiomics analysis (41). Shape features provide evidence linking lesion geometry to the underlying vascular anatomy and collateral perfusion (42). Larger or irregularly shaped lesions may indicate more extensive vascular occlusion or failure of collateral circulation, both of which are associated with poor prognosis (43, 44). Moreover, regions with poor perfusion are more prone to displaying irregular lesion morphologies (45). These findings highlight the capability of CBF radiomics features to reflect the extent and heterogeneity of tissue damage, demonstrating their relevance to clinical prognosis of AIS.

This study must acknowledge several limitations. Firstly, the small sample size may restrict the generalizability of the results. Despite utilizing LOOCV and permutation tests to mitigate this issue, larger multi-center datasets are essential to confirm the model and broaden its external applicability. Secondly, the exclusion of posterior circulation infarction cases restricted the model's generalizability. Future research should incorporate posterior circulation cases into larger datasets to construct subtype-specific models. Thirdly, despite efforts to ensure consistency through ICC analysis, manual delineation of infarcted areas may lead to observer variability (46). Future research should explore automated or semi-automated segmentation methods to reduce subjectivity and improve reproducibility. Fourthly, this study focused exclusively on the multi-PLD ASL sequence. Future studies should explore integrating multimodal imaging techniques, such as quantitative susceptibility mapping and diffusion-prepared ASL, to better understand AIS progression by delineating the ischemic penumbra and assessing blood–brain barrier integrity (47–50). Finally, future studies could integrate radiomics features with network-based approaches, which have proven valuable in neuropsychiatric disorders, to better understand how ischemic lesions disrupt brain networks and influence prognosis of AIS (51–53).

5 Conclusion

In this study, we established new prognostic prediction models for AIS utilizing multi-PLD ASL technology. The results indicate that the combined model, which integrates clinical data and CBF radiomics features, accurately predicts AIS prognosis. This model has the potential to assist clinicians in identifying individualized treatment approaches to improve patient prognosis. This strategy presents a feasible alternative for assessing the prognosis of AIS, especially in individuals for whom the use of contrast agents is contraindicated.

Data availability statement

The original contributions presented in the study are included in the article/Supplementary material, further inquiries can be directed to the corresponding authors.

Ethics statement

The studies involving humans were approved by the Ethics Committee of the Yancheng Third People's Hospital. The studies were conducted in accordance with the local legislation and institutional requirements. The participants provided their written informed consent to participate in this study. Written informed consent was obtained from the individual(s) for the publication of any potentially identifiable images or data included in this article.

Author contributions

ZW: Methodology, Writing – original draft. YS: Supervision, Writing – review & editing. XZ: Formal analysis, Methodology, Writing – review & editing. QL: Conceptualization, Data curation, Writing – review & editing. CD: Data curation, Methodology, Writing – review & editing. SW: Conceptualization, Data curation, Writing – review & editing. HS: Conceptualization, Methodology, Supervision, Writing – review & editing. MC: Methodology, Supervision, Writing – review & editing. XX: Data curation, Methodology, Writing – review & editing. PP: Conceptualization, Methodology, Writing – review & editing. ZD: Project administration, Supervision, Writing – review & editing. FC: Data curation, Supervision, Writing – review & editing.

Funding

The author(s) declare financial support was received for the research, authorship, and/or publication of this article. This work was supported by the Elderly Health Research Project of Jiangsu Province (No. LKM2024050), the Research Foundation of Science and Technology Bureau of Yancheng (No. YCBK2023041), the Medical and Scientific Development Program of Yancheng of Jiangsu Province of China (No. YK2020070, YK2023088), the Special Project of Clinical Medicine of Nantong University (No. YXY-Z2023003, 2024LZ004), the Special Funds for Science Development of the Yancheng Third People's Hospital of Jiangsu Vocational College of Medicine (No. 20229103), and the School-Local Collaborative Innovation Research Project of Jiangsu Vocational College of Medicine (No. 20239102).

Acknowledgments

We would like to thank all the individuals who took part in the study.

Conflict of interest

The authors declare that the research was conducted in the absence of any commercial or financial relationships that could be construed as a potential conflict of interest.

Generative AI statement

The author(s) declare that no Gen AI was used in the creation of this manuscript.

Publisher's note

Supplementary material

The Supplementary material for this article can be found online at: https://www.frontiersin.org/articles/10.3389/fneur.2024.1544578/full#supplementary-material

References

1. Feigin VL, Brainin M, Norrving B, Martins S, Sacco RL, Hacke W, et al. World stroke organization (WSO): global stroke fact sheet 2022. *Int J Stroke*. (2022) 17:18–29. doi: 10.1177/17474930211065917

2. Feigin VL, Stark BA, Johnson CO, Roth GA, Bisignano C, Abady GG, et al. Global, regional, and national burden of stroke and its risk factors, 1990–2019: a systematic analysis for the global burden of disease study 2019. *Lancet Neurol*. (2021) 20:795–820. doi: 10.1016/S1474-4422(21)00252-0

3. Saini V, Guada L, Yavagal DR. Global epidemiology of stroke and access to acute ischemic stroke interventions. *Neurology*. (2021) 97:S6–S16. doi: 10.1212/WNL.0000000000012781

4. Wu S, Wu B, Liu M, Chen Z, Wang W, Anderson CS, et al. Stroke in China: advances and challenges in epidemiology, prevention, and management. *Lancet Neurol*. (2019) 18:394–405. doi: 10.1016/S1474-4422(18)30500-3

5. Béjot Y, Bailly H, Graber M, Garnier L, Laville A, Dubourget L, et al. Impact of the ageing population on the burden of stroke: the Dijon stroke registry. *Neuroepidemiology*. (2019) 52:78–85. doi: 10.1159/000492820

6. Hofmeister J, Bernava G, Rosi A, Vargas MI, Carrera E, Montet X, et al. Clot-based Radiomics predict a mechanical Thrombectomy strategy for successful recanalization in acute ischemic stroke. *Stroke*. (2020) 51:2488–94. doi: 10.1161/STROKEAHA.120.030334

7. Nakamura K, Ago T. Pericyte-mediated molecular mechanisms underlying tissue repair and functional recovery after ischemic stroke. *J Atheroscler Thromb*. (2023) 30:1085–94. doi: 10.5551/jat.RV22007

8. Dani KA, Thomas RGR, Chappell FM, Shuler K, MacLeod MJ, Muir KW, et al. Computed tomography and magnetic resonance perfusion imaging in ischemic stroke: definitions and thresholds. *Ann Neurol*. (2011) 70:384–401. doi: 10.1002/ana.22500

9. Bivard A, Stanwell P, Levi C, Parsons M. Arterial spin labeling identifies tissue salvage and good clinical recovery after acute ischemic stroke. *J Neuroimaging*. (2013) 23:391–6. doi: 10.1111/j.1552-6569.2012.00728.x

10. Haller S, Zaharchuk G, Thomas DL, Lovblad KO, Barkhof F, Golay X. Arterial spin labeling perfusion of the brain: emerging clinical applications. *Radiology*. (2016) 281:337–56. doi: 10.1148/radiol.2016150789

11. Hernandez-Garcia L, Lahiri A, Schollenberger J. Recent progress in ASL. *Neuroimage*. (2019) 187:3–16. doi: 10.1016/j.neuroimage.2017.12.095

12. Lindner T, Bolar DS, Achten E, Barkhof F, Bastos-Leite AJ, Detre JA, et al. Current state and guidance on arterial spin labeling perfusion MRI in clinical neuroimaging. *Magn Reson Med*. (2023) 89:2024–47. doi: 10.1002/mrm.29572

13. Sui B, Gao P. Imaging evaluation of acute ischemic stroke. *J Int Med Res*. (2020) 48:1–5. doi: 10.1177/0300060518802530

14. Golay X, Ho M-L. Multidelay ASL of the pediatric brain. *Br J Radiol*. (2022) 95:20220034. doi: 10.1259/bjr.20220034

15. Mutsaerts HJMM, Petr J, Václavů L, van Dalen JW, Robertson AD, Caan MW, et al. The spatial coefficient of variation in arterial spin labeling cerebral blood flow images. *J Cereb Blood Flow Metab*. (2017) 37:3184–92. doi: 10.1177/0271678X16683690

16. Woods JG, Achten E, Asllani I, Bolar DS, Dai W, Detre JA, et al. Recommendations for quantitative cerebral perfusion MRI using multi-timepoint arterial spin labeling: acquisition, quantification, and clinical applications. *Magn Reson Med*. (2024) 92:469–95. doi: 10.1002/mrm.30091

17. Arrarte Terreros N, van Willigen BG, Niekolaas WS, Tolhuisen ML, Brouwer J, Coutinho JM, et al. Occult blood flow patterns distal to an occluded artery in acute ischemic stroke. *J Cereb Blood Flow Metab*. (2021) 42:292–302. doi: 10.1177/0271678X211044941

18. Yan C, Yu F, Zhang Y, Zhang M, Li J, Wang Z, et al. Multidelay arterial spin labeling versus computed tomography perfusion in penumbra volume of acute ischemic stroke. *Stroke*. (2023) 54:1037–45. doi: 10.1161/STROKEAHA.122.040759

19. Xu X, Tan Z, Fan M, Ma M, Fang W, Liang J, et al. Comparative study of multi-delay Pseudo-continuous arterial spin labeling perfusion MRI and CT perfusion in ischemic stroke disease. *Front Neuroinform*. (2021) 15:719719. doi: 10.3389/fninf.2021.719719

20. Wang DJJ, Alger JR, Qiao JX, Gunther M, Pope WB, Saver JL, et al. Multi-delay multi-parametric arterial spin-labeled perfusion MRI in acute ischemic stroke — comparison with dynamic susceptibility contrast enhanced perfusion imaging. *Neuroimage Clin*. (2013) 3:1–7. doi: 10.1016/j.nicl.2013.06.017

21. Sasahara M, Yamanaka M, Matsushita T, Abe T, Otomo M, Yamamoto Y, et al. Evaluation of the ischemic penumbra and prognosis in acute cerebral infarction using cerebral blood flow and delay time derived from multi-delay pCASL imaging. *J Med Investig*. (2024) 71:286–92. doi: 10.2152/jmi.71.286

22. Li Q, Jiang C, Qian L, Yang J, Mu T, Dong C, et al. Prognostic value of multi-PLD ASL-based cerebral perfusion ASPECTS in acute ischemic stroke. *Front Neurol*. (2024) 15:15. doi: 10.3389/fneur.2024.1476937

23. Mayerhoefer ME, Materka A, Langs G, Häggström I, Szczypiński P, Gibbs P, et al. Introduction to Radiomics. *J Nucl Med*. (2020) 61:488–95. doi: 10.2967/jnumed.118.222893

24. Guiot J, Vaidyanathan A, Deprez L, Zerka F, Danthine D, Frix AN, et al. A review in radiomics: making personalized medicine a reality via routine imaging. *Med Res Rev*. (2022) 42:426–40. doi: 10.1002/med.21846

25. Guo Y, Yang Y, Wang M, Luo Y, Guo J, Cao F, et al. The combination of whole-brain features and local-lesion features in DSC-PWI may improve ischemic stroke outcome prediction. *Life*. (2022) 12:1847. doi: 10.3390/life12111847

26. Mendelson SJ, Prabhakaran S. Diagnosis and Management of Transient Ischemic Attack and Acute Ischemic Stroke. *JAMA*. (2021) 325:1088. doi: 10.1001/jama.2020.26867

27. Cheng J, Dekkers JCM, Fernando RL. Cross-validation of best linear unbiased predictions of breeding values using an efficient leave-one-out strategy. *J Anim Breed Genet*. (2021) 138:519–27. doi: 10.1111/jbg.12545

28. Aracki-Trenkic A, Law-Ye B, Radovanovic Z, Stojanov D, Dormont D, Pyatigorskaya N. ASL perfusion in acute ischemic stroke: the value of CBF in outcome prediction. *Clin Neurol Neurosurg*. (2020) 194:105908. doi: 10.1016/j.clineuro.2020.105908

29. Hernandez-Garcia L, Aramendía-Vidaurreta V, Bolar DS, Dai W, Fernández-Seara MA, Guo J, et al. Recent technical developments in ASL: a review of the state of the art. *Magn Reson Med*. (2022) 88:2021–42. doi: 10.1002/mrm.29381

30. Yang J, Cai H, Liu N, Huang J, Pan Y, Zhang B, et al. Application of radiomics in ischemic stroke. *J Int Med Res*. (2024) 52:3000605241238141. doi: 10.1177/03000605241238141

31. Demler OV, Pencina MJ, D'Agostino RB. Misuse of DeLong test to compare AUCs for nested models. *Stat Med*. (2012) 31:2577–87. doi: 10.1002/sim.5328

32. Dragoş HM, Stan A, Pintican R, Feier D, Lebovici A, Panaitescu PS, et al. MRI radiomics and predictive models in assessing ischemic stroke outcome-a systematic review. *Diagnostics*. (2023) 13:857. doi: 10.3390/diagnostics13050857

33. Chung C-C, Su EC-Y, Chen J-H, Chen Y-T, Kuo C-Y. XGBoost-based simple three-item model accurately predicts outcomes of acute ischemic stroke. *Diagnostics*. (2023) 13:842. doi: 10.3390/diagnostics13050842

34. Ding G-y, Xu J-h, He J-h, Nie Z-y. Clinical scoring model based on age, NIHSS, and stroke-history predicts outcome 3 months after acute ischemic stroke. *Front Neurol*. (2022) 13:13. doi: 10.3389/fneur.2022.935150

35. Shrestha S, Poudel RS, Khatiwada D, Thapa L. Stroke subtype, age, and baseline NIHSS score predict ischemic stroke outcomes at 3 months: a preliminary study from Central Nepal. *J Multidiscip Healthc*. (2015) 8:443–8. doi: 10.2147/JMDH.S90554

36. Kwah LK, Diong J. National Institutes of Health Stroke Scale (NIHSS). *J Physiother*. (2014) 60:61. doi: 10.1016/j.jphys.2013.12.012

37. Ahmed R, Mhina C, Philip K, Patel SD, Aneni E, Osondu C, et al. Age- and sex-specific trends in medical complications after acute ischemic stroke in the United States. *Neurology*. (2023) 100:e1282–95. doi: 10.1212/WNL.0000000000206749

38. Gutchess A. Plasticity of the aging brain: new directions in cognitive neuroscience. *Science*. (2014) 346:579–82. doi: 10.1126/science.1254604

39. Lee J, Yoo SK, Kim K, Lee BM, Park VY, Kim JS, et al. Machine learning-based radiomics models for prediction of locoregional recurrence in patients with breast cancer. *Oncol Lett*. (2023) 26:422. doi: 10.3892/ol.2023.14008

40. Bai J, He M, Gao E, Yang G, Yang H, Dong J, et al. Radiomic texture analysis based on neurite orientation dispersion and density imaging to differentiate glioblastoma from solitary brain metastasis. *BMC Cancer*. (2023) 23:1231. doi: 10.1186/s12885-023-11718-0

41. Brown CE, Li P, Boyd JD, Delaney KR, Murphy TH. Extensive turnover of dendritic spines and vascular remodeling in cortical tissues recovering from stroke. *J Neurosci*. (2007) 27:4101–9. doi: 10.1523/JNEUROSCI.4295-06.2007

42. Pensato U, Demchuk AM, Menon BK, Nguyen TN, Broocks G, Campbell BCV, et al. Cerebral infarct growth: pathophysiology, pragmatic assessment, and clinical implications. *Stroke*. (2024) 56:219–29. doi: 10.1161/STROKEAHA.124.049013

43. Liu S, Fan D, Zang F, Gu N, Yin Y, Ge X, et al. Collateral circulation detected by arterial spin labeling predicts outcome in acute ischemic stroke. *Acta Neurol Scand*. (2022) 146:635–42. doi: 10.1111/ane.13694

44. Meng X, Ji J. Infarct volume and outcome of cerebral ischaemia, a systematic review and meta-analysis. *Int J Clin Pract*. (2021) 75:e14773. doi: 10.1111/ijcp.14773

45. Abels B, Klotz E, Tomandl BF, Kloska SP, Lell MM. Perfusion CT in acute ischemic stroke: a qualitative and quantitative comparison of deconvolution and maximum slope approach. *AJNR Am J Neuroradiol*. (2010) 31:1690–8. doi: 10.3174/ajnr.A2151

46. Sherer MV, Lin D, Elguindi S, Duke S, Tan L-T, Cacicedo J, et al. Metrics to evaluate the performance of auto-segmentation for radiation treatment planning: a critical review. *Radiother Oncol*. (2021) 160:185–91. doi: 10.1016/j.radonc.2021.05.003

47. Uchida Y, Kan H, Kano Y, Onda K, Sakurai K, Takada K, et al. Longitudinal changes in iron and myelination within ischemic lesions associate with neurological outcomes: a pilot study. *Stroke*. (2024) 55:1041–50. doi: 10.1161/STROKEAHA.123.044606

48. Uchida Y, Kan H, Inoue H, Oomura M, Shibata H, Kano Y, et al. Penumbra detection with oxygen extraction fraction using magnetic susceptibility in patients with acute ischemic stroke. *Front Neurol*. (2022) 13:752450. doi: 10.3389/fneur.2022.752450

49. Uchida Y, Kan H, Furukawa G, Onda K, Sakurai K, Takada K, et al. Relationship between brain iron dynamics and blood-brain barrier function during childhood: a quantitative magnetic resonance imaging study. *Fluids Barriers CNS*. (2023) 20:60. doi: 10.1186/s12987-023-00464-x

50. Uchida Y, Kan H, Sakurai K, Horimoto Y, Hayashi E, Iida A, et al. APOE ε4dose associates with increased brain iron and β-amyloid via blood–brain barrier dysfunction. *J Neurol Neurosurg Psychiatry*. (2022) 93:772–8. doi: 10.1136/jnnp-2021-328519

51. Mo F, Zhao H, Li Y, Cai H, Song Y, Wang R, et al. Network localization of state and trait of auditory verbal hallucinations in schizophrenia. *Schizophr Bull*. (2024) 50:1326–36. doi: 10.1093/schbul/sbae020

52. Zhang X, Xu R, Ma H, Qian Y, Zhu J. Brain structural and functional damage network localization of suicide. *Biol Psychiatry*. (2024) 95:1091–9. doi: 10.1016/j.biopsych.2024.01.003

53. Cheng Y, Cai H, Liu S, Yang Y, Pan S, Zhang Y, et al. Brain network localization of gray matter atrophy and neurocognitive and social cognitive dysfunction in schizophrenia. *Biol Psychiatry*. (2025) 97:148–56. doi: 10.1016/j.biopsych.2024.07.021

frontiers | Frontiers in Neurology

TYPE Original Research
PUBLISHED 15 January 2025
DOI 10.3389/fneur.2024.1514711

OPEN ACCESS

EDITED BY
Shuai Ren,
Affiliated Hospital of Nanjing University of Chinese Medicine, China

REVIEWED BY
Huilin Zhao,
Shanghai Jiao Tong University, China
Xiao-er Wei,
Shanghai Jiao Tong University, China
Mingming Lu,
Characteristic Medical Center of Chinese People's Armed Police Force, China

*CORRESPONDENCE
Tianle Wang
✉ wangtianle9192@163.com
Li Zhu
✉ ntyyyxkzhuli@163.com

RECEIVED 21 October 2024
ACCEPTED 30 December 2024
PUBLISHED 15 January 2025

CITATION
Shao S, Wang T, Zhu L, Gao Y, Fan X, Lu Y, Qian C, Zhang M and Qian J (2025) Correlation of intracranial and extracranial carotid atherosclerotic plaque characteristics with ischemic stroke recurrence: a high-resolution vessel wall imaging study. *Front. Neurol.* 15:1514711. doi: 10.3389/fneur.2024.1514711

Correlation of intracranial and extracranial carotid atherosclerotic plaque characteristics with ischemic stroke recurrence: a high-resolution vessel wall imaging study

Shengyu Shao, Tianle Wang*, Li Zhu*, Yin Gao, Xian Fan, Yu Lu, Chengqun Qian, Manyu Zhang and Jinhua Qian

Department of Medical Imaging, The Second Affiliated Hospital of Nantong University, Nantong, China

Objectives: To evaluate the ability of the plaque characteristics of extracranial carotid and intracranial arteries to predict large atherosclerotic ischemic stroke recurrence via head and neck combined high-resolution vessel wall imaging (HR-VWI).

Methods: This prospective cohort study included 169 patients with large atherosclerotic ischemic stroke who underwent head and neck combined HR-VWI from April 2022 to May 2023. The baseline clinical data and atherosclerotic plaque characteristics of the intracranial and extracranial carotid arteries were collected, and the patients were followed up for 1 year, with the endpoint event defined as recurrent ischemic stroke. Clinical and imaging data were compared between the recurrent and nonrecurrent groups. Independent risk factors associated with stroke recurrence were assessed via multivariate Cox regression analysis. The receiver operating characteristic (ROC) curves of the relevant variables were also plotted, and the area under the curve (AUC) was calculated to assess their ability to predict stroke recurrence. Kaplan–Meier survival curves were used to compare the probability of stroke recurrence.

Results: During the 12-month follow-up, stroke recurrence occurred in 35 of the 169 patients. Multivariate Cox regression analysis revealed that the total number of intracranial and extracranial carotid plaques ($p = 0.010$) and coexisting extracranial carotid plaques and intracranial significantly enhanced plaques ($p = 0.047$) were independent risk factors for recurrent ischemic stroke. The AUCs for predicting stroke recurrence were 0.787 and 0.710, respectively. The Kaplan–Meier survival curve revealed that the risk of stroke recurrence was significantly greater in patients whose total number of intracranial and extracranial carotid plaques was >4.5 than in patients whose total number of plaques was <4.5 ($p < 0.001$) and was significantly greater in patients with coexisting extracranial carotid plaques and intracranial significantly enhanced plaques than in patients without coexisting plaques ($p < 0.001$).

Conclusion: A greater total number of intracranial and extracranial carotid plaques and the coexistence of extracranial carotid plaques and intracranially

significantly enhanced plaques are independent risk factors associated with recurrent ischemic stroke. Head and neck combined HR-VWI may provide new indicators for the prediction of stroke recurrence, thus helping clinicians identify high-risk patients and target therapy to reduce the recurrence of ischemic events.

KEYWORDS

ischemic stroke, stroke recurrence, high-resolution vessel wall imaging, atherosclerosis, plaque characteristics

Introduction

Stroke is a common clinical cerebrovascular disease with high morbidity, disability, mortality, recurrence and economic burden and is the leading cause of death and disability among adults in China (1). Ischemic stroke is the main type of stroke, accounting for more than 80% of all strokes (2); it has an unstable prognosis and is prone to recurrence, especially in the early stages.

Atherosclerosis of the intracranial arteries and extracranial carotid arteries is the most common cause of ischemic stroke, and previous studies (3, 4) have demonstrated that many atherosclerotic plaque characteristics, including hyperintensity on T1-weighted imaging (T1WI), positive remodeling, plaque enhancement, and plaque burden, are correlated with the recurrence of ischemic stroke. However, atherosclerotic disease, as a systemic disease, usually affects multiple vascular beds. Therefore, simultaneous assessment of coexisting intracranial and extracranial atherosclerotic plaques may have greater predictive value for future cerebrovascular events than assessment of atherosclerotic plaques in a single vascular bed (5, 6).

Traditional vascular imaging techniques, such as computed tomography angiography (CTA), magnetic resonance angiography (MRA), and digital subtraction angiography (DSA), can only reveal the degree of stenosis and simple vessel wall information. Head and neck combined high-resolution vessel wall imaging (HR-VWI) can not only accurately assess the degree of stenosis but also has the unique advantages of providing potential pathological information within the vessel wall, visualizing plaque components, and accurately evaluating the morphology and signal characteristics of the arterial wall qualitatively and quantitatively. It is a repeatable and effective technique for the assessment of atherosclerotic disease (7).

This study aimed to evaluate the predictive value of extracranial carotid and intracranial plaque characteristics, as well as coexisting extracranial carotid and intracranial plaque characteristics, for large atherosclerotic ischemic stroke recurrence via head and neck combined HR-VWI and to identify the independent risk factors associated with stroke recurrence to provide guidance and assistance for the individualized treatment of patients with ischemic stroke.

Materials and methods

Patients

This was a single-center prospective cohort study. Patients with acute ischemic stroke who underwent head and neck combined HR-VWI from April 2022 to May 2023 at the Second Affiliated Hospital of Nantong University were included in this study. The inclusion criteria were as follows: (1) age > 18 years; (2) acute ischemic stroke confirmed by DWI and clinically; (3) head and neck combined HR-VWI performed within 2 weeks of symptom onset; and (4) intracranial large atherosclerosis determined to be the etiology of the stroke by a multidisciplinary consultation. (5) Complete clinical information. The exclusion criteria were as follows: (1) nonatherosclerotic intracranial or extracranial arterial diseases, such as vasculitis, moyamoya disease, and dissection; (2) cardiac risk factors for embolism, such as rheumatic heart disease, myocardial infarction, and subacute bacterial endocarditis; (3) reperfusion therapy for stroke (intravenous thrombolysis/intravascular thrombus extraction/angioplasty/stenting); (4) angioplasty/stenting/eroticization during the follow-up period; (5) a history of malignancy or newly diagnosed malignancy at the time of follow-up; and (6) poor imaging quality. The patient selection flowchart is shown in Figure 1. This study followed the Declaration of Helsinki and was approved by the Ethics Committee of the Second Affiliated Hospital of Nantong University (2023KT208).

Clinical data

Clinical data, including sex, age, history of hypertension, diabetes mellitus, smoking history, blood pressure, blood glucose, glycosylated hemoglobin, lipids, and renal function, were extracted from the clinical record system. Patients were also assessed for the National Institutes of Health Stroke Scale (NIHSS) score and Essen Stroke Risk Scale (ESRS) score.

HR-VWI examination

A 3.0 T Siemens Magnetom Prisma MRI scanner (Siemens Healthcare, Erlangen, Germany) with a 64-channel combined head and neck coil was used. In addition to the routine DWI and TOF-MRA scanning sequences, 3D-T1-SPACE sequences were added before the contrast agent was injected and 10 min later. The subjects were kept in a supine position during image acquisition, with the head placed in the center of the coil, the head was fixed with an elastic cushion to avoid artifacts caused by head movement resulting in blurred images, and acoustic sponges were used in both ears to reduce noise hazards during scanning. The axial plane was positioned parallel to the anterior–posterior joint line, and the sagittal plane was positioned parallel to the midline of the brain. The scanning sequence and its parameters were as follows: TR 700 ms, TE 15 ms; FOV 220 mm × 220 mm, matrix 320 × 320, and voxel

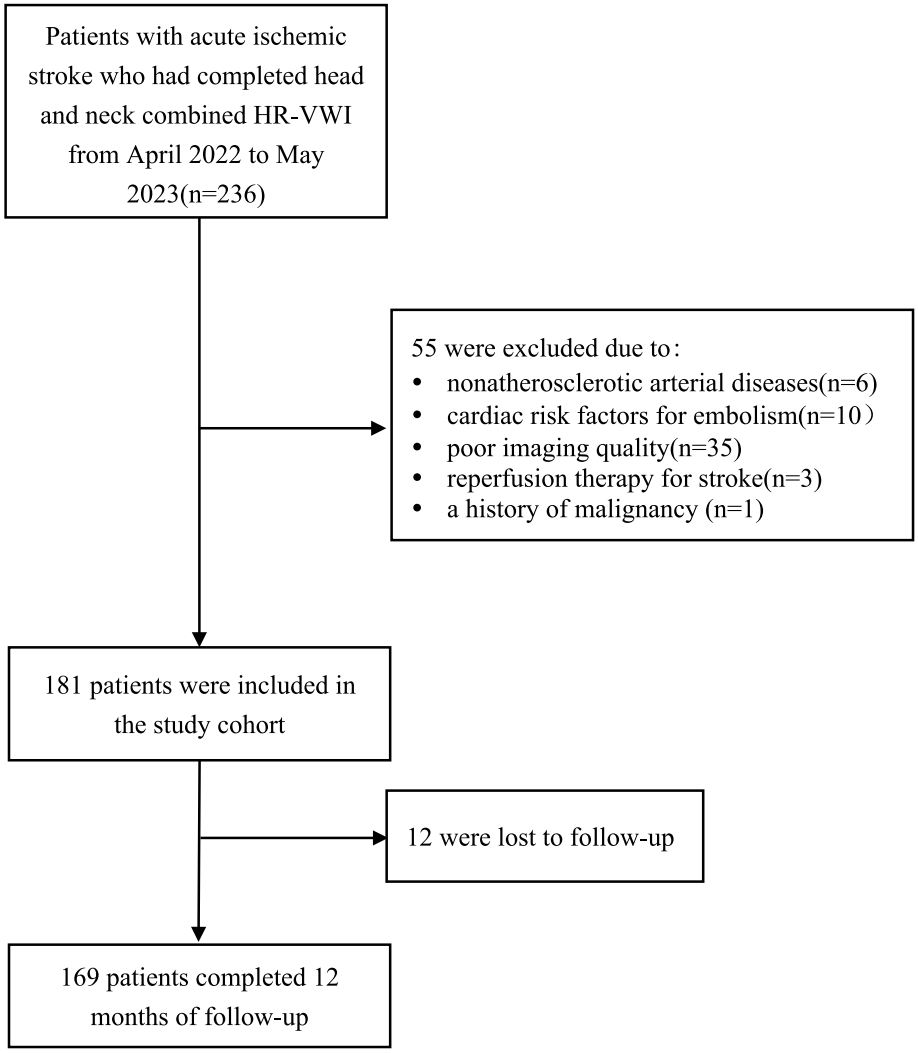

FIGURE 1
Flowchart showing the selection of patients.

0.3 mm × 0.3 mm × 0.7 mm. Gadopentetate dextran was used as the contrast agent at a dose of 0.1 mmol/kg.

Image analysis

Image postprocessing was performed via a Siemens workstation. A second-year graduate neuroimaging-oriented student and a neuroradiologist with 5 years of experience analyzed the images. The intracranial arteries were evaluated mainly as the anterior cerebral artery A1–A2 segment, the middle cerebral artery M1–M2 segment, the posterior cerebral artery P1–P2 segment, the vertebral artery V4 segment, the basilar artery, and the internal carotid artery C3–C7 segment, and the extracranial carotid arteries were evaluated mainly as the common carotid artery end and the internal carotid artery C1–C2 segment. The location of atherosclerotic plaques was determined by 3D-T1-SPACE sequences combined with sagittal, coronal, and axial images, i.e., the presence of focal wall thickening with or without significant luminal stenosis. The location of the culprit plaque was also determined with reference to the intracranial vascular supply zone, which was the only lesion within the supplying artery in the area of the infarct focus or the most stenotic lesion in the presence of multiple plaques.

Intracranial culprit plaque characteristics were assessed on 3D-T1-SPACE images that optimally revealed the plaque by adjusting the images to be perpendicular to the long-axis level of the vessel, and the following indices were measured: outer wall area (OWA) at the plaque, lumen area (LA) at the plaque, OWA at the reference site, and wall area (WA) at the plaque = OWA-LA at the plaque. The degree of stenosis was measured on HR-VWI images with reference to the Warfain Apisin symptomatic intracranial arterial disease test (WASID) (8). The remodeling ratio (RR) = OWA at the plaque/OWA at the reference site, with positive remodeling occurring when the RR > 1.05 and negative remodeling occurring when the RR < 0.95 (9). Plaque burden = WA at the plaque/OWA at the plaque. The degree of plaque enhancement was determined by outlining the region of interest covering the whole plaque on 3D-T1-SPACE images before and after enhancement and recording the signal intensity (SI) before and after plaque enhancement. The plaque enhancement ratio = (SIpost-SIpre/SIpre), where SIpost is the SI of the enhanced plaque and where SIpre is the SI of the flat-scan plaque. Significant enhancement is defined when the SI of the enhanced plaque

is equal to or greater than the enhancement signal of the pituitary stalk (10). Intraplaque hemorrhage (IPH) was defined as a high signal within the plaque on preenhancement 3D-T1-SPACE images that exceeded 150% of the adjacent muscle signal (11).

Extracranial carotid plaques are measured by the following indices: degree of stenosis, RR, IPH, and lipid-rich necrotic core (LRNC). The degree of stenosis was measured via the North American Symptomatic Carotid Endarterectomy Trial (NASCET) (12). LRNC is an iso-signal on TOF-MRA images and a high signal on 3D-T1-SPACE images and has no significant enhancement after enhancement (13).

Finally, extracranial carotid and intracranial atherosclerotic plaques were assessed simultaneously, the total number of intracranial and extracranial carotid plaques was calculated, and the presence of the following coexisting combinations was examined: (1) extracranial carotid plaques + intracranial plaques; (2) extracranial carotid plaques + intracranial stenosis (≥50%); (3) extracranial carotid plaques + intracranial positive remodeling; (4) extracranial carotid plaques + intracranial IPH; and (5) extracranial carotid plaques + intracranial significantly enhanced plaques.

We selected randomly 30 patients to test the intra-observer and inter-observer reproducibility of the quantitative and qualitative date. A 1-month interval was set to determine the intra-observer reproducibility to minimize memory bias.

Follow-up and outcome assessment

Patients were followed up via face–to-face conversation or telephone at 3, 6, 9, and 12 months after discharge, with the endpoint event being recurrent ischemic stroke in the same vascular territory during the follow-up period. Recurrent stroke was defined as the worsening of neurological deficits or new neurological deficits and the presence of a new lesion in the relevant area of the brain, as confirmed by diffusion–weighted imaging (DWI) (14). The follow-up time was defined as the time of the endpoint event or, if no event occurred, the time of the most recent follow-up. Patients were categorized into recurrent and nonrecurrent groups on the basis of follow-up results.

Statistical analysis

SPSS 26.0 software was used for statistical analysis. The normality of the quantitative data was tested via the Shapiro–Wilk test. Variables that conformed to a normal distribution are presented as the means ± standard deviations, and differences between groups were analyzed via two independent samples t tests. Information that was not normally distributed was described by medians and interquartile ranges, and differences between groups were analyzed via nonparametric tests. Count data are described as cases (%), and differences were analyzed via the chi-square test. Variables with $p < 0.05$ in the univariable Cox regression analysis were included in the multivariable Cox regression analysis to obtain independent characteristics associated with stroke recurrence. The receiver operating characteristic (ROC) curves of the relevant variables were also plotted, and the area under the curve (AUC) was calculated and compared via the Delong test. In addition, Kaplan–Meier survival curves and log-rank tests were used to compare the probability of recurrence after stroke for the variables of interest. The inter-observer and intra-observer reproducibility of quantitative date was evaluated by intraclass correlation coefficient (ICC) using a two-way random model with absolute agreement. The inter-observer and intra-observer reproducibility of qualitative date was evaluated by Cohen's kappa value. A value of ICC and kappa≥0.75 indicates excellent agreement. $p < 0.05$ was considered a statistically significant difference.

Results

Baseline clinical data of patients

A total of 169 patients were included in this study, 35 of whom experienced stroke recurrence during an average follow-up time of 10.7 months. The median stroke recurrence time was 5 (2, 9.5) months. The median age of the patients in the recurrence group was 70 (65, 73) years, of which 62.9% were male, and the median age of the patients in the nonrecurrence group was 65 (56, 73) years, of which 61.9% were male. The age of the patients in the recurrence group was significantly greater than that of the patients in the nonrecurrence group ($p = 0.024$), and the remaining differences in the clinical data between the two groups were not statistically significant ($p > 0.05$), as shown in Table 1.

Plaque characteristics of patients

The intracranial and extracranial carotid plaque characteristics of the recurrent and nonrecurrent groups are shown in Table 2. Compared with the nonrecurrent group, the recurrent group had a greater total number of intracranial and extracranial carotid plaques and a greater incidence of positive remodeling of extracranial carotid arteries ($p < 0.001$), extracranial carotid plaques + intracranial plaques ($p = 0.001$), extracranial carotid plaques + intracranial stenosis (≥50%; $p = 0.004$), extracranial carotid plaques + intracranial IPH ($p = 0.004$), and extracranial carotid plaques + intracranial significantly enhanced plaques ($p < 0.001$). The results were statistically significant. The other characteristics were not significantly different between the two groups ($p > 0.05$). Typical imaging images of patients in the recurrent and nonrecurrent groups are shown in Figures 2, 3.

The kappa values were, respectively, 1.00, 0.95, 0.90, 0.89, 1.00, 0.98 and 0.93 for the intra-observer reproducibility in the identification of intracranial IPH, intracranial significantly enhanced plaques, intracranial positive remodeling, extracranial carotid stenosis (≥50%), extracranial carotid IPH, extracranial carotid LRNC and extracranial carotid positive remodeling. For the inter-observer reproducibility, the values of the same parameters were 0.98, 0.92, 0.88, 0.85, 0.99, 0.93 and 0.90, respectively. The intra-observer ICC values of plaque thickness, plaque burden, degree of stenosis and remodeling ratio of intracranial culprit plaques were 0.95 (95% CI 0.90–0.98), 0.89 (95% CI 0.75–0.94), 0.87 (95% CI 0.73–0.95) and 0.80 (95% CI 0.62–0.89), respectively. The inter-observer ICC values for the same parameters were as follows: 0.96 (95% CI 0.92–0.99), 0.94 (95% CI 0.85–0.97), 0.85 (95% CI 0.72–0.91) and 0.84 (95% CI 0.72–0.91).

Independent risk factor analysis for stroke recurrence

Univariable and multivariable Cox regression analyses were used to detect risk factors associated with stroke recurrence and variables

TABLE 1 Comparison of baseline clinical data between the recurrent and nonrecurrent groups.

Index	Recurrence group (n = 35)	Non-recurrence group (n = 134)	t/z/χ^2	p value
Age, years	70(65, 73)	65(56, 73)	2.254	0.024
Male, n (%)	22(62.9%)	83(61.9%)	0.01	0.921
Systolic blood pressure, mmHg	146.37 ± 19.74	146.91 ± 20.60	−0.139	0.89
Diastolic blood pressure, mmHg	83(76, 90)	82.5(74, 91)	0.208	0.836
History of hypertension, n (%)	30(85.7%)	96(71.6%)	2.897	0.089
Diabetes mellitus, n (%)	14(40%)	46(34.3%)	0.39	0.532
Smoking history, n (%)	8(22.9%)	39(29.1%)	0.539	0.463
blood glucose, mmol/L	5.61(4.68, 6.99)	5.62(4.73, 7.40)	−0.671	0.502
Glycosylated hemoglobin, mmol/L	6.2(5.9, 7.6)	6.2(5.7,7.88)	0.132	0.895
Triglycerides, mmol/L	1.57(1.25, 1.88)	1.53(1.03, 1.98)	0.345	0.73
Total cholesterol, mmol/L	4.11(3.64, 4.49)	4.27(3.68, 4.95)	−0.793	0.428
HDL, mmol/L	1.03(0.92, 1.24)	1.11(0.97, 1.33)	−1.187	0.235
LDL, mmol/L	2.54(2.23, 2.86)	2.63(2.03, 3.14)	−0.202	0.840
Lipoprotein a, mmol/L	130(71, 290)	115(53.75, 252.75)	0.987	0.323
Urea nitrogen, mmol/L	5.20(4.04, 6.85)	5.37(4.28, 6.38)	−0.132	0.895
Creatinine, mmol/L	63(58.3, 70)	63.5(51.95, 72.55)	0.415	0.678
Uric acid, mmol/L	318(274, 387)	313.95(268.15, 363.95)	0.921	0.357
Hemoglobin,g/L	136.71 ± 17.28	138.38 ± 17.48	−0.503	0.615
NIHSS score	2(1, 4)	2(0, 4)	0.406	0.685
ESRS	2(2, 3)	2(1, 3)	1.420	0.156

HDL, high-density lipoprotein; LDL, low-density lipoprotein; NIHSS, National Institute of Health Stroke Scale; ESRS, Essen stroke risk score.

with $p < 0.05$ in the univariable analysis were included in the multivariable Cox regression model. The results revealed that the total number of intracranial and extracranial carotid plaques (HR = 1.327; 95% CI 1.070–1.647; $p = 0.010$) and coexisting extracranial carotid plaques and intracranial significantly enhanced plaques (HR = 5.375; 95% CI 1.025–28.171; $p = 0.047$) were independent risk factors for stroke recurrence, as shown in Tables 3, 4.

We plotted ROC curves for coexisting extracranial carotid plaques and intracranial significantly enhanced plaques, the total number of intracranial and extracranial carotid plaques, and ESRS to predict stroke recurrence (Figure 4). On the basis of the ROC curve analysis, the optimal cutoff value of the total number of plaques to predict stroke recurrence was 4.5, with an AUC value of 0.787 (95% CI 0.705–0.869), a sensitivity of 74.3%, and a specificity of 69.4%. The AUC value of coexisting extracranial carotid plaques and intracranial significantly enhanced plaques to predict stroke recurrence was 0.710 (95% CI 0.607–0.814), with a sensitivity of 60% and specificity of 82.1%. The AUC value for the ESRS was 0.575 (95% CI 0.473–0.677). The Delong test revealed a statistically significant difference between the AUC values of coexisting extracranial carotid plaques and intracranially significantly enhanced plaques and the ESRS ($z = 2.399$, $p = 0.016$) and between the AUC values of the total number of plaques and the ESRS ($z = 3.943$, $p < 0.001$).

Kaplan–Meier survival curve analysis

We used Kaplan–Meier survival curve analysis to determine the risk of stroke recurrence according to the optimal cutoff value for the total number of intracranial and extracranial carotid plaques (4.5) and the coexistence of extracranial carotid plaques and significantly enhanced intracranial plaques. The vertical axis represents the rate of no recurrence and the horizontal axis represents the follow-up time. By log-rank tests we found that the risk of stroke recurrence was significantly greater in patients with a total number of plaques>4.5 than in patients with a total number of plaques<4.5 ($p < 0.001$), and the risk of stroke recurrence was significantly greater in patients with coexisting extracranial carotid plaques and intracranially significantly enhanced plaques than in patients without coexisting plaques ($p < 0.001$), as shown in Figure 5.

Discussion

In this prospective cohort study, we found that a greater total number of intracranial and extracranial carotid plaques and the coexistence of extracranial carotid plaques and intracranially significantly enhanced plaques were independent risk factors associated with ischemic stroke recurrence. Both had good predictive ability for stroke recurrence, whereas ESRS did not.

Atherosclerosis is a systemic disease, and no independent risk factors associated with stroke recurrence were found when extracranial carotid and intracranial atherosclerotic plaque characteristics were analyzed separately in this study, whereas coexisting plaques and the total number of plaques in the intracranial and extracranial carotid arteries were significantly associated with stroke recurrence, suggesting that simultaneous assessment of multiple vascular beds is more valuable than

TABLE 2 Comparison of plaque characteristics between the recurrent and nonrecurrent groups.

Characteristic	Recurrence group (n = 35)	Non-recurrence group (n = 134)	t/z/χ^2	p value
Total number of plaques	6(4, 7)	4(3, 5)	5.302	<0.001
Intracranial culprit plaque				
Degree of stenosis, %	55(30, 75)	40(26.75, 65)	1.205	0.228
Plaque burden	0.79 ± 0.099	0.76 ± 0.098	1.614	0.108
Remodeling ratio	1.10(0.89, 1.15)	1.06(0.92, 1.13)	0.921	0.357
Positive remodeling, n (%)	21(60%)	69(51.5%)	0.807	0.369
Plaque thickness, mm	1.7(1.4, 2.2)	1.6(1.4, 1.9)	1.738	0.082
Enhancement ratio	1.56(0.82, 1.76)	1.09(0.72, 1.51)	1.755	0.079
IPH, n (%)	11(31.4%)	40(29.9%)	0.033	0.856
Significant enhancement, n (%)	20(57.1%)	58(43.3%)	2.145	0.143
Extracranial carotid plaque				
Stenosis (≥50%), n (%)	4(11.4%)	3(2.2%)	3.815	0.051
Positive remodeling, n (%)	19(54.3%)	32(23.9%)	12.176	<0.001
LRNC, n (%)	3(8.6%)	12(9%)	0.005	0.943
IPH, n (%)	2(5.7%)	3(2.2%)	0.271	0.603
Coexisting atherosclerotic plaques				
Extracranial carotid plaques + intracranial plaques, n (%)	23(65.7%)	45(33.6%)	11.915	0.001
Extracranial carotid plaques + intracranial stenosis (≥50%), n (%)	14(40%)	23(17.2%)	8.463	0.004
Extracranial carotid plaques + intracranial positive remodeling, n (%)	12(34.3%)	29(21.6%)	2.415	0.120
Extracranial carotid plaques + intracranial IPH, n (%)	12(34.3%)	18(13.4%)	8.265	0.004
Extracranial carotid plaques + intracranial significantly enhanced plaques, n (%)	21(60%)	24(17.9%)	25.164	<0.001

IPH, Intraplaque hemorrhage; LRNC, lipid-rich necrotic core.

assessment of a single vascular bed in the prediction of stroke recurrence. In line with previous studies, Suo et al. (15) analyzed the relationship between intracranial and extracranial large atherosclerosis and prognosis through multivariate Cox regression by enrolling 806 patients with less severe acute stroke and finally reported that the coexistence of atherosclerosis with >50% stenosis in the intracranial and extracranial arteries can result in a significant increase in the rate of stroke recurrence by a factor of approximately 3.4. Another study (16) also found that patients with symptomatic vascular disease in multiple arterial beds had a poor long-term prognosis for stroke or TIA, and that the prognosis worsened with the number of vessels involved. This may be due to the increased risk of plaque rupture due to more plaques and the involvement of more vascular beds, further increasing the probability of stroke recurrence. Moreover, the number of atherosclerotic risk factors increases with the number of affected vascular beds, including lipids and smoking, which are independently associated with stroke recurrence and are important targets for secondary prevention of stroke (17). Thus, the number of affected vascular beds may be able to be used as a summative measure to predict stroke recurrence, which further demonstrates the additive value of multivessel bed assessment for stroke recurrence prediction. Clinicians can try to include assessment of the carotid artery to further predict the prognosis of stroke patients.

However, owing to the limitations of the examination technique, most of the previous studies were limited to the coexistence of intracranial and extracranial atherosclerosis and the degree of stenosis and did not involve other characteristics of the plaques. In this study, head and neck combined HR-VWI was employed to perform the examination. Magnetic resonance can provide high spatial resolution and excellent soft tissue contrast, which can not only identify atherosclerotic plaques with mild to moderate stenosis more accurately but also visualize and characterize the vessel wall and reveal more pathological characteristics of plaques (18) to further analyze the relationship between the coexistence of high-risk plaque characteristics and stroke recurrence. A similar study was previously performed by Wu et al. (19). They followed up 97 stroke patients who underwent head and neck combined HR-VWI, and 21 patients experienced stroke recurrence. Multivariate Cox regression analysis revealed that the coexistence of intracranial T1WI high-signal plaques and extracranial carotid atherosclerotic plaques was an independent risk factor for stroke recurrence, with greater predictive value than the assessment of extracranial carotid atherosclerosis alone. Jiang et al. (20) also reported that the coexistence of severe stenosis of intracranial arteries with greater plaque burden, intraplaque calcification, and LRNC in extracranial carotid arteries was independently associated with ipsilateral acute cerebrovascular events through magnetic resonance vessel wall imaging. Although both of these results differ from the final results

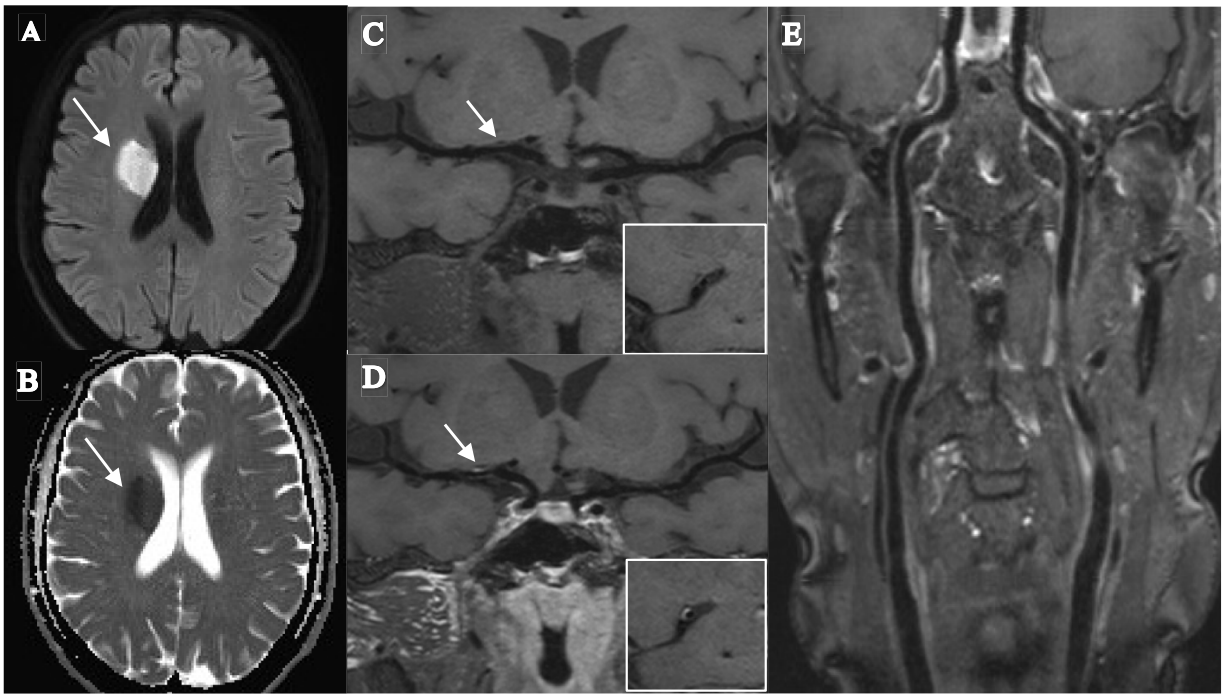

FIGURE 2
Female, 56 years old, was admitted to the hospital with orofacial tilt and left lower limb weakness for 2 days, and did not experience stroke recurrence during the 12-month follow-up. **(A,B)** DWI image shows a patchy hyperdense shadow in the right radiocoronal area with a corresponding reduced ADC value (arrow). **(C,D)** T1-SPACE images before and after enhancement show the presence of plaque in the M1 segment of the right middle cerebral artery (arrow), with low plaque burden, isosignal plaque before enhancement, mild enhancement after enhancement, and mild stenosis. **(E)** T1-SPACE image of the extracranial carotid artery does not show the presence of plaque.

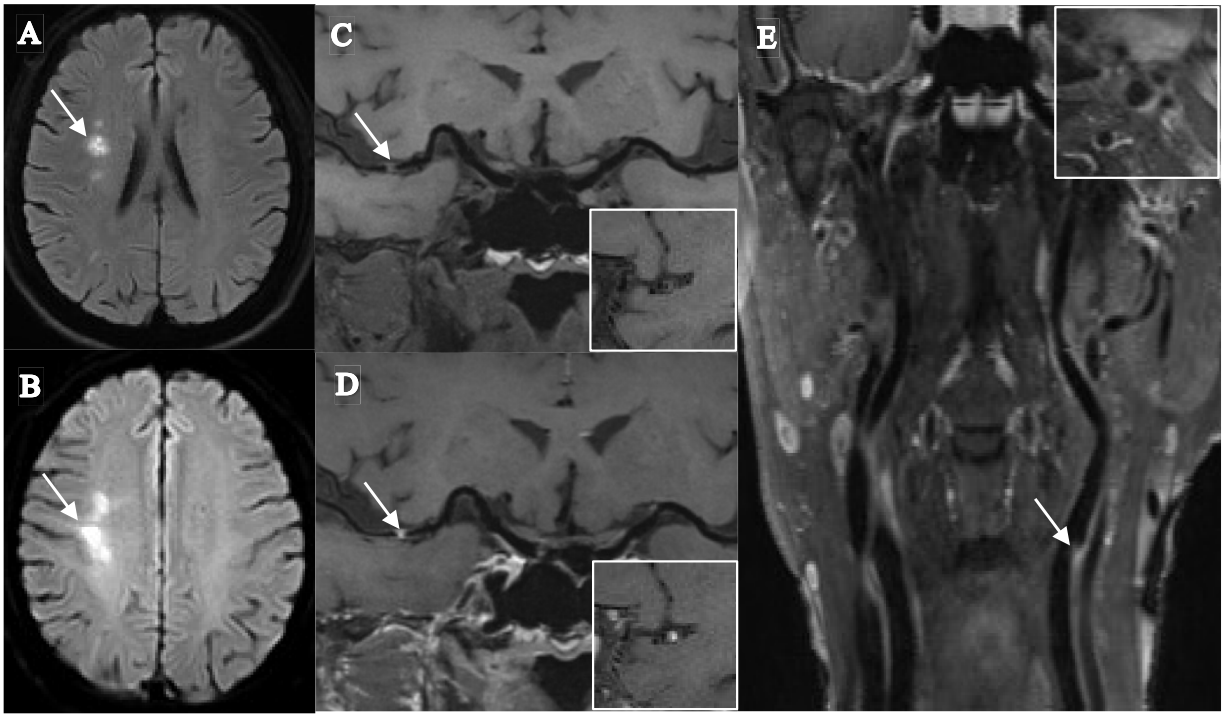

FIGURE 3
Female, 68 years old, was admitted to the hospital with numbness in the left limb, and stroke recurrence occurred at the 4-month follow-up. **(A)** DWI images before recurrence shows a patchy hyperdense shadow visible in the right corona radiata (arrow). **(B)** DWI images after recurrence shows a clumpy hyperdense shadow visible in the right centrum semiovale (arrow). **(C,D)** T1-SPACE images before and after enhancement show the presence of plaque in the M1 segment of the right middle cerebral artery (arrow), with high plaque burden, significant enhancement after enhancement, and severe stenosis. **(E)** T1-SPACE image of the extracranial carotid artery shows the presence of plaque at the beginning of the left internal carotid artery (arrow).

TABLE 3 Univariable cox regression of the significant indicators associated with stroke recurrence.

Risk factors	HR(95%CI)	*p* value
Age	1.043(1.007,1.080)	0.018
Total number of intracranial and extracranial carotid plaques	1.568(1.334,1.844)	<0.001
Positive remodeling of extracranial carotid arteries	3.052(1.569,5.938)	0.001
Extracranial carotid plaques + intracranial plaques	3.171(1.577,6.376)	0.001
Extracranial carotid plaques + intracranial stenosis (≥50%)	2.755(1.400,5.422)	0.003
Extracranial carotid plaques + intracranial IPH	2.903(1.443,5.837)	0.003
Extracranial carotid plaque + intracranial significantly enhanced plaques	5.094(2.586,10.034)	<0.001

IPH, Intraplaque hemorrhage; HR hazard ratio; CI confidence interval.

TABLE 4 Multivariate cox regression of the significant indicators associated with stroke recurrence.

Risk factors	HR(95%CI)	*p* value
Age	1.032(0.990,1.075)	0.136
Total number of intracranial and extracranial carotid plaques	1.327(1.070,1.647)	0.010
Positive remodeling of extracranial carotid arteries	1.326(0.433,4.062)	0.621
Extracranial carotid plaques + intracranial plaques	0.248(0.038,1.604)	0.143
Extracranial carotid plaques + intracranial stenosis (≥50%)	1.809(0.727,4.503)	0.203
Extracranial carotid plaques + intracranial IPH	0.822(0.323,2.089)	0.680
Extracranial carotid plaque + intracranial significantly enhanced plaques	5.375(1.025,28.171)	0.047

IPH, Intraplaque hemorrhage; HR hazard ratio; CI confidence interval.

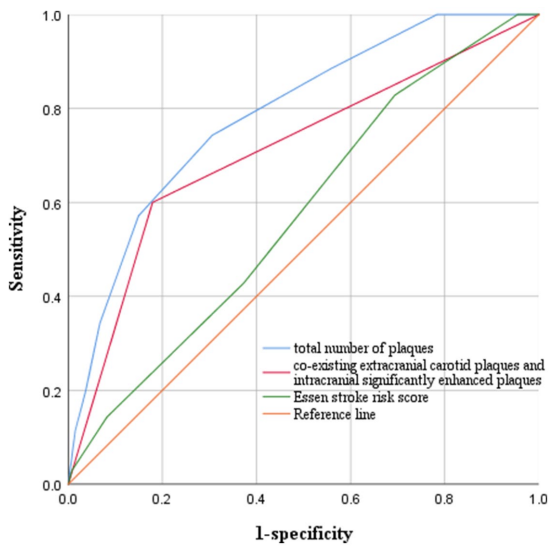

FIGURE 4
ROC curves for predicting stroke recurrence. The optimal cutoff value of the total number of plaques to predict stroke recurrence was 4.5, with an AUC value of 0.787, a sensitivity of 74.3%, and a specificity of 69.4%. The AUC value of coexisting extracranial carotid plaques and intracranial significantly enhanced plaques to predict stroke recurrence was 0.710, with a sensitivity of 60% and a specificity of 82.1%. The AUC value for ESRS was 0.575.

of the present study, the coexistence of plaque characteristics found by HR-VWI is more valuable for the prediction of stroke recurrence than the coexistence of atherosclerosis alone is, and this could be further explored in the future.

As one of the important characteristics of plaque vulnerability, significant plaque enhancement has been demonstrated in many previous studies to be correlated with ischemic stroke recurrence (21, 22). In this study, although we did not observe a strong relationship between significant enhancement of intracranial plaques and stroke recurrence, the coexistence of extracranial carotid plaques and intracranial significantly enhanced plaques was independently associated with stroke recurrence, indicating that significant plaque enhancement can still significantly improve the ability to predict recurrence. This may be because significant plaque enhancement generally represents plaque inflammation, macrophage infiltration and neovascularization, and the accumulation of inflammatory cells in specific areas of the plaque can further lead to plaque hemorrhage and rupture, which increases the instability of the plaque and consequently leads to the occurrence of stroke (23). However, a sufficiently reliable pathological basis for the correlation between plaque enhancement and stroke recurrence is still lacking, and larger prospective studies are needed for further validation.

In addition, the degree of arterial stenosis is one of the traditional predictors of stroke recurrence, and a study by Li et al. (24) reported that the stenosis rate of the responsible vessel was significantly greater in patients with recurrent ischemic stroke than in patients without recurrence, which can be used as an independent risk factor for predicting stroke recurrence. However, our study did not find a significant association between moderate-to-severe stenosis of extracranial carotid and intracranial arteries and stroke recurrence, and the fact that the majority of plaques showed positive remodeling may be one of the main reasons. Plaques with positive remodeling are considered to have a greater risk of rupture and are more likely to lead to the occurrence and recurrence of stroke (25), whereas plaques with

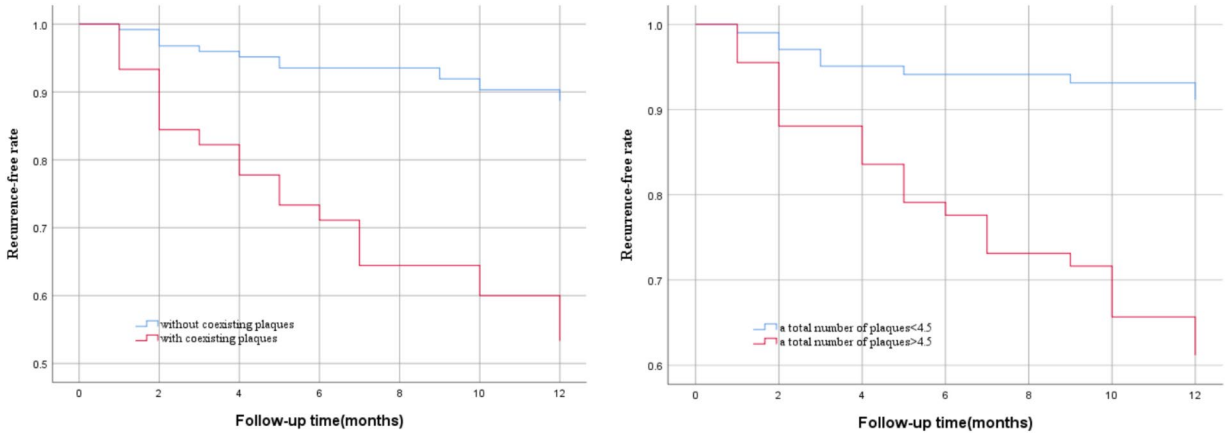

FIGURE 5
Kaplan–Meier survival curves of stroke recurrence probability. Patients with a total number of plaques> 4.5 ($p < 0.001$) and coexisting extracranial carotid plaques and intracranial significantly enhanced plaques ($p < 0.001$) had a higher risk of stroke recurrence during follow-up.

positive remodeling often show mild stenosis; thus, there is a limitation in judging the vulnerability of plaques by the degree of stenosis, neglecting the effect of plaque remodeling. Plaque burden and IPH are also important characteristics indicating plaque vulnerability (26), and many previous studies (27, 28) have shown that both are significantly associated with ischemic stroke recurrence and are important predictors of stroke recurrence. However, this is contrary to the results of our study, which did not find a significant association between a larger plaque burden and the presence of IPH with stroke recurrence, which may be due to the low occurrence of both in all plaques and the fact that our study was a single-center, smaller-sample-size trial, which led to the masking of the association between both and stroke recurrence. Thus, more multicenter trials with large sample sizes are needed to explore this topic further in the future.

The study also revealed that the ESRS score was not a good predictor of stroke recurrence, with an AUC of only 0.575, and a retrospective cohort study by Lv et al. (29) also revealed that the AUC of the ESRS score for the prediction of stroke recurrence was 0.595, which was similar to our study, indicating that the indicators included in the score lacked good predictive ability for stroke recurrence. In contrast, the AUCs for the total number of intracranial and extracranial carotid plaques and the coexistence of extracranial carotid plaques and intracranially significantly enhanced plaques were significantly greater than those of the ESRS, suggesting that the clinic may try to apply these two indicators to assess the risk of stroke recurrence, in addition to traditional assessment tools.

Our study also has the following limitations. First, this is a single-center study with a small sample size, which may obscure the association between certain low-incidence plaque characteristics and stroke recurrence, and further multicenter studies with large sample sizes are needed in the future. Second, atherosclerosis is a systemic disease, and only intracranial arteries and extracranial carotid arteries were evaluated in the present study. Research on more vessels should be included in the future. Third, in addition to plaque characteristics, hemodynamics and collateral circulation formation are strongly associated with stroke recurrence and should be included in future studies. Finally, atherosclerosis is a dynamic process, and HR-VWI was not performed during the follow-up period in this study.

Conclusion

In conclusion, a greater total number of intracranial and extracranial carotid plaques and the coexistence of extracranial carotid plaques and significantly enhanced intracranial plaques are independent risk factors associated with ischemic stroke recurrence. Head and neck combined HR-VWI may provide new indicators for the prediction of stroke recurrence, thus helping clinicians identify high-risk patients and target therapy to reduce the recurrence of ischemic events.

Data availability statement

The raw data supporting the conclusions of this article will be made available by the authors, without undue reservation.

Ethics statement

The studies involving humans were approved by the Ethics Committee of the Second Affiliated Hospital of Nantong University (2023KT208). The studies were conducted in accordance with the local legislation and institutional requirements. The participants provided their written informed consent to participate in this study.

Author contributions

SS: Writing – original draft. TW: Writing – review & editing. LZ: Writing – review & editing. YG: Writing – original draft. XF: Writing – original draft. YL: Writing – original draft. CQ: Writing – original draft. MZ: Writing – original draft. JQ: Writing – original draft.

Funding

The author(s) declare that financial support was received for the research, authorship, and/or publication of this article. This work was supported by Science and Technology Project of Nantong City (MS2023068), Nantong University Clinical Medicine Special Project (2023LQ003), Nantong Municipal Health Commission (MS2024026).

Conflict of interest

The authors declare that the research was conducted in the absence of any commercial or financial relationships that could be construed as a potential conflict of interest.

Generative AI statement

The authors declare that no Generative AI was used in the creation of this manuscript.

Publisher's note

All claims expressed in this article are solely those of the authors and do not necessarily represent those of their affiliated organizations, or those of the publisher, the editors and the reviewers. Any product that may be evaluated in this article, or claim that may be made by its manufacturer, is not guaranteed or endorsed by the publisher.

References

1. Wang LD, Peng B, Zhang HQ. Brief report on stroke prevention and treatment in China, 2020. *Chin J Cerebrovasc Dis*. (2022) 19:136–44. doi: 10.3969/j.issn.1672-5921.2022.02.011

2. Wang Y, Li Z, Wang Y, Zhao X, Liu L, Yang X, et al. Chinese stroke center Alliance: a national effort to improve healthcare quality for acute stroke and transient ischaemic attack: rationale, design and preliminary findings. *Stroke Vasc Neurol*. (2018) 3:256–62. doi: 10.1136/svn-2018-000154

3. Saba L, Saam T, Jäger HR, Yuan C, Hatsukami TS, Saloner D, et al. Imaging biomarkers of vulnerable carotid plaques for stroke risk prediction and their potential clinical implications. *Lancet Neurol*. (2019) 18:559–72. doi: 10.1016/S1474-4422(19)30035-3

4. Song JW, Pavlou A, Xiao J, Kasner SE, Fan Z, Messé SR. Vessel Wall magnetic resonance imaging biomarkers of symptomatic intracranial atherosclerosis: a Meta-analysis. *Stroke*. (2021) 52:193–202. doi: 10.1161/STROKEAHA.120.031480

5. Xu Y, Yuan C, Zhou Z, He L, Mi D, Li R, et al. Co-existing intracranial and extracranial carotid artery atherosclerotic plaques and recurrent stroke risk: a three-dimensional multicontrast cardiovascular magnetic resonance study. *J Cardiovasc Magn Reson*. (2016) 18:90. doi: 10.1186/s12968-016-0309-3

6. Li J, Li D, Yang D, Huo R, Chen X, Xu Y, et al. Co-existing cerebrovascular atherosclerosis predicts subsequent vascular event: a multi-contrast cardiovascular magnetic resonance imaging study. *J Cardiovasc Magn Reson*. (2020) 22:4. doi: 10.1186/s12968-019-0596-6

7. Xu W. High-resolution MRI of intracranial large artery diseases: how to use it in clinical practice. *Stroke Vasc Neurol*. (2019) 4:102–4. doi: 10.1136/svn-2018-000210

8. Chimowitz MI, Lynn MJ, Howlett-Smith H, Stern BJ, Hertzberg VS, Frankel MR, et al. Comparison of warfarin and aspirin for symptomatic intracranial arterial stenosis. *N Engl J Med*. (2005) 352:1305–16. doi: 10.1056/NEJMoa043033

9. Qiao Y, Anwar Z, Intrapiromkul J, Liu L, Zeiler SR, Leigh R, et al. Patterns and implications of intracranial arterial remodeling in stroke patients. *Stroke*. (2016) 47:434–40. doi: 10.1161/STROKEAHA.115.009955

10. Skarpathiotakis M, Mandell DM, Swartz RH, Tomlinson G, Mikulis DJ. Intracranial atherosclerotic plaque enhancement in patients with ischemic stroke. *AJNR Am J Neuroradiol*. (2013) 34:299–304. doi: 10.3174/ajnr.A3209

11. Alexander MD, Yuan C, Rutman A, Tirschwell DL, Palagallo G, Gandhi D, et al. High-resolution intracranial vessel wall imaging: imaging beyond the lumen. *J Neurol Neurosurg Psychiatry*. (2016) 87:589–97. doi: 10.1136/jnnp-2015-312020

12. Inzitari D, Eliasziw M, Gates P, Sharpe BL, Chan RKT, Meldrum HE, et al. The causes and risk of stroke in patients with asymptomatic internal-carotid-artery stenosis. North American symptomatic carotid endarterectomy trial collaborators. *N Engl J Med*. (2000) 342:1693–701. doi: 10.1056/NEJM200006083422302

13. Yuan C, Mitsumori LM, Ferguson MS, Polissar NL, Echelard D, Ortiz G, et al. In vivo accuracy of multispectral magnetic resonance imaging for identifying lipid-rich necrotic cores and intraplaque hemorrhage in advanced human carotid plaques. *Circulation*. (2001) 104:2051–6. doi: 10.1161/hc4201.097839

14. Coull AJ, Rothwell PM. Underestimation of the early risk of recurrent stroke: evidence of the need for a standard definition. *Stroke*. (2004) 35:1925–9. doi: 10.1161/01.STR.0000133129.58126.67

15. Suo Y, Jing J, Pan Y, Chen W, Zhou H, Li H, et al. Concurrent intracranial and extracranial artery stenosis and the prognosis of transient ischaemic symptoms or imaging-negative ischaemic stroke. *Stroke Vasc Neurol*. (2021) 6:33–40. doi: 10.1136/svn-2020-000377

16. Heldner MR, Li L, Lovett NG, Kubiak MM, Lyons S, Rothwell PM. Long-term prognosis of patients with transient ischemic attack or stroke and symptomatic vascular disease in multiple arterial beds. *Stroke*. (2018) 49:1639–46. doi: 10.1161/STROKEAHA.118.020913

17. Xu J, Zhang X, Jin A, Pan Y, Li Z, Meng X, et al. Trends and risk factors associated with stroke recurrence in China, 2007-2018. *JAMA Netw Open*. (2022) 5:e2216341. doi: 10.1001/jamanetworkopen.2022.16341

18. Makowski MR, Botnar RM. MR imaging of the arterial vessel wall: molecular imaging from bench to bedside. *Radiology*. (2013) 269:34–51. doi: 10.1148/radiol.13102336

19. Wu G, Zhu C, Wang H, Fu D, Lu X, Cao C, et al. Co-existing intracranial and extracranial carotid atherosclerosis predicts large-artery atherosclerosis stroke recurrence: a single-center prospective study utilizing combined head-and-neck vessel wall imaging. *Eur Radiol*. (2023) 33:6970–80. doi: 10.1007/s00330-023-09654-5

20. Jiang C, Zhang J, Zhu J, Wang X, Wen Z, Zhao X, et al. Association between coexisting intracranial artery and extracranial carotid artery atherosclerotic diseases and ipsilateral cerebral infarction: a Chinese atherosclerosis risk evaluation (CARE-II) study. *Stroke Vasc Neurol*. (2021) 6:595–602. doi: 10.1136/svn-2020-000538

21. Quan G, Wang X, Liu Y, Gao L, Gao G, Tan G, et al. Refined imaging features of culprit plaques improve the prediction of recurrence in intracranial atherosclerotic stroke within the middle cerebral artery territory. *Neuroimage Clin*. (2023) 39:103487. doi: 10.1016/j.nicl.2023.103487

22. Cheng X, Liu J, Li H, Yang JL, Zhou CS, Zhi BB, et al. Incremental value of enhanced plaque length for identifying intracranial atherosclerotic culprit plaques: a high-resolution magnetic resonance imaging study. *Insights Imaging*. (2023) 14:99. doi: 10.1186/s13244-023-01449-y

23. Benson JC, Saba L, Bathla G, Brinjikji W, Nardi V, Lanzino G. MR imaging of carotid artery atherosclerosis: updated evidence on high-risk plaque features and emerging trends. *AJNR Am J Neuroradiol*. (2023) 44:880–8. doi: 10.3174/ajnr.A7921

24. Li F, Wang Y, Du Y, Hu T, Wu Y. Correlation of the middle cerebral artery atherosclerotic plaque characteristics with ischemic stroke recurrence: a vessel wall magnetic resonance imaging study. *Aging (Albany NY)*. (2023) 15:7844–52. doi: 10.18632/aging.204950

25. Rentrop KP. Thrombi in acute coronary syndromes: revisited and revised. *Circulation*. (2000) 101:1619–26. doi: 10.1161/01.CIR.101.13.1619

26. Hu YN, Zhao Z, Ding J, Zhang Y. Imaging evaluation of vulnerability of intracranial atherosclerotic plaques. *Int J Cerbrovasc Dis*. (2022) 30:927–33. doi: 10.3760/cma.j.issn.1673-4165.2022.12.008

27. Sun B, Wang L, Li X, Zhang J, Zhang J, Liu X, et al. Intracranial atherosclerotic plaque characteristics and burden associated with recurrent acute stroke: a 3D quantitative Vessel Wall MRI study. *Front Aging Neurosci*. (2021) 13:706544. doi: 10.3389/fnagi.2021.706544

28. Yuan W, Liu X, Yan Z, Wu B, Lu B, Chen B, et al. Association between high-resolution magnetic resonance vessel wall imaging characteristics and recurrent stroke in patients with intracranial atherosclerotic steno-occlusive disease: a prospective multicenter study. *Int J Stroke*. (2024) 19:569–76. doi: 10.1177/17474930241228203

29. Lv Y, Ma X, Zhao W, Ju J, Yan P, Li S, et al. Association of plaque characteristics with long-term stroke recurrence in patients with intracranial atherosclerotic disease: a 3D high-resolution MRI-based cohort study. *Eur Radiol*. (2024) 34:3022–31. doi: 10.1007/s00330-023-10278-y

frontiers | Frontiers in Neurology

TYPE Original Research
PUBLISHED 29 January 2025
DOI 10.3389/fneur.2024.1527861

OPEN ACCESS

EDITED BY
Shuai Ren,
Affiliated Hospital of Nanjing University of Chinese Medicine, China

REVIEWED BY
Binyin Li,
Shanghai Jiao Tong University, China
Zhen Luo,
First Hospital of Tsinghua University, China

*CORRESPONDENCE
Fei Dong
✉ dngfei@zju.edu.cn

†These authors have contributed equally to this work

RECEIVED 13 November 2024
ACCEPTED 30 December 2024
PUBLISHED 29 January 2025

CITATION
Li Q, Mao J, Wang Q, Yao L, Xu F and Dong F (2025) Standard b-value DWI-derived stiffness index analysis may provide a way to evaluate the development of intracerebral hematoma.
Front. Neurol. 15:1527861.
doi: 10.3389/fneur.2024.1527861

Standard b-value DWI-derived stiffness index analysis may provide a way to evaluate the development of intracerebral hematoma

Qian Li†, Jin Mao†, Qiyuan Wang, Liding Yao, Fangfang Xu and Fei Dong*

Department of Radiology, The Second Affiliated Hospital, Zhejiang University School of Medicine, Hangzhou, China

Background and purpose: The development of intracerebral hemorrhage (ICH) is closely related to mechanical forces. However, noninvasively evaluating mechanical forces for ICH patients in the current clinical setting is challenging. In this study, we aimed to build an easily accessible stiffness index (STI) and evaluate the stiffness of the perihematomal edema (PHE) region in ICH patients.

Materials and methods: In this retrospective study, two cohorts of 57 patients were included. One cohort (the exploratory cohort) comprised patients with both standard b-value diffusion-weighted imaging (sDWI) (b-values of 0 and 1,000 s/mm^2, b0 and b1000) and higher b-value diffusion-weighted imaging (hDWI) (b-values of 200 and 1,500 s/mm^2). Another cohort (the hemorrhage cohort) consisted of patients who were diagnosed with ICH and who underwent sDWI within 48 h from onset. The hDWI-based virtual shear modulus (μdiff) was calculated and correlated with the sDWI data in the exploratory cohort. In the hemorrhage cohort, STI maps that were used to estimate μdiff were generated. The mean STI (mSTI) and coefficient of variation (COV) of the STI were computed on the basis of the STI maps in the whole and largest-slice PHE regions.

Results: The STI could be calculated with the Equation 0.047697*S1000-0.022944*S0 + 5.359883, where S1000 and S0 represent the signal intensities of the b1000 and b0 images, respectively. In the whole and largest-slice PHE regions, both the mSTI and COV were correlated with the hematoma volume ($p < 0.01$), but neither were correlated with the time from onset.

Conclusion: The standard b-value DWI-derived stiffness index analysis may provide a noninvasive and easily accessible way to evaluate the development of ICH.

KEYWORDS

elasticity imaging techniques, shear modulus, diffusion magnetic resonance imaging, cerebral hemorrhage, stiffness index, magnetic resonance elastography

1 Introduction

Intracerebral hemorrhage (ICH) is a devastating form of stroke (1), with 3.41 million cases occurring each year worldwide, accounting for 27.9% of all stroke patients (2). The median fatality was 40·4% at 1 month and 54·7% after 1 year (3).

ICH is typically divided into five stages based on the breakdown products of blood, including hyperacute (<12 h), acute (12 h–48 h), early subacute (2 days–7 days), late subacute (8 days–1 month), and chronic (>1 month) stages (4). The first 48 h are very important period. During this period of ICH development, it involves hematoma expansion (4, 5), the occurrence of perihematomal edema (6), primary and secondary brain injury (5), and is correlated with high mortality (7).

It has been reported that the development of ICH is closely related to mechanical force (8–10), and the perihematomal area serves as a critical interface for both deleterious and beneficial effects (8). Furthermore, stiffness reflects the ability of a structure to resist deformation under force (11). Therefore, measuring the stiffness of the perihematomal area may be valuable for evaluating the development of incipient ICH from a mechanical viewpoint and may provide a target for monitoring and treatment for ICH patients.

Although magnetic resonance elastography (MRE) provides a quantitative method for evaluating tissue stiffness and has been used in various central nervous system diseases (12), it is necessary to consider that there may be a potential risk of exacerbating the disease due to mechanical vibrations during the examination. Currently, MRE has not been found to be used for ICH patients.

Recently, diffusion-weighted (DW) MRI-based elastography or virtual MRE (vMRE) has been proposed. This method involves fitting the shear modulus with DWI parameters to avoid the need for mechanical vibration. It has demonstrated excellent agreement with MRE in staging liver fibrosis (13), and has shown consistent results compared to surgery in cases of meningiomas and pituitary adenomas (14, 15). In these studies, higher b-value (200 s/mm^2 and 1,500 s/mm^2, or 200 s/mm^2 and 1,000 s/mm^2) were used. However, standard b-value (0 s/mm^2 and 1,000 s/mm^2) DWI is more commonly used in clinical settings.

In this study, we aimed to build an easily accessible standard b-value DWI-derived stiffness index (STI) and evaluate the stiffness of the perihematomal edema (PHE) region, which is an important region of the perihematomal area (16), in ICH patients within 48 h from onset.

2 Materials and methods

The retrospective study was approved by the Local Ethics Committee of our hospital, and the requirement for patient informed consent was waived.

2.1 Study population

We retrospectively included two cohorts (the exploratory cohort and hemorrhage cohort) of adult patients who underwent brain MRI examination at our hospital between January 2020 and October 2023. Patients in the exploratory cohort, including patients with both standard b-value DWI (sDWI, with b-values of 0 and 1,000 s/mm^2, b0 and b1000 images) and higher b-value DWI (hDWI, with b-values of 200 and 1,500 s/mm^2, b200 and b1500 images), were used to investigate the relationships between sDWI parameters and virtual shear modulus. Patients in the hemorrhage cohort, including ICH patients with sDWI within 48 h from onset, were analyzed to assess the stiffness (the magnitude of the shear modulus is sometimes called stiffness, a term that is intuitive to both the general public and clinicians (17)) of the PHE region. For the exploratory cohort, all patients underwent MRI examinations due to symptoms such as discomfort, headaches, and dizziness, and patients with significant intracranial diseases on MR images were excluded. For the hemorrhage cohort, patients who had undergone surgical intervention or who had ICH secondary to brain trauma, vascular malformation, brain tumor, and hemorrhagic infarction were excluded (18). The age and sex for both cohorts, as well as the baseline blood pressure and time from onset to MRI scan of each patient in the hemorrhage cohort, were recorded.

2.2 Image acquisition

For the exploratory cohort cases, MRI was performed using a 1.5 T MAGNETOM Altea scanner (Siemens Medical Solutions) and a 3.0T uMR 790 scanner (United Imaging). DWI was acquired with the following parameters: repetition time (TR), 3,740–4,510 ms; echo time (TE), 79.26 or 84.26 ms; section thickness, 6.0 mm; b-values, 0 and 1,000 s/mm^2 or 200 and 1,500 s/mm^2 for the MAGNETOM Altea scanner. And TR, 2600 ms; TE, 84.6 ms; section thickness, 5.5 mm; b-values, 0 and 1,000 s/mm^2 or 200 and 1,500 s/mm^2 for the uMR 790 scanner. For the hemorrhage cohort cases, MRI was performed with 1.5 T Aera scanners (Siemens Medical Solutions). The DWI was acquired with the following parameters: TR, 3900–5,300 ms; TE, 104–115 ms; section thickness, 6 mm; b-value, 0 and 1,000 s/mm^2.

2.3 Image preprocessing and segmentation

A series of image preprocessing steps was carried out to minimize discrepancies caused by variations in MR image acquisition conditions. Utilizing b0 images as reference images, registration was conducted for the other images, and eddy current correction was applied to all images using FSL[1]. Gibbs ringing artifacts were removed using MRtrix3[2]. N4 bias field correction and denoising was performed using CaPTK[3] (19, 20).

Manual segmentation for all the cases was performed by two radiologists on b0 images using ITK-SNAP software[4]. For the exploratory cohort, 10 regions of interest (ROIs, 5 mm × 5 mm × 5 mm) were delineated on b0 images for each patient. The ROIs were chosen in the centrum semiovale, periventricular white matter, basal ganglia, thalamus, and cerebellar hemisphere on both sides. For the hemorrhage cohort, four ROIs were delineated, including the whole hematoma region, the whole PHE region, the largest-slice hematoma region and the largest-slice PHE region. The whole hematoma and whole PHE regions were delineated slice by slice for all the hematoma and PHE lesions, respectively. The largest-slice hematoma and the largest-slice PHE regions were delineated in the hematoma and edema regions, respectively, on the slice with the largest hematoma size that was evaluated by the two doctors. Ten patients in the hemorrhage cohort were randomly selected to evaluate the consistency of the segmentation performed by the two doctors, with the segmented regions including the whole PHE region and the largest-slice PHE region.

1 https://fsl.fmrib.ox.ac.uk/fsl/fslwiki/
2 http://www.mrtrix.org/
3 https://www.nitrc.org/projects/captk/
4 http://www.itksnap.org

The mean signal intensity of b0 images, b1000 images, b200 images, and b1500 images (S0, S1000, S200, and S1500) in each ROI for the exploratory cohort cases was computed using Python software[5]. The apparent diffusion coefficient (ADC) value for standard DWI was calculated by the following formula: ADC = ln (S0/S1000)/1,000 (21). The virtual shear modulus (μdiff) was calculated by the following formula: μdiff = −9.8 ln (S200/S1500) + 14 (21).

For the exploratory cohort cases, four parameters derived from sDWI, including S0, S1000, S0/S1000, and ADC value were used to build a model (μModel) to predict μdiff. The entire exploratory cohort dataset was randomly split into training (70%) and test (30%) datasets. For the hemorrhage cohort, according to the algorithm of the μModel, virtual magnetic resonance elastography (STI map) was generated using sDWI parameters and FSL software. The signal intensity value was extracted by Python software from the ROIs of the STI maps. The mean STI (mSTI) and coefficient of variation (COV, standard deviation/mSTI) as the STI parameters in the whole PHE region and the largest-slice PHE region were recorded and represented by the whole mSTI, whole COV, largest-slice mSTI, and largest-slice COV, respectively.

2.4 Statistical analysis

The continuous variables were presented as the mean or medians, according to whether or not a normal distribution was present. Categorical data were presented as proportions. Univariate linear regression was performed to select parameters derived from sDWI for the exploratory cohort cases. Multiple linear regression was then used to evaluate the independent association of the selected parameters with μdiff. The correlation between two continuous variables was assessed using either Pearson or Spearman correlation methods and linear regression analysis. The Dice coefficient was used to evaluate the consistency of segmentation performed by the two doctors. The statistical significance levels were two-sided, with the statistical significance level set at 0.05. The statistical analyses were performed using the R software (version 4.4.1).[6]

3 Results

3.1 Participant characteristics

Fifty-seven patients, 32 (56.1%) men and 25 (43.9%) women, were included in this study. In the exploratory cohort, there were 17 patients, including 8 (47.1%) men and 9 (52.9%) women, and the age was 52.8 ± 14.8 years. In the hemorrhage cohort, there were 40 patients (Table 1 and Figure 1).

TABLE 1 Patient characteristics, hematoma and edema volumes, and STI features.

Characteristics	Values
Age, years	
Mean (sd)	57.1 (15.0)
Gender, *n* (%)	
Male, female	24 (60.0%), 16 (40.0%)
Time, hours	
Mean (sd)	24.6 (12.8)
SBP, mmHg	
Median (range)	150.5 (113.0–235.0)
DBP, mmHg	
Mean (sd)	84.5 (61.0–129.0)
Whole hematoma volume, mm^3	
Median (range)	6562.9 (897.6–82759.5)
Largest-slice hematoma volume, mm^3	
Median (range)	2643.6 (344.3–12408.8)
Whole edema volume, mm^3	
Median (range)	7100.9 (609.6–55348.7)
Largest-slice edema volume, mm^3	
Median (range)	2259.6 (475.3–7273.8)
Whole mSTI	
Mean (sd)	3.50 (1.80)
Largest-slice mSTI	
Mean (sd)	3.64 (2.06)
Whole COV	
Median (range)	0.56 (−4.15–3.74)
largest-slice COV	
Median (range)	0.45 (−5.88–9.54)

SBP, systolic blood pressure; DBP, diastolic blood pressure; sd, standard deviation; STI, stiffness index; mSTI, mean stiffness index; COV, coefficient of variation.

3.2 μModel building and validation

Univariate logistic regression revealed that each parameter, including S0 ($p = 0.038$), S1000 ($p < 0.001$), ADC ($p < 0.001$), and S0/S1000 ($p < 0.001$) contributed significantly to the prediction of μdiff. However, multivariable logistic regression showed that only S0 ($p = 0.036$) and S1000 ($p = 0.043$) were independent predictors (Figure 2). Using the model, the STI could be calculated with the Equation 0.047697*S1000-0.022944*S0 + 5.359883 (Figure 3), where S1000 and S0 represented the mean signal intensity of the ROIs on the b1000 and b0 images, respectively. The model showed an adjusted R-squared of 0.643 for the training dataset and 0.626 for the test dataset. The variance inflation factor was 3.04, which means that there was no serious multicollinearity between the two parameters.

3.3 Segmentation of the PHE region

The median Dice coefficient was 0.79 (range, 0.74–0.89) for the segmentation by the two doctors of the whole PHE region and 0.80 (range, 0.71–0.88) for the largest-slice PHE region, respectively. The median volumes of the whole PHE region and the largest-slice PHE region were 7100.9 mm^3 and 2259.6 mm^3, respectively (Table 1).

5 https://www.python.org/

6 http://www.r-project.org/

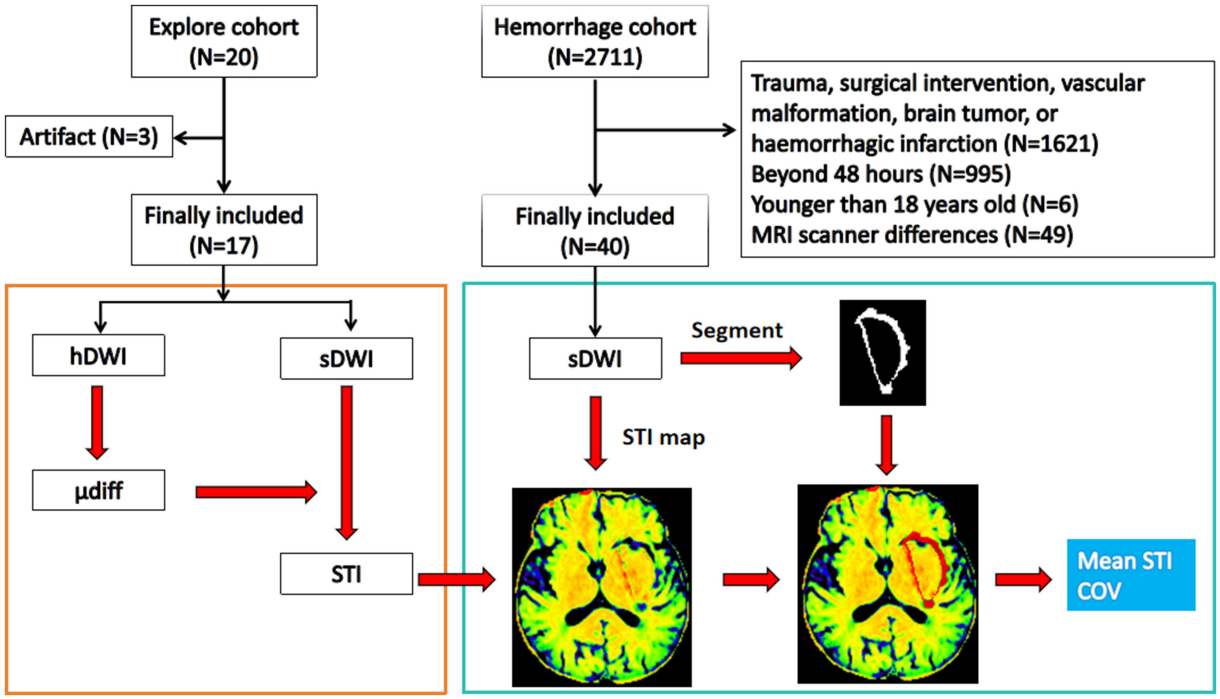

FIGURE 1
Flow diagram. The exploratory cohort is used to build the stiffness predicting model using standard b-value DWI, and the hemorrhage cohort is used to study the stiffness features of the perihematomal edema region. hDWI, high b-value diffusion weighted imaging; sDWI, standard b-value diffusion weighted imaging; STI, stiffness index; μdiff, diffusion-based virtual shear modulus; COV, coefficient of variation.

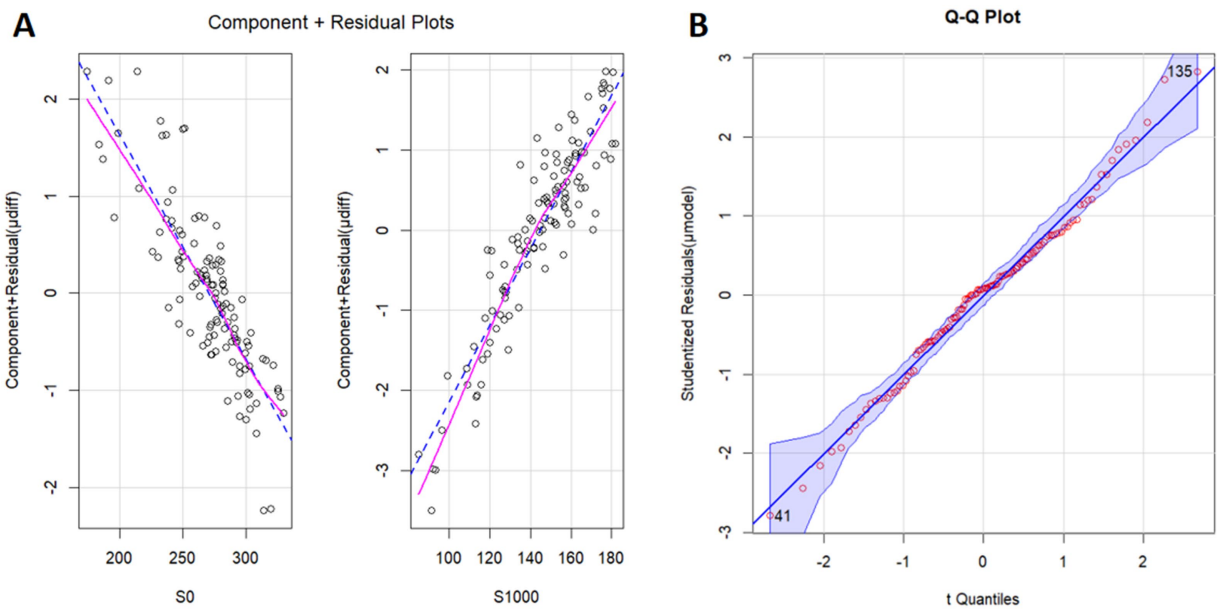

FIGURE 2
Component plus residual plot **(A)** and Q–Q plot **(B)**. The relationships between S0 and μdiff and between S1000 and μdiff are linear. S0, the signal intensity of b0 image (diffusion weighted imaging, b = 0 s/mm^2); S1000, the signal intensity of b1000 image (diffusion weighted imaging, b = 1,000 s/mm^2); μdiff, virtual shear modulus computed by diffusion weighted imaging using b = 200 and 1,500 s/mm^2; μModel, model to predicting μdiff.

3.4 Evaluation of the STI

The mSTIs exhibited a normal distribution, whereas the COVs exhibited a nonnormal distribution (Table 1). Overall, the largest-slice mSTI was positively correlated with the whole mSTI (r = 0.93), and the largest-slice COV was positively correlated with the whole COV (r = 0.91). Both the whole and the largest-slice mSTIs were negatively correlated with the largest-slice COV and with the whole COV (Figure 4).

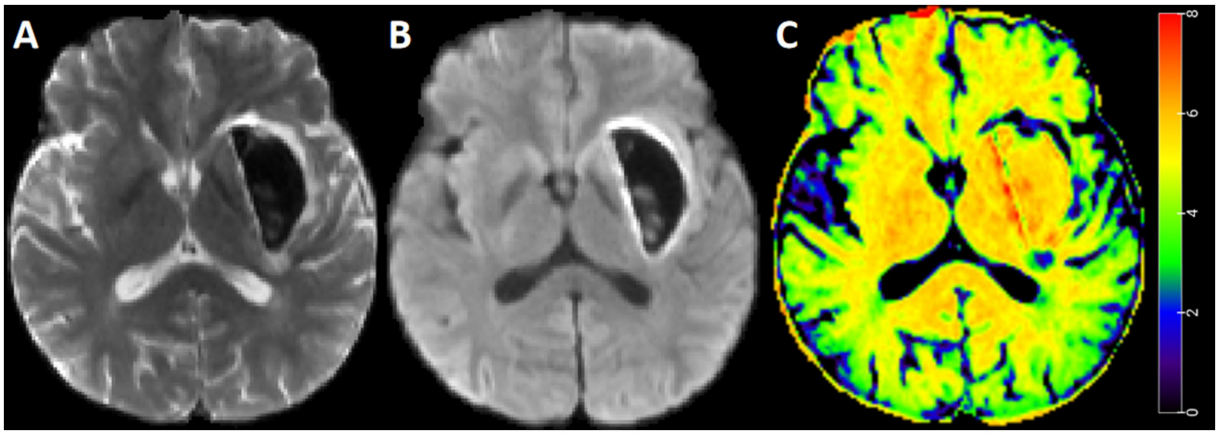

FIGURE 3
Standard b-value DWI and STI map for representative case. A 45-year-old man with intracerebral hemorrhage. Diffusion weighted imaging with b = 0 s/mm^2 **(A)**, diffusion weighted imaging with b = 1,000 s/mm^2 **(B)**, and STI map **(C)**. The STI in the perihematomal edema region was heterogeneous, with a relatively greater value in the deep region.

Both the whole and largest-slice mSTIs were negatively correlated with the hematoma volume and PHE volume (p values, <0.01). However, both the whole COV and the largest-slice COV were positively correlated with the volumes (p values, <0.001) (Figure 4).

Neither the mSTIs nor the COV in the whole PHE region and the largest-slice PHE region were significantly correlated with the time from onset or blood pressure (Figures 4, 5).

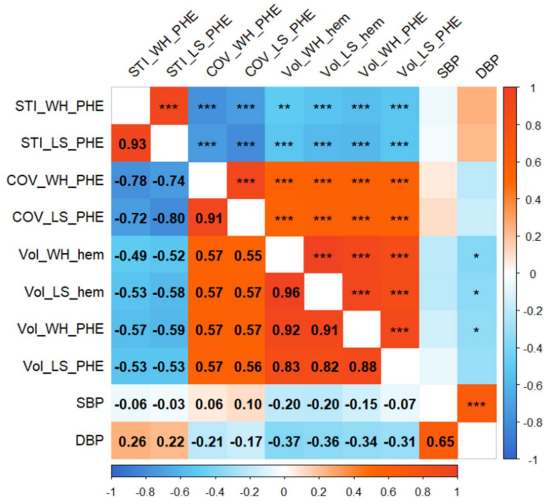

FIGURE 4
Correlogram. The numbers in the boxes indicate the correlation coefficient between the two variables. Significance is indicated by single asterisks (p < 0.05), double asterisks (p < 0.01), or triple asterisks (p < 0.001). STI_WH_PHE, mean stiffness index in the whole perihematomal edema region; STI_LS_PHE, mean stiffness index in the largest-slice perihematomal edema region; COV_WH_PHE, coefficient of variation of stiffness index in the whole perihematomal edema region; COV_LS_PHE, coefficient of variation of stiffness index in the largest-slice perihematomal edema region; Vol_WH_hem, the whole volume of hematoma; Vol_LS_hem, the largest-slice volume of hematoma; Vol_WH_PHE, the whole volume of perihematomal edema region; Vol_LS_PHE, the largest-slice volume of perihematomal edema region; DBP, diastolic blood pressure; SBP, systolic blood pressure.

4 Discussion

Measuring the stiffness of perihematomal tissue may help us evaluate the development of ICH from a mechanical viewpoint. In this study, we built STI maps based on standard b-value DWI and evaluated the stiffness in the PHE regions. We found that the STI parameters in the PHE regions was closely correlated with the hematoma volume.

Stiffness is an important physical property of a substance. It is related to biological characteristics of tissues, and it can reflect the histopathological changes, as well as mechanical information in the tissues (22). In fact, brain has viscoelastic properties (with both viscosity and elasticity) (23), and exhibits heterogeneous stiffness due to the tissue heterogeneity (24–26). For ICH patients, the PHE region correlates with secondary brain injury (27), and undergoes pathological changes continuously over time (6), which may lead to a constant change in its stiffness.

Although magnetic resonance elastography (MRE) has a significant potential for application in brain diseases (28), it remains difficult to implement widely in current clinical practice. At present, the resolution of MRE is limited, and it should be treated with caution when comparing MRE results across studies as it may be affected by acquisition parameters, post-processing, and some other factors (29).

We know that DWI can reflect the diffusion of water molecules in tissues, and sDWI is one of the most commonly used sequences for MR imaging of brain diseases. In this study, we built a model for predicting virtual shear modulus using sDWI, and it showed good predictive performance. It is close to the result of a previous study that predicted liver shear modulus using sDWI parameters (21). This suggests that through sDWI examination, additional stiffness information may be obtained alongside diffusion restriction evaluation, making it easier to assess stiffness features of brain tissues affected by intracerebral hemorrhage or other diseases.

Our results showed that the STI parameters, including the mSTI and COV, in the largest-slice PHE region were significantly positively

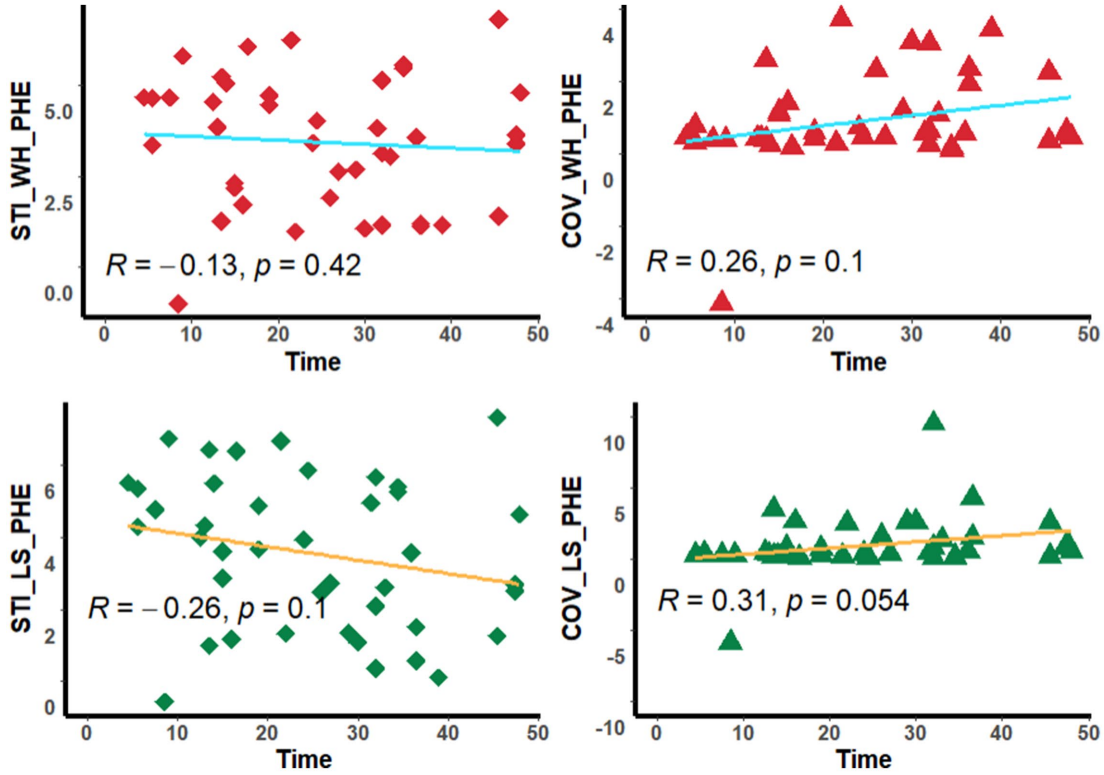

FIGURE 5
Scatter diagram. The diagram shows the corrlation between the stiffness index and time. STI_WH_PHE, mean stiffness index in the whole perihematomal edema region; STI_LS_PHE, mean stiffness index in the largest-slice perihematomal edema region; COV_WH_PHE, coefficient of variation of stiffness index in the whole perihematomal edema region; COV_LS_PHE, coefficient of variation of stiffness index in the largest-slice perihematomal edema region; Time, the time from onset to MRI scan.

correlated with those in the whole PHE region. Also, the largest-slice mSTI and the COV showed a comparable correlation coefficient with the hematoma volume. These findings are very interesting. A previous study showed that the long axis of most hematomas is in the anterior–posterior direction, and the longitudinal axis type is unchanged in 90% of HE patients (30). This finding may indicate that the largest-slice stiffness in PHE regions have a potential value for evaluating the trend of hematoma development.

In this study, we found that the STI parameters in the PHE region are closely related to the hematoma volume; that is, the larger the hematoma volume is, the smaller the mSTI and the larger the COV of the STI. This might be because the increasing volume of the hematoma may cause pronounced edema (16), which may lead to a reduction in stiffness. The increasing COV value may indicate that the heterogeneity of the PHE region increases with increasing hematoma volumes.

It is known that time and blood pressure are important factors for ICH. However, our study revealed that neither the time from onset nor blood presure was significantly correlated with the STI parameters. This may be due to the complex pathological changes in the PHE regions over time (6), as well as the factors influencing the hematoma volume. This deserves further study.

An important application of our findings is to assess the possible direction of hematoma expansion using the STI map. Due to the heterogeneity of the tissue stiffness surrounding the hematoma, the hematoma may be more likely to expand to sites with less stiffness. The previous study revealed that HE in cerebral hemorrhage is asymmetrical in direction, and its shape becomes increasingly irregular with the expansion of the hematoma (30). Based on the STI map, the tissue stiffness around the hematoma can be measured to predict the direction of hematoma expansion, and timely treatment to avoid the involvement of important functional regions may be possible. Furthermore, as ICH is accompanied by damage to the surrounding brain tissue, therefore, stiffness evaluation by STI may be useful for quantitatively assessing the extent of brain injury.

There are several limitations in this study. First, the sample size of this study was small, and the results need to be further validated in a large multicenter sample. Second, we analyze only the correlations between the STI parameters and time from onset within 48 h. Subgroup analyses or a more detailed division of time point studies can be performed in the future to better understand the changes in the STI parameters with the development of ICH over time. Thirdly, although multistep preprocessing was performed, there may still be some effects near the hematoma when extracting the STI parameters from the PHE region. Fourthly, the blood pressure data used in this study were collected at the time of admission, and the data collected just before MRI examination may better reflect the relationship between blood pressure and stiffness around the hematoma. Fifthly, this study presents an evaluation of the STI of the tissue around the hematoma, which may reflect the relative magnitude of the stiffness, but there may be some differences from the true stiffness value.

5 Conclusion

In conclusion, we constructed STI maps using sDWI and evaluated the stiffness of PHE regions in ICH patients and showed that the STI parameters of PHE regions is closely correlated with the hematoma volume. This study may provide a way to evaluate ICH development from a mechanical point of view and also provide a target for ICH monitoring and treatment.

Data availability statement

The datasets presented in this article are not readily available because the raw data supporting the conclusions of this article are available from the corresponding author upon reasonable request. Requests to access the datasets should be directed to Fei Dong, dngfei@zju.edu.cn.

Ethics statement

The studies involving humans were approved by the Ethics Committee of the Second Affiliated Hospital of Zhejiang University. The studies were conducted in accordance with the local legislation and institutional requirements. The ethics committee/institutional review board waived the requirement of written informed consent for participation from the participants or the participants' legal guardians/next of kin due to the retrospective nature of the study.

Author contributions

QL: Conceptualization, Data curation, Investigation, Methodology, Validation, Writing – original draft. JM: Data curation, Investigation, Resources, Validation, Writing – review & editing. QW: Data curation, Investigation, Validation, Writing – review & editing. LY: Data curation, Investigation, Writing – review & editing. FX: Data curation, Investigation, Writing – review & editing. FD: Conceptualization, Formal analysis, Investigation, Methodology, Software, Supervision, Visualization, Writing – review & editing.

Funding

The author(s) declare that no financial support was received for the research, authorship, and/or publication of this article.

Conflict of interest

The authors declare that the research was conducted in the absence of any commercial or financial relationships that could be construed as a potential conflict of interest.

Generative AI statement

The authors declare that no Gen AI was used in the creation of this manuscript.

Publisher's note

All claims expressed in this article are solely those of the authors and do not necessarily represent those of their affiliated organizations, or those of the publisher, the editors and the reviewers. Any product that may be evaluated in this article, or claim that may be made by its manufacturer, is not guaranteed or endorsed by the publisher.

References

1. Magid-Bernstein J, Girard R, Polster S, Srinath A, Romanos S, Awad IA, et al. Cerebral hemorrhage: pathophysiology, treatment, and future directions. *Circ Res*. (2022) 130:1204–29. doi: 10.1161/CIRCRESAHA.121.319949

2. GBD 2019 Stroke Collaborators. Global, regional, and national burden of stroke and its risk factors, 1990-2019: a systematic analysis for the global burden of disease study 2019. *Lancet Neurol*. (2021) 20:795–820. doi: 10.1016/S1474-4422(21)00252-0

3. van Asch CJ, Luitse MJ, Rinkel GJ, van der Tweel I, Algra A, Klijn CJ. Incidence, case fatality, and functional outcome of intracerebral haemorrhage over time, according to age, sex, and ethnic origin: a systematic review and meta-analysis. *Lancet Neurol*. (2010) 9:167–76. doi: 10.1016/S1474-4422(09)70340-0

4. Kidwell CS, Wintermark M. Imaging of intracranial haemorrhage. *Lancet Neurol*. (2008) 7:256–67. doi: 10.1016/S1474-4422(08)70041-3

5. Jain A, Malhotra A, Payabvash S. Imaging of spontaneous intracerebral hemorrhage. *Neuroimaging Clin N Am*. (2021) 31:193–203. doi: 10.1016/j.nic.2021.02.003

6. Lim-Hing K, Rincon F. Secondary hematoma expansion and perihemorrhagic edema after intracerebral hemorrhage: from bench work to practical aspects. *Front Neurol*. (2017) 8:74. doi: 10.3389/fneur.2017.00074

7. Han Q, Li M, Su D, Zuo Z, Fu A, Zhu J, et al. Development and validation of a nomogram for predicting death within 2 days after intracerebral hemorrhage. *J Stroke Cerebrovasc Dis*. (2020) 29:105159. doi: 10.1016/j.jstrokecerebrovasdis.2020.105159

8. Puy L, Parry-Jones AR, Sandset EC, Dowlatshahi D, Ziai W, Cordonnier C. Intracerebral haemorrhage. *Nat Rev Dis Primers*. (2023) 9:14. doi: 10.1038/s41572-023-00424-7

9. Wang W, Jin W, Feng H, Wu G, Wang W, Jia J, et al. Higher cerebral blood flow predicts early hematoma expansion in patients with intracerebral hemorrhage: a clinical study. *Front Neurol*. (2021) 12:735771. doi: 10.3389/fneur.2021.735771

10. Cardona S, Baqai H, Mikdashi F, Aligabi A, Solomon J, Frederick H, et al. Intracranial and blood pressure variability and in-hospital outcomes in intracranial device-monitored patients with spontaneous intracerebral hemorrhage. *Neurocrit Care*. (2023) 39:357–67. doi: 10.1007/s12028-023-01677-6

11. Handorf AM, Zhou Y, Halanski MA, Li WJ. Tissue stiffness dictates development, homeostasis, and disease progression. *Organogenesis*. (2015) 11:1–15. doi: 10.1080/15476278.2015.1019687

12. Hersh AM, Weber-Levine C, Jiang K, Young L, Kerensky M, Routkevitch D, et al. Applications of elastography in operative neurosurgery: a systematic review. *J Clin Neurosci*. (2022) 104:18–28. doi: 10.1016/j.jocn.2022.07.019

13. Kromrey ML, Le Bihan D, Ichikawa S, Motosugi U. Diffusion-weighted MRI-based virtual elastography for the assessment of liver fibrosis. *Radiology*. (2020) 295:127–35. doi: 10.1148/radiol.2020191498

14. Aunan-Diop JS, Andersen MCS, Friismose AI, Halle B, Pedersen CB, Mussmann B, et al. Virtual magnetic resonance elastography predicts the intraoperative consistency of meningiomas. *J Neuroradiol*. (2023) 50:396–401. doi: 10.1016/j.neurad.2022.10.006

15. Lagerstrand K, Gaedes N, Eriksson S, Farahmand D, De Coursey E, Johansson G, et al. Virtual magnetic resonance elastography has the feasibility to evaluate preoperative pituitary adenoma consistency. *Pituitary*. (2021) 24:530–41. doi: 10.1007/s11102-021-01129-4

16. Jiang C, Guo H, Zhang Z, Wang Y, Liu S, Lai J, et al. Molecular, pathological, clinical, and therapeutic aspects of perihematomal edema in different stages of intracerebral hemorrhage. *Oxidative Med Cell Longev*. (2022) 2022:3948921–38. doi: 10.1155/2022/3948921

17. Manduca A, Bayly PJ, Ehman RL, Kolipaka A, Royston TJ, Sack I, et al. MR elastography: principles, guidelines, and terminology. *Magn Reson Med*. (2021) 85:2377–90. doi: 10.1002/mrm.28627

18. Li Q, Dong F, Wang Q, Xu F, Zhang M. A model comprising the blend sign and black hole sign shows good performance for predicting early intracerebral haemorrhage

expansion: a comprehensive evaluation of Ct features. *Eur Radiol*. (2021) 31:9131–8. doi: 10.1007/s00330-021-08061-y

19. Horiuchi D, Shimono T, Tatekawa H, Tsukamoto T, Takita H, Matsushita S, et al. Brain temperature remains stable during the day: a study of diffusion-weighted imaging thermometry in healthy individuals. *Neuroradiology*. (2023) 65:1239–46. doi: 10.1007/s00234-023-03142-9

20. Li Q, Dong F, Jiang B, Zhang M. Exploring MRI characteristics of brain diffuse midline gliomas with the H3 K27m mutation using radiomics. *Front Oncol*. (2021) 11:646267. doi: 10.3389/fonc.2021.646267

21. Le Bihan D, Ichikawa S, Motosugi U. Diffusion and intravoxel incoherent motion MR imaging-based virtual elastography: a hypothesis-generating study in the liver. *Radiology*. (2017) 285:609–19. doi: 10.1148/radiol.2017170025

22. Yang JY, Qiu BS. The advance of magnetic resonance elastography in tumor diagnosis. *Front Oncol*. (2021) 11:722703. doi: 10.3389/fonc.2021.722703

23. Joo B, Won SY, Sinkus R, Lee SK. Viscoelastic property of the brain assessed with magnetic resonance elastography and its association with glymphatic system in neurologically normal individuals. *Korean J Radiol*. (2023) 24:564–73. doi: 10.3348/kjr.2022.0992

24. Burman Ingeberg M, Van Houten E, Zwanenburg JJM. Estimating the viscoelastic properties of the human brain at 7T MRI using intrinsic MRE and nonlinear inversion. *Hum Brain Mapp*. (2023) 44:6575–91. doi: 10.1002/hbm.26524

25. Budday S, Sarem M, Starck L, Sommer G, Pfefferle J, Phunchago N, et al. Towards microstructure-informed material models for human brain tissue. *Acta Biomater*. (2020) 104:53–65. doi: 10.1016/j.actbio.2019.12.030

26. Jamal A, Bernardini A, Dini D. Microscale characterisation of the time-dependent mechanical behaviour of brain white matter. *J Mech Behav Biomed Mater*. (2022) 125:104917. doi: 10.1016/j.jmbbm.2021.104917

27. Dierksen F, Tran AT, Zeevi T, Maier IL, Qureshi AI, Sanelli PC, et al. Peri-hematomal edema shape features related to 3-month outcome in acute supratentorial intracerebral hemorrhage. *Eur Stroke J*. (2024) 9:383–90. doi: 10.1177/23969873231223814

28. Yin Z, Romano AJ, Manduca A, Ehman RL, Huston J 3rd. Stiffness and beyond: what Mr elastography can tell us about brain structure and function under physiologic and pathologic conditions. *Top Magn Reson Imaging*. (2018) 27:305–18. doi: 10.1097/RMR.0000000000000178

29. Aunan-Diop JS, Halle B, Pedersen CB, Jensen U, Munthe S, Harbo F, et al. Magnetic resonance elastography in intracranial neoplasms: a scoping review. *Top Magn Reson Imaging*. (2022) 31:9–22. doi: 10.1097/RMR.0000000000000292

30. Jianbo C, Ting X, Yihao C, Xiaoning W, Hong S, Qinghua Z, et al. The patterns of morphological change during intracerebral hemorrhage expansion: a multicenter retrospective cohort study. *Front Med*. (2021) 8:774632. doi: 10.3389/fmed.2021.774632

frontiers | Frontiers in Neurology

TYPE Original Research
PUBLISHED 12 February 2025
DOI 10.3389/fneur.2025.1550014

OPEN ACCESS

EDITED BY
Shuai Ren,
Affiliated Hospital of Nanjing University of Chinese Medicine, China

REVIEWED BY
Yu-Chen Chen,
Nanjing No. 1 Hospital, China
Kusnandar Anggadiredja,
Bandung Institute of Technology, Indonesia

*CORRESPONDENCE
Yan Gu
guyan2020@njmu.edu.cn

RECEIVED 22 December 2024
ACCEPTED 27 January 2025
PUBLISHED 12 February 2025

CITATION
Chu T, Guo Z, Zhang Y, Liu Y and Gu Y (2025) Study on the correlation between carotid plaque calcification types and acute ischemic stroke. *Front. Neurol.* 16:1550014. doi: 10.3389/fneur.2025.1550014

Study on the correlation between carotid plaque calcification types and acute ischemic stroke

Tianyu Chu, Zhongping Guo, Yonggang Zhang, Ying Liu and Yan Gu*

Department of Radiology, Lianyungang Clinical College of Nanjing Medical University, The First People's Hospital of Lianyungang, Lianyungang, China

Introduction: Computed tomography angiography (CTA) was used to explore the correlation between the calcification types of carotid plaques and ipsilateral acute ischemic stroke. This could provide new insights into the clinical evaluation and treatment of ischemic stroke.

Methods: This study obtained information on patients undergoing head and neck CTA examinations at the First People's Hospital of Lianyungang between September 2022 and August 2023 to investigate the clinical differences in baseline data between the acute ischemic stroke and control groups. Patients meeting the inclusion and exclusion criteria were classified into 1 to 6 groups according to their plaque calcification characteristics. The correlation between calcified plaque type and ipsilateral acute ischemic anterior circulation stroke was analyzed using paired sample chi-square and Spearman correlation tests.

Results: Based on the inclusion and exclusion criteria, this study included 589 patients with plaques at the bifurcation of the carotid arteries. In both the acute ischemic stroke and control groups, sex, smoking, alcohol consumption, systolic blood pressure, blood sugar, cholesterol, high-density lipoprotein, and homocysteine levels were statistically significant ($p < 0.05$). During the Spearman correlation analysis between calcification type and acute stroke (1,178 carotid arteries), different calcification types of plaques were linked with ipsilateral acute anterior circulation stroke with statistically significant differences ($p < 0.001$). Finally, the chi-squared test of the paired samples showed that the grade of plaque calcification is often higher on the side of acute infarction than on the side without acute infarction, and the difference is statistically significant ($p < 0.001$).

Discussion: Carotid plaque calcification is associated with acute ischemic stroke. Our findings provide novel insights into the study of calcification in carotid atherosclerotic plaques and additional radiological evidence to clinically assess the risk of ischemic stroke.

KEYWORDS

atherosclerosis, carotid plaque, calcified plaque, stroke, computed tomography angiography

1 Introduction

Based on the latest statistical data, stroke is the second leading cause of death worldwide and the third leading cause of death and disability (1), possessing a heavy disease burden (2). Carotid atherosclerosis is a degenerative disease that can cause ischemia when plaques rupture (3), inducing severe neurological deficits. Calcification is universally present in atherosclerotic plaques; however, the underlying mechanism is not entirely understood. They often appear during atherosclerotic disease progression, where apoptotic cells, the extracellular matrix, and necrotic core substances become

sources of calcium microcrystals. They can progress and fuse to form more extensive calcified deposits (4). However, research on the calcification inside plaques remains controversial. Calcified plaques are structural markers of plaque stability and protective factors against ipsilateral ischemic stroke, and are negatively associated with cerebrovascular diseases. However, recent studies have indicated that different calcification characteristics affect the plaque stability (5). Most studies have focused on a single characteristic of carotid plaque calcification. The classification method used in this study encompasses the size, location, and shape of the plaque calcification. Hence, six types of calcifications have been proposed by Saba et al. (6): type 1, no calcification inside the plaque; type 2, intima or superficial calcification; type 3, deep or large calcification; type 4, adventitial calcification with internal soft plaque thickness <2 mm; type 5, mixed type with intima and significant calcification; and type 6, positive rim sign. The prevalence of cerebrovascular events was highest in patients with type 6 calcification.

The current study selected calcifications, elements which are easily observable in CT, to explore the correlation between each type of carotid plaque calcification and ipsilateral acute ischemic anterior circulation stroke according to the six calcifications types. This could provide a better radiological basis for evaluating carotid plaque vulnerability and early patient treatment.

2 Materials and methods

2.1 Study type

This is a single-center retrospective study.

2.2. Study subjects

2.2.1. Study population

This study retrospectively obtained data from patients who underwent head and neck CTA examinations at Lianyungang First People's Hospital between September 2022 and August 2023. This study was reviewed by the Lianyungang First People's Hospital Medical Ethics (KY-20220726002-01).

2.2.2. Inclusion criteria

Patients who underwent head and neck CTA for atherosclerotic plaques at the carotid bifurcation were included in this study. At the same time, the patient underwent an MR examination within a week.

2.2.3. Exclusion criteria

The exclusion criteria included patients having incomplete imaging or clinical data. Non-intracranial atherosclerotic diseases, including aneurysms, vasculitis, Moyamoya disease, intracranial arterial dissection, reversible cerebral vasoconstriction syndrome, and vertebrobasilar dolichoectasia. Patients with suspected cardiogenic thrombus depicted by cardiac Doppler ultrasound or cardiac CTA, validated coagulation dysfunction, heart failure or respiratory failure, and renal dysfunction (serum creatinine > 133 μmol/L) were excluded. Furthermore, patients with severe disturbance of consciousness Intracranial hemorrhage, a history of cranial surgery, carotid stent placement, or carotid endarterectomy were excluded. Patients with a history of brain infarction having a diameter >1.5 cm (no hyperintensity in DWI) observed on MR were also excluded. The brain infarction could be seen in the posterior circulation supply area.

2.3 Examination plan and image analysis technology

2.3.1 Scanning technology

2.3.1.1. Equipment and reagents

A SIEMENS SOMATOM Definition Flash dual-source CT scanner was utilized, and the scanning parameters were set as follows: current, 125 mA; voltage, 100 kV; collimation, 16 × 0.6 mm, and slice thickness 0.75 mm. A venous catheter, double-pole release injector, and an iodixanol contrast medium (320 mg I/ml, Jiangsu Hengrui Pharmaceutical Co., Ltd., China) were used. A 320 mgI/ml contrast agent (iodoxanol, a non-ionic contrast agent with iodine) was administered using an 18-G catheter inserted within the antecubital vein at 3–5 ml/s, and 30 ml of physiological saline was injected at the same rate after injecting the contrast agent. The total amount and flow rate of the contrast agent were individualized according to the patient's weight and scanning range.

2.3.1.2 CTA scanning protocol

None of the patients who underwent carotid CTA had a history of heart failure or contraindications for iodinated contrast agents. The patients were placed in the supine position, and CT coverage ranged between the aortic arch and carotid siphon. Patients were scanned from their feet to their heads. The images were tested before and after contrast agent injection. Scanning was performed from the lower edge of the aortic arch to the top of the skull. The scanning time was 8–12 s. Contrast agent tracing was applied to determine the CT value within the aortic arch or carotid level of interest. When the CT value was more than 100 HU, the scan was automatically triggered after a 4 s delay. After reaching the threshold, the patients were instructed to hold their breath and start scanning after a 4 s interval. Experienced radiologists conducted all imaging examinations. The patients were instructed not to swallow or move their head or body while scanning to obtain the desired vascular images using three-dimensional reconstruction technology.

2.3.2 Image analysis technology

2.3.2.1 Image analysis

Image analysis was performed on the improved phase of CTA examination inside the GPACS system (WW = 800, WL = 240).

2.3.2.2 Carotid plaque calcification analysis

Two radiologists who had over 5 years of experience with head and neck imaging reviewed each image. Both reviewers were unaware of the patients' clinical data, and a third senior physician's opinion was sought in case of a disagreement.

The plaque at the carotid bifurcation was selected and evaluated as a whole. Calcification typing and plaque grouping were determined based on the morphology of the carotid plaque calcification by vision assessment.

2.3.2.3 Carotid plaque calcification type

The various calcification types on CTA images are depicted in Figure 1.

2.4. Demographic characteristics

Blood pressure, blood sugar, triglycerides (TG), total cholesterol (TC), low-density lipoprotein (LDL), high-density lipoprotein (HDL), lipoprotein A (LA), and homocysteine levels were measured while fasting in the morning for the first 48 h after admission. Medical history of diabetes, hypertension, coronary heart disease, and valvular heart disease. History of consumption of smoking and alcohol history.

2.5 Statistical methods

Data analysis was performed using SPSS version 26.0. Normally distributed continuous variables were expressed as the mean ± standard deviation, and analysis of variance helped conduct a comparison between groups. Quantitatively skewed distribution data are expressed as M (P25, P75). Moreover, a comparison between groups was performed using the Mann-Whitney U test. Categorical variables are expressed as frequencies and percentages. Additionally, the chi-square test was used to determine statistically significant differences between the groups. Kappa consistency testing was used to analyze inter-observer and intra-observer consistencies. *P*-values <0.05 were considered statistically significant. Thus, Spearman's correlation analysis was used to analyze the correlation between the plaque type and acute ischemic anterior circulation stroke.

3 Results

3.1 Patient baseline data with carotid plaque calcification

After screening based on the predetermined inclusion and exclusion criteria, 589 patients, with plaques at the carotid bifurcation were included, with an average age of 65.3(30–90) years, including 351(59.6%) male patients. When analyzing the clinical baseline data between the acute and non-acute ischemic stroke groups, sex, smoking, alcohol consumption, systolic blood pressure, blood sugar, cholesterol, low-density lipoprotein, and homocysteine showed statistical significance ($p < 0.05$). The demographic and clinical data of the study population are presented in Table 1.

3.2 The correlation analysis between calcification types and acute stroke

By observing 1,178 cases of carotid plaque and the occurrence of acute stroke in their blood supply area. We found that 68 cases in type 1 (68/478, 14.22%) had acute stroke, 54 cases in type 2

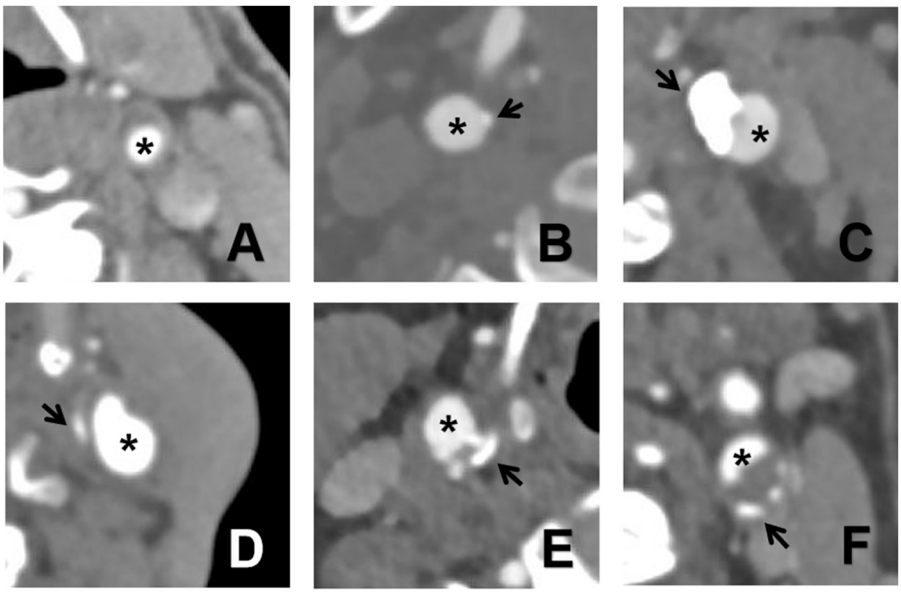

FIGURE 1
The six types of calcifications on CTA images. **(A)** no calcification inside the plaque; **(B)** intima or superficial calcification; **(C)** deep or large calcification; **(D)** adventitia calcification having internal soft plaque thickness <2 mm; **(E)** mixed type with intima and significant calcification; and **(F)** positive rim sign. The asterisk indicates a lumen and the *arrow* indicates calcification.

TABLE 1 Clinical baseline characteristics between the acute stroke group and the non-acute stroke group ($n = 589$).

	The acute stroke group	The non-acute stroke group	*P*-value
Age (years)	67 (59, 74)	66 (58, 73)	0.233
Sex/male (*n*, %)	158, 65%	193, 55.78%	0.024
Smoking (*n*, %)	92, 37.86%	101, 29.19%	0.027
Drinking (*n*, %)	86, 35.39%	89, 25.72%	0.011
SBP, mmHg	148 (139, 161)	141 (130, 155)	<0.001
DBP, mmHg	83 (78, 96)	81 (77, 93)	0.058
BS, mmol/L	5.34 (4.61, 7.66)	5.02 (4.45, 6.14)	0.001
TG, mmol/L	1.36 (1, 2.06)	1.31 (0.93, 1.80)	0.107
TC, mmol/L	4.70 (3.97, 5.53)	4.40 (3.50, 5.14)	<0.001
LDL, mmol/L	3.02 (2.48, 3.57)	2.74 (2.06, 3.31)	<0.001
HDL, mmol/L	1.12 (0.93, 1.32)	1.07 (0.91, 1.25)	0.134
LA, mg/L	177.7 (81.13, 341.10)	168.75 (87, 360.28)	0.799
Homocysteine, μmol/L	14.3 (11.3, 18.7)	12.8 (10.25, 16.70)	0.003

P-values <0.05 were considered statistically significant.
SBP, Systolic blood pressure; DBP, Diastolic blood pressure; BS, blood sugar; TG, triglycerides; TC, total cholesterol; LDL, low-density lipoprotein; HDL, high-density lipoprotein; LA, lipoprotein A.

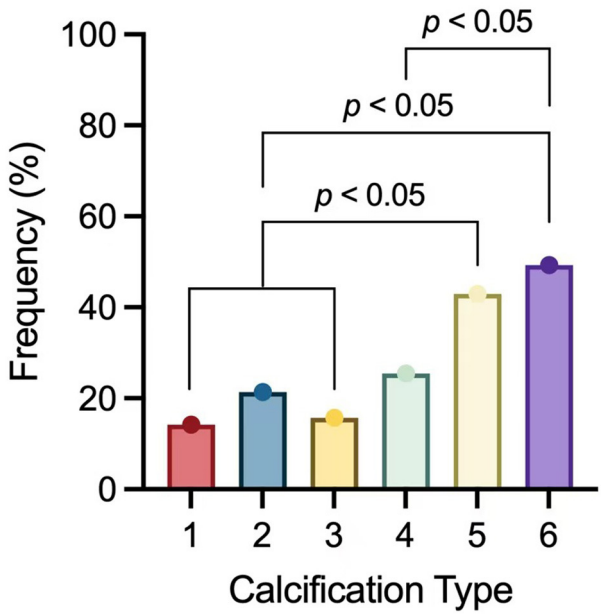

FIGURE 2
The incidence of ipsilateral acute stroke in type 1–6.

(54/253, 21.34%), 24 cases in type 3 (24/153, 15.69%), 26 cases in type 4 (26/102, 25.49%), and 52 cases in type 5 (52/121, 42.98%), 35 patients in the 6 type had acute stroke (35/71, 49.30%). Figure 2 presents the results of this study.

TABLE 2 Plaque calcification types on the acute and non-acute infarction sides of the same patient.

The non-acute Infarction sides	The acute infarction sides						
	1	2	3	4	5	6	Total
1	50	20	4	8	3	3	88
2	9	17	9	4	7	8	54
3	3	2	4	2	11	8	30
4	4	4	3	5	3	4	23
5	0	1	1	3	12	8	25
6	1	0	1	0	3	2	7
Total	67	44	22	22	39	33	227

The Spearman test was used to analyze the correlation between the carotid plaque calcification type and ipsilateral acute anterior circulation infarction. Moreover, the results indicated a weak positive correlation between different calcified plaque types and ipsilateral acute anterior circulation stroke ($r = 0.217$, $p < 0.001$).

3.3 Paired sample chi-square test of carotid plaque calcification types and acute cerebral infarction

A paired-sample chi-square test was performed on the bilateral calcified plaque types in (227 patients) unilateral acute cerebral infarction. Calcified plaque types on the side with acute infarction were significantly higher than those on the side without acute infarction differences ($p < 0.001$). The results are presented in Table 2.

4 Discussion

This study did not start with the traditional high-risk and low-risk plaques but focused on the more common calcification during clinical work. We grouped common calcified carotid plaques in clinical practice using CTA technology and developed a new classification method for calcified carotid plaques. We explored their associations with the occurrence of acute ipsilateral anterior circulation stroke. Type 6 calcified plaques are associated with acute ipsilateral anterior circulation strokes. This could help patients receive active and effective treatments before acute stroke.

Two radiologists who had been diagnosing head and neck images for more than 5 years reviewed the images in our study. Type 2 calcifications are easily distinguishable. In contrast, types 3 and 5 calcifications are difficult to distinguish. According to Kappa consistency testing, there was good inter-observer consistency ($\kappa = 0.92$).

First, the morphology of calcified plaques at the carotid bifurcation was examined, and the correlation between plaque calcification type and ipsilateral anterior circulation acute stroke

was analyzed (considering 1,178 carotid arteries). Type 6 calcified plaques, that is, edge-sign-positive plaques, had the highest risk of ipsilateral anterior circulation acute stroke. Thirty-five of the 71 patients experienced acute ipsilateral anterior circulation stroke. This was confirmed by Spearman correlation analysis, which indicated a statistically significant correlation between the calcified plaque type and acute stroke. In the paired sample chi-square analysis, the carotid plaque calcification types on the side with acute stroke were often higher than those on the side without acute stroke. It was not difficult to identify the acute stroke proportion in type 6 calcified plaques, which was the most common type, by combining the overall proportion of each calcification type. The acute stroke prevalence in type 6 plaques in our study was much lower than the symptoms of type 6 calcified plaques observed by Saba et al. (6). This is because we introduced the definition of acute stroke. Based on the high signal intensity observed on DWI, false-positive patients were excluded. Simultaneously, patients with a history of larger infarctions were excluded, which reduced the incidence of false-negatives in the control group. In a retrospective cohort study, adventitial calcification with positive internal soft plaque edge signs was observed on CTA. This could predict intraplaque hemorrhage inside the carotid plaques (7). Kashiwazaki et al. observed that thin calcifications were associated with intraplaque hemorrhage, demonstrating a different clinical significance from that of thick calcifications (8), consistent with our research findings.

Gupta et al. observed that every increase of 1 mm can enhance the risk of stroke or transient ischemic attack by 2.7 times for soft plaques (9). Similar findings were made in our type 4 and type 6. Xu et al. reported intraplaque hemorrhage and lipid-rich necrotic cores combined with small punctate calcifications (10). Nandalur et al. discovered that the proportion of carotid plaque calcification, not the absolute volume, was associated with plaque stability. Specifically, the plaque may demonstrate better stability in some patients when calcification in carotid plaques accounts for more than 45% of the total plaque volume (11). However, similar results were not observed for type 1, 2, and 3. This is because calcification mechanisms and acute stroke are complex (12) and require further investigation. Type 5 refers to mixed type with intima and significant calcification and its complex mechanism needs to be further studied.

Secondly, our study identified that some baseline data between the acute and non-acute infarction groups showed significant statistical differences, which is consistent with previous studies. Sex, smoking, alcohol consumption, hypertension, hyperglycemia, and hyperlipidemia are the risk factors for ischemic stroke (13). Moreover, the consistency of systematic evaluations in observational studies (cohort and case-control studies) indicated a strong, positive, and dose-dependent correlation between serum total homocysteine concentration and stroke risk (14). Therefore, daily blood pressure, blood sugar, and blood lipid management while actively quitting smoking and alcohol consumption can help prevent the occurrence of stroke. However, patients depend on medications for disease management (15).

Similarly, we tried to exclude acute stroke caused by cardiac embolism or intracranial atherosclerotic plaques because baseline data inclusion and exclusion were performed by two experienced clinical doctors. However, patients with scattered lacunar infarctions identified by MR were not excluded. Because lacunar cerebral infarction has always been caused by cerebral small vessel disease (16), a common cause of cerebral small vessel disease is small artery sclerosis, which is a cerebral microvascular disease (17).

Our study had certain limitations. First, we could not avoid selection bias in the retrospective studies. Secondly, more complex plaques are difficult to describe using a single calcification type. Hence, typing carotid plaque calcifications is challenging.

This calcified plaque typing model must be validated using prospective and longitudinal cohort studies to establish its clinical reference value. The results of this study are clinically significant. A causal correlation between plaque calcification and acute stroke has not yet been established, although calcification is an accompanying phenomenon in atherosclerosis. However, the study results have established that the morphology of plaque calcification is associated with the occurrence of acute ischemic stroke.

Data availability statement

The raw data supporting the conclusions of this article will be made available by the authors, without undue reservation.

Ethics statement

The studies involving humans were approved by the Lianyungang First People's Hospital Medical Ethics Committee (Approval number: KY-20220726002-01). The studies were conducted in accordance with the local legislation and institutional requirements. Written informed consent for participation was not required from the participants or the participants' legal guardians/next of kin in accordance with the national legislation and institutional requirements.

Author contributions

TC: Writing – original draft, Conceptualization. ZG: Writing – review & editing, Formal analysis. YZ: Writing – review & editing, Data curation. YL: Writing – review & editing, Methodology. YG: Writing – review & editing, Supervision.

Funding

The author(s) declare financial support was received for the research, authorship, and/or publication of this article. This work was supported by the Lianyungang City Health Commission Surface of State Project Foundation (Grant no. 202204).

Acknowledgments

Thanks to all the staff of the Department of Radiology of The First People's Hospital of Lianyungang for their help and support.

Conflict of interest

The authors declare that the research was conducted in the absence of any commercial or financial relationships that could be construed as a potential conflict of interest.

Generative AI statement

The author(s) declare that no Gen AI was used in the creation of this manuscript.

Publisher's note

All claims expressed in this article are solely those of the authors and do not necessarily represent those of their affiliated organizations, or those of the publisher, the editors and the reviewers. Any product that may be evaluated in this article, or claim that may be made by its manufacturer, is not guaranteed or endorsed by the publisher.

References

1. GBD 2019 Stroke Collaborators. Global, regional, and national burden of stroke and its risk factors, 1990–2019: a systematic analysis for the Global Burden of Disease Study 2019. *Lancet Neurol.* (2021) 20:795–820. doi: 10.1016/S1474-4422(21)00252-0

2. GBD 2016 Neurology Collaborators. Global, regional, and national burden of neurological disorders, 1990–2016: a systematic analysis for the Global Burden of Disease Study 2016. *Lancet Neurol.* (2019) 18:459–480. doi: 10.1016/S1474-4422(18)30499-X

3. Lammie GA, Sandercock PA, Dennis MS. Recently occluded intracranial and extracranial carotid arteries. Relevance of the unstable atherosclerotic plaque. *Stroke.* (1999) 30:1319–25. doi: 10.1161/01.STR.30.7.1319

4. Bentzon JF, Otsuka F, Virmani R, Falk E. Mechanisms of plaque formation and rupture. *Circ Res.* (2014) 114:1852–66. doi: 10.1161/CIRCRESAHA.114.302721

5. Shi X, Gao J, Lv Q, Cai H, Wang F, Ye R, et al. Calcification in atherosclerotic plaque vulnerability: friend or foe? *Front Physiol.* (2020) 11:56. doi: 10.3389/fphys.2020.00056

6. Saba L, Chen H, Cau R, Rubeis GD, Zhu G, Pisu F, et al. Impact analysis of different CT configurations of carotid artery plaque calcifications on cerebrovascular events. *AJNR Am J Neuroradiol.* (2022) 43:272–9. doi: 10.3174/ajnr.A7401

7. Eisenmenger LB, Aldred BW, Kim SE, Stoddard GJ, de Havenon A, Treiman GS, et al. Prediction of carotid intraplaque hemorrhage using adventitial calcification and plaque thickness on CTA. *AJNR Am J Neuroradiol.* (2016) 37:1496–503. doi: 10.3174/ajnr.A4765

8. Kashiwazaki D, Yamamoto S, Hori E, Akioka N, Noguchi K, Kuroda S. Thin calcification (<2 mm) can highly predict intraplaque hemorrhage in carotid plaque: the clinical significance of calcification types. *Acta Neurochir.* (2022) 164:1635–43. doi: 10.1007/s00701-022-05205-x

9. Gupta A, Baradaran H, Kamel H, Pandya A, Mangla A, Dunning A, et al. Evaluation of computed tomography angiography plaque thickness measurements in high-grade carotid artery stenosis. *Stroke.* (2014) 45:740–5. doi: 10.1161/STROKEAHA.113.003882

10. Xu X, Hua Y, Liu B, Zhou F, Wang L, Hou W. Correlation between calcification characteristics of carotid atherosclerotic plaque and plaque vulnerability. *Ther Clin Risk Manag.* (2021) 17:679–90. doi: 10.2147/TCRM.S303485

11. Nandalur KR, Hardie AD, Raghavan P, Schipper MJ, Baskurt E, Kramer CM. Composition of the stable carotid plaque: insights from a multidetector computed tomography study of plaque volume. *Stroke.* (2007) 38:935–40. doi: 10.1161/01.STR.0000257995.74834.92

12. Saba L, Nardi V, Cau R, Gupta A, Kamel H, Suri JS, et al. Carotid artery plaque calcifications: lessons from histopathology to diagnostic imaging. *Stroke.* (2022) 53:290–7. doi: 10.1161/STROKEAHA.121.035692

13. Boehme AK, Esenwa C, Elkind MS. Stroke Risk Factors, Genetics, and Prevention. *Circ Res.* (2017) 120:472–95. doi: 10.1161/CIRCRESAHA.116.308398

14. Hankey GJ, Eikelboom JW. Homocysteine and stroke. *Lancet.* (2005) 365:194–6. doi: 10.1016/S0140-6736(05)70126-4

15. Senoner T, Plank F, Langer C, Beyer C, Steinkohl F, Barbieri F, et al. Smoking and obesity predict high-risk plaque by coronary CTA in low coronary artery calcium score (CACS). *J Cardiovasc Comput Tomogr.* (2021) 15:499–505. doi: 10.1016/j.jcct.2021.04.003

16. Horowitz DR, Tuhrim S, Weinberger JM, Rudolph SH. Mechanisms in lacunar infarction. *Stroke.* (1992) 23:325–7. doi: 10.1161/01.STR.23.3.325

17. Wardlaw JM, Smith C, Dichgans M. Small vessel disease: mechanisms and clinical implications. *Lancet Neurol.* (2019) 18:684–96. doi: 10.1016/S1474-4422(19)30079-1

frontiers | Frontiers in Neurology

TYPE Original Research
PUBLISHED 12 February 2025
DOI 10.3389/fneur.2025.1545631

OPEN ACCESS

EDITED BY
Shuai Ren,
Affiliated Hospital of Nanjing University of Chinese Medicine, China

REVIEWED BY
Jiaming Lu,
Nanjing Drum Tower Hospital, China
Yuto Uchida,
Johns Hopkins Medicine, United States
Hang Qu,
Affiliated Hospital of Yangzhou University, China
Songyu Chen,
Tongji University, China

*CORRESPONDENCE
Lina Song
songln2023@yeah.net
Peng An
drpengan@foxmail.com

†These authors have contributed equally to this work

RECEIVED 15 December 2024
ACCEPTED 14 January 2025
PUBLISHED 12 February 2025

CITATION
Wu X, Yang J, Ji X, Ye Y, Song P, Song L and An P (2025) Delta radiomics modeling based on CTP for predicting hemorrhagic transformation after intravenous thrombolysis in acute cerebral infarction: an 8-year retrospective pilot study.
Front. Neurol. 16:1545631.
doi: 10.3389/fneur.2025.1545631

Delta radiomics modeling based on CTP for predicting hemorrhagic transformation after intravenous thrombolysis in acute cerebral infarction: an 8-year retrospective pilot study

Xiaxia Wu[1,2†], Jinfang Yang[1,2†], Xianqun Ji[1†], Yingjian Ye[1], Ping Song[1], Lina Song[1*] and Peng An[1,2*]

[1]Department of Radiology and Surgery, Xiangyang No.1 People's Hospital, Hubei University of Medicine, Xiangyang, China, [2]Department of Neurology, NICU and Epidemiology, Xiangyang Key Laboratory of Maternal-Fetal Medicine on Fetal Congenital Heart Disease, Xiangyang No.1 People's Hospital, Hubei University of Medicine, Xiangyang, Hubei, China

Objective: To explore the value of delta radiomics from cerebral CT perfusion (CTP) in predicting hemorrhagic transformation after intravenous thrombolysis for acute cerebral infarction (HT-ACI).

Methods: Clinical and imaging data of 419 patients with acute cerebral infarction who underwent CTP after treatment between November 2016 and August 2024 were retrospectively collected. Based on post-thrombolysis cranial CT or MRI results, patients were divided into the HT-ACI group (114 cases) and the non-HT-ACI group (305 cases). The dataset was split into a training set and a test set in a 7:3 ratio based on time nodes. In the training set, regions of interest (ROI) within the cerebral infarction area on CTP images were delineated using 3D slicer software, and delta radiomic features were extracted. Hemodynamic parameters such as cerebral blood volume (CBV), cerebral blood flow (CBF), and time to peak (TTP) were obtained using CTP techniques. These were combined with baseline patient data (e.g., age, sex, NIHSS score, medical history) to establish various models for predicting HT-ACI through multivariable logistic regression analysis. The predictive performance of the models was compared using DeLong curves, clinical net benefit was assessed using decision curves, and model predictions were validated using the XGboost algorithm. These results were then validated in the test set, and a nomogram and calibration curve were constructed for clinical application.

Results: In the training set, significant differences were observed between the two groups in NIHSS score, pre-illness usually use of anticoagulants, age, infarction size, ADC difference, CBF, and Delta radscore ($P < 0.05$). The combined model [AUC 0.878, OR 0.0217, 95%CI 0.835–0.913] demonstrated superior predictive performance compared to the clinical model [AUC 0.725, OR 0.0310, 95%CI 0.670–0.775] and the imaging model [AUC 0.818, OR 0.0259, 95%CI 0.769–0.861]. This was confirmed by the XGboost algorithm, and decision curves confirmed the higher clinical net benefit of the combined model. Similar results were validated in the test set, and a novel nomogram was constructed to simplify the prediction process for HT-ACI.

Conclusion: The combined model established based on delta radiomics from CTP may provide early insights into the hemodynamic status of acutely ischemic brain tissue, holding significant clinical importance for predicting HT-ACI. This method could offer a powerful imaging reference for clinical decision-making in patients with ACI, helping to reduce the risk of HT-ACI and improve patient outcomes.

KEYWORDS

acute cerebral infarction, intravenous thrombolysis, hemorrhagic transformation, CT perfusion imaging, delta radiomics, prediction model

Introduction

Acute cerebral infarction, characterized by high incidence, disability, and mortality rates, remains a significant clinical challenge. The prognosis of this disease is poor, especially when complicated by hemorrhagic transformation after intravenous thrombolysis for acute cerebral infarction (HT-ACI). HT-ACI occurs due to secondary hemorrhage resulting from blood–brain barrier (BBB) disruption and reperfusion injury in ischemic brain tissue following acute cerebral infarction. This process can occur at any stage of the natural course of acute cerebral infarction or after stroke treatment. Statistics indicate that the incidence of HT-ACI is as high as 10–20%, with 30 to 40% being progressive, profoundly impacting patients' treatment plans and prognosis (1–4). Given the severe consequences of HT-ACI, clinicians urgently need a method to predict the risk of post-treatment rebleeding in patients early, thereby enhancing the safety of endovascular treatment and improving patient outcomes. However, traditional assessment methods based on clinical symptoms and conventional imaging features have certain limitations. Clinical symptom evaluation is often subjective and lacks accuracy, while conventional imaging findings cannot provide timely and accurate diagnoses. Therefore, identifying sensitive predictive markers for HT-ACI is crucial (5–7). In recent years, the rapid development of radiomics has offered new opportunities for HT-ACI prediction. By mining and screening a vast amount of quantitative feature information from acute cerebral infarction images, radiomics can establish classifiers to aid in the judgment of HT-ACI occurrence, enabling precise diagnosis and prediction. This approach is expected to overcome the limitations of traditional assessment methods and improve prediction accuracy. Currently, some studies have effectively predicted the occurrence of HT-ACI using radiomics combined with machine learning models or artificial intelligence, but these are all based on static radiomics, that is, radiomic parameters extracted from non-contrast head CT scans, which may introduce certain biases (8–10). Therefore, this study aims to construct a model for predicting HT-ACI based on delta radiomic features derived from cerebral CT perfusion (CTP) images. This not only contributes to a deeper understanding of the pathogenesis of HT-ACI but also provides clinicians with a novel and more accurate predictive tool to guide clinical treatment decisions and improve patient prognosis.

Materials and methods

Study materials

We retrospectively collected and analyzed clinical and imaging data from 537 patients with acute cerebral infarction who were diagnosed by MRI and CTA and received intravenous thrombolysis treatment at Xiangyang NO.1 People's Hospital Affiliated to Hubei University of Medicine between November 2016 and August 2024. Inclusion Criteria: ① Met the diagnostic criteria for acute cerebral infarction outlined in the 2020 Chinese Guidelines for the Diagnosis and Treatment of Acute Ischemic Stroke. ② Exhibited clear neurological dysfunction with a National Institutes of Health Stroke Scale (NIHSS) score ranging from 4 to 22. ③ Onset of symptoms within 4.5 h, which is the effective time window for intravenous thrombolysis. ④ No history of contrast agent allergy, no claustrophobia, and normal liver and kidney function. ⑤ Met the standards outlined in the 2020 Chinese Guidelines for Intravenous Thrombolysis in Acute Ischemic Stroke and the Guidelines for Early Endovascular Treatment of Acute Ischemic Stroke. ⑥ Underwent CTP (CT Perfusion Imaging) examination after thrombolysis and received a follow-up plain CT scan 24–48 h later. Exclusion Criteria: ① Patients with a history of previous stroke. ② Patients with severe metabolic disorders, tumors, or other serious systemic diseases. ③ Contraindications for thrombolysis. ④ Pregnant and lactating women. ⑤ Patients who had already experienced hemorrhage before the CTP follow-up scan. ⑥ Patients with head trauma, cerebral infarction, or myocardial infarction within the past 3 months. ⑦ Patients with a platelet count <100×10^9/L or fasting blood glucose <2.7 mmol/L (11, 12). Final Enrollment: After rigorous screening and exclusion, 419 patients were enrolled, including 234 males and 185 females, aged between 36 and 85 years, with an average age of (57.6 ± 18.5) years. The patients were closely followed up for their disease outcomes. Based on CT or MRI results, patients were divided into the HT-ACI group (114 patients) and the non-HT-ACI group (305 patients) (Figure 1).

Examination methods

Equipment: Siemens SOMATOM Drive Dual-Source 64-Slice CT scanners were used. Patient Position: Patients were placed in a supine position on the examination table. Scanning Baseline: The scanning baseline was set at the orbitomeatal line. Plain Scan Parameters: Tube

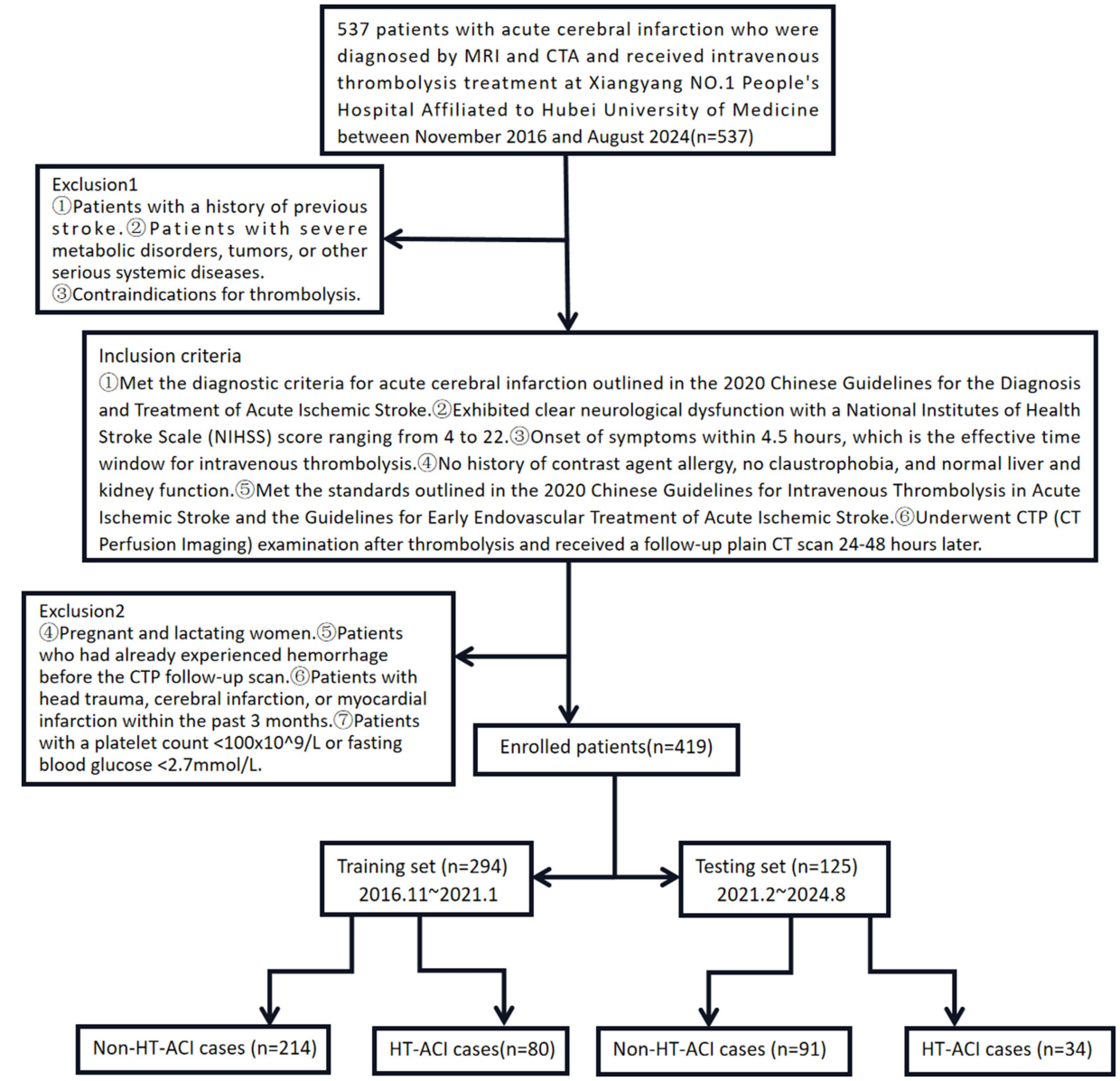

FIGURE 1
Inclusion and exclusion criteria, and case grouping method for this study.

voltage: 120 kV, tube current: 300 mA, slice thickness: 3 mm, slice interval: 1 mm. CTP Scan: Based on the plain CT scan results, a total of 23 slices covering the whole brain were determined. Iopromide contrast agent (350 mg/mL) was injected as a bolus through the right elbow vein using a high-pressure injector at a rate of 4.5 mL/s. Scanning began 5 s after the injection. Scanning Parameters: Tube voltage: 80 kV, tube current: 200 mAs, matrix: 512×512, slice thickness: 1 mm, slice interval: 1, interval: 2 s, continuous scanning for 45 s, scanning range: 200 mm. A total of 700–900 frames of images were obtained. CTP Image Processing and Data Analysis, Image Transfer: The reconstructed dynamic images were transferred to the GE ADW4.6 workstation. Software Processing: The BRAIN STROKE Perfusion software (non-deconvolution/deconvolution algorithm) was used for image post-processing. Data Obtained: Time-intensity curves, CT perfusion images, CBF maps, CBV maps, and TTP maps of the region of interest (ROI). Image Analysis: Two senior imaging specialists with over 10 years of experience analyzed the images using a double-blind method. The area centered on the infarct lesion was designated as the ROI, avoiding blood vessels and sulci of the brain. The absolute values of CBF, CBV, and TTP in the infarcted side and the corresponding contralateral region were calculated (13, 14). ADC Difference: The lowest ADC value (mm^2/s) in the core of the infarct lesion and the ADC value (mm^2/s) in the contralateral mirror region were measured on the ADC sequence of brain MRI, and the ADC difference between the contralateral and infarcted sides was calculated.

Image segmentation and radiomic feature extraction in cerebral infarct regions

Using the 3D slicer software (version 4.11), the region of interest (ROI) for the entire cerebral infarct region was segmented layer by layer on 1.0 mm thin-slice CTP images. The criteria for identifying the infarct region were defined as follows: based on a comprehensive assessment of the DWI sequence from MR and plain CT scans, the entire infarct region on CTP was delineated as the ROI. The ROI for the infarct region encompassed the core infarct area and the ischemic penumbra within 3–10 mm around it, excluding surrounding cerebral sulci, cisterns, subarachnoid spaces, and bone tissue. After manually delineating the ROI for the infarct region layer by layer, revisions were made with reference to coronal and sagittal MR images. The segmentation process of the infarct region was manually conducted by two radiologists with over 10 years of experience in neurological radiology, and the intraclass correlation coefficient (ICC) was used to evaluate the consistency of segmentation parameters and the reproducibility of radiomic feature extraction between the two radiologists. An ICC > 0.75 indicated good consistency and reproducibility of radiomic feature extraction. The Radiomics plugin in Slicer was utilized to extract radiomic features, with image resampling and nearest-neighbor interpolation performed prior to this to standardize the CTP images. A total of 879×2 radiomic features were extracted, including shape features, first-order statistical features, texture features, and higher-order features. Subsequently, the LASSO algorithm and 10-fold cross-validation were employed to generate the Radscore based on the remaining features; Radscore1 represented the radiomic score derived from texture parameters extracted from plain CT scans, while Delta Radscore represented the radiomic score calculated as (CTP cerebral perfusion phase texture parameters – plain CT scan phase texture parameters)/CTP cerebral perfusion phase texture parameters (15) (Figure 2).

Overview of statistical methods

Statistical analysis was conducted using SPSS 22.0 and R software. Firstly, the enrolled cases were divided into a training set and a test set based on a 7:3 ratio and time points. All continuous variables underwent tests for homogeneity of variance and normal distribution. Measurement data for the two groups (normally distributed) were expressed as $X \pm S$ and compared using *t*-tests; measurement data for the two groups (non-normally distributed) were expressed as ranges (median, 25–75%) and compared using rank-sum tests. Categorical variables were expressed as percentages (%) or specific case numbers and compared using chi-square tests or Fisher's exact tests. For radiomic parameters, the LASSO algorithm and 10-fold cross-validation were used to adjust elastic network parameters to avoid overfitting, thereby selecting the optimal texture features to generate the radiomic score (Radscore). In the training set, three prediction models (clinical model, imaging model, and combined model) were established using multivariate logistic regression. The predictive performance of the models was compared using DeLong's test, and the clinical net benefit of the most valuable model was assessed using decision curves. These results were then validated in the test set and further verified using the XGboost machine learning model by outputting SHAP values. Finally, a novel nomogram was established and corresponding clinical trials

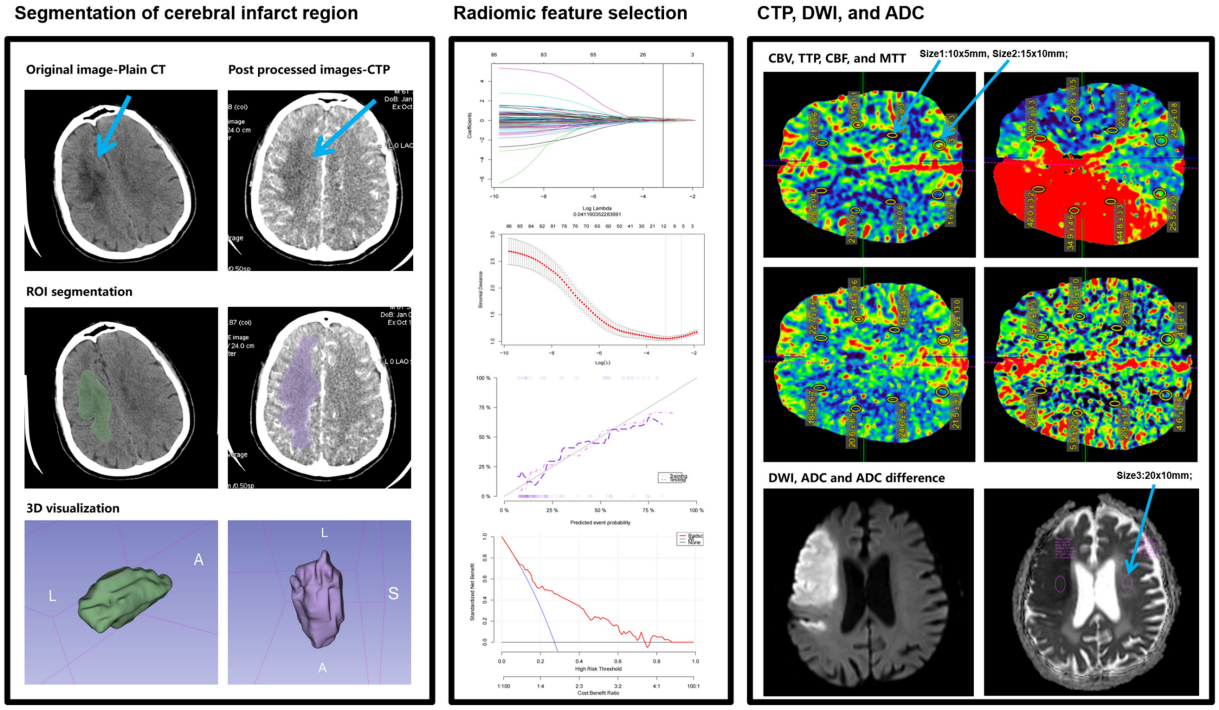

FIGURE 2
A simple schematic diagram of ROI delineation and radiomic feature extraction in cerebral infarct regions in this study.

and applications were conducted. A p-value <0.05 indicated statistical significance (16).

Results

A total of 537 patients with acute ischemic stroke caused by anterior circulation vascular occlusion underwent non-contrast CT, CTP, and CTA examinations, with the time from stroke onset to CT imaging being ≤6 h were enrolled. One hundred and eighteen patients were excluded due to reasons such as poor image quality or motion artifacts, presence of old cerebral infarction, lack of follow-up imaging data, contrast agent extravasation, occurrence of hemorrhage before CTP reexamination, and patients with cerebral infarction or myocardial infarction. Ultimately, 419 patients met the study criteria, with an average age of (57.6 ± 18.5) years. Univariate regression analysis revealed no statistically significant differences between the two patient groups in terms of gender, history of coronary heart disease, history of atrial fibrillation, previous stroke or transient ischemic attack (TIA), history of hypertension, history of diabetes, smoking history, alcohol consumption history, prothrombin time (PT), body mass index (BMI), infarct location, pulmonary infection (PI), white blood cell count, D-dimer levels, platelet-to-lymphocyte ratio (PLR), neutrophil-to-lymphocyte ratio (NLR), cerebral blood volume (CBV), time to peak (TTP), and Radscore 1 ($p > 0.05$). Significant statistical differences were observed between the two groups in infarct size, National Institutes of Health Stroke Scale (NIHSS) score, pre-illness regular use of anticoagulants, age, cerebral blood flow (CBF), ADC difference, and Delta Radscore ($p < 0.05$). Multivariate regression analysis confirmed that infarct size, age, CBF, and Delta Radscore were independent risk factors for the occurrence of hemorrhagic transformation after acute cerebral infarction (HT-ACI).

Based on these risk factors, we established clinical, imaging, and combined models. In the training set, the combined model demonstrated the highest predictive performance [AUC 0.878, OR 0.0217, 95% CI 0.835–0.913, sensitivity 86.92%, specificity 77.51%], significantly outperforming the clinical model [AUC 0.725, OR 0.0310, 95% CI 0.670–0.775, sensitivity 72.15%, specificity 60.81%, $p < 0.05$] and the imaging model [AUC 0.818, OR 0.0259, 95% CI 0.769–0.861, sensitivity 81.70%, specificity 70.15%, $p < 0.05$]. Similar results were validated in the test set, with the combined model showing superior predictive performance [AUC: 0.867, OR 0.0353, 95% CI: 0.794–0.921, sensitivity 82.35%, specificity 81.32%] compared to the clinical model [AUC: 0.729, OR 0.0448, 95% CI: 0.642–0.804, sensitivity 69.51%, specificity 71.32%, $p = 0.001$] and the imaging model [AUC: 0.818, OR 0.0422, 95% CI: 0.739–0.882, sensitivity 80.61%, specificity 75.19%, $p = 0.04$]. Decision curve analysis (DCA) confirmed that the combined model had higher clinical net benefit in both groups, and the XGboost machine learning model also verified the association of infarct size, age, CBF, and Delta Radscore with the occurrence of HT-ACI (all $p < 0.05$). Subsequently, a nomogram and calibration curve based on the combined model were developed and received clinical application and positive feedback (Tables 1–3 and Figures 3–6).

Discussion

With the intensification of domestic environmental pollution and the aggravation of social aging, the incidence rate of stroke has reached 200/100,000, with ischemic stroke accounting for 69.6% of all strokes. Intravenous thrombolysis is currently one of the most effective treatments for acute cerebral infarction. Hemorrhagic transformation after acute cerebral infarction (HT-ACI) refers to secondary hemorrhage within the cerebral infarction area or hemorrhage in adjacent areas due to the restoration of blood flow perfusion in the ischemic area of the brain after cerebral infarction. HT-ACI is a serious complication of intravenous thrombolysis, significantly affecting its therapeutic effect. It is also one of the main reasons for neurological deterioration in patients with cerebral infarction after intravenous thrombolysis and for medical disputes. Previous studies have suggested that low serum albumin levels, smoking history, diabetes mellitus, coagulation time, and CTP parameters [cerebral blood volume (CBV), time to peak (TTP), mean transit time (MTT)] are associated with poor prognosis in patients with stroke, but these factors lack specificity (17–19). Furthermore, conventional CT and MR have certain difficulties and limitations in predicting HT-ACI, mainly due to the complexity of HT-ACI, limitations of imaging techniques, and individual differences among patients. The mechanisms of HT-ACI involve multiple aspects, including post-infarction ischemic injury, reperfusion injury, coagulation dysfunction, and blood–brain barrier disruption. These factors interact with each other, making the occurrence of HT-ACI highly complex and uncertain. Restricted by the examination time window, CT and MR have low sensitivity to small or micro-hemorrhage points, which are difficult to distinguish from surrounding brain tissue, potentially leading to delayed detection of HT-ACI and exacerbation of the condition (20, 21). Our team has found that radiomic parameters based on delta changes in cerebral infarction areas, extracted from enhanced CT cerebral perfusion imaging and plain CT, are helpful in predicting HT-ACI. Therefore, this study established a novel nomogram for predicting HT-ACI based on clinical parameters combined with the Delta radscore, which has received favorable clinical evaluations. This nomogram is non-invasive and requires no additional costs, with a high AUC value of 0.878, providing a new method for the prediction and treatment evaluation of HT-ACI.

This study found that HT-ACI is correlated with certain factors, including the NIHSS score, pre-illness usually use of anticoagulants, age, infarct size, ADC difference, CBF, and Delta radscore. The NIHSS score (National Institutes of Health Stroke Scale score) is a crucial indicator for assessing stroke severity. Research has shown that the NIHSS score is closely related to the risk of HT-ACI, with a higher NIHSS score generally indicating a higher risk of HT-ACI. It has been reported that patients with an NIHSS score ≥ 20 have an increased risk of fatal hemorrhagic transformation, reaching 6.8%. The routine use of anticoagulants (such as Warfarin, Clopidogrel Sulfate, Aspirin, etc.) before illness also increases the risk of HT-ACI. Anticoagulants prevent thrombus formation by inhibiting the coagulation process but simultaneously increase the risk of bleeding. When administering intravenous thrombolysis to patients using anticoagulants, it is necessary to more cautiously assess the risk of HT-ACI and closely monitor the patient's bleeding status. Age is an important risk factor for HT-ACI. As age increases, the blood–brain barrier becomes

TABLE 1 Presents the logistic regression analysis results of the clinical model predicting HT-ACI based on clinical features, with *$p < 0.05$ indicating statistical significance.

Clinical model	Univariate analysis		Multivariate analysis	
Factors	*P*	Hazard ratio	*P*	Hazard ratio
Gender	0.36	1.27 (0.76–2.10)		
History of coronary heart disease	0.69	1.14 (0.58–2.22)		
History of atrial fibrillation	0.41	1.27 (0.71–2.24)		
Previous stroke or transient ischemic attack (TIA)	0.13	1.35 (0.91–1.98)		
History of hypertension	0.54	1.01 (0.97–1.05)		
History of diabetes	0.13	1.04 (0.98–1.09)		
Smoking history	0.37	1.02 (0.98–1.05)		
Alcohol consumption history	0.15	1.02 (0.99–1.04)		
Prothrombin time (PT)	0.12	1.15 (0.96–1.38)		
BMI	0.13	1.09 (0.97–1.20)		
Infarct location	0.34	1.15 (0.86–1.54)		
Pulmonary infection (PI)	0.38	1.18 (0.82–1.72)		
White blood cell count	0.19	1.09 (0.96–1.24)		
D-dimer levels	0.61	0.94 (0.77–1.17)		
PLR	0.11	1.04 (0.99–1.09)		
NLR	0.12	1.05 (1.98–1.10)		
Infarct size	<0.05*	1.09 (1.05–1.13)	<0.05*	1.09 (1.04–1.12)
NIHSS	<0.05*	1.28 (1.12–1.48)	0.01*	1.24 (1.07–1.43)
Pre-illness regular use of anticoagulants	0.01*	1.68 (1.15–2.47)		
Age	0.04*	1.03 (1.01–1.07)		

*Multivariate regression confirmed that the Infarct size and NIHSS were influential factors for HT-ACI.

TABLE 2 Displays the logistic regression analysis results of the imaging model predicting HT-ACI based on imaging features, with *$P < 0.05$ indicating statistical significance.

Imaging model	Univariate analysis		Multivariate analysis	
Factors	*P*	Hazard ratio	*P*	Hazard ratio
CBF	0.04*	1.49 (1.01–2.23)		
ADC difference	0.04*	1.01 (1.00–1.02)	0.03*	1.01 (1.00–1.02)
CBV	0.43	1.32 (0.66–2.61)		
TTP	0.22	2.84 (0.54–14.92)		
Delta Radscore	<0.05*	2.34 (1.85–2.96)	<0.05*	2.41 (1.89–3.07)
Radscore 1	>0.05			

*Multivariate regression confirmed that the ADC difference and Delta Radscore were influential factors for HT-ACI.

relatively fragile, and the elasticity and toughness of blood vessel walls gradually decrease, making them more prone to rupture and bleeding. Therefore, the risk of HT-ACI significantly increases in elderly patients undergoing intravenous thrombolysis. Generally, the larger the infarct size, the higher the risk of HT-ACI. Large cerebral infarcts can lead to significant brain edema, exerting pressure on surrounding capillaries. When reperfusion is restored and collateral circulation opens up, it may cause blood vessels to rupture, resulting in a marked increase in the incidence of HT-ACI. This study confirms that patients with large infarcts (maximum infarct area ≥ 50 cm^2 or infarct volume ≥ 145 mL) have a sixfold increase in the incidence of HT-ACI compared to patients with smaller infarcts (21, 22). In this study, ADC difference, CBF, and Delta radscore are newly identified predictors of HT-ACI. The ADC (apparent diffusion coefficient) difference reflects differences in water molecule diffusion capacity between the infarct core and normal regions. In this study, the ADC difference in the HT-ACI group was significantly higher than that in the normal group ($p < 0.05$), which may be related to ischemia, hypoxia, vascular

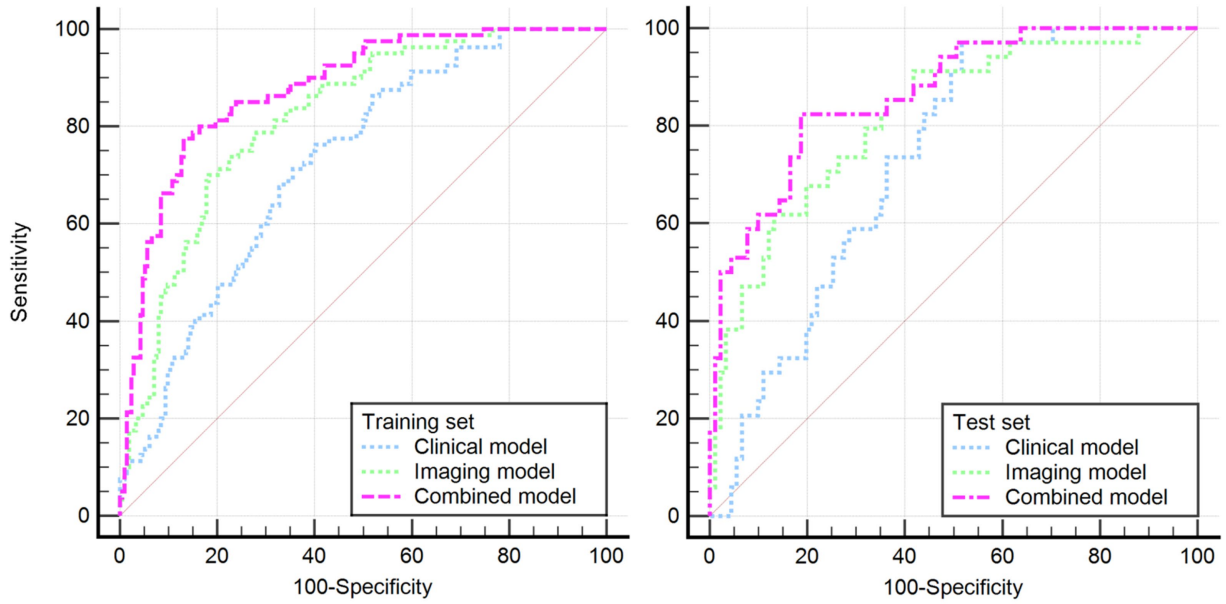

FIGURE 3
Illustrates the DeLong's non-parametric curves for both the training and test sets, revealing that the combined model has the largest area under the ROC curve, confirming its optimal predictive performance.

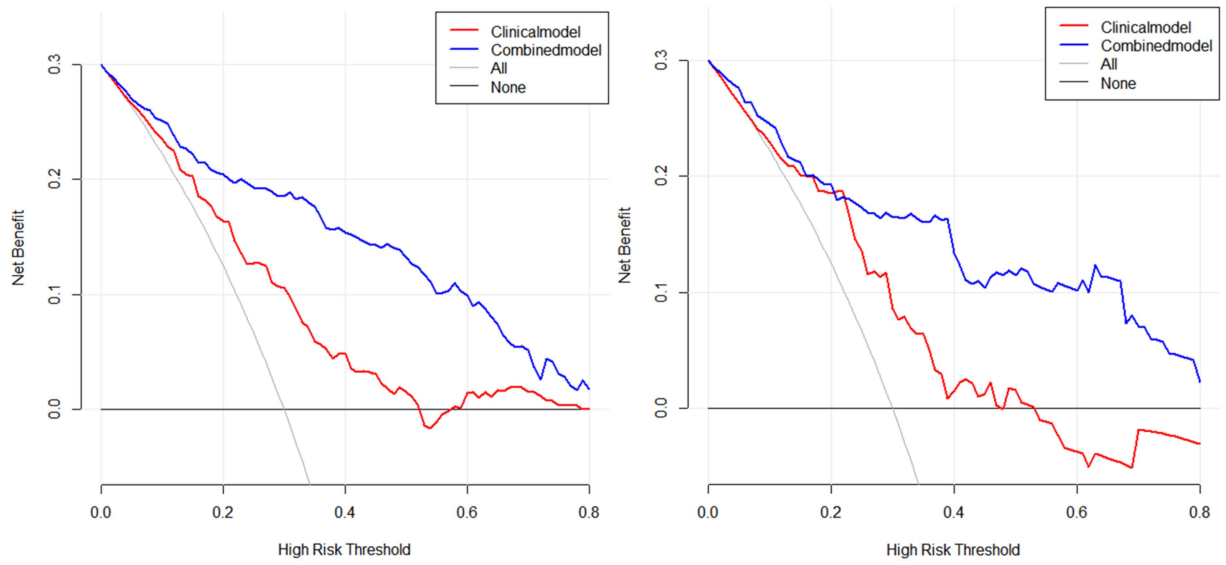

FIGURE 4
Presents the DCA analysis conducted using R software for both the training and test sets, further confirming the higher clinical net benefit of the combined model (left: training set, right: test set).

damage, and blood–brain barrier disruption caused by acute cerebral infarction. Ongoing ischemia and hypoxia in the brain tissue of patients with acute cerebral infarction can lead to cytotoxic edema, increased DWI signals, and significantly reduced ADC values. The ADC difference is collected and calculated from the mirror position of brain tissue in the same individual, effectively avoiding individual differences caused by factors such as the concentration and viscosity of intracellular and extracellular water and body temperature. This allows for an objective and accurate assessment of the cerebral infarction area, thus aiding in the prediction of HT-ACI. Additionally, we found that when the CBF value exceeds 3.12, the incidence of HT-ACI significantly increases. An overly rapid or excessive restoration of cerebral blood flow can lead to an increase in cerebral reperfusion, potentially elevating the risk of hemorrhagic transformation. This is because the damaged vascular walls, upon the resumption of blood flow, may rupture and bleed due to the intense impact of the blood. Furthermore, the dosage and timing of thrombolytic drugs also affect the restoration of cerebral blood flow

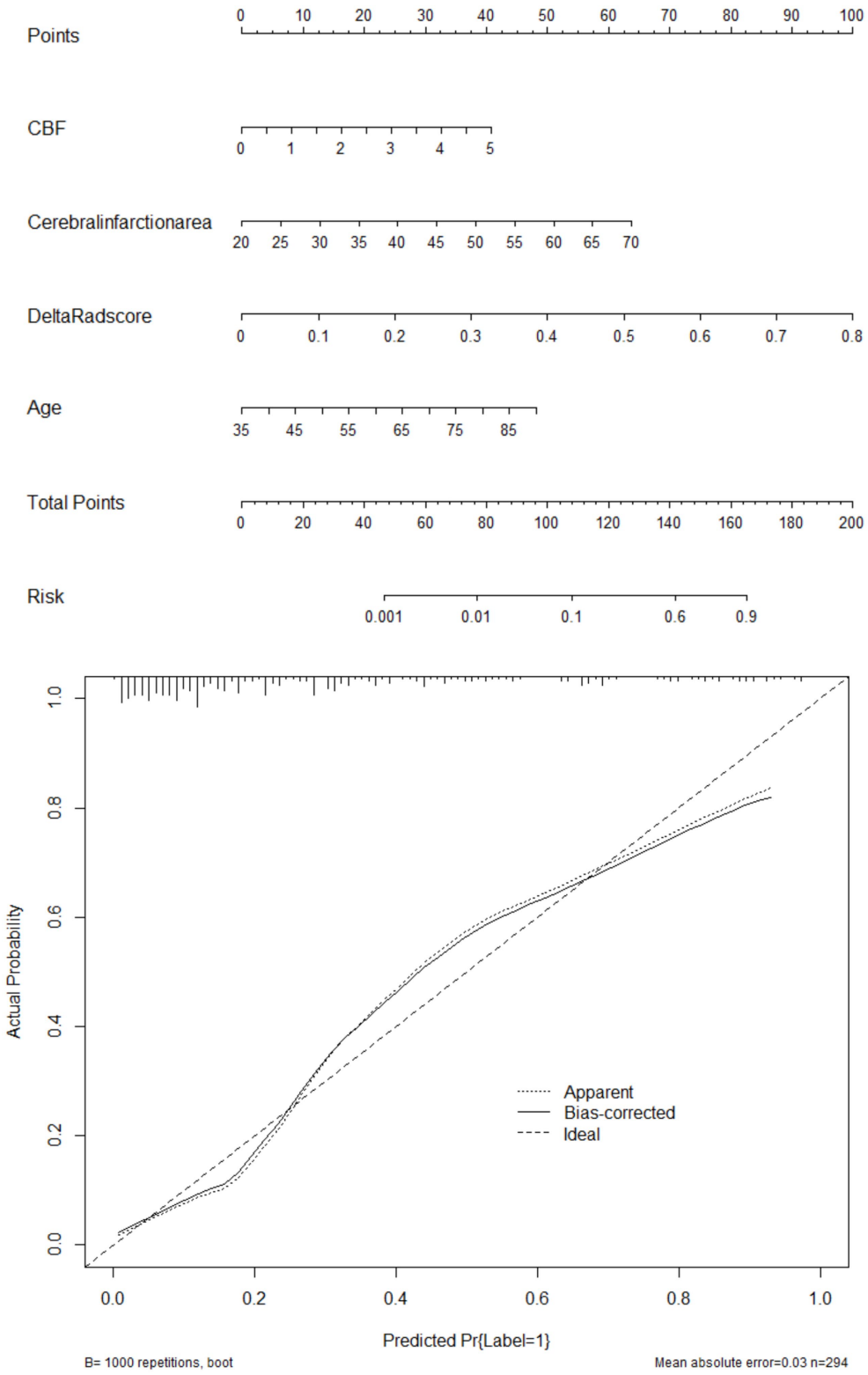

FIGURE 5
Showcases the clinically well-regarded nomogram prediction tool based on risk factors from the combined model (above: nomogram, below: calibration curve). This tool simplifies the assessment process for HT-ACI by assigning scores to each risk factor and summing them up to calculate the final risk value. For example, in Case 501, the CBF of 4.5 corresponds to 37.5 points, the infarct area of 40 corresponds to 25 points, the Delta Radscore of 0.6 corresponds to 75 points, and the age of 70 corresponds to 37.5 points, totaling 175 points, which corresponds to a risk value >0.9. It is inferred that this patient has a high probability of developing HT-ACI, consistent with the clinical outcome.

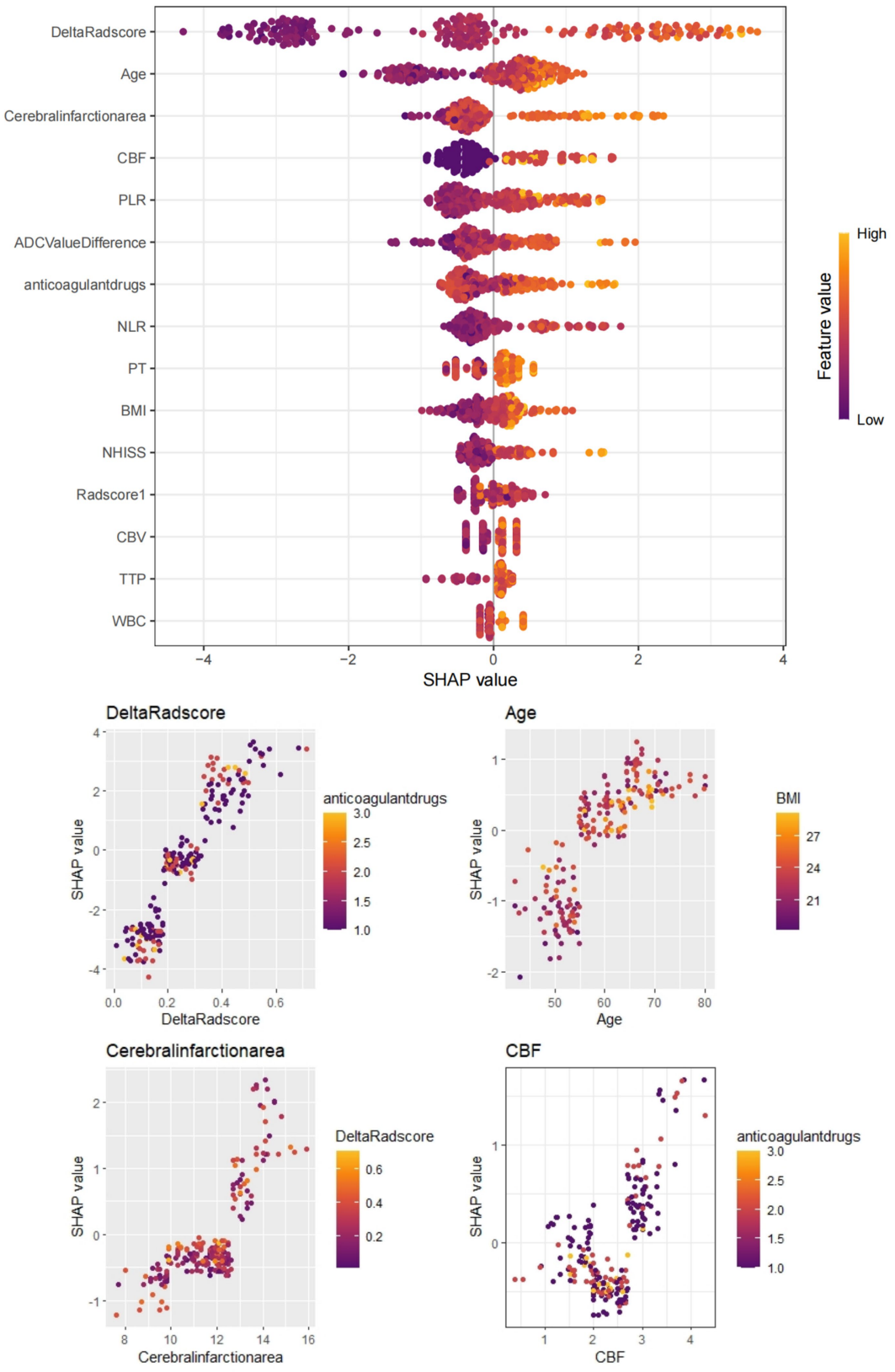

FIGURE 6
Depicts the SHAP value plot output by the XGBoost machine learning model. The SHAP values confirm that infarct size (cut-off value 51.30), age (55.81), CBF (3.12), Delta Radscore (0.31), etc., are important factors influencing the occurrence of HT-ACI, aligning with our research findings. Red represents lower values, while yellow represents higher values.

TABLE 3 Shows the logistic regression analysis results of the combined model predicting HT-ACI based on the valuable factors mentioned above, with *$P < 0.05$ indicating statistical significance.

Combined model	Univariate analysis		Multivariate analysis	
Factors	*P*	Hazard ratio	*P*	Hazard ratio
Infarct size	<0.05*	1.09 (1.05–1.13)	<0.05*	1.09 (1.04–1.15)
NIHSS	<0.05*	1.28 (1.12–1.48)		
Pre-illness regular use of anticoagulants	0.01*	1.68 (1.15–2.47)		
Age	0.04*	1.03 (1.01–1.07)	<0.05*	1.06 (1.02–1.11)
CBF	0.04*	1.49 (1.01–2.23)	<0.05*	1.92 (1.14–3.24)
ADC difference	0.04*	1.01 (1.00–1.02)		
Delta radscore	<0.05*	2.34 (1.85–2.96)	<0.05*	2.66 (2.02–3.51)

*Multivariate regression confirmed that the Infarct size, age, CBF and Delta Radscore were influential factors for HT-ACI.

and the risk of hemorrhagic transformation. If the dosage of thrombolytic drugs is too high or the timing is inappropriate, it may result in an overly rapid restoration of cerebral blood flow, thereby increasing the risk of HT-ACI (23, 24).

Radiomics is an advanced technique that extracts a large number of features (such as shape, intensity, texture, etc.) from medical imaging data and performs high-throughput analysis. These features can reflect the biological characteristics and malignant progression potential of lesions, providing reliable auxiliary information for disease diagnosis. In the diagnosis and treatment of multisystem tumors, radiomics technology can analyze medical imaging data such as CT and MRI to extract quantitative features related to tumors, thereby assisting doctors in early diagnosis and decision-making. It is reported that prediction models built using radiomics technology can effectively classify four types of brain tumors, including craniopharyngioma, glioma, glioblastoma, and metastasis, with high accuracy demonstrated in various validation sets. Moreover, radiomics models based on machine learning algorithms have shown higher accuracy than traditional imaging methods in differentiating these brain tumors. Therefore, for the prediction of HT-ACI, we have incorporated the relatively novel Delta radscore. This high-quality data, based on perfusion changes in enhanced CT, helps to extract CT grayscale texture changes before and after thrombolysis in the acute cerebral infarction area, providing reliable data to evaluate the degree of blood flow perfusion and cerebral tissue infarction within the infarcted area, and further guiding the treatment of acute cerebral infarction and predicting HT-ACI. In this study, based on CTP (CT Perfusion) images, a total of 879 × 2 radiomic features were extracted from the ROI (Region of Interest) of the whole infarcted area. After screening for redundant features, 859 × 2 radiomic features were ultimately retained, including morphological features such as Sphericity, and high-order texture features such as RunLengthNonUniformity.0.732, Skewness.0.588, and Kurtosis.0.393. Sphericity is a shape feature in radiomics that intuitively reflects the texture features of the image or object surface, describing the shape, roughness, smoothness, and grayscale differences of the tissue. A larger value indicates greater differences, which may be related to tissue ischemia, necrosis, and softening. This study found that acute cerebral infarction patients with lower Sphericity values are more prone to HT-ACI, suggesting that patients with acute cerebral infarction where the infarcted tissue has not completely softened and necrosed should be cautious about the dosage during thrombolysis to avoid excessive perfusion leading to HT-ACI. High-order texture features generated through frequency domain denoising methods such as Fourier transform and wavelet transform emphasize areas of grayscale change and their texture heterogeneity, allowing more valuable radiomic features to be extracted from the original image. RunLengthNonUniformity.0.732 reflects the uniformity or orderliness of grayscale distribution within the image or infarcted ROI, with a smaller value indicating a more uniform and ordered grayscale distribution. Skewness.0.588 and Kurtosis.0.393 measure the difference in grayscale values between adjacent pixels within the image or ROI. A smaller value indicates smaller differences in grayscale values between adjacent pixels, resulting in a smoother image; a larger value indicates larger differences, resulting in a rougher image. Both can more finely assess the grayscale texture differences and perfusion differences between the infarcted area and surrounding tissues, with a quantization degree of tissue differences significantly higher than that of human visual recognition (25–28). Therefore, the combined model based on CTP radiomics has shown good prediction results for HT-ACI, outperforming clinical and imaging models. The combined model can provide strong support for neurologists to develop personalized treatment plans and provide prognostic guidance. Meanwhile, this study employed dynamic radiomics techniques, which offer certain advantages over previous CTP studies. It emphasizes the radiomic texture changes before and after treatment, avoiding the gray areas that are indistinguishable by the naked eye, thus supplementing the deficiencies of previous research and promoting new developments in CTP radiomics. More importantly, this study incorporated machine learning models and used SHAP plots to verify the predictive factors of the nomogram, and conducted corresponding clinical practical applications (29).

Limitations

Firstly, due to the single-center nature of the study, the sample size remains relatively small, and the study population is primarily Han Chinese, with potential differences in dietary and lifestyle habits. Consequently, biases may inevitably exist in the study results. Future research will involve multi-center and multi-regional studies to validate the conclusions of this study. The use of unsupervised fully or semi-automatic delineation of infarcted regions of interest (ROIs) was not employed, potentially introducing errors. The exclusion of radiomic parameters from MR plain scans and multi-phase enhanced scans may

have omitted meaningful variables. Additionally, this study did not utilize radiomics to assess the impact of HT-ACI status on patient prognosis, which may limit or challenge clinical decisions based on these study results. This study focuses on anterior circulation ischemic stroke and does not investigate the value of CTP radiomics in middle-posterior circulation stroke or venous stroke. However, we believe that this research also holds certain value in other subtypes of stroke, and we anticipate future studies with larger sample sizes to validate this conclusion. Although we included patients' age and gender as calibration factors in our multivariate statistical analysis, and we also tried our best to balance the proportion of positive patients in the training and test sets to enhance the reliability and robustness of this study, differences in sample size are inevitable, which has raised concerns about the generality and reliability of the results. In the future, we plan to expand our sample size to 5,000 cases to reduce the error caused by this imbalance, and we believe that the results of this study hold some significance (30).

Conclusion

In summary, the Delta radscore has demonstrated significant clinical value in the study of HT-ACI. The novel nomogram established based on the Delta radscore may simplify and effectively predict HT-ACI, aiding in improving treatment decisions for patients with acute cerebral infarction and enhancing perioperative care. With continuous advancements in imaging technology and deepening research, the application of radiomics in the field of cerebral hemorrhage will become increasingly widespread, offering more possibilities for disease prevention, diagnosis, and treatment.

Data availability statement

The original contributions presented in the study are included in the article/supplementary material, further inquiries can be directed to the corresponding authors.

Ethics statement

The research protocol was developed in accordance with the guidelines of the Helsinki Declaration and has been reviewed and approved by the Human Ethics Committee of Xiangyang No.1 People's Hospital affiliated with Hubei University of Medicine (Approval no. XYYYE20240011). The studies were conducted in accordance with the local legislation and institutional requirements. The participants provided their written informed consent to participate in this study.

Author contributions

XW: Conceptualization, Data curation, Writing – original draft. JY: Data curation, Formal analysis, Writing – original draft. XJ: Methodology, Writing – original draft. YY: Data curation, Formal analysis, Software, Writing – original draft. PS: Investigation, Methodology, Writing – original draft. LS: Data curation, Supervision, Writing – review & editing. PA: Software, Supervision, Validation, Writing – review & editing.

Funding

The author(s) declare that financial support was received for the research, authorship, and/or publication of this article. This research was funded by the "323" Major Chronic Disease Project of the Hubei Health Commission and Xiangyang No.1 People's Hospital (XYY2022-323). General Program of the Natural Science Foundation of Hubei Province (Exploring the Prediction of Immunophenotyping and Prognosis Modeling for Oropharyngeal Cancer through Multi-modality Imaging-Pathomics Combined with Generalized Machine Learning – JCZRYB202501213-belonged to Peng An). Innovative Research Program of Xiangyang No.1 People's Hospital (XYY2025QN16 and XYY2025SD17). This study was supported by the Xiangyang Science and Technology Plan Key Project Fund (2022YL31B).

Conflict of interest

The authors declare that the research was conducted in the absence of any commercial or financial relationships that could be construed as a potential conflict of interest.

Generative AI statement

The authors declare that no Generative AI was used in the creation of this manuscript.

Publisher's note

References

1. Uchida Y, Kan H, Kano Y, Onda K, Sakurai K, Takada K, et al. Longitudinal changes in iron and myelination within ischemic lesions associate with neurological outcomes: a pilot study. *Stroke*. (2024) 55:1041–50. doi: 10.1161/STROKEAHA.123.044606

2. Wang R, Zeng J, Wang F, Zhuang X, Chen X, Miao J. Risk factors of hemorrhagic transformation after intravenous thrombolysis with rt-PA in acute cerebral infarction. *QJM*. (2019) 112:323–6. doi: 10.1093/qjmed/hcy292

3. Xu X, Li C, Wan T, Gu X, Zhu W, Hao J, et al. Risk factors for hemorrhagic transformation after intravenous thrombolysis in acute cerebral infarction: a retrospective single-center study. *World Neurosurg*. (2017) 101:155–60. doi: 10.1016/j.wneu.2017.01.091

4. Liu X, Zhang J, Tian C, Wang J. The relationship of leukoaraiosis, haemorrhagic transformation and prognosis at 3 months after intravenous thrombolysis in elderly patients aged ≥ 60 years with acute cerebral infarction. *Neurol Sci*. (2020) 41:3195–200. doi: 10.1007/s10072-020-04398-2

5. Ren H, Song H, Wang J, Xiong H, Long B, Gong M, et al. A clinical-radiomics model based on non-contrast computed tomography to predict hemorrhagic

transformation after stroke by machine learning: a multicenter study. *Insights Imaging*. (2023) 14:52. doi: 10.1186/s13244-023-01399-5

6. Pilato F, Silva S, Valente I, Distefano M, Broccolini A, Brunetti V, et al. Predicting factors of functional outcome in patients with acute ischemic stroke admitted to neuro-intensive care unit-a prospective cohort study. *Brain Sci*. (2020) 10:911. doi: 10.3390/brainsci10120911

7. Heo J, Sim Y, Kim BM, Kim D, Kim Y, Nam H, et al. Radiomics using non-contrast CT to predict hemorrhagic transformation risk in stroke patients undergoing revascularization. *Eur Radiol*. (2024) 34:6005–15. doi: 10.1007/s00330-024-10618-6

8. Ru X, Zhao S, Chen W, Wu J, Yu R, Wang D, et al. A weakly supervised deep learning model integrating non-contrasted computed tomography images and clinical factors facilitates haemorrhagic transformation prediction after intravenous thrombolysis in acute ischaemic stroke patients. *Biomed Eng Online*. (2023) 22:129. doi: 10.1186/s12938-023-01193-w

9. Sun T, Yu HY, Zhan CH, Guo HL, Luo MY. Non-contrast CT radiomics-clinical machine learning model for futile recanalization after endovascular treatment in anterior circulation acute ischemic stroke. *BMC Med Imaging*. (2024) 24:178. doi: 10.1186/s12880-024-01365-7

10. Hao Y, Zhou H, Pan C, Xie G, Hu J, Zhang B, et al. CASE II investigators. Prediction factors and clinical significance of different types of hemorrhagic transformation after intravenous thrombolysis. *Eur J Med Res*. (2023) 28:509. doi: 10.1186/s40001-023-01503-x

11. Ma Y, Xu DY, Liu Q, Chen HC, Chai EQ. Nomogram prediction model for the risk of intracranial hemorrhagic transformation after intravenous thrombolysis in patients with acute ischemic stroke. *Front Neurol*. (2024) 15:1361035. doi: 10.3389/fneur.2024.1361035

12. Uchida Y, Kan H, Inoue H, Oomura M, Shibata H, Kano Y, et al. Penumbra detection with oxygen extraction fraction using magnetic susceptibility in patients with acute ischemic stroke. *Front Neurol*. (2022) 13:752450. doi: 10.3389/fneur.2022.752450

13. Zhang Y, Xie G, Zhang L, Li J, Tang W, Wang D, et al. Constructing machine learning models based on non-contrast CT radiomics to predict hemorrhagic transformation after stoke: a two-center study. *Front Neurol*. (2024) 15:1413795. doi: 10.3389/fneur.2024.1413795

14. Cao YZ, Zhao LB, Jia ZY, Liu QH, Xu XQ, Shi HB, et al. Cerebral blood volume Alberta stroke program early computed tomography score predicts intracranial hemorrhage after thrombectomy in patients with acute ischemic stroke in an extended time window. *Acta Radiol*. (2022) 63:393–400. doi: 10.1177/0284185121990843

15. Shi L, Rong Y, Daly M, Dyer B, Benedict S, Qiu J, et al. Cone-beam computed tomography-based delta-radiomics for early response assessment in radiotherapy for locally advanced lung cancer. *Phys Med Biol*. (2020) 65:015009:015009. doi: 10.1088/1361-6560/ab3247

16. Xu Q, Zhu Y, Zhang X, Kong D, Duan S, Guo L, et al. Clinical features and FLAIR radiomics nomogram for predicting functional outcomes after thrombolysis in ischaemic stroke. *Front Neurosci*. (2023) 17:1063391. doi: 10.3389/fnins.2023.1063391

17. Li W, Qi Z, Kang H, Qin X, Song H, Sui X, et al. Serum occludin as a biomarker to predict the severity of acute ischemic stroke, hemorrhagic transformation, and patient prognosis. *Aging Dis*. (2020) 11:1395–406. doi: 10.14336/AD.2020.0119

18. Gu Y, Xu C, Zhang Z, Fang C, Yu J, He D, et al. Association between infarct location and haemorrhagic transformation of acute ischaemic stroke after intravenous thrombolysis. *Clin Radiol*. (2024) 79:e401–7. doi: 10.1016/j.crad.2023.11.024

19. Wen X, Xiao Y, Hu X, Chen J, Song F. Prediction of hemorrhagic transformation via pre-treatment CT radiomics in acute ischemic stroke patients receiving endovascular therapy. *Br J Radiol*. (2023) 96:20220439. doi: 10.1259/bjr.20220439

20. Uchida Y, Kan H, Furukawa G, Onda K, Sakurai K, Takada K, et al. Relationship between brain iron dynamics and blood-brain barrier function during childhood: a quantitative magnetic resonance imaging study. *Fluids Barriers CNS*. (2023) 20:60. doi: 10.1186/s12987-023-00464-x

21. Mohd Said MR, Mohd Firdaus MAB. Haemorrhagic transformation: a serious complication of massive ischemic stroke. *Med J Malaysia*. (2021) 76:258–60.

22. You S, Wang Y, Wang X, Maeda T, Ouyang M, Han Q, et al. Twenty-four-hour post-thrombolysis NIHSS score as the strongest prognostic predictor after acute ischemic stroke: ENCHANTED study. *J Am Heart Assoc*. (2024) 13:e036109:e036109. doi: 10.1161/JAHA.124.036109

23. Meng Y, Wang H, Wu C, Liu X, Qu L, Shi Y. Prediction model of hemorrhage transformation in patient with acute ischemic stroke based on multiparametric MRI Radiomics and machine learning. *Brain Sci*. (2022) 12:858. doi: 10.3390/brainsci12070858

24. Froelich MF, Thierfelder KM, Rotkopf LT, Fabritius M, Kellert L, Tiedt S, et al. Impact of collateral filling delay on the development of subacute complications after acute ischemic stroke. *Clin Neuroradiol*. (2020) 30:331–7. doi: 10.1007/s00062-019-00760-w

25. Zhai D, Wu Y, Cui M, Liu Y, Zhou X, Hu D, et al. Combinations of clinical factors, CT signs, and Radiomics for differentiating high-density areas after mechanical Thrombectomy in patients with acute ischemic stroke. *AJNR Am J Neuroradiol*. (2025) 46:66–74. doi: 10.3174/ajnr.A8434

26. Jiang YL, Zhao QS, Li A, Wu ZB, Liu LL, Lin F, et al. Advanced machine learning models for predicting post-thrombolysis hemorrhagic transformation in acute ischemic stroke patients: a systematic review and meta-analysis. *Clin Appl Thromb Hemost*. (2024) 30:10760296241279800. doi: 10.1177/10760296241279800

27. Xie G, Li T, Ren Y, Wang D, Tang W, Li J, et al. Radiomics-based infarct features on CT predict hemorrhagic transformation in patients with acute ischemic stroke. *Front Neurosci*. (2022) 16:1002717. doi: 10.3389/fnins.2022.1002717

28. Liu C, Dong Z, Xu L, Khursheed A, Dong L, Liu Z, et al. MR image features predicting hemorrhagic transformation in acute cerebral infarction: a multimodal study. *Neuroradiology*. (2015) 57:1145–52. doi: 10.1007/s00234-015-1575-8

29. Han S, Huang R, Yao F, Lu Z, Zhu J, Wang H, et al. Pre-treatment spectral CT combined with CT perfusion can predict hemorrhagic transformation after thrombolysis in patients with acute ischemic stroke. *Eur J Radiol*. (2022) 156:110543:110543. doi: 10.1016/j.ejrad.2022.110543

30. Honig A, Molad J, Horev A, Simaan N, Sacagiu T, Figolio A, et al. Predictors and Prognostic Implications of Hemorrhagic Transformation Following Cerebral Endovascular Thrombectomy in Acute Ischemic Stroke: A Multicenter Analysis. *Cardiovasc Intervent Radiol*. (2022) 45:826–833. doi: 10.1007/s00270-022-03115-0

frontiers | Frontiers in Neurology

TYPE Original Research
PUBLISHED 06 March 2025
DOI 10.3389/fneur.2025.1508148

OPEN ACCESS

EDITED BY
Liang Jiang,
Nanjing Medical University, China

REVIEWED BY
Romella Durrani,
University of Calgary, Canada
Juha Lempiäinen,
Helsinki University Central Hospital, Finland

*CORRESPONDENCE
Brian T. Gold
✉ brian.gold@uky.edu

RECEIVED 08 October 2024
ACCEPTED 10 February 2025
PUBLISHED 06 March 2025

CITATION
Bauer CE, Zachariou V, Pappas C, Maillard P, DeCarli C, Caprihan A and Gold BT (2025) Healthy dietary intake diminishes the effect of cerebral small vessel disease on cognitive performance in older adults.
Front. Neurol. 16:1508148.
doi: 10.3389/fneur.2025.1508148

Healthy dietary intake diminishes the effect of cerebral small vessel disease on cognitive performance in older adults

Christopher E. Bauer[1], Valentinos Zachariou[2], Colleen Pappas[1], Pauline Maillard[3,4], Charles DeCarli[3,4], Arvind Caprihan[5] and Brian T. Gold[1,6,7]*

[1]Departments of Neuroscience, University of Kentucky, Lexington, KY, United States, [2]Behavioral Science, University of Kentucky, Lexington, KY, United States, [3]Departments of Neurology, University of California, Davis, Davis, CA, United States, [4]Center for Neurosciences, University of California, Davis, Davis, CA, United States, [5]The Mind Research Network, Albuquerque, NM, United States, [6]Sanders-Brown Center on Aging, University of Kentucky, Lexington, KY, United States, [7]Magnetic Resonance Imaging and Spectroscopy Center, University of Kentucky, Lexington, KY, United States

Introduction: We evaluated whether regular dietary intake of nutrients commonly found in fish, unsaturated oils, and nuts would moderate the associations between neuroimaging biomarkers of cerebral small vessel disease (cSVD) and cognitive function in older adults.

Methods: Dietary information, Montreal Cognitive Assessment (MoCA) scores, and magnetic resonance imaging (MRI) scans were collected from 71 older adults without dementia (60–86 years). MRI biomarkers of cSVD were calculated for each participant. Multivariate linear regression models were computed using dietary intake as the moderating variable. Covariates included age, sex, and estimated intracranial volume.

Results: Dietary intake moderated the association between several cSVD biomarkers and MoCA scores such that the expected negative association between cSVD biomarkers and cognition was seen at low levels of healthy dietary intake, but not at medium or high levels. A dietary intake by age moderation was not observed.

Discussion: Our findings indicate that healthy dietary intake may confer cognitive reserve against cSVD in older adults.

KEYWORDS

cerebral small vessel disease, cerebrovascular disease, vascular contributions to cognitive impairment and dementia, peak width of skeletonized mean diffusivity, Mediterranean diet, cognitive reserve, nutrition, free water

1 Introduction

Vascular contributions to cognitive impairment and dementia (VCID) are very common in older adults and represent a growing public health risk (1–3). VCID commonly results from cerebral small vessel disease (cSVD), which can be assessed *in vivo* using magnetic resonance imaging (MRI), including several recently developed and validated MRI biomarkers (4). It is known that cSVD can increase significantly with age and contributes to cognitive impairment years prior to the development of dementia (2, 5). Risk factors for cSVD include hypertension, hyperlipidemia, unhealthy diet, sedentary lifestyle, and smoking, among others (2, 5).

Despite the knowledge of risk factors, relatively little is known about how modifiable lifestyle variables confer reserve against cSVD and/or its effects on cognition. According to recent consensus frameworks, the term "reserve" serves as an umbrella that can take three specific forms: cognitive reserve, brain reserve, and brain maintenance (6, 7). Cognitive reserve (sometimes called "resilience") refers to cases in which one's cognitive function is better than expected by their brain health. Brain reserve refers to cases in which having more brain resources (e.g., larger brains or less cSVD, leaving more viable brain tissue available) is associated with better cognitive function. Finally, brain maintenance (sometimes called "resistance") refers to less decline in neural resources than expected by one's age, that is associated with better cognitive performance (6–8).

Brain reserve, cognitive reserve, and brain maintenance have all been studied extensively in the context of Alzheimer's disease (AD) pathology (6, 7, 9). In contrast, only a handful of studies have explored potential reserve variables in cSVD (10–15). However, findings from this research have been mixed, with some studies finding evidence of cognitive reserve (13, 15–18) or brain maintenance (11), and others reporting null effects [cognitive reserve; (10, 14); brain maintenance (12, 15)].

Several factors could contribute to these discrepant findings. First, the reserve variables explored in these studies (early life education, occupational attainment, leisure activities, etc.) are selected based on evidence of reserve typically seen in the context of AD pathology (10, 13), yet the sensitivity of these factors to reserve against cSVD is relatively unknown. Several of these factors are also considered "static," or not modifiable at an advanced age (early life education, occupational attainment). Further, most studies report results from only one reserve factor such as education or leisure activities. Additional research is needed to explore multiple reserve factors in the same study participants to assess the specificity of potential factors providing reserve against cSVD.

Dietary patterns are an important but underexplored potential reserve variable against cSVD given the known association between dietary intake and cSVD generally (19–22). The Mediterranean diet (23) in particular has been identified as a potential candidate for cSVD prevention (19, 20, 24, 25). The Mediterranean diet is also strongly associated with improved cognitive performance and reduced risk of cognitive impairment and risk of dementia (26, 27).

These findings warrant the investigation of dietary intake, particularly dietary intake containing core components of the Mediterranean diet, as a factor that potentially builds reserve against cSVD. Here we explored this possibility using a cross-sectional design. While reserve is optimally measured longitudinally, cross-sectional studies remain important, particularly in emerging fields such as this, in that they can provide preliminary data to develop hypotheses for more expensive and time consuming longitudinal studies and aid in formulation of conceptual frameworks (9). We investigated whether dietary factors might contribute to brain reserve, cognitive reserve, or brain maintenance using cross-sectional analyses recommended by the consensus criteria for each type of reserve (6, 7).

Specifically, evidence for brain reserve would come from a main effect of cSVD on cognitive function (i.e., having less cSVD results in better cognitive performance). Evidence of cognitive reserve would come from a statistical interaction between dietary intake and cSVD on cognitive function. For example, older adults with high cSVD may perform better than expected by their brain status if they practice healthy dietary intake, possibly due to molecular, cellular or network alterations. Finally, evidence of brain maintenance (i.e., resistance) would come from an interaction between dietary intake and chronological age on cSVD biomarkers (i.e., older adults show less cSVD than expected by their age if they practice healthy dietary intake).

As our interest here relates to cSVD, we used three extensively validated MRI biomarkers of cSVD from the MarkVCID consortium [white matter hyperintensity volume (WMH volume) (28), free water (FW) (28, 29), peak width of skeletonized mean diffusivity (PSMD) (28, 30)]. Cognition was assessed using a validated measure of cognitive status, the Montreal Cognitive Assessment (MoCA), a test routinely used in clinical settings due to its sensitivity to detect early cognitive dysfunction (31). Finally, we assessed the specificity of our findings related to healthy dietary intake by testing for the presence of similar relationships when using the Cognitive Reserve Index questionnaire (CRIq) (32) as the potential reserve variable.

2 Materials and methods

2.1 Participants

Seventy-one participants were recruited from the Sanders-Brown Center on Aging (SBCoA) longitudinal cohort (33) and the greater Lexington community. Inclusion criteria for enrollment in the SBCoA longitudinal cohort are neurological and cognitive normality at enrollment (examination based on clinical consensus), willingness to undergo annual physical, neurological, and cognitive examinations, blood draw, appointment of a designated informant for structured interviews, and a minimum of 60 years of age. Exclusion criteria are major psychiatric illness, untreated depression, current substance abuse, medical illnesses that are nonstable, impairing, or affect the CNS, chronic infectious diseases, stroke or transient ischemic attack, epilepsy, meningitis, encephalitis, or a history of head injury. Participants recruited from the community had the same exclusion criteria.

Additional exclusion criteria for the current study were MRI-related contraindications (i.e., claustrophobia, metal implants, metal fragments, pacemakers), brain abnormalities discovered through imaging, or disease affecting the blood (heart disease, kidney disease, anemia). Additional inclusion criteria for the current study was the absence of dementia at the time of the MRI scan, the completion of a nutrient questionnaire ["Newly Developed Antioxidant Nutrient Questionnaire" (NDANQ) (34)], the Cognitive Reserve Index questionnaire (CRIq) (32) and the Montreal Cognitive Assessment (MoCA) (31). Absence of

Abbreviations: cSVD, Cerebral Small Vessel Disease; CVD, Cerebrovascular Disease; VCID, Vascular Contributions to Cognitive Impairment and Dementia; AD, Alzheimer's Disease; FON, Fish Oils and Nuts; WMH volume, White Matter Hyperintensity Volume; FW, Free Water; PSMD, peak Width of Skeletonized Mean Diffusivity; CR, Cognitive Reserve; CRIq, Cognitive Reserve Index Questionnaire; MoCA, Montreal Cognitive Assessment.

dementia was determined by annual clinical consensus diagnosis or a score of 18 or greater on the MoCA (31), where 18 is the lower cutoff value for mild cognitive impairment.[1] The MoCA was completed for each participant within 13 months of the scan date.

A total of 71 older adults (ages 60–86) met initial eligibility criteria for the present study. All participants provided informed consent under a protocol approved by the Institutional Review Board of the University of Kentucky.

2.2 Image acquisition

Images were acquired from a 3 Tesla Siemens Magnetom Prisma MRI scanner with a 64-channel head coil at the University of Kentucky's Magnetic Resonance Imaging and Spectroscopy Center (MRISC). Data from four sequences were collected in the following order: (1) a 3D multi-echo, T1-weighted magnetization prepared rapid gradient echo (T1) sequence; (2) a 3D fluid-attenuated inversion recovery (FLAIR) sequence; (3) a spin-echo, echo-planar multi-shell diffusion-weighted sequence, and (4) a spin-echo, echo-planar diffusion-weighted sequence with reverse phase-encoding direction from the main diffusion sequence. Data from several other sequences pertaining to unrelated scientific questions were also collected during the session and are not further described here.

The T1 scan had four echoes [first echo time (TE) = 1.69 ms, echo spacing = 1.86 ms], and covered the entire brain [256 × 256 × 176 mm acquisition matrix (176 slices), repetition time (TR) = 2,530 ms, 1 mm isotropic voxels, flip angle = 7°, scan duration = 5.88 min]. The 3D FLAIR sequence covered the entire brain (256 × 256 × 176 mm acquisition matrix, TR = 5,000 ms, TE = 38 ms, 1 mm isotropic voxels, inversion time = 1800 ms, scan duration = 6.45 min). The main multi-shell diffusion sequence was acquired with 126 separate diffusion directions [232 × 232 × 162 mm acquisition matrix (81 slices), TR = 3,400 ms, TE = 71 ms, 2 mm isotropic voxels, posterior-to-anterior phase encoding direction, multislice acceleration factor = 3, phase partial Fourier = 6/8, and scan duration = 7.45 min] divided between 4 b-values [0 s/mm^2 (12 directions), 500 s/mm^2 (6 directions), 1,000 s/mm^2 (48 directions), and 2000 s/mm^2 (60 directions)]. The short (28-s) diffusion sequence was collected using the same parameters as the main diffusion sequence but used the reverse-phase encoding direction (anterior-to-posterior phase encoding direction) and 2 b-values (0 and 2000 s/mm^2). The non-diffusion weighted (b = 0 s/mm^2) images were used to correct for susceptibility-induced distortions as recommended by FSL's topup (35).

2.3 T1 segmentation

The four echoes from the multi-echo T1 scan were averaged into a root mean square (RMS) image, as described previously (36). The RMS T1 images were then examined visually to ensure no participants had significant brain abnormalities, motion artifacts, or poor contrast that could interfere with segmentation accuracy. All T1 images passed quality control criteria and were automatically segmented into gray matter, white matter and cerebrospinal fluid (CSF) using the recon-all option in FreeSurfer 6.0 (37). Estimated intracranial volume (eICV, mm^3) was used as a covariate in subsequent analyses.

2.4 White matter hyperintensity analyses

White matter hyperintensity volume (WMH volume) was computed using a validated 4-tissue segmentation method (38, 39) used in the Alzheimer's Disease Neuroimaging Initiative (ADNI) analysis pipeline and the MarkVCID consortium (28).[2] First, participant's FLAIR images were registered to their T1 image (RMS image; see *section 2.3*) using FLIRT from the FMRIB Software Library version 6.0.1 [FSL; (40)]. FLAIR images were then corrected for inhomogeneities using local histogram normalization (41) and were non-linearly aligned to a minimal deformation template (39).

FLAIR images were then segmented in template space using Bayesian probability based on histogram fitting and prior probability maps. Voxels segmented as WMHs must also have exceeded 3.5 SDs above the mean WM signal intensity. WMHs were visually examined to ensure quality segmentation and volume estimation. Manual editing was accomplished by labeling false positive FLAIR hyperintensities as background, typically in the septum pellucidum and other membranes surrounding the ventricular areas. The segmented WMH volumes were then back-transformed to native space where the total volume for each participant was reported in cubic millimeters. Finally, each participant's WMH volume was log transformed, as WMH volume was non-normally distributed in our sample.

2.5 Free water and peak width of skeletonized mean diffusivity analysis

2.5.1 Diffusion-weighted imaging preprocessing

Pre-processing and processing for diffusion MRI data has been described in our previous work (42). Briefly, each participant's diffusion data was corrected for susceptibility induced distortions using a reverse phase-encoded scan in FSL's topup (35), skull-stripped with BET (43), and corrected for eddy currents and participant motion with eddy (44). All diffusion MRI data was examined visually to ensure quality. No participants had 2 mm or greater average head motion across volumes as assessed using eddy QC tools [eddyqc tools: QUality Assessment for DMRI (QUAD) and Study-wise QUality Assessment for DMRI (SQUAD)], and therefore no participants were excluded for excessive motion.

1 https://mocacognition.com/faq/

2 https://markvcid.partners.org

2.5.2 Diffusion-tensor processing

Fractional anisotropy (FA) maps were calculated using FSL's DTIFIT. This function computes the diffusion tensor model and eigenvalues within each voxel from each participant's preprocessed diffusion MRI data.

2.5.3 Free water processing

Free water (FW) maps were computed for each participant using the FW kit, developed and validated through the MarkVCID consortium (28), which in this study was adapted for multi-shell diffusion data. FW maps were calculated for each participant using a two-compartment model of the multi-shell Free Water Diffusion Tensor Imaging algorithm (45) from the open-source software package Diffusion Imaging in Python [DIPY; (46)]. FW maps were then transformed into standard space (standard FSL template FMRIB 1-mm FA template) using parameters calculated by registering the participant's FA map to the same standard space. White matter throughout the brain (global white matter) is then defined using the FMRIB 1-mm FA template after applying a 0.3 threshold to reduce cerebrospinal fluid partial volume contamination. This thresholded template is then used an as ROI mask. The mean value of all voxels in the FW map within this ROI are then extracted to produce the mean free water value for each participant.

2.5.4 Peak width of skeletonized mean diffusivity processing

Peak width of skeletonized mean diffusivity (PSMD) (47) was computed for each participant using the PSMD kit developed and validated through the MarkVCID consortium (28). First, each participant's FA map was registered to a standard FSL template (FMRIB 1-mm FA). FSL's Tract-Based Spatial Statistics (TBSS) pipeline was then used to produce a group FA skeleton, with each participants' FA data projected onto the skeleton. A threshold of 0.2 was then used exclude non-WM voxels. Each participant's MD map is then projected onto the thresholded FA skeleton using the FA-derived projection parameters, and further thresholded with a template skeleton mask to reduce CSF volume contamination. Finally, PSMD is calculated as the difference between the 95th and 5th percentiles in MD values within the skeleton.

2.6 Calculation of CRIq scores

The CRIq was administered according to the published instructions (32). Broadly, the CRIq asks participants about frequency and the number of years engaged in several leisure activities throughout the lifespan (CRIq-Leisure Time), the number of years worked in various occupations throughout the lifespan (CRIq-Working Activity), and the number of years of early life education (CRIq-Education). Scores from each of the three subscales are then calculated based on residuals from linear regression models (32). The total CRIq score is then calculated as the average of the three subscores (32).

2.7 Nutrition data acquisition and analysis

The nutrition factor used in this study (which represents nutrients commonly found in fish, healthy oils and nuts: FON factor) was identified as part of our previous work exploring the role of dietary factors on brain iron levels in older adults (48). Three nutrition factors were identified in that work, as described below. In the present work, we focused on dietary factor 2 (FON factor) as a potential reserve variable against cSVD because it constitutes a core component of the Mediterranean diet (49) and was the only factor that was correlated with cognitive performance in our previous work (48).

Participants completed an online version of the "Newly Developed Antioxidant Nutrient Questionnaire" (NDANQ) (34), where they self-reported the quantity they consumed per day of 92 food items and 15 over-the-counter supplements/multivitamins during the preceding month (48). Survey data was processed using in-house developed software (48) to convert foods consumed per day into milligrams (mg) of nutrients per day on a total of 122 nutrients. This conversion was done automatically using the United States Department of Agriculture (USDA) Research Service databases: the National Nutrient Database for Standard Reference,[3] the flavonoid values for USDA survey foods and beverages (50),[4] and the food and nutrient database for dietary studies.[5] A literature review was then used to narrow the nutrient list down to only a subset that can cross the blood brain barrier and either chelate brain iron or reduce oxidative stress. Following this criteria the nutrient subset was narrowed to vitamin C, vitamin E, quercetin, lysine, epigallocatechin 3-gallate, β-carotene, β-cryptoxanthin, docosahexaenoic acid omega-3 (DHA), and omega-6 polyunsaturated fatty acids (PUFAs) (51).

Nutrients that co-varied were grouped into largely independent nutrition factors (48) using exploratory factor analysis in SPSS 27 (IBM, Chicago, IL, United States). The analysis used the nutrients identified in the previous paragraph as inputs, with principal components as the extraction method under the assumption that factors may not be independent (48). Factor scores were created for the nutrition factors using the regression method (52). Ultimately, 3 dietary factors were identified with this analysis. Vitamin C, quercetin, β-carotene, and β-cryptoxanthin loaded onto dietary factor 1, vitamin E, lysine, docosahexaenoic acid omega-3, and omega-6 polyunsaturated fatty acids loaded onto dietary factor 2, while epigallocatechin 3-gallate loaded onto dietary factor 3. In terms of food groups, dietary factor 1 largely represents nutrients derived from common vegetables and fruits (VF factor), dietary factor 2 largely represents nutrients derived from fish, (healthy) oils, and nuts (FON factor), while dietary factor 3 represents epigallocatechin 3-gallate, which is found in many herbs and tea (48).

2.8 Statistical analyses

We first explored whether reduced cSVD would be associated with better cognition (brain reserve) and/or whether FON dietary intake may interact with cSVD when predicting cognition (cognitive reserve). Three multivariate linear regression models were conducted to test FON factor,

3 release 28; May 2016; https://www.ars.usda.gov/northeast-area/beltsville-md-bhnrc/beltsville-human-nutrition-research-center/methods-and-application-of-food-composition-laboratory/mafcl-site-pages/sr11-sr28/

4 https://www.ars.usda.gov/northeast-area/beltsville-md-bhnrc/beltsville-human-nutrition-research-center/food-surveys-research-group/docs/fndds-flavonoid-database/

5 https://www.ars.usda.gov/northeast-area/beltsville-md-bhnrc/beltsville-human-nutrition-research-center/food-surveys-research-group/docs/fndds-download-databases/

VCID biomarkers, and the interaction between FON factor and VCID biomarkers, as predictors of MoCA scores. Each model used a different VCID biomarker (WMH volume, FW, or PSMD) as a predictor. All models were corrected for age (years), sex, education (years), and estimated intracranial volume (eICV; mm^3).

We then explored whether FON dietary intake might help preserve brain health relative to chronological age (as a brain maintenance variable). Three additional multivariate linear regression models were conducted to test FON factor, age, and the interaction between FON factor and age, as predictors of VCID biomarkers. Each model used a different VCID biomarker (WMH volume, FW, PSMD) as the dependent variable. Sex, education (years) and estimated intracranial volume (eICV; mm^3) were included as covariates in each model.

Finally, we assessed the potential specificity of FON dietary intake as a reserve factor by substituting in a more traditional reserve proxy in all models. All six multivariate linear regression models described above were re-run replacing FON factor with the CRIq (32). Covariates remained the same as they were in the original models, except that education was removed as a covariate due to its similarity to the CRIq.

Statistical analyses were conducted using SPSS 28 (IBM, Chicago, IL, United States). Results were considered statistically significant at $p < 0.05$ using a false discovery rate (FDR) approach (53). Both MoCA scores and WMH volume were not normally distributed and were therefore log transformed. Statistical outliers were defined as values greater than 3.29 standard deviations from the group mean and were excluded from relevant analyses. Error residuals in all linear regression models were examined for the assumption of normality. Multivariate linear regression models with moderation were conducted through the PROCESS macro (version 4.0) in SPSS (54). Moderator variables were mean centered. Significant interactions were probed using the pick-a-point approach, which uses all the data (no grouping) to demonstrate moderation effects at 16% (low), 50% (medium), and 84% (high) of the moderator value (which corresponds to the mean value + − 1 SD) (54). VCID biomarkers were considered to be the independent variable while reserve variables (FON factor, CRIq scores) were considered to be the moderator when probing interactions for cognitive reserve. Statistics for significance (p-values) in moderation probing indicate whether the slope of the line at the chosen moderation point (low, medium, or high) is significantly different from zero, and are included to fully describe our results.

3 Results

Participant demographics are summarized in Table 1. One participant was an outlier for MoCA scores, one participant was an outlier for PSMD, and one participant was an outlier for WMH volume. Data from these participants were excluded from the analyses in which they were outliers. Error residuals followed an approximate normal distribution in all regression models. All results reported below pertain to findings after correction for multiple comparisons, although uncorrected p-values are also reported for transparency.

We first explored associations between VCID biomarkers (WMH volume, FW or PSMD) and MoCA scores. There were trends but no main effects of WMH volume (uncorrected $p = 0.091$), FW (uncorrected $p = 0.053$) or PSMD (uncorrected $p = 0.070$) on MoCA scores. However, there was an interaction between the FON factor and both FW (uncorrected $p = 0.009$) and PSMD (uncorrected $p = 0.008$; Table 2; Figure 1) when predicting MoCA scores. There was no interaction between FON factor and WMH volume (uncorrected $p = 0.137$) when predicting MoCA scores.

TABLE 1 Group demographics, biomarker metrics, and Montreal cognitive assessment (MoCA) scores.

	Mean (S.D.)	*N*
Age (Years)	70.1 (5.9)	71
Sex Ratio (F:M)	43:28	71
Education (Years)	16.7 (2.3)	71
WMH volume	4.71 (5.44)	70
Free water	0.258 (0.015)	71
PSMD	0.27 (0.050)	70
CRIq score	134.6 (17.8)	71
MoCA	26.6 (2.5)	70

CRIq, Cognitive Reserve Index questionnaire; F:M, female to male; standard deviation; MoCA, Montreal Cognitive Assessment; PSMD, Peak Skeletonized Mean Diffusivity; S.D., standard deviation; WMH, White Matter Hyperintensity. The table lists the female/male ratio and mean (± sd) age (years), education (years), white matter hyperintensity volume (cm^3), free water (fraction), peak skeletonized mean diffusivity ($mm^2/s \times 10^{-3}$), total Cognitive Reserve Index questionnaire (CRIq) scores, and MoCA scores for the full sample.

We decomposed the significant interactions between VCID biomarkers (FW and PSMD) and the FON factor on MoCA scores using the pick-a-point approach as described by Hayes (54). This approach determines if the slope of the partial regression plot line between VCID biomarkers and MoCA scores is significantly different from zero at three different values of the moderator [FON factor; 16% (low), 50% (medium), 84% (high)] and provides better characterization of the observed interaction than the interaction terms alone (54). Using this approach, there was a significant negative association between FW and MoCA at low values of the FON factor (Unstandardized $\beta = -1.9627$, 95% CI = −3.0440 – −0.8813, $p < 0.001$) but not between FW and MoCA at medium values of the FON factor ($p = 0.055$) or high values of the FON factor ($p = 0.562$; Figure 1A). Similarly, there was a negative association between PSMD and MoCA at low values of the FON factor (Unstandardized β = −0.5953, 95% CI = −0.9742 – −0.2165, $p = 0.003$), but not at medium ($p = 0.071$) or high ($p = 0.399$) values (Figure 1B).

We then explored potential main effects of age on VCID biomarkers (WMH volume, FW, PSMD) and whether those effects were moderated by the FON factor. There was a main effect of age on each of the VCID biomarkers [WMH volume (uncorrected $p = 0.002$), FW (uncorrected $p < 0.001$), and PSMD (uncorrected $p < 0.001$)]. However, the FON factor did not moderate the association between age and VCID biomarkers in any of the models (Table 3).

When total CRIq scores were used as our reserve variable, there were no main effects of WMH volume (uncorrected $p = 0.695$), FW (uncorrected $p = 0.047$), or PSMD (uncorrected $p = 0.251$) on MoCA scores (Table 4). There were no interactions between total CRIq scores and WMH volume (uncorrected $p = 0.436$), FW (uncorrected $p = 0.311$), or PSMD (uncorrected $p = 0.695$) when predicting MoCA scores. In the three models exploring brain maintenance, CRIq scores also did not moderate the association between age and VCID biomarkers (Table 5). There were no significant main effects or interactions when replacing total CRIq scores with scores specific to any of its subscales

TABLE 2 Associations between VCID biomarkers and MoCA scores using the FON factor as the reserve variable.

Predictor	Unstandardized β	95% CI for β	p value
Model 1			
Age	−0.0009	−0.0030 – 0.0013	0.427
Sex	−0.0309	−0.0602 – −0.0015	0.040*
Education	0.0014	−0.0034 – 0.0062	0.567
Estimated intracranial volume	0.0000	0.0000–0.0001	0.346
FON factor	0.0040	−0.0067 – 0.0146	0.457
WMH volume	−0.0218	−0.0471 – 0.0036	0.091
FON factor x WMH volume	0.0191	−0.0060 – 0.0442	0.137
Model 2			
Age	−0.0007	−0.0027 – 0.0014	0.515
Sex	−0.0310	−0.0578 – −0.0042	0.024*
Education	0.0016	−0.0029 – 0.0061	0.485
Estimated intracranial volume	0.0000	0.0000–0.0001	0.261
FON factor	0.0033	−0.0065 – 0.0132	0.503
Free Water	−0.8128	−1.6379 –0.0123	0.053
FON factor x Free water	1.2239	0.3152–2.1325	0.009*
Model 3			
Age	−0.0008	−0.0029 – 0.0013	0.447
Sex	−0.0278	−0.0552 – −0.0003	0.047*
Education	0.0023	−0.0024 – 0.0069	0.337
Estimated intracranial volume	0.0000	0.0000–0.0001	0.405
FON factor	0.0050	−0.0052 – 0.0152	0.331
PSMD	−0.2274	−0.4743 – 0.0194	0.070
FON factor x PSMD	0.3885	0.1044–0.6727	0.008*

CI, confidence interval; FON, fish oils and nuts; MoCA, Montreal Cognitive Assessment; PSMD, Peak Skeletonized Mean Diffusivity; WMH, White Matter Hyperintensity. #$p < 0.05$ before, *$p < 0.05$ after correction for multiple comparisons. The table displays the unstandardized β estimates, the 95% confidence intervals (CI) for β estimates, and the p values for each predictor in the linear regression models. A different VCID biomarker is explored in each model.

(CRIq-Education, CRIq-Working Activity, or CRIq-Leisure Time) in any models.

As noted above, our analyses focused on the FON factor as it was the only dietary factor that was correlated with cognitive performance in our previous work (48). However, supplementary analyses were conducted to investigate potential moderation effects between VCID biomarkers and nutrients derived from common vegetables and fruits (VF factor; section 2.7) on MoCA scores, due to fruits and vegetables also being a component of the Mediterranean diet (20, 24, 25). Results indicated that, as with FON factor, there was a significant interaction between the VF factor and FW when predicting MoCA scores (uncorrected $p = 0.011$; Supplementary Table S1). However, there was no interaction between VF factor and either PSMD (uncorrected $p = 0.083$) or WMH volume (uncorrected $p = 0.215$) when predicting MoCA scores (Supplementary Table S1).

4 Discussion

Our results indicated that dietary intake of specific nutrients moderated the relationship between MRI markers of VCID and cognition. Specifically, our findings revealed negative associations between several MRI markers of cSVD (FW, PSMD) and MoCA scores in those with low intake of fish, (healthy) oils, and nuts (FON), but not in those with medium or high FON intake. In contrast, FON intake did not moderate the relationship between age and MRI markers of cSVD. Finally, a different potential reserve variable, scores on the Cognitive Reserve Index questionnaire (CRIq), did not moderate either of these relationships. Our findings suggest that the intake of certain dietary nutrients may build cognitive reserve against cSVD in older adults.

4.1 Dietary intake moderates the relationship between diffusion MRI measures of cSVD and cognitive function

Our results demonstrated that the relationships between several established MRI markers of cSVD and cognition were moderated by dietary intake. Specifically, high FW and PSMD values were associated with lower MoCA scores in those with low FON values, but not those with medium or high values. This suggests that healthy dietary intake may promote cognitive reserve against cSVD. Both FW and PSMD are thought to capture subtle cSVD damage associated with VCID (28).

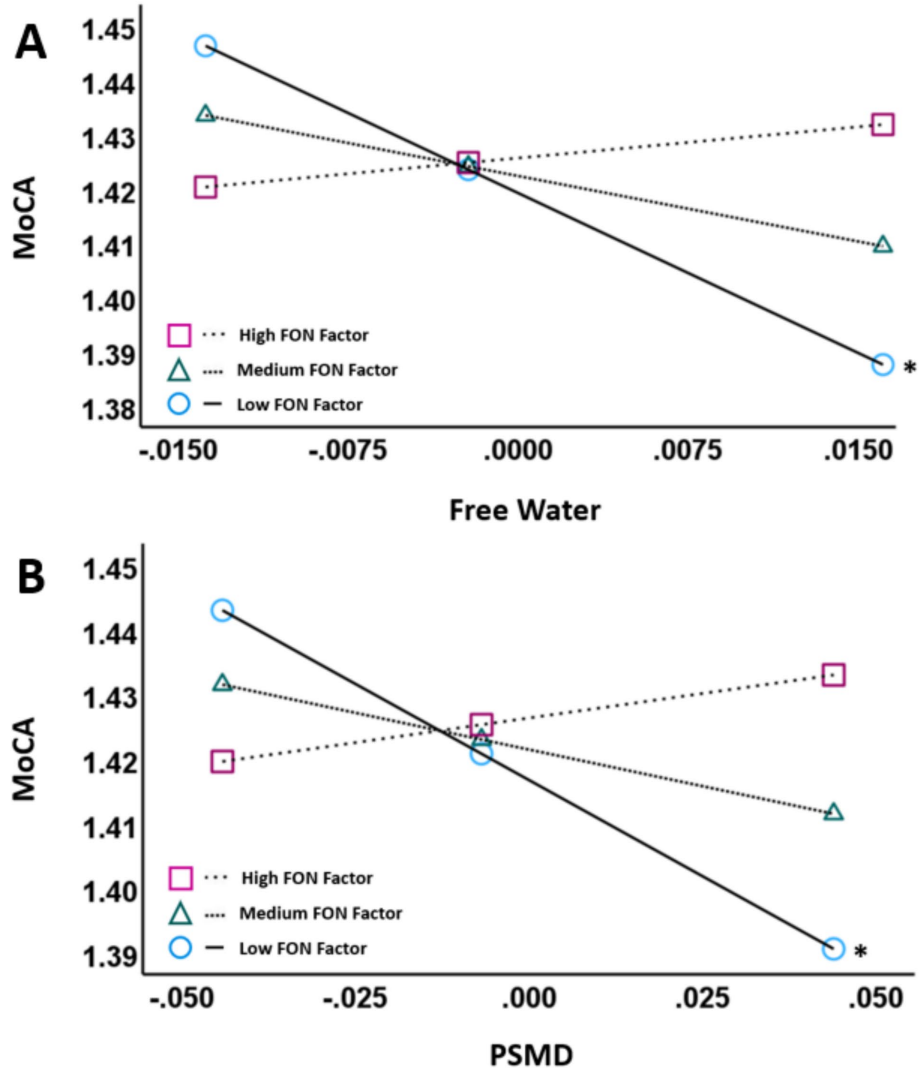

FIGURE 1
Partial regression plots showing FW **(A)** and PSMD **(B)** against MoCA scores. The pick-a-point approach was used to determine whether the slope of the regression line between VCID biomarkers (FW, PSMD; residualized; X-axis) and MoCA scores (log-transformed; Y-axis) were significantly different from zero at 3 different moderator values [High FON factor, Medium FON factor, and Low FON factor]. Both plots control for age, sex, education and ICV. The moderator variable was mean centered. The figures illustrate that there is a negative association between the VCID biomarkers and MoCA scores at low FON factor intake values ($p < 0.01$) but not at medium or high FON factor intake values. Abbreviations: MoCA, Montreal Cognitive Assessment; PSMD, Peak Skeletonized Mean Diffusivity. *$p < 0.05$.

Biologically, high FW primarily reflects increased extracellular water content and has been linked to elevated blood pressure and arterial stiffness (arteriosclerosis) (55), while PSMD reflects heterogeneity of the mean diffusivity values across WM tracts (47) and high PSMD has been linked to lower blood flow (56).

In contrast to the moderation described above, the FON factor did not moderate the relationship between WMH volume and cognitive performance. This may be because macrostructural WMHs reflect more advanced cSVD than microstructural diffusion metrics of FW and PSMD. Specifically, WMHs have been linked with gliosis, axonal degeneration, myelin loss, vacuolation and BBB damage/dysfunction (5, 57, 58). This possibility is in-keeping with evidence that FW and PSMD precede WMH development (47, 55), and that diffusion measures are able to detect alterations in normal-appearing WM (59). Other studies have reported that potential reserve variables (education, reading and vocabulary scores, involvement in social activities, physical activity) do not moderate the relationship between WMH volume and cognition (10, 14), although positive findings have also been reported (13, 16, 18). The present results suggest that certain lifestyle variables build cognitive reserve against relatively early/minor cSVD (microscopic diffusion alterations), but may become overwhelmed as cSVD becomes more advanced (i.e., significant WMH burden).

Our results did not find evidence for dietary intake as a measure of brain reserve. While there were trends found in our results, none of the relationships between cSVD biomarkers and MoCA scores reached significance. These findings are somewhat surprising in that high FW and/or PSMD have been associated with poorer cognitive performance in a number of studies, including validation studies as part of the MarkVCID consortium (29, 83). However, FW and PSMD

TABLE 3 Associations between age and vascular biomarkers using FON factor as the reserve variable.

Predictor	Unstandardized β	95% CI for β	p value
Model 1: WMH volume is DV			
Age	0.0296	0.0111–0.0481	0.002*
Sex	−0.1802	−0.4647 – 0.1042	0.210
Education	0.0010	−0.0464 – 0.0484	0.967
Estimated intracranial volume	0.0011	0.0003–0.0018	0.007*
FON factor	−0.0290	−0.1373 – 0.0794	0.595
Age x FON factor	0.0074	−0.0127 – 0.0276	0.462
Model 2: Free water is DV			
Age	0.0010	0.0005–0.0016	< 0.001*
Sex	0.0009	−0.0072 – 0.0090	0.829
Education	−0.0002	−0.0015 – 0.0012	0.789
Estimated intracranial volume	0.0000	0.0000–0.0001	0.005*
FON factor	0.0001	−0.0030 – 0.0032	0.937
Age x FON factor	0.0003	−0.0003 – 0.0009	0.311
Model 3: PSMD is DV			
Age	0.0040	0.0022–0.0058	< 0.001*
Sex	−0.0008	−0.0289 – 0.0272	0.952
Education	−0.0001	−0.0049 – 0.0047	0.967
Estimated intracranial volume	0.0001	0.0000–0.0002	0.018*
FON factor	−0.0005	−0.0113 – 0.0102	0.921
Age x FON factor	0.0005	−0.0015 – 0.0025	0.610

CI, confidence interval; DV, Dependent Variable; FON, fish oils and nuts; PSMD, Peak Skeletonized Mean Diffusivity; WMH, White Matter Hyperintensity. #$p < 0.05$ before, *$p < 0.05$ after correction for multiple comparisons. The table displays the unstandardized β estimates, the 95% confidence intervals (CI) for β estimates, and the p values for each predictor in the linear regression models. In each model, there is a different vascular biomarker as the dependent variable.

TABLE 4 Associations between VCID biomarkers and MoCA scores using total CRIq scores as the reserve variable.

Predictor	Unstandardized β	95% CI for β	p value
Model 1			
Age	−0.0009	−0.0030 – 0.0014	0.406
Sex	−0.0360	−0.0646 – −0.0069	0.014*
Estimated intracranial volume	0.0000	0.0000–0.0001	0.228
CRIq scores	0.0005	−0.0003 – 0.0013	0.231
WMH volume	−0.0242	−0.0506 – 0.0023	0.069
CRIq x WMH volume	−0.0007	−0.0023 – 0.0009	0.436
Model 2			
Age	−0.0006	−0.0029 – 0.0016	0.589
Sex	−0.0262	−0.0531 – 0.0007	0.056
Estimated intracranial volume	0.0001	0.0000–0.0001	0.196
CRIq scores	0.0003	−0.0004 – 0.0009	0.433
Free water	−0.8763	−1.7390 – 0.0135	0.047#
CRIq x Free water	−0.0203	−0.0601 – 0.0194	0.311
Model 3			
Age	−0.0013	−0.0036 – 0.0010	0.279
Sex	−0.0259	−0.0536 – 0.0018	0.067
Estimated intracranial volume	0.0000	0.0000–0.0001	0.417
CRIq scores	0.0005	−0.0003 – 0.0012	0.200
PSMD	−0.1604	−0.4373 – 0.1164	0.251
CRIq x PSMD	−0.0028	−0.0170 – 0.0114	0.695

CI, confidence interval; CRIq, Cognitive Reserve Index Questionnaire; MoCA, Montreal Cognitive Assessment; PSMD, Peak Skeletonized Mean Diffusivity; WMH, White Matter Hyperintensity. #$p < 0.05$ before, *$p < 0.05$ after correction for multiple comparisons. The table displays the unstandardized β estimates, the 95% confidence intervals (CI) for β estimates, and the p values for each predictor in the linear regression models. A different VCID biomarker is explored in each model.

TABLE 5 Associations between age and vascular biomarkers using CRIq scores as the reserve variable.

Predictor	Unstandardized β	95% CI for β	p value
Model 1: WMH volume is DV			
Age	0.0296	0.0108–0.0484	0.003*
Sex	−0.1891	−0.4690 – 0.0908	0.182
Estimated intracranial volume	0.0011	0.0004–0.0019	0.004*
CRIq scores	−0.0010	−0.0075 – 0.0055	0.757
Age x CRIq scores	−0.0004	−0.0016 – 0.0008	0.533
Model 2: Free water is DV			
Age	0.0011	0.0006–0.0017	0.001*
Sex	0.0008	−0.0070 – 0.0086	0.842
Estimated intracranial volume	0.0000	0.0000–0.0001	0.001*
CRIq scores	−0.0002	−0.0003 – 0.0000	0.082
Age x CRIq scores	0.0000	0.0000–0.0000	0.560
Model 3: PSMD is DV			
Age	0.0043	0.0024–0.0061	< 0.001*
Sex	0.0016	−0.0288 – 0.0256	0.907
Estimated intracranial volume	0.0001	0.0000–0.0002	0.008*
CRIq scores	−0.0003	−0.0010 – 0.0003	0.285
Age x CRIq scores	0.0000	−0.0001 – 0.0001	0.612

CI, confidence interval; CRIq, Cognitive Reserve Index questionnaire; DV, Dependent Variable; PSMD, Peak Skeletonized Mean Diffusivity; WMH, White Matter Hyperintensity. #$p < 0.05$ before, *$p < 0.05$ after correction for multiple comparisons. The table displays the unstandardized β estimates, the 95% confidence intervals (CI) for β estimates, and the p values for each predictor in the linear regression models. In each model, there is a different vascular biomarker as the dependent variable.

were validated in relation to composite cognitive metrics composed of scores on multiple National Alzheimer's Coordinating Center (NACC) Uniform Data Set 3 (UDS-3) measures, whereas the MoCA measure used here is less sensitive to performance on specific cognitive domains. Nonetheless, MoCA performance remains an important measure to use in the field of reserve given that it is a sensitive and widely used measure of global cognitive functioning (60). Future studies are needed to determine which cognitive domains may be most preserved by maintaining cerebrovascular health (i.e., brain reserve).

4.2 Dietary intake does not moderate the relationship between chronological age and MRI measures of cSVD

Evidence for brain maintenance would come from a finding that a putative reserve variable (here dietary intake) mitigates the negative effects of aging on brain health (here cSVD) (6–8). We did not find supportive evidence for brain maintenance in this study. As expected, all of the cSVD biomarkers in our study (WMH volume, FW, PSMD) were negatively associated with chronological age, consistent with other findings (61–68). However, FON factor intake did not moderate the association between age and any of the VCID biomarkers in our study.

As this is the first study to use the MarkVCID MRI biomarkers of FW and PSMD in an experiment focused on dietary intake as a reserve variable, there does not exist a literature in which we can draw comparisons related to our null findings concerning brain maintenance. However, WMH volume has been used in a number of studies on reserve. In general, our null results concerning brain maintenance are similar to others reporting that neither dietary intake (25, 69) nor education (12) protect against WMHs over time in older adults. In contrast, our previous work has shown that high cardiorespiratory fitness (CRF) does diminish the effects of age on WMH volume, such that age is more strongly associated with WMH volume in older adults with low CRF compared to those with high CRF (11). Together, these findings suggest that reserve factors more directly related to blood flow, such as exercise (11), may be more likely than dietary intake to promote brain maintenance (i.e., resistance to the development of age-related WMHs).

4.3 Traditional cognitive reserve measures do not moderate the relationship between diffusion MRI measures of cSVD and cognitive function

Our results further suggest some specificity concerning variables that build cognitive reserve against cSVD. Specifically, unlike healthy dietary intake, scores on the Cognitive Reserve Index questionnaire (CRIq) did not moderate the association between any of the cSVD biomarkers used in this study and MoCA scores. Broadly, the CRIq is comprised of more traditional cognitive reserve variables such as early life education, occupational history, and engagement in recreational activities. Previous work has found that such variables often mitigate the effects of brain pathology on cognitive function (70–73) although null effects have also been reported (74, 75).

Notably, findings related to CRIq as a reserve variable have been reported largely within the context of biomarkers of Alzheimer's disease (AD). Much less work has been conducted exploring CRIq components as potential reserve variables against biomarkers of cSVD. The few studies that have been conducted report fairly mixed findings (10, 14, 15, 17). Overall, the evidence that more traditional cognitive reserve variables actually provide reserve appears less consistent in cSVD than AD.

4.4 Dietary intake as a cognitive reserve variable: some potential underlying mechanisms

The FON factor we used is comprised of the nutrients vitamin E, lysine, DHA, and omega-6 polyunsaturated fatty acids (PUFAs), which are commonly found in the Mediterranean Diet (49). PUFAs [which include DHA (which is an omega-3 PUFA) and omega-6 PUFAs] in particular are well documented in their positive relationship with cardiovascular function (76–79) through a variety of factors including the lowering of blood pressure (76, 78, 79) and plasma cholesterol levels (77–79), increasing general endothelial function (76, 79), and the reduction of atherosclerosis (76, 79).

Recent evidence also suggests omega-3 PUFAs may protect blood–brain barrier (BBB) integrity and alleviate glymphatic dysfunction (78) which are critical to cerebrovascular health. Furthermore, all nutrients included in the FON factor have antioxidant properties (48), which may counteract damage to the endothelium and BBB caused by cSVD-induced oxidative stress (80, 81). The consumption of these nutrients in older adults may then help to counteract (and thereby provide some reserve against) cSVD disease processes captured by FW and PSMD, which would help to preserve cognitive function across the numerous domains associated with the Mediterranean diet (26, 27).

Nevertheless, we do not conclude that nutrients comprising the FON factor are the only ones that may build cognitive reserve against cSVD. In particular, fruits and vegetables (VF factor) represent a component of the Mediterranean diet known to be beneficial to cerebrovascular health (20, 24, 25). In our supplementary analysis, we also found that VF factor moderated the association between FW and MoCA scores, suggesting that the intake of vegetables and fruit may contribute some reserve against cSVD. Additional studies will be required to determine the separate and possibly joint effects of different dietary factors on cognitive reserve. Future work using functional neuroimaging should also assess if the cognitive reserve effects associated with healthy dietary intake result from better maintenance of network connectivity, or perhaps reorganization of functional brain networks in aging.

4.5 Strengths and limitations

Strengths of the study include the use of multiple, validated biomarkers of VCID (WMH volume, FW, PSMD) (28–30, 82) developed by a multicenter consortium,[6] in the context of a study on reserve. Future work is needed to establish standardized VCID biomarker cutoff thresholds for group comparisons as is done with AD using PET amyloid positivity/negativity. Further, FON factor itself has been previously validated and demonstrated to be strongly associated with cognitive performance using composite measures (48). Finally, our use of statistical moderation models to test for potential reserve is the "gold standard" in the field (7).

One primary limitation of our study is the cross-sectional design which limits interpretation and prevents causal inferences. Brain maintenance in particular is best investigated longitudinally (6, 7). In addition, our measure of nutrient intake (NDANQ) and responses on the CRIq were based on self-report. Future research investigating nutrient patterns as a potential reserve proxy in VCID should ideally use fluid-based nutrient markers. The MoCA, while clinically relevant, is also not a comprehensive measure of cognitive function. Finally, our highly educated, primarily white sample may limit the external validity of our results to more diverse cohorts. Nevertheless, this work is one of the first to investigate dietary patterns as a measure of reserve against cSVD, and the results may aid in the development of longitudinal studies.

5 Conclusion

In conclusion, our results suggest that regular intake of nutrients commonly found in fish, healthy oils and nuts may contribute to cognitive reserve against cSVD. This effect appeared relatively specific to healthy dietary intake as a composite score of early life education, occupational history, and engagement in recreational activities did not protect cognition from cSVD in this study. Future research should attempt to replicate these findings longitudinally and expand the types of reserve variables explored with respect to cSVD in aging populations.

Data availability statement

The raw data supporting the conclusions of this article will be made available by the authors, without undue reservation.

Ethics statement

The studies involving humans were approved by Institutional Review Board of the University of Kentucky. The studies were conducted in accordance with the local legislation and institutional requirements. The participants provided their written informed consent to participate in this study.

Author contributions

CB: Conceptualization, Data curation, Formal analysis, Methodology, Software, Validation, Visualization, Writing – original draft, Writing – review & editing. VZ: Conceptualization, Data curation, Investigation, Methodology, Resources, Software, Writing – review & editing. CP: Conceptualization, Formal analysis, Investigation, Methodology, Software, Writing – original draft, Writing – review & editing. PM: Investigation, Methodology,

6 MarkVCID: https://markvcid.partners.org/

Resources, Software, Writing – review & editing. CD: Methodology, Software, Writing – review & editing. AC: Methodology, Software, Writing – review & editing. BG: Conceptualization, Data curation, Formal analysis, Funding acquisition, Methodology, Project administration, Resources, Supervision, Validation, Visualization, Writing – original draft, Writing – review & editing.

Funding

The author(s) declare that financial support was received for the research, authorship, and/or publication of this article. The present study was supported by the National Institutes of Health (grant nos. NIA P30 AG072946, NIA P30 AG028383 -15S1, NIA R01 AG055449, NIA R01 AG068055, NINDS RF1 NS122028, and NIGMS S10 OD023573). The content is solely the responsibility of the authors and does not necessarily represent the official views of these granting agencies.

Acknowledgments

The authors thank the dedicated research volunteers at our Sanders-Brown Center on Aging. We also thank Beverly Meacham, Eric Forman, Stephen Dundon, and Beatriz Rodolpho for their assistance with MRI scanning, and David Powell for assistance with pulse sequence programming and harmonization.

Conflict of interest

The authors declare that the research was conducted in the absence of any commercial or financial relationships that could be construed as a potential conflict of interest.

Generative AI statement

The authors declare that no Gen AI was used in the creation of this manuscript.

Publisher's note

Supplementary material

The Supplementary material for this article can be found online at: https://www.frontiersin.org/articles/10.3389/fneur.2025.1508148/full#supplementary-material

References

1. Corriveau RA, Bosetti F, Emr M, Gladman JT, Koenig JI, Moy CS, et al. The science of vascular contributions to cognitive impairment and dementia (VCID): a framework for advancing research priorities in the cerebrovascular biology of cognitive decline. *Cell Mol Neurobiol.* (2016) 36:281–8. doi: 10.1007/s10571-016-0334-7

2. Gorelick PB, Scuteri A, Black SE, Decarli C, Greenberg SM, Iadecola C, et al. Vascular contributions to cognitive impairment and dementia: a statement for healthcare professionals from the American Heart Association/American Stroke Association. *Stroke.* (2011) 42:2672–713. doi: 10.1161/STR.0b013e3182299496

3. Zlokovic BV, Gottesman RF, Bernstein KE, Seshadri S, McKee A, Snyder H, et al. Vascular contributions to cognitive impairment and dementia (VCID): a report from the 2018 National Heart, Lung, and Blood Institute and National Institute of Neurological Disorders and Stroke workshop. *Alzheimers Dement.* (2020) 16:1714–33. doi: 10.1002/alz.12157

4. Lu H, Kashani AH, Arfanakis K, Caprihan A, DeCarli C, Gold BT, et al. MarkVCID cerebral small vessel consortium: II. Neuroimaging protocols. *Alzheimers Dement.* (2021) 17:716–25. doi: 10.1002/alz.12216

5. Wardlaw JM, Valdés Hernández MC, Muñoz-Maniega S. What are white matter hyperintensities made of? Relevance to vascular cognitive impairment. *J Am Heart Assoc.* (2015) 4:001140. doi: 10.1161/JAHA.114.001140

6. Stern Y, Barnes CA, Grady C, Jones RN, Raz N. Brain reserve, cognitive reserve, compensation, and maintenance: operationalization, validity, and mechanisms of cognitive resilience. *Neurobiol Aging.* (2019) 83:124–9. doi: 10.1016/j.neurobiolaging.2019.03.022

7. Stern Y, Arenaza-Urquijo EM, Bartrés-Faz D, Belleville S, Cantilon M, Chetelat G, et al. Whitepaper: defining and investigating cognitive reserve, brain reserve, and brain maintenance. *Alzheimers Dement.* (2020) 16:1305–11. doi: 10.1016/j.jalz.2018.07.219

8. Nyberg L, Lövdén M, Riklund K, Lindenberger U, Bäckman L. Memory aging and brain maintenance. *Trends Cogn Sci.* (2012) 16:292–305. doi: 10.1016/j.tics.2012.04.005

9. Stern Y, Albert M, Barnes CA, Cabeza R, Pascual-Leone A, Rapp PR. A framework for concepts of reserve and resilience in aging. *Neurobiol Aging.* (2023) 124:100–3. doi: 10.1016/j.neurobiolaging.2022.10.015

10. Durrani R, Friedrich MG, Schulze KM, Awadalla P, Balasubramanian K, Black SE, et al. Effect of cognitive reserve on the Association of Vascular Brain Injury with Cognition: analysis of the PURE and CAHHM studies. *Neurology.* (2021) 97:E1707–16. doi: 10.1212/WNL.0000000000012765

11. Johnson NF, Bahrani AA, Powell DK, Jicha GA, Gold BT. Cardiorespiratory fitness diminishes the effects of age on white matter hyperintensity volume. *PLoS One.* (2020) 15:236–44. doi: 10.1371/journal.pone.0236986

12. Pettigrew C, Soldan A, Zhu Y, Cai Q, Wang MC, Moghekar A, et al. Cognitive reserve and rate of change in Alzheimer's and cerebrovascular disease biomarkers among cognitively normal individuals. *Neurobiol Aging.* (2020) 88:33–41. doi: 10.1016/j.neurobiolaging.2019.12.003

13. Pinter D, Enzinger C, Fazekas F. Cerebral small vessel disease, cognitive reserve and cognitive dysfunction. *J Neurol.* (2015) 262:2411–9. doi: 10.1007/s00415-015-7776-6

14. Soldan A, Pettigrew C, Zhu Y, Wang MC, Gottesman RF, DeCarli C, et al. Cognitive reserve and midlife vascular risk: cognitive and clinical outcomes. *Ann Clin Transl Neurol.* (2020) 7:1307–17. doi: 10.1002/acn3.51120

15. Zahodne LB, Mayeda ER, Hohman TJ, Fletcher E, Racine AM, Gavett B, et al. The role of education in a vascular pathway to episodic memory: brain maintenance or cognitive reserve? *Neurobiol Aging.* (2019) 84:109–18. doi: 10.1016/j.neurobiolaging.2019.08.009

16. Brickman AM, Siedlecki KL, Muraskin J, Manly JJ, Luchsinger JA, Yeung LK, et al. White matter hyperintensities and cognition: testing the reserve hypothesis. *Neurobiol Aging.* (2011) 32:1588–98. doi: 10.1016/j.neurobiolaging.2009.10.013

17. Jokinen H, Melkas S, Madureira S, Verdelho A, Ferro JM, Fazekas F, et al. Cognitive reserve moderates long-term cognitive and functional outcome in cerebral small vessel disease. *J Neurol Neurosurg Psychiatry.* (2016) 87:1296–302. doi: 10.1136/jnnp-2016-313914

18. Vemuri P, Lesnick TG, Przybelski SA, Knopman DS, Preboske GM, Kantarci K, et al. Vascular and amyloid pathologies are independent predictors of cognitive decline in normal elderly. *Brain.* (2015) 138:761–71. doi: 10.1093/brain/awu393

19. Del Brutto OH, Recalde BY, Mera RM. Dietary oily fish intake is inversely associated with severity of white matter Hyperintensities of presumed vascular origin. A population-based study in frequent fish consumers of Amerindian ancestry. *J Stroke Cerebrovasc Dis.* (2021) 30:105778. doi: 10.1016/j.jstrokecerebrovasdis.2021.105778

20. Gu Y, Scarmeas N. Diet and neuroimaging markers of cerebrovascular disease. *Curr Nutr Rep.* (2013) 2:81–9. doi: 10.1007/s13668-013-0044-4

21. Liu D, Zhang Q, Xing S, Wei F, Li K, Zhao Y, et al. Excessive salt intake accelerates the progression of cerebral small vessel disease in older adults. *BMC Geriatr.* (2023) 23:263–10. doi: 10.1186/s12877-023-03877-3

22. Makin SDJ, Mubki GF, Doubal FN, Shuler K, Staals J, Dennis MS, et al. Small vessel disease and dietary salt intake: cross-sectional study and systematic review. *J Stroke Cerebrovasc Dis*. (2017) 26:3020–8. doi: 10.1016/j.jstrokecerebrovasdis.2017.08.004

23. Keys A, Menotti A, Karvonen MJ, Aravanis C, Blackburn H, Buzina R, et al. The diet and 15-year death rate in the seven countries study. *Am J Epidemiol*. (1986) 124:903–15. doi: 10.1093/oxfordjournals.aje.a114480

24. Gardener H, Scarmeas N, Gu Y, Boden-Albala B, Elkind MS, Sacco RL, et al. Mediterranean diet and white matter hyperintensity volume in the northern Manhattan study. *Arch Neurol*. (2012) 69:251–6. doi: 10.1001/archneurol.2011.548

25. Song S, Gaynor AM, Cruz E, Lee S, Gazes Y, Habeck C, et al. Mediterranean diet and white matter Hyperintensity change over time in cognitively intact adults. *Nutrients*. (2022) 14:1–14. doi: 10.3390/nu14173664

26. Lourida I, Soni M, Thompson-Coon J, Purandare N, Lang IA, Ukoumunne OC, et al. Mediterranean diet, cognitive function, and dementia: a systematic review. *Epidemiology*. (2013) 24:479–89. doi: 10.1097/EDE.0b013e3182944410

27. Petersson SD, Philippou E. Mediterranean diet, cognitive function, and dementia: a systematic review of the evidence. *Adv Nutr*. (2016) 7:889–904. doi: 10.3945/an.116.012138

28. Maillard P, Lu H, Arfanakis K, Gold BT, Bauer CE, Zachariou V, et al. Instrumental validation of free water, peak-width of skeletonized mean diffusivity, and white matter hyperintensities: MarkVCID neuroimaging kits. *Alzheimers Dement*. (2022) 14:e12261–14. doi: 10.1002/dad2.12261

29. Maillard P, Hillmer LJ, Lu H, Arfanakis K, Gold BT, Bauer CE, et al. MRI free water as a biomarker for cognitive performance: validation in the MarkVCID consortium. *Alzheimers Dement*. (2022) 14:e12362–12. doi: 10.1002/dad2.12362

30. Satizabal CL, Beiser AS, Maillard P, Himali JJ, DeCarli C, Fornage M, et al. PSMD, a novel marker of small vessel disease, and its association with cognitive function in the community. *Alzheimers Dement*. (2020) 16:41993. doi: 10.1002/alz.041993

31. Nasreddine ZS, Phillips NA, Bédirian V, Charbonneau S, Whitehead V, Collin I, et al. The Montreal cognitive assessment, MoCA: a brief screening tool for mild cognitive impairment. *J Am Geriatr Soc*. (2005) 53:695–9. doi: 10.1111/j.1532-5415.2005.53221.x

32. Nucci M, Mapelli D, Mondini S. Cognitive reserve index questionnaire (CRIq): a new instrument for measuring cognitive reserve. *Aging Clin Exp Res*. (2012) 24:218–26. doi: 10.1007/BF03654795

33. Schmitt F, Nelson PT, Abner E, Scheff S, Jicha GA, Smith C, et al. University of Kentucky Sanders-Brown healthy brain aging volunteers: donor characteristics, procedures and neuropathology. *Curr Alzheimer Res*. (2012) 9:724–33. doi: 10.2174/156720512801322591

34. Satia JA, Watters JL, Galanko JA. Validation of an antioxidant nutrient questionnaire in whites and African Americans. *J Am Diet Assoc*. (2009) 109:502–508.e6. doi: 10.1016/j.jada.2008.11.033

35. Andersson JLR, Skare S, Ashburner J. How to correct susceptibility distortions in spin-echo echo-planar images: application to diffusion tensor imaging. *NeuroImage*. (2003) 20:870–88. doi: 10.1016/S1053-8119(03)00336-7

36. Bauer CE, Zachariou V, Seago E, Gold BT. White matter Hyperintensity volume and location: associations with WM microstructure, brain Iron, and cerebral perfusion. *Front Aging Neurosci*. (2021) 13:1–12. doi: 10.3389/fnagi.2021.617947

37. Fischl B, van der Kouwe A, Destrieux C, Halgren E, Ségonne F, Salat DH, et al. Automatically parcellating the human cerebral cortex. *Cereb Cortex*. (2004) 14:11–22. doi: 10.1093/cercor/bhg087

38. DeCarli C, Fletcher E, Ramey V, Harvey D, Jagust WJ. Anatomical mapping of white matter hyperintensities (WMH): exploring the relationships between periventricular WMH, deep WMH, and total WMH burden. *Stroke*. (2005) 36:50–5. doi: 10.1161/01.STR.0000150668.58689.f2

39. Decarli C, Maillard P, Fletcher E. *Four tissue segmentation in ADNI II, Department of Neurology and Center for neuroscience, University of California at Davis*. Alzheimer's Disease Neuroimaging Initiative. (2013). Available at: https://www.alz.washington.edu/WEB/adni_proto.pdf.

40. Jenkinson M, Beckmann CF, Behrens TEJ, Woolrich MW, Smith SM. FSL. *NeuroImage*. (2012) 62:782–90. doi: 10.1016/j.neuroimage.2011.09.015

41. Decarli C, Murphy D, Teichberg D, Campbell G, Sobering G. Local histogram correction of MRI spatially dependent image pixel intensity nonuniformity. *J Magn Reson Imaging*. (1996) 6:519–28. doi: 10.1002/jmri.1880060316

42. Bauer CE, Zachariou V, Maillard P, Caprihan A, Gold BT. Multi-compartment diffusion magnetic resonance imaging models link tract-related characteristics with working memory performance in healthy older adults. *Front Aging Neurosci*. (2022) 14:1–15. doi: 10.3389/fnagi.2022.995425

43. Smith SM. Fast robust automated brain extraction. *Hum Brain Mapp*. (2002) 17:143–55. doi: 10.1002/hbm.10062

44. Andersson JLR, Sotiropoulos SN. An integrated approach to correction for off-resonance effects and subject movement in diffusion MR imaging. *NeuroImage*. (2016) 125:1063–78. doi: 10.1016/j.neuroimage.2015.10.019

45. Henriques RN, Rokem A, Garyfallidis E, St-Jean S, Peterson ET, Correia MM. [Re] optimization of a free water elimination two-compartment model for diffusion tensor imaging. *bioRxiv*. (2017) 2017:795. doi: 10.1101/108795

46. Garyfallidis E, Brett M, Amirbekian B, Rokem A, van der Walt S, Descoteaux M, et al. 'Dipy, a library for the analysis of diffusion MRI data', Frontiers. *Neuroinformatics*. (2014) 8:1–17. doi: 10.3389/fninf.2014.00008

47. Baykara E, Gesierich B, Adam R, Tuladhar AM, Biesbroek JM, Koek HL, et al. A novel imaging marker for small vessel disease based on Skeletonization of white matter tracts and diffusion histograms. *Ann Neurol*. (2016) 80:581–92. doi: 10.1002/ana.24758

48. Zachariou V, Bauer CE, Seago ER, Panayiotou G, Hall ED, Butterfield DA, et al. Healthy dietary intake moderates the effects of age on brain iron concentration and working memory performance. *Neurobiol Aging*. (2021) 106:183–96. doi: 10.1016/j.neurobiolaging.2021.06.016

49. Davis C, Bryan J, Hodgson J, Murphy K. Definition of the mediterranean diet: a literature review. *Nutrients*. (2015) 7:9139–53. doi: 10.3390/nu7115459

50. Sebastian RS. *Flavonoid values for USDA survey foods and beverages*. Food Surveys Research, pp. 1–30. (2016).

51. Zachariou V, Bauer CE, Pappas C, Gold BT. High cortical iron is associated with the disruption of white matter tracts supporting cognitive function in healthy older adults. *Cereb Cortex*. (2022) 33:4815–28. doi: 10.1093/cercor/bhac382

52. DiStefano C, Zhu M, Mîndrilă D. Understanding and using factor scores: considerations for the applied researcher. *Pract Assess Res Eval*. (2009) 14:2–11. doi: 10.7275/da8t-4g52

53. Benjamini Y, Hochberg Y. Controlling the false discovery rate: a practical and powerful approach to multiple testing. *J R Stat Soc*. (1995) 57:289–300. doi: 10.1111/j.2517-6161.1995.tb02031.x

54. Hayes AF. Introduction to mediation, moderation, and conditional Process analysis: A regression-based approach. *3rd* ed. New York: Guilford Press (2022).

55. Maillard P, Mitchell GF, Himali JJ, Beiser A, Fletcher E, Tsao CW, et al. Aortic stiffness, increased white matter free water, and altered microstructural integrity: a continuum of injury. *Stroke*. (2017) 48:1567–73. doi: 10.1161/STROKEAHA.116.016321

56. Rimmele DL, Petersen EL, Schlemm E, Kessner SS, Petersen M, Mayer C, et al. Association of Carotid Plaque and Flow Velocity with White Matter Integrity in a middle-aged to elderly population. *Neurology*. (2022) 99:E2699–707. doi: 10.1212/WNL.0000000000201297

57. Gouw AA, Seewann A, van der Flier WM, Barkhof F, Rozemuller AM, Scheltens P, et al. Heterogeneity of small vessel disease: a systematic review of MRI and histopathology correlations. *J Neurol Neurosurg Psychiatry*. (2011) 82:126–35. doi: 10.1136/jnnp.2009.204685

58. Valdés Hernández M, Allerhand M, Glatz A, Clayson L, Muñoz Maniega S, Gow A, et al. Do white matter hyperintensities mediate the association between brain iron deposition and cognitive abilities in older people? *Eur J Neurol*. (2016) 23:1202–9. doi: 10.1111/ene.13006

59. de Groot M, Verhaaren BFJ, de Boer R, Klein S, Hofman A, van der Lugt A, et al. Changes in Normal-appearing white matter precede development of white matter lesions. *Stroke*. (2012) 44:1037–42. doi: 10.1161/STROKEAHA.112.680223

60. Julayanont P, Nasreddine ZS. Montreal cognitive assessment (MoCA): concept and clinical review In: AJ Larner, editor. Cognitive Screening Instruments: A Practical Approach. Berlin: Springer Science and Business Media (2017). 139–95.

61. Beaudet G, Tsuchida A, Petit L, Tzourio C, Caspers S, Schreiber J, et al. Age-related changes of peak width skeletonized mean diffusivity (PSMD) across the adult life span: a multi-cohort study. *Front Psych*. (2020) 11:1–13. doi: 10.3389/fpsyt.2020.00342

62. Beck D, de Lange AMG, Maximov II, Richard G, Andreassen OA, Nordvik JE, et al. White matter microstructure across the adult lifespan: a mixed longitudinal and cross-sectional study using advanced diffusion models and brain-age prediction. *NeuroImage*. (2021) 224:117441. doi: 10.1016/j.neuroimage.2020.117441

63. Chad JA, Pasternak O, Salat DH, Chen JJ. Re-examining age-related differences in white matter microstructure with free-water corrected diffusion tensor imaging. *Neurobiol Aging*. (2018) 71:161–70. doi: 10.1016/j.neurobiolaging.2018.07.018

64. Garnier-Crussard A, Bougacha S, Wirth M, André C, Delarue M, Landeau B, et al. White matter hyperintensities across the adult lifespan: relation to age, a β load, and cognition. *Alzheimers Res Ther*. (2020) 12:127. doi: 10.1186/s13195-020-00669-4

65. Kubicki M, Baxi M, Pasternak O, Tang Y, Karmacharya S, Chunga N, et al. Lifespan trajectories of white matter changes in Rhesus monkeys. *Cereb Cortex*. (2019) 29:1584–93. doi: 10.1093/cercor/bhy056

66. Moura AR, Lee S, Habeck C, Razlighi Q, Stern Y. The relationship between white matter hyperintensities and cognitive reference abilities across the life span. *Neurobiol Aging*. (2019) 83:31–41. doi: 10.1016/j.neurobiolaging.2019.08.024

67. Pieciak T, París G, Beck D, Maximov II, Tristán-Vega A, de Luis-García R, et al. Spherical means-based free-water volume fraction from diffusion MRI increases non-linearly with age in the white matter of the healthy human brain. *NeuroImage*. (2023) 279:120324. doi: 10.1016/j.neuroimage.2023.120324

68. Raz N, Yang Y, Dahle CL, Land S. (2012) 'volume of white matter hyperintensities in healthy adults: contribution of age, vascular risk factors, and inflammation-related genetic variants'. *Biochim Biophys Acta Mol basis Dis*. (1822) 1822:361–9. doi: 10.1016/j.bbadis.2011.08.007

69. Pelletier A, Barul C, Féart C, Helmer C, Bernard C, Periot O, et al. Mediterranean diet and preserved brain structural connectivity in older subjects. *Alzheimers Dement*. (2015) 11:1023–31. doi: 10.1016/j.jalz.2015.06.1888

70. Meng X, D'Arcy C. Education and dementia in the context of the cognitive reserve hypothesis: a systematic review with meta-analyses and qualitative analyses. *PLoS One*. (2012) 7:e38268. doi: 10.1371/journal.pone.0038268

71. Stern Y. What is cognitive reserve? Theory and research application of the reserve concept. *J Int Neuropsychol Soc*. (2002) 8:448–60. doi: 10.1017/S1355617702813248

72. Stern Y. Cognitive reserve in ageing and Alzheimer's disease. *Lancet Neurol*. (2012) 11:1006–12. doi: 10.1016/S1474-4422(12)70191-6

73. Wang HX, Xu W, Pei JJ. (2012) 'Leisure activities, cognition and dementia'. *Biochim Biophys Acta Mol basis Dis*. (1822) 1822:482–91. doi: 10.1016/j.bbadis.2011.09.002

74. Bauer CE, Brown CA, Gold BT. Education does not protect cognitive function from brain pathology in the ADNI 2 cohort. *Neurobiol Aging*. (2020) 90:147–9. doi: 10.1016/j.neurobiolaging.2019.11.017

75. Wada M, Noda Y, Shinagawa S, Chung JK, Sawada K, Ogyu K, et al. Effect of education on Alzheimer's disease-related neuroimaging biomarkers in healthy controls, and participants with mild cognitive impairment and Alzheimer's disease: a cross-sectional study. *J Alzheimers Dis*. (2018) 63:861–9. doi: 10.3233/JAD-171168

76. Colussi G, Catena C, Novello M, Bertin N, Sechi LA. Impact of omega-3 polyunsaturated fatty acids on vascular function and blood pressure: relevance for cardiovascular outcomes. *Nutr Metab Cardiovasc Dis*. (2017) 27:191–200. doi: 10.1016/j.numecd.2016.07.011

77. Kris-Etherton PM, Hecker KD, Binkoski AE. Polyunsaturated fatty acids and cardiovascular health. *Nutr Rev*. (2004) 62:414–26. doi: 10.1111/j.1753-4887.2004.tb00013.x

78. Wen J, Satyanarayanan SK, Li A, Yan L, Zhao Z, Yuan Q, et al. (2024) 'unraveling the impact of Omega-3 polyunsaturated fatty acids on blood-brain barrier (BBB) integrity and glymphatic function'. *Brain Behav Immun*. (2023) 115:335–55. doi: 10.1016/j.bbi.2023.10.018

79. Zehr KR, Walker MK. Function in humans at risk for atherosclerosis: a review. *Prostaglandins Ohter Lipid Mediat*. (2019) 134:131–40. doi: 10.1016/j.prostaglandins.2017.07.005.Omega-3

80. Grochowski C, Litak J, Kamieniak P, Maciejewski R. Oxidative stress in cerebral small vessel disease. Role of reactive species. *Free Radic Res*. (2018) 52:1–13. doi: 10.1080/10715762.2017.1402304

81. Mustapha M, Nassir CMN, Hay YK, Yee FW, Hamid HA. Neuroprotective potentials of natural vitamin E for cerebral small vessel disease In: M Mustapha, editor. Neuroprotection–new approaches and prospects. London: Intechopen (2020)

82. Sur S, Lin Z, Li Y, Yasar S, Rosenberg P, Moghekar A, et al. Association of cerebrovascular reactivity and Alzheimer pathologic markers with cognitive performance. *Neurology*. (2020) 95:E962–72. doi: 10.1212/WNL.0000000000010133

83. Luckey AM, Ghosh S, Wang C-P, Beiser A, Bernal R, Li Z, et al. 'Biological validation of peak-width of skeletonized mean diffusivity as a VCID biomarker: The MarkVCID Consortium', *Alzheimer's and Dementia*, (September), (2024) pp. 8814–24. doi: 10.1002/alz.14345

frontiers | Frontiers in Neurology

TYPE Original Research
PUBLISHED 11 March 2025
DOI 10.3389/fneur.2025.1566395

OPEN ACCESS

EDITED BY
Shuai Ren,
Affiliated Hospital of Nanjing University of Chinese Medicine, China

REVIEWED BY
Hongmei Zhang,
Chinese Academy of Medical Sciences and Peking Union Medical College, China
Juntao Ran,
First Hospital of Lanzhou University, China
Wei Guo,
Peking University Third Hospital, China

*CORRESPONDENCE
Yankai Meng
✉ mengyankai@126.com

RECEIVED 24 January 2025
ACCEPTED 24 February 2025
PUBLISHED 11 March 2025

CITATION
Zhang H, Long J, Wang C, Liu X, Lu H, Xu W, Sun X, Dou P, Zhou D, Zhu L, Xu K and Meng Y (2025) Development of a nomogram model for predicting acute stroke events based on dual-energy CTA analysis of carotid intraplaque and perivascular adipose tissue. *Front. Neurol.* 16:1566395. doi: 10.3389/fneur.2025.1566395

Development of a nomogram model for predicting acute stroke events based on dual-energy CTA analysis of carotid intraplaque and perivascular adipose tissue

He Zhang[1,2,3,4], Juan Long[1,2,3], Chenzi Wang[1,2,3], Xiaohan Liu[1,2,3], He Lu[4], Wenbei Xu[1,2,3], Xiaonan Sun[1,2,3], Peipei Dou[1,2,3], Dexing Zhou[4], Lili Zhu[5], Kai Xu[1,2,3] and Yankai Meng[1,2,3]*

[1]Department of Radiology, The Affiliated Hospital of Xuzhou Medical University, Xuzhou, China, [2]College of Medical Imaging, Xuzhou Medical University, Xuzhou, China, [3]Jiangsu Medical Imaging and Digital Medical Engineering Research Center, Xuzhou Medical University, Xuzhou, China, [4]Department of Radiology, Jiawang District People's Hospital, Xuzhou, China, [5]Department of Medical Imaging, Xuzhou New Health Hospital, Xuzhou, China

Objective: To evaluate the predictive value of dual-energy CT angiography (DECTA) parameters of carotid intraplaque and perivascular adipose tissue (PVAT) in acute stroke events.

Methods: A retrospective analysis was conducted using clinical, laboratory, and imaging data from patients who underwent dual-energy carotid CTA and cranial MRI. Acute cerebral infarctions occurring in the ipsilateral anterior circulation were classified as the symptomatic group (STA group), while other cases were categorized as the asymptomatic group (ATA group). LASSO regression was employed to identify key predictors. These predictors were used to develop three models: the intraplaque model (IP_Model), the perivascular adipose tissue model (PA_Model), and the nomogram model (Nomo_Model). The predictive accuracy of the models was evaluated using receiver operating characteristic (ROC) analysis, calibration curves, and decision curve analysis. Statistical significance was defined as $p < 0.05$.

Results: Seventy-five patients (mean age: 68.7 ± 8.7 years) were analyzed. LASSO regression identified seven significant variables (IP_Zeff, IP_40KH, IP_K, PA_FF, PA_VNC, PA_Rho, PA_K) for model construction. The Nomo_Model demonstrated superior predictive performance compared to the IP_Model and PA_Model, achieving an area under the curve (AUC) of 0.962, with a sensitivity of 95.8%, specificity of 82.4%, precision of 82.6%, an F1 score of 0.809, and an accuracy of 88.0%. The clinical decision curve analysis further validated the Nomo_Model's significant clinical utility.

Conclusion: DECTA imaging parameters revealed significant differences in carotid intraplaque and PVAT characteristics between the STA and ATA groups. Integrating these parameters into the nomogram (Nomo_Model) resulted in a highly accurate and clinically relevant tool for predicting acute stroke risk.

KEYWORDS

dual-energy CT, CT angiography, carotid plaque, perivascular fat, acute stroke

Introduction

Stroke remains the leading cause of cardiovascular disease-related mortality in China (1). Among the numerous risk factors, vulnerable carotid artery plaques on the ipsilateral side are key contributors to acute stroke incidents (2). Studies have shown that active inflammation, the presence of a large lipid-rich necrotic core (LRNC), and intraplaque hemorrhage (IPH) are central in promoting plaque instability (3). Moreover, perivascular adipose tissue (PVAT) plays a significant role in enhancing plaque vulnerability by secreting pro-inflammatory cytokines that accelerate atherosclerosis (4, 5).

The vulnerability of carotid plaques has been extensively evaluated using high-resolution MRI, which provides significant value (6–8). However, MRI is constrained by long scan times, high costs, and patient compliance issues. Consequently, researchers have increasingly turned to CT angiography (CTA) to investigate the relationship between carotid plaques and acute stroke, yielding promising results (9, 10). Traditional CTA struggles to differentiate plaque types, limiting its ability to assess plaque vulnerability accurately. In contrast, dual-energy CT (DECT), which utilizes X-rays at varying energies, offers an innovative approach. Compared to MRI, DECT provides a faster, more affordable alternative with comparable or superior diagnostic capabilities, particularly for assessing carotid plaques and perivascular adipose tissue. Additionally, DECT enhances tissue characterization, enabling more precise identification of plaque components and improving stroke risk prediction.

Through advanced post-processing, DECT generates virtual non-contrast (VNC) images, fat fraction (FF), iodine concentration (IC), electron density (Rho), effective atomic number (Zeff), and the slope of the energy spectrum curve (K). Each of these parameters provides insights into material composition changes to varying extents (11–13). While some research has applied DECT to detect symptomatic carotid plaques (14, 15), its potential to predict acute stroke events by assessing fat content within and surrounding carotid plaques remains to be fully understood.

Thus, this study aims to evaluate the predictive value of dual-energy CTA (DECTA) parameters of carotid intraplaque and PVAT for the occurrence of acute stroke events.

Methods

Patients

This retrospective study has been approved by the Medical Ethics Committee of the Affiliated Hospital of Xuzhou Medical University, and the Institutional Review Board of this institution has waived the requirement for informed consent. All methods are in compliance with relevant ethical and regulatory requirements and adhere to the principles outlined in the Declaration of Helsinki.

This study enrolled 75 consecutive patients between January 2023 and August 2024, all of whom presented with neurological symptoms and/or exhibited positive findings during physical examinations. Each participant underwent dual-energy carotid CTA and cranial MRI.

Patients were eligible for inclusion based on the following criteria: (1) the interval between carotid CTA and cranial MRI did not exceed three days; (2) the presence of measurable carotid plaques (either unilateral or bilateral); (3) identifiable PVAT (either unilateral or bilateral); and (4) the absence of measurable atherosclerotic plaques in the ipsilateral anterior or middle cerebral arteries.

Patients were excluded for the following reasons: (1) poor image quality of CTA or MRI due to significant artifacts that would preclude post-processing analysis; (2) evidence of intracranial large vessel disease in the anterior circulation (e.g., stenosis or dissection); (3) underlying autoimmune vasculitis or intracranial vascular malformations; or (4) changes following stenting of the common carotid, internal carotid, or intracranial large arteries.

DECTA scanning protocol

Dual-energy head and neck CTA scans were conducted using a Siemens third-generation dual-source CT scanner (SOMATOM Driver), covering the range from the aortic arch to the vertex of the skull. The scanning parameters included tube voltages of 80 kV and 140 kV; tube currents of 200 mAs and 100 mAs; a pitch of 1.1; a reconstruction layer thickness of 0.6 mm; an interval of 0.6 mm; a convolution kernel of Br40; and a rotation time of 0.5 s.

The contrast agent utilized was a non-ionic iodine medium, Iohexol (produced by Nanjing Zhengda Tianqing Pharmaceutical; trade name: Qinglidai; concentration: 100 mg/mL). A high-pressure injector (Medrad Stellant, Bayer AG) administered the contrast agent at a dosage of 1.0–1.2 mL/kg body weight, at an injection rate of 4.0 mL/s, followed by a 30 mL saline flush.

Cranial MRI scanning protocol

Cranial MRI scans were performed using a GE 3.0 T magnetic resonance scanner (SIGNA Architect) and a Toshiba 1.5 T scanner (Vantage Elan). For the GE 3.0 T diffusion-weighted imaging (DWI) sequence, the scanning parameters were as follows: repetition time (TR) of 3,966 ms; echo time (TE) of 75.9 ms; slice thickness of 5 mm; spacing of 1.5 mm; field of view (FOV) of 240 mm × 240 mm; and a b-value of 1,000 s/mm^2. For the Toshiba 1.5 T DWI sequence, parameters included: TR of 3,291 ms; TE of 100 ms; slice thickness of 6 mm; spacing of 1 mm; FOV of 240 mm × 240 mm; and a b-value of 800 s/mm^2.

Dual-energy carotid CTA image analysis

Two senior radiologists, each with over 15 years of experience in CTA post-processing, conducted the analysis of head and neck CTA images using a Siemens workstation (Syngo. Via VB40B). Regions of interest (ROIs) were strategically placed in the most prominent slices of the carotid plaques and PVAT gaps under the Liver VNC, Rho/Z, and Mono E modes.

One ROI was positioned within the plaque to encompass the entire structure in a single slice, ensuring the exclusion of high-density contrast medium effects. Two additional ROIs were placed in the PVAT gaps, ensuring each was located more than 1 mm from the edge of the carotid artery and surrounding tissues, in accordance with the measurement methodology proposed by Baradaran et al. (9), while avoiding surrounding soft tissues or small penetrating vessels. The average values from the two ROIs were subsequently utilized for

statistical analysis. In cases of disagreement, the radiologists consulted to achieve consensus.

To resolve any disagreements between the two senior radiologists, a consensus-based approach was adopted. Both radiologists independently reviewed the images and identified the ROIs of the carotid plaques and PVAT gaps. If discrepancies in their measurements or interpretations arose, they engaged in direct consultation to reach a final decision. This collaborative process, leveraging both radiologists' extensive experience, ensured that any conflicting views were thoroughly discussed and resolved. This approach ensured that both radiologists were aligned on the criteria for image analysis, improving the reliability and reproducibility of the measurements.

The DECTA parameters for the carotid plaque (Intraplaque, IP_) and perivascular adipose tissue (PA_) encompassed fat fraction (FF), virtual non-contrast (VNC) values, iodine concentration (IC), electron density (Rho), effective atomic number (Zeff), energy spectrum curve, and corresponding CT values for 40 keV (40KH) and 90 keV (90KH), as well as the slope of the intraplaque energy spectrum curve K. The formula employed is $K_{HU/keV} = (90KH-40KH) / 50_{keV}$ (Supplementary Figure S1). FF refers to the proportion of fat tissue within the plaque or surrounding perivascular adipose tissue, offering insights into the composition and stability of the plaque.

Assessment of the acute cerebrovascular events

MRI images of patients' brains were evaluated by two senior radiologists specialized in neuroimaging, using a Picture Archiving and Communication System (PACS). According to established guidelines, lesions exhibiting significantly high signals on diffusion-weighted imaging (DWI) and significantly low signals on the apparent diffusion coefficient (ADC) sequence are defined as acute cerebrovascular events (16).

Acute cerebral infarctions occurring in the anterior circulation supply area on the same side are classified as the symptomatic group (STA group), while those without acute infarction in the same-side anterior circulation supply area are classified as the asymptomatic group (ATA group) (Figure 1).

Clinical data collection

Clinical data were meticulously retrieved from the case management system by a radiologist (C.S) specializing in cardiovascular imaging. We retrospectively gathered comprehensive data, including gender, age, body mass index (BMI), history of hypertension, diabetes, transient ischemic attack (TIA), smoking history, alcohol consumption, and serum biomarker levels (total cholesterol, triglycerides, high-density lipoprotein, low-density lipoprotein). The interval between the collection of clinical laboratory data and CTA examinations did not exceed one week.

Statistic

Data processing was conducted using SPSS version 23.0 and R software packages, including pROC, rms, glmnet, regplot and ggplot2. The normality of continuous variables was assessed using the Kolmogorov–Smirnov test. Continuous variables that followed a normal distribution were presented as ($x \pm s$), while those with a non-normal distribution were expressed as M (Q1, Q3). Categorical variables were represented as percentages (%).

Comparisons of qualitative data between groups were performed using the χ^2 test, whereas the *t*-test was applied for continuous data. For non-normally distributed data, the Mann–Whitney *U* test was used. Univariate variables with $p < 0.05$ were included in LASSO analysis, and selected variables were incorporated to construct the intraplaque model (IP_Model), the perivascular adipose tissue model (PA_Model) and the nomogram model (Nomo-Model). The models performance were evaluated using ROC analysis, calibration curve, clinical decision curve analysis and compared with the DeLong test. A *p* value of <0.05 was considered statistically significant.

Data availability

The datasets used and/or analysed during the current study are available from the corresponding author on reasonable request.

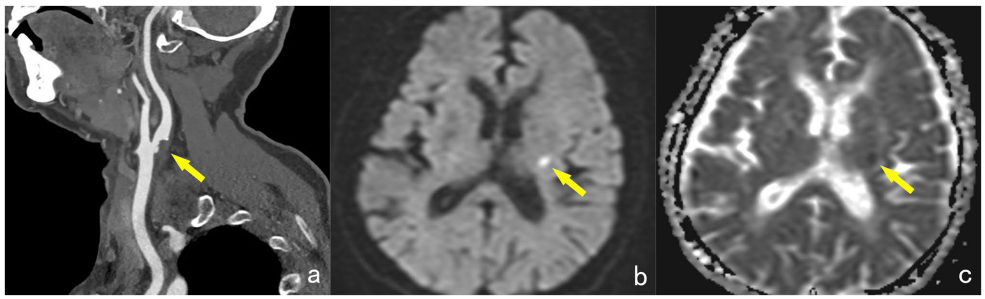

FIGURE 1
A 65-year-old female, showing a non-calcified plaque (yellow arrow) at the starting point of the left internal carotid artery on DECTA, with a narrowing degree of approximately 45% **(a)**. MRI examination reveals patchy high signals (yellow arrow) in the contralateral basal ganglia region on the DWI sequence **(b)**. The ADC map shows low signals (yellow arrow) in the lesion, with an ADC value of approximately 0.549×10^{-3} mm^2/s, diagnosed as acute cerebral infarction and classified into the STA group **(c)**.

Results

Comparison of clinical characteristics between the STA and ATA groups

No statistically significant differences were observed in clinical characteristics between the STA and ATA groups (all p values >0.05) (Table 1).

Comparison of DECTA parameters for intraplaque between the STA and ATA groups

For DECTA parameters of intraplaque, in the STA group, the iodine concentration (IP_IC), effective atomic number (IP_Zeff), and CT values corresponding to the 40 keV energy spectrum curve (IP_40KH) were all greater than those in the ATA group.

The average value of the energy spectrum curve slope (IP_K) was lower in the STA group than in the ATA group, with all differences being statistically significant (p values <0.05) (Table 2).

Comparison of DECTA parameters for PVAT between the STA and ATA groups

The PVAT fat fraction (PA_FF) in the STA group was less than that in the ATA group ($p < 0.001$). In the STA group, the virtual non-contrast CT value (PA_VNC), electron density (PA_Rho), and CT values at 40 keV of the energy spectrum curve (PA_40KH) were all higher than those in the ATA group, while the slope of the energy spectrum curve (PA_K) was lower in the STA group than in the ATA group, with all differences being statistically significant (Table 3).

LASSO regression analysis and variable selection

Nine univariate variables with $p < 0.05$ from group comparisons were included in the LASSO regression analysis. The optimal regularization parameter λ was determined using 10-fold cross-validation (Supplementary Figure S2). At the point of minimum cross-validation error, seven variables (IP_Zeff, IP_40KH, IP_K, PA_FF, PA_VNC, PA_Rho, PA_K) were selected for further model

TABLE 1 Clinical data for STA and ATA groups (N = 75).

Clinical data	STA (n = 24) (%)	ATA (n = 51) (%)	P value
Male	16 (66.70)	36 (70.60)	0.731
Age (years)	68 (61.00, 74.50)	71 (64.50, 76.00)	0.481
BMI (kg/m^2)	23.82 ± 2.89	25.18 ± 3.41	0.960
History of hypertension			0.370
Yes	16 (66.70)	39 (76.50)	
No	8 (33.30)	12 (23.50)	
History of diabetes			0.057
Yes	3 (12.50)	17 (33.30)	
No	21 (87.50)	34 (66.70)	
History of coronary heart disease			0.884
Yes	3 (12.50)	7 (13.70)	
No	21 (87.50)	44 (86.30)	
History of TIA			0.316
Yes	7 (29.20)	21 (41.20)	
No	17 (70.80)	30 (58.80)	
History of smoking			0.600
Yes	9 (37.50)	16 (31.40)	
No	15 (62.50)	35 (68.60)	
History of alcohol consumption			0.110
Yes	3 (12.50)	15 (29.40)	
No	21 (87.50)	36 (70.60)	
Total cholesterol (mmol/L)	4.41 ± 1.16	4.41 ± 1.22	0.999
Triglycerides (mmol/L)	1.05 (0.75, 1.65)	1.36 (1.06, 1.72)	0.113
HDL (mmol/L)	1.21 ± 0.32	1.11 ± 0.23	0.109
LDL (mmol/L)	2.57 ± 0.92	2.69 ± 1.01	0.604

BMI, body mass index; TIA, transient ischemic attack; HDL, high-density lipoprotein; LDL, low-density lipoprotein. Age and triglycerides do not follow a normal distribution and are expressed as M (Q1, Q3). TIA means transient ischemic attacks.

TABLE 2 DECTA parameters for plaque between STA and ATA groups (*N* = 75).

DECTA parameters	STA (*n* = 24)	ATA (*n* = 51)	*P* value
IP_FF	22.90 ± 18.28	18.72 ± 19.62	0.382
IP_IC	0.39 ± 0.94	−0.18 ± 1.01	0.022*
IP_VNC	24.09 ± 22.09	24.35 ± 18.69	0.958
IP_Rho	24.55 ± 15.64	27.08 ± 17.63	0.551
IP_Zeff	7.675 (7.42, 7.84)	7.35 (7.16, 7.60)	0.003*
IP_40KH	58.63 ± 51.87	7.96 ± 39.47	<0.001*
IP_90KH	30.14 ± 15.94	28.33 ± 17.86	0.673
IP_K	−0.57 ± 0.98	0.41 ± 0.87	<0.001*

IP_, Intraplaque; FF, fat fraction; IC, iodine concentration; VNC, virtual non-contrast; Rho, electron density; Zeff, effective atomic number; 40KH, CT values at 40 keV; 90KH, CT values at 90 keV; K, the slope of the energy spectrum curve. IP_Zeff is expressed as M (Q1, Q3) due to non-normal distribution. * $p < 0.05$.

TABLE 3 DECTA parameters for PVAT between STA and ATA groups (*N* = 75).

DECTA parameters	STA (*n* = 24)	ATA (*n* = 51)	*P* value
PA_FF	75.41 ± 13.07	90.49 ± 16.38	<0.001*
PA_IC	−0.125 (−0.50, 0.00)	0 (0.00, 0.03)	0.075
PA_VNC	−79.25 (−92.75, −59.75)	−101 (−113.00, −90.65)	<0.001*
PA_Rho	−57.46 ± 21.52	−72.76 ± 15.33	<0.001*
PA_Zeff	6.775 (6.57, 7.01)	6.65 (6.40, 6.97)	0.233
PA_40KH	−94.93 ± 45.79	−168.39 ± 57.57	<0.001*
PA_90KH	−71.14 ± 28.03	−74.63 ± 22.98	0.570
PA_K	0.48 ± 0.83	1.88 ± 1.25	<0.001*

PA_, Perivascular Fat; FF, fat fraction; IC, iodine concentration; VNC, virtual non-contrast; Rho, electron density; Zeff, effective atomic number; 40KH, CT values at 40 keV; 90KH, CT values at 90 keV; K, the slope of the energy spectrum curve. PA_IC, PA_VNC, and PA_Zeff is expressed as M (Q1, Q3) due to non-normal distribution. * $p < 0.05$.

construction (Supplementary Figure S3). The regression coefficients for these variables were presented in Supplementary Table S1.

The logistic regression equation is as follows:

$$\begin{aligned}\mathrm{Logit}(P) = {} & 1.913 + 1.414 \times \mathrm{IP\_Zeff} + 0.023 \times \mathrm{IP\_40KH} \\ & + -0.517 \times \mathrm{IP\_K} + -0.081 \times \mathrm{PA\_FF} + 0.054 \\ & \times \mathrm{PA\_VNC} + 0.011 \times \mathrm{PA\_Rho} + -1.531 \times \mathrm{PA\_K}\end{aligned}$$

Construction of the nomogram model for predicting SAT

The seven variables identified through LASSO regression were incorporated into a logistic regression analysis to construct a dynamic nomogram model (Nomo_Model) for predicting the risk of acute stroke. The dynamic nomogram is accessible online at: https://dual-energy-carotid-cta.shinyapps.io/dynnomapp-1/ (Figure 2).

Predictive performance of DECTA models

The Nomo_Model demonstrated superior predictive performance compared to the intraplaque (IP_Model) and perivascular adipose tissue (PA_Model) models. The Nomo_Model achieved an area under the curve (AUC) of 0.962, with a sensitivity of 95.8%, specificity of 82.4%, and an accuracy of 88.0% (Table 4; Supplementary Figure S4; Figure 3).

The results of the DeLong test confirmed that the predictive efficacy of the Nomo_Model was significantly higher than that of all univariate variables, as well as the IP_Model and PA_Model ($p < 0.05$).

Calibration and clinical decision curve analysis

The calibration curve, generated through 1,000 bootstrap iterations, demonstrated strong agreement between the Nomo_Model's predicted probabilities and observed outcomes (Supplementary Figure S5).

The clinical decision curve analysis indicated that the Nomo_Model provides substantial clinical benefit, particularly at intermediate and higher threshold probabilities (Figure 4).

Discussion

In this study, we employed LASSO regression to select significant variables from dual-energy CTA-derived carotid plaque and PVAT parameters, aiming to reduce multicollinearity and prevent overfitting. These selected variables were then incorporated into a logistic regression nomogram model to predict SAT. The model demonstrated high predictive capability and clinical benefit.

Prior research has established that PVAT significantly influences atherosclerotic plaque progression. It does so by secreting inflammatory factors and active mediators that exacerbate vascular oxidation and inflammation, thereby increasing plaque vulnerability. Additionally, PVAT sequesters peroxides through an "inside-out" mechanism, which upregulates adiponectin gene expression and facilitates lipolysis. Conversely, inflammatory factors hinder the maturation of adipocyte precursors, resulting in decreased PVAT volume and heightened risk of acute cerebrovascular events (17–19). Therefore, unlike previous studies that have focused exclusively on PVAT (20), our approach integrates the dual-energy characteristics of both intraplaque and PVAT, providing a more comprehensive assessment of plaque vulnerability and enhancing predictive capabilities for acute stroke event.

In comparison to earlier investigations linking mixed-energy CTA with acute cerebrovascular events, our findings demonstrate superior predictive efficacy using dual-energy parameters. This enhancement may be attributed to the contamination of PVAT by high-density iodine contrast agents during CTA, which can compromise measurement accuracy. In contrast, virtual non-contrast images obtained from dual-energy computed tomography effectively separate iodine contrast, yielding clearer imaging (14). Moreover, low-density materials—such as loose connective tissue, fibrous tissue, lipid-rich necrotic cores, and adipose tissue—exhibit pronounced attenuation differences at low kiloelectron volts (keV), thereby improving the predictive efficacy of dual-energy CTA (21). Our results indicate that, whether in plaques or

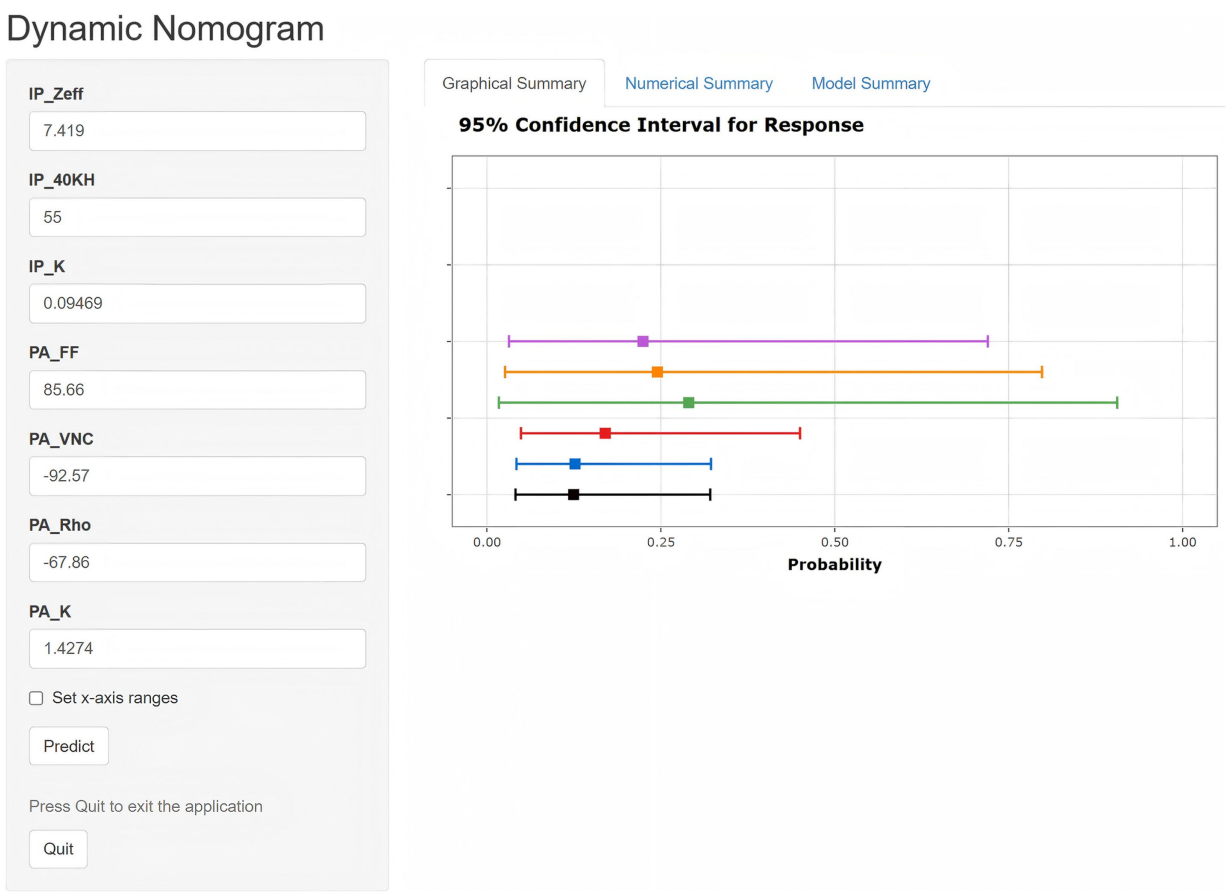

FIGURE 2
Dynamic nomogram illustrating DECTA parameters used for predicting SAT risk.

TABLE 4 Predictive performance of DECTA parameters for SAT.

DECTA parameters	AUC (95%CI)	Sensitivity (%)	Specificity (%)
IntraPlaque (IP-)			
IP_Zeff	0.713 (0.578, 0.848)	70.8	70.6
IP_40KH	0.797 (0.674, 0.919)	66.7	88.2
IP_K	0.795 (0.676, 0.915)	75.0	82.4
IP_Model	0.805 (0.683, 0.926)	66.7	88.2
Perivascular fat (PA-)			
PA_FF	0.777 (0.670, 0.883)	91.7	62.7
PA_VNC	0.811 (0.711, 0.912)	75.0	72.5
PA_Rho	0.725 (0.594, 0.855)	70.8	74.5
PA_K	0.839 (0.745, 0.932)	83.3	76.5
PA_Model	0.913 (0.845, 0.980)	83.3	86.3
Overall combined variables			
Nomo_Model	0.962 (0.925, 1.000)	95.8	82.4

FF, fat fraction; IC, iodine concentration; VNC, virtual non-contrast; Rho, electron density; Zeff, effective atomic number; 40KH, CT values at 40 keV; 90KH, CT values at 90 keV; K, the slope of the energy spectrum curve; IP_Model, the plaque model; PA_Model, perivascular adipose tissue model; Nomo_Model, nomogram model.

PVAT, 40 keV Hounsfield units (40KH) serve as the most reliable indicator for STA, underscoring the advantages of employing lower keV to distinguish low-density materials.

Furthermore, neovascularization within plaques is intricately linked to increased plaque activity, contributing to a heightened risk of neovascular rupture, bleeding, and inflammation (22). Several studies have documented a correlation between plaque enhancement and the extent of neovascularization (23). Specifically, in our analysis, the STA group exhibited a higher iodine concentration (IP_IC) compared to the ATA group, suggesting maybe greater neovascularization within STA plaques.

The effective atomic number (Zeff), which reflects the average atomic number of materials within a ROI, provides insights into tissue composition (11). Notably, higher density materials lead to a reduced slope of the energy spectrum curve and relatively elevated 40KH values (13). Our observations reveal that the slope of the energy spectrum curve (IP_K) in the STA group was lower than in the ATA group, while IP_40KH was higher, indicating the presence of denser components in the STA plaques. In support of this, international studies have demonstrated a robust correlation between IPH and acute cerebrovascular events (24, 25). Thus, we speculate that the STA group may harbor a higher proportion of IPH, necessitating further verification through high-resolution MRI.

Traditional CTA lacks the sensitivity required to assess tissue composition within the PVAT, limiting its ability to provide detailed information on plaque vulnerability. In contrast, DECTA enables precise measurements of iodine concentration and fat fraction in PVAT, offering critical insights into tissue characteristics associated

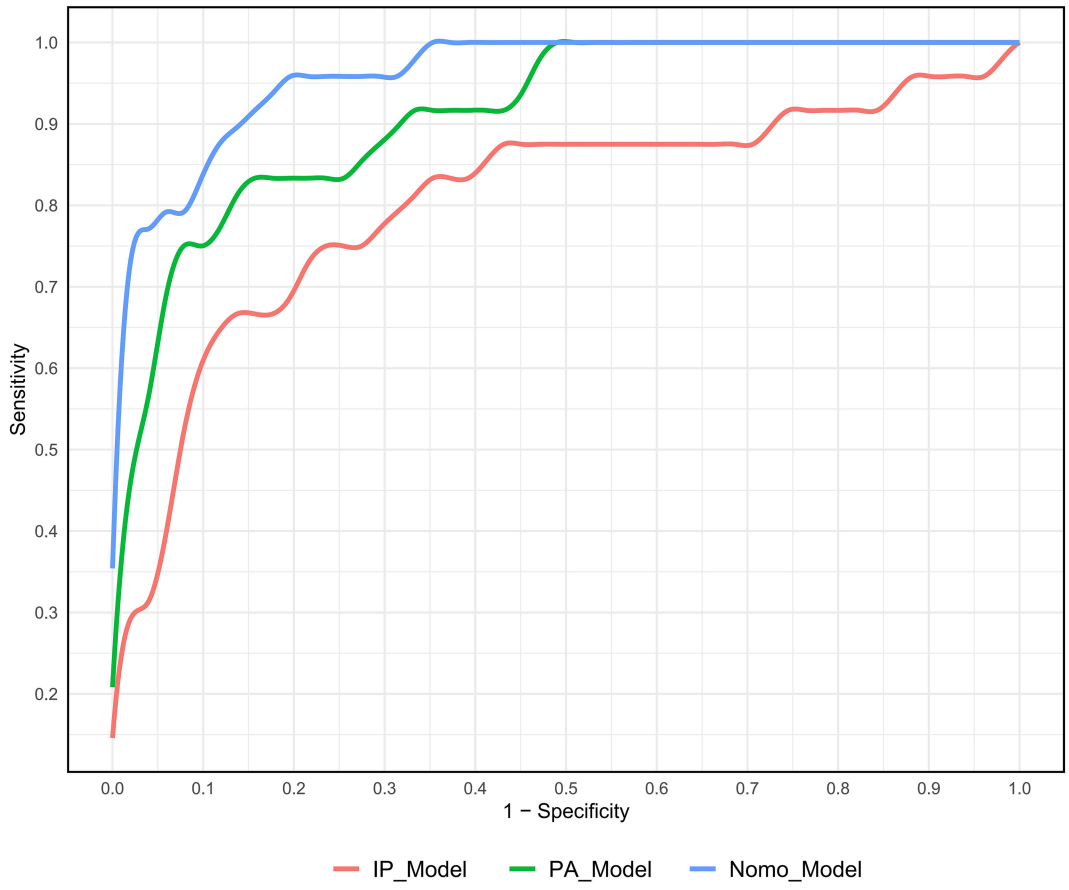

FIGURE 3
ROC curve analysis of three different DECTA models for predicting SAT.

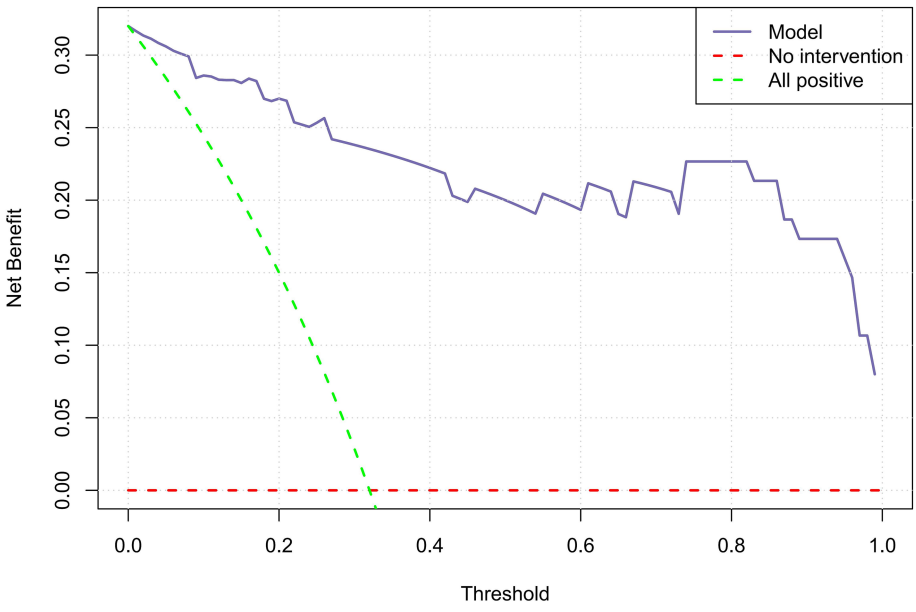

FIGURE 4
Clinical decision curve illustrating the net benefit of the Nomo_Model.

with stroke risk. This capability facilitates a comprehensive evaluation of plaque stability and inflammation, both of which are key factors in stroke prediction.

The study underscores the value of DECTA imaging in identifying imaging biomarkers that enhance risk prediction for acute stroke. The significant differences in intraplaque and PVAT parameters between STA and ATA groups demonstrate the importance of combining both tissue-specific and vascular imaging in clinical assessments. The dynamic nomogram provides a practical and accessible tool for clinicians to estimate individual stroke risk. By incorporating multiple DECTA parameters, the model improves predictive accuracy and facilitates personalized treatment planning. Traditional clinical characteristics often fail to differentiate between STA and ATA groups. The integration of DECTA-derived parameters offers a non-invasive and precise method to evaluate plaque vulnerability and perivascular tissue characteristics, ultimately improving diagnostic outcomes.

The nomogram model provides a valuable non-invasive tool for screening patients at high risk of acute stroke. By incorporating DECTA parameters from carotid plaques and PVAT, it helps identify vulnerable plaques, allowing clinicians to prioritize high-risk patients for intensive monitoring and intervention. The model also aids in risk stratification, guiding decisions on whether additional diagnostic tests, such as MRI or cerebral angiography, are necessary. For low-risk patients, the nomogram helps optimize resource allocation and avoid unnecessary testing. Ultimately, it supports personalized treatment strategies, such as aggressive risk factor management or surgical intervention for high-risk individuals. Integrating the model into clinical decision support systems could enhance routine practice and streamline workflows in stroke centers.

While this study focused on DECTA, future research could enhance the nomogram by incorporating additional imaging techniques. High-resolution MRI could offer further details on plaque composition, such as LRNC and IPH, improving stroke risk prediction. Carotid ultrasound combined with elastography could assess plaque stiffness, providing complementary data. Including biomarkers, like lipid profiles and inflammatory markers, could also add valuable insights into the biological processes driving plaque instability. Finally, prospective validation in larger, multi-center cohorts is essential to test the model's accuracy and generalizability across diverse clinical settings. These steps would refine the model and increase its clinical utility in patient risk assessment and management.

While DECTA offers advantages in distinguishing low-density tissues and assessing plaque vulnerability, factors such as radiation dosage, scanning parameters, and iodine contrast effects on surrounding tissues can influence its effectiveness. Excessive radiation or inconsistent parameters may introduce artifacts or variations in fat fraction and iodine concentration, compromising the accuracy of plaque and PVAT evaluations. Future studies should focus on standardizing scanning protocols to minimize these effects and ensure reproducibility. Additionally, high-resolution MRI is essential for validating DECTA findings, particularly for the accurate assessment of plaque and PVAT characteristics.

This study has several limitations: (1) the sample size is relatively small; we plan to expand this research by conducting a multi-center study with a larger cohort of patients from diverse clinical settings; (2) as a single-center retrospective clinical investigation, it lacks external validation. We intend to collaborate with other medical institutions to validate our nomogram model in independent cohorts, using standardized DECTA imaging protocols to minimize variability and enhance reproducibility; and (3) the assessment of plaques requires further validation through high-resolution MRI.

Conclusion

DECTA imaging parameters revealed significant differences in carotid intraplaque and PVAT characteristics between the STA and ATA groups. Integrating these parameters into the nomogram (Nomo_Model) resulted in a highly accurate and clinically relevant tool for predicting acute stroke risk. However, the small sample size and lack of external validation limit the model's generalizability.

Data availability statement

The datasets presented in this article are not readily available because they may require compliance with ethical and privacy protection requirements, and approval according to relevant agreements. Requests to access the datasets should be directed to YM, mengyankai@126.com.

Ethics statement

The studies involving humans were approved by the Medical Ethics Committee of the Affiliated Hospital of Xuzhou Medical University. The studies were conducted in accordance with the local legislation and institutional requirements. Written informed consent for participation was not required from the participants or the participants' legal guardians/next of kin in accordance with the national legislation and institutional requirements.

Author contributions

HZ: Data curation, Investigation, Methodology, Software, Visualization, Writing – original draft, Writing – review & editing. JL: Data curation, Writing – review & editing. CW: Data curation, Writing – review & editing. XL: Data curation, Writing – review & editing. HL: Data curation, Writing – review & editing. WX: Data curation, Writing – review & editing. XS: Data curation, Writing – review & editing. PD: Writing – review & editing, Data curation. DZ: Supervision, Writing – review & editing. LZ: Supervision, Writing – review & editing. KX: Supervision, Writing – review & editing. YM: Conceptualization, Data curation, Investigation, Methodology, Resources, Supervision, Writing – original draft, Writing – review & editing.

Funding

The author(s) declare that financial support was received for the research, authorship, and/or publication of this article. This study was supported by the Jiangsu Provincial Health Commission's Elderly Health Research Project (LKM2022018); the Jiangsu Provincial Traditional Chinese Medicine Science and Technology Development Plan Project (MS2021100); and the Xuzhou City Science and Technology Program

Project (ZYSH20230498, KC23342); Xuzhou Municipal Health Commission Science and Technology Project (XWKYHT20240086).

Conflict of interest

The authors declare that the research was conducted in the absence of any commercial or financial relationships that could be construed as a potential conflict of interest.

Generative AI statement

The author(s) declare that no Gen AI was used in the creation of this manuscript.

Publisher's note

All claims expressed in this article are solely those of the authors and do not necessarily represent those of their affiliated organizations, or those of the publisher, the editors and the reviewers. Any product that may be evaluated in this article, or claim that may be made by its manufacturer, is not guaranteed or endorsed by the publisher.

Supplementary material

The Supplementary material for this article can be found online at: https://www.frontiersin.org/articles/10.3389/fneur.2025.1566395/full#supplementary-material

SUPPLEMENTARY FIGURE S1
In the Siemens workstation's liver VNC mode **(a)** and Rho/Z mode **(b)**, ROIs were placed at the most prominent areas of the plaque (yellow circles). In the Mono E mode, the slope of the energy spectrum curve (IP_K) was acquired (white line) **(c)**. In the Siemens workstation's Liver VNC mode **(d)** and Rho/Z mode **(e)**, two ROIs were placed in the thickest PVAT gaps around the plaque (yellow circles). In the Mono E mode, the slope of the energy spectrum curve (PA_K) was calculated (white line) **(f)**.

SUPPLEMENTARY FIGURE S2
Selection of the optimal regularization parameter λ using 10-fold cross-validation. The dashed lines represent two λ values: one minimizing cross-validation error, and the other representing one standard error.

SUPPLEMENTARY FIGURE S3
Coefficient paths for variables in LASSO regression model. The dashed line represents the optimal value of λ. The asterisk (*) indicates the variables retained after selection.

SUPPLEMENTARY FIGURE S4
Confusion matrix heatmap of the Nomo_Model.

SUPPLEMENTARY FIGURE S5
Calibration curve showing the alignment between predicted and observed probabilities for the Nomo_Model.

References

1. Fu J, Deng Y, Ma Y, Man S, Yang X, Yu C, et al. National and provincial-level prevalence and risk factors of carotid atherosclerosis in Chinese adults. *JAMA Netw Open*. (2024) 7:e2351225. doi: 10.1001/jamanetworkopen.2023.51225

2. Kamtchum-Tatuene J, Wilman A, Saqqur M, Shuaib A, Jickling GC. Carotid plaque with high-risk features in embolic stroke of undetermined source: systematic review and Meta-analysis. *Stroke*. (2020) 51:311–4. doi: 10.1161/strokeaha.119.027272

3. Naghavi M, Libby P, Falk E, Casscells SW, Litovsky S, Rumberger J, et al. From vulnerable plaque to vulnerable patient: a call for new definitions and risk assessment strategies: part I. *Circulation*. (2003) 108:1664–72. doi: 10.1161/01.Cir.0000087480.94275.97

4. Hu H, Garcia-Barrio M, Jiang ZS, Chen YE, Chang L. Roles of perivascular adipose tissue in hypertension and atherosclerosis. *Antioxid Redox Signal*. (2021) 34:736–49. doi: 10.1089/ars.2020.8103

5. Ross R. Atherosclerosis--an inflammatory disease. *N Engl J Med*. (1999) 340:115–26. doi: 10.1056/nejm199901143400207

6. Boussel L, Arora S, Rapp J, Rutt B, Huston J, Parker D, et al. Atherosclerotic plaque progression in carotid arteries: monitoring with high-spatial-resolution MR imaging--multicenter trial. *Radiology*. (2009) 252:789–96. doi: 10.1148/radiol.2523081798

7. Bianda N, di Valentino M, Periat D, Segatto JM, Oberson M, Moccetti M, et al. Progression of human carotid and femoral atherosclerosis: a prospective follow-up study by magnetic resonance vessel wall imaging. *Eur Heart J*. (2012) 33:230–7. doi: 10.1093/eurheartj/ehr332

8. Saam T, Cai J, Ma L, Cai YQ, Ferguson MS, Polissar NL, et al. Comparison of symptomatic and asymptomatic atherosclerotic carotid plaque features with in vivo MR imaging. *Radiology*. (2006) 240:464–72. doi: 10.1148/radiol.2402050390

9. Baradaran H, Myneni PK, Patel P, Askin G, Gialdini G, al-Dasuqi K, et al. Association between carotid artery perivascular fat density and cerebrovascular ischemic events. *J Am Heart Assoc*. (2018) 7:e010383. doi: 10.1161/jaha.118.010383

10. Zhang S, Yu X, Gu H, Kang B, Guo N, Wang X. Identification of high-risk carotid plaque by using carotid perivascular fat density on computed tomography angiography. *Eur J Radiol*. (2022) 150:110269. doi: 10.1016/j.ejrad.2022.110269

11. Hua CH, Shapira N, Merchant TE, Klahr P, Yagil Y. Accuracy of electron density, effective atomic number, and iodine concentration determination with a dual-layer dual-energy computed tomography system. *Med Phys*. (2018) 45:2486–97. doi: 10.1002/mp.12903

12. Duan X, Li Z, Yu L, Leng S, Halaweish AF, Fletcher JG, et al. Characterization of urinary Stone composition by use of third-generation dual-source dual-energy CT with increased spectral separation. *AJR Am J Roentgenol*. (2015) 205:1203–7. doi: 10.2214/ajr.15.14348

13. Chen JF, Yang J, Chen WJ, Wei X, Yu XL, Huang DD, et al. Mono+ algorithm assessment of the diagnostic value of dual-energy CT for high-risk factors for colorectal cancer: a preliminary study. *Quant Imaging Med Surg*. (2024) 14:432–46. doi: 10.21037/qims-23-291

14. Zhang J, Li S, Wu L, Wang H, Wang C, Zhou Y, et al. Application of dual-layer spectral-detector computed tomography angiography in identifying symptomatic carotid atherosclerosis: a prospective observational study. *J Am Heart Assoc*. (2024) 13:e032665. doi: 10.1161/jaha.123.032665

15. Wang LJ, Zhai PQ, Xue LL, Shi CY, Zhang Q, Zhang H. Machine learning-based identification of symptomatic carotid atherosclerotic plaques with dual-energy computed tomography angiography. *J Stroke Cerebrovasc Dis*. (2023) 32:107209. doi: 10.1016/j.jstrokecerebrovasdis.2023.107209

16. Mendelson SJ, Prabhakaran S. Diagnosis and Management of Transient Ischemic Attack and Acute Ischemic Stroke: a review. *JAMA*. (2021) 325:1088–98. doi: 10.1001/jama.2020.26867

17. Katsiki N, Mikhailidis DP. Perivascular adipose tissue: pathophysiological links with inflammation, atherosclerosis, and thrombosis. *Angiology*. (2022) 73:195–6. doi: 10.1177/00033197211014676

18. Kim HW, Shi H, Winkler MA, Lee R, Weintraub NL. Perivascular adipose tissue and vascular perturbation/atherosclerosis. *Arterioscler Thromb Vasc Biol*. (2020) 40:2569–76. doi: 10.1161/atvbaha.120.312470

19. Lombardo A, Biasucci LM, Lanza GA, Coli S, Silvestri P, Cianflone D, et al. Inflammation as a possible link between coronary and carotid plaque instability. *Circulation*. (2004) 109:3158–63. doi: 10.1161/01.Cir.0000130786.28008.56

20. Cau R, Anzalone N, Mannelli L, Edjlali M, Balestrieri A, Nardi V, et al. Pericarotid fat as a marker of cerebrovascular risk. *AJNR Am J Neuroradiol*. (2024) 45:1635–41. doi: 10.3174/ajnr.A8300

21. Li Z, Cao J, Bai X, Gao P, Zhang D, Lu X, et al. Utility of dual-layer spectral detector CTA to characterize carotid atherosclerotic plaque components: an imaging-histopathology comparison in patients undergoing endarterectomy. *AJR Am J Roentgenol*. (2022) 218:517–25. doi: 10.2214/ajr.21.26540

22. Falk E. Pathogenesis of atherosclerosis. *J Am Coll Cardiol*. (2006) 47:C7–C12. doi: 10.1016/j.jacc.2005.09.068

23. Saba L, Lai ML, Montisci R, Tamponi E, Sanfilippo R, Faa G, et al. Association between carotid plaque enhancement shown by multidetector CT angiography and histologically validated microvessel density. *Eur Radiol*. (2012) 22:2237–45. doi: 10.1007/s00330-012-2467-5

24. Saam T, Hetterich H, Hoffmann V, Yuan C, Dichgans M, Poppert H, et al. Meta-analysis and systematic review of the predictive value of carotid plaque hemorrhage on cerebrovascular events by magnetic resonance imaging. *J Am Coll Cardiol*. (2013) 62:1081–91. doi: 10.1016/j.jacc.2013.06.015

25. Saba L, Saam T, Jäger HR, Yuan C, Hatsukami TS, Saloner D, et al. Imaging biomarkers of vulnerable carotid plaques for stroke risk prediction and their potential clinical implications. *Lancet Neurol*. (2019) 18:559–72. doi: 10.1016/s1474-4422(19)30035-3

Glossary

LRNC - large lipid-rich necrotic core

IPH - intraplaque hemorrhage

PVAT - perivascular adipose tissue

CTA - CT angiography

DECT - Dual-energy CT

VNC - virtual non-contrast

FF - fat fraction

IC - iodine concentration

Rho - electron density

Zeff - effective atomic number

K - the slope of the energy spectrum curve

40KH - the CT value corresponding to 40 keV on the energy spectrum curve

90KH - the CT value corresponding to 90 keV on the energy spectrum curve

TR - repetition time

TE - echo time

FOV - field of view

ROI - Regions of interest

PACS - Picture Archiving and Communication System

DWI - diffusion-weighted imaging

ADC - apparent diffusion coefficient

ICA - internal carotid artery

BMI - body mass index

TIA - transient ischemic attack

ROC - receiver operating characteristic

keV - kiloelectron volts

DCA - decision curve analysis

frontiers | Frontiers in Neurology

TYPE Original Research
PUBLISHED 21 March 2025
DOI 10.3389/fneur.2025.1514679

OPEN ACCESS

EDITED BY
Liang Jiang,
Nanjing Medical University, China

REVIEWED BY
Jacopo Scaggiante,
Gemelli Hospital, Italy
Sergio Manuel Solis-Barquero,
University Clinic of Navarra, Spain

*CORRESPONDENCE
Ling Li
✉ l.l0622@foxmail.com
Xuejiao Yan
✉ qywmsfw@163.com

RECEIVED 21 October 2024
ACCEPTED 27 February 2025
PUBLISHED 21 March 2025

CITATION
Li L, Pan P, Zhang N, Wen Y, Tang M, Ai K, Zhang X, Lei X and Yan X (2025) Distinguishing stroke from transient ischemic attack using plaque characteristics and arterial transit artifacts.
Front. Neurol. 16:1514679.
doi: 10.3389/fneur.2025.1514679

Distinguishing stroke from transient ischemic attack using plaque characteristics and arterial transit artifacts

Ling Li[1]*, Peichun Pan[2], Na Zhang[1], Yu Wen[1], Min Tang[1], Kai Ai[3], Xiaoling Zhang[1], Xiaoyan Lei[1] and Xuejiao Yan[1]*

[1]Shaanxi Provincial People's Hospital, Xi'an, China, [2]Faculty of Medical Technology, Shaanxi University of Chinese Medicine, Xianyang, China, [3]Department of Clinical Science, Philips Healthcare, Xi'an, China

Purpose: We aimed to investigate the differences in plaque characteristics and hemodynamics in patients with ischemic stroke and transient ischemic attack (TIA), comparing the diagnostic abilities of high-resolution magnetic resonance imaging (HRMRI) and arterial spin labeling (ASL) for ischemic stroke.

Methods: This retrospective analysis included patients who underwent HRMRI and ASL between October 2020 and December 2023. We compared clinical risk factors, vascular plaque characteristics, and the presence of arterial transit artifacts (ATAs) at post-labeling delays (PLDs) of 1.5-s and 2.5-s between stroke and TIA groups. Multivariate logistic regression analysis was used to evaluate the diagnostic performance of different prediction models combining clinical factors, differential plaque characteristics, and the presence of ^PLD ATAs.

Results: A total of 147 patients (mean age, 57.12 ± 13.08 years; 102 men) were initially included in this study, divided into stroke (79) and TIA (68) groups. Significant differences in vascular positive remodeling, intraplaque hemorrhage, enhancement ratio, and the presence of 1.5-s and 2.5-s ATAs ($p < 0.05$) were observed between groups. Combined HRMRI and ASL performed best in distinguishing ischemic stroke and TIA (area under the curve [AUC], 0.926; 95% confidence interval [CI], 0.885–0.967), with no significant difference in ischemic stroke diagnostic performance between HRMRI and ASL (95% CI, −0.039 to 0.087, $Z = 0.742$, $p = 0.458$).

Conclusion: A model combined with plaque characteristics and ATAs showed good diagnostic performance in distinguishing between TIA and stroke in patients with intracranial atherosclerotic stenosis. ASL provides a simpler imaging evaluation method than HRMRI, and ATA evaluation may become a more widely used imaging marker in clinical practice.

KEYWORDS

arterial spin labeling, arterial transit artifacts, high-resolution MRI, transient ischemic attack, stroke

Introduction

Ischemic stroke is a common cerebrovascular disease which has become one of the main causes of disease-related death in China (1, 2). Intracranial atherosclerotic stenosis (ICAS), which most commonly involves the middle cerebral artery (MCA), is the main cause of transient ischemic attack (TIA) and ischemic stroke (3, 4). TIA is a clinical precursor to the onset of ischemic stroke: approximately 7.5 to 17.4% of patients with TIA develop an ischemic stroke within 3 months (5, 6). Therefore, differences in plaque characteristics and hemodynamics between patients with ischemic stroke and TIA must be evaluated. This facilitates clinical risk stratification to guide specific treatment in patients with symptomatic atherosclerotic stenosis.

In clinical practice, the standard diagnostic approach for intracranial atherosclerotic stenosis (ICAS) primarily relies on vascular imaging to evaluate the degree of stenosis and plaque morphology (4). High-resolution magnetic resonance imaging (HRMRI) can non-invasively characterize lumen and plaque features of intracranial atherosclerosis, such as plaque morphology and plaque burden, which are associated with ischemic events (4, 7, 8). However, patients with ICAS rarely undergo MRI assessments using techniques for evaluating hemodynamic injuries, such as dynamic sensitivity contrast-enhanced (DSC) perfusion-weighted imaging (PWI) or arterial spin labeling (ASL) (9, 10). Consequently, studies distinguishing the plaque and hemodynamic features in patients with TIA and irreversible infarction are limited. Although DSC-PWI findings are associated with neurological impairment (11), DSC-PWI is an invasive procedure that requires complex post-processing, making it cumbersome and unsuitable for patient populations such as those with renal dysfunction (12).

Unlike DSC-PWI, ASL allows convenient and non-invasive visual assessment of arterial transport artifacts (ATAs), which occur when labeled blood remains in the supplying arteries/arterioles without being distributed to the microvascular system and tissues. These artifacts appear as bright signals in blood vessels on the surface of the brain and can indicate collateral blood flow and arterial stenosis/occlusion (13). Two single ASL scans performed with different post-labeling delays (PLDs), such as 1,500 and 2,500 ms, can visualize collateral circulation, providing valuable information and facilitating diagnoses (14, 15).

A multimodal approach combining plaque characteristics, hemodynamic parameters, and clinical risk factors may help to understand the mechanism of stroke occurrence. However, studies of differences between TIA and stroke patients have focused on plaque characteristics, and few studies have used ASL for assessment (11). We aimed to investigate differential characteristics of plaque in MCA and hemodynamics in patients with ischemic stroke and TIA and to compare the ability of HRMRI and ASL with two PLDs to predict the occurrence of ischemic stroke.

Abbreviations: ASL, Arterial spin labeling; ATA, Arterial transit artifact; AUC, Area under the curve; DSC, Dynamic sensitivity contrast-enhanced; DWI, Diffusion-weighted imaging; HRMRI, High-resolution magnetic resonance imaging; ICAS, Intracranial atherosclerotic stenosis; ICC, Intraclass correlation coefficient; MCA, Middle cerebral artery; MLN, Maximum lumen narrowing; PLD, Post-labeling delay; PWI, Perfusion-weighted imaging; ROC, Receiver operating characteristic; T1W1, T1-weighted imaging; T2WI, T2-weighted imaging; TIA, Transient ischemic attack; TOF-MRA, Time-of-flight magnetic resonance angiography.

Materials and methods

Ethics

The study was approved by the ethics committee of our institution and was performed in accordance with the tenets of the 1964 Declaration of Helsinki and its later amendments or comparable ethical standards. The need for informed consent was waived.

Patients

The data of symptomatic ICAS patients with moderate-to-severe MCA stenosis who underwent intracranial HRMRI and ASL examinations between October 2020 and December 2023 were selected from the hospital database for retrospective analysis.

The inclusion criteria were as follows: (1) clinical and imaging diagnosis of acute or subacute ischemic stroke or TIA in the MCA region within 2 weeks of symptom onset; (2) unilateral MCA stenosis detected in time-of-flight magnetic resonance angiography (TOF-MRA); and (3) at least one intracranial atherosclerotic plaque. Exclusion criteria were as follows: (1) ultrasound or magnetic resonance angiography or computed tomography angiography revealed a bilateral internal carotid artery or contralateral MCA stenosis of >50%; (2) non-ICAS diseases such as Moyamoya disease, arterial dissection, or vasculitis; (3) suspected cardioembolism; (4) incomplete clinical data or laboratory results; and (5) unsatisfactory image quality. A previously established 4-point scale was used to assess the MRI quality (1 = poor quality, 2 = acceptable, 3 = good quality, 4 = excellent). Images rated as poor quality were excluded from the final study. Figure 1 provides a flowchart of inclusion and exclusion criteria.

The patients were classified into stroke and TIA groups according to the results of diffusion-weighted imaging (DWI) and neurological examinations. TIA was defined as a transient episode of neurological dysfunction caused by focal cerebral ischemia that is not accompanied by acute cerebral infarction. In contrast, acute ischemic stroke was defined as sudden neurologic dysfunction caused by focal brain ischemia lasting more than 24 h or with evidence of acute infarction on brain imaging and diffusion restriction on DWI (6). Among the 147 patients included in the study, 79 and 68 were categorized into the ischemic stroke and TIA groups, respectively.

Clinical data collection

The following clinical information was obtained: age; sex; smoker; BMI; hypertension [self-reported high blood pressure history, mean blood pressure > 140/90 mmHg, or the use of antihypertensive medication (16)]; diabetes [patients using insulin or oral hypoglycemic agents or newly diagnosed with diabetes based on hemoglobin A1C ≥6.5% (17)]; hyperlipidemia [total cholesterol ≥5.2 mmol/L, triglycerides ≥1.7 mmol/L, high-density lipoprotein cholesterol ≤1.0 mmol/L, low-density lipoprotein cholesterol ≥3.4 mmol/L (18)]; hyperhomocysteinemia (homocysteine ≥15 μmol/L); and history of coronary artery disease (19).

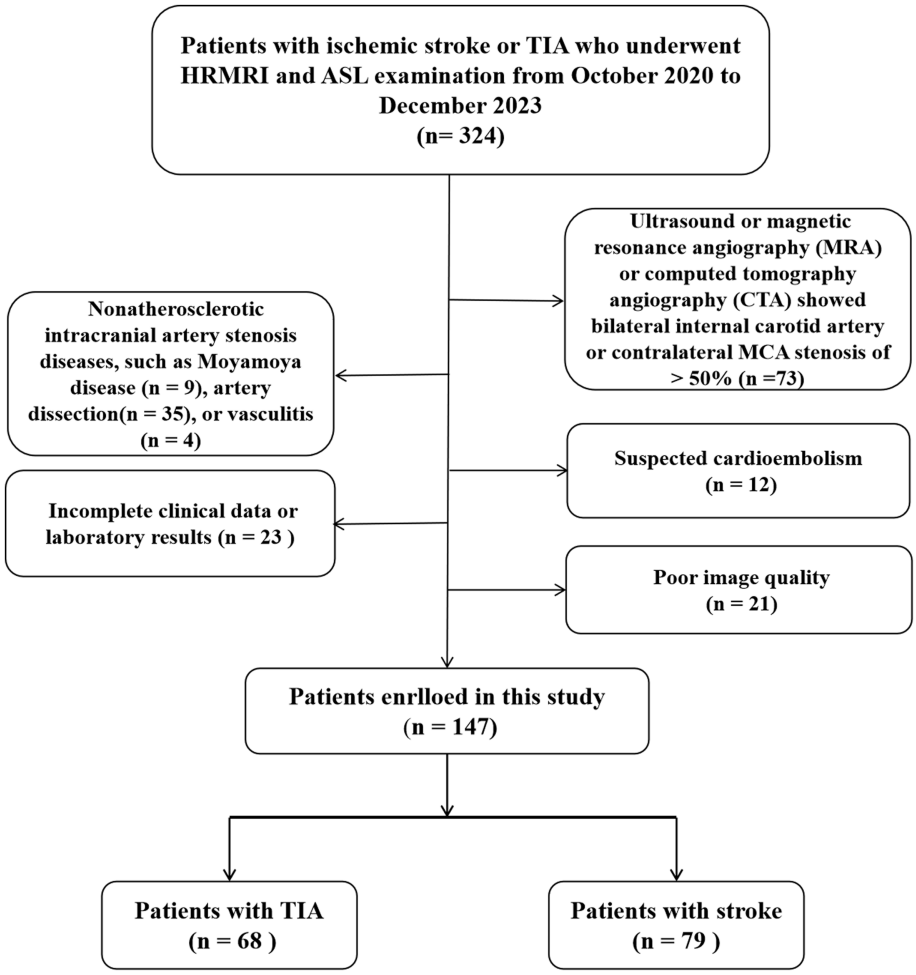

FIGURE 1
Flowchart of the study population. TIA, transient ischemic attack; HRMRI, high-resolution magnetic resonance imaging; ASL, arterial spin labeling.

MRI protocol

Imaging was performed on a 3.0-T Philips Ingenia CX scanner. The scan protocols included a head MRI routine examination (T1-weighted imaging [T1WI], T2-weighted imaging [T2WI], and fluid attenuation inversion recovery) and DWI examination. HRMRI was performed within 1 week of symptom onset, including three-dimensional (3D)-TOF MRA, 3D-T1WI-Volume-isotropic TSE acquisition (VISTA), T2WI-Turbo Spin Echo (TSE), 3D-T1-Vista enhanced imaging, and 2-PLD ASL-PWI. The parameters of these sequences are provided in Table 1.

Image analysis

All MRI data were transferred to semiautomatic software[1] for analysis. Plaque characterization and ASL visual assessment were performed on a workstation by two experienced neuroradiologists (with 10 and 6 years of experience in neuroimaging diagnosis, respectively) who had no knowledge of the patient's clinical information or previous imaging data. For qualitative assessments, a third senior neuroradiologist (with 17 years of experience) was consulted to review the images and help reach a consensus. For quantitative evaluations, the average of the measurements from the two radiologists was used in the final analysis. Atherosclerotic plaque was defined as significantly eccentric or focal thickening of the vessel wall on reconstructed HRMRI images, with the thinnest wall ≤50% of the thickest (20). The plaque characteristics of MCA maximum lumen stenosis (MLN) were analyzed. First, the post-contrast T1WI images were reconstructed using a multi-plane reconstruction tool, according to the vascular orientation of the MLN site. Then, the inner and outer walls of the lumen on the short-axis reconstructed image were manually sketched using post-processing software. The reference site was the lumen without plaque closest to the proximal or distal end of the MLN site. Maximum wall thickness, total vascular area, and lumen area were measured three times and averaged for final statistical analysis. The plaque characteristics were evaluated as follows (21, 22):

a. Plaque burden = [1 − lumen $area_{(MLN)}$/total vessel $area_{(MLN)}$] × 100%.

1 tsimaging.net

TABLE 1 Imaging parameters for each sequence.

Imaging parameters	TR (ms)	TE (ms)	FOV (mm)	Matrix (mm)	Slice thickness (mm)	Slice gap (mm)
T1WI	2000	20	230 × 180	512 × 512	6	1
T2WI	2,500	80	230 × 180	512 × 512	6	1
FLAIR	6,000	120	230 × 180	480 × 480	6	1
DWI	2,562	94	230 × 230	224 × 224	6	1
TOF-MRA	20	3.6	180 × 180	512 × 512	0.5	0
3D-T1WI-VISTA	700	16	180 × 180	256 × 256	0.6	0
T2WI-TSE	3,000	90	140 × 100	288 × 288	2.0	0.2
1.5 s-ASL	3,935	9.8	240 × 240	80 × 80	6.0	0
2.5 s-ASL	3,935	9.8	240 × 240	80 × 80	6.0	0

TR, repetition time; TE, echo time; FOV, field of view. Post-contrast T1WI was performed 5 min after injecting a single dose (0.1 mmol/kg of body weight) of gadolinium-based contrast agent (Magnevist; Bayer HealthCare Pharmaceuticals).

b. Degree of stenosis = [1 − lumen area$_{(MLN)}$/lumen area$_{(reference)}$] × 100%.
c. Remodeling index = total vessel area$_{(MLN)}$/total vessel area$_{(reference)}$.

Remodeling index ≥1.05 and < 1.05 indicated positive and non-positive remodeling, respectively.

d. Eccentricity index = maximum wall thickness – minimum wall thickness/maximum wall thickness.
e. Intraplaque hemorrhage was defined as the T1WI signal in the plaque being ≥150% of the T1WI signal in the adjacent muscle or pons.
f. Enhancement was assessed by comparing pre- and post-enhancement HRMRI. Plaque enhancement was classified into three grades: grade 2 (enhancement equal to or greater than the pituitary funnel), grade 1 (enhancement greater than the normal intracranial vascular wall but less than the pituitary funnel), and grade 0 (enhancement equal to or less than the normal intracranial vascular wall). The enhanced ratio was estimated as follows: enhanced ratio = (Signal$_{post}$ − Signal$_{pre}$)/Signal$_{pre}$.
g. ATAs were defined by the presence of highlighted signals in blood vessels covering the surface of the brain. Our study used ASL of two PLDs (1.5 s and 2.5 s) and evaluated the presence of ATAs on two PLD (hereafter referred to as 2-PLD ATAs) images (10).

Statistical analysis

The normality of continuous variables was assessed using the Shapiro–Wilk test. Normally distributed data are presented as mean ± standard deviation and analyzed with the Student's *t*-test, while non-normally distributed data are presented as median (25th–75th percentile) and analyzed using the Mann–Whitney U-test. Categorical variables are presented as counts and percentages and compared using the chi-square test or Fisher's exact test when the expected frequency was below 5. Inter-reader reliability was analyzed using intraclass correlation efficient (ICC) values. Variables were selected for multivariate analysis through (1) statistical significance threshold ($p < 0.05$) in univariate analyses, and (2) variables with established biological or clinical relevance, such as age and gender, were included in the multivariate analysis, regardless of their univariate statistical significance. Models using different combinations of risk factors were constructed, and the diagnostic performance of each model was assessed using receiver operating characteristic (ROC) curves. The Z-test was used to compare the area under the curve (AUC) of the different models. The above statistics were two-sided and performed using SPSS (version 26, IBM) or R (version 4.0.4, R Foundation for Statistical). A $p < 0.05$ is considered statistically significant.

Results

Patient demographics and clinical characteristics

A total of 147 patients (mean age, 57.12 ± 13.08 years; 29–88 years, 102 men) were initially included in this study, including 68 patients (59.82 ± 13.38 years, 46 men) in the TIA group and 79 patients (54.79 ± 12.44 years, 56 men) in the stroke group. Demographic and clinical characteristics of the enrolled patients are presented in Table 2. Compared with TIA patients, stroke patients were younger and had a significantly higher prevalence of hypertension ($p = 0.001$). The remaining clinical characteristics showed no significant differences between the two groups.

Inter-reader agreement

Measurement of plaque characteristics and ASL showed good-to-excellent inter-reader agreement (ICC = 0.796–0.966; $p < 0.001$), as shown in Supplementary Table 1.

Intergroup differences in plaque characteristics and the presence of 2-PLD ATAs

The comparison of plaque characteristics and the presence of 2-PLD ATAs between the two groups are shown in Table 3.

TABLE 2 Demographic and clinical characteristics of the enrolled patients.

Characteristics	Total sample (n = 147)	TIA group (n = 68)	Stroke group (n = 79)	p-value
Age (years)	57.12 ± 13.08	59.82 ± 13.38	54.79 ± 12.44	0.021[a,*]
Male sex	102 (69.39)	46 (67.65)	56 (70.89)	0.806
Smoker	92 (62.59)	46 (67.65)	46 (58.23)	0.315
BMI	24.38 [22.51, 26.08]	24.80 [22.62, 26.44]	24.00 [22.51, 25.89]	0.367
Hypertension	95 (64.63)	35 (51.47)	60 (75.95)	0.003*
Diabetes mellitus	50 (34.01)	24 (35.29)	26 (32.91)	0.926
HbA1c	5.90 [5.60, 6.55]	5.90 [5.60, 6.73]	5.80 [5.50, 6.40]	0.227
Hyperlipidemia	62 (42.18)	24 (35.29)	38 (48.10)	0.161
TC (mmol/L)	3.70 [3.15, 4.63]	3.76 [3.12, 4.70]	3.70 [3.20, 4.26]	0.556
TG (mmol/L)	1.21 [0.95, 1.60]	1.21 [0.94, 1.78]	1.17 [0.96, 1.43]	0.281
LDL (mmol/L)	0.99 [0.86, 1.20]	1.03 [0.90, 1.20]	0.93 [0.84, 1.10]	0.075
HDL (mmol/L)	2.21 [1.71, 2.73]	2.20 [1.70, 2.82]	2.23 [1.77, 2.66]	0.804
Hyperhomocysteinemia	73 (49.66)	29 (42.65)	44 (55.70)	0.158
Homocysteine (μmol/L)	15.60 [12.80, 24.00]	15.25 [12.80, 24.00]	15.80 [12.95, 23.85]	0.659
History of coronary artery disease	29 (19.73)	9 (13.24)	20 (25.32)	0.104

All values are presented as number (%) or median [interquartile range] unless otherwise indicated. HbA1c, glycosylated hemoglobin; TC, total cholesterol; TG, triglyceride; HDL, high-density lipoprotein cholesterol; LDL, low-density lipoprotein cholesterol. * $p < 0.05$ indicates a significant difference between the two groups.
[a]Data presented as mean ± standard deviation.

TABLE 3 Comparison of HRMRI and ASL characteristics in the two groups.

Characteristics	Total sample (n = 147)	TIA group (n = 68)	Stroke group (n = 79)	p-value
Plaque burden (%)	41.72 ± 14.92	33.77 ± 14.79	48.57 ± 11.23	<0.001*[,a]
Degree of stenosis (%)	72.62 [56.09, 82.45]	62.06 [48.76, 77.77]	77.64 [68.68, 86.63]	<0.001*
Remodeling index	1.06 [0.98, 1.19]	1.03 [0.92, 1.08]	1.13 [1.02, 1.23]	<0.001*
Positive remodeling	76 (51.70)	20 (29.41)	56 (70.89)	<0.001*
Eccentricity index	0.59 ± 0.15	0.60 ± 0.14	0.58 ± 0.16	0.628[a]
Intraplaque hemorrhage	44 (29.93)	8 (11.76)	36 (45.57)	<0.001*
Enhancement ratio (%)	42.77 [17.58, 73.37]	20.52 [7.25, 42.92]	59.88 [35.28, 90.35]	<0.001*
Enhanced grade (%)				<0.001*
Grade 0	21 (14.29)	18 (26.47)	3 (3.80)	
Grade 1	58 (39.46)	42 (61.76)	16 (20.25)	
Grade 2	68 (46.26)	8 (11.76)	60 (75.95)	
1.5-s ATAs present (%)	105 (71.43)	33 (48.53)	72 (91.14)	<0.001*
2.5-s ATAs present (%)	69 (46.94)	11 (16.18)	58 (73.42)	<0.001*

All values are presented as numbers (%) or median [interquartile range] unless otherwise indicated. HRMRI, high-resolution magnetic resonance imaging; TIA, transient ischemic attack; ATA, arterial transit artifacts. * $p < 0.05$ indicates a significant difference between the two groups.
[a]Data presented as mean ± standard deviation.

In the stroke group, plaque burden ($p < 0.001$), degree of stenosis ($p < 0.001$), remodeling index ($p < 0.001$), the prevalence of positive remodeling ($p < 0.001$) and intraplaque hemorrhage ($p < 0.001$), enhanced ratio ($p < 0.001$), and enhanced grade ($p < 0.001$) were significantly higher than in the TIA group. The presence of 1.5-s ATAs and 2.5-s ATAs was more common in the stroke group than in the TIA group ($p < 0.001$).

The ability of plaque characteristics and ASL visual assessment to differentiate ischemic stroke

In the univariate analysis, plaque burden, degree of stenosis, positive remodeling, intraplaque hemorrhage, enhancement ratio, and the presence of 1.5-s and 2.5-s ATAs were associated with stroke ($p < 0.05$, Table 4). We combined the differential plaque characteristics

and the presence of 2-PLD ATAs with clinical factors to establish three models: model 1 (clinical risk factors + plaque characteristics), model 2 (clinical risk factors + presence of 2-PLD ATAs), and model 3 (clinical risk factors + plaque characteristics + presence of 2-PLD ATAs).

In the multivariate logistic regression analysis of model 1, hypertension (OR = 3.2088; 95% CI, 1.214–8.995), positive remodeling (OR = 3.966; 95% CI, 1.323–12.57), intraplaque hemorrhage (OR = 4.580; 95% CI, 1.534–15.45), and enhancement ratio (OR = 1.022; 95% CI, 1.008–1.039) were independent predictors of stroke events. In the multivariate logistic regression analysis of model 2, hypertension (OR = 3.461; 95% CI, 1.376–9.215) and the presence of 1.5-s ATAs (OR = 4.700; 95% CI, 1.673–14.44) and 2.5-s ATAs (OR = 8.743; 95% CI, 3.617–22.69) were independent predictors of stroke events. In the multivariate logistic regression analysis of model 3, positive remodeling (OR = 4.055; 95% CI, 1.243–14.52), enhancement ratio (OR = 1.018; 95% CI, 1.003–1.036), and the presence of 1.5-s ATAs (OR = 4.604; 95% CI, 1.301–17.97) and 2.5-s ATAs (OR = 4.950; 95% CI, 1.610–16.77) were independent predictors of stroke events (Table 4). Figures 2, 3 show a typical example of two groups of patients.

All three models showed excellent diagnostic performance in distinguishing between ischemic stroke and TIA. Model 3 (AUC, 0.926; 95% CI, 0.885–0.967) demonstrated superior diagnostic performance compared to Model 1 (AUC, 0.894; 95% CI, 0.845–0.944, Z = −1.982, $p = 0.047$) and Model 2 (AUC, 0.870; 95% CI, 0.812–0.929, Z = 2.552, $p = 0.011$), while no significant difference was observed between Model 1 and Model 2 (95% CI, −0.039 to 0.087, Z = 0.742, $p = 0.458$). The sensitivities of Model 1, Model 2, and Model 3 were 83.54, 82.28, and 89.87%, respectively; the specificities were 80.88, 80.88, and 85.29%; the positive predictive values were 83.54, 83.33, and 87.65%; the negative predictive values were 80.88, 79.71, and 87.88%; and the accuracies were 82.31, 81.63, and 87.76%, respectively. The ROC curves of the three models are shown in Figure 4.

Discussion

The existing studies on stroke mainly focus on the structure and composition of plaques, and hemodynamic injuries have been less investigated (7, 8, 11). This study combined plaque and hemodynamic

TABLE 4 Multivariate logistic analyses for ischemic stroke appearance.

	Univariable analysis		Multivariable analysis	
	OR (95 CI)	*p*-value	OR (95 CI)	*p*-value
Model 1				
Age (year)	0.97 (0.944–0.995)	0.022*		
Men	0.859 (0.424–1.739)	0.671		
Hypertension	2.977 (1.49–6.093)	0.002*	3.208 (1.214–8.995)	0.021*
Plaque burden	1.09 (1.058–1.128)	<0.001*		
Degree of stenosis	1.047 (1.026–1.071)	<0.001*		
Positive remodeling	5.843 (2.911–12.15)	<0.001*	3.966 (1.323–12.57)	0.016*
Intraplaque hemorrhage	6.279 (2.771–15.76)	0.002*	4.580 (1.534–15.45)	0.009*
Enhancement ratio	1.035 (1.022–1.05)	<0.001*	1.022 (1.008–1.039)	0.004*
Model 2				
Age (year)	0.97 (0.944–0.995)	0.022*		
Men	0.859 (0.424–1.739)	0.671		
Hypertension	2.977 (1.49–6.093)	0.002*	3.461 (1.376–9.215)	0.010*
1.5-s ATAs present	10.909 (4.62–29.14)	<0.001*	4.700 (1.673–14.44)	0.004*
2.5-s ATAs present	14.312 (6.54–33.72)	<0.001*	8.743 (3.617–22.69)	<0.001*
Model 3				
Age (year)	0.97 (0.944–0.995)	0.022*		
Men	0.859 (0.424–1.739)	0.671		
Hypertension	2.977 (1.49–6.093)	0.002*		
Plaque burden	1.09 (1.058–1.128)	<0.001*		
Degree of stenosis	1.047 (1.026–1.071)	<0.001*		
Positive remodeling	5.843 (2.911–12.15)	<0.001*	4.055 (1.243–14.52)	0.024*
Intraplaque hemorrhage	6.279 (2.771–15.76)	0.002*		
Enhancement ratio	1.035 (1.022–1.05)	<0.001*	1.018 (1.003–1.036)	0.024*
1.5-s ATAs present	10.909 (4.62–29.14)	<0.001*	4.604 (1.301–17.97)	0.021*
2.5-s ATAs present	14.312 (6.54–33.72)	<0.001*	4.950 (1.610–16.77)	0.007*

OR, odds ratio; CI, confidence interval; ATAs, arterial transit artifacts. Model 1, clinical risk factors + plaque characteristics; Model 2, clinical risk factors + 2-PLD ATAs present; and Model 3, clinical risk factors + plaque characteristics + 2-PLD ATAs present. * $p < 0.05$ indicates a significant difference.

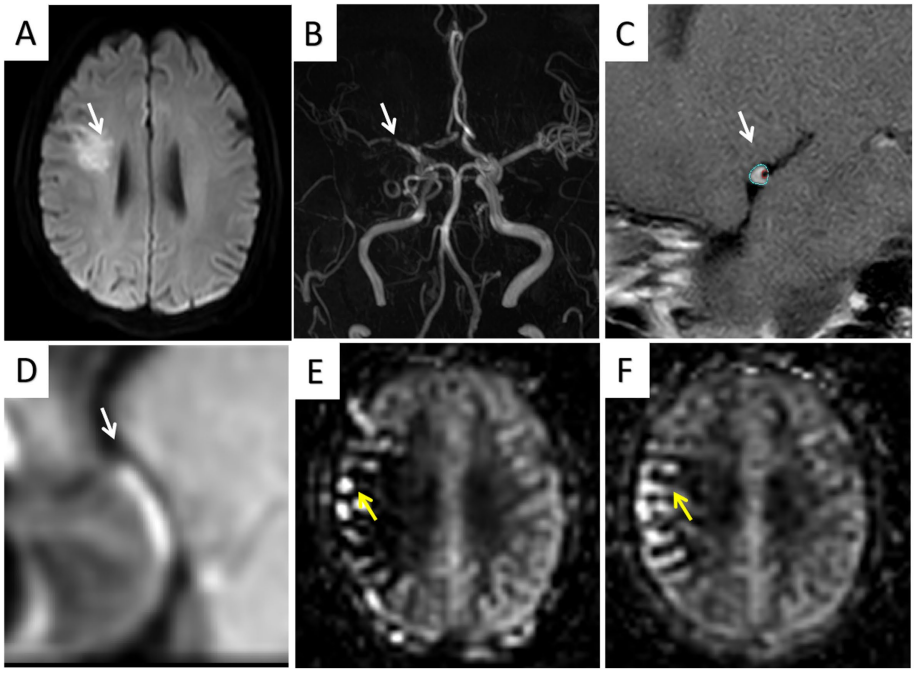

FIGURE 2
A stroke patient (age 73 years) showing a adjacent to the right lateral ventricle infarction **(A)** and right MCA stenosis **(B)**; HRMRI showed significant enhancement of the eccentric plaque **(C,D)**; ATA was present in the lesion area on 1.5-s ASL images **(E)**, and was still present in the lesion area, but with a reduced range, on 2.5-s ASL images **(F)**.

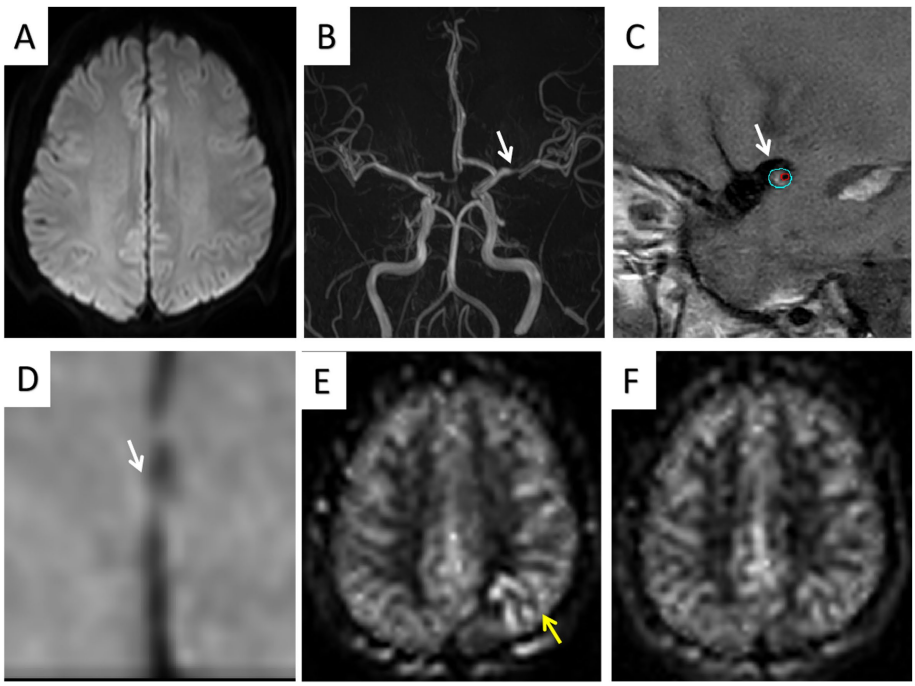

FIGURE 3
One TIA patient (age 67 years) showed no infarct area **(A)** and left MCA stenosis **(B)**; HRMRI showed moderate enhancement of the eccentric plaque **(C,D)**; ATA was present in the lesion area on 1.5-s ASL images **(E)** but was absent in the lesion area on 2.5-s ASL images **(F)**.

characteristics to explore the relationship between TIA and stroke patients, yielding three important findings: First, plaque characteristics (positive remodeling, intraplaque hemorrhage, and enhancement ratio) and the presence of 2-PLD ATAs were independently related to the incidence of stroke. Second, in comparison with HRMRI, the combination of 2-PLD ATAs with clinical risk factors showed no significant difference in distinguishing between patients with TIA and stroke. Third, the multimodal model that integrated positive remodeling,

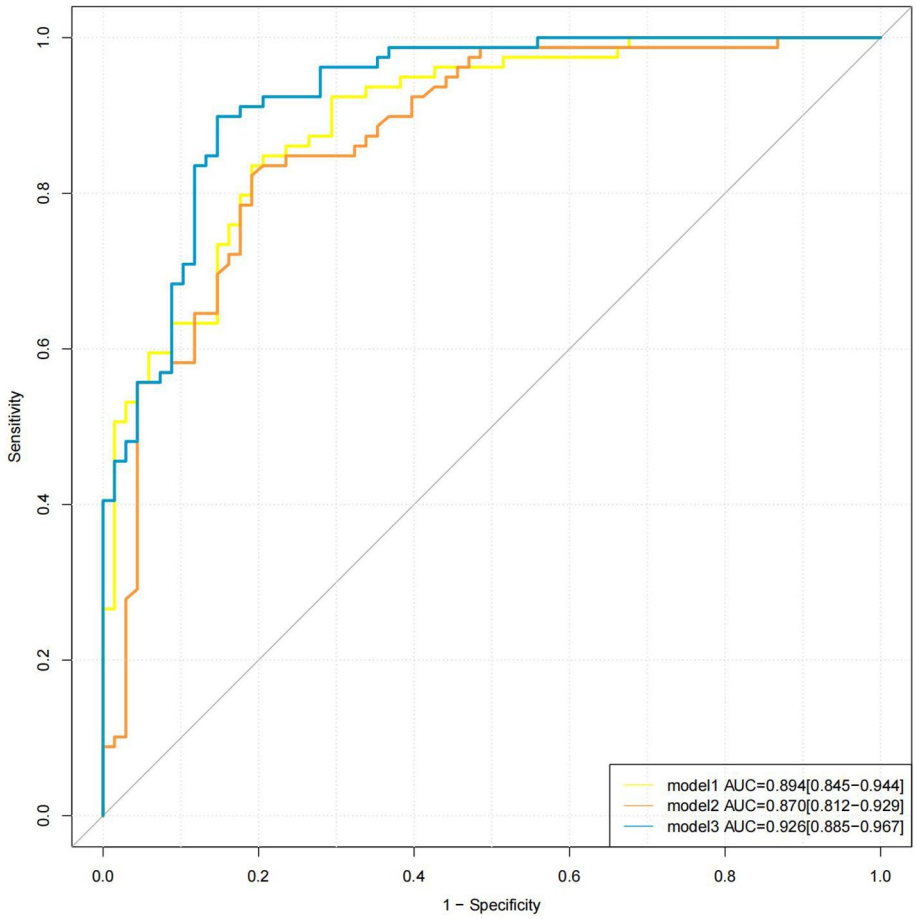

FIGURE 4
Different models for detection of stroke. The AUC values of models 1, 2, and 3 were 0.894, 0.870, and 0.926, respectively. AUC, area under the curve.

enhancement ratio, and the presence of 2-PLD ATAs demonstrated strong diagnostic performance in predicting stroke occurrence.

ATAs are caused by residual labeled blood in the supplying arteries that have not yet been distributed to microvessels and tissues. In this study, the stroke group exhibited a significantly higher incidence of 1.5-s and 2.5-s ATAs, indicating more severe hemodynamic impairment. A previous study using ASL found that ATAs were the only factor associated with recent ischemic symptoms in participants with carotid stenosis, while other plaque features were unrelated to symptom status (10). Thus, compared to plaques, ATAs are more indicative of symptomatic ischemic patients. Similarly, Liu et al. reported a significantly higher incidence of brain tissue volume with Tmax >6.0 s on DSC-PWI in the stroke group (11), suggesting that hypoperfusion can reduce blood flow in cortical or boundary areas, leading to arterio-arterial embolic infarctions. These findings align with the results of this study.

In Model 3, the presence of 1.5-s ATAs and 2.5-s ATAs was significantly associated with stroke. While ATAs can be corrected in multi-PLD acquisition, PLD changes help distinguish early hypersignal from true hyperperfusion in large vessels. However, this process is complex and challenging (15). ASL is particularly sensitive to hemodynamic changes, so delays in blood flow from the neck to the imaging area can lead to the appearance of ATAs. However, the presence of ATA has been associated with collateral circulation compensation (23). Our findings indicate that the presence of 1.5-s ATAs and 2.5-s ATAs are independently associated with stroke. This suggests that stroke patients experience longer blood flow delays to brain tissue, indicating more severe cerebral hemodynamic injury and a higher risk of infarction. ATAs not only provide information about collateral circulation but also reflect the severity of hemodynamic impairment. Consequently, prolonged PLD highlights the differences in blood flow abnormalities between TIA and stroke patients. ASL with multiple PLDs thus holds significant clinical value.

Another advantage of ASL over DSC-PWI is its use of endogenous water-molecule labeling instead of exogenous contrast agents (10). ATAs can be easily assessed through visual inspection of ASL-PWI scans, demonstrating good agreement and reproducibility in this study. Furthermore, combining clinical risk factors with ASL findings showed strong diagnostic efficacy in distinguishing stroke patients from those with TIA. Therefore, ATA assessments could become a widely used imaging marker in clinical practice.

HRMRI has become a valuable tool for directly assessing atherosclerotic plaques (24, 25). Numerous studies have utilized HRMRI to identify imaging biomarkers of symptomatic MCA plaques (26), providing unique radiological insights for diagnosing and treating ischemic stroke. Our study revealed significant differences in plaque morphology and composition between patients with ischemic stroke and those with TIA. These findings could advance research on the mechanisms of ischemic stroke and the potential links between TIA and stroke.

Our results indicated that luminal-positive remodeling, intraplaque hemorrhage, and plaque enhancement ratio were independently associated with stroke. Consistent with previous studies, these plaque characteristics are strong imaging biomarkers of patients with ischemic

stroke (26). Furthermore, our findings revealed distinct pathological differences between stroke and TIA patients. Positive remodeling, a marker of plaque vulnerability, is associated with a higher likelihood of microemboli formation at the MLN site (27). Intraplaque hemorrhage, another independent risk factor for ischemic stroke, plays a significant role in the progression and recurrence of ischemic events. Plaque hyperintensity has been identified as a sign of intraplaque hemorrhage, often resulting from the rupture of thin-walled microvessels or vasotrophic vessels (28). Additionally, plaque enhancement may result from inflammation, neovascularization, or gadolinium leakage due to endothelial dysfunction (29). Lu et al. reported a significant correlation between the degree of MCA plaque enhancement and the presence of downstream acute infarction (30). Our findings indicated a higher incidence of positive remodeling, intraplaque hemorrhage, and an increased plaque enhancement ratio in the stroke group. This suggests that these patients may have more unstable plaques, a greater risk of plaque rupture, a higher tendency for microthrombosis formation in the lumen, and an elevated stroke risk. The plaque characteristics described above may have contributed to the abnormal distal blood flow that enhanced ATAs in stroke patients.

The strength of our study is the combination of two advanced MRI techniques (HRMRI and ASL) to simultaneously assess the differences in hemodynamic features and arterial plaque characteristics in stroke and TIA patients. Our results suggest that ASL may allow simpler detection of impaired cerebral hemodynamics and a better understanding of the differences in arterial plaque and hemodynamics underlying transient ischemic attack and stroke.

Nevertheless, this study has some limitations. First, selection bias may exist due to the cross-sectional study design. Second, the relatively small sample size necessitates larger studies to validate our findings. Third, certain important plaque features, such as plaque volume, fibrous cap, and lipid necrotic core, were not evaluated due to the small size of intracranial plaques and the challenges of accurate measurement. Finally, the lack of follow-up data limits our understanding of the relationship between these findings and patient outcomes. Future longitudinal studies are needed to confirm the stability and applicability of our model.

Conclusion

A model incorporating plaque characteristics and ATAs demonstrated strong diagnostic performance in distinguishing TIA from stroke in patients with intracranial atherosclerotic stenosis. Compared to HRMRI, ASL offers a simpler imaging evaluation method, and the assessment of ATAs has the potential to become a widely adopted imaging marker in clinical practice.

Data availability statement

The original contributions presented in the study are included in the article/Supplementary material, further inquiries can be directed to the corresponding authors.

Ethics statement

The studies involving humans were approved by the Ethics Committee of Shaanxi Provincial People's Hospital. The studies were conducted in accordance with the local legislation and institutional requirements. Written informed consent for participation was not required from the participants or the participants' legal guardians/next of kin in accordance with the national legislation and institutional requirements.

Author contributions

LL: Conceptualization, Data curation, Formal analysis, Funding acquisition, Investigation, Methodology, Project administration, Resources, Software, Supervision, Validation, Visualization, Writing – original draft, Writing – review & editing. PP: Conceptualization, Formal analysis, Investigation, Methodology, Project administration, Software, Validation, Visualization, Writing – original draft, Writing – review & editing. NZ: Formal analysis, Investigation, Methodology, Project administration, Resources, Validation, Visualization, Writing – review & editing. YW: Data curation, Formal analysis, Methodology, Resources, Software, Supervision, Validation, Writing – review & editing. MT: Conceptualization, Investigation, Methodology, Project administration, Resources, Software, Supervision, Validation, Writing – review & editing. KA: Formal analysis, Methodology, Resources, Software, Visualization, Writing – review & editing. XZ: Conceptualization, Formal analysis, Investigation, Methodology, Project administration, Resources, Supervision, Visualization, Writing – review & editing. XL: Conceptualization, Investigation, Methodology, Resources, Software, Supervision, Validation, Visualization, Writing – review & editing. XY: Conceptualization, Funding acquisition, Investigation, Methodology, Project administration, Resources, Software, Supervision, Validation, Writing – original draft, Writing – review & editing.

Funding

The author(s) declare that financial support was received for the research and/or publication of this article. This study has received funding by the Key Research and Development Program of Shaanxi Province of China [2024SF-YBXM-051] and [2023-YBSF-418], the Science and Technology Talent Support Program of Shaanxi Provincial People's Hospital of China (grant number 2022JY-10).

Conflict of interest

The authors declare that the research was conducted in the absence of any commercial or financial relationships that could be construed as a potential conflict of interest.

Generative AI statement

The author(s) declare that no Gen AI was used in the creation of this manuscript.

Publisher's note

All claims expressed in this article are solely those of the authors and do not necessarily represent

those of their affiliated organizations, or those of the publisher, the editors and the reviewers. Any product that may be evaluated in this article, or claim that may be made by its manufacturer, is not guaranteed or endorsed by the publisher.

Supplementary material

The Supplementary material for this article can be found online at: https://www.frontiersin.org/articles/10.3389/fneur.2025.1514679/full#supplementary-material

References

1. Collaborators GBDSRF. Global, regional, and national burden of stroke and its risk factors, 1990-2021: a systematic analysis for the Global Burden of Disease Study 2021. *Lancet Neurol*. (2024) 23:973–1003. doi: 10.1016/S1474-4422(24)00369-7

2. Greco A, Occhipinti G, Giacoppo D, Agnello F, Laudani C, Spagnolo M, et al. Antithrombotic Therapy for Primary and Secondary Prevention of Ischemic Stroke: JACC State-of-the-Art Review. *J Am Coll Cardiol*. (2023) 82:1538–57. doi: 10.1016/j.jacc.2023.07.025

3. Barnard ZR, Alexander MJ. Update in the treatment of intracranial atherosclerotic disease. *Stroke Vasc Neurol*. (2020) 5:59–64. doi: 10.1136/svn-2019-000279

4. Gutierrez J, Turan TN, Hoh BL, Chimowitz MI. Intracranial atherosclerotic stenosis: risk factors, diagnosis, and treatment. *Lancet Neurol*. (2022) 21:355–68. doi: 10.1016/S1474-4422(21)00376-8

5. Garg A, Limaye K, Shaban A, Leira EC, Adams HP. Risk of Ischemic Stroke after an Inpatient Hospitalization for Transient Ischemic Attack in the United States. *Neuroepidemiology*. (2021) 55:40–6. doi: 10.1159/000511829

6. Mendelson SJ, Prabhakaran S. Diagnosis and Management of Transient Ischemic Attack and Acute Ischemic Stroke: A Review. *JAMA*. (2021) 325:1088–98. doi: 10.1001/jama.2020.26867

7. Zhao JJ, Lu Y, Cui JY, Ma LQ, Zhang RP, Xu Z. Characteristics of symptomatic plaque on high-resolution magnetic resonance imaging and its relationship with the occurrence and recurrence of ischemic stroke. *Neurol Sci*. (2021) 42:3605–13. doi: 10.1007/s10072-021-05457-y

8. Yang D, Liu J, Yao W, Huang K, Zhou C, Bi J, et al. The MRI enhancement ratio and plaque steepness may be more accurate for predicting recurrent ischemic cerebrovascular events in patients with intracranial atherosclerosis. *Eur Radiol*. (2022) 32:7004–13. doi: 10.1007/s00330-022-08893-2

9. Haller S, Zaharchuk G, Thomas DL, Lovblad KO, Barkhof F, Golay X. Arterial Spin Labeling Perfusion of the Brain: Emerging Clinical Applications. *Radiology*. (2016) 281:337–56. doi: 10.1148/radiol.2016150789

10. Di Napoli A, Cheng SF, Gregson J, Atkinson D, Markus JE, Richards T, et al. Arterial Spin Labeling MRI in Carotid Stenosis: Arterial Transit Artifacts May Predict Symptoms. *Radiology*. (2020) 297:652–60. doi: 10.1148/radiol.2020200225

11. Liu S, Tang R, Xie W, Chai S, Zhang Q, Luo Y, et al. Plaque characteristics and hemodynamics contribute to neurological impairment in patients with ischemic stroke and transient ischemic attack. *Eur Radiol*. (2021) 31:2062–72. doi: 10.1007/s00330-020-07327-1

12. Schellinger PD, Bryan RN, Caplan LR, Detre JA, Edelman RR, Jaigobin C, et al. Evidence-based guideline: The role of diffusion and perfusion MRI for the diagnosis of acute ischemic stroke: report of the Therapeutics and Technology Assessment Subcommittee of the American Academy of Neurology. *Neurology*. (2010) 75:177–85. doi: 10.1212/WNL.0b013e3181e7c9dd

13. Zaharchuk G. Arterial spin-labeled perfusion imaging in acute ischemic stroke. *Stroke*. (2014) 45:1202–7. doi: 10.1161/STROKEAHA.113.003612

14. Lyu J, Ma N, Liebeskind DS, Wang DJ, Ma L, Xu Y, et al. Arterial Spin Labeling Magnetic Resonance Imaging Estimation of Antegrade and Collateral Flow in Unilateral Middle Cerebral Artery Stenosis. *Stroke*. (2016) 47:428–33. doi: 10.1161/STROKEAHA.115.011057

15. Lindner T, Bolar DS, Achten E, Barkhof F, Bastos-Leite AJ, Detre JA, et al. Current state and guidance on arterial spin labeling perfusion MRI in clinical neuroimaging. *Magn Reson Med*. (2023) 89:2024–47. doi: 10.1002/mrm.29572

16. McEvoy JW, McCarthy CP, Bruno RM, Brouwers S, Canavan MD, Ceconi C, et al. 2024 ESC Guidelines for the management of elevated blood pressure and hypertension. *Eur Heart J*. (2024) 45:3912–4018. doi: 10.1093/eurheartj/ehae178

17. Kim YH, Her AY, Jeong MH, Kim BK, Hong SJ, Kim S, et al. Effects of stent generation on clinical outcomes after acute myocardial infarction compared between prediabetes and diabetes patients. *Sci Rep*. (2021) 11:9364. doi: 10.1038/s41598-021-88593-x

18. Li JJ, Zhao SP, Zhao D, Lu GP, Peng DQ, Liu J, et al. China Guidelines for Lipid Management. *J Geriatr Cardiol*. (2023) 20:621–63. doi: 10.26599/1671-5411.2023.09.008

19. Sellos-Moura M, Glavin F, Lapidus D, Evans K, Lew CR, Irwin DE. Prevalence, characteristics, and costs of diagnosed homocystinuria, elevated homocysteine, and phenylketonuria in the United States: a retrospective claims-based comparison. *BMC Health Serv Res*. (2020) 20:183. doi: 10.1186/s12913-020-5054-5

20. Tao L, Li XQ, Hou XW, Yang BQ, Xia C, Ntaios G, et al. Intracranial Atherosclerotic Plaque as a Potential Cause of Embolic Stroke of Undetermined Source. *J Am Coll Cardiol*. (2021) 77:680–91. doi: 10.1016/j.jacc.2020.12.015

21. Zhang R, Zhang Q, Ji A, Lv P, Zhang J, Fu C, et al. Identification of high-risk carotid plaque with MRI-based radiomics and machine learning. *Eur Radiol*. (2021) 31:3116–26. doi: 10.1007/s00330-020-07361-z

22. Li L, Tang M, Yan X, Gao J, Ma N, Shi X, et al. Plaque Characteristics in Young Adults With Symptomatic Intracranial Atherosclerotic Stenosis: A Preliminary Study. *Front Neurol*. (2022) 13:825503. doi: 10.3389/fneur.2022.825503

23. de Havenon A, Haynor DR, Tirschwell DL, Majersik JJ, Smith G, Cohen W, et al. Association of Collateral Blood Vessels Detected by Arterial Spin Labeling Magnetic Resonance Imaging With Neurological Outcome After Ischemic Stroke. *JAMA Neurol*. (2017) 74:453–8. doi: 10.1001/jamaneurol.2016.4491

24. Mandell DM, Mossa-Basha M, Qiao Y, Hess CP, Hui F, Matouk C, et al. Intracranial Vessel Wall MRI: Principles and Expert Consensus Recommendations of the American Society of Neuroradiology. *AJNR Am J Neuroradiol*. (2017) 38:218–29. doi: 10.3174/ajnr.A4893

25. Li H, Liu J, Dong Z, Chen X, Zhou C, Huang C, et al. Identification of high-risk intracranial plaques with 3D high-resolution magnetic resonance imaging-based radiomics and machine learning. *J Neurol*. (2022) 269:6494–503. doi: 10.1007/s00415-022-11315-4

26. Song JW, Pavlou A, Xiao J, Kasner SE, Fan Z, Messe SR. Vessel Wall Magnetic Resonance Imaging Biomarkers of Symptomatic Intracranial Atherosclerosis: A Meta-Analysis. *Stroke*. (2021) 52:193–202. doi: 10.1161/STROKEAHA.120.031480

27. Shi MC, Wang SC, Zhou HW, Xing YQ, Cheng YH, Feng JC, et al. Compensatory remodeling in symptomatic middle cerebral artery atherosclerotic stenosis: a high-resolution MRI and microemboli monitoring study. *Neurol Res*. (2012) 34:153–8. doi: 10.1179/1743132811Y.0000000065

28. Wu F, Song H, Ma Q, Xiao J, Jiang T, Huang X, et al. Hyperintense Plaque on Intracranial Vessel Wall Magnetic Resonance Imaging as a Predictor of Artery-to-Artery Embolic Infarction. *Stroke*. (2018) 49:905–11. doi: 10.1161/STROKEAHA.117.020046

29. Millon A, Boussel L, Brevet M, Mathevet JL, Canet-Soulas E, Mory C, et al. Clinical and histological significance of gadolinium enhancement in carotid atherosclerotic plaque. *Stroke*. (2012) 43:3023–8. doi: 10.1161/STROKEAHA.112.662692

30. Lu SS, Ge S, Su CQ, Xie J, Mao J, Shi HB, et al. MRI of plaque characteristics and relationship with downstream perfusion and cerebral infarction in patients with symptomatic middle cerebral artery stenosis. *J Magn Reson Imaging*. (2018) 48:66–73. doi: 10.1002/jmri.25879

frontiers | Frontiers in Neurology

TYPE Original Research
PUBLISHED 30 April 2025
DOI 10.3389/fneur.2025.1553357

OPEN ACCESS

EDITED BY
Xindao Yin,
Nanjing Medical University, China

REVIEWED BY
Ozge Altintas Kadirhan,
Kırklareli University, Türkiye
Miao Li,
China-Japan Union Hospital of Jilin University, China
Weili Li,
Shandong Provincial Qianfoshan Hospital, China

*CORRESPONDENCE
Manhua Ding
✉ dingmanhuab@126.com
Yang Zhang
✉ huayingliehuo@163.com

†These authors have contributed equally to this work and share first authorship

‡These authors have contributed equally to this work and share last authorship

RECEIVED 30 December 2024
ACCEPTED 07 April 2025
PUBLISHED 30 April 2025

CITATION
Chen S, Chen G, Zhao C, Wang E, Zhou Y, Ding M and Zhang Y (2025) Infarct core growth rate and 90-day outcomes in ischemic stroke: subgroup analysis based on onset-to-recanalization time.
Front. Neurol. 16:1553357.
doi: 10.3389/fneur.2025.1553357

Infarct core growth rate and 90-day outcomes in ischemic stroke: subgroup analysis based on onset-to-recanalization time

Sha Chen[1,2†], Guofang Chen[3†], Changzhi Zhao[2], Enle Wang[4], Yewen Zhou[4], Manhua Ding[5*‡] and Yang Zhang[3,6*‡]

[1]Jiangsu Key Laboratory of New Drug Research and Clinical Pharmacy, Xuzhou Medical University, Xuzhou, China, [2]Department of Neurosurgery, Xuzhou Center Hospital, Xuzhou Clinical School of Xuzhou Medical University, Southeast University Affiliated Xuzhou Central Hospital, Xuzhou, China, [3]Department of Neurology, Xuzhou Center Hospital, Xuzhou Clinical School of Xuzhou Medical University, Southeast University Affiliated Xuzhou Central Hospital, Xuzhou, China, [4]Southeast University School of Medicine, Southeast University School, Nanjing, China, [5]Department of Radiotherapy, Xuzhou Cancer Hospital, Xuzhou, China, [6]Department of Neurology and Clinical Research Center of Neurological Disease, The Second Affiliated Hospital of Soochow University, Suzhou, China

Background: It is essential to understand the factors that influence patient outcomes in stroke research. The infarct core growth rate (ICGR) is emerging as a potentially valuable marker, but its relationship with patient outcomes, especially concerning the onset-to-recanalization time (ORT), requires further clarification. This study investigates the impact of ICGR on 90-day (90d) outcomes in acute ischemic stroke patients and explores whether stratifying ICGR analysis based on ORT provides more detailed prognostic insights.

Methods: This study retrospectively analyzed patients with acute ischemic stroke with anterior circulation large vessel occlusion (AIS-ACLVO) who underwent endovascular treatment (EVT) between January 2021 and December 2023. Their clinical characteristics, baseline and imaging data were recorded upon admission. Clinical outcomes were evaluated using the modified Rankin Scale (mRS) at 90 days post-procedure. The least absolute shrinkage and selection operator (LASSO) regression was employed for data screening. Multivariable logistic regression analysis was performed to explore the relationship between ICGR and 90-day (90d) clinical outcome. Additionally, a stratified analysis based on ORT was conducted to compare the diagnostic performance of ICGR and infarct core volume (ICV) at different time points.

Results: A total of 153 patients were included in the analysis. Univariate and Lasso regression analyses showed that the group with unfavorable outcomes had statistically significant differences in ICGR, age, history of atrial fibrillation, history of drinking, admission blood glucose level, Alberta Stroke Program Early CT Score (ASPECTS), and National Institutes of Health Stroke Scale (NIHSS) score compared to the favorable outcome group (all $p < 0.05$). Furthermore, multivariate logistic regression analysis indicated that ICGR was independently associated with clinical outcome in AIS-ACLVO patients [Odds Ratio (OR) 1.101, 95% confidence interval (CI) 1.029–1.178; $p = 0.005$]. When stratified by median ORT, the ICGR remained a strong predictor of outcome within 8 h (OR 1.188, 95% CI 1.048–1.347; $p = 0.007$), and proved to be a better predictor than ICV [area under the Receiver Operating Characteristic (AUROC) curve, 0.816 vs. 0.750, $p = 0.024$].

Conclusion: Our research indicates that the ICGR correlates with 90d clinical outcomes in AIS-ACLVO patients: a faster rate is associated with poorer outcomes. Within 8 h of ORT, the ICGR serves as a better predictor of 90d outcome than ICV.

KEYWORDS

infarct core growth rate, infarct core volume, onset-to-recanalization time, endovascular treatment, outcome

Introduction

The global incidence of stroke has been increasing in recent years (1). Acute ischemic stroke with anterior circulation large vessel occlusion (AIS-ACLVO) is one subtype of acute ischemic stroke that generally has a poorer prognosis (2). Research has shown that administering endovascular thrombectomy (EVT) within 24 h after the onset of symptoms, as opposed to relying on medical treatment alone, can significantly improve both short-term and long-term outcomes for most patients, while also reducing mortality rates (3–6). Nonetheless, a considerable percentage of patients—between 40% and 60%—still face poor outcomes (7, 8).

For patients with AIS-ACLVO, computed tomography perfusion (CTP) imaging has been widely utilized to identify reversible ischemic regions (ischemic penumbra) and irreversible ischemic regions (infarct core) (9). Yu et al. (10) used whole-brain CTP to calculate the optimal threshold for identifying the ischemic core in Chinese individuals, establishing that a relative cerebral blood flow (rCBF) of 30% or less, with a delay time of 3 s or more, is indicative of this condition. However, despite using the infarct core volume (ICV) and clinical characteristics as guidelines for surgical selection and individualized treatment for patients experiencing stroke due to large vessel occlusion, there was still an inaccurate prediction of prognosis for some patients.

Patients exhibiting identical ICV may experience disparate outcomes, depending upon the temporal discrepancy between the onset of symptoms and the restoration of blood flow in the impacted vessel (11). The rate of infarction, in synergy with the magnitude of the ICV and the interval from the onset of stroke to the acquisition of imaging, provides a holistic representation of the evolution of cerebral infarction. Infarct core growth rate (ICGR) = ICV (rCBF $\leq$ 30%)/time from symptom onset to imaging. ICGR has emerged as a critical metric for evaluating EVT efficacy. Alebers et al. (12) hypothesized that slower core growth dynamics might explain the superior outcomes of EVT over conservative management in late time-window clinical trials. This mechanistic insight has led to the clinical consensus that patients with rapid ICGR derive limited benefit from EVT.

The rapid ICGR defined in previous studies typically ranges from > 5–15 mL/h (12–14). Using a linear infarct core expansion model, one study demonstrated that patients with target mismatch and baseline ICV < 70 mL within early time windows exhibited significantly faster ICGR (>25 mL/h) compared to previously reported values (15). Intriguingly, these individuals with accelerated ICGR derived greater absolute benefit from EVT than thrombolysis-alone groups (9). However, consistent with prior investigations, this therapeutic advantage was restricted to specific populations characterized by relatively small baseline ICV and favorable imaging profiles.

To date, no consensus exists on the definition of rapid ICGR, and its impact on EVT outcomes remains controversial. This study aims to investigate the relationship between ICGR and the outcomes of patients at a 90-day follow-up after EVT.

Methods

Study design

This research was a single-center retrospective analysis, and consecutively included patients diagnosed with AIS-ACLVO who were seen in the outpatient or emergency green channel of our hospital from January 2021 to December 2023. All patients undergoing intravenous thrombolysis or EVT received written informed consent from the patient or their authorized representative prior to treatment. The study was approved by the Ethics Committee of Xuzhou Central Hospital. Demographic, clinical, and imaging data were prospectively collected and analyzed to evaluate treatment outcomes. Original datasets supporting this study's conclusions are accessible from the corresponding author upon reasonable request.

Patients population

The inclusion criteria for our study were as follows: (1) patients had acute stroke symptoms; (2) all patients underwent baseline imaging assessment, including noncontrast computed tomography (NCCT), CT angiography (CTA), and CT perfusion (CTP) scans; (3) CTA confirmed occlusion of the cervical internal carotid artery, as well as the M1 segment or proximal portion of the M2 segment of the middle cerebral artery; (4) age $\geq$ 18 years; (5) preoperative NIHSS score $\geq$ 6 upon admission; (6) onset-to-door time $\leq$ 24 h; (7) ICV $\leq$ 100 mL. The exclusion criteria were as follows: (1) CT scan of the brain showed hemorrhage; (2) occlusion of the posterior circulation or involvement of both circulations; (3) mRS score $\geq$ 2 before the onset of the disease; (4) severe dysfunction of important organs such as the heart, lungs, liver, and kidneys, with an expected life span of less than 6 months; (5) the time from symptom onset to imaging examination is unclear and imaging data is incomplete or unreadable; (6) expanded Thrombolysis in Cerebral Infarction (eTICI) grade < 2b50 after EVT (16); (7) patients who have not completed follow-up. Collected baseline data on the patients, including age, gender, vascular risk factors, blood pressure at admission, laboratory tests, stroke etiological classification, imaging studies, and time intervals.

Imaging protocol and analysis

Imaging was conducted utilizing a Toshiba Aquilion One Vision 64-slice spiral CT scanner. CT parameters were 80 kV, 300 mA, 0.5 mm slice thickness, 0.5 mm slice interval, 220 × 220 mm field of view, 160 mm detector collimation, and 0.75 s/r gantry rotation speed. 50 mL of iopromide contrast agent was injected via the cubital vein at 4.0 mL/s, followed by a 30 mL saline flush at 4.0 mL/s. Dynamic volume scanning was performed with a 7 s delay. NCCT and CTA raw data were uploaded to a Shu-kun workstation, and CTP data were uploaded to iStroke 3.15 software for automated processing using a convolution algorithm. The software automatically calculated the ICV (rCBF < 30%), Ischemic volume (time to maximum, a key CTP parameter measuring when blood contrast reaches a specific brain region and peaks > 6 s), and mismatch volume (ischemic volume—ICV). Two experienced neurologists with over 5 years of experience jointly interpreted the images and calculated the Alberta Stroke Program Early CT Score (ASPECTS) (17), and disagreements were resolved through negotiation.

EVT procedure

Clinical symptoms and imaging assessments were performed on AIS-ACLVO patients. For patients with an onset-to-door time of ≤4.5 h who were free of contraindications and had obtained informed consent, 0.9 mg/kg alteplase was administered intravenously for thrombolysis (18). The standard approach is to select the right femoral artery as the puncture site. After the puncture is successful, a cerebral angiography is conducted to identify the precise location of vascular occlusion and evaluate the status of collateral circulation. The American Society of Interventional and Therapeutic Neuroradiology/Society of Interventional Radiology (ASITN/SIR) grading system is employed for assessment (19). Then, a thrombus aspiration system was introduced and placed near the proximal occluded vessel. Under the guidance of the roadmap, a microcatheter and microguidewire were used to enter the occluded area. The microguidewire was then withdrawn, and a suitable-sized stent was placed to perform stent thrombectomy.

Outcome evaluation

Patients were followed up via phone or outpatient clinic, after 90-day (90d) following EVT, by the same experienced neurologist using mRS for outcome assessment. A score of 0–2 was defined as a favorable outcome, while a score of 3–6 was defined as an unfavorable outcome, with a score of 6 signifying death (3).

Statistical analysis

Statistical analysis was carried out with the help of IBM SPSS Statistics 27.0 and R 4.4.2 software. Continuous quantitative data adhering to a normal distribution were presented as $\overline{x} \pm s$, and group comparisons were conducted using an independent samples t-test. Data with non-normal distributions were reported as median and interquartile range (IQR), and the Mann–Whitney U test was used for comparison between the two groups. Count data was expressed as frequency and percentage, and the chi-square (χ^2) test or Fisher's exact test was used for comparison between the two groups. The "glmnet" package in R software was used to build the least absolute shrinkage and selection operator (LASSO) regression model and conduct data feature selection to reduce model collinearity and overfitting. Multivariate logistic regression analysis was used to identify the independent risk factors for unfavorable outcomes, and the odds ratios (OR) along with 95% confidence intervals (CI) were computed. The receiver operating characteristic (ROC) curve was plotted, and the area under the ROC curve (AUROC) was calculated. The DeLong test was used to evaluate the discriminatory power of different groups. It was considered statistically significant when the two-sided value of P was less than 0.05.

Results

Baseline characteristic of patients

The research flowchart is shown in Figure 1. During the study, a total of 205 patients with AIS-LVO undergoing EVT were enrolled. After excluding 24 patients with involvement of both posterior and anterior circulations, 7 patients with incomplete baseline data, 3 patients with preoperative mRS score of ≥2, 8 patients with missing or degraded imaging data affecting interpretation, and 3 patients with postoperative eTICI grade <2b50, 153 patients were included in the subsequent analysis. There were 86 males (56.2%) with a median age of 70 (IQR 60, 77) years. 70 (45.8%) had a favorable prognosis, while 83 (54.2%) had an unfavorable outcome, including 36 deaths (23.5%).

Univariate analysis and clinical feature selection

Univariate analysis revealed statistically significant differences between the unfavorable prognosis group and the favorable prognosis group in terms of age, gender, history of atrial fibrillation, coronary heart disease, history of alcohol consumption, admission blood glucose, ASPECTS score, NIHSS score, ASITN/SIR score, ICV, ischemic volume, and ICGR (all $p < 0.05$; see Table 1). Incorporating the aforementioned metrics into the Lasso regression model. Owing to the pronounced collinearity between the ICV and the ICGR, the ICV was omitted from the Lasso regression analysis. The findings indicated that gender, a history of coronary heart disease, ischemic volume, and the ASITN/SIR score were not retained in the model (Figure 2).

Multivariate logistic regression

The variables selected by Lasso regression were incorporated into the multivariate logistic regression analysis. The results showed that ICGR (OR 1.101, 95% CI 1.029–1.178; $p = 0.005$), ASPECTS score (OR 0.042, 95% CI 0.466–0.985; $p = 0.039$), and preoperative NIHSS score (OR 1.078, 95% CI 1.022–1.138; $p = 0.006$) were independent risk factors for poor outcomes in patients with anterior circulation stroke (Figure 3A).

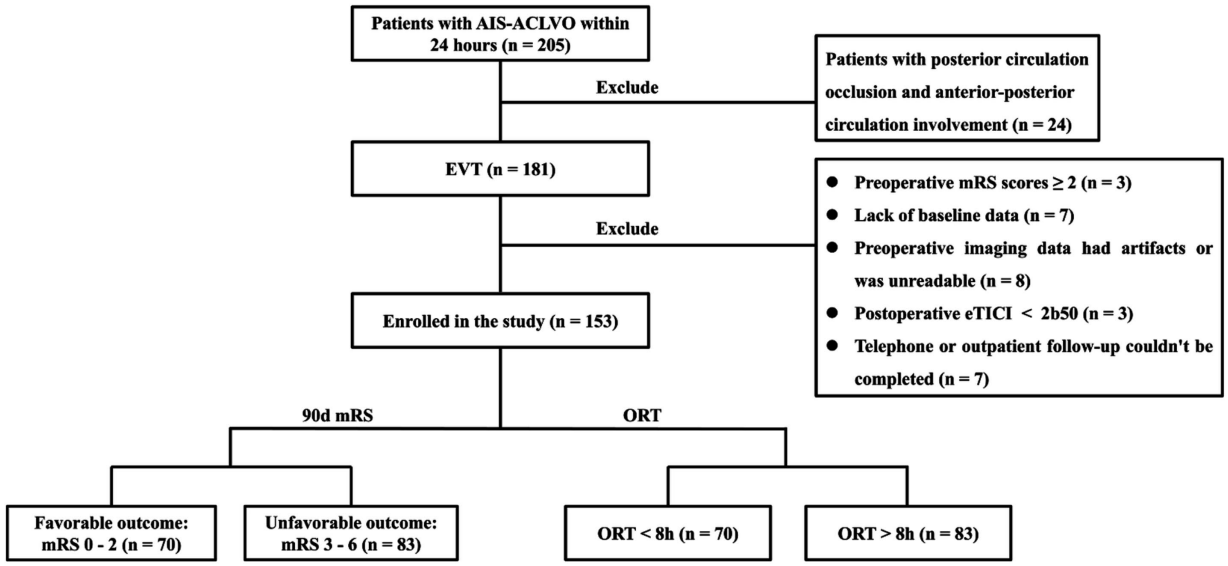

FIGURE 1
Patient selection flow-chart. AIS-ACLVO, Acute Ischemic Stroke with Anterior Circulation Large Vessel Occlusion; EVT, Endovascular Treatment; mRS, modified Rankin Scale; eTICI, expanded Thrombolysis in Cerebral Infarction; 90d, 90-day; ORT, Onset-to-recanalization time.

Subgroup analysis with ORT

We divided the patients into two groups based on the median time from onset-to-recanalization time (ORT) of 8 h. We again used a multivariable logistic regression analysis, and found that the subpopulation with a time from ORT < 8 h had an independent effect on the 90d prognosis of AIS-ACLVO patients (OR 1.188, 95% CI 1.048–1.347; $p = 0.007$), as shown in Figure 3B. However, another group with ORT > 8 h, the ICGR no longer showed statistical significance (Figure 3C).

A single-factor logistic regression analysis was performed on the ICGR and ICV for different groups, and ROC curves were drawn and the AUC results were compared to show that in the subgroup with a time from ORT of 8 h or less, the AUROC curve for ICGR was higher than that for ICV (0.816 vs. 0.750), with a sensitivity of 74.4% and a specificity of 74.2%. Following the application of the Delong test for analytical purposes, a statistically significant disparity was observed between the two cohorts ($p = 0.024$), suggesting that the ICGR is a superior predictor of the 90d prognosis in AIS-ACLVO patients, within the 8-h window from ORT, in comparison with the ICV. No significant discrepancies were noted in the remaining groups (Table 2; Figure 4).

Comparison of ICGR and ICV

There were a total of 70 (45.8%) patients with AIS-ACLVO who had a reperfusion time of 8 h or less, with the ICGR group having a median of 9.56 (IQR 2.67, 16.08) ml/h. Another group for patients with a reperfusion time of more than 8 h had a median of 2.64 (IQR 0.75, 4.77) ml/h, ($Z = 4.601$, $p < 0.001$), as shown in Figure 5A. The median ICV for patients with a reperfusion time of 8 h or less was 19.60 (IQR 6.1, 35.70) ml, while another group was 24.60 (IQR 7.70, 42.50) ml, ($Z = -0.751$, $p = 0.453$), as shown in Figure 5B.

Discussion

Our study reports four key findings in patients eligible for thrombectomy: (1) Within 24 h of symptom onset, ICGR correlated significantly with 90-day clinical outcomes, with slower ICGR strongly associated with favorable prognoses. (2) ICGR independently predicted patient outcomes, demonstrating significant prognostic value within the first 8 h but no statistical significance beyond this time window. (3) Within the 8-h timeframe, ICGR exhibited stronger predictive efficacy for clinical outcomes compared to ICV. (4) ICGR was significantly higher within the first 8 h post-onset than after 8 h, whereas ICV did not differ significantly between these intervals.

The site of a cerebral infarction is commonly delineated into the infarct core and the ischemic penumbra (salvageable tissue). The magnitude of the infarct core and the ischemic penumbra tends to fluctuate in correlation with the progression of the infarction over time. The prolonged duration of infarction progression is positively correlated with an increase in the volume of the infarct core and a concomitant decrease in the extent of salvageable tissue. DEFUSE 3 trial found that EVT in patients with AIS-ACLVO and ICV measuring 70 mL or less within the first 16 h from the onset of symptoms often resulted in superior efficacy in terms of functional outcome endpoints (90d mRS score of 0–2) (3). Recent randomized controlled trials have demonstrated that EVT maintains clinical efficacy in patients with moderate-to-large ICV (70–100 mL) defined by NCCT and CTP (20–22). Notably, a study published last year in Lancet Neurology demonstrated that EVT in patients with AIS-ACLVO and large infarct core (ASPECTS score 3–5, corresponding to ICV < 100 mL) (23) within 12 h of symptom onset resulted in superior functional outcomes, survival rates, and quality of life compared to medical management alone at 12-month follow-up. These findings highlight the short-term and durable benefits of EVT in this population (24). Nonetheless, there is a paucity of reported research on the efficacy of thrombectomy for core infarctions exceeding 100 mL. In this study, there were 144

TABLE 1 Factors affecting outcomes in patients with AIS-ACLVO.

Indicator	All (*n* = 153)	Favorable (*n* = 70)	Unfavorable (*n* = 83)	Statistic	*p*-value
Demography					
Age (y; *M*, *IQR*)	70.00 (60.00,77.00)	64.00 (56.00,74.00)	73.00 (67.00,78.00)	−3.990	<0.001
Male [*n* (%)]	86 (56.2)	46 (65.7)	40 (48.2)	4.736	0.030
Vascular risk factors [*n* (%)]					
Atrial fibrillation	57 (37.3)	16 (22.9)	41 (49.4)	11.443	<0.001
Coronary heart disease	49 (32.0)	16 (22.9)	33 (39.8)	4.983	0.026
Smoking	31 (20.3)	19 (27.1)	12 (14.5)	3.782	0.052
Drinking	26 (17.0)	7 (10.0)	19 (22.9)	4.474	0.034
Baseline data					
SBP (mmHg[a]; *M*, *IQR*)	145.00 (131.50,165.00)	145.00 (130.00,165.00)	146.00 (134.00,168.00)	−0.704	0.482
DBP (mmHg[a]; *M*, *IQR*)	80.00 (75.00,90.00)	80.50 (75.00,87.75)	80.00 (75.00,90.00)	0.526	0.599
Admitted blood glucose (mmol/L; *M*, *IQR*)	7.27 (5.85,9.10)	6.92 (5.35,8.26)	7.66 (6.52,9.83)	−2.478	0.013
Preoperative NIHSS (*M*, *IQR*)	18.00 (12.00,24.00)	14.00 (8.00,19.00)	21.00 (17.00,26.00)	−5.209	<0.001
Radiologic characteristic					
ASPECTS (*M*, *IQR*)	8.00 (7.00,9.00)	9.00 (8.00,10.00)	8.00 (7.00,9.00)	2.976	0.003
ASITN/SIR (*M*, *IQR*)	1.75 (1.00,2.00)	2.00 (1.00,2.64)	1.41 (1.00,2.00)	2.179	0.029
ICV (ml; *M*, *IQR*)	21.00 (6.60,41.00)	9.10 (1.78,24.85)	27.60 (17.70,49.30)	−5.565	<0.001
Ischemic volume (ml; *M*, *IQR*)	173.40 (105.40,238.20)	150.10 (83.53,230.58)	185.50 (144.60,244.90)	−2.382	0.017
Mismatch (*M*, *IQR*)	148.4 (83.65,214.05)	130.40 (74.80,215.50)	158.70 (107.40,197.60)	−1.241	0.214
ICGR (ml/h; *M*, *IQR*)	3.50 (1.18,10.84)	1.44 (0.39,5.67)	5.39 (2.70,15.27)	−5.334	<0.001
Occlusion site				3.816	0.165
ICA	23 (15.0)	11 (15.7)	12 (14.5)		
MCA	105 (68.6)	52 (74.3)	53 (63.9)		
ICA + MCA	25 (16.3)	7 (10.0)	18 (21.7)		
Interval time (h; *M*, *IQR*)					
Onset-to-door	3.97 (1.76,7.47)	3.98 (1.93,7.51)	3.60 (1.50,7.43)	0.185	0.853
Onset-to-imaging	5.12 (2.66,8.33)	5.24 (2.91,8.25)	4.98 (2.00,8.65)	0.809	0.418
Onset-to-recanalization	8.30 (5.63,12.22)	8.33 (6.06,12.36)	8.23 (5.50,11.90)	0.401	0.688
IVT [*n* (%)]	51 (33.3)	24 (34.3)	27 (32.5)	0.053	0.818
Tandem [*n* (%)]	22 (14.4)	9 (12.9)	13 (15.7)	0.243	0.622
Stroke etiology [*n* (%)]				—	0.140[b]
LAA	88 (57.5)	47 (67.1)	41 (49.4)		
CE	46 (30.1)	16 (22.9)	30 (36.1)		
SOE	4 (2.6)	2 (2.9)	2 (2.4)		
SUE	15 (9.8)	5 (7.1)	10 (12.0)		

[a]1 mmHg = 0.133 kPa; [b]Fisher's exact test; *IQR*, Interquartile Range; *M*, Median; SBP, systolic blood pressure; DBP, diastolic blood pressure; NIHSS, National Institutes of Health Stroke Scale; ASPECTS, Alberta Stroke Program Early CT Score; ASITN/SIR, American Society of Interventional and Therapeutic Neuroradiology/Society of Interventional Radiology; ICV, Infarct core volume; Mismatch, (Ischemic volume—ICV); ICGR, Infarct core growth rate; ICA, Internal carotid artery; MCA, Middle cerebral artery; IVT, Intravenous thrombolysis; LAA, Large-artery atherosclerosis; CE, Cardiogenic embolism; SOE, Stroke of other determined etiology; SUE, Stroke of undetermined etiology.

patients with ICV of 0–70 mL, accounting for approximately 94.12%, while others of 70–100 mL, accounting for 5.88%. The size of the ICV is related to the clinical prognosis of the patient. The larger the infarction core volume, the worse the prognosis of the patient (25–27). Our research further supports this view. However, in clinical practice, we have found that for patients with identical infarction volumes, yet shorter onset intervals, may have poor 90d outcomes (mRS scores of 3–6) after EVT, so we introduced the concept of ICGR. Prior research has demonstrated that the median growth rate of the infarcted core was in the range of 3–7 mL/h, with rapid progression of the infarcted core being delineated as an expansion exceeding 5 mL/h (13). Our dataset revealed a median growth rate of the infarcted core at 3.50 mL/h, and

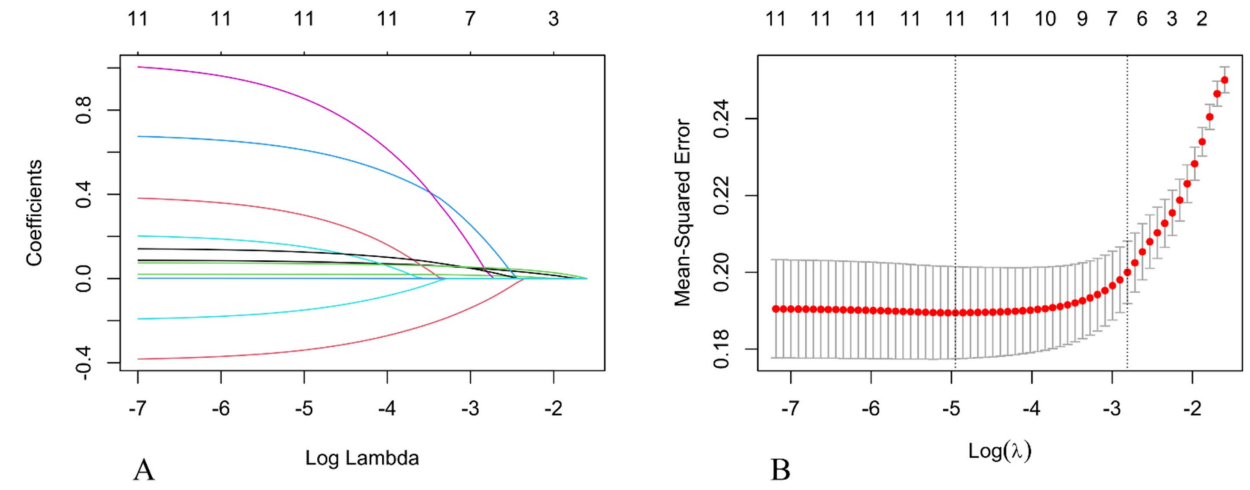

FIGURE 2
Selection of the optimal prognostic factors by LASSO regression analysis. **(A)** LASSO coefficient profiles of potential predictors. **(B)** Screening of the optimal penalization coefficient in the LASSO regression. LASSO, The Least Absolute Shrinkage and Selection Operator.

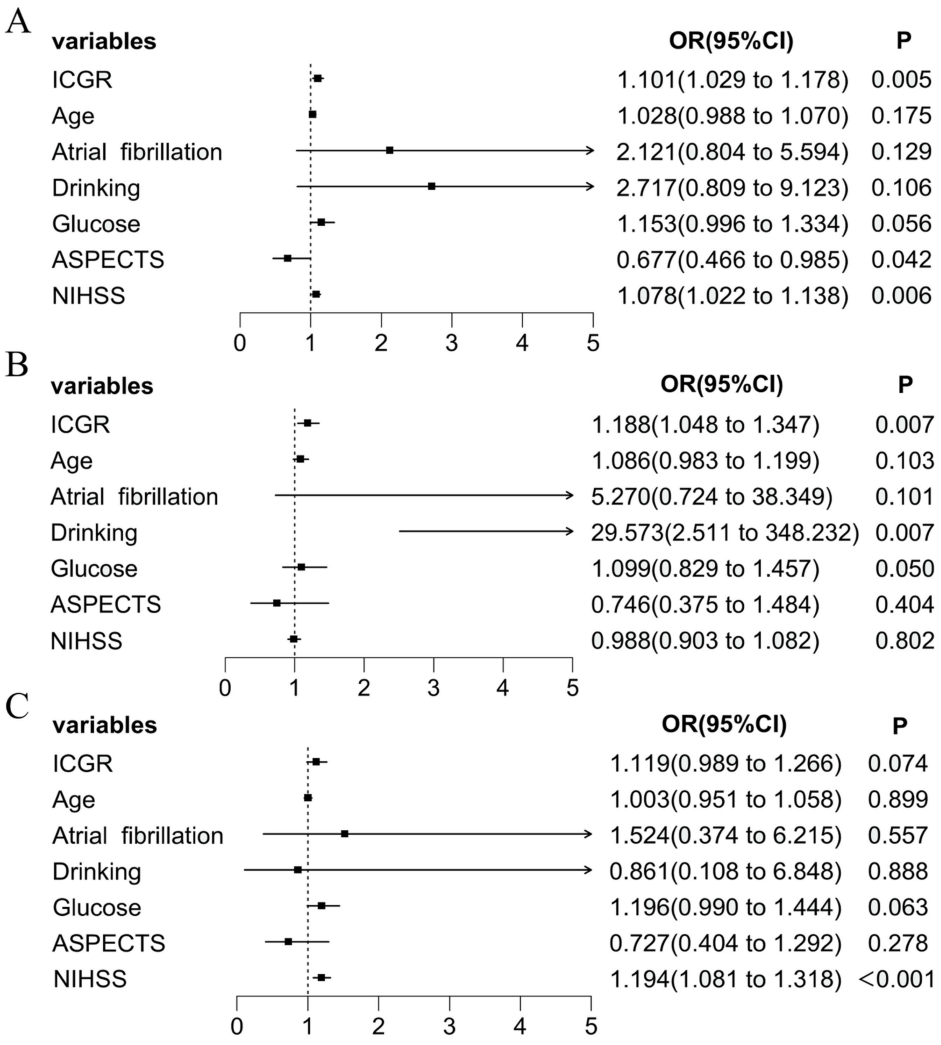

FIGURE 3
Forest plot of multivariate logistic regression analysis for poor prognosis. **(A)** Patients within 24 h of onset. **(B)** Patients within 8 h of ORT. **(C)** Patients beyond 8 h of ORT. ICGR, Infarct core growth rate; ASPECTS, Alberta Stroke Program Early CT Score; NIHSS, National Institutes of Health Stroke Scale; ORT, Onset-to-recanalization time.

TABLE 2 Assess the predictive power of ICGR and ICV in various infarction subgroups.

Variable	All		≤8 h		>8 h	
	AUC	Delong	AUC	Delong	AUC	Delong
ICGR	0.751	$p = 0.686$	0.816	P = 0.024	0.740	$p = 0.193$
ICV	0.761		0.750		0.773	

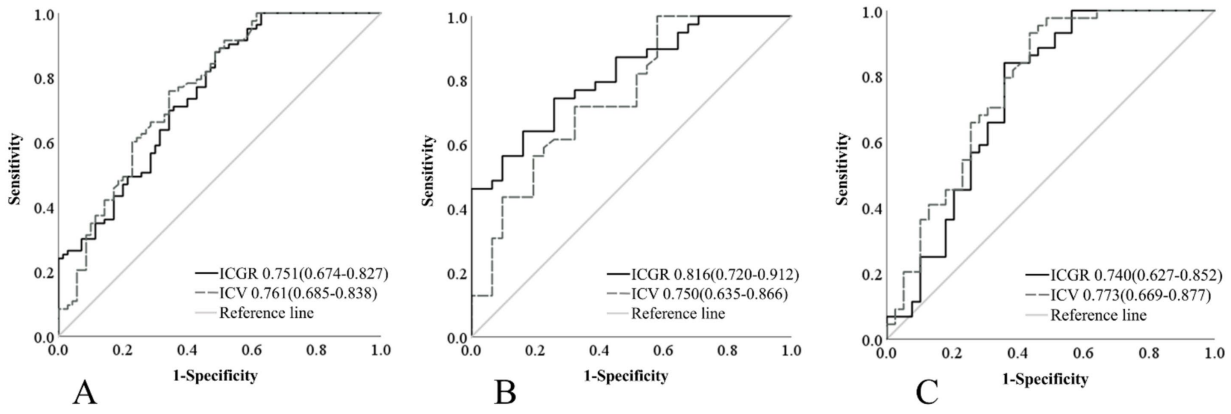

FIGURE 4
Comparison of ROC curves for ICGR and ICV among different groups. **(A)** Patients within 24 h of onset. **(B)** Patients within 8 h of ORT. **(C)** Patients beyond 8 h of ORT. ROC, Receiver operating characteristic; ICGR, Infarct core growth rate; ICV, Infarct core volume; ORT, Onset-to-recanalization time.

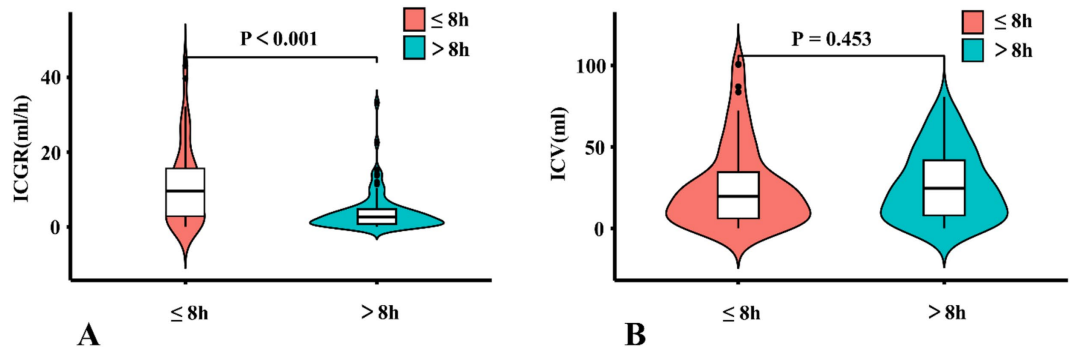

FIGURE 5
A violin plots comparing ICGR and ICV. **(A)** Comparison of the distribution and quartiles of ICV in patients. **(B)** Comparison of the distribution and quartiles of ICV in patients. ICGR, Infarct core growth rate; ICV, Infarct core volume.

the majority of patients exhibiting unfavorable prognoses demonstrated rapid progression of the infarcted core, with a median value of 5.39 mL/h. Furthermore, our analysis indicated that patients with a more rapid progression of the infarcted core were of advanced age, presented with higher NIHSS score, and exhibited reduced ASPECTS score, aligning with the findings of prior research studies (14, 28).

Within a 24-h window following symptom onset, the ICGR not only significantly influenced the clinical outcomes of patients with AIS-ACLVO, but it also correlated with the patients' functional recovery at the 90d outcome, even after adjusting for conventional prognostic variables such as age, baseline glucose levels, history of drinking, history of atrial fibrillation, ASPECTS score, and NIHSS score. An increase of 1 mL/h in the rate of infarct core expansion is associated with a 10.2% rise in the likelihood of an unfavorable outcome. Nonetheless, in univariate analysis, there is no statistically significant discrepancy in its prognostic impact when compared to the ICV.

We categorized the data based on the median ORT of 8 h. The findings suggested that, in patients with an onset-to-reopening time of 8 h or less, the ICGR served as a more reliable predictor of clinical outcomes compared to ICV. In the initial stages of a cerebrovascular accident, the brain parenchyma demonstrates a degree of tolerance to ischemic and hypoxic conditions. It is observed that a higher infarction ratio correlates with a diminished capacity for collateral circulation compensation, thereby implying that the penumbra—an area of potentially salvageable brain tissue—is at a greater risk of progressing to irreversible ischemic damage, even with timely interventions aimed at restoring cerebral blood flow (14, 15). Although the ischemic core region will continue to grow for at least

72 h after stroke onset (24), ICGR no longer independently predicts patient outcomes when the ORT exceeds 8 h. In this scenario, ICGR demonstrates no significant predictive superiority over ICV for clinical outcomes. Moreover, although our data showed no significant differences, existing literature suggests that ICGR may be related to the location of vascular occlusion, and occlusion of the internal carotid artery can predict ICGR (29). Proximity of the affected vessel to the distal extremity correlates inversely with the perfusion area's size; hence, the penumbral tissue is more rapidly perfused by collateral circulation from the pial surface, which in turn retards the growth of the infarct core. Consequently, patients are more likely to exhibit enhanced functional independence 90 days subsequent to the incident.

When the duration of ORT exceeds 8 h, the ICGR no longer independently affects the prognosis of patients. At this point, the ICGR is no more advantageous than the ICV in predicting the clinical outcome of patients. Interestingly, we observed that the median ICGR for patients treated within 8 h of ORT was 9.56 mL/h, while for another subgroup only 2.64 mL/h, indicating a significant difference. However, no notable difference in ICV was observed between the two groups. This phenomenon may be explained by the fact that the maximum allowable ICV, as stated in the thrombectomy eligibility criteria, is 100 mL. In instances where the ORT is protracted and the rate of infarction is expedited, the infarcted volume in these patients significantly surpasses the 100 mL threshold, precluding them from thrombectomy within the framework of the EVT. By this time, the majority of brain tissue has suffered from extended ischemia, and the cumulative impact of the ICV becomes more pronounced. Consequently, for patients with AIS-ACLVO, the volume of infarction imposes constraints on the investigation of rapid ICGR.

The limitations of this study include the following aspects: (1) The sample size for this study is relatively limited, and there is a need to increase the sample size for more comprehensive analysis; (2) Our investigation constitutes a single-center study, with the potential for subsequent external validation to corroborate the findings; (3) This investigation omitted individuals exhibiting ICV exceeding 100 mL, particularly those with an expedited expansion of the infarcted core. Subsequent prospective clinical trials are imperative to address the management of these patients in the future.

Conclusion

Our study findings suggest that the ICGR and the ICV measured within 24 h of onset in AIS-ACLVO patients are closely related to the 3-month outcomes. Within 8 h of ORT, we can predict the prognosis of patients by measuring the ICGR. This information can assist doctors in implementing more effective and rational treatment measures, ultimately helping patients achieve better clinical outcomes.

Data availability statement

The raw data supporting the conclusions of this article will be made available by the authors, without undue reservation.

Ethics statement

The studies involving humans were approved by Ethics Committee of Xuzhou Central Hospital. The studies were conducted in accordance with the local legislation and institutional requirements. The participants provided their written informed consent to participate in this study.

Author contributions

SC: Data curation, Investigation, Software, Validation, Writing – original draft. GC: Data curation, Methodology, Validation, Writing – original draft. CZ: Data curation, Validation, Visualization, Writing – original draft. EW: Data curation, Writing – original draft. YeZ: Data curation, Writing – original draft, Software. MD: Methodology, Supervision, Writing – review & editing. YaZ: Data curation, Funding acquisition, Methodology, Resources, Supervision, Validation, Writing – original draft, Writing – review & editing.

Funding

The author(s) declare that financial support was received for the research and/or publication of this article. This work was supported by the General Project of Traditional Chinese Medicine Science and Technology Development Plan in Jiangsu Province, China (MS2023077); General Project of Open Project of Key Laboratories in Jiangsu Province, China (XZSYSKF2023016); Key Research and Development Project of Xuzhou Science and Technology Bureau, China (KC22169); and Development Fund of Affiliated Hospital of Xuzhou Medical University (XYFM202410).

Conflict of interest

The authors declare that the research was conducted in the absence of any commercial or financial relationships that could be construed as a potential conflict of interest.

Generative AI statement

The author(s) declare that no Gen AI was used in the creation of this manuscript.

Publisher's note

References

1. Ding Q, Liu S, Yao Y, Liu H, Cai T, Han L. Global, regional, and national burden of ischemic stroke, 1990-2019. *Neurology*. (2022) 98:e279–90. doi: 10.1212/WNL.0000000000013115

2. Benz AP, Meinel TR, Salerno A, Beyeler M, Strambo D, Kaesmacher J, et al. Prevalence and distribution of intracranial vessel occlusion on angiography and its association with functional outcome in patients with atrial fibrillation presenting with ischemic stroke. *Ann Neurol*. (2024) 96:1115–23. doi: 10.1002/ana.27084

3. Albers GW, Marks MP, Kemp S, Christensen S, Tsai JP, Ortega-Gutierrez S, et al. Thrombectomy for stroke at 6 to 16 hours with selection by perfusion imaging. *N Engl J Med*. (2018) 378:708–18. doi: 10.1056/NEJMoa1713973

4. Nogueira RG, Jadhav AP, Haussen DC, Bonafe A, Budzik RF, Bhuva P, et al. Thrombectomy 6 to 24 hours after stroke with a mismatch between deficit and infarct. *N Engl J Med*. (2018) 378:11–21. doi: 10.1056/NEJMoa1706442

5. Jovin TG, Li C, Wu L, Wu C, Chen J, Jiang C, et al. Trial of thrombectomy 6 to 24 hours after stroke due to basilar-artery occlusion. *N Engl J Med*. (2022) 387:1373–84. doi: 10.1056/NEJMoa2207576

6. Tao C, Nogueira RG, Zhu Y, Sun J, Han H, Yuan G, et al. Trial of endovascular treatment of acute basilar-artery occlusion. *N Engl J Med*. (2022) 387:1361–72. doi: 10.1056/NEJMoa2206317

7. van de Graaf RA, Samuels N, Chalos V, Nijeholt GJ LA, Van Beusekom H, Yoo AJ, et al. Predictors of poor outcome despite successful endovascular treatment for ischemic stroke: results from the MR CLEAN registry. *J Neurointerv Surg*. (2022) 14:660–5. doi: 10.1136/neurintsurg-2021-017726

8. Liu J, Zhou Y, Zhang L, Li Z, Chen W, Zhu Y, et al. Balloon guide catheters for endovascular thrombectomy in patients with acute ischaemic stroke due to large-vessel occlusion in China (PROTECT-MT): a multicentre, open-label, blinded-endpoint, randomised controlled trial. *Lancet*. (2024) 404:2165–74. doi: 10.1016/S0140-6736(24)02315-8

9. Lin L, Wang Y, Chen C, Bivard A, Butcher K, Garcia-Esperon C, et al. Exploring ischemic core growth rate and endovascular therapy benefit in large core patients. *J Cereb Blood Flow Metab*. (2024) 44:1593–604. doi: 10.1177/0271678X241242911

10. Yu Y, Han Q, Ding X, Chen Q, Ye K, Zhang S, et al. Defining core and penumbra in ischemic stroke: a voxel- and volume-based analysis of whole brain CT perfusion. *Sci Rep*. (2016) 6:20932. doi: 10.1038/srep20932

11. Ryu W, Hong K, Jeong S, Park JE, Kim BJ, Kim J, et al. Association of ischemic stroke onset time with presenting severity, acute progression, and long-term outcome: a cohort study. *PLoS Med*. (2022) 19:e1003910. doi: 10.1371/journal.pmed.1003910

12. Albers GW. Late window paradox. *Stroke*. (2018) 49:768–71. doi: 10.1161/STROKEAHA.117.020200

13. Renú Jornet A, Urra X, Laredo C, Montejo C, Rudilosso S, Llull L, et al. Benefit from mechanical thrombectomy in acute ischemic stroke with fast and slow progression. *J Neurointerv Surg*. (2020) 12:132–5. doi: 10.1136/neurintsurg-2019-015064

14. Sarraj A, Hassan AE, Grotta J, Blackburn S, Day A, Abraham M, et al. Early infarct growth rate correlation with endovascular thrombectomy clinical outcomes: analysis from the SELECT study. *Stroke*. (2021) 52:57–69. doi: 10.1161/STROKEAHA.120.030912

15. Lin L, Zhang H, Chen C, Bivard A, Butcher K, Garcia-Esperon C, et al. Stroke patients with faster core growth have greater benefit from endovascular therapy. *Stroke*. (2021) 52:3998–4006. doi: 10.1161/STROKEAHA.121.034205

16. Liebeskind DS, Bracard S, Guillemin F, Jahan R, Jovin TG, Majoie CB, et al. ETICI reperfusion: defining success in endovascular stroke therapy. *J Neurointerv Surg*. (2019) 11:433–8. doi: 10.1136/neurintsurg-2018-014127

17. Barber PA, Demchuk AM, Zhang J, Buchan AM. Validity and reliability of a quantitative computed tomography score in predicting outcome of hyperacute stroke before thrombolytic therapy. ASPECTS study group. Alberta stroke programme early CT score. *Lancet*. (2000) 355:1670–4. doi: 10.1016/s0140-6736(00)02237-6

18. Emberson J, Lees KR, Lyden P, Blackwell L, Albers G, Bluhmki E, et al. Effect of treatment delay, age, and stroke severity on the effects of intravenous thrombolysis with alteplase for acute ischaemic stroke: a meta-analysis of individual patient data from randomised trials. *Lancet*. (2014) 384:1929–35. doi: 10.1016/S0140-6736(14)60584-5

19. Ben Hassen W, Malley C, Boulouis G, Clarençon F, Bartolini B, Bourcier R, et al. Inter- and intraobserver reliability for angiographic leptomeningeal collateral flow assessment by the american society of interventional and therapeutic neuroradiology/society of interventional radiology (ASITN/SIR) scale. *J Neurointerv Surg*. (2019) 11:338–41. doi: 10.1136/neurintsurg-2018-014185

20. Bendszus M, Fiehler J, Subtil F, Bonekamp S, Aamodt AH, Fuentes B, et al. Endovascular thrombectomy for acute ischaemic stroke with established large infarct: multicentre, open-label, randomised trial. *Lancet*. (2023) 402:1753–63. doi: 10.1016/S0140-6736(23)02032-9

21. Huo X, Ma G, Tong X, Zhang X, Pan Y, Nguyen TN, et al. Trial of endovascular therapy for acute ischemic stroke with large infarct. *N Engl J Med*. (2023) 388:1272–83. doi: 10.1056/NEJMoa2213379

22. Sarraj A, Hassan AE, Abraham MG, Ortega-Gutierrez S, Kasner SE, Hussain MS, et al. Trial of endovascular thrombectomy for large ischemic strokes. *N Engl J Med*. (2023) 388:1259–71. doi: 10.1056/NEJMoa2214403

23. de Margerie-Mellon C, Turc G, Tisserand M, Naggara O, Calvet D, Legrand L, et al. Can DWI-ASPECTS substitute for lesion volume in acute stroke? *Stroke*. (2013) 44:3565–7. doi: 10.1161/STROKEAHA.113.003047

24. Thomalla G, Fiehler J, Subtil F, Bonekamp S, Aamodt AH, Fuentes B, et al. Endovascular thrombectomy for acute ischaemic stroke with established large infarct (TENSION): 12-month outcomes of a multicentre, open-label, randomised trial. *Lancet Neurol*. (2024) 23:883–92. doi: 10.1016/S1474-4422(24)00278-3

25. Campbell BCV, Mitchell PJ, Kleinig TJ, Dewey HM, Churilov L, Yassi N, et al. Endovascular therapy for ischemic stroke with perfusion-imaging selection. *N Engl J Med*. (2015) 372:1009–18. doi: 10.1056/NEJMoa1414792

26. Yi T, Wu Y, Lin D, Lang F, Yang Y, Pan Z, et al. Association of baseline core volume and early midline shift in acute stroke patients with a large ischaemic core. *Front Neurol*. (2022) 13:1077824. doi: 10.3389/fneur.2022.1077824

27. Gu Y, Ding Y, Hang Y, Cao Y, Jia Z, Zhao L, et al. Smaller baseline subcortical infarct volume predicts good outcomes in patients with a large core in early acute ischemic stroke after endovascular treatment. *Front Neurosci*. (2023) 17:1063478. doi: 10.3389/fnins.2023.1063478

28. Seners P, Yuen N, Olivot J, Mlynash M, Heit JJ, Christensen S, et al. Factors associated with fast early infarct growth in patients with acute ischemic stroke with a large vessel occlusion. *Neurology*. (2023) 101:e2126–37. doi: 10.1212/WNL.0000000000207908

29. Simonsen CZ, Mikkelsen IK, Karabegovic S, Kristensen PK, Yoo AJ, Andersen G. Predictors of infarct growth in patients with large vessel occlusion treated with endovascular therapy. *Front Neurol*. (2017) 8:574. doi: 10.3389/fneur.2017.00574

frontiers | Frontiers in Neurology

TYPE Original Research
PUBLISHED 02 May 2025
DOI 10.3389/fneur.2025.1571205

OPEN ACCESS

EDITED BY
Sonu Bhaskar,
National Cerebral and Cardiovascular Center, Japan

REVIEWED BY
Shihua Shi,
ETH Zürich, Switzerland
Wei Pan,
Sun Yat-sen University, China

*CORRESPONDENCE
Jian Wu
✉ wujianxuanwu@126.com

†These authors share first authorship

RECEIVED 05 February 2025
ACCEPTED 21 April 2025
PUBLISHED 02 May 2025

CITATION
Song X, Zhao H, Pengmao Z, Hou D, Zhao X, Zheng Z and Wu J (2025) Serum calcium and phosphate levels and carotid atherosclerotic plaque characteristics: a retrospective study by high-resolution MR vessel wall imaging.
Front. Neurol. 16:1571205.
doi: 10.3389/fneur.2025.1571205

Serum calcium and phosphate levels and carotid atherosclerotic plaque characteristics: a retrospective study by high-resolution MR vessel wall imaging

Xiaowei Song[1†], Hongliang Zhao[1†], Zhuoma Pengmao[1], Duoduo Hou[1], Xihai Zhao[1,2], Zhuozhao Zheng[1] and Jian Wu[1,3*]

[1]Beijing Tsinghua Changgung Hospital, School of Clinical Medicine, Tsinghua University, Beijing, China, [2]Center for Biomedical Imaging Research, Department of Biomedical Engineering, School of Medicine, Tsinghua University, Beijing, China, [3]IDG/McGovern Institute for Brain Research, School of Medicine, Tsinghua University, Beijing, China

Background and aims: Serum calcium (Ca), phosphate (P), and calcium-phosphate product (CPP) are associated with cardiovascular disease and atherosclerosis in patients with chronic kidney disease. However, it remains unclear whether this relationship persists in individuals with carotid artery atherosclerosis of acute ischemic stroke. We investigated the association between serum Ca, P, as well as CPP, and carotid artery atherosclerotic plaque in acute ischemic stroke patients.

Methods and results: A total of 251 ischemic stroke participants with carotid artery atherosclerosis (mean age: 68 years; male: 80.1%) were retrospectively enrolled at a comprehensive stroke center. Serum Ca and P levels were obtained from blood tests after admission. Carotid artery plaque burden and vulnerability were evaluated using high-resolution magnetic resonance vessel wall imaging. Subsequently, the associations between serum Ca, P, as well as CPP, and the characteristics of atherosclerotic plaques were analyzed using multivariate linear and logistic regression analyses. Finally, the consistency of these associations was also explored across different subgroups. As a result, serum P and CPP levels were associated with carotid artery plaque burden, presented as maximum wall thickness (max WT), wall area, and lipid-rich necrotic core (LRNC), in univariate analysis, with β = −0.205, 95% CI (−0.348, −0.061), β = −0.258, 95% CI (−0.405, −0.113), OR = 0.182, 95% CI (0.034, 0.975) for P, and β = −0.203, 95% CI (−0.346, −0.059), β = −0.221, 95% CI (−0.366, −0.074), OR = 0.466, 95% CI (0.237, 0.915) for CPP, respectively. In multivariate regression analysis, the serum P level was independently associated with wall area, β = −0.211, 95% CI (−0.367, −0.052).

Conclusion: Lower serum phosphorus levels are associated with an increased carotid artery plaque wall area.

KEYWORDS

ischemic stroke, atherosclerosis, carotid artery, calcium, phosphate

Introduction

Previous studies have demonstrated the association between serum calcium/phosphate metabolism and atherosclerosis, as well as a relationship with cardiovascular disease (1). Most studies conducted on patients with coronary artery disease indicated a positive correlation between serum calcium-phosphate levels and coronary artery calcification (2, 3). However, conclusions regarding its association with cerebrovascular atherosclerosis, particularly atherosclerotic plaque vulnerability, have not been established.

Few studies investigating the relationship between serum calcification/phosphate levels and cerebrovascular atherosclerosis have yielded inconsistent results. A Korean retrospective study investigated the association between serum calcium phosphate level and intracranial atherosclerosis in stroke-free patients, and the results suggested that corrected serum calcium concentrations are positively associated with the presence of intracranial atherosclerosis on MRA, but no association was found between uncorrected serum calcium, phosphate, and intracranial atherosclerosis (4). Another study conducted in type 2 diabetes mellitus (T2DM) without kidney disease compared the serum calcium phosphate level in patients with and without subclinical carotid atherosclerosis (defined as presence of carotid plaque on carotid ultrasound imaging), and the results demonstrated that patients with subclinical carotid atherosclerosis have a higher serum phosphate and calcium-phosphate product level than those without subclinical carotid atherosclerosis. After further adjustment for confounders, serum calcium-phosphate product is associated with subclinical carotid atherosclerosis independently (5). In addition, a retrospective study including 1,034 patients with first-ever stroke suggested that serum phosphate level was related to neither intracranial nor extracranial atherosclerosis on DSA (6). However, most of these studies focused on specific populations, such as individuals with chronic kidney disease or diabetes, making it difficult to extrapolate the findings to all stroke patients; and the evaluations of atherosclerosis also varied, as no carotid artery plaque compositions were involved.

The aim of this study was to investigate the association between serum calcium, phosphate, as well as calcium-phosphate product levels, and carotid artery atherosclerotic plaque, both plaque burden and vulnerability, as assessed by high-resolution MR vessel wall imaging (HR MR-VWI).

Methods

Study design

Retrospective study.

Subjects

Ischemic stroke associated with carotid artery atherosclerosis patients admitted to a comprehensive stroke center during 2019–2022 were consecutively screened. The inclusion criteria are as follows: (1) acute ischemic stroke confirmed by brain MRI, (2) symptom onset within 2 weeks, (3) stroke was caused by carotid artery atherosclerosis, and (4) availability of carotid artery plaque MRI vessel wall imaging. Subjects were excluded if they met any of the following criteria: (1) non-atherosclerotic carotid artery lesions, (2) concurrent ipsilateral severe (>50%) intracranial atherosclerosis evaluated on MRA, (3) poor image quality, and (4) parathyroid function disorders.

A total of 251 subjects who met the criteria mentioned above were ultimately included in the study. Subjects were excluded from the analysis for the following reasons: carotid artery occlusion 25, dissection 6, and coexisting severe intracranial stenosis 12.

The study protocol was approved by the local ethics committee, and the requirement for subjects' consent was waived due to the retrospective analysis. All the data obtained were de-identified to protect patient confidentiality.

Demographic characteristics and assessment of vascular risk factors

Demographic characteristics and atherosclerotic risk factors—including hypertension, diabetes, hyperlipidemia, coronary heart disease (CAD), and smoking—were obtained from electronic health records.

Serum calcium and phosphate measurement

Blood samples were collected early in the morning after an overnight fast, with the last meal typically consumed 10 h prior to the blood draw. The samples were analyzed to measure serum calcium, phosphate, albumin, glucose, total cholesterol, high-density lipoprotein (HDL) cholesterol, and triglycerides. Low-density lipoprotein (LDL) cholesterol was estimated using the method described by Friedewald et al. (7). Measurements of serum calcium, phosphate, and albumin concentrations were conducted using standard autoanalyzer techniques (Modular DP analyzer, Roche Diagnostics, Mannheim, Germany). The serum calcium concentration was corrected for serum albumin concentration using the following formula: corrected calcium (mmol/L) = measured total calcium (mmol/)- [0.02 × serum albumin(g/L)] + 0.8. All the blood samples were processed in the same lab with the same protocol.

Carotid artery MR vessel wall imaging

Magnetic resonance imaging was conducted using a Philips 3.0 T MR scanner (Achieva TX, Philips Healthcare, Best, the Netherlands) equipped with a custom-designed 36-channel neurovascular coil. The MR imaging parameters were as follows: 3D MERGE: fast field echo (FFE), repetition time (TR)/echo time (TE) 9.2/4.3 msec, flip angle 6°, field of view (FOV) $4 \times 16 \times 25$ cm^3, and spatial resolution of $0.8 \times 0.8 \times 0.8$ mm^3; T2-VISTA: turbo spin echo, TR/TE 2500/278 msec, flip angle 90°, FOV $4 \times 16 \times 25$ cm^3, and spatial resolution $0.8 \times 0.8 \times 0.8$ mm^3; Simultaneous Non-contrast Angiography and intraPlaque Hemorrhage (SNAP): FFE, TR/TE 9.9/4.8 msec, flip angle 11/5°, FOV $4 \times 16 \times 25$ cm^3, and spatial resolution $0.8 \times 0.8 \times 0.8$ mm^3.

Image interpretation

Carotid artery MR vessel wall images were analyzed by two reviewers with >5 years experience in neurovascular imaging, using an MR workstation (Extended MR Work Space 2.6.3.4, Best, the Netherlands). The reviewers worked independently, and in cases of inconsistency, a third senior radiologist was involved to reach a consensus. The presence or absence of atherosclerotic plaque at each carotid artery was determined; the atherosclerotic plaque is defined as the eccentric thickening of the vessel wall. The degree of arterial luminal stenosis was measured using the NASCET criteria (8). The carotid artery plaque burden index included maximum carotid wall thickness (max WT), which is the maximum segmental wall thickness of 12 segments measured at the slice with the largest lipid core area, or the maximum segmental wall thickness if no core was present; wall area; normalized wall index (wall area /[lumen area + wall area]), and degree of stenosis. The carotid artery plaque stability index included intraplaque hemorrhage (IPH), defined as the presence of IPH in each plaque when hyperintensity on SNAP images exhibited a signal intensity ≥1.5 times that of adjacent muscle or cerebral parenchyma; calcification; lipid-rich necrotic core (LRNC); thinned ruptured fibrous cap (TRFC); and irregular surface (9). The consistency test for image interpretation between the two readers was good, with kappa = 1.0 ($p < 0.01$) for diagnosing IPH and an ICC = 0.94 (95% CI: 0.85–0.97) for determining the max WT measurements.

Statistical analysis

Continuous variables with a normal distribution were described as mean ± standard deviation. T-tests were used for comparisons between groups, while categorical variables were presented as numbers (percentages), with chi-square tests used for group comparisons. Linear regression was utilized to assess the association between calcium and phosphate levels and plaque burden (max WT and wall area). Logistic regression was applied to identify the association between calcium and phosphate levels and atherosclerotic plaque vulnerability (IPH, calcification, TRFC, and LNRC). In the multivariate regression analysis, we adjusted for demographic characteristics and risk factors step by step. All *p*-values were set at 0.05, and all statistical analyses were performed using SPSS version 22.0 (IBM, New York, USA). Subgroup analysis forest plots were generated using Stata 17.0.

Result

Basic characteristic of subjects included

A total of 251 acute ischemic stroke patients with carotid atherosclerosis were included in the study, with a mean age of 68 years. Of these patients, 80.1% were male. The prevalence of coexisting hypertension, diabetes, and hyperlipidemia was 75.2, 41.7, and 50.8%, respectively. The mean serum calcium and phosphorus levels were 2.26 ± 0.11 mmol/L and 1.16 ± 0.19 mmol/L, retrospectively (see Table 1).

TABLE 1 Basic characteristics of subjects included.

Variables, M ± SD or *n* (%)	Total (*N* = 251)
Age (years)	68 ± 10
Male	205 (80.1)
Hypertension	191 (75.2)
Diabetes	105 (41.7)
Hyperlipidemia	129 (50.8)
CAD	58 (23.1)
Smoking	174 (69.6)
Hcy (umol/L)	17.4 ± 8.3
SBP (mmHg)	145 ± 20
DBP (mmHg)	78 ± 13
Glucose (mmol/L)	6.12 ± 2.00
TC (mmol/L)	4.03 ± 0.94
TG (mmol/L)	1.46 ± 0.78
LDL-C(mmol/L)	2.53 ± 0.94
HDL-C(mmol/L)	0.98 ± 0.25
eGFR(ml/min/1.73m^2)	86.53 ± 19.63
Ca(mmol/L)	2.26 ± 0.11
P(mmol/L)	1.16 ± 0.19
Ca*P	2.63 ± 0.46

Carotid artery plaque burden and vulnerability in subjects included

Carotid artery plaque characteristics are presented in Table 2. Among the included patients, 53.0% exhibited less than 50% stenosis, with a mean max WT of 4.29 mm. Additionally, 42.0% of the patients had IPH, while 39.4% showed atherosclerotic plaque calcification. Furthermore, 35.5% of the patients exhibited LRNC and TRFC characteristics, respectively.

Association between Ca, P with carotid artery plaque burden and vulnerability

Table 3 demonstrates the association between serum Ca, P, as well as CPP and atherosclerotic plaque characteristics in a univariate analysis. Both P and CPP were correlated with max WT, wall area, and LRNC in univariate regression. However, no positive associations between Ca and atherosclerotic plaque features were detected in this analysis.

Association between serum P, CPP, and plaque characteristics in multivariate regression

In multivariate regression, after adjusting for age and sex in Model 1, as well as cardiovascular risk factors in Model 2, serum P is independently associated with wall area, with $\beta = -0.211$, 95% CI (−0.367, −0.052). Additionally, CPP is marginally correlated with

TABLE 2 Carotid atherosclerotic plaque burden and vulnerability.

Carotid atherosclerotic plaque characteristics M ± SD or *n* (%)	Total (*n* = 251)	95% CI
Stenosis		
≤30%	92 (36.8)	
30–49%	41 (16.3)	
50–69%	44 (17.5)	
70–99%	74 (29.4)	
Max WT (mm)	4.29 ± 1.45	
Lumen area(mm^2)	0.22 ± 0.15	
Wall area (mm^2)	0.50 ± 0.19	
NWI	0.70 ± 0.13	
Eccentricity index	0.66 ± 0.14	
IPH	97(42.0)	35.5,48.1
Calcification	91 (39.4)	32.9,45.9
Irregular surface	73 (31.6)	26.0, 38.1
LRNC	82 (35.5)	29.4, 41.6
TRFC	82 (35.5)	29.4, 41.6

wall area, with β = −0.157, 95% CI (−0.314, 0.004), $p = 0.056$ (see Table 4).

Association between serum P, CPP, and carotid artery atherosclerosis in different subgroups

We explored the relationship between P, CPP, and carotid atherosclerotic plaque characteristics across various subgroups, including age, sex, hypertension, diabetes, and CKD subgroups (Supplementary Tables 1, 2). After adjusted cofounding, the results indicated that P is associated with max WT in hypertensive subgroups, $\beta = -0.248$, 95% CI (−0.430, −0.068) (Figure 1A), also associated with wall area in individuals over 65 years of age($\beta = -0.222$, 95% CI [−0.400, −0.011]), male participants ($\beta = -0.219$, 95% CI [−0.446, −0.045]), and those with hypertension ($\beta = -0.314$, 95% CI [−0.513, −0.130]) (Figure 1B). Additionally, the positive relationship between CPP and carotid artery plaque burden (max WT and wall area) can still be established in the hypertensive subgroup, with $\beta = -0.249$, 95% CI (−0.436, −0.067), and $\beta = -0.259$, 95% CI (−0.461, −0.068) (Figures 1C,D). No other significant differences were identified in the remaining subgroups.

Discussion

This study investigated the association between serum calcium phosphate levels and carotid atherosclerosis, assessed comprehensively through HR-MR VWI, focusing on atherosclerotic plaque burden and vulnerability. The results demonstrated a positive relationship between serum phosphate levels and carotid atherosclerosis, as indicated by wall area, after adjusting for confounding factors. CPP was associated with the wall area marginally. Further subgroup analysis suggested potential differences in this correlation based on age, sex, and

TABLE 3 Association between serum calcium phosphate and carotid atherosclerotic plaque characteristics in univariate analysis.

	Max WT			Wall area			NWI			Eccentricity index			IPH			Calcification			TRFC			LRNC		
	β	95%CI	*p*	β	95% CI	*p*	β	95%CI	*p*	β	95% CI	*p*	OR	95% CI	*p*	OR	95%CI	*p*	OR	95%CI	*p*	OR	95%CI	*p*
Ca	−0.073	−2.742, 0.826	0.291	0.001	−0.144, 0.145	0.994	−0.082	−0.227, 0.059	0.248	−0.016	−0.160, 0.127	0.820	2.020	0.208, 19.657	0.545	0.672	0.066, 6.873	0.738	1.969	0.169, 22.866	0.588	0.214	0.018, 2.509	0.219
P	−0.205	−0.348, −0.061	0.006	−0.258	−0.405, −0.113	0.001	−0.044	−0.190, 0.105	0.568	−0.128	−0.281, 0.020	0.090	0.415	0.092, 1.881	0.254	0.307	0.064, 1.476	0.140	0.396	0.078, 2.002	0.263	0.182	0.034, 0.975	0.047
Adjusted Ca*	−0.080	−0.218, 0.057	0.247	−0.011	−0.149, 0.128	0.881	−0.055	−0.191, 0.084	0.443	−0.068	−0.208, 0.070	0.327	0.859	0.061, 12.103	0.911	0.779	0.051, 11.860	0.857	0.669	0.036, 12.448	0.788	0.044	0.001, 1.831	0.101
Ca*P	−0.203	−0.346, −0.059	0.006	−0.221	−0.366, −0.074	0.003	−0.070	−0.214, 0.078	0.360	−0.123	−0.275, 0.026	0.103	0.733	0.401, 1.340	0.313	0.638	0.341, 1.194	0.160	0.733	0.385, 1.395	0.345	0.466	0.237, 0.915	0.027

*Adjusted Ca: albumin-corrected calcium.

10.3389/fneur.2025.1571205

TABLE 4 Association between serum P, CPP levels, and carotid artery atherosclerotic plaque in multivariate regression.

	Max WT						Wall area						LRNC					
	Model 1			Model 2			Model 1			Model 2			Model 1			Model 2		
	β	95% CI	*p*	β	95% CI	*p*	β	95% CI	*p*	β	95% CI	*p*	OR	95% CI	*p*	OR	95% CI	*p*
P	−0.115	−0.264, 0.035	0.131	−0.134	−0.286, 0.021	0.091	−0.190	−0.344, −0.036	0.016	−0.211	−0.367, −0.052	0.010	0.309	0.052, 1.843	0.198	0.249	0.040, 1.563	0.128
Ca*P	−0.112	−0.261, 0.037	0.141	−0.128	−0.280, 0.028	0.108	−0.147	−0.300, 0.008	0.063	−0.157	−0.314, 0.004	0.056	0.572	0.280, 1.171	0.126	0.532	0.254, 1.114	0.094

Adjust age and sex in model 1. Adjust age, sex, hypertension, diabetes, hyperlipidemia, smoking, and eGFR in model 2.

hypertension status. The results of this study could provide some insight into serum mineral metabolism and carotid atherosclerosis.

Serum phosphate level and atherosclerosis

Serum phosphate has been established as a risk factor for cardiac calcification, cardiovascular disease, and mortality in populations with chronic kidney disease (10), has also been recognized as a risk factor for ischemic stroke in hemodialysis patients (11, 12). Additionally, some studies suggest that phosphate levels within the conventional normal range may also contribute to cardiovascular disease (10). A meta-analysis of the general population indicated that elevated serum phosphate is associated with cardiovascular mortality and subclinical coronary atherosclerosis (13). However, data about serum phosphate and carotid artery atherosclerosis were limited. In a study of 1,034 patients with first-ever acute cerebral infarction, serum phosphate was associated with neither intracranial nor extracranial atherosclerosis (6). Another cross-sectional study in the general population demonstrated that a high phosphate level is correlated with cardiovascular disease, while a lower phosphate level is correlated with metabolic syndrome (14). Our study did find the association between serum phosphate level and carotid atherosclerosis after adjusting for confounding, especially max WT, wall area, and LRNC. This finding is in contrast to the results in the coronary artery. The inconsistency can be explained by the population included, the vascular bed heterogeneity, as well as the atherosclerosis definitions. In this study, we included acute ischemic stroke patients with carotid artery atherosclerosis, and we used HR-MR VWI to quantitatively assess carotid atherosclerosis, which is more sensitive than intracranial artery stenosis on MRA. While previous study on coronary artery disease usually evaluates atherosclerosis on CTA. The mechanism of low serum phosphate contributes to atherosclerosis could be caused by glucose metabolism or malnutrition–inflammation complex syndrome (12). As we know, phosphate is a component of cell membranes and plays an important role in mediating intracellular signaling, so lower serum phosphate levels may have adverse implications for vascular biology and may affect several organ systems (15). There is one study validated that low serum phosphate level is associated with glucose tolerance, insulin sensitivity in non-diabetic subjects (16). While we did not find a significant difference in P and carotid atherosclerosis in the diabetes and non-diabetes subgroups due to the limited sample size. From a pathophysiological perspective, animal experiments demonstrated that excess phosphate intake decreased atherosclerosis formation partly by changing the profile of peripheral monocytes or inducing apoptosis of macrophages in apolipoprotein E-deficient mice (17). However, our exploratory findings could not validate the causality; more longitudinal studies are needed in the future.

We also find that the positive associations between serum phosphate and carotid artery atherosclerosis differ in different sex groups; the main results can be established in males but not in females. A previous study regarding phosphate and subclinical carotid atherosclerosis also suggested the sex difference (18). As for the causes of this result, there are more male patients included in our study,

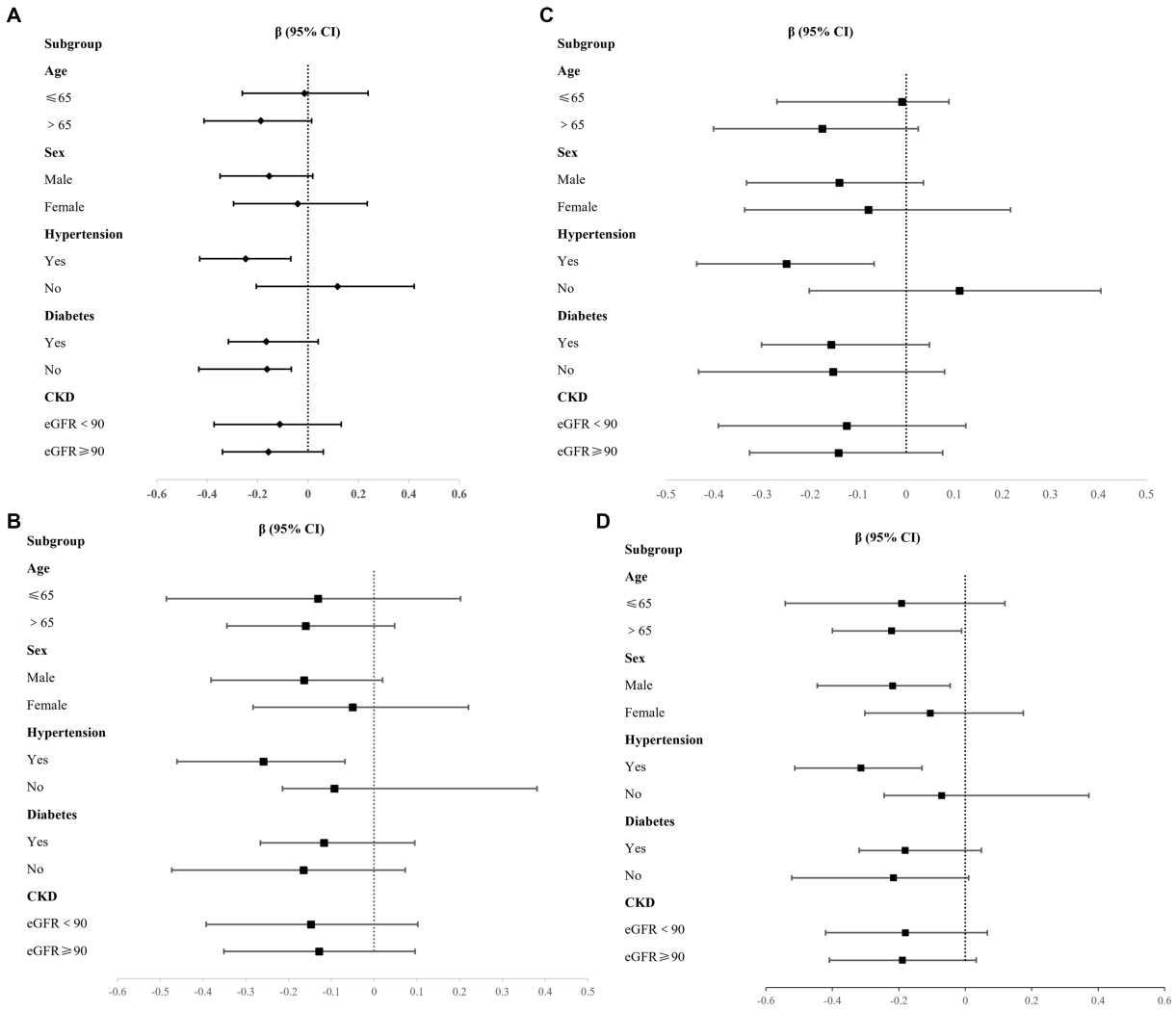

FIGURE 1
Association between P, CPP and plaque burden in different subgroups. **(A)** P and Max WT; **(B)** P and Wall area; **(C)** CPP and Max WT; **(D)** CPP and Wall area.

which could result in some population bias; Second, age and associated hormone levels could also affect the result. Therefore, more balanced data, including different age and sex groups, are needed to validate the results.

Ca-P product and atherosclerosis

The relationship between CPP and atherosclerosis or cardiovascular disease has not been concluded. Data from Atherosclerosis Risk in Communities (ARIC) study suggested that the calcium-phosphate product is associated with stroke in a prospective cohort (HR = 1.15, 95% CI 1.05–10.26, $p = 0.0017$) (19). Association between CPP and coronary atherosclerosis assessed by cardiac computed tomography angiography had been established in a cohort of 7,553 participants with normal kidney function, especially with the presence of calcified coronary atherosclerotic plaque (3). As for CPP and subclinical carotid atherosclerosis, a study of 303 subjects was conducted in patients with type 2 diabetes mellitus (T2DM) without kidney disease or previous cardiovascular disease, clinical variables and carotid ultrasound imaging were obtained. Subclinical atherosclerosis was defined as the presence of carotid artery atherosclerotic plaques (main study outcome), and the result suggested that CPP was positively associated with the presence of carotid plaques (OR(adj) = 1.078; 95% CI: 1.017–1.142) (5). Our result demonstrated the association between CPP and max WT, wall area, and LRNC in univariate analysis, but with limited significance in multivariate analysis. The possible reasons for this result could be contributed to the population included, sample size, and some cofounding factors, a prospective study with larger sample size is needed to validate the result in the future.

Significance and limitations

To our best knowledge, this is the first study to investigate serum calcification-phosphate metabolism and carotid artery atherosclerosis quantitatively on HR-MR VWI. The results of our study could provide

some insights about serum mineral levels and carotid artery atherosclerosis in acute ischemic stroke, as well as some potential differences in different subgroups.

There are some innovations of our study. First, we use HR-MR VWI to quantitatively evaluate atherosclerotic plaque burden and vulnerability, which is different from previous calcification scores on CCTA. Second, we investigate the calcium phosphate levels and carotid artery atherosclerosis in all acute ischemic stroke patients, but not diabetes or chronic kidney disease. The results of our study could be helpful in the exploration of the potential risk factors of carotid artery atherosclerosis, also provide some evidence for future mechanism studies.

There were some limitations about this study, first, the population in this study is limited to a single center in China, with a male-dominated cohort. This limits the generalizability of findings to other populations, particularly women and non-Asian ethnic groups. A larger population with more balanced sex distribution is still needed in the future. Second, the cross-sectional analysis fails to validate the causal relationship between serum mineral levels and atherosclerosis. Finally, no other dietary intake of calcium phosphate, as well as vitamin D levels, were included in this study. More details of factors in calcium and phosphorus metabolism will be helpful in the mechanism explanation. Further study, including serum calcium phosphate intake and Vitamin D supplement, will be needed in the future.

Conclusion

Serum phosphate was independently associated with carotid atherosclerotic plaque burden in acute ischemic stroke. And this correlation could be significant in males, older age, and hypertension subgroups.

Data availability statement

The original contributions presented in the study are included in the article/Supplementary material, further inquiries can be directed to the corresponding author.

Ethics statement

The studies involving humans were approved by Beijing Tsinghua Changgung Ethics Committee. The studies were conducted in accordance with the local legislation and institutional requirements. The ethics committee/institutional review board waived the requirement of written informed consent for participation from the participants or the participants' legal guardians/next of kin because retrospective study and data analysis.

Author contributions

XS: Conceptualization, Writing – original draft, Writing – review & editing. HZ: Data curation, Formal analysis, Investigation, Writing – review & editing, Methodology, Resources, Software. ZP: Investigation, Methodology, Resources, Software, Writing – review & editing. DH: Project administration, Resources, Supervision, Writing – review & editing. XZ: Supervision, Validation, Writing – review & editing. ZZ: Investigation, Methodology, Writing – review & editing. JW: Conceptualization, Funding acquisition, Writing – review & editing.

Funding

The author(s) declare that financial support was received for the research and/or publication of this article. This work was financially supported by National Natural Science Foundation of China (82401555), National Key R&D Program of China (2023YFC2506600), Tsinghua Precision Medicine, Tsinghua University (20219990033), and Capital's Funds for Health Improvement and Research (2020-1-2241).

Conflict of interest

The authors declare that the research was conducted in the absence of any commercial or financial relationships that could be construed as a potential conflict of interest.

Generative AI statement

The author(s) declare that no Gen AI was used in the creation of this manuscript.

Publisher's note

All claims expressed in this article are solely those of the authors and do not necessarily represent those of their affiliated organizations, or those of the publisher, the editors and the reviewers. Any product that may be evaluated in this article, or claim that may be made by its manufacturer, is not guaranteed or endorsed by the publisher.

Supplementary material

The Supplementary material for this article can be found online at: https://www.frontiersin.org/articles/10.3389/fneur.2025.1571205/full#supplementary-material

References

1. Dhingra R, Sullivan LM, Fox CS, Wang TJ, D'Agostino RS, Gaziano JM, et al. Relations of serum phosphorus and calcium levels to the incidence of cardiovascular disease in the community. *Arch Intern Med*. (2007) 167:879–85. doi: 10.1001/archinte.167.9.879

2. Gronhoj MH, Gerke O, Mickley H, Steffensen FH, Lambrechtsen J, Sand NPR, et al. Associations between calcium-phosphate metabolism and coronary artery calcification; a cross-sectional study of a middle-aged general population. *Atherosclerosis*. (2016) 251:101–8. doi: 10.1016/j.atherosclerosis.2016.06.001

3. Shin S, Kim KJ, Chang HJ, Cho I, Kim YJ, Choi BW, et al. Impact of serum calcium and phosphate on coronary atherosclerosis detected by cardiac computed tomography. *Eur Heart J*. (2012) 33:2873–81. doi: 10.1093/eurheartj/ehs152

4. Kang K. Serum calcium and phosphate concentrations and intracranial atherosclerosis. *Atherosclerosis*. (2014) 232:249–53. doi: 10.1016/j.atherosclerosis.2013.11.030

5. Ramirez-Morros A, Granado-Casas M, Alcubierre N, Martinez-Alonso M, Real J, Castelblanco E, et al. Calcium phosphate product is associated with subclinical carotid atherosclerosis in type 2 diabetes. *J Diabetes Res*. (2017) 2017:1–8. doi: 10.1155/2017/3498368

6. Kim J, Song TJ, Song D, Lee HS, Nam CM, Nam HS, et al. Serum alkaline phosphatase and phosphate in cerebral atherosclerosis and functional outcomes after cerebral infarction. *Stroke*. (2013) 44:3547–9. doi: 10.1161/STROKEAHA.113.002959

7. Friedewald WT, Levy RI, Fredrickson DS. Estimation of the concentration of low-density lipoprotein cholesterol in plasma, without use of the preparative ultracentrifuge. *Clin Chem*. (1972) 18:499–502. doi: 10.1093/clinchem/18.6.499

8. Ferguson GG, Eliasziw M, Barr HW, Clagett GP, Barnes RW, Wallace MC, et al. The north American symptomatic carotid endarterectomy trial: surgical results in 1415 patients. *Stroke*. (1999) 30:1751–8. doi: 10.1161/01.STR.30.9.1751

9. Brunner G, Virani SS, Sun W, Liu L, Dodge RC, Nambi V, et al. Associations between carotid artery plaque burden, plaque characteristics, and cardiovascular events: the ARIC carotid magnetic resonance imaging study. *JAMA Cardiol*. (2021) 6:79–86. doi: 10.1001/jamacardio.2020.5573

10. Foley RN. Phosphate levels and cardiovascular disease in the general population. *Clin J Am Soc Nephrol*. (2009) 4:1136–9. doi: 10.2215/CJN.01660309

11. Chen TS, Chen CH, Chen CA, Chou LP, Liu CC. Low serum phosphate is associated with ischemic stroke in hemodialysis patients. *Clin Exp Nephrol*. (2018) 22:1182–7. doi: 10.1007/s10157-018-1578-y

12. Yamada S, Tsuruya K, Taniguchi M, Tokumoto M, Fujisaki K, Hirakata H, et al. Association between serum phosphate levels and stroke risk in patients undergoing hemodialysis: the Q-cohort study. *Stroke*. (2016) 47:2189–96. doi: 10.1161/STROKEAHA.116.013195

13. Torrijo-Belanche C, Moreno-Franco B, Munoz-Cabrejas A, Calvo-Galiano N, Casasnovas JA, Sayon-Orea C, et al. High serum phosphate is associated with cardiovascular mortality and subclinical coronary atherosclerosis: systematic review and Meta-analysis. *Nutrients*. (2024) 16:599. doi: 10.3390/nu16111599

14. Park W, Kim BS, Lee JE, Huh JK, Kim BJ, Sung KC, et al. Serum phosphate levels and the risk of cardiovascular disease and metabolic syndrome: a double-edged sword. *Diabetes Res Clin Pract*. (2009) 83:119–25. doi: 10.1016/j.diabres.2008.08.018

15. Michigami T, Yamazaki M, Razzaque MS. Extracellular phosphate, inflammation and cytotoxicity. *Adv Exp Med Biol*. (2022) 1362:15–25. doi: 10.1007/978-3-030-91623-7_3

16. Haap M, Heller E, Thamer C, Tschritter O, Stefan N, Fritsche A. Association of serum phosphate levels with glucose tolerance, insulin sensitivity and insulin secretion in non-diabetic subjects. *Eur J Clin Nutr*. (2006) 60:734–9. doi: 10.1038/sj.ejcn.1602375

17. Shiota A, Taketani Y, Maekawa Y, Yasutomo K, Sata M, Sakai T, et al. High phosphate diet reduces atherosclerosis formation in apolipoprotein E-deficient mice. *J Clin Biochem Nutr*. (2011) 49:109–14. doi: 10.3164/jcbn.10-150

18. Martin M, Valls J, Betriu A, Fernandez E, Valdivielso JM. Association of serum phosphorus with subclinical atherosclerosis in chronic kidney disease sex makes a difference. *Atherosclerosis*. (2015) 241:264–70. doi: 10.1016/j.atherosclerosis.2015.02.048

19. Foley RN, Collins AJ, Ishani A, Kalra PA. Calcium-phosphate levels and cardiovascular disease in community-dwelling adults: the atherosclerosis risk in communities (ARIC) study. *Am Heart J*. (2008) 156:556–63. doi: 10.1016/j.ahj.2008.05.016

frontiers | Frontiers in Neurology

TYPE Original Research
PUBLISHED 15 May 2025
DOI 10.3389/fneur.2025.1583451

OPEN ACCESS

EDITED BY
Liang Jiang,
Nanjing Medical University, China

REVIEWED BY
Shaowu Li,
Beijing Neurosurgical Institute, China
Hongyan Chen,
Capital Medical University, China
Wen Jiang,
Beijing Jishuitan Hospital, China

*CORRESPONDENCE
Peiyao Zhang
✉ 15011353102@163.com

RECEIVED 25 February 2025
ACCEPTED 16 April 2025
PUBLISHED 15 May 2025

CITATION
Li L, Song S, Hu Y, Luo Y, Wang L and Zhang P (2025) Altered cerebral perfusion in Parkinson's disease patients with anxiety: an arterial spin labeling MRI study.
Front. Neurol. 16:1583451.
doi: 10.3389/fneur.2025.1583451

Altered cerebral perfusion in Parkinson's disease patients with anxiety: an arterial spin labeling MRI study

Lu Li[1], Shiyuan Song[1], Yingying Hu[1], Yuan Luo[1], Lu Wang[2] and Peiyao Zhang[1]*

[1]Department of Radiology, China-Japan Friendship Hospital, Beijing, China, [2]Department of Neurology, China-Japan Friendship Hospital, Beijing, China

Purpose: In this study, we used arterial spin labeling (ASL) to explore altered cerebral blood flow perfusion in Parkinson's disease (PD) patients with anxiety and assessed the relationship between anxiety and perfusion in various brain regions to determine the pathophysiologic basis for the occurrence of anxiety in patients with PD.

Materials and methods: Seventy-three patients with PD who were treated at China-Japan Friendship Hospital from September 2023 to November 2024 were enrolled: 36 PD patients with anxiety (PD-A) and 37 PD patients without anxiety (PD-NA); in addition, 37 healthy volunteers were recruited as healthy controls (HCs). All the subjects underwent three-dimensional T1-weighted imaging (3D-T1WI) and pseudo-continuous arterial spin labeling (pCASL) sequential scans via 3.0-T MRI, and cerebral blood flow (CBF) values were obtained from the whole brain. Independent samples *t* tests and non-parametric Mann–Whitney U tests were applied to test the differences in the CBF values of each brain region between the PD and HC groups, and between the PD-A and PD-NA groups. The relationships between CBF values and anxiety scores in the PD group were also investigated.

Results: CBF values in the bilateral frontal lobes, parietal lobes, temporal lobes, occipital lobes, substantia nigra, striatum, caudate nuclei, left pallidum, and bilateral cerebellum were lower in the PD group than in the HC group ($P < 0.05$). Compared with those in the PD-NA group, the CBF values of the bilateral frontal lobes, temporal lobes, left putamen and left pallidum were lower in the PD-A group ($P < 0.05$). CBF values in the left frontal lobe ($r = -0.265$, $P = 0.024$), right frontal lobe ($r = -0.283$, $P = 0.015$), left temporal lobe ($r = -0.287$, $P = 0.014$), and right temporal lobe ($r = -0.275$, $P = 0.019$) were negatively correlated with Hamilton Anxiety Scale (HAMA) scores in PD patients.

Conclusion: The development of PD-A may be associated with dysfunctional brain perfusion in multiple brain regions, notably the bilateral frontal lobes, temporal lobes, left putamen, and left pallidum. Abnormal CBF in these brain regions may serve as a neuroimaging marker for early PD-A diagnosis. Using ASL to identify perfusion changes in core regions may advance our understanding of the pathophysiological mechanisms underlying PD-A.

KEYWORDS

Parkinson's disease, anxiety, arterial spin labeling, magnetic resonance imaging, cerebral blood flow

1 Introduction

Parkinson's disease (PD) is the second most common neurodegenerative disorder (1) and is characterized by bradykinesia, rigidity, resting tremor, postural instability, gait impairment, and numerous non-motor and behavioral symptoms (2). Cognitive impairment and psychiatric disorders are common non-motor symptoms that may manifest in early stages of the disease, sometimes even before the appearance of classic motor symptoms (3, 4). Furthermore, the onset and progression of non-motor symptoms have a greater impact on PD patients than motor symptoms do (5). Anxiety is one of the most common non-motor symptoms in PD patients, and the prevalence of PD with anxiety (Parkinson's disease patients with anxiety [PD-A]) is approximately 31% (6), which affects patient's quality of life. The neuropathological hallmarks of PD are neuronal loss in the substantia nigra, which causes striatal dopaminergic deficiency, and α-synuclein accumulation in intraneuronal inclusions (1). The underlying mechanisms of PD-A remain largely unknown, and exploration of their neurobiological alterations can assist in the further diagnosis and treatment of PD-A patients.

Arterial spin labeling (ASL) is a noninvasive magnetic resonance imaging (MRI) technique that uses magnetically labeled blood water as an endogenous tracer for perfusion measurements (7). The absence of dopaminergic neurons alters the microvascular environment and affects cerebral blood perfusion (8). Recent studies have demonstrated that PD patients exhibit cortical hypoperfusion in brain regions that are associated with motor and non-motor symptoms (9–11). Reduced CBF in PD patients is an important measure for assessing motor symptoms, non-motor symptoms, and dopamine treatment (12, 13). Prior investigations of cerebral perfusion in PD-A patients have focused predominantly on single-photon emission computed tomography (SPECT) (14). SPECT-based imaging necessitates the use of radiotracers, which may pose potential risks and limitations related to invasiveness and radiation exposure. In contrast, ASL is a non-invasive, radiation-free technique that offers enhanced safety, faster acquisition times, and superior reproducibility. These attributes render ASL a promising modality by which to elucidate regional perfusion alterations in PD-A patients.

In this study, we used the ASL technique to explore cerebral perfusion in PD-A patients and to assess the relationship between anxiety scores and CBF values to determine the pathophysiologic basis for the development of anxiety in PD patients.

2 Materials and methods

2.1 Participants

This prospective study was approved by the Ethics Committee of the China-Japan Friendship Hospital. All participants were informed of the study details and methods and provided written informed consent. A total of 81 patients with PD who were treated at China-Japan Friendship Hospital between September 2023 and November 2024 were prospectively enrolled. The inclusion criteria were as follows: (1) diagnosis and evaluation by two experienced neurologists according to the Movement Disorder Society (MDS) clinical diagnostic criteria for Parkinson's disease; (2) modified Hoehn & Yahr (H&Y) stage of 1–2.5; and (3) right-handedness. The exclusion criteria were as follows: (1) history of head trauma, stroke, central nervous system infection, or tumor ($n = 3$); (2) contraindications to MRI examination, such as claustrophobia or the presence of metallic implants ($n = 2$); (3) significant motion artifacts in the scan images ($n = 3$); and (4) severe psychiatric or cognitive disorders. Ultimately, 73 PD patients met the inclusion criteria and were enrolled in the study.

Thirty-seven healthy volunteers were recruited from the community to serve as the healthy controls (HCs). The inclusion criteria for the HCs were as follows: (1) no history of traumatic brain injury or stroke and no psychiatric or cognitive disorders; (2) Hamilton Anxiety Scale (HAMA) score <7; (3) right-handedness; and (4) no contraindications to MRI examination.

2.2 Clinical information collection and neuropsychological scale assessment

PD patients were evaluated by senior neurologists with specialized training on the basis of the diagnostic criteria for anxiety attacks outlined in the Diagnostic and Statistical Manual of Mental Disorders, 4th edition (DSM-IV). PD patients were categorized into two groups according to HAMA score: the PD-A group and the PD-NA group. Specifically, a HAMA score ≥ 7 was used to identify PD patients with anxiety (PD-A, $n = 36$), whereas those with a HAMA score < 7 were classified as PD patients without anxiety (PD-NA, $n = 37$). The severity of PD was assessed using the H&Y staging system, and cognitive function was evaluated using the Mini-Mental State Examination (MMSE). The motor function of PD patients was assessed with the MDS modified version of the Unified Parkinson's Disease Rating Scale motor examination (UPDRS-III).

2.3 MRI data acquisition and processing

All participants completed MRI examinations on a 3.0-T MR scanner (GE Healthcare, Discovery MR 750, United States) with an 8-channel head coil. All PD patients discontinued any dopamine replacement therapy for at least 48 h prior to evaluation. The participants were instructed to keep their eyes closed, their bodies relaxed, and their heads still during the scanning process. The scanning sequences included three-dimensional T1-weighted imaging (3D-T1WI) and pseudo-continuous arterial spin labeling (pCASL). Three-dimensional T1-weighted imaging (3D-T1WI) were acquired with the following parameters: repetition time (TR), 6.7 ms; echo time (TE), 2.5 ms; flip angle, 12°; slice thickness, 1 mm; number of slices, 192; and field of view (FOV), 256 mm × 256 mm. The perfusion-weighted images were acquired at pCASL with a post label delay (PLD) of 2,025 ms. The scan parameters were as follows: TR, 5,029 ms; TE, 14.6 ms; bandwidth,

TABLE 1 Demographic and clinical characteristics of the samples.

Groups	HC ($n = 37$)	PD-NA ($n = 37$)	PD-A ($n = 36$)	$\chi^2/t/F/Z$	P
Gender (M/F)	12/25	17/20	14/22	1.420[a]	0.492
Age (years)	63.24 ± 8.37	65.54 ± 10.55	63.42 ± 9.16	0.682[b]	0.508
MDS-UPDRS-III score	-	21.38 ± 13.31	28.83 ± 12.93	−2.427[c]	0.018
Disease course (months)	-	36.0 (24.0, 48.0)	36.0 (15.0, 60.0)	−0.067[d]	0.947
Hoehn & Yahr stage	-	2.0 (1.0, 2.0)	2.0 (1.5, 2.4)	−1.414[d]	0.157
HAMA score	3.0 (2.0, 5.0)	3.0 (1.0, 5.0)	10.0 (8.3, 13.8)*#	72.621[e]	<0.001
MMSE score	29.0 (27.0, 30.0)	29.0 (27.0, 30.0)	28.0 (26.3, 29.0)	2.456[e]	0.293
HAMD score	3.0 (2.0, 4.0)	3.0 (2.0, 5.0)	3.0 (2.0, 4.0)	−0.992[e]	0.321

*Indicates a statistically significant difference compared with HCs ($P < 0.05$), #indicates a statistically significant difference compared with PD-NA patients ($P < 0.05$). [a]χ^2 test; [b]one-way ANOVA; [c]two independent samples t-test; [d]Mann–Whitney U test; [e]Kruskal–Wallis H test. HC, healthy control; PD-NA, Parkinson's disease without anxiety; PD-A, Parkinson's disease with anxiety.

62.5 kHz; slice thickness, 4 mm; number of slices, 36; and FOV, 240 mm × 240 mm.

The ASL data were post processed via CereFlow software (Translational MRI, LLC, Los Angeles, CA, United States) using the following steps: (1) The raw ASL data and CBF data were converted into parametric cerebral perfusion maps to obtain the mCBF (mean cerebral blood flow). (2) The brain perfusion parameter maps were normalized to the Montreal Neurological Institute (MNI) standard brain templates, resampled after normalization, and spatially smoothed. (3) Brain mapping of the arterial blood supply region and automatic anatomical labeling brain mapping for overlay were conducted. (4) The mean value of perfusion within each partitioned volume was obtained. The perfusion regions of interest (ROIs) included the frontal lobe, parietal lobe, temporal lobe, occipital lobe, substantia nigra, striatum, caudate, putamen, pallidum, and cerebellum.

2.4 Statistical analysis

Statistical analysis was conducted using SPSS 26.0 (IBM, Armonk, New York, USA). Categorical data, such as gender, are expressed as the number of cases, and comparisons among the three groups were performed using the χ^2 test. For continuous data (age, scale scores, and CBF values), data that conformed to a normal distribution were described as the mean ± standard deviation ($\bar{x} \pm s$), whereas those not conforming to a normal distribution were described as the median and interquartile range (M, P25–P75).

Comparisons between two groups for normally distributed variables were performed using the independent samples t test, whereas comparisons among multiple groups were conducted using one-way analysis of variance (ANOVA). For non-normally distributed variables, comparisons between two groups were performed using the Mann–Whitney U test, and comparisons among multiple groups were conducted using the Kruskal–Wallis H test.

Spearman correlation analysis was employed to assess the relationships between HAMA scores and CBF values in different brain regions among PD patients. All hypothesis tests were two-sided, with $P < 0.05$ indicating statistical significance.

3 Results

3.1 Analysis of clinical data

There were no statistically significant differences among the three groups (HC, PD-NA, and PD-A) in terms of age, gender, MMSE score, or Hamilton Depression Scale (HAMD) score ($P > 0.05$). Additionally, no significant differences were observed between the PD-NA and PD-A groups regarding disease duration, UPDRS-III score, or H&Y stage ($P > 0.05$). In terms of the HAMA score, no significant difference was found between the HC and PD-NA groups ($P > 0.05$). However, significant differences were observed between the HC and PD-A groups, as well as between the PD-NA and PD-A groups ($P < 0.05$). Specifically, the HAMA scores of the PD-A group were higher than those of the HC and PD-NA groups. Detailed results are presented in Table 1.

3.2 Comparison of CBF values

Compared with the HCs, the PD patients presented reduced CBF values in multiple brain regions, including the bilateral frontal lobes, parietal lobes, temporal lobes, occipital lobes, substantia nigra, striatum, caudate nuclei, left pallidum, and bilateral cerebellum (Figure 1, Table 2).

Further comparisons revealed that PD-A patients presented significantly lower perfusion in the bilateral frontal lobes, temporal lobes, left putamen, and left pallidum than PD-NA patients (Figure 1, Table 3).

3.3 Correlation between the CBF value and HAMA score

The HAMA score and CBF value of each brain region in the PD group were analyzed for correlation, and the results indicated that the HAMA scores were negatively correlated with the CBF values in

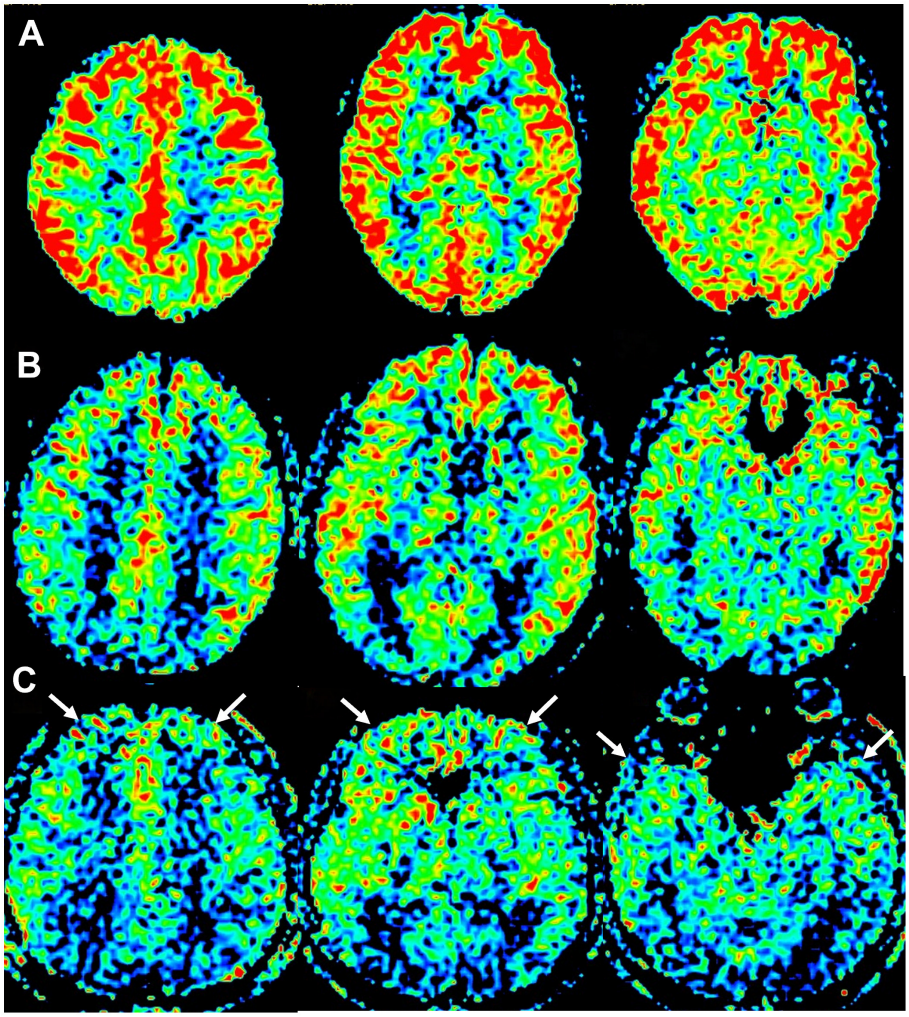

FIGURE 1
Fused images of cerebral blood flow (CBF). **(A)** Image of a healthy control (HC) participant (female, 55 years old). **(B)** Image of a participant in the Parkinson's disease without anxiety (PD-NA) group (male, 51 years old). **(C)** Image of a participant in the Parkinson's disease with anxiety (PD-A) group (female, 66 years old). Compared to the HC group **(A)**, both PD-NA **(B),** and PD-A **(C)** demonstrate widespread hypoperfusion in multiple brain regions. The PD-A group **(C)** exhibits further reduced perfusion in bilateral frontal and temporal lobes compared to PD-NA **(B)** (white arrows).

the left frontal lobe ($r = -0.265$, $P = 0.024$), right frontal lobe ($r = -0.283$, $P = 0.015$), left temporal lobe ($r = -0.287$, $P = 0.014$), and right temporal lobe ($r = -0.275$, $P = 0.019$), as shown in Figure 2 and Table 4.

4 Discussion

ASL is a brain imaging technique that uses labeled blood water from cerebral supply arteries as an endogenous tracer to obtain information about relevant cerebral perfusion and offers a non-invasive and highly reproducible method for assessing cerebral hemodynamics (15–17). In this study, we assessed alterations in the perfusion of brain regions between PD patients and healthy controls via the ASL technique. Our results revealed multiple brain regions with reduced perfusion in PD patients. Further analysis was conducted to compare perfusion patterns between PD-A and PD-NA patients. We found significant reductions in perfusion within the bilateral frontal lobes, temporal lobes, left putamen, and left pallidum in the PD-A group compared with the PD-NA group. Additionally, the CBF values in the bilateral frontal and temporal lobes of PD patients were negatively correlated with their HAMA scores. Through this study, we explored the neurological alterations associated with anxiety in PD patients by examining regional perfusion differences across groups, thereby providing imaging-based evidence to elucidate the underlying mechanisms involved.

In the present study, PD patients exhibited widespread cerebral hypoperfusion compared with HCs in the bilateral frontal lobes, parietal lobes, temporal lobes, occipital lobes, substantia nigra, striatum, caudate nuclei, left pallidum, and bilateral cerebellum, findings that are largely consistent with prior research (18–21). A study by Lin et al. (18) demonstrated extensive perfusion deficits in the bilateral frontal, parietal, and temporal lobes of PD patients. Cheng et al. (19) reported reduced CBF values in the left frontal lobe, right cerebellum and left caudate nucleus in PD patients, which are partially consistent with our findings. Melzer

TABLE 2 Brain regions with perfusion differences between the HC group and the PD group.

Brain regions	HC ($n = 37$)	PD ($n = 73$)	t/Z	P
Frontal L	53.87 (49.34, 59.54)	48.49 (41.69, 51.95)	25.523	<0.001*
Frontal R	48.25 (45.79, 54.87)	44.41 (40.03, 49.29)	18.908	<0.001*
Parietal L	51.83 (47.22, 56.13)	43.33 (37.15, 49.42)	29.028	<0.001*
Parietal R	47.19 (44.22, 50.65)	39.15 (32.42, 44.15)	30.781	<0.001*
Temporal L	54.26 (50.37, 56.69)	46.33 (41.53, 50.84)	28.840	<0.001*
Temporal R	52.13 (48.95, 55.74)	44.56 (39.00, 50.12)	31.592	<0.001*
Occipital L	55.47 (51.00, 62.17)	46.05 (37.98, 51.38)	30.924	<0.001*
Occipital R	54.36 (50.30, 59.22)	46.04 (37.77, 51.33)	30.015	<0.001*
Substantia Nigra L	43.76 ± 6.57	40.29 ± 7.47	2.393	0.018*
Substantia Nigra R	44.50 ± 6.94	40.93 ± 6.94	2.552	0.012*
Striatum L	37.98 (35.29, 39.79)	34.93 (33.01, 38.26)	10.757	0.005*
Striatum R	39.29 (36.62, 43.51)	38.27 (34.68, 41.57)	6.337	0.042*
Caudate L	33.83 (31.91, 37.99)	30.37 (27.49, 34.92)	11.527	0.003*
Caudate R	38.89 (35.60, 42.01)	35.99 (32.18, 38.75)	10.289	0.006*
Putamen L	41.44 ± 5.86	40.01 ± 5.18	1.309	0.193
Putamen R	41.84 ± 6.30	40.05 ± 5.19	1.588	0.115
Pallidum L	35.73 (33.39, 38.49)	34.36 (32.20, 38.52)	6.303	0.043*
Pallidum R	37.95 (35.79, 44.29)	38.08 (35.49, 42.75)	1.771	0.412
Cerebellum L	54.59 ± 10.13	46.33 ± 8.76	4.428	<0.001*
Cerebellum R	55.08 ± 10.40	46.71 ± 8.83	4.419	<0.001*

*Statistically significant difference ($P < 0.05$), PD, Parkinson's disease patients.

TABLE 3 Brain regions with perfusion differences between the PD-NA group and the PD-A group.

Brain regions	PD-NA ($n = 37$)	PD-A ($n = 36$)	t/Z	P
Frontal L	49.39 ± 7.03	45.62 ± 7.06	2.284	0.025*
Frontal R	46.36 ± 6.98	42.3 ± 6.56	2.564	0.012*
Parietal L	44.62 ± 8.51	41.56 ± 7.95	1.586	0.117
Parietal R	40.14 ± 8.12	36.9 ± 7.93	1.723	0.089
Temporal L	48.70 ± 7.70	44.44 ± 7.03	2.468	0.016*
Temporal R	46.82 ± 7.76	42.42 ± 7.13	2.519	0.014*
Occipital L	46.12 ± 9.26	42.79 ± 10.25	1.460	0.149
Occipital R	47.91 (38.61, 53.71)	43.27 (36.01, 49.97)	−1.589	0.112
Substantia Nigra L	40.20 ± 7.53	40.39 ± 7.52	−0.108	0.914
Substantia Nigra R	41.98 ± 6.55	39.85 ± 7.26	1.315	0.193
Striatum L	36.46 ± 5.57	34.56 ± 4.11	1.653	0.103
Striatum R	38.63 ± 4.92	37.43 ± 4.78	1.055	0.295
Caudate L	31.44 ± 6.90	30.91 ± 5.00	0.376	0.708
Caudate R	35.56 ± 5.67	35.26 ± 4.98	0.241	0.810
Putamen L	41.32 ± 5.26	38.67 ± 4.80	2.254	0.027*
Putamen R	40.84 ± 5.08	39.23 ± 5.25	1.336	0.186
Pallidum L	37.00 ± 4.93	34.27 ± 4.36	2.507	0.014*
Pallidum R	40.05 ± 5.80	38.3 ± 5.59	1.309	0.195
Cerebellum L	47.65 ± 9.10	44.97 ± 8.30	1.314	0.193
Cerebellum R	48.71 ± 8.56	44.66 ± 8.74	1.998	0.052

*Statistically significant difference ($P < 0.05$).

et al. (20) characterized metabolic and perfusion abnormalities in patients with PD and reported significant reductions in cerebral perfusion within the parieto-occipital cortex, cuneus, precuneus, and middle frontal gyrus, whereas smaller decreases were noted in additional cortical areas (parietal, frontal, and temporal regions) and subcortical structures (thalamus and caudate nucleus). Syrimi et al. (21) investigated the perfusion basis of cognitive changes in PD patients without dementia and reported decreased CBF in the posterior parietal lobe, precuneus, and posterior cingulate gyrus. Our findings partially align with these findings, as most brain regions in PD patients exhibit a hypoperfusion pattern, with only the right pallidum showing mildly increased perfusion. However, some previous studies are somewhat inconsistent with the present study (22, 23). Wang et al. (22) reported reduced CBF in the frontal, parietal, and occipital lobes of PD patients, whereas CBF was increased in the thalamus, and chiasmatic nucleus. Similarly, Liu et al. (23) reported lower CBF in the frontal, parietal, and temporal lobes of PD patients than in those of healthy volunteers, whereas the CBF was greater in the bilateral hippocampus, red nucleus, right substantia nigra, thalamus, and most cerebellar regions. The discrepancy between our results and those of prior ASL studies may be due to differences between the subject groups. Liu's research focused on advanced PD patients (H&Y $\geq$ 3), whereas our subjects were early-stage PD patients. Advanced PD may exhibit compensatory phenomena in certain brain regions characterized by hypoperfusion in cortical regions and hyperperfusion in subcortical and cerebellar regions (23). The cerebellar cortex may play an important role in both motor and non-motor performance. For example, lobules I–V of the anterior lobe, adjacent parts of lobule VI and lobule VIII of the posterior lobe support sensorimotor function. Lobules VI and VII support cognitive functions (24, 25). The primary pathological hallmark of PD is the degeneration of nigrostriatal dopaminergic neurons, which disrupts the normal functioning of basal ganglia circuits. Dopaminergic neuronal loss modifies the microvascular environment and may affect cerebral blood perfusion. Neurodegeneration and reduced metabolism may subsequently disturb CBF (26). In PD patients, impaired motor and cognitive functions are influenced by the cerebello-thalamo-cortical (CTC) circuit and the striatal-thalamo-cortical (STC) circuit. Dopaminergic deficits may lead to the suppression of the function of these circuits, which can result in a decrease in metabolic demand and a reduction in CBF in relevant brain regions. Additionally, dopaminergic medications are commonly used in PD patients and their effects on cerebral blood flow warrant further investigation. Hershey et al. (27) concluded that levodopa had a minimal effect on cerebral blood flow perfusion in PD patients undergoing initial levodopa treatment. In contrast, Xiong et al.

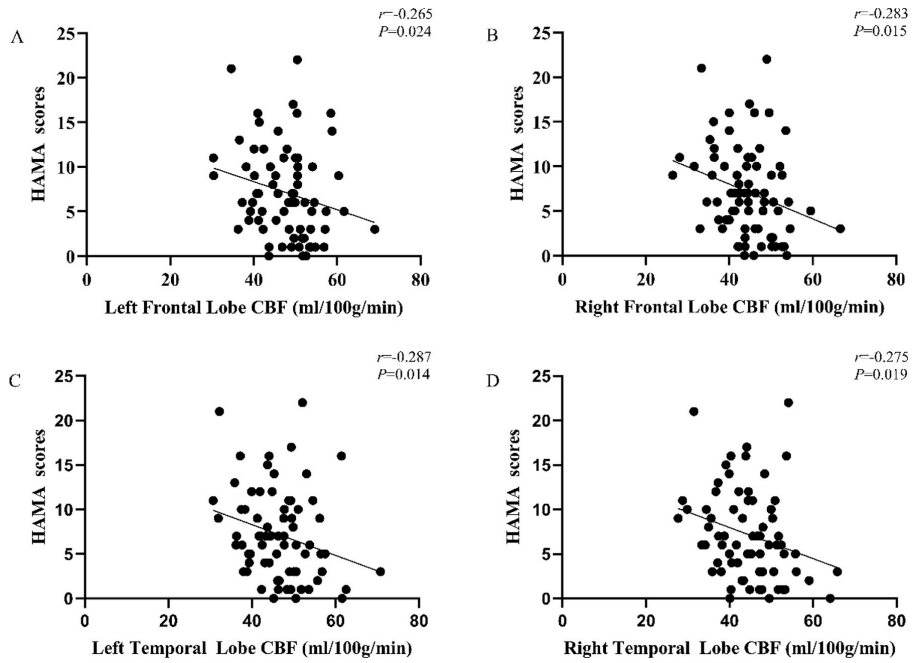

FIGURE 2
Correlation between CBF value and Hamilton Anxiety Scale (HAMA) score in PD patients. **(A)** The CBF values of left frontal lobe were negatively correlated with the HAMA scores ($r = -0.265$, $P = 0.024$); **(B)** the CBF values of right frontal lobe were negatively correlated with the HAMA scores ($r = -0.283$, $P = 0.015$); **(C)** the CBF values of left temporal lobe were negatively correlated with the HAMA scores ($r = -0.287$, $P = 0.014$); **(D)** the CBF values of right temporal lobe were negatively correlated with the HAMA scores ($r = -0.275$, $P = 0.019$).

(28) recently reported that levodopa could increase CBF values in corresponding brain regions by dilating intracranial arteries. In order to minimize the influence of medication on the results of this study, the PD subjects included in our study discontinued dopaminergic medications for 48 h prior to evaluation. Differences in the results of relevant clinical studies may also be related to variations in disease duration, disease staging, and drug administration between subjects.

In this study, we investigated the differences in perfusion between PD-A and PD-NA patients. Compared with the PD-NA group, the PD-A group presented reduced perfusion in the bilateral frontal lobes, temporal lobes, left putamen, and left pallidum. Additionally, correlation analyses revealed that perfusion values in the bilateral frontal and temporal lobes were negatively correlated with HAMA scores, which suggests that these regions may serve as key brain regions involved in the pathophysiology of anxiety-related mechanisms. The prefrontal cortex, a key brain region associated with emotional disorders, is crucial for functions such as decision-making, emotional regulation, and social cognition (29). A longitudinal study suggested that reduced prefrontal perfusion may underlie the progression of cognitive impairment during the early stages of PD (30). Zhang et al. (31) demonstrated that patients with PD-A exhibit significantly reduced levels of oxygenated hemoglobin in the left inferior frontal gyrus (IFG), which is negatively correlated with the severity of anxiety symptoms. The pathological mechanisms of anxiety in PD patients are closely associated with structural and functional abnormalities in the temporal lobe, particularly neurodegenerative changes and hemodynamic disturbances in the medial temporal lobe (e.g., hippocampus and amygdala) and lateral temporal regions (e.g., superior temporal gyrus and temporal pole). Structural magnetic resonance imaging (sMRI) studies have demonstrated that decreased gray matter volume (GMV) in the frontal and temporal lobes is associated with PD-A patients compared to PD patients without anxiety, indicating that these regions are involved in emotional regulation and cognitive control functions (32, 33). Deep brain stimulation (DBS) studies have demonstrated that the functional connectivity (FC) between specific brain regions (e.g., olfactory cortex- inferior frontal gyrus pars orbitalis connectivity and inferior temporal gyrus- posterior orbital gyrus connectivity) is significantly correlated with anxiety improvement rates in PD-A patients, which indicates that these regions play critical roles in both the generation and progression of anxiety symptoms (34, 35). Cortical structural and functional abnormalities in the frontal and temporal lobes may lead to changes in CBF in corresponding brain regions that are associated with cognitive and non-motor symptoms in PD patients. Vriend et al. (36) reported that the severity of anxiety symptoms in PD patients is associated with decreased availability of dopamine transporter proteins in the striatum. A positron emission tomography (PET) correlation study showed that changes in dopamine levels at different sites elicit distinct mood alterations. Specifically, reduced dopamine in the ventral striatum is correlated with the severity of apathy, whereas decreased dopamine level within the limbic system is often associated with the onset of anxiety (37). Anxiety symptoms in PD patients are negatively correlated with dopamine transporter density in the bilateral pallidum and the left putamen (38), which suggests that dysfunction in the pallidum and putamen may contribute to anxiety development through neurotransmitter imbalance or local blood flow changes. Anxiety may be associated

TABLE 4 Correlation analysis between the CBF values and HAMA scores in different brain regions.

Brain regions	HAMA scores	
	r-value	*P* value
Frontal L	−0.265	0.024*
Frontal R	−0.283	0.015*
Parietal L	−0.228	0.052
Parietal R	−0.222	0.059
Temporal L	−0.287	0.014*
Temporal R	−0.275	0.019*
Occipital L	−0.163	0.168
Occipital R	−0.197	0.095
Substantia Nigra L	−0.081	0.494
Substantia Nigra R	−0.173	0.144
Striatum L	−0.026	0.829
Striatum R	−0.067	0.575
Caudate L	0.045	0.708
Caudate R	0.005	0.969
Putamen L	−0.117	0.324
Putamen R	−0.102	0.389
Pallidum L	−0.161	0.174
Pallidum R	−0.094	0.427
Cerebellum L	−0.120	0.311
Cerebellum R	−0.208	0.077

*Statistically significant difference ($P < 0.05$).

with dysfunction in the limbic cortico-striato-thalamocortical circuits (6), which may exacerbate hypoperfusion in associated brain regions through neurotransmitter imbalance or changes in metabolic demands.

This study has several limitations. First, this study is limited by its cross-sectional, single-center design with a relatively small sample size. Therefore, validation of the current findings through a multicenter, large-sample longitudinal study is essential. Additionally, due to inherent limitations in the accuracy of scale assessments, only patients with early to mid-stage PD were included. Further investigations are warranted to determine the consistency of these findings in patients with advanced PD.

5 Conclusion

In this study, we applied ASL technology to investigate the differences in cerebral perfusion between PD patients and HCs, as well as between PD patients with and without anxiety. Our results demonstrated that PD patients exhibit significant alterations in cerebral perfusion, which are predominantly characterized by a hypoperfusion pattern. Specifically, the reduction in perfusion in the bilateral frontal and temporal lobes is correlated with the occurrence of anxiety in PD patients. These findings will help to provide a theoretical basis for the study of the pathophysiological mechanisms underlying anxiety in PD.

Data availability statement

The original contributions presented in the study are included in the article/supplementary material, further inquiries can be directed to the corresponding author.

Ethics statement

The studies involving humans were approved by Ethics Committee of China-Japan Friendship Hospital. The studies were conducted in accordance with the local legislation and institutional requirements. The participants provided their written informed consent to participate in this study. Written informed consent was obtained from the individual(s) for the publication of any potentially identifiable images or data included in this article.

Author contributions

LL: Data curation, Writing – original draft, Writing – review & editing. SS: Data curation, Resources, Writing – review & editing. YH: Data curation, Resources, Writing – review & editing. YL: Software, Resources, Writing – review & editing. LW: Methodology, Resources, Writing – review & editing. PZ: Supervision, Funding acquisition, Writing – review & editing.

Funding

The author(s) declare that financial support was received for the research and/or publication of this article. This study was supported by National High Level Hospital Clinical Research Funding (2023-NHLHCRF-YYPPLC-TJ-08).

Conflict of interest

The authors declare that the research was conducted in the absence of any commercial or financial relationships that could be construed as a potential conflict of interest.

Generative AI statement

The author(s) declare that no Gen AI was used in the creation of this manuscript.

Publisher's note

References

1. Aarsland D, Batzu L, Halliday GM, Geurtsen GJ, Ballard C, Ray Chaudhuri K, et al. Parkinson disease-associated cognitive impairment. *Nat Rev Dis Primers.* (2021) 7:47. doi: 10.1038/s41572-021-00280-3

2. Bloem BR, Okun MS, Klein C. Parkinson's disease. *Lancet.* (2021) 397:2284–303. doi: 10.1016/S0140-6736(21)00218-X

3. Liao H, Yi J, Cai S, Shen Q, Liu Q, Zhang L, et al. Changes in degree centrality of network nodes in different frequency bands in Parkinson's disease with depression and without depression. *Front Neurosci.* (2021) 15:638554. doi: 10.3389/fnins.2021.638554

4. Chen X, Chen L, Chen X, Ye Q, Cai G, Zeng Y. Assessing the impact of immersive virtual reality technology on the psychological recovery of patients with Parkinson's disease depression: study protocol of a randomized controlled trial. *Trials.* (2024) 25:715. doi: 10.1186/s13063-024-08552-5

5. Gulunay A, Cakmakli GY, Yon MI, Ulusoy EK, Karakoc M. Frequency of non-motor symptoms and their impact on the quality of life in patients with Parkinson's disease: a prospective descriptive case series. *Psychogeriatrics.* (2020) 20:206–11. doi: 10.1111/psyg.12489

6. Carey G, Görmezoglu M, de Jong JJA, Hofman PAM, Backes WH, Dujardin K, et al. Neuroimaging of anxiety in parkinson's disease: a systematic review. *Mov Disord.* (2021) 36:327–39. doi: 10.1002/mds.28404

7. Lindner T, Bolar DS, Achten E, Barkhof F, Bastos-Leite AJ, Detre JA, et al. Current state and guidance on arterial spin labeling perfusion MRI in clinical neuroimaging. *Magn Reson Med.* (2023) 89:2024–47. doi: 10.1002/mrm.29572

8. Joshi D, Prasad S, Saini J, Ingalhalikar M. Role of arterial spin labeling (ASL) images in Parkinson's disease (PD): a systematic review. *Acad Radiol.* (2023) 30:1695–708. doi: 10.1016/j.acra.2022.11.001

9. Jeong SH, Kim SH, Park CW, Lee HS, Lee PH, Kim YJ, et al. Differential implications of cerebral hypoperfusion and hyperperfusion in Parkinson's disease. *Mov Disord.* (2023) 38:1881–90. doi: 10.1002/mds.29565

10. Pelizzari L, Di Tella S, Rossetto F, Laganà MM, Bergsland N, Pirastru A, et al. Parietal perfusion alterations in Parkinson's disease patients without dementia. *Front Neurol.* (2020) 11:562. doi: 10.3389/fneur.2020.00562

11. Madhyastha TM, Askren MK, Boord P, Zhang J, Leverenz JB, Grabowski TJ. Cerebral perfusion and cortical thickness indicate cortical involvement in mild Parkinson's disease. *Mov Disord.* (2015) 30:1893–900. doi: 10.1002/mds.26128

12. Rane S, Koh N, Oakley J, Caso C, Zabetian CP, Cholerton B, et al. Arterial spin labeling detects perfusion patterns related to motor symptoms in Parkinson's disease. *Parkinsonism Relat Disord.* (2020) 76:21–8. doi: 10.1016/j.parkreldis.2020.05.014

13. Azamat S, Betul Arslan D, Erdogdu E, Kicik A, Cengiz S, Eryürek K, et al. Detection of visual and frontoparietal network perfusion deficits in Parkinson's disease dementia. *Eur J Radiol.* (2021) 144:109985. doi: 10.1016/j.ejrad.2021.109985

14. Valli M, Mihaescu A, Strafella AP. Imaging behavioural complications of Parkinson's disease. *Brain Imaging Behav.* (2019) 13:323–32. doi: 10.1007/s11682-017-9764-1

15. Togao O, Obara M, Yamashita K, Kikuchi K, Wada T, Murazaki H, et al. Arterial spin labeling-based MR angiography for cerebrovascular diseases: principles and clinical applications. *J Magn Reson Imaging.* (2024) 60:1305–24. doi: 10.1002/jmri.29119

16. Golay X, Ho ML. Multidelay ASL of the pediatric brain. *Br J Radiol.* (2022) 95:20220034. doi: 10.1259/bjr.20220034

17. Sollmann N, Hoffmann G, Schramm S, Reichert M, Hernandez Petzsche M, Strobel J, et al. Arterial spin labeling (ASL) in neuroradiological diagnostics - methodological overview and use cases. *Rofo.* (2024) 196:36–51. doi: 10.1055/a-2119-5574

18. Lin WC, Chen PC, Huang CC, Tsai NW, Chen HL, Wang HC, et al. Autonomic function impairment and brain perfusion deficit in Parkinson's disease. *Front Neurol.* (2017) 8:246. doi: 10.3389/fneur.2017.00246

19. Cheng L, Wu X, Guo R, Wang Y, Wang W, He P, et al. Discriminative pattern of reduced cerebral blood flow in Parkinson's disease and Parkinsonism-Plus syndrome: an ASL-MRI study. *BMC Med Imaging.* (2020) 20:78. doi: 10.1186/s12880-020-00479-y

20. Melzer TR, Watts R, MacAskill MR, Pearson JF, Rüeger S, Pitcher TL, et al. Arterial spin labelling reveals an abnormal cerebral perfusion pattern in Parkinson's disease. *Brain.* (2011) 134:845–55. doi: 10.1093/brain/awq377

21. Syrimi ZJ, Vojtisek L, Eliasova I, Viskova J, Svatkova A, Vanicek J, et al. Arterial spin labelling detects posterior cortical hypoperfusion in non-demented patients with Parkinson's disease. *J Neural Transm (Vienna).* (2017) 124:551–7. doi: 10.1007/s00702-017-1703-1

22. Wang X, Wang L, Wu Y, Lv X, Xu Y, Dou W, et al. Intracerebral hemodynamic abnormalities in patients with Parkinson's disease: Comparison between multi-delay arterial spin labelling and conventional single-delay arterial spin labelling. *Diagn Interv Imaging.* (2024) 105:281–91. doi: 10.1016/j.diii.2024.01.006

23. Liu Z, Zhang Y, Wang H, Xu D, You H, Zuo Z, et al. Altered cerebral perfusion and microstructure in advanced Parkinson's disease and their associations with clinical features. *Neurol Res.* (2022) 44:47–56. doi: 10.1080/01616412.2021.1954842

24. Stoodley CJ, Schmahmann JD. Functional topography in the human cerebellum: a meta-analysis of neuroimaging studies. *Neuroimage.* (2009) 44:489–501. doi: 10.1016/j.neuroimage.2008.08.039

25. Stoodley CJ, Schmahmann JD. Evidence for topographic organization in the cerebellum of motor control versus cognitive and affective processing. *Cortex.* (2010) 46:831–44. doi: 10.1016/j.cortex.2009.11.008

26. Paul G, Elabi OF. Microvascular changes in Parkinson's disease-focus on the neurovascular unit. *Front Aging Neurosci.* (2022) 14:853372. doi: 10.3389/fnagi.2022.853372

27. Hershey T, Black KJ, Carl JL, McGee-Minnich L, Snyder AZ, Perlmutter JS. Long term treatment and disease severity change brain responses to levodopa in Parkinson's disease. *J Neurol Neurosurg Psychiatry.* (2003) 74:844–51. doi: 10.1136/jnnp.74.7.844

28. Xiong Y, Ji L, He L, Chen L, Zhang X, Chen Z, et al. Effects of levodopa therapy on cerebral arteries and perfusion in parkinson's disease patients. *J Magn Reson Imaging.* (2022) 55:943–53. doi: 10.1002/jmri.27903

29. Zhang B, Qi S, Liu S, Liu X, Wei X, Ming D. Altered spontaneous neural activity in the precuneus, middle and superior frontal gyri, and hippocampus in college students with subclinical depression. *BMC Psychiatry.* (2021) 21:280. doi: 10.1186/s12888-021-03292-1

30. Wang J, Zhang W, Zhou Y, Jia J, Li Y, Liu K, et al. Altered prefrontal blood flow related with mild cognitive impairment in Parkinson's disease: a longitudinal study. *Front Aging Neurosci.* (2022) 14:896191. doi: 10.3389/fnagi.2022.896191

31. Zhang H, Shan AD, Wan CH, Cao XY, Yuan YS, Ye SY, et al. Transcutaneous auricular vagus nerve stimulation improves anxiety symptoms and cortical activity during verbal fluency task in Parkinson's disease with anxiety. *J Affect Disord.* (2024) 361:556–63. doi: 10.1016/j.jad.2024.06.083

32. Jia M, Yang S, Li S, Chen S, Wu L, Li J, et al. Early identification of Parkinson's disease with anxiety based on combined clinical and MRI features. *Front Aging Neurosci.* (2024) 16:1414855. doi: 10.3389/fnagi.2024.1414855

33. He G, Huang X, Sun H, Xing Y, Gu S, Ren J, et al. Gray matter volume alterations in de novo Parkinson's disease: a mediational role in the interplay between sleep quality and anxiety. *CNS Neurosci Ther.* (2024) 30:e14867. doi: 10.1111/cns.14867

34. Chang B, Mei J, Ni C, Xiong C, Chen P, Jiang M, et al. Development and validation of a prediction model for anxiety improvement after deep brain stimulation for Parkinson disease. *Brain Sci.* (2023) 13:219. doi: 10.3390/brainsci13020219

35. Chang B, Mei J, Ni C, Niu C. Functional connectivity and anxiety improvement after subthalamic nucleus deep brain stimulation in Parkinson's disease. *Clin Interv Aging.* (2023) 18:1437–45. doi: 10.2147/CIA.S422605

36. Vriend C, Boedhoe PS, Rutten S, Berendse HW, van der Werf YD, van den Heuvel OA, et al. smaller amygdala is associated with anxiety in Parkinson's disease: a combined FreeSurfer-VBM study. *J Neurol Neurosurg Psychiatry.* (2016) 87:493–500. doi: 10.1136/jnnp-2015-310383

37. Navailles S, Bioulac B, Gross C, De Deurwaerdère P. Serotonergic neurons mediate ectopic release of dopamine induced by L-DOPA in a rat model of Parkinson's disease. *Neurobiol Dis.* (2010) 38:136–43. doi: 10.1016/j.nbd.2010.01.012

38. Wen MC, Chan LL, Tan LC, Tan EK. Depression, anxiety, and apathy in Parkinson's disease: insights from neuroimaging studies. *Eur J Neurol.* (2016) 23:1001–19. doi: 10.1111/ene.13002

frontiers | Frontiers in Neurology

TYPE Original Research
PUBLISHED 24 July 2025
DOI 10.3389/fneur.2025.1554539

OPEN ACCESS

EDITED BY
Shuai Ren,
Affiliated Hospital of Nanjing University of Chinese Medicine, China

REVIEWED BY
Takeshi Hiu,
Nagasaki University, Japan
Nima Broomand Lomer,
University of Pennsylvania, United States

*CORRESPONDENCE
Jiansong Ji
✉ jjstcty@wmu.edu.cn

†These authors have contributed equally to this work

RECEIVED 02 January 2025
ACCEPTED 10 June 2025
PUBLISHED 24 July 2025

CITATION
Luo M, Lin G, Chen D, Chen W, Xia S, Hui J, Chen P, Chen M, Ye W and Ji J (2025) MRI-based multiregional radiomics for preoperative prediction of Ki-67 expression in meningiomas: a two-center study. *Front. Neurol.* 16:1554539. doi: 10.3389/fneur.2025.1554539

MRI-based multiregional radiomics for preoperative prediction of Ki-67 expression in meningiomas: a two-center study

Ming Luo[1,2†], Guihan Lin[1†], Duoning Chen[1,2], Weiyue Chen[1], Shuiwei Xia[1], Junguo Hui[1], Pengjun Chen[1], Minjiang Chen[1], Wangyang Ye[1,2] and Jiansong Ji[1*]

[1]Zhejiang Key Laboratory of Imaging and Interventional Medicine, Key Laboratory of Precision Medicine of Lishui City, Zhejiang Engineering Research Center of Interventional Medicine Engineering and Biotechnology, The Fifth Affiliated Hospital of Wenzhou Medical University, Lishui, China, [2]Department of Neurosurgery, The Fifth Affiliated Hospital of Wenzhou Medical University, Lishui, China

Background: High expression of Ki-67 in meningioma is significantly associated with higher histological grade and worse prognosis. The non-invasive and dynamic assessment of Ki-67 expression levels in meningiomas is of significant clinical importance and is urgently required. This study aimed to develop a predictive model for the Ki-67 index in meningioma based on preoperative magnetic resonance imaging (MRI).

Methods: This study included 196 patients from one center (internal cohort) and 92 patients from another center (external validation cohort). Meningioma had to have been pathologically confirmed for inclusion. The Ki-67 index was classified as high (Ki-67 ≥ 5%) and low (Ki-67 < 5%). The internal cohort was randomly assigned to training and validation sets at a 7:3 ratio. Radiomics features were selected from contrast-enhanced T1-weighted MRI using the least-absolute shrinkage and selection operator and random forest methods. Then, we constructed a predictive model based on the identified semantic and radiomics features, aiming to distinguish high and low Ki-67 expression. The model's performance was evaluated through internal cross-validation and validated in the external cohort.

Results: Among the clinical features, peritumoral edema (p = 0.001) and heterogeneous enhancement (p = 0.001) were independent predictors of the Ki-67 index in meningiomas. The radiomics model using a combined 8 mm volume of interest demonstrated optimal performance in the training (area under the receiver operating characteristic curve [AUC] = 0.883) and validation (AUC = 0.811) sets. A nomogram integrating clinical and radiomic features was constructed, achieving an AUC of 0.904 and enhancing the model's predictive accuracy for high Ki-67 expression.

Conclusion: This study developed clinical-radiomic models to non-invasively predict Ki-67 expression in meningioma and provided a novel preoperative strategy for assessing tumor proliferation.

KEYWORDS

meningiomas, radiomics, intratumoral, peritumoral, Ki-67

1 Introduction

Meningioma, rank as the second most common primary tumor of the central nervous system, accounting for approximately 39.7% of all intracranial tumors (1–3). Growth patterns differ among the different meningioma subtypes. Benign meningiomas have a five-year survival rate of 85.5% because of their slow growth. However, even after complete surgical resection, the five-year recurrence rate of benign meningiomas ranges from 7 to 25%, demonstrating a potential conversion to a high-grade subtype (2, 4). The resection status and histological grade significantly influence the management and prognosis of meningioma (5). The Ki-67 index is a critical biomarker of tumor proliferation in meningioma. Higher Ki-67 expression levels have been firmly established as a prognostic risk factor associated with unfavorable outcomes and increased risk of recurrence in affected individuals (6). Consequently, understanding the Ki-67 expression index in patients with meningioma is essential for managing risk stratification and clinical decision-making (7, 8).

In meningioma, the Ki-67 index is predominantly assessed in postoperative specimens using the immunohistochemical (IHC) technique. However, it's invasive nature and reliance on retrospective tissue sampling restrict its clinical utility for preoperative therapeutic planning and longitudinal progression monitoring. Many patients with meningioma require long-term follow-up, and since Ki-67 expression is a valuable prognostic marker, a tailored follow-up strategy is necessary to balance patient well-being with effective disease management, as traditional imaging methods struggle to assess tumor proliferation accurately (9). As a result, there is still an urgent clinical need for a readily accessible method for assessing the Ki-67 index. Previous studies indicate that preoperative magnetic resonance imaging (MRI) features, such as tumor heterogeneity on enhanced T1 images, apparent diffusion coefficient images, irregular tumor shape, and peritumoral brain edema, are valuable for evaluating the grade and histopathological characteristics of meningiomas (10–13). Radiomics incorporates automated calculation methods into precise quantitative analysis techniques, and applies them to imaging diagnosis, establishing classification models through analysis and screening (14). It streamlines the diagnostic process, minimizes the necessity for invasive procedures, and accelerates treatment planning. As radiomics technology evolves, its application in predicting the pathological grade and clinical prognosis of brain tumors has gained increasing recognition (12, 15). A focused systematic review and meta-analysis evaluated the performance of MRI-derived radiomics models for predicting Ki-67 status, demonstrating the growing interest and promising results in this area. These studies provide a foundation for our research, which leverages a multiregional radiomics approach based on MRI to preoperatively predict Ki-67 expression in meningiomas (16).

This study aimed to derive radiomics features from the peritumoral and intratumoral regions, providing valuable insights into predicting the Ki-67 expression status of patients with meningioma. To achieve this aim, we developed and validated a model that integrated clinical semantic features with radiomics features using machine learning algorithms, intending to non-invasively predict the Ki-67 expression status of these patients.

2 Materials and methods

2.1 Patients

This study initially enrolled 296 patients from the Fifth Affiliated Hospital of Wenzhou Medical University (Center 1) and 151 from the Sixth Affiliated Hospital of Wenzhou Medical University (Center 2) between November 2009 and May 2023. The meningioma diagnoses were confirmed through surgical pathology. The inclusion criteria were as follows: (1) patients who underwent MRI plain and enhanced scans 1 month before surgery, with complete clinical data; (2) patients who had not received radiotherapy or any other treatment before the MRI scan and had no history of head surgery; (3) patients with confirmed postoperative pathology and a determined Ki-67 index. The exclusion criteria were as follows: (1) patients with incomplete clinical data or poor MRI image quality; (2) patients lacking Ki-67 proliferation index results; (3) patients who had undergone radiation therapy and chemotherapy. Ultimately, 288 patients (196 from Center 1 and 92 from Center 2) were included in this study. The data from Center 1 were used for model development, while the data from Center 2 were used for external validation. Lesions from Center 1 were randomly assigned into training ($n = 136$) and validation ($n = 60$) sets at a ratio of 7:3. The detailed patient enrollment process is outlined in Figure 1. All study protocols and procedures were conducted in compliance with the Declaration of Helsinki. The requirement for informed consent from patients was waived due to the retrospective nature of this study.

2.2 MRI protocol

Preoperative MRI examinations were performed at two hospitals. At Center 1, MRI examinations were performed on a 3 T scanner (Magnetom Skyra; Siemens Healthineers, Erlangen, Germany). The imaging protocols included the following sequences: T1-weighted imaging (T1WI; repetition time [TR]/echo time [TE] = 2,540/9.4 ms, matrix size = 384 × 269), T2-weighted imaging (T2WI; TR/TE = 3,700/100 ms, matrix size = 448 × 311), fluid-attenuated inversion recovery (FLAIR; TR/TE = 7,000/86 ms, matrix size = 384 × 230), and contrast-enhanced T1WI (CE-T1WI; TR/TE = 149/3.4 ms, matrix size = 480 × 381). All images were taken with a field of view (FOV) of 230 × 230 mm, a slice thickness of 4 mm, and no interslice gaps. Contrast-enhanced MRI scans were performed following a bolus dose of 0.2 mL/kg of a contrast agent.

At Center 2, MRI examinations were performed using a 3 T scanner (Discovery 750; GE Healthcare, Chicago, IL, United States). The detailed protocol included the following sequences: T1WI (TR/TE = 2,200/11 ms, matrix = 320 × 256), T2WI (TR/TE = 3,900/87 ms, matrix = 512 × 384), FLAIR (TR/TE = 6,800/113 ms, matrix = 384 × 256), and CE-T1WI (TR/TE = 294/3.6 ms, matrix = 384 × 256). All images were taken with a FOV of 230–240 × 230–240 mm, a slice thickness of 5 mm, and a gap of 0.5 mm. The CE-T1WI images were acquired after a bolus dose of 0.2 mL/kg of a contrast agent.

2.3 Data collection

The patients' baseline clinical data were collected, including sex, age, headache history, history of epilepsy, history of malignancy,

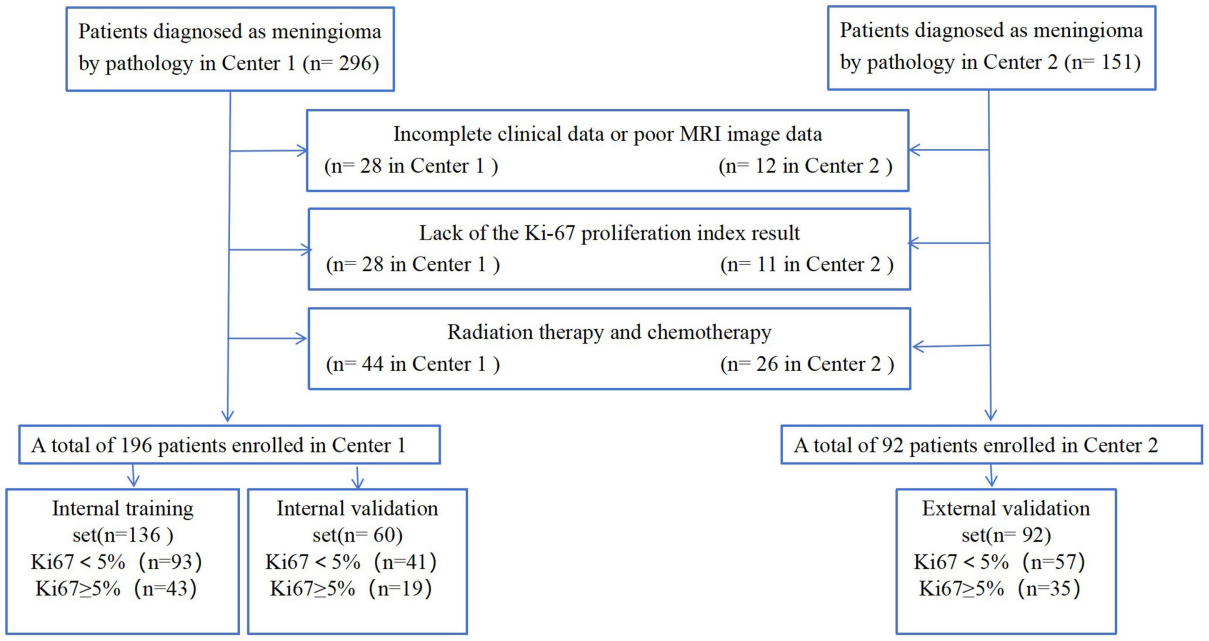

FIGURE 1
Flowchart of the patient selection criteria.

diabetes mellitus, hypertension, history of allergies, history of alcohol abuse, and history of tobacco addiction, along with their laboratory test results, including leucocyte, neutrophil, lymphocyte, and monocyte counts; plasma fibrinogen level; and serum albumin level. Two attending physicians with 5 and 11 years of neuroimaging diagnostic experience were assigned to analyze the images using a post-processing workstation. Their evaluations primarily focused on tumor location, morphology, peritumoral edema, necrosis, and enhancement characteristics. In cases where they disagreed on the interpretation results, consensus was achieved through collaborative consultation.

2.4 Pathological analysis

The surgical tissue samples were initially fixed in a 10% formaldehyde solution, then dehydrated and embedded in paraffin for IHC staining of Ki-67. Under microscopic examination, cells exhibiting dark brown granules within their nuclei were identified as Ki-67+. The Ki-67 index was determined by calculating the percentage of Ki-67 + cells relative to the total cell count. A Ki-67 index of <5% was classified as low expression, and a Ki-67 index of ≥5% was classified as high expression (11, 12, 17).

2.5 Image segmentation and feature extraction

Delineation of the tumor volume of interest (VOI) and segmentation for radiomics feature extraction were conducted using the Radcloud platform. Before extracting features, all images were resampled to a uniform voxel size of $1 \times 1 \times 1$ mm^3 using B-Spline interpolation, ensuring consistent slice thickness and preserving rotational symmetry. Additionally, to address differences in pixel brightness between two distinct MRI machines, the intensity of gray levels in all image datasets was normalized to a range of 0–255 after removing pixels with anomalous values. The normalization pipeline involves applying N4 bias field correction to address intensity inhomogeneities followed by Z-score normalization to standardize the data scale and mitigate feature variations caused by intensity differences. CE-T1WI images were used for delineation, carefully excluding non-brain tissues such as the skull. Image normalization was conducted before feature selection to minimize grayscale variability and individual differences. Initially, an attending physician with 5 years of neuroimaging diagnostic experience manually traced the tumor boundaries layer-by-layer to define the intratumoral VOI. The peritumoral VOI was generated using automated software, expanding at intervals of 2, 4, 6, 8, and 10 mm from the tumor outline. After delineation, another attending physician with 11 years of neuroimaging diagnostic experience reviewed the VOIs. In cases of inconsistency, the two physicians reached a consensus through discussion. Both were blinded to patient groupings. The extracted radiomic features included first-order statistics, morphological features, and texture features. First-order statistics quantitatively describe the intensity distribution of voxels within MRI images. Morphological features represent three-dimensional aspects, reflecting the shape and size of the lesion. Texture features assess heterogeneity within the VOI.

2.6 Feature filtering and machine learning classifier building

Radiomics features were screened using variance threshold, SelectKBest method, and least absolute shrinkage and selection

operator (LASSO) logistic regression. A threshold of 0.8 was set, and features with variance below this value were excluded. Using the SelectKBest method, features with a p-value < 0.05 were retained. The LASSO algorithm was used for cross-verification, identifying the optimal radiomics features characterized by non-zero regression coefficients. A series of distinct models were constructed using a Random Forest (RF) classifier: (1) a clinical semantic model; (2) a tumoral radiomics model; (3) five peritumoral radiomics models at incremental distances of 2, 4, 6, 8, and 10 mm from the tumor outline; (4) five combined radiomics models integrating intratumoral features with five widths of peritumoral features; and (5) a comprehensive model that merged clinical semantic and radiomics features. Clinical features with a p-value <0.05 in the univariate analyses were included in the multivariate logistic regression to screen for clinical risk factors and establish clinical models. Ultimately, a comprehensive model integrating clinical risk factors and the best radiomic features was constructed, and a nomogram was developed. An overview of the clinical and radiomic feature analyses is provided in Figure 2.

The Rad-score signature was generated using a Random Forest (RF) classifier to combine the radiomics features into a single signature. The RF classifier was trained using the filtered radiomics features and the corresponding patient outcomes (high or low Ki-67 expression). The resulting Rad-score signature was then used as an input feature in the nomogram model.

2.7 Statistical analysis

All statistical analyses were conducted using Python (version 3.7.6) and the R (version 4.3.1) statistical software. The Kolmogorov–Smirnov test was used to assess the normality of continuous variables. Student's t-test was used to compare normally distributed continuous variables, the Mann–Whitney U test was used to compare non-normally distributed continuous variables, and the chi-square test was used to compare categorical variables. The R packages used in this study included "glmnet" (for LASSO regression), "rms" (for logistic regression analysis and calibration curves), "rmda" (for decision curve analysis [DCA]), and "PredictABEL" (for calculating the net reclassification improvement [NRI] and integrated discrimination improvement [IDI]). Receiver operating characteristic (ROC) analysis was conducted using MedCalc, and the DeLong test was used to compare the differences in the area under the ROC curve (AUC) between models. All tests were two-tailed, and a $p < 0.05$ was considered statistically significant.

3 Results

3.1 Patient characteristics and clinical model construction

The clinical and radiological characteristics of the enrolled patients are summarized in Table 1. The training set comprised 136 patients and the validation set comprised 60 patients. In both the training and validation sets, the sex distribution, histories of chronic conditions (e.g., malignancy, diabetes, and hypertension), and laboratory research indices did not vary substantially between the high and low Ki-67 expression groups. However, in both cohorts, patients with peritumoral edema and those with heterogeneous enhancement were significantly more common in the high Ki-67 expression group (all $p < 0.05$).

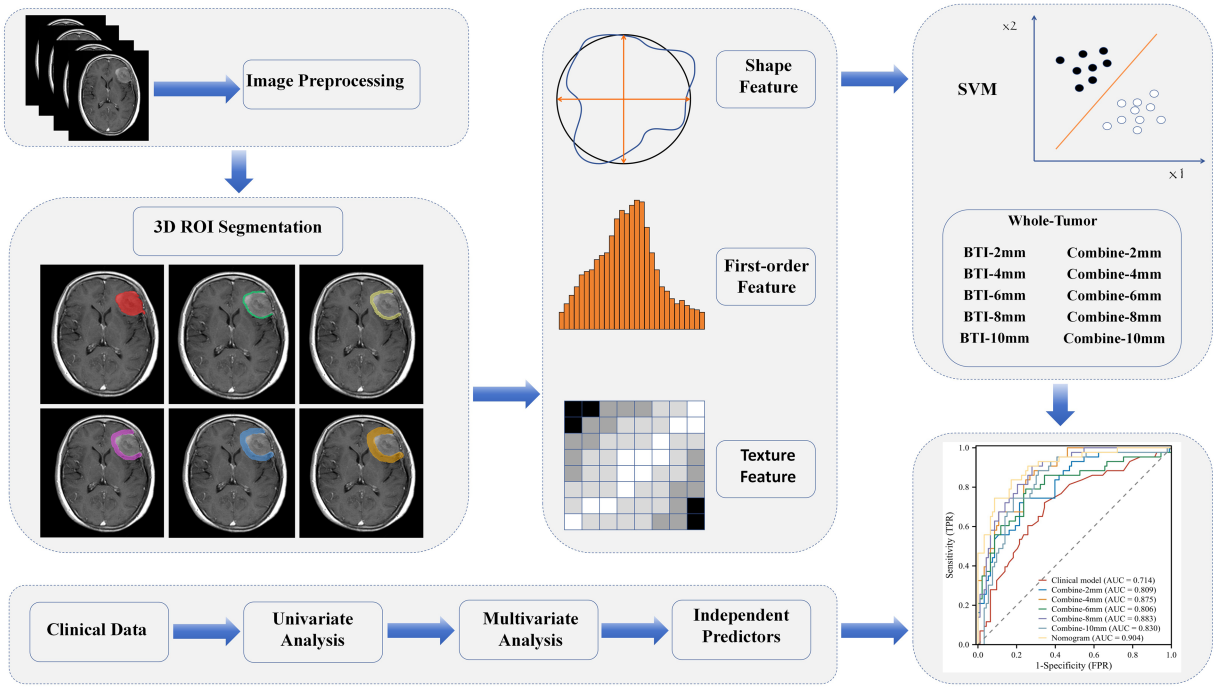

FIGURE 2
Study workflow.

TABLE 1 The clinical and radiological characteristics of the enrolled patients.

Characteristic	Internal training set		*p* value	Internal validation set		*p* value	External validation set		*p* value
	Ki-67 < 5% (*n* = 93)	Ki-67 ≥ 5% (*n* = 43)		Ki-67 < 5% (*n* = 41)	Ki-67 ≥ 5% (*n* = 19)		Ki-67 < 5% (*n* = 57)	Ki-67 ≥ 5% (*n* = 35)	
Age (year, mean ± SD)	55.30 ± 9.24	60.14 ± 10.64	0.008	52.44 ± 8.69	58.79 ± 13.44	0.032	59.18 ± 9.10	57.77 ± 8.75	0.468
Gender			0.130			0.839			0.170
Male	21 (22.6)	15 (34.9)		14 (34.1)	7 (36.8)		15 (26.3)	14 (40.0)	
Female	72 (77.4)	28 (65.1)		27 (65.9)	12 (63.2)		42 (73.7)	21 (60.0)	
History of Headache			0.566			0.872			0.597
Negative	58 (62.4)	29 (67.4)		25 (61.0)	12 (63.2)		42 (73.7)	24 (68.6)	
Positive	35 (37.6)	14 (32.6)		16 (39.0)	7 (36.8)		15 (26.3)	11 (31.4)	
History of epilepsy			0.243			0.663			0.864
Negative	83 (89.2)	41 (95.3)		35 (85.4)	17 (89.5)		55 (96.5)	34 (97.1)	
Positive	10 (10.8)	2 (4.7)		6 (14.6)	2 (10.5)		2 (3.5)	1 (2.9)	
History of malignancy			0.530			0.492			0.615
Negative	86 (92.5)	41 (95.3)		40 (97.6)	19 (100.0)		55 (96.5)	33 (94.3)	
Positive	7 (7.5)	2 (4.7)		1 (2.4)	0 (0.0)		2 (3.5)	2 (5.7)	
History of diabetes			0.511			0.558			0.255
Negative	89 (95.7)	40 (93.0)		37 (90.2)	18 (94.7)		53 (93.0)	30 (85.7)	
Positive	4 (4.3)	3 (7.0)		4 (9.8)	1 (5.3)		4 (7.0)	5 (14.3)	
History of hypertension			0.263			0.303			0.710
Negative	65 (69.9)	34 (79.1)		27 (65.9)	15 (78.9)		38 (66.7)	22 (62.9)	
Positive	28 (30.1)	9 (20.9)		14 (34.1)	4 (21.1)		19 (33.3)	13 (37.1)	
History of allergic			0.164			0.139			0.864
Negative	91 (97.8)	40 (93.0)		41 (100.0)	18 (94.7)		55 (96.5)	34 (97.1)	
Positive	2 (2.2)	3 (7.0)		0 (0.0)	1 (5.3)		2 (3.5)	1 (2.9)	
Alcohol abuse			0.859			0.079			0.466
Negative	88 (94.6)	41 (95.3)		35 (85.4)	19 (100.0)		53 (93.0)	31 (88.6)	
Positive	5 (5.4)	2 (4.7)		6 (14.6)	0 (0.0)		4 (7.0)	4 (11.4)	
Cigarette addict			0.383			0.150			0.716
Negative	81 (87.1)	35 (81.4)		33 (80.5)	18 (94.7)		32 (56.1)	21 (60.0)	
Positive	12 (12.9)	8 (18.6)		8 (19.5)	1 (5.3)		25 (43.9)	14 (40.0)	

(Continued)

10.3389/fneur.2025.1554539

TABLE 1 (Continued)

Characteristic	Internal training set		*p* value	Internal validation set		*p* value	External validation set		*p* value
	Ki-67 < 5% (*n* = 93)	Ki-67 ≥ 5% (*n* = 43)		Ki-67 < 5% (*n* = 41)	Ki-67 ≥ 5% (*n* = 19)		Ki-67 < 5% (*n* = 57)	Ki-67 ≥ 5% (*n* = 35)	
Tumor morphology			0.030			0.432			0.636
Regular	71 (76.3)	25 (58.1)		28 (68.3)	11 (57.9)		37 (64.9)	21 (60.0)	
Irregular	22 (23.7)	18 (41.9)		13 (31.7)	8 (42.1)		20 (35.1)	14 (40.0)	
Peritumoral edema			0.001			0.017			0.002
Negative	62 (66.7)	19 (44.2)		32 (78.0)	9 (47.4)		45 (78.9)	16 (45.7)	
Positive	31 (33.3)	24 (55.8)		9 (22.0)	10 (52.6)		12 (21.1)	19 (54.3)	
Necrosis			0.012			0.498			0.299
Negative	87 (93.5)	34 (79.1)		37 (90.2)	16 (84.2)		34 (59.6)	17 (48.6)	
Positive	6 (6.5)	9 (20.9)		4 (9.8)	3 (15.8)		23 (40.4)	18 (51.4)	
Enhancement			0.001			<0.001			0.001
Uniform	72 (77.4)	21 (48.8)		32 (78.0)	5 (26.3)		48 (84.2)	18 (51.4)	
Heterogeneous	21 (22.6)	22 (51.2)		9 (22.0)	14 (73.7)		9 (15.8)	17 (48.6)	
Tumor location			0.504			0.784			0.546
Convexity	55 (59.1)	29 (67.4)		28 (68.3)	13 (68.4)		37 (64.9)	26 (74.3)	
Skull base	37 (39.8)	13 (30.2)		12 (29.3)	6 (31.6)		9 (15.8)	8 (22.9)	
Ventricle	1 (1.1)	1 (2.3)		1 (2.4)	0 (0.0)		1 (1.8)	1 (2.9)	
Leucocyte count	6.49 ± 2.62	6.42 ± 3.37	0.891	7.39 ± 3.46	7.78 ± 4.15	0.709	8.172.67	7.92 ± 4.21	0.468
Neutrophil count	4.16 ± 2.60	4.25 ± 3.35	0.855	5.15 ± 3.40	5.58 ± 3.92	0.669	4.85 ± 2.41	4.52 ± 4.34	0.641
Lymphocyte count	1.76 ± 0.58	1.61 ± 0.53	0.168	1.59 ± 0.48	1.60 ± 0.55	0.976	1.61 ± 0.49	1.56 ± 0.48	0.581
Monocyte count	0.40 ± 0.17	0.37 ± 0.15	0.356	0.50 ± 0.27	0.46 ± 0.23	0.537	0.44 ± 0.22	0.43 ± 0.14	0.733
Plasma fibrinogen	2.91 ± 0.83	3.07 ± 0.84	0.320	3.47 ± 0.93	3.39 ± 0.75	0.748	3.28 ± 1.01	3.16 ± 0.91	0.544
Serum-albumin	40.66 ± 3.94	38.92 ± 3.48	0.014	40.44 ± 3.45	39.70 ± 3.93	0.462	35.98 ± 9.10	57.77 ± 8.75	0.067

P represents the difference in each clinicopathological variable between the high and low Ki-67 expression groups. The chi-square test was used to compare the difference in categorical variables (all variables except age), while a Student's t-test was used to compare the difference in age.

10.3389/fneur.2025.1554539

TABLE 2 Univariate and multivariate analyses for predicting Ki-67 expression.

Features	Univariate logistic	*p*	Multivariate logistic	*p*
	OR (95% CI)		OR (95% CI)	
Age	1.052 (1.012–1.094)	0.010		
Gender	1.837 (0.831–4.061)	0.133		
History of Headache	0.800 (0.373–1.717)	0.567		
History of epilepsy	0.405 (0.085–1.934)	0.257		
History of malignancy	0.599 (0.119–3.013)	0.534		
History of diabetes	1.669 (0.357–7.806)	0.515		
History of hypertension	0.615 (0.261–1.449)	0.266		
History of allergic	3.412 (0.549–21.219)	0.188		
Alcohol abuse	0.858 (0.160–4.612)	0.859		
Cigarette addict	1.543 (0.580–4.105)	0.385		
Tumor morphology	2.324 (1.074–5.028)	0.032		
Peritumoral edema	3.733 (1.744–7.991)	0.001	2.943 (1.329–6.516)	0.008
Necrosis	3.838 (1.269–11.605)	0.017		
Enhancement	3.592 (11.662–7.762)	0.001	2.722 (1.211–6.120)	0.015
Tumor location	0.765 (0.374–1.562)	0.462		
Leucocyte count	0.991 (0.871–1.127)	0.890		
Neutrophil count	1.012 (0.893–1.147)	0.854		
Lymphocyte count	0.626 (0.321–1.220)	0.169		
Monocyte count	0.312 (0.026–3.714)	0.357		
Plasma fibrinogen	1.243 (0.810–1.907)	0.320		
Serum-albumin	0.885 (0.800–0.980)	0.018		

OR, odds ratio; CI, Confidence interval.

16 clinical features and 5 radiological features were utilized to construct the clinical model. Among the clinical parameters, peritumoral edema (odds ratio [OR] = 3.733, 95% confidence interval [CI] = 1.744–7.991, $p = 0.001$) and heterogeneous enhancement (OR = 3.592, 95% CI = 11.662–7.762, $p = 0.001$) were identified as significant predictors of high Ki-67 expression (Table 2). These results suggested that patients presenting with these radiological features were more likely to have a higher Ki-67 index.

3.2 Model construction

The ROC curves for the tumoral and peritumoral radiomics models are shown in Figure 3, illustrating the diagnostic performance of the model in distinguishing patients with high and low Ki-67 expression. Multivariate logistic analysis showed that peritumoral edema, heterogeneous enhancement, and 8 mm-based radiomics signature were independent predictors of high Ki-67 expression. These predictors were incorporated into a comprehensive model that merged clinical semantic and radiomics features. The radiomics signature was derived from the combined-8 mm (the whole tumor plus 8 mm peritumoral area) model, which demonstrated superior performance compared to other peritumoral widths (2, 4, 6, 10 mm). Then, these independent predictors were incorporated into a model and presented as a nomogram. The calibration curves and DCA for the diagnostic nomogram are shown in Figure 4. These analyses thoroughly assessed the model's predictive performance and diagnostic accuracy.

3.3 Comparison of performance among VOIs

In total, 1,688 radiomic features were extracted from each tumor and its surrounding tissues. The VOIs included intratumoral and peritumoral VOIs expanding 2, 4, 6, 8, and 10 mm from the tumor outline and their combinations. The ROC curve was used to evaluate the sensitivity and specificity of the nomogram (Figure 4). Among the radiomic-based predictive models for Ki-67 expression, the one based on combined-8 mm radiomic features demonstrated superior diagnostic performance (Tables 3, 4). This model was derived from features selected using LASSO and classified using a random forest algorithm (Figure 5). In the training set, its AUC, accuracy, sensitivity, and specificity for high Ki-67 expression were 0.883, 77.05, 90.7, and 72.04%, respectively. However, they were generally lower in the validation set (AUC = 0.820, accuracy = 80.73%, sensitivity = 63.16%, and specificity = 90.68%). After extensive analysis, combined-8 mm was determined to be the most predictive radiomic model, demonstrating its potential for clinical application in diagnosing meningiomas.

3.4 The diagnostic performance of the prediction models

In the ROC analysis, the radiomics-based model outperformed the clinical parameter-based model for predicting Ki-67 expression in

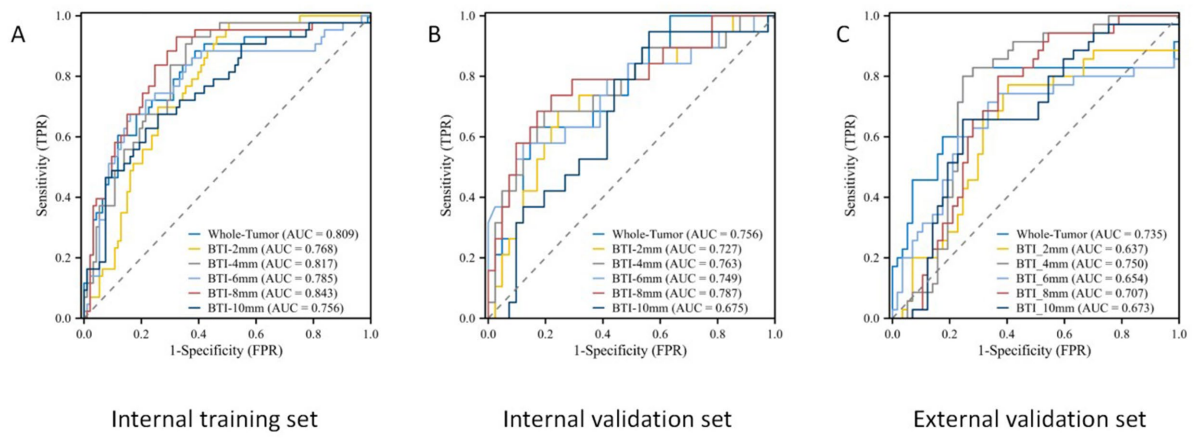

FIGURE 3
The ROC curves for the tumoral and peritumoral radiomics model. ROC curves in the **(A)** internal training set, **(B)** internal validation set, and **(C)** external validation set.

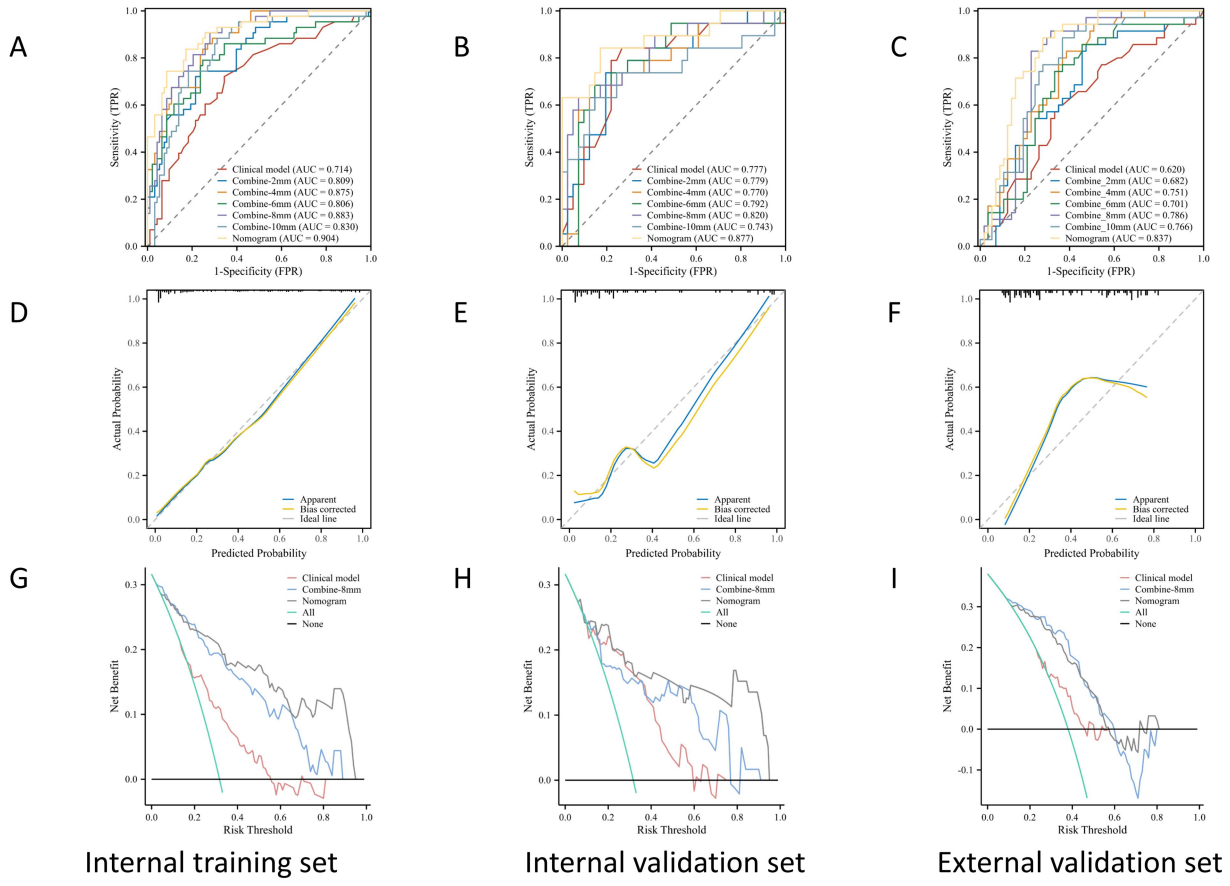

FIGURE 4
The ROC, calibration, and DCA curves. ROC curves in the **(A)** internal training set, **(B)** internal validation set, and **(C)** the external validation set. Calibration curves in the **(D)** internal training set, **(E)** internal validation set, and **(F)** external validation set. The prediction results were consistent with the diagonal line, indicating the accurate prediction results. The DCA curves for the diagnostic nomogram in the **(G)** internal training set, **(H)** internal validation set, and **(I)** external validation set.

both the training and validation sets. The clinical-radiomic model merged clinical predictors (peritumoral edema, heterogeneous enhancement) with the combined-8 mm radiomics features. Optimal predictive accuracy was achieved when the clinical and radiomic models were integrated, resulting in a clinical-radiomic model. In the training set, the integrated model had an AUC of 0.904, accuracy of

TABLE 3 Predictive model performance for Ki-67 expression in the intratumoral and peritumoral VOI.

Model	Training set				Internal validation set				External validation set			
	AUC (95% CI)	SEN (%)	SPE (%)	ACC (%)	AUC (95% CI)	SEN (%)	SPE (%)	ACC (%)	AUC (95% CI)	SEN (%)	SPE (%)	ACC (%)
Whole-Tumor	0.809 (0.761–0.857)	88.37	61.29	67.87	0.756 (0.700–0.812)	63.16	85.37	76.82	0.735 (0.673–0.797)	74.38	75.21	74.89
BTI-2 mm	0.768 (0.716–0.820)	97.67	49.46	58.61	0.727 (0.665–0.789)	68.42	75.61	73.17	0.637 (0.559–0.715)	77.14	59.65	65.28
BTI-4 mm	0.817 (0.771–0.863)	93.02	62.37	69.62	0.763 (0.711–0.815)	68.42	80.49	76.23	0.750 (0.694–0.806)	78.49	75.44	76.57
BTI-6 mm	0.785 (0.735–0.835)	67.44	81.87	76.68	0.749 (0.693–0.805)	57.89	87.80	75.45	0.654 (0.584–0.724)	71.43	66.67	68.40
BTI-8 mm	0.843 (0.801–0.885)	93.03	67.74	74.11	0.787 (0.739–0.835)	73.68	78.05	76.61	0.707 (0.649–0.765)	79.98	63.16	68.65
BTI-10 mm	0.756 (0.700–0.812)	67.44	74.19	71.91	0.675 (0.605–0.745)	94.74	43.90	52.89	0.673 (0.607–0.739)	65.71	75.44	71.42

AUC, area under the curve.

TABLE 4 Predictive model performance of the clinical, combined VOI, and clinical-radiomic models.

Model	Training set				Internal validation set				External validation set			
	AUC (95% CI)	SEN (%)	SPE (%)	ACC (%)	AUC (95% CI)	SEN (%)	SPE (%)	ACC (%)	AUC (95% CI)	SEN (%)	SPE (%)	ACC (%)
Clinical model	0.714 (0.648–0.780)	72.09	65.59	67.51	0.777 (0.715–0.839)	84.21	73.17	76.34	0.620 (0.535–0.705)	60.02	64.91	62.96
Combine-2 mm	0.809 (0.761–0.857)	74.42	76.34	75.72	0.779 (0.719–0.839)	73.68	80.49	78.20	0.682 (0.606–0.758)	85.71	52.63	61.69
Combine-4 mm	0.875 (0.839–0.911)	88.37	70.97	75.68	0.770 (0.706–0.834)	63.17	87.80	78.15	0.751 (0.689–0.813)	82.86	61.40	68.11
Combine-6 mm	0.806 (0.754–0.858)	79.07	75.27	76.43	0.792 (0.734–0.850)	68.42	85.37	79.16	0.701 (0.629–0.773)	74.29	66.67	69.38
Combine-8 mm	0.883 (0.851–0.915)	90.70	72.04	77.05	0.820 (0.770–0.870)	63.16	92.68	80.73	0.786 (0.734–0.838)	82.86	75.16	77.91
Combine-10 mm	0.830 (0.772–0.888)	88.37	68.82	74.00	0.743 (0.671–0.815)	73.68	75.61	74.99	0.766 (0.700–0.832)	88.54	63.16	70.89
Nomogram	0.904 (0.876–0.932)	83.72	84.95	84.56	0.877 (0.843–0.911)	84.21	82.93	83.33	0.837 (0.793–0.881)	88.57	71.31	77.02

AUC, area under the curve.

10.3389/fneur.2025.1554539

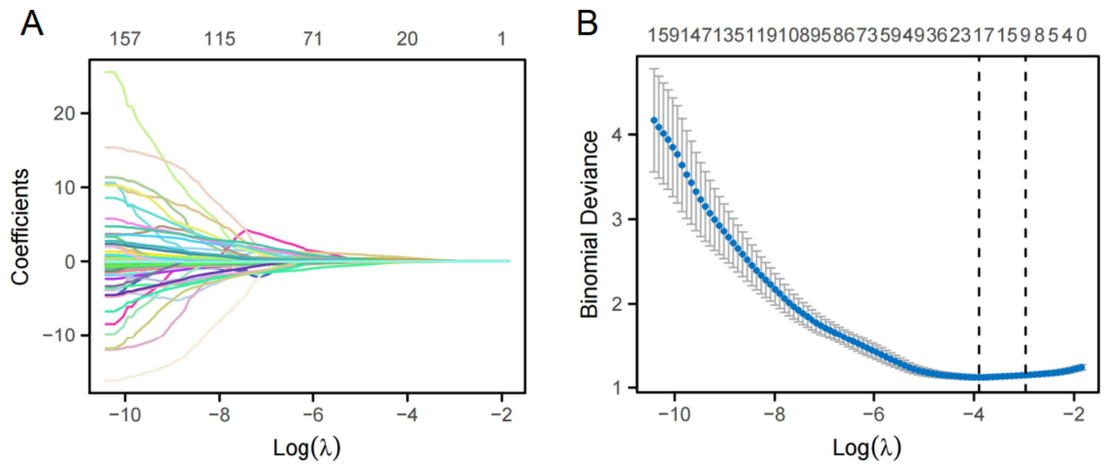

FIGURE 5
LASSO regression was used for feature selection. **(A)** LASSO coefficient selection: The optimal value of λ and the corresponding coefficients were identified using the coefficient plot. **(B)** LASSO variable trajectories: The feature importance plot was used to identify the most important features and the optimal value of λ.

84.56%, sensitivity of 83.72%, and specificity of 84.95%. In the validation set, its performance was slightly lower but still robust, with an AUC of 0.877, accuracy of 83.33%, sensitivity of 84.21%, and specificity of 82.93%. Furthermore, in the external validation set, it maintained a high level of performance, with an AUC of 0.837, accuracy of 77.02%, sensitivity of 88.57%, and specificity of 71.31% (Table 4). These results indicate that the diagnostic model has better discrimination ability than the single radiomics-based and clinical parameter-based models. Additionally, the calibration curve for the nomogram, used for preoperative prediction of high Ki-67 expression in patients with meningioma, was highly concordant with actual outcomes, indicating that this prediction model has good reliability for preoperatively assessing Ki-67 expression.

3.5 Evaluation of the diagnostic nomogram through DCA

DCA was used to evaluate the diagnostic performance of the diagnostic nomogram and each single predictor model (Figure 6). The decision curve indicates the net benefit of patients when the intervention is performed under various threshold probabilities. The net benefit of the diagnostic nomogram model was the highest when the prediction model threshold probabilities were 0.21 ~ 0.66 (training set) and 0.58 ~ 1.09 (validation set), followed by the single radiomics-based model. Notably, the diagnostic nomogram model consistently provided a greater net benefit than the single predictor models, including the radiomics-based model. The example flowchart of prediction is shown in Supplementary Figure 1. The DCA and flowchart provided insights into the diagnostic performance of the prediction model.

4 Discussion

Our study revealed that meningioma with an elevated Ki-67 index was associated with an increased risk of peritumoral edema and heterogeneous enhancement, which are recognized indicators of brain invasion. We also demonstrated that VOI radiomics models based on CE-T1WI images, including intra- and peri-tumoral regions, can improve the accuracy in predicting Ki-67 expression levels in meningiomas. Then, we assessed the predictive performance of radiomics models with different VOI ranges for the peritumoral region. Among the examined radiomics feature ranges, the 8 mm was identified as the optimal peritumoral region. Then, we developed a combined clinical-radiomics model, integrating radiomics features from the intratumoral and 8 mm peritumoral regions. This integrated model demonstrated superior predictive efficacy. Ultimately, we developed an integrated clinico-radiomic model incorporating peritumoral edema, enhancement pattern, and tumor-peritumoral 8 mm radiomic features. This integrated model outperformed the individual radiomic and clinical models in terms of AUC, accuracy, and predictive efficacy for Ki-67 expression. The DCA and flowchart provide valuable insights into the diagnostic performance of the prediction model, enabling clinicians to make well-informed decisions regarding patient management strategies.

The Ki-67 expression is considered an indicator of the biological behavior of meningioma (18). Preoperative evaluation of Ki-67 expression can provide valuable supplementary information for clinical decision-making (19, 20). Systematic reviews have underscored the significance of accurately predicting Ki-67 status using radiological methods. For instance, a systematic review by Helal et al. (21) synthesized evidence on the accuracy and prognostic value of radiological predictions of Ki-67 in meningiomas, highlighting their potential to inform treatment strategies. Similarly, Broomand Lomer et al. (16) conducted a meta-analysis specifically on MRI-derived radiomics models, demonstrating their effectiveness in predicting Ki-67 index status. A higher Ki-67 index is generally associated with a more aggressive tumor phenotype and potentially poorer outcomes. Therefore, these findings suggest that patients presenting with these radiological features may require more intensive monitoring and treatment. However, since the Ki-67 assessment is susceptible to tumor

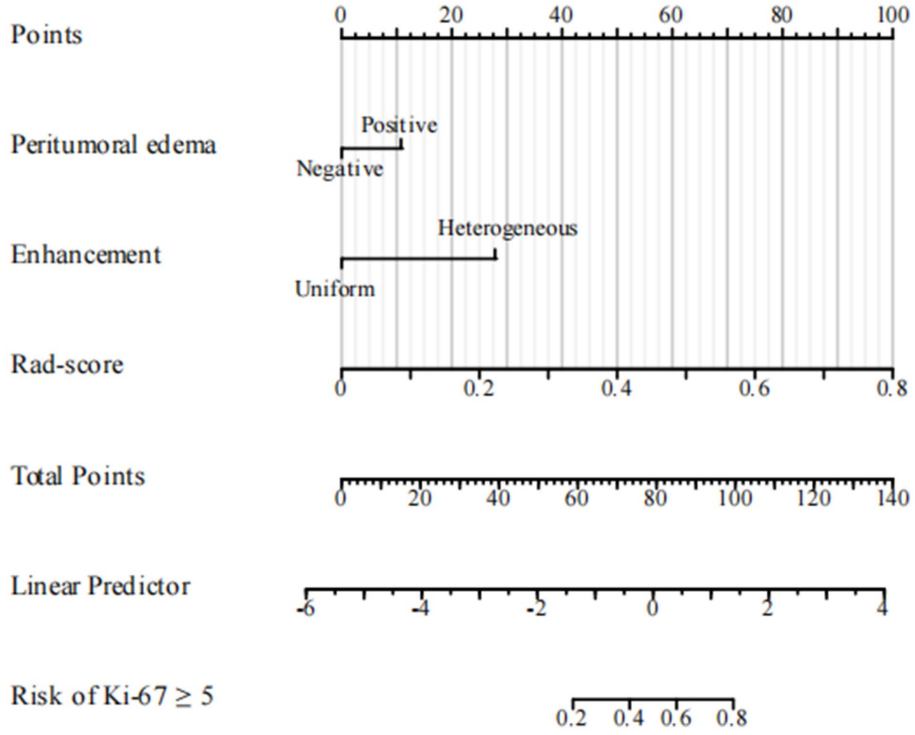

FIGURE 6
Diagnostic nomogram. The nomogram was constructed from peritumoral edema and contrast enhancement.

heterogeneity, it is essential to evaluate the entire specimen, not only the core biopsy (22, 23).

MRI-based radiomics models have been reported to predict Ki-67 expression levels in meningiomas. Khanna et al. (12) predicted high Ki-67 expression in World Health Organization grade I meningioma using features extracted from multiple MRI sequences, with an AUC of 0.84 in their testing set. In Zhao's study (11), the AUC for predicting the Ki-67 index in meningiomas was 0.837 in the internal validation set and 0.700 in the external validation set. These studies suggest that radiomics feature-based models can effectively predict both the grade of meningioma and the Ki-67 index. Both studies were based on intratumoral models. Recent advancements in MRI-based radiomics has demonstrated potential in preoperative prediction of meningioma Ki-67 expression. Li et al. (24) created machine learning models using multiparametric MRI to evaluate meningioma malignancy by WHO grading and prediction of Ki-67 index with AUCs of 0.92 and 0.87 in multicenter validation. Their study recognized the complementarity of clinical features and radiomics in stratification of tumor aggressiveness. Based on this, Duan et al. (25) developed a deep transfer learning radiomics nomogram that integrates multiparametric MRI features to make predictions of Ki-67 proliferation status with an AUC of 0.84 in external validation and highlights the technical advantages of combining domain-adaptive deep learning with traditional radiomics. Ouyang et al. (26) further advanced this field by constructing a contrast-enhanced MRI radiomics nomogram for Ki-67 prediction in two independent centers (AUC: 0.86), i.e., determining the clinical utility of texture features of arterial and venous phase images. While these studies together emphasize the diagnostic value of MRI radiomics in meningioma proliferation assessment, they are primarily founded on single-region tumor analysis. Previous research has indicated that peritumoral radiomics features offer greater insight into tumor heterogeneity. Our research builds upon previous studies by incorporating both intratumoral and peritumoral radiomics features into our predictive model. By integrating radiomics characteristics from the tumor core and its periphery, we aim to provide a comprehensive and encompassing assessment of the meningioma grade and Ki-67 index.

However, the peritumoral range for the VOI used in past radiological studies remains controversial. One study extracted imaging characteristics from various interfaces, including tumors and the brain (at distances of 1, 2, 3, 4, and 5 mm), establishing models that demonstrated superior generalization performance compared to current methods (27). Another study analyzed MRI radiomic features from intratumoral and peritumoral regions (at 5, 10, 15, and 20 mm distances) in a cohort of 92 patients with glioma. It found that models based on features from the 10 and 20 mm ranges were more effective at predicting Ki-67 levels and the expression of tumor protein p53 (TP53) (28). A further study involving 719 patients with meningioma revealed that including 4 mm peritumoral MRI radiomic features in the intratumoral model significantly improved diagnostic performance for meningioma invasion (29).

Evidently, a consistent criterion for the peritumoral boundary remains ambiguous. Therefore, we developed multiple VOI radiomics models with different peritumoral ranges to explore the distinct regions of highly aggressive meningioma. Considering that the actual tumor boundary extends beyond the image, we established five distinct peritumoral VOI ranges, extending the intratumoral VOI by 2, 4, 6, 8, and 10 mm. The VOI delineation methods for tumor and peritumoral regions with variable margins are illustrated in

Supplementary Figure 2. Our results showed that the AUC for the 8 mm peritumoral region was 0.843 in the training set and 0.787 in the validation set. This region was identified as the most effective VOI, designating the 8 mm peritumoral area as the optimal selection. The radiomics model based on the 8 mm VOI encompassed the most predictive radiomics features.

Combining radiomics features from various categories resulted in the most robust predictive performance. While interpreting the complex relationship between pathophysiological processes and tumor structural features is challenging, tumors with greater structural heterogeneity are often more aggressive. Increased heterogeneity in meningiomas indicates a higher probability of infiltration into adjacent tissues. Greater heterogeneity is manifested in MRI as increased grayscale inhomogeneity and elevated image complexity. These features may indicate aggressive tumor behavior, such as breaching the tumor capsule and invading surrounding non-neoplastic tissues, which leads to increased intra- and peri-tumoral heterogeneity and reflects the underlying oncobiological and heterogeneity characteristics (30).

Integrating intratumoral and peritumoral radiological features offers superior advantages over relying exclusively on single-tumor radiomics, emphasizing the importance of combining intratumoral and peritumoral characteristics to enhance clinical insights (31). Further analysis revealed that the combined intratumoral and peritumoral 8 mm model achieved an AUC of 0.883 in the validation set, outperforming both the intratumoral model (AUC = 0.809) and the peritumoral 8 mm model (AUC = 0.843). This finding is consistent with Beig et al. (32), who demonstrated that lung adenocarcinomas and granulomas could be more effectively differentiated by combining radiomics features from within and around pulmonary nodules. With an AUC of 0.80, this integrated approach outperformed the single internal nodule model (AUC = 0.75), further emphasizing the importance of the peritumoral microenvironment in oncological research. These results highlight the need to consider the entire tumor environment for more accurate diagnostic and prognostic evaluations.

Regarding clinical factors, previous studies have demonstrated that characteristics such as tumor volume, tumor margin, and tumor-brain interface correlate with Ki-67 expression in meningioma (33), which is consistent with our findings. Pathological grade is a crucial prognostic factor in meningiomas (34), and there is a close correlation between grade and Ki-67 expression. High-grade pathology implies higher recurrence and worse prognosis. Existing studies have confirmed a significant correlation between Ki-67 expression and the invasion of pial/cortical and arachnoidal structures (35), and the Ki-67 proliferation index also serves as a predictor of recurrence timing (36). Our clinical model demonstrated only moderate predictive performance, suggesting that basic clinicopathological factors alone may not be sufficient.

Meticulous segmentation enables a thorough examination of the heterogeneity across multiple radiographic VOIs. Furthermore, there is an increased focus on the predictive value of Ki-67 expression in meningiomas, recognizing its established role as a proliferation marker closely associated with tumor aggressiveness and recurrence potential. By targeting this critical biomarker, the goal is not only identifying the optimal peritumoral VOI but also refining risk stratification strategies for patients. This dual focus highlights the contribution of our study in advancing both the scientific understanding and clinical management of meningioma.

Nonetheless, our study had several limitations. Firstly, its retrospective design and small sample size limited its power, highlighting the need for prospective studies with large sample sizes to verify our findings. Secondly, specific indicators of the tumor microenvironment, such as radiological features of immune cells, were not included in the developed model. Their inclusion could have provided a more comprehensive understanding of the relationship between radiological features and the peritumoral microenvironment. One of the major limitations of our research is the inhomogeneity of WHO grade data throughout the cohort. WHO grading data were not consistently available for all cases in our dataset. The WHO grading system represents a valuable pathological parameter with a well-documented association with Ki-67 expression, and its omission can restrict the generalizability and interpretability of our results. Future research including WHO grade data will be necessary for a more thorough assessment of the association between imaging characteristics and tumor biology.

5 Conclusion

In summary, this study developed innovative clinical-radiomic models to predict Ki-67 expression in meningiomas before surgery. By integrating radiomic features with clinical data, these models offer a novel non-invasive strategy for assessing tumor status, potentially enhancing the accuracy of preoperative evaluations and aiding in developing personalized treatment plans for patients with meningioma.

Data availability statement

The raw data supporting the conclusions of this article will be made available by the authors, without undue reservation.

Ethics statement

The studies involving humans were approved by Ethics Committee of Lishui Central Hospital (Approval number: 495-2023). The studies were conducted in accordance with the local legislation and institutional requirements. Written informed consent for participation was not required from the participants or the participants' legal guardians/next of kin in accordance with the national legislation and institutional requirements.

Author contributions

ML: Conceptualization, Writing – original draft. GL: Conceptualization, Writing – original draft. DC: Data curation, Formal analysis, Writing – review & editing. WC: Formal analysis, Writing – review & editing. SX: Software, Writing – review & editing. JH: Software, Writing – review & editing. PC: Software, Writing – review & editing. MC: Conceptualization, Supervision, Writing – review & editing. WY: Data curation, Writing – review & editing. JJ: Supervision, Writing – review & editing.

Funding

The author(s) declare that financial support was received for the research and/or publication of this article. This work was supported by the the medical and health research project of Zhejiang province (Project No. 2025KY484).

Conflict of interest

The authors declare that the research was conducted in the absence of any commercial or financial relationships that could be construed as a potential conflict of interest.

Generative AI statement

The author(s) declare that Gen AI was used in the creation of this manuscript. During the preparation of this work the authors used chatGPT in order to improve language and readability. After using this tool, the authors reviewed and edited the content as needed and take full responsibility for the content of the publication.

Publisher's note

All claims expressed in this article are solely those of the authors and do not necessarily represent those of their affiliated organizations, or those of the publisher, the editors and the reviewers. Any product that may be evaluated in this article, or claim that may be made by its manufacturer, is not guaranteed or endorsed by the publisher.

Supplementary material

The Supplementary material for this article can be found online at: https://www.frontiersin.org/articles/10.3389/fneur.2025.1554539/full#supplementary-material

References

1. Simpson D. The recurrence of intracranial meningiomas after surgical treatment. *J Neurol Neurosurg Psychiatry*. (1957) 20:22–39. doi: 10.1136/jnnp.20.1.22

2. Domingues PH, Sousa P, Otero Á, Gonçalves JM, Ruiz L, de Oliveira C, et al. Proposal for a new risk stratification classification for meningioma based on patient age, WHO tumor grade, size, localization, and karyotype. *Neuro-Oncology*. (2014) 16:735–47. doi: 10.1093/neuonc/not325

3. Ostrom QT, Price M, Neff C, Cioffi G, Waite KA, Kruchko C, et al. CBTRUS statistical report: primary brain and other central nervous system tumors diagnosed in the United States in 2015-2019. *Neuro-Oncology*. (2022) 24:v1–v95. doi: 10.1093/neuonc/noac202

4. Narla S, Uppin MS, Saradhi MV, Sahu BP, Purohit AK, Sundaram C. Assessment of expression of epidermal growth factor receptor and p53 in meningiomas. *Neurol India*. (2014) 62:37–41. doi: 10.4103/0028-3886.128276

5. Louis DN, Perry A, Wesseling P, Brat DJ, Cree IA, Figarella-Branger D, et al. The 2021 WHO classification of tumors of the central nervous system: a summary. *Neuro-Oncology*. (2021) 23:1231–51. doi: 10.1093/neuonc/noab106

6. Baumgarten P, Gessler F, Schittenhelm J, Skardelly M, Tews DS, Senft C, et al. Brain invasion in otherwise benign meningiomas does not predict tumor recurrence. *Acta Neuropathol*. (2016) 132:479–81. doi: 10.1007/s00401-016-1598-1

7. Telugu RB, Chowhan AK, Rukmangadha N, Patnayak R, Phaneendra BV, Prasad BC, et al. Histopathological and immunohistochemical evaluation of meningiomas with reference to proliferative markers p53 and Ki-67. *J Clin Diagn Res*. (2016) 10:Ec15–9. doi: 10.7860/JCDR/2016/15661.7117

8. Wang L, Cao Y, Zhang G, Sun D, Zhou W, Li W, et al. A radiomics model enables prediction venous sinus invasion in meningioma. *Ann Clin Transl Neurol*. (2023) 10:1284–95. doi: 10.1002/acn3.51797

9. Roser F, Samii M, Ostertag H, Bellinzona M. The Ki-67 proliferation antigen in meningiomas. Experience in 600 cases. *Acta Neurochir*. (2004) 146:37–44. doi: 10.1007/s00701-003-0173-4

10. Baskan O, Silav G, Bolukbasi FH, Canoz O, Geyik S, Elmaci I. Relation of apparent diffusion coefficient with Ki-67 proliferation index in meningiomas. *Br J Radiol*. (2016) 89:20140842. doi: 10.1259/bjr.20140842

11. Zhao Y, Xu J, Chen B, Cao L, Chen C. Efficient prediction of Ki-67 proliferation index in Meningiomas on MRI: from traditional radiological findings to a machine learning approach. *Cancers*. (2022) 14:637. doi: 10.3390/cancers14153637

12. Khanna O, Fathi Kazerooni A, Farrell CJ, Baldassari MP, Alexander TD, Karsy M, et al. Machine learning using multiparametric magnetic resonance imaging Radiomic feature analysis to predict Ki-67 in World Health Organization grade I Meningiomas. *Neurosurgery*. (2021) 89:928–36. doi: 10.1093/neuros/nyab307

13. Morin O, Chen WC, Nassiri F, Susko M, Magill ST, Vasudevan HN, et al. Integrated models incorporating radiologic and radiomic features predict meningioma grade, local failure, and overall survival. *Neurooncol Adv*. (2019) 1:vdz011. doi: 10.1093/noajnl/vdz011

14. Gillies RJ, Kinahan PE, Hricak H. Radiomics: images are more than pictures, they are data. *Radiology*. (2016) 278:563–77. doi: 10.1148/radiol.2015151169

15. Ehteshami Bejnordi B, Veta M, Johannes van Diest P, van Ginneken B, Karssemeijer N, Litjens G, et al. Diagnostic assessment of deep learning algorithms for detection of lymph node metastases in women with breast Cancer. *JAMA*. (2017) 318:2199–210. doi: 10.1001/jama.2017.14585

16. Broomand Lomer N, Khalaj F, Ghorani H, Mohammadi M, Ghadimi DJ, Zakavi S, et al. MRI-derived radiomics models for prediction of Ki-67 index status in meningioma: a systematic review and meta-analysis. *Clin Imaging*. (2025) 120:110436. doi: 10.1016/j.clinimag.2025.110436

17. Park CJ, Choi SH, Eom J, Byun HK, Ahn SS, Chang JH, et al. An interpretable radiomics model to select patients for radiotherapy after surgery for WHO grade 2 meningiomas. *Radiat Oncol*. (2022) 17:147. doi: 10.1186/s13014-022-02090-7

18. Abry E, Thomassen IØ, Salvesen ØO, Torp SH. The significance of Ki-67/MIB-1 labeling index in human meningiomas: a literature study. *Pathol Res Pract*. (2010) 206:810–5. doi: 10.1016/j.prp.2010.09.002

19. Tang Y, Dundamadappa SK, Thangasamy S, Flood T, Moser R, Smith T, et al. Correlation of apparent diffusion coefficient with Ki-67 proliferation index in grading meningioma. *AJR Am J Roentgenol*. (2014) 202:1303–8. doi: 10.2214/AJR.13.11637

20. Pavelin S, Becic K, Forempoher G, Mrklic I, Pogorelic Z, Titlic M, et al. Expression of Ki-67 and p53 in meningiomas. *Neoplasma*. (2013) 60:480–5. doi: 10.4149/neo_2013_062

21. Helal A, Hammam E, Ovenden CD, Candy NG, Chaurasia B, Atallah O, et al. A systematic review of radiological prediction of ki 67 proliferation index of meningioma. *Neurosurg Rev*. (2024) 47:881. doi: 10.1007/s10143-024-03074-9

22. Wang QS, Chen C, Zhan J, Fang XF, Chen GG, Yang SL, et al. Peritumoral overexpression of ZBP-89 is associated with unfavorable disease-free survival rates in patients with hepatocellular carcinoma following hepatectomy. *Oncol Lett*. (2018) 15:7828–36. doi: 10.3892/ol.2018.8353

23. Li C, Song L, Yin J. Intratumoral and Peritumoral Radiomics based on functional parametric maps from breast DCE-MRI for prediction of HER-2 and Ki-67 status. *J Magn Reson Imaging*. (2021) 54:703–14. doi: 10.1002/jmri.27651

24. Li M, Liu L, Qi J, Qiao Y, Zeng H, Jiang W, et al. MRI-based machine learning models predict the malignant biological behavior of meningioma. *BMC Med Imaging*. (2023) 23:141. doi: 10.1186/s12880-023-01101-7

25. Duan C, Hao D, Cui J, Wang G, Xu W, Li N, et al. An MRI-based deep transfer learning Radiomics nomogram to predict Ki-67 proliferation index of meningioma. *J Imaging Inform Med*. (2024) 37:510–9. doi: 10.1007/s10278-023-00937-3

26. Ouyang ZQ, He SN, Zeng YZ, Zhu Y, Ling BB, Sun XJ, et al. Contrast enhanced magnetic resonance imaging-based radiomics nomogram for preoperatively predicting expression status of Ki-67 in meningioma: a two-center study. *Quant Imaging Med Surg*. (2023) 13:1100–14. doi: 10.21037/qims-22-689

27. Cheng J, Liu J, Yue H, Bai H, Pan Y, Wang J. Prediction of glioma grade using Intratumoral and Peritumoral Radiomic features from multiparametric MRI images. *IEEE/ACM Trans Comput Biol Bioinform*. (2022) 19:1084–95. doi: 10.1109/TCBB.2020.3033538

28. Sun X, Pang P, Lou L, Feng Q, Ding Z, Zhou J. Radiomic prediction models for the level of Ki-67 and p53 in glioma. *J Int Med Res*. (2020) 48:300060520914466. doi: 10.1177/0300060520914466

29. Xiao D, Zhao Z, Liu J, Wang X, Fu P, le Grange JM, et al. Diagnosis of invasive meningioma based on brain-tumor Interface Radiomics features on brain MR images: a multicenter study. *Front Oncol*. (2021) 11:708040. doi: 10.3389/fonc.2021.708040

30. Li N, Mo Y, Huang C, Han K, He M, Wang X, et al. A clinical semantic and Radiomics nomogram for predicting brain invasion in WHO grade II meningioma based on tumor and tumor-to-brain Interface features. *Front Oncol*. (2021) 11:752158. doi: 10.3389/fonc.2021.752158

31. Joo L, Park JE, Park SY, Nam SJ, Kim YH, Kim JH, et al. Extensive peritumoral edema and brain-to-tumor interface MRI features enable prediction of brain invasion in meningioma: development and validation. *Neuro-Oncology*. (2021) 23:324–33. doi: 10.1093/neuonc/noaa190

32. Beig N, Khorrami M, Alilou M, Prasanna P, Braman N, Orooji M, et al. Perinodular and Intranodular Radiomic features on lung CT images distinguish adenocarcinomas from granulomas. *Radiology*. (2019) 290:783–92. doi: 10.1148/radiol.2018180910

33. Moon CM, Lee YY, Kim DY, Yoon W, Baek BH, Park JH, et al. Preoperative prediction of Ki-67 and p53 status in meningioma using a multiparametric MRI-based clinical-radiomic model. *Front Oncol*. (2023) 13:1138069. doi: 10.3389/fonc.2023.1138069

34. Li J, Liang R, Song C, Xiang Y, Liu Y. Prognostic value of Ki-67/MIB-1 expression in meningioma patients: a Meta-analysis. *Crit Rev Eukaryot Gene Expr*. (2019) 29:141–50. doi: 10.1615/CritRevEukaryotGeneExpr.2019025430

35. Bečulić H, Skomorac R, Jusić A, Alić F, Mašović A, Burazerović E, et al. Correlation of PERITUMORAL BRAIN edema with morphological characteristics and KI67 proliferative index in resected intracranial MENINGIOMAS. *Acta Clin Croat*. (2019) 58:42–9. doi: 10.20471/acc.2019.58.01.06

36. Mirian C, Skyrman S, Bartek J, Jensen LR, Kihlström L, Förander P, et al. The Ki-67 proliferation index as a marker of time to recurrence in intracranial meningioma. *Neurosurgery*. (2020) 87:1289–98. doi: 10.1093/neuros/nyaa226

Frontiers in Neurology

Explores neurological illness to improve patient care

The third most-cited clinical neurology journal explores the diagnosis, causes, treatment, and public health aspects of neurological illnesses. Its ultimate aim is to inform improvements in patient care.

Discover the latest Research Topics

See more →

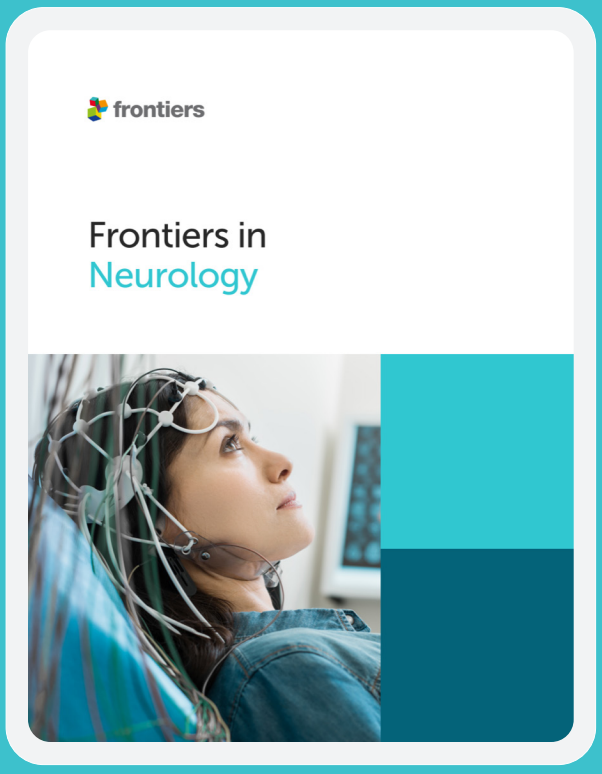

Frontiers

Avenue du Tribunal-Fédéral 34
1005 Lausanne, Switzerland
frontiersin.org

Contact us

+41 (0)21 510 17 00
frontiersin.org/about/contact